

Report BSD-TR-63-34

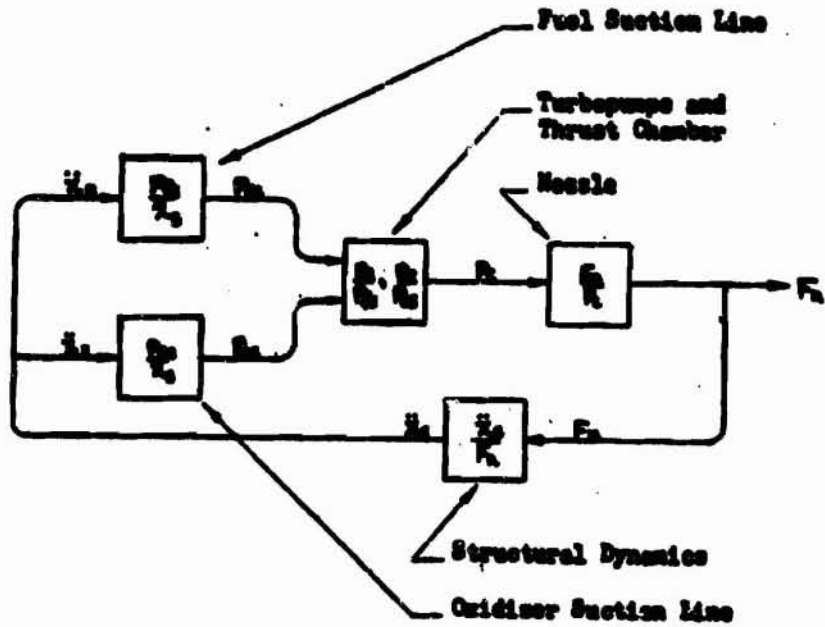


Figure 1. Closed-Loop Flow Diagram for Engine-Vehicle System in Flight

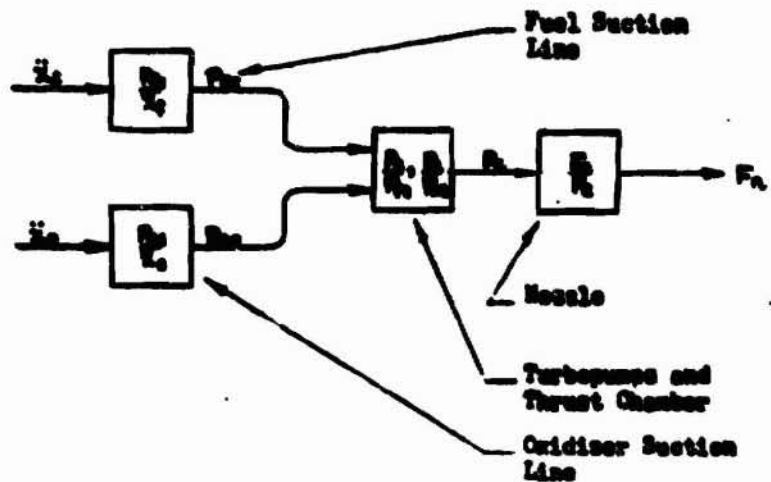
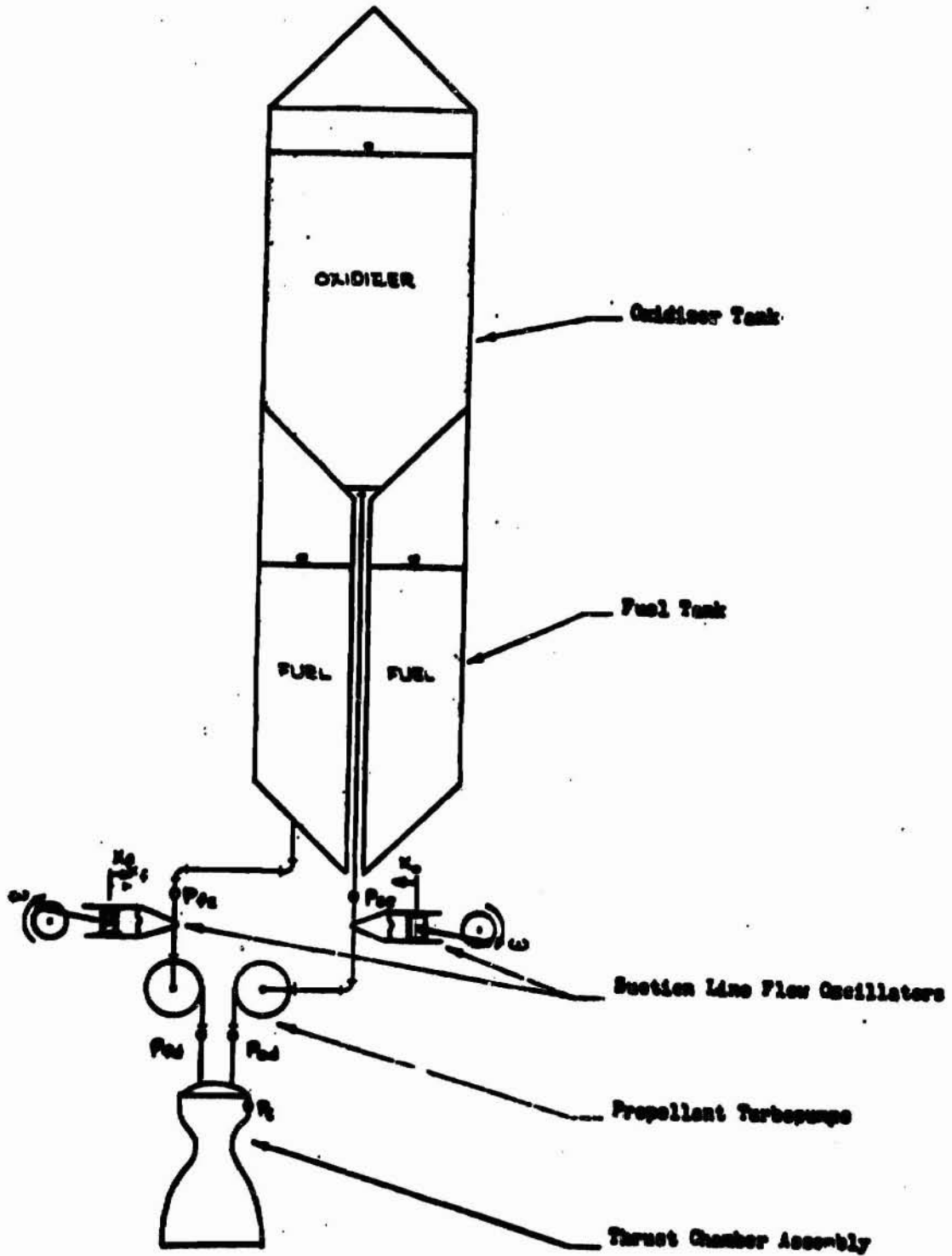


Figure 2. Open-Loop Flow Diagram for Engine-Transfer Function-Test Program

Figure 1 and Figure 2

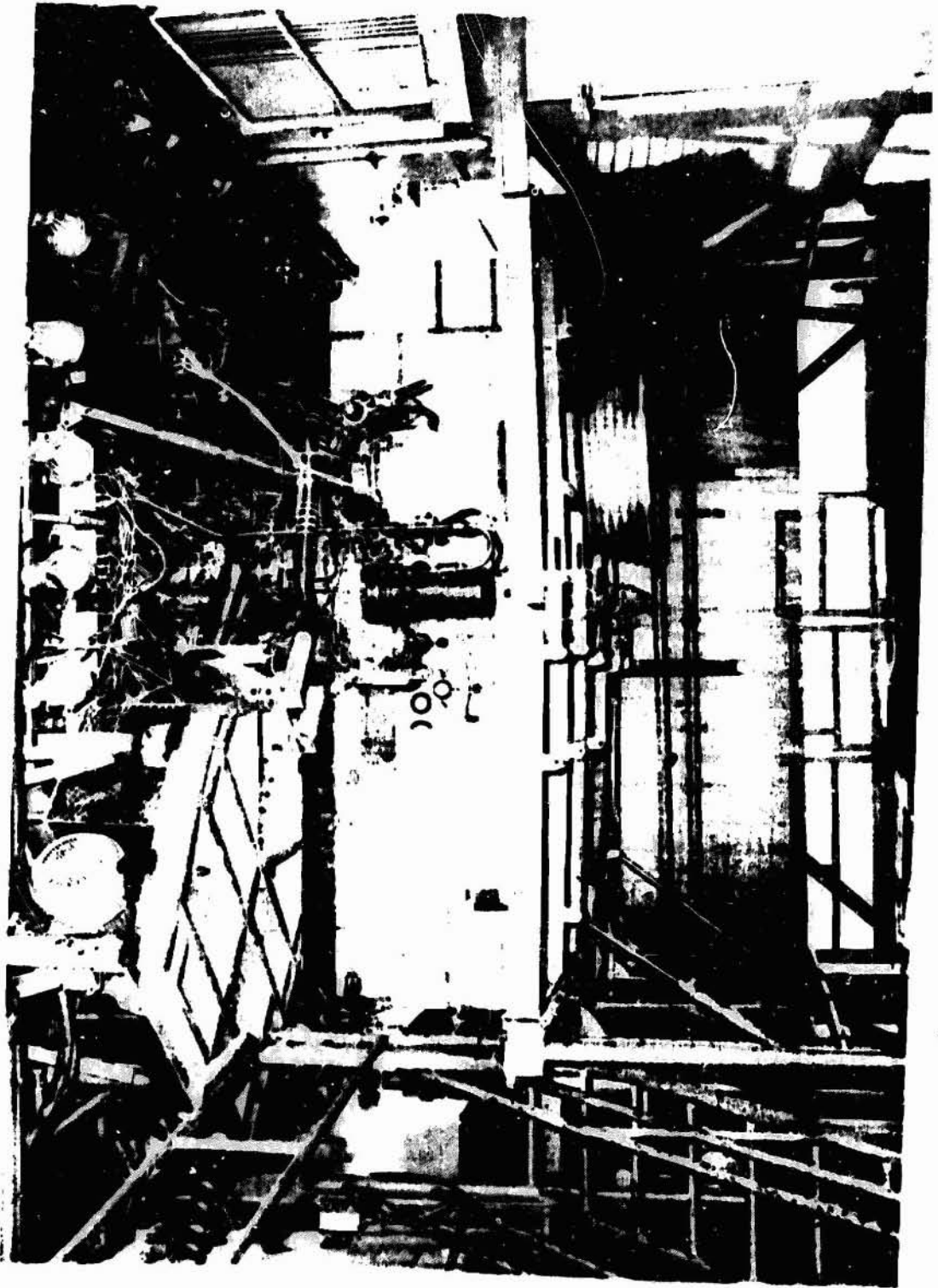
BLANK PAGE

Report BSD-TR-65-54



Schematic Diagram of Engine-Transfer Function-Test Apparatus

Figure 3



E-6 "ROGO" Test Stand

Figure 4

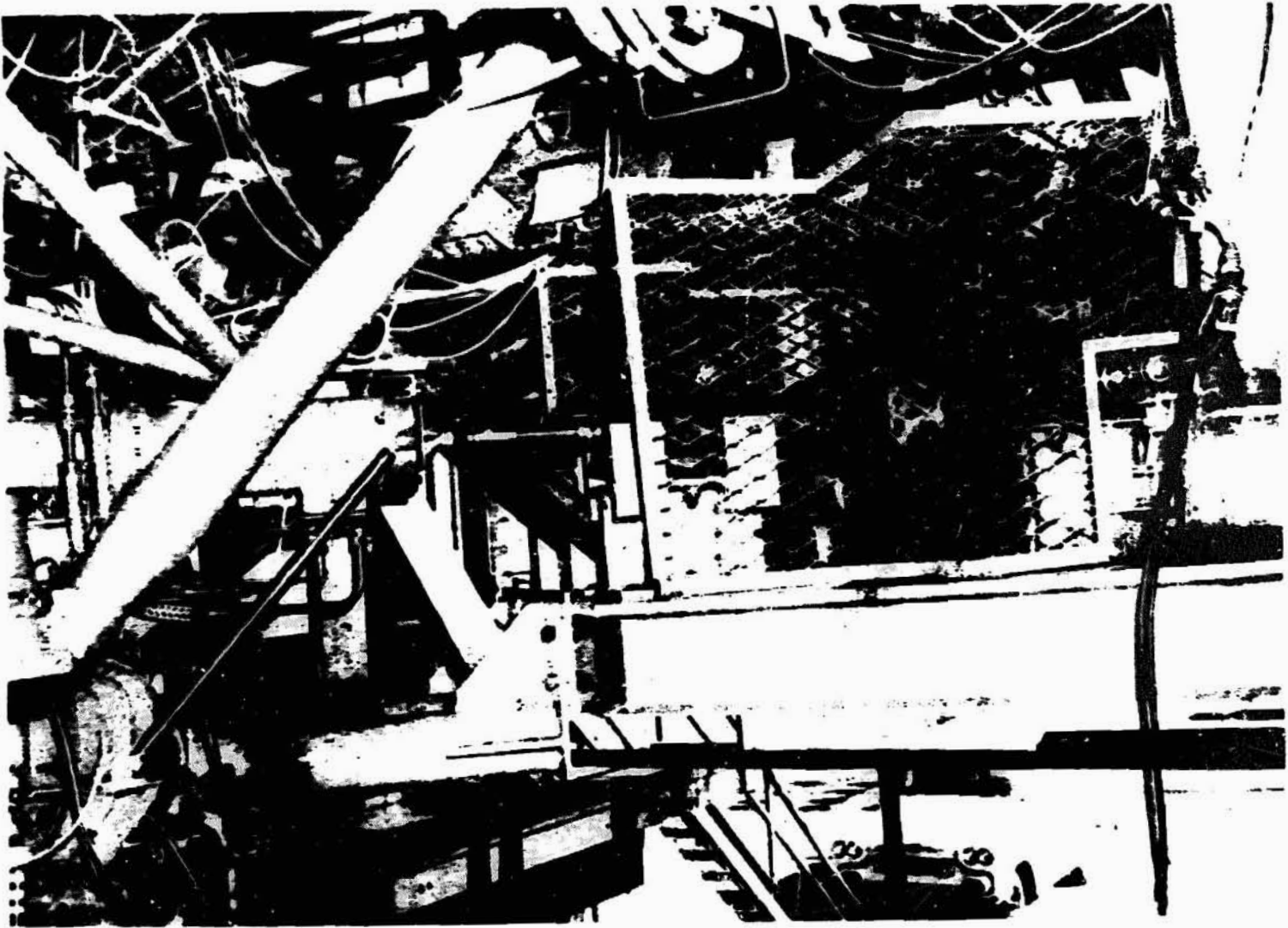


Figure 5

E-6 Stand, Fuel-System Pulsing Assembly

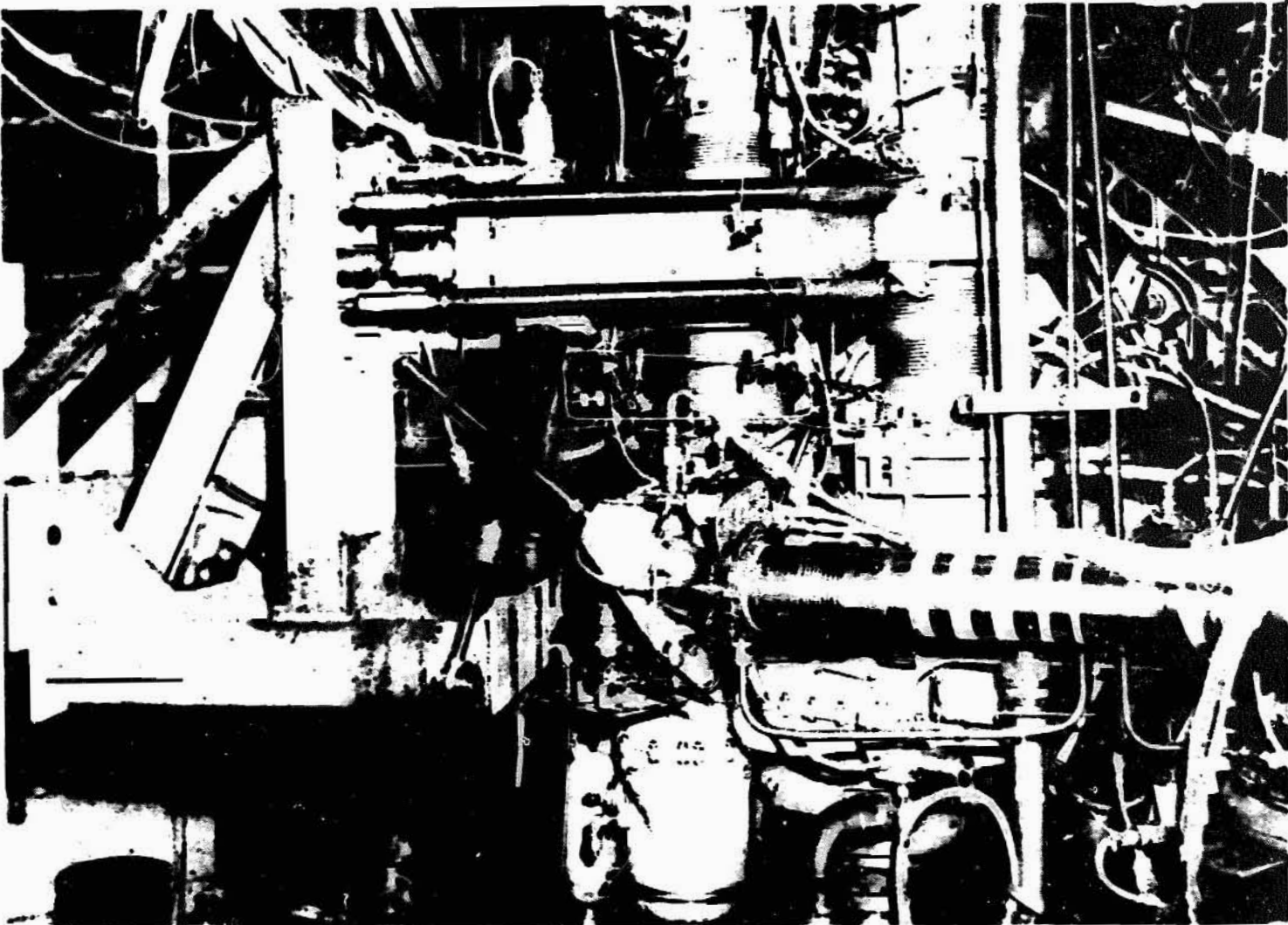
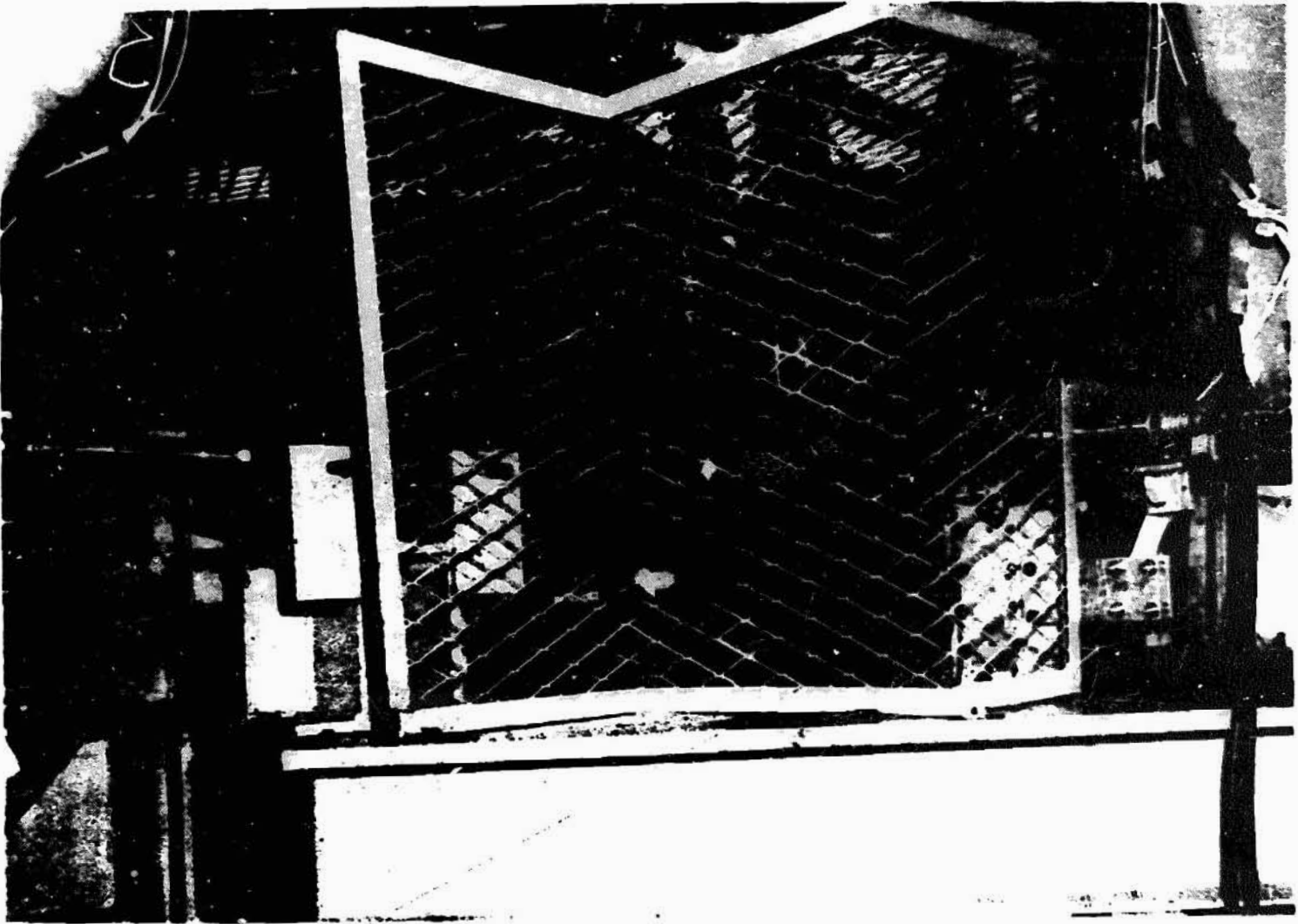


Figure 6

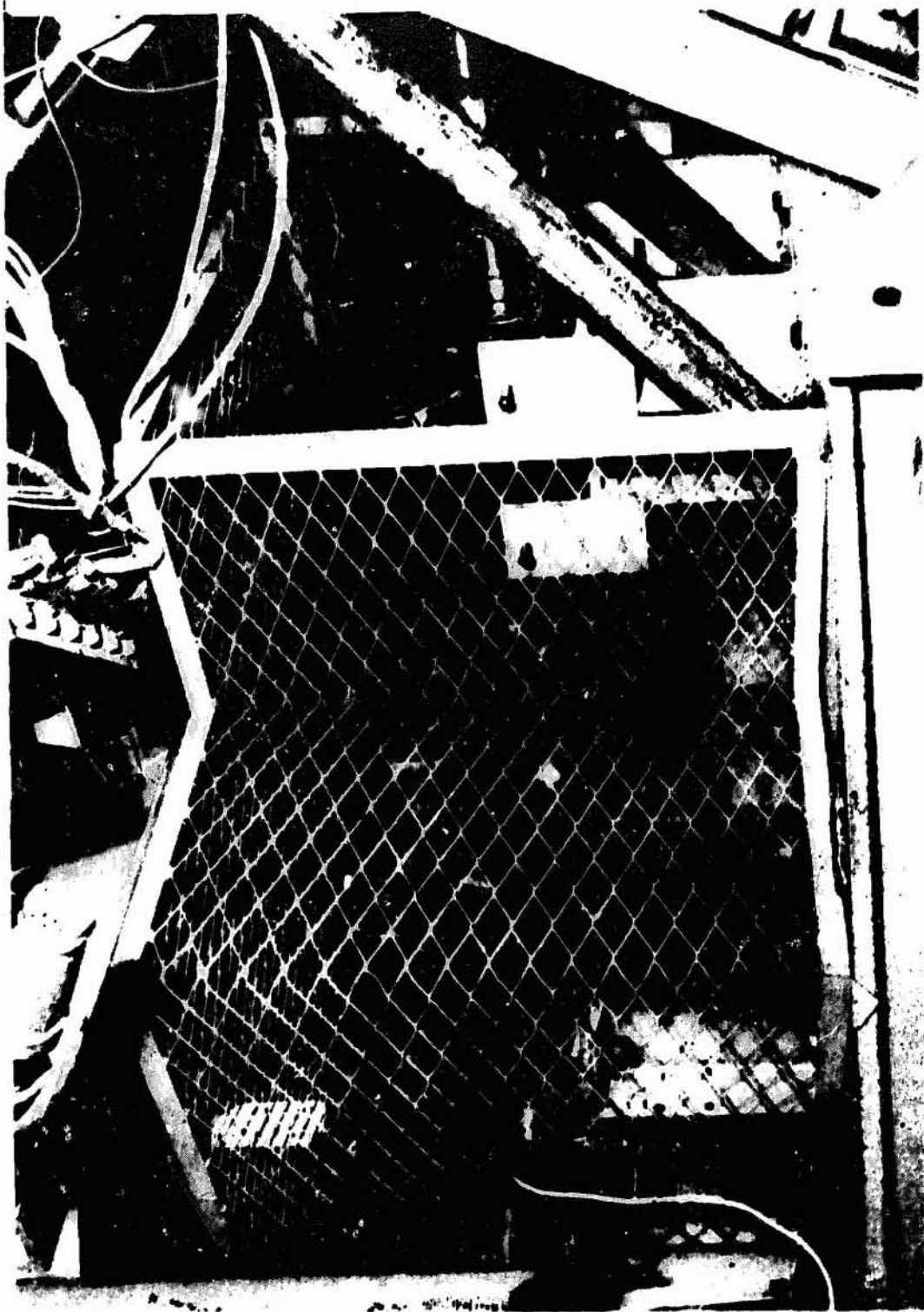
E-6 Stand, Oxidizer-System Pulsing Assembly



Report BSD-TR-65-54

Figure 7

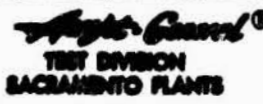
B-6 Stand, Fuel-System Slave Motor and Pulsing Assembly

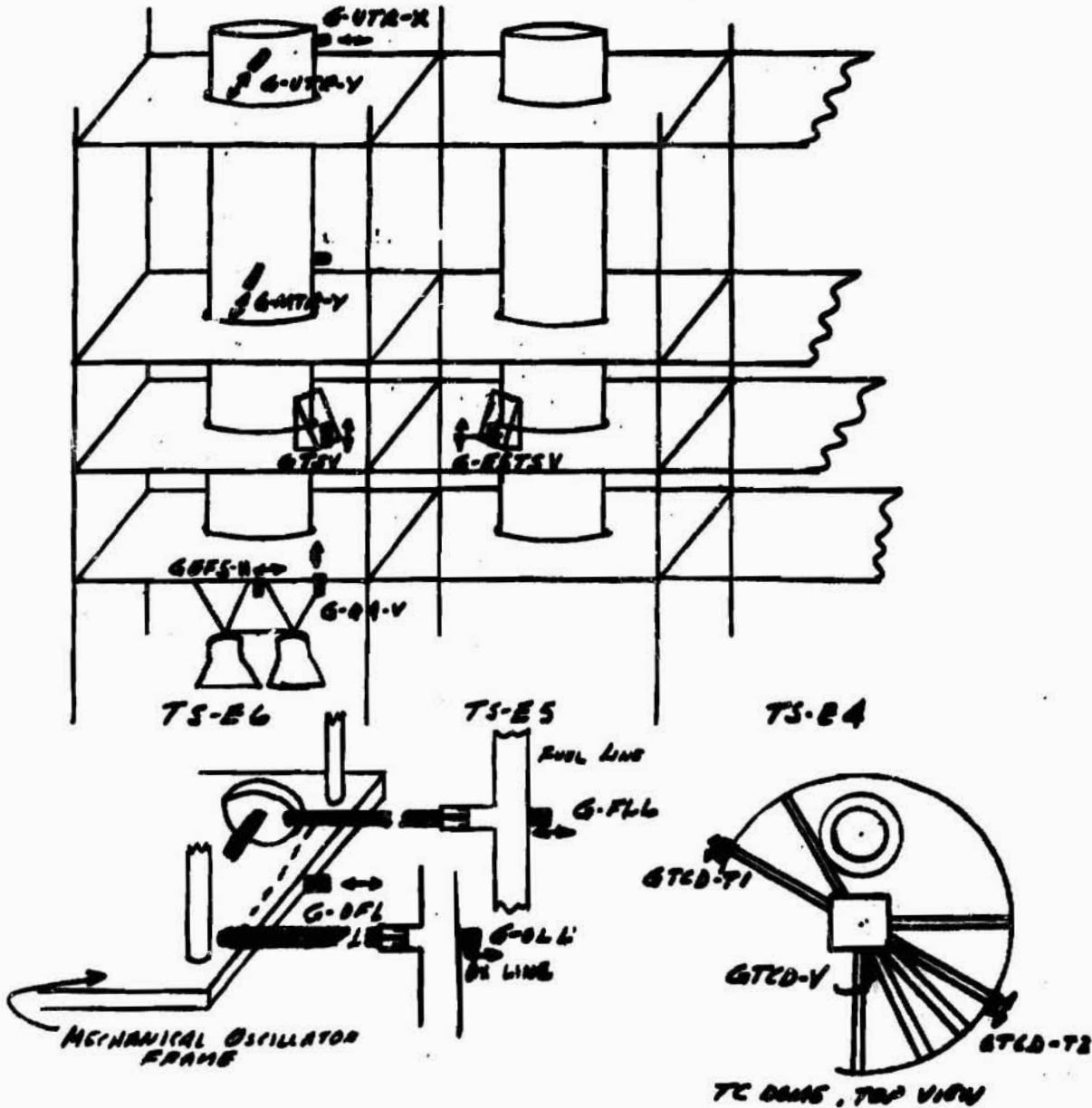


E-6 Stand, Oxidizer System Slave Motor and Pulsing Assembly

Figure 8

Report ESD-TR-65-54

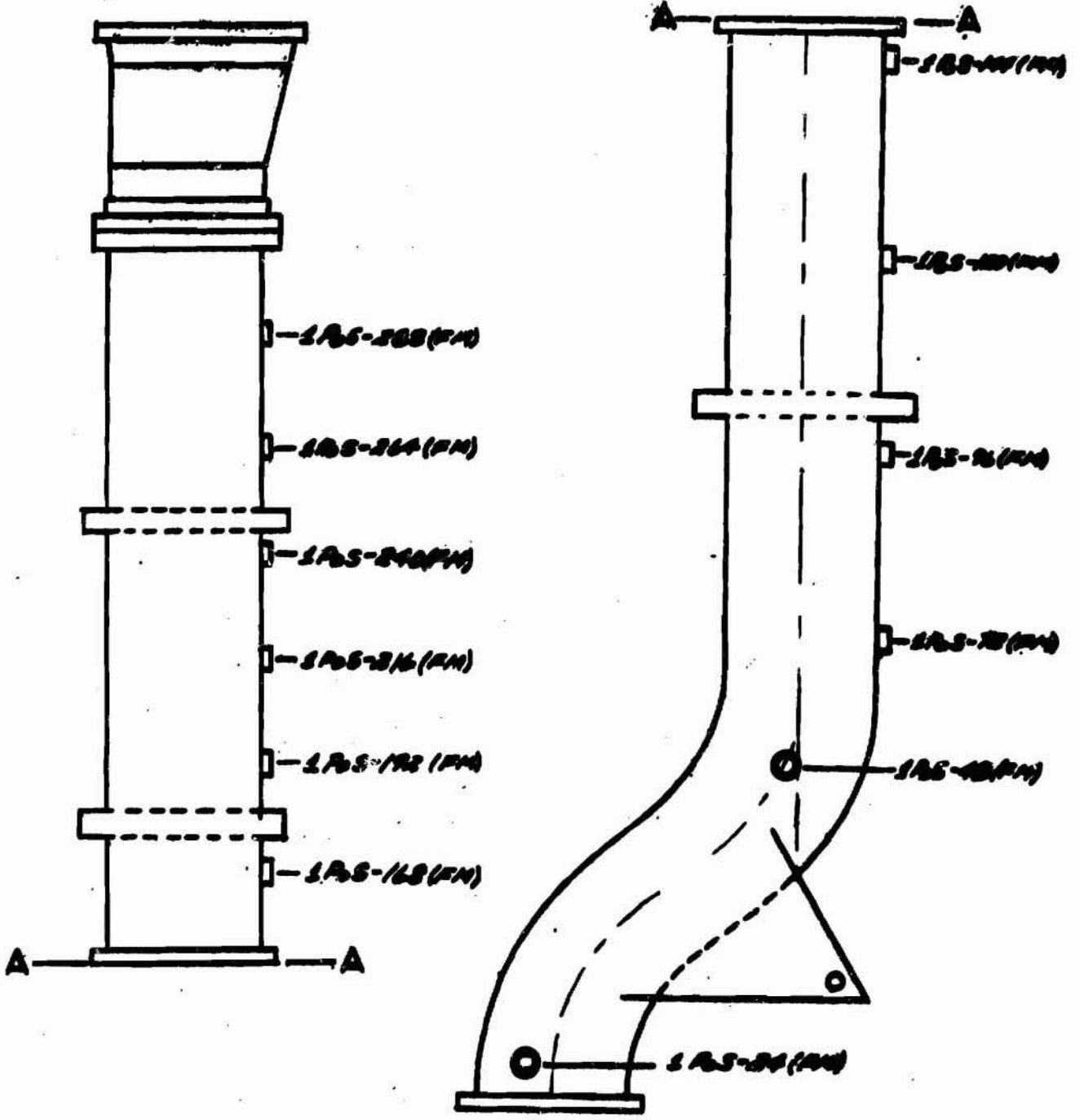
AEC-8-204  TEST DIVISION SACRAMENTO PLANTS	DESIGNED _____	DRAWN _____	VDB _____	ELECTRONIC ENGINEERING
	CHECKED _____	APPROVED _____	DATE _____	



Test Stand and Test Hardware Accelerometer Locations

Figure 9

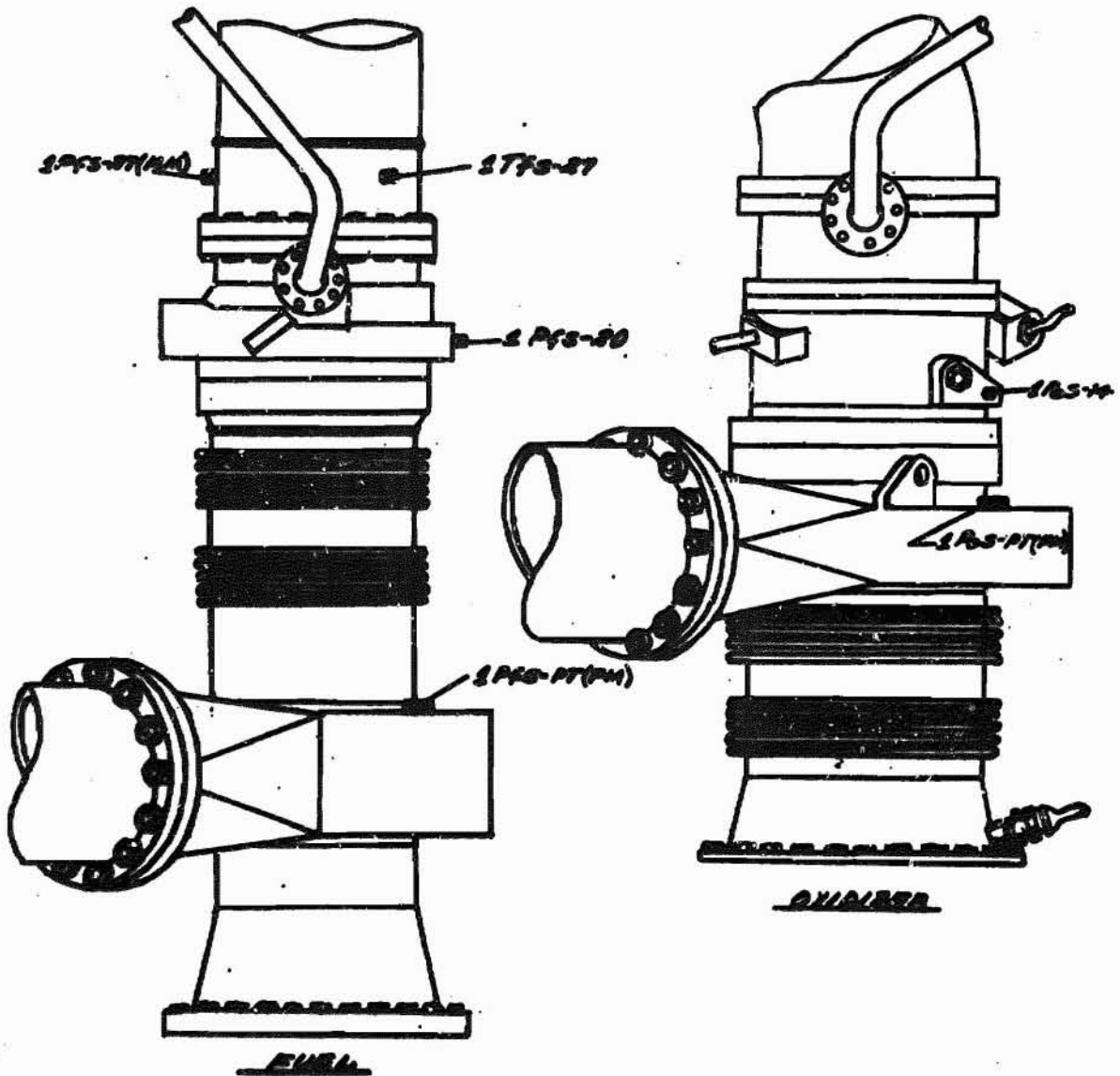
Report BSD-TR-63-34



Oxidizer Section-Line Transducers

Figure 10

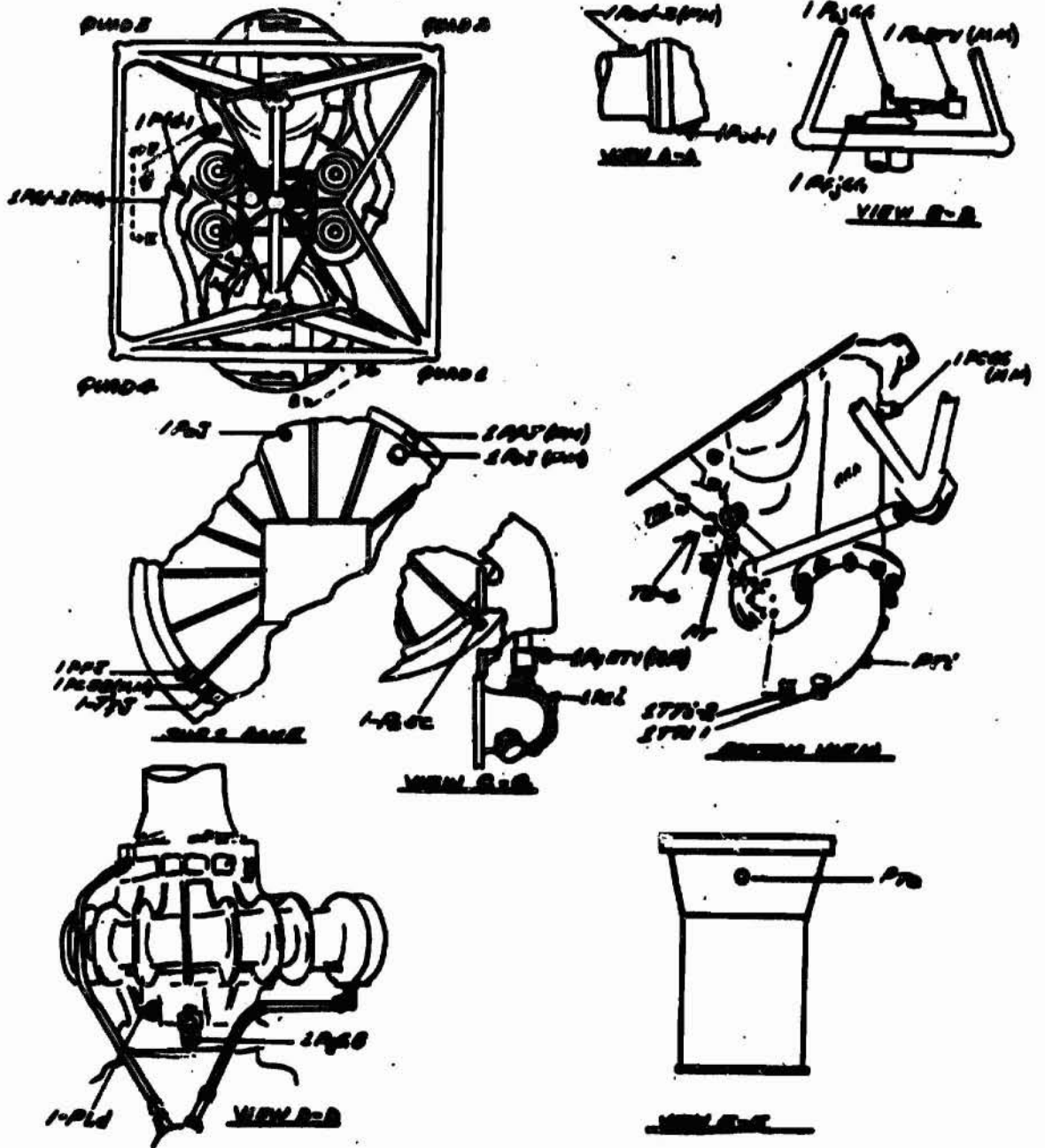
Report BMD-TR-65-54



Fuel and Oxidizer Suction-Line Toruses and Transducers

Figure 11

Report BDD-TR-63-54



Engine Parameter Instrumentation

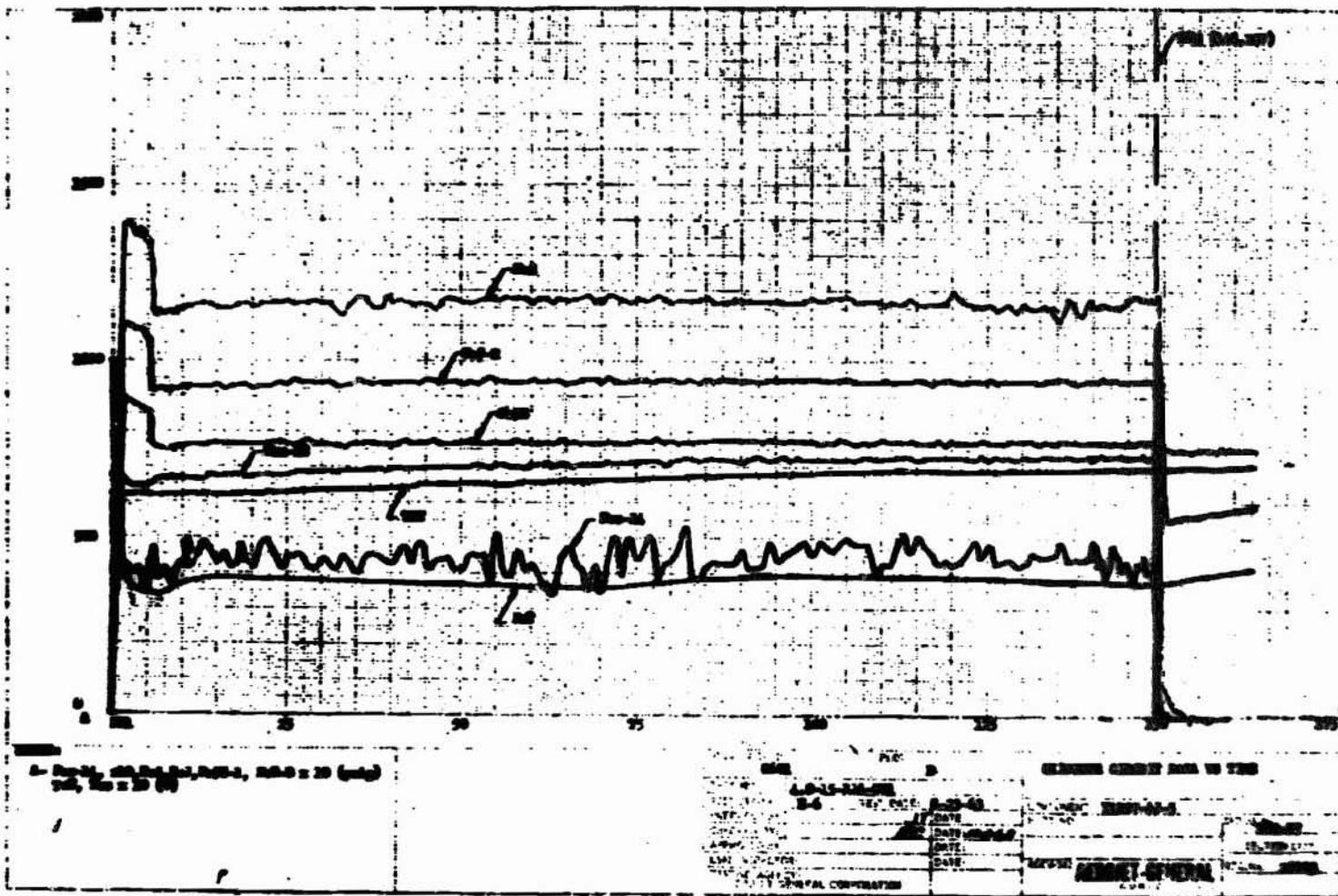
Figure 12



B-6 Stand, Flush-Mounted Transducer on Oxidizer Torus

Figure 13

Figure 15



Test 4.0-15-RJA-001--Plot B, Oxidizer Circuit Data vs Time

Report ASD-TR-63-54

Report BDD-TR-65-34

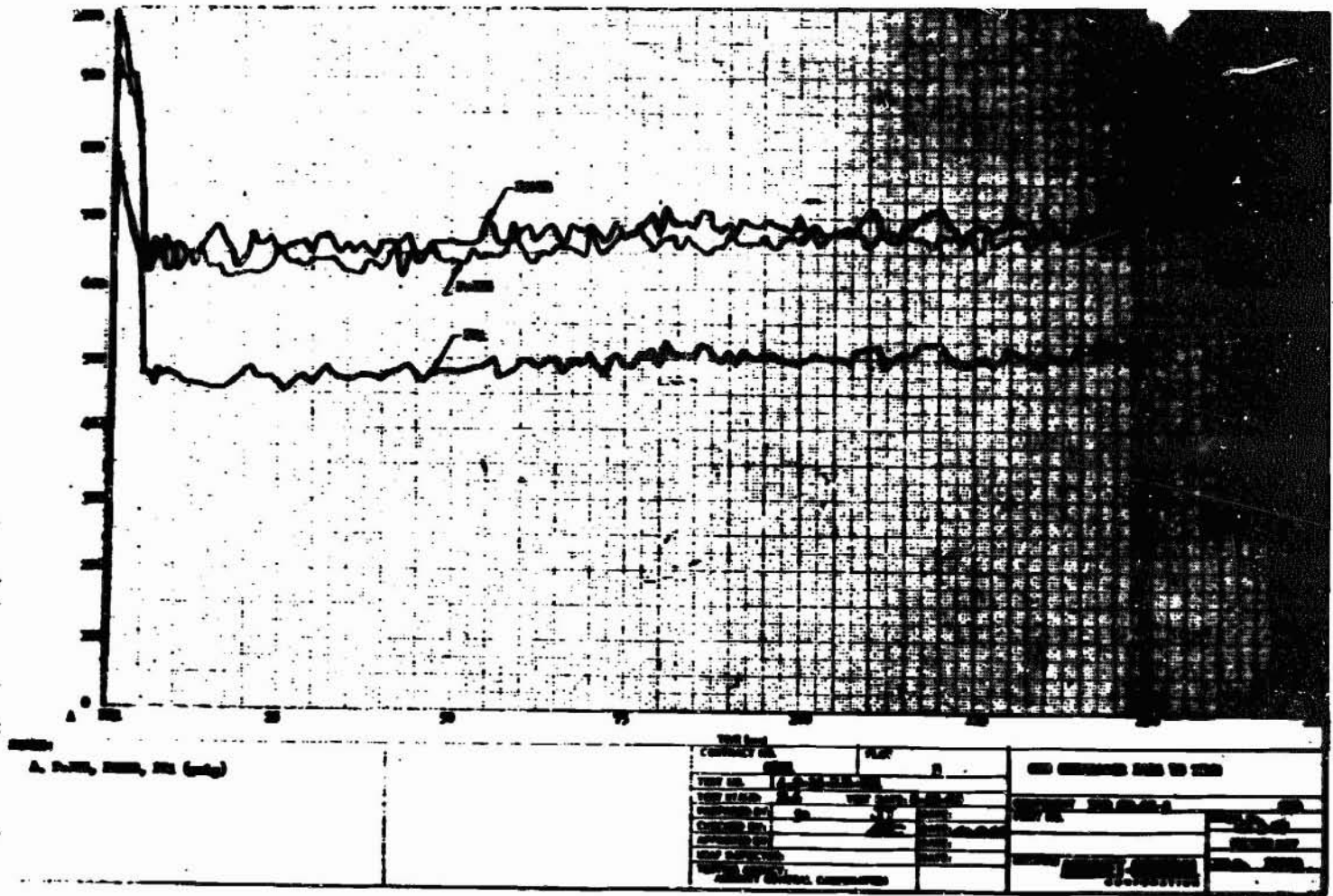
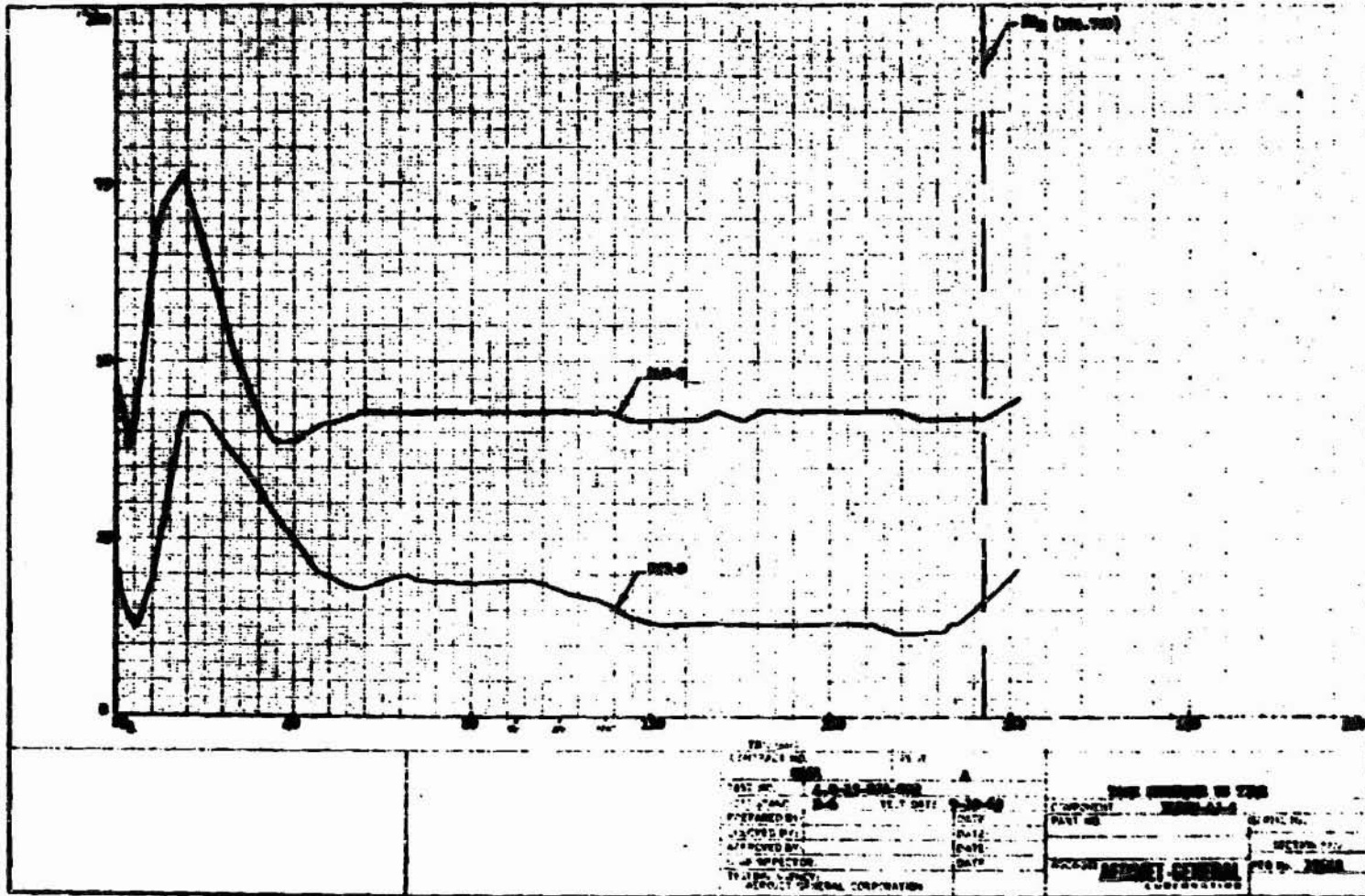


Figure 17

Test 4.0-15-RM-001--Plot B, Oxidizer Circuit Data vs Time

Figure 10



Test 4.0-15-RJA-002—Plot A, Tank-Pressure Data vs Time

Report RBD-TR-45-54

REPRODUCIBILITY OF THE ORIGINAL PAGE IS POOR

Report BSD-TR-65-54

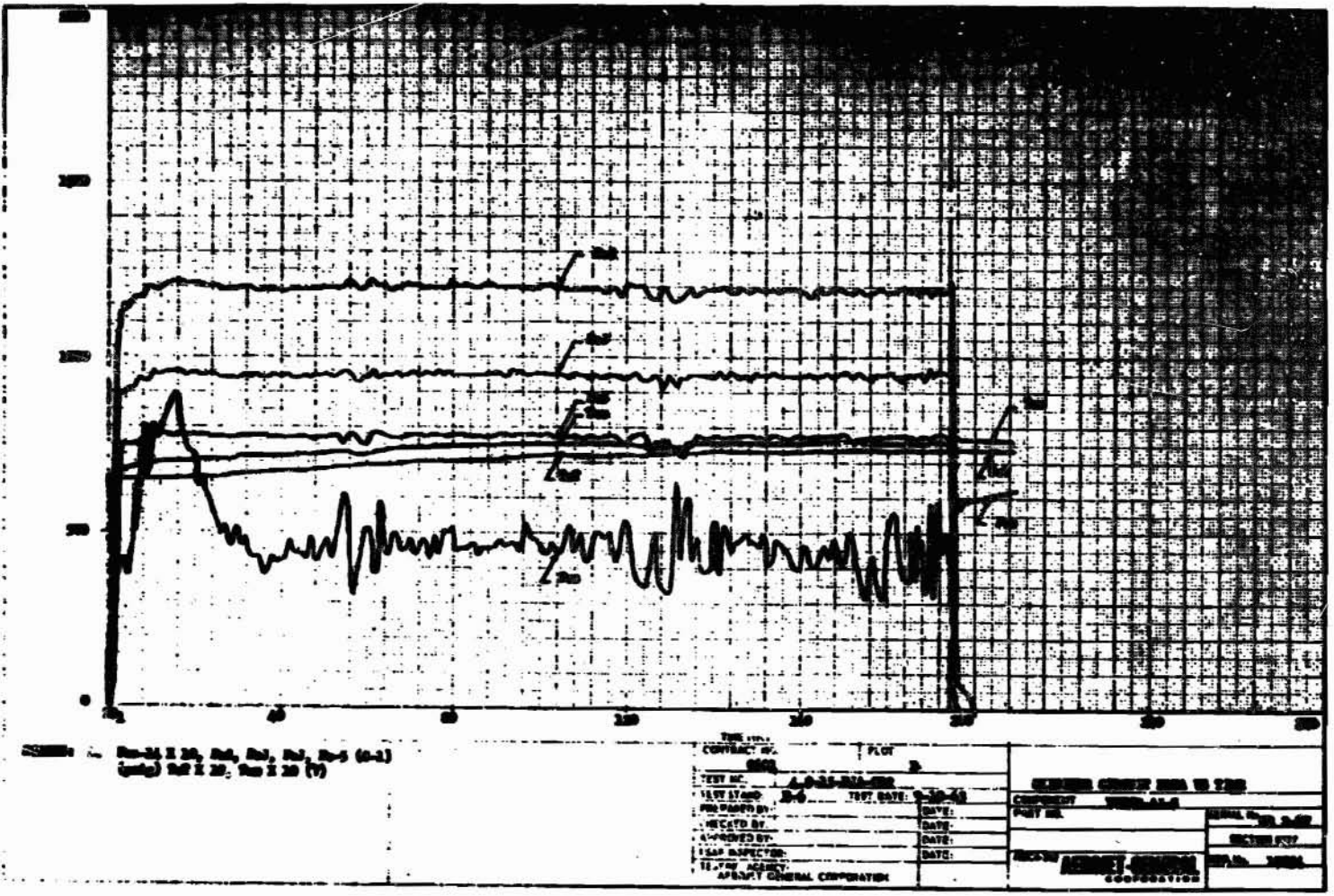


Figure 19

Test 4.0-15-RJA-002--Plot B, Oxidizer-Circuit Data vs Time

Report: RMA-200-34

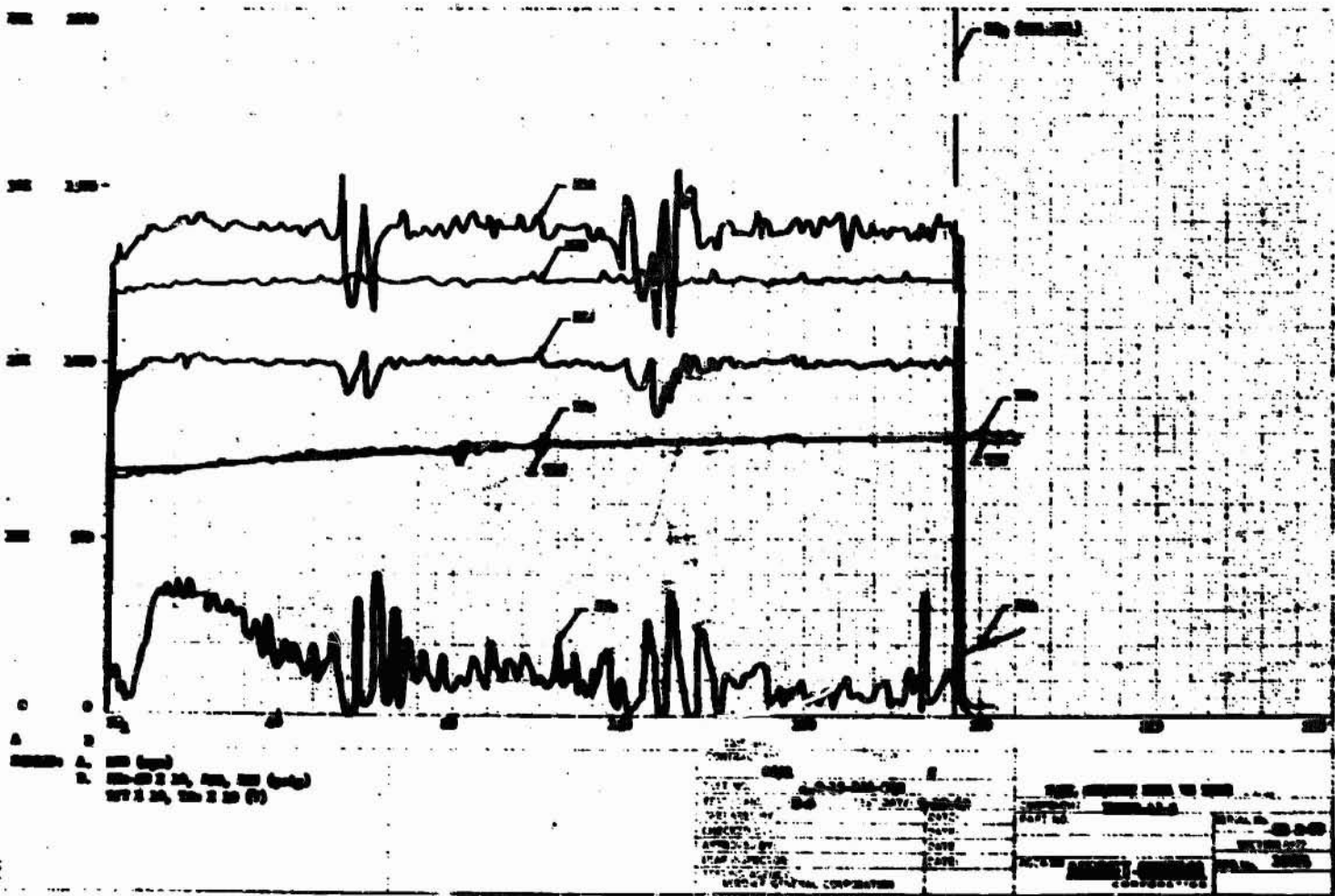
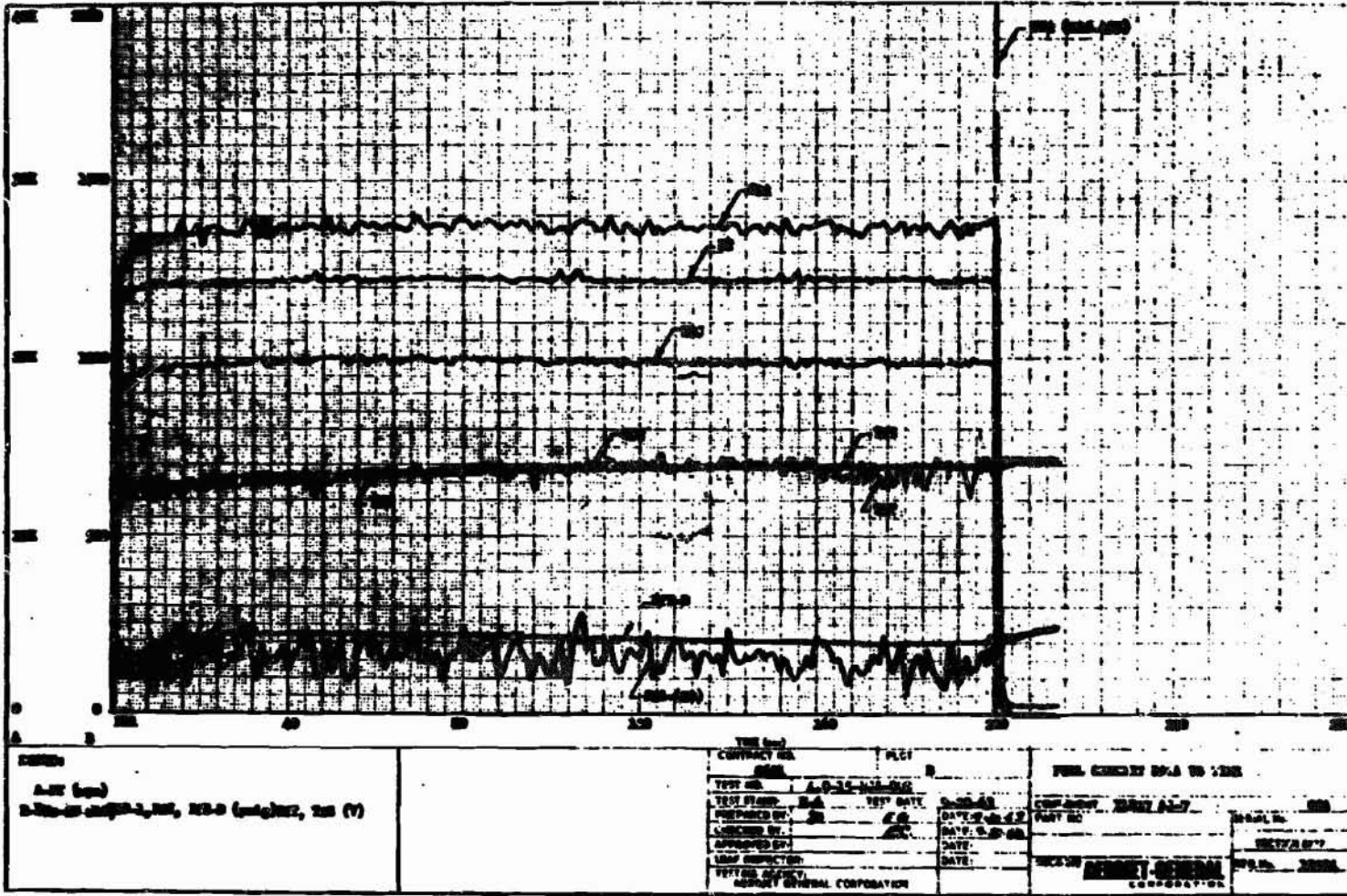


Figure 30

Test 4.0-15-RM-032-Plot C, Poul-Circuit Data vs Time

Figure 23



Test 4.0-15-RJA-003--Plot B, Fuel-Circuit Data vs Time

Report ASD-TR-65-54

REPRODUCIBILITY OF THE ORIGINAL PAGE IS POOR

Report BDD-TR-65-34

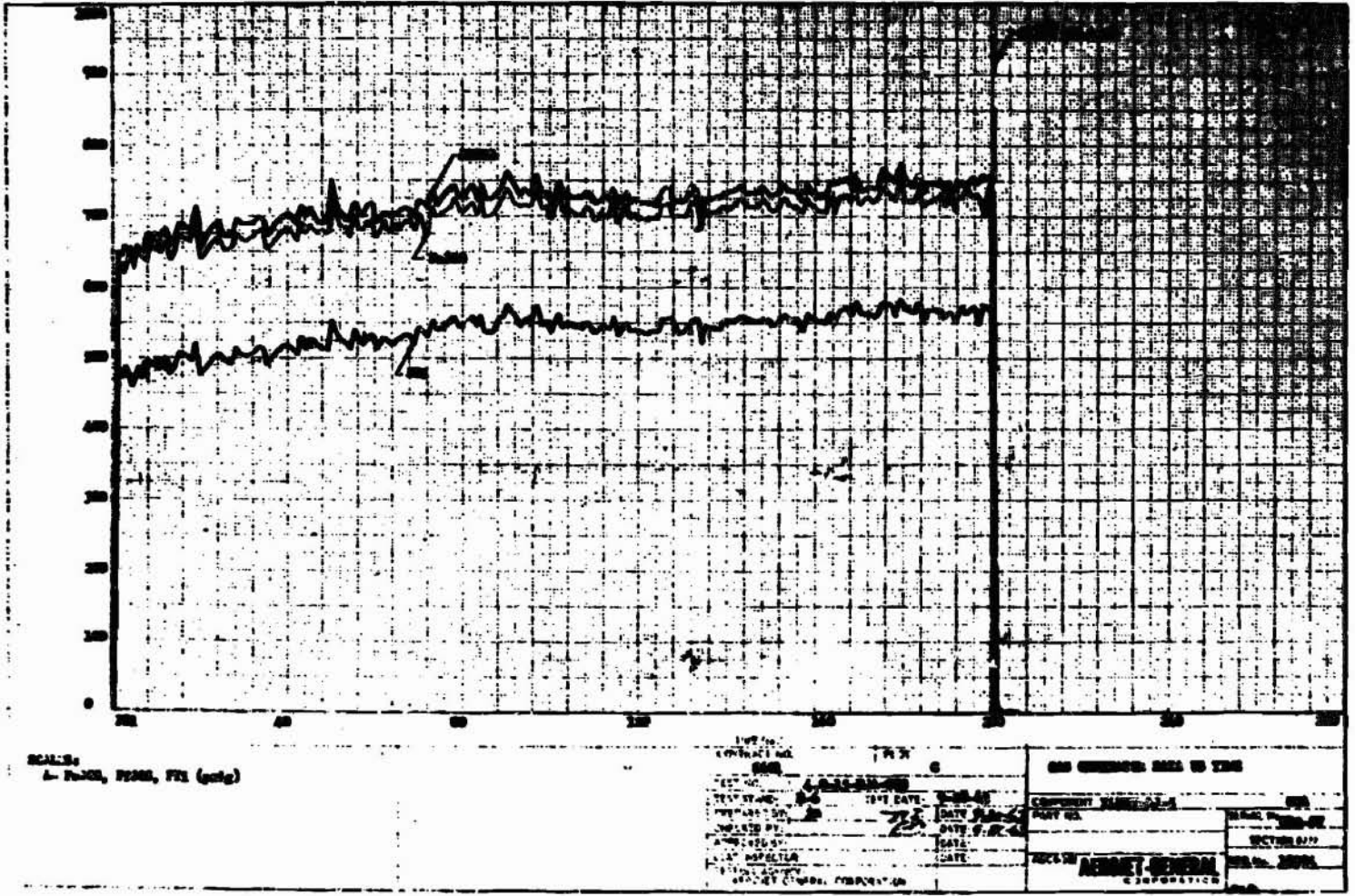
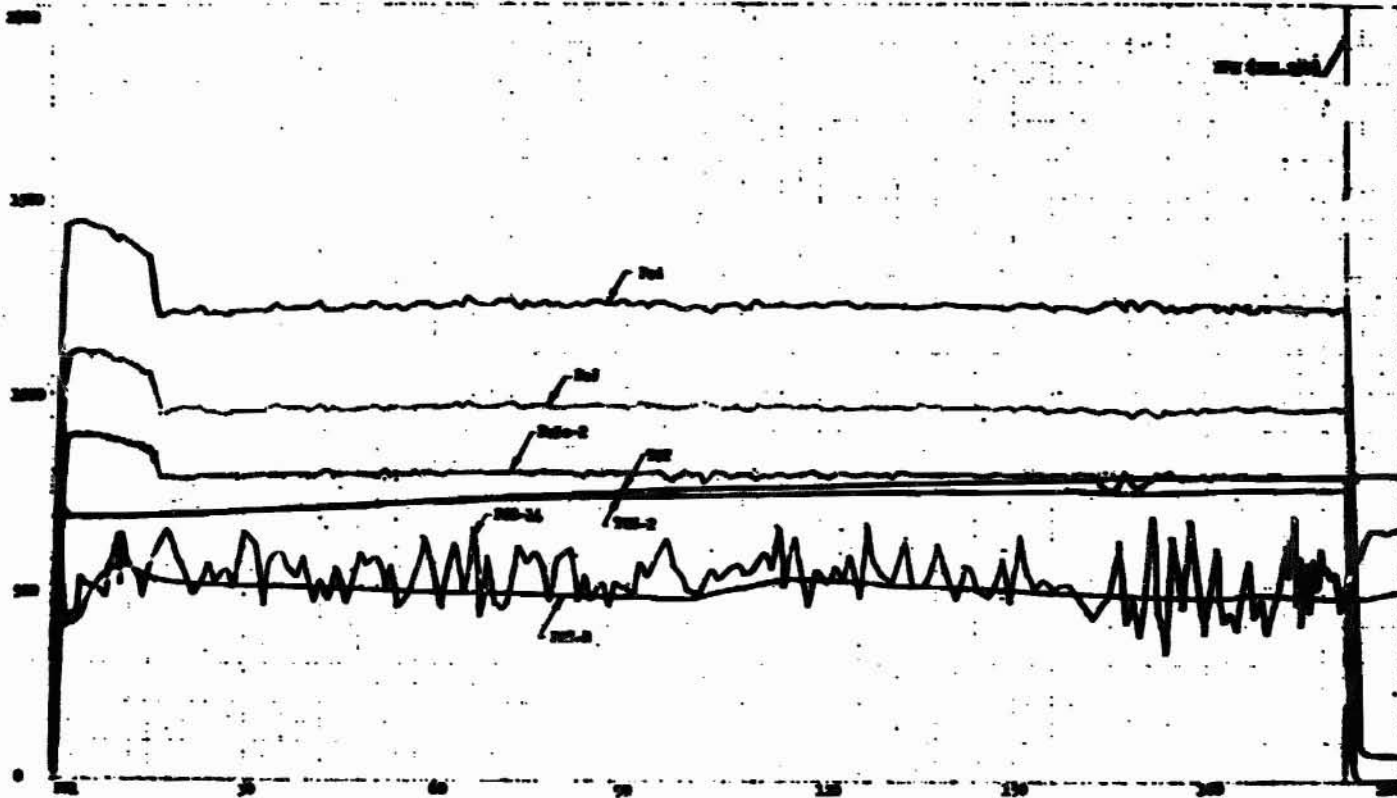


Figure 24

Test 4.0-15-RM-003--Plot C, Gas-Generator Data vs Time



A. For 4.0-15-RJA-004, Plot A, Oxidizer-Circuit Data vs Time
 Scale: 100 = 10, 200 = 10 (V)

4.0-15-RJA-004
 9-25-65
 9-27-65
 AIR FORCE RESEARCH AND DEVELOPMENT COMMAND
 WRIGHT-PATTERSON AIR FORCE BASE
 OHIO 45433-6100

Report RDD-TR-65-54

Test 4.0-15-RJA-004--Plot A, Oxidizer-Circuit Data vs Time

REPRODUCIBILITY OF THE ORIGINAL PAGE IS POOR

Report ASD-TR-65-54

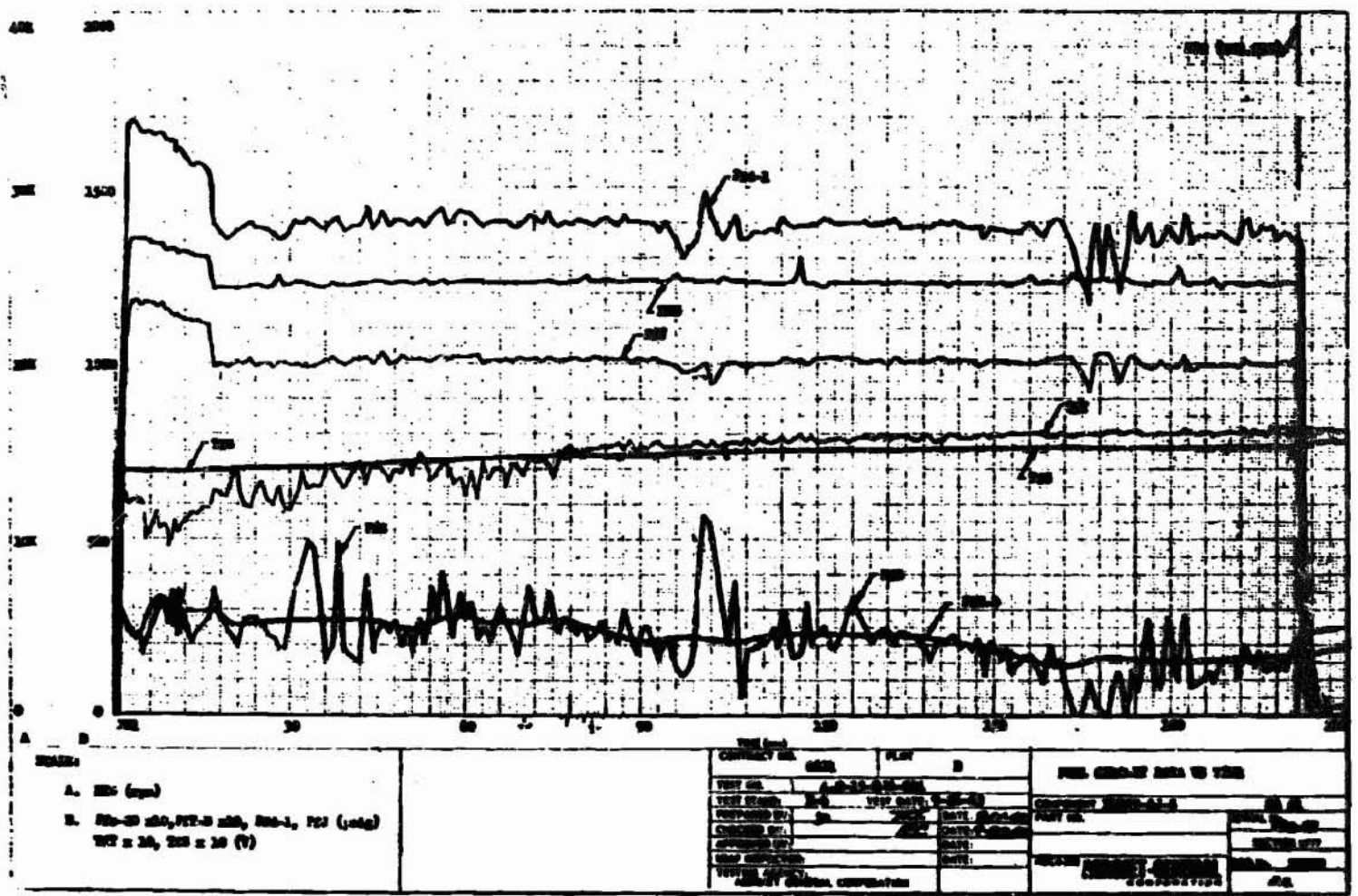


Figure 26

Test 4.0-15-RJA-004--Plot B, Fuel-Circuit Data vs Time

Report BSD-TR-65-54

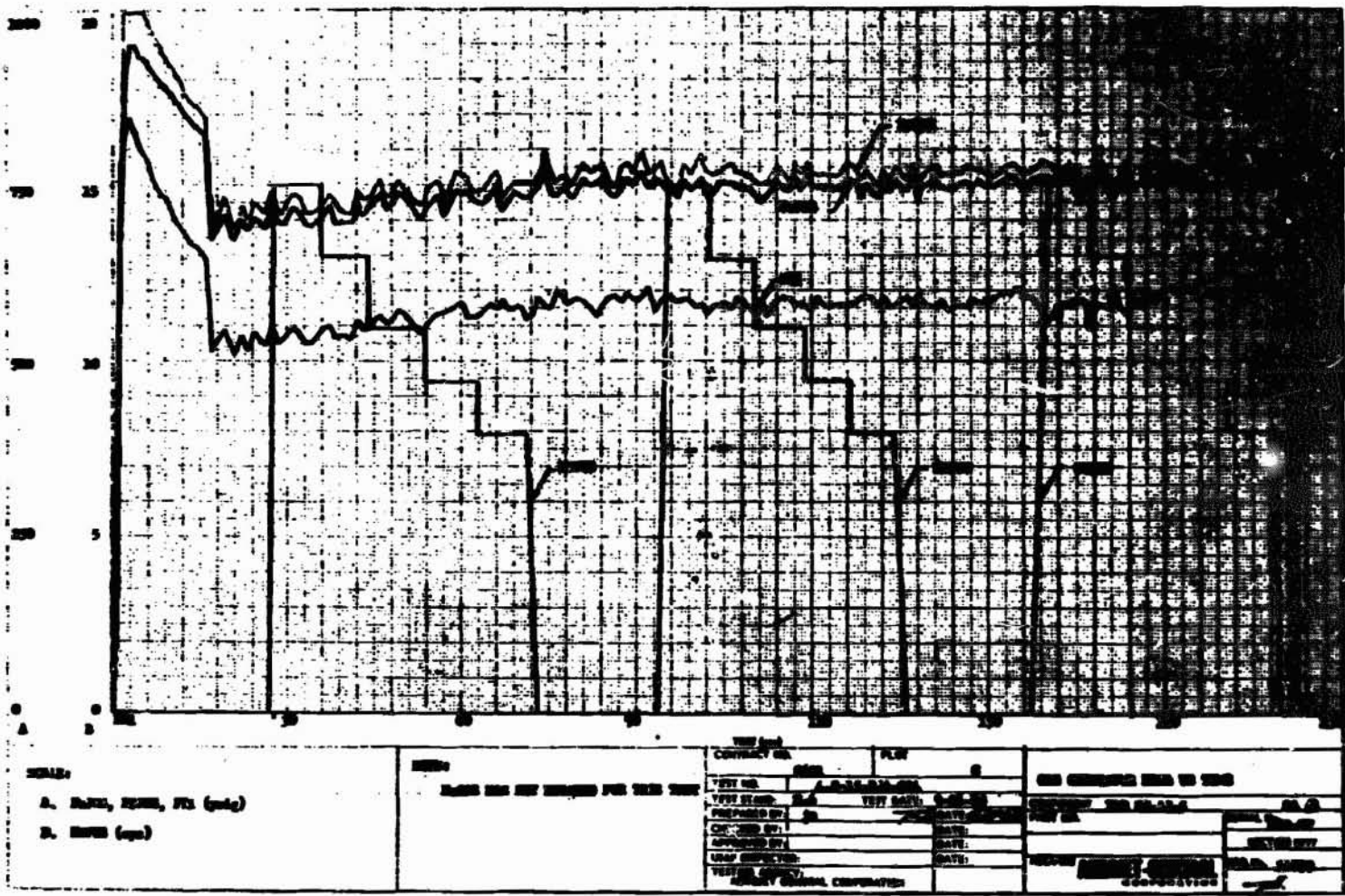


Figure 27

Test 4.0-15-RJA-004--Plot C, Gas-Generator Data vs Time

Report ASD-TR-63-54

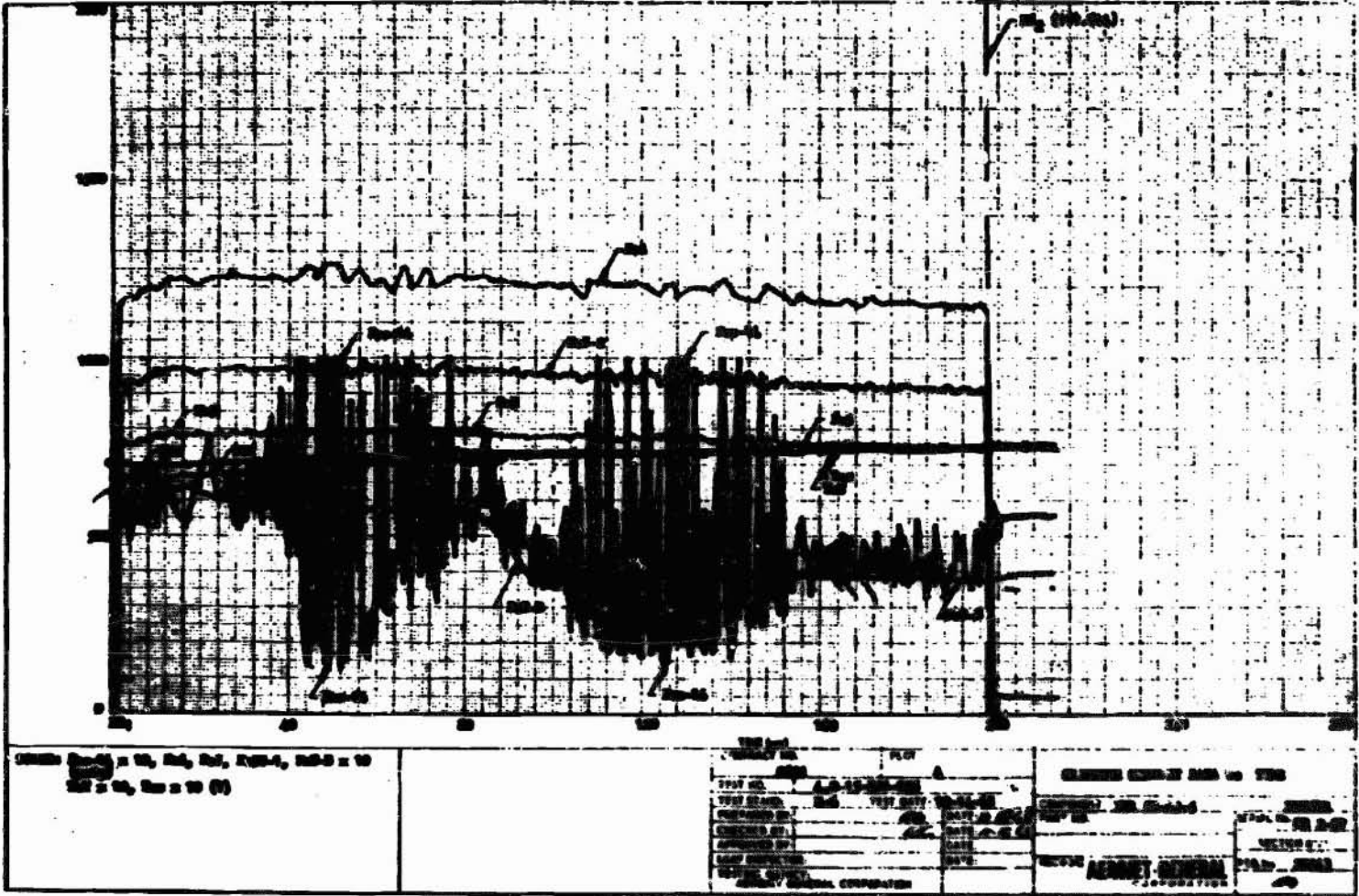
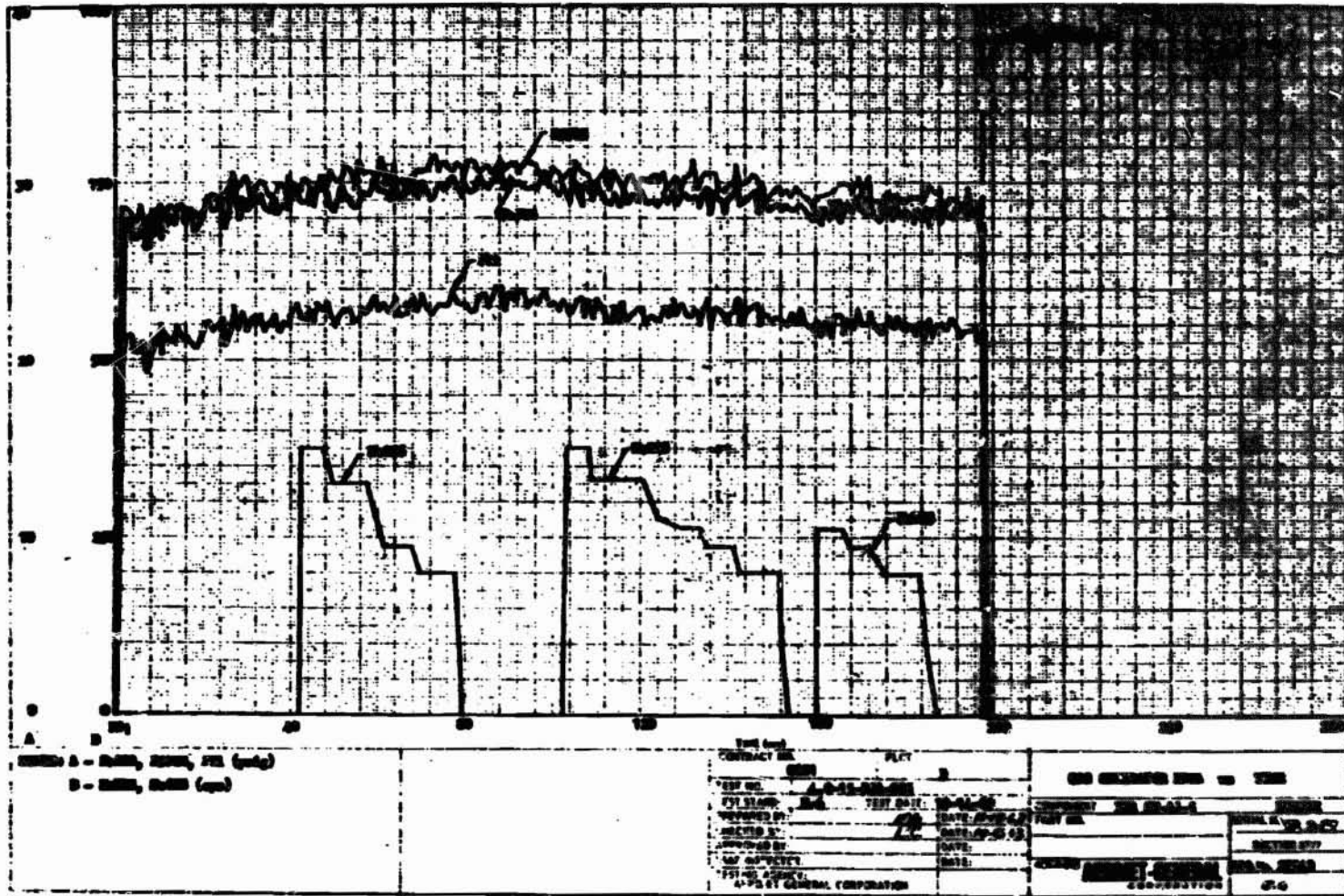


Figure 28

Test 4.0-15-2JA-005--Plot A, Oxidizer-Circuit Data vs Time



Test 4.0-15-RJA-005--Plot B, Gas-Generator Data vs Time

Report MD-TR-65-54

Report: DSD-TR-65-54

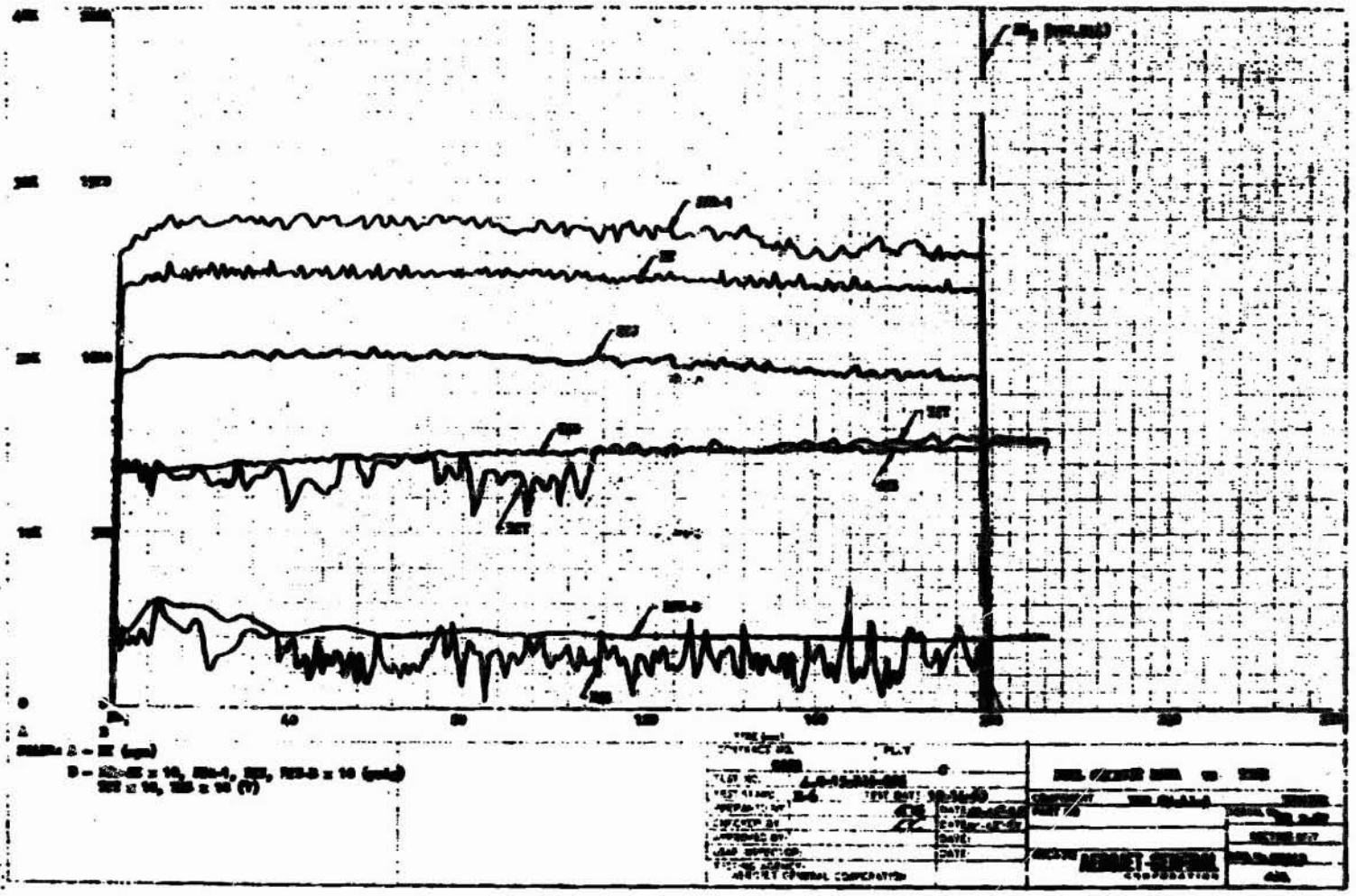
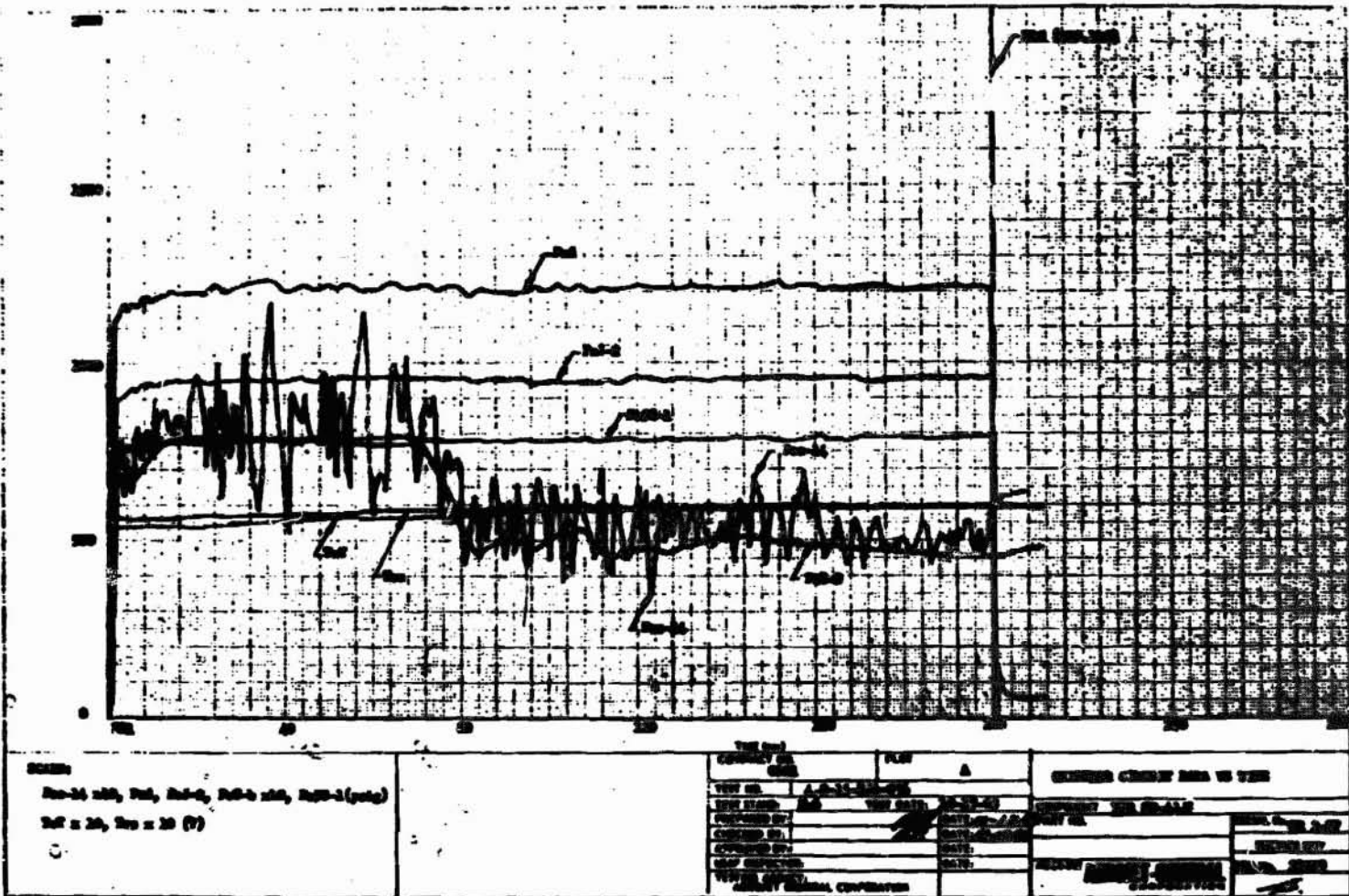


Figure 30

Test 4.0-15-RJA-005—Plot C, Fuel-Circuit Data vs Time

Figure 31

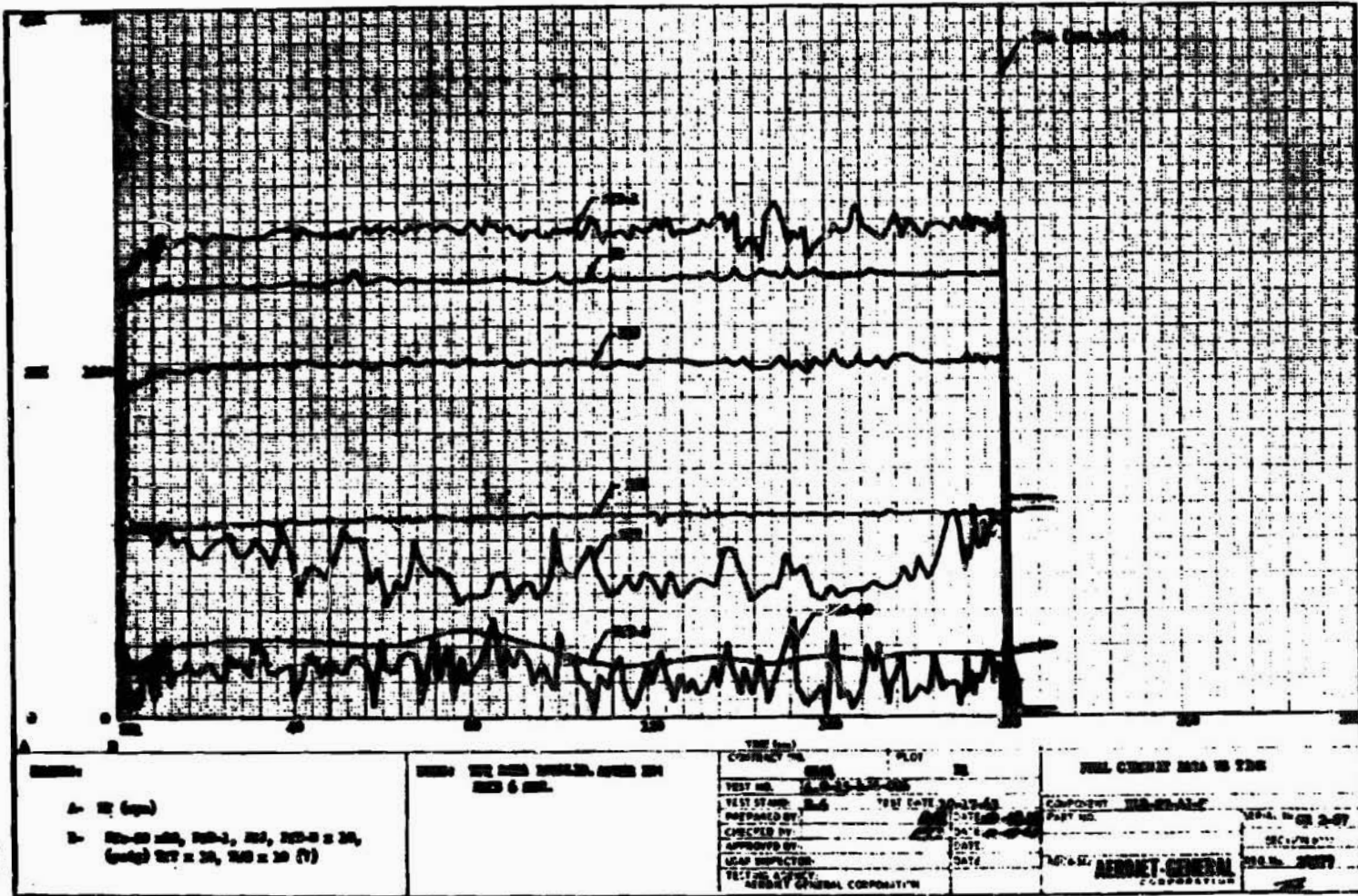


Test 4.0-15-RJA-006--Plot A, Oxidizer Circuit Data vs Time

Report RJA-TR-65-54

REPRODUCIBILITY OF THE ORIGINAL PAGE IS POOR

Figure 32



Test 4.0-15-RJA-006--Plot B, Fuel-Circuit Data vs Time

Report BSD-TM-65-54

REPRODUCIBILITY OF THE ORIGINAL PAGE IS POOR

Report MSD-TR-65-54

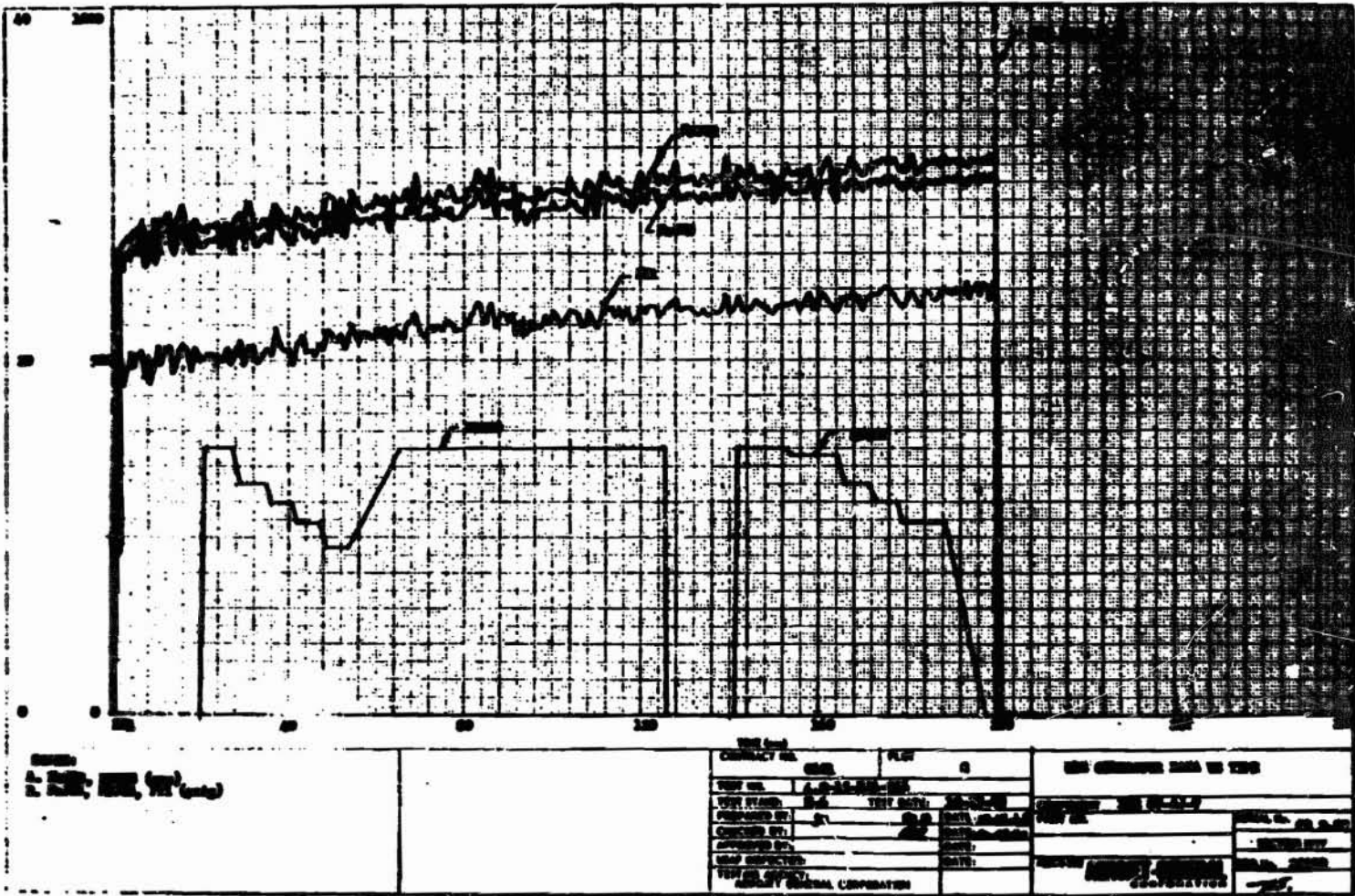
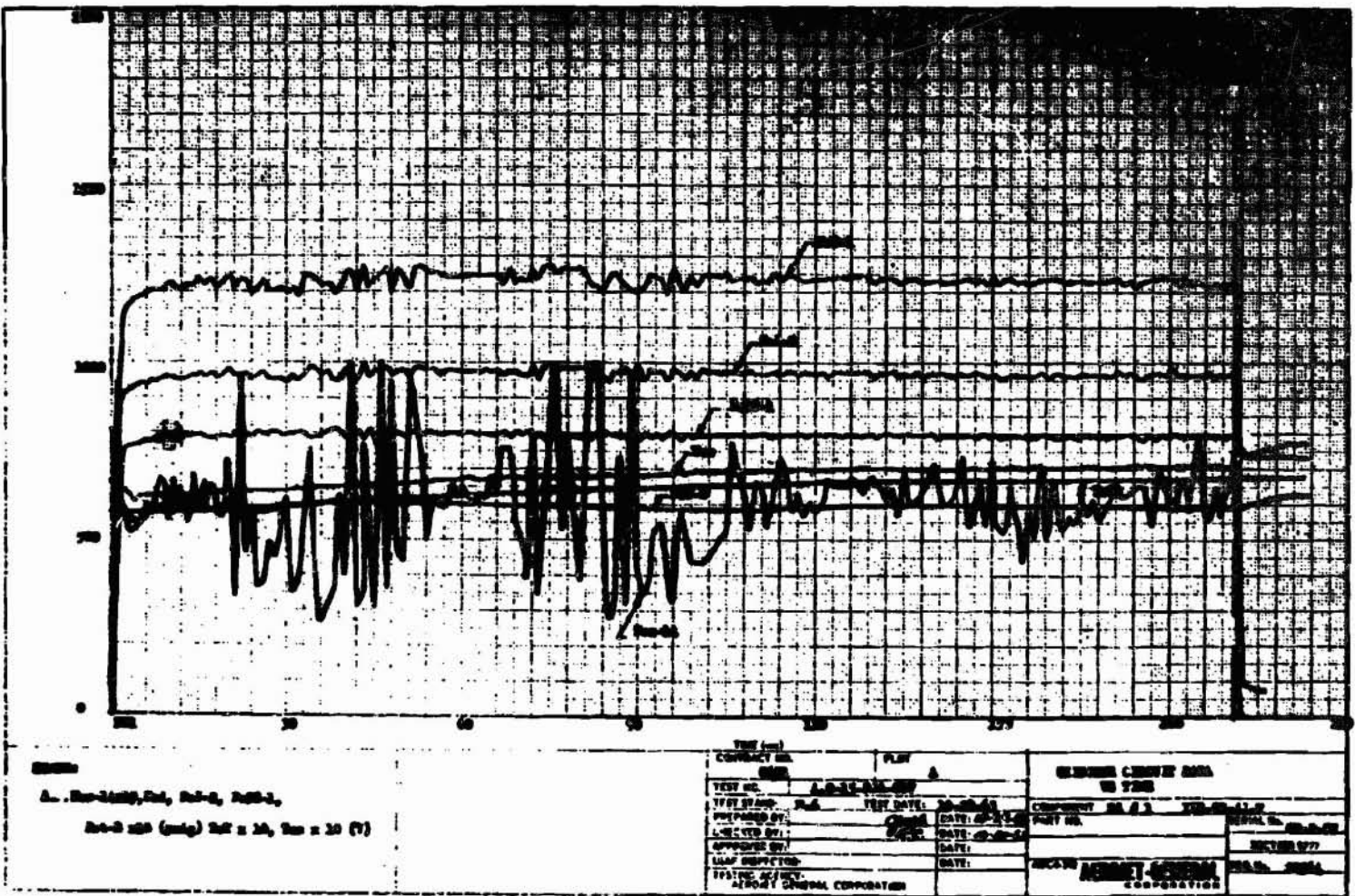


Figure 33

Plot C, Gas-Generator Data vs
 Test 4.0-15-RJA-006--Plot C, Gas Generator Data vs Time

Report # BSD-TR-65-54

Figure 34

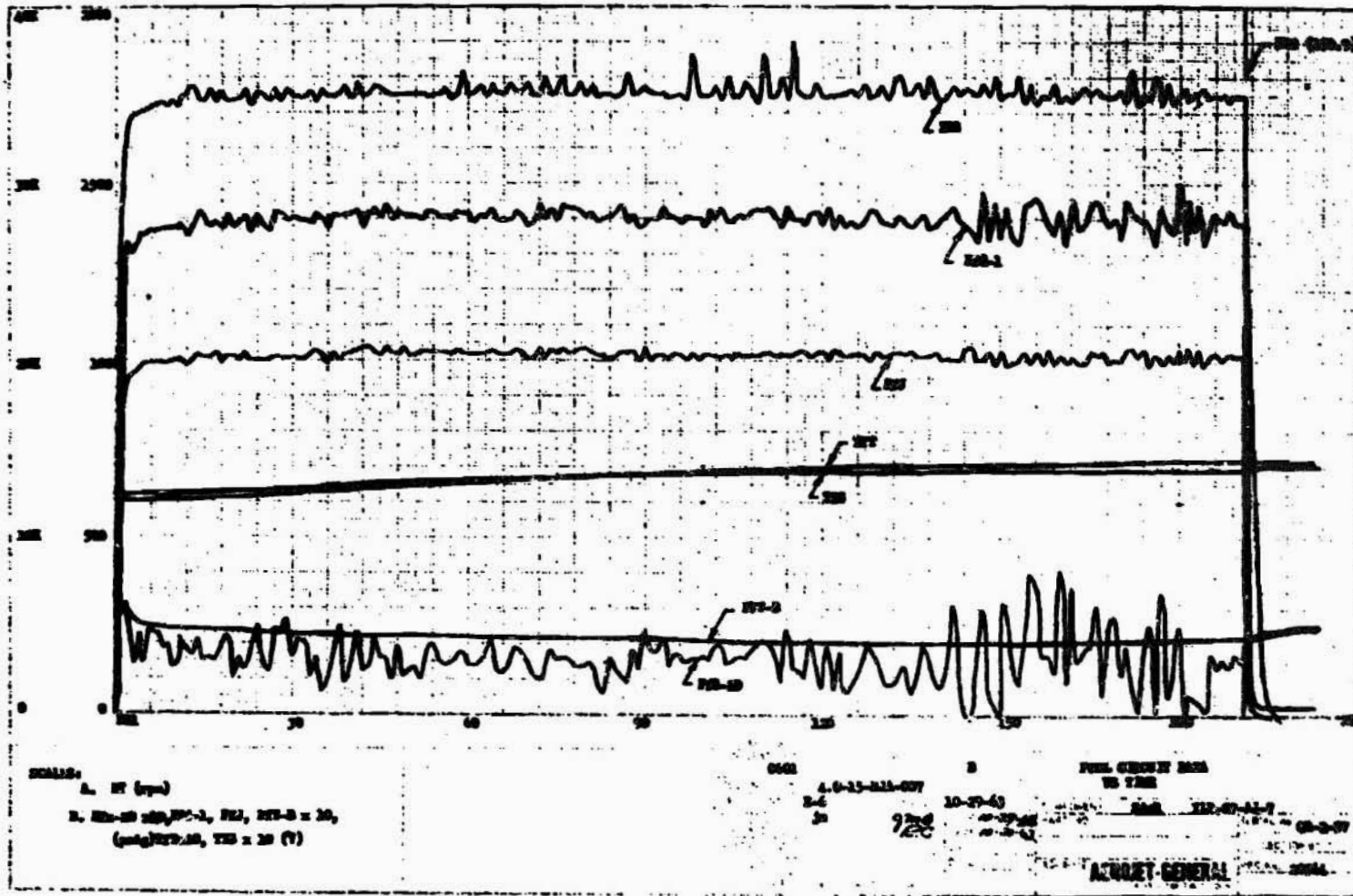


A. 4.0-15-RJA-007, Plot A, Oxidizer-Circuit Data vs Time
 4.0-15-RJA-007 (orig) 20 x 10, 20 x 10 (7)

TEST (min)		FLY		ELEMENT CIRCUIT DATA	
CONDUCT IN		A		IS 728	
TEST NO.	4.0-15-RJA-007	TEST DATE:	10-28-64	COMPONENT NO. 1	TEST NO. 111
TEST ROOM:	PLA	DATE:	10-28-64	PART NO.	10-28-64
DESIGNED BY:	CHAM	DATE:	10-28-64	SECTION 077	
APPROVED BY:	CHAM	DATE:		REMARKS	
DATE RECEIVED:		DATE:		REMARKS	
TESTING AGENCY:		ALBERT EINSTEIN CORPORATION			

Test 4.0-15-RJA-007--Plot A, Oxidizer-Circuit Data vs Time

Figure 25



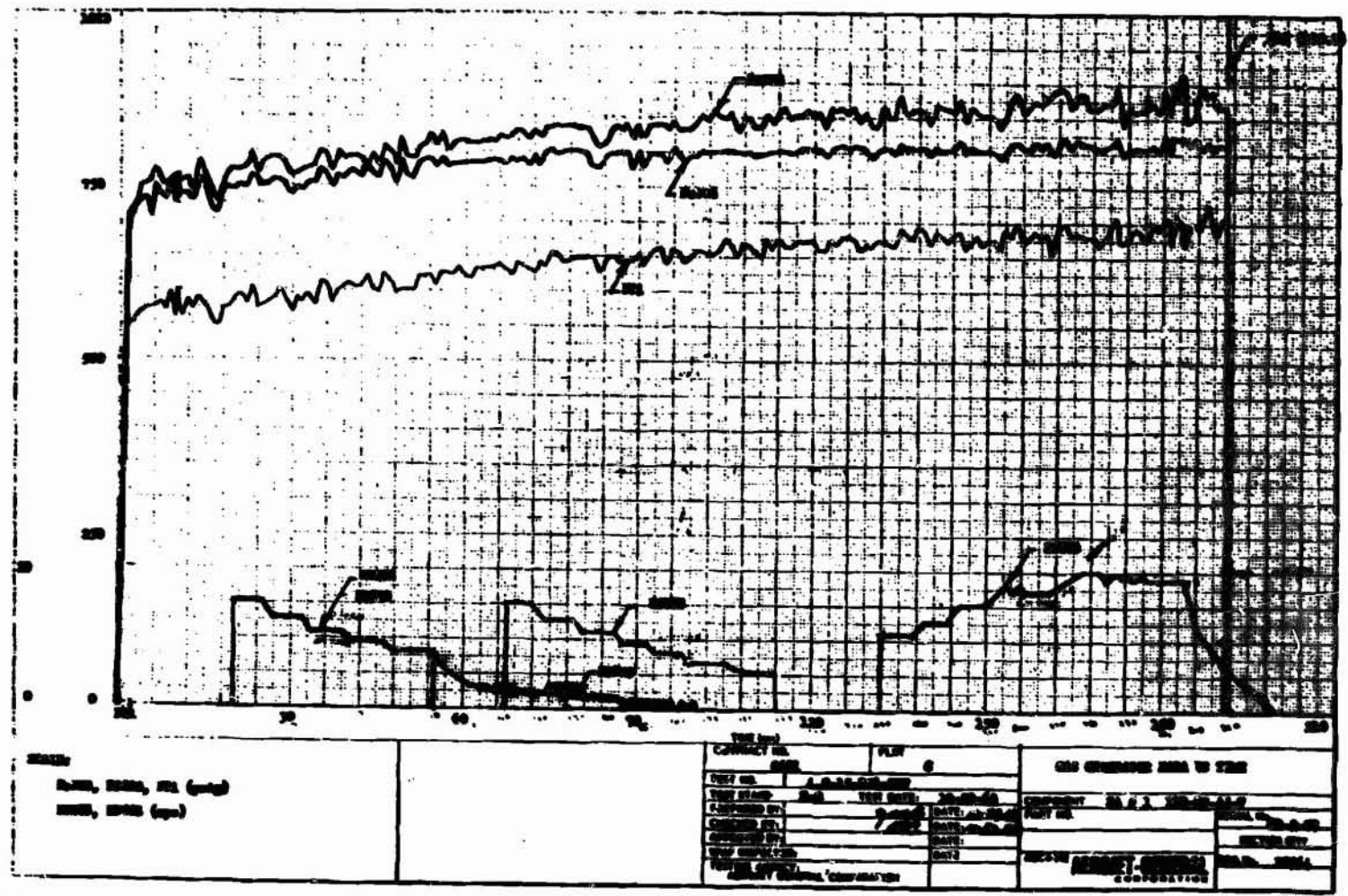
Test 4.0-15-RJA-007--Plot B, Fuel-Circuit Data vs Time

Report BDD-TR-65-34

REPRODUCIBILITY OF THE ORIGINAL PAGE IS POOR

Report ASD-TR-65-54

Figure 36



Test 4.0-15-RJA-007--Plot C, Gas-Generator Data vs Time

Report ASD-TR-65-54

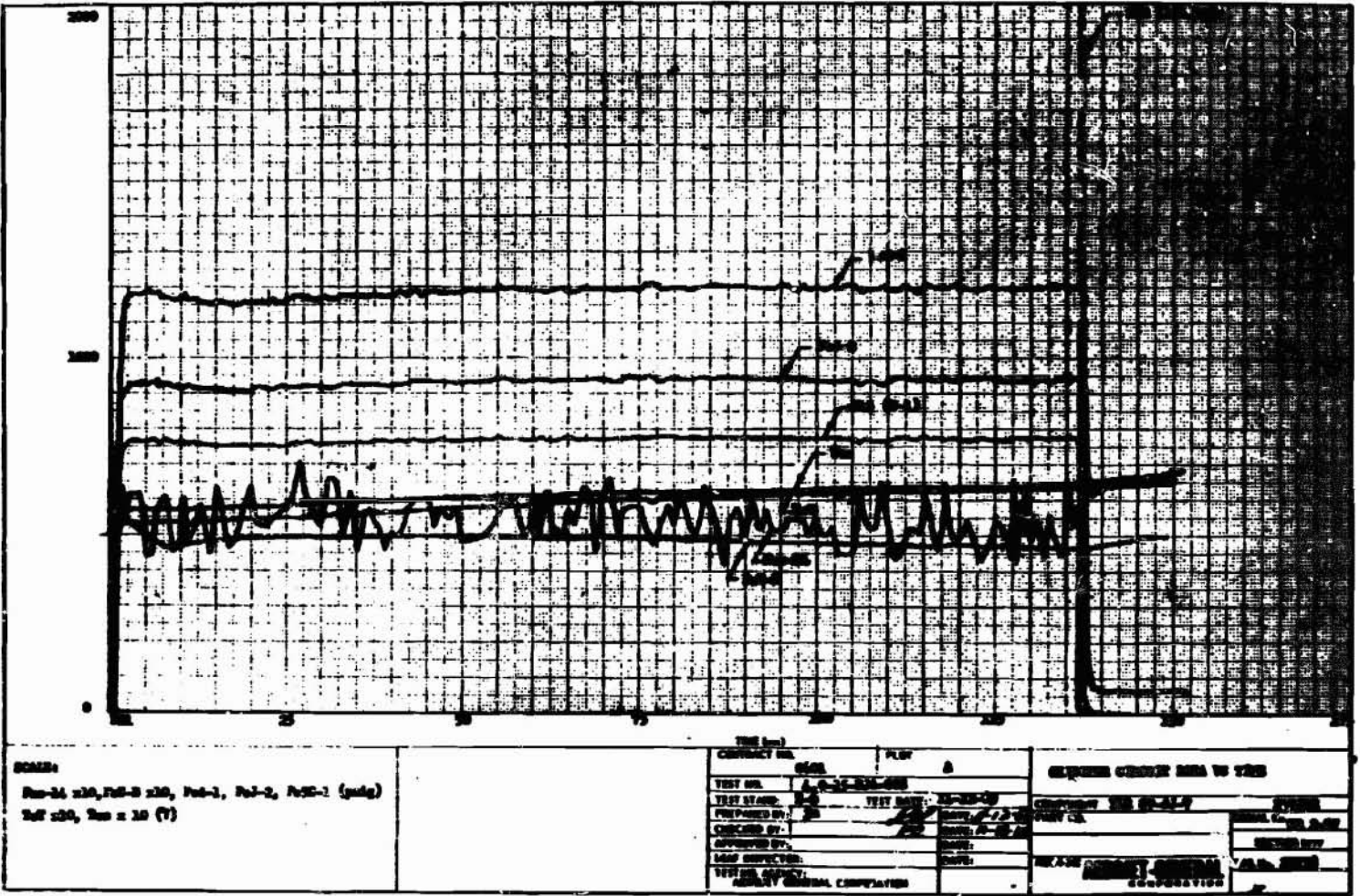


Figure 37

Test 4.0-15-BJA-008—Plot A, Oxidizer-Circuit Data vs Time

Report BSD-TR-65-54

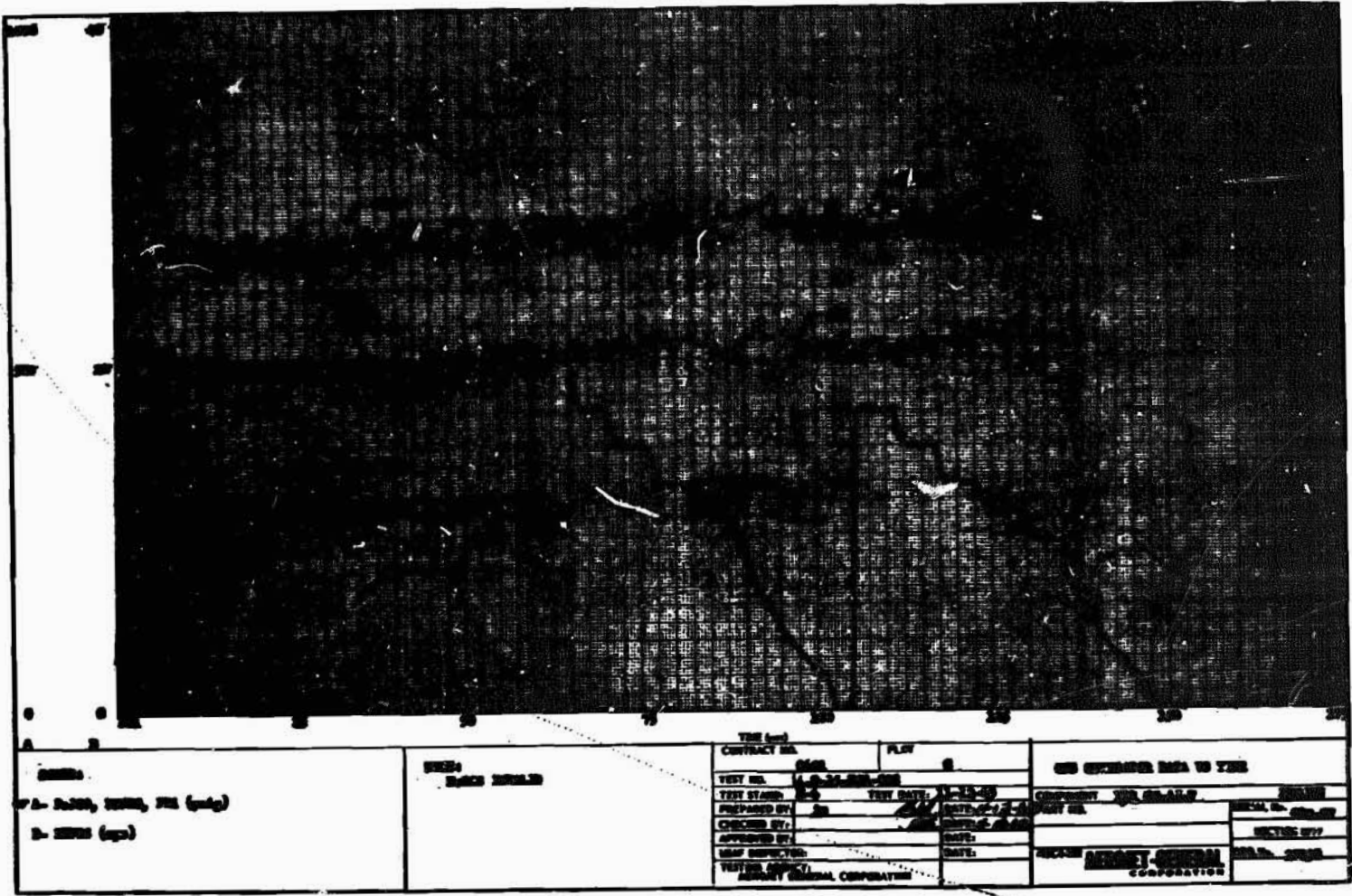
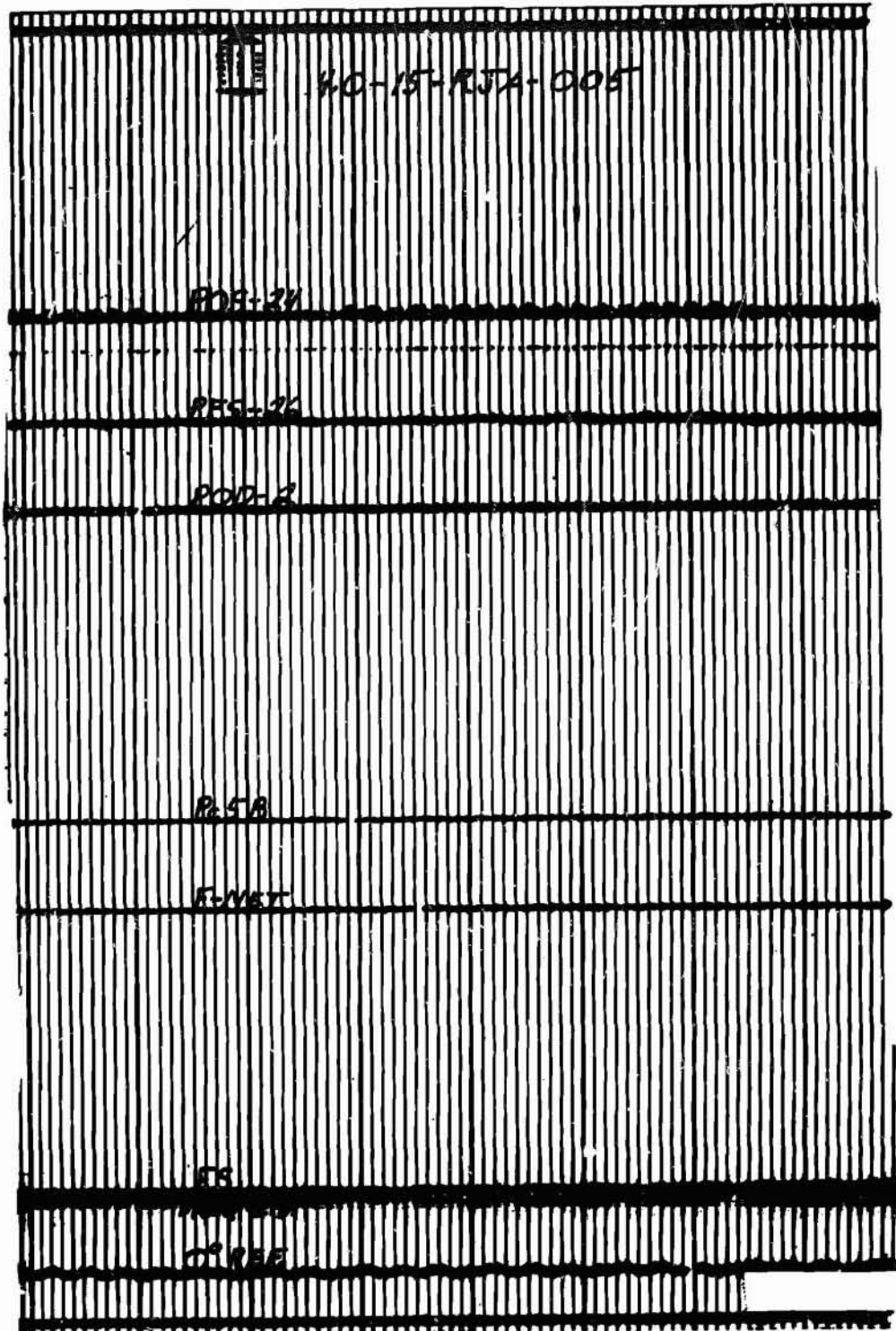


Figure 39

TITLE: A. RJA, 1958, 72 (gag) B. 1958 (gag)	INDEX: NONE KNOWN	TEST NO. 4.0-15-RJA-008 TEST STAGE 1 PREPARED BY JH CHECKED BY JH APPROVED BY JH TEST DIR. (gag) ARMY GENERAL CORPORATION	FILE # 2 TEST DATE 1-15-58 DATE OF 1-1-58 DATE 1-1-58 DATE	USE GENERATOR DATA IN THE COMMENTS: YES OR NO YES SECTION 107 ARMY GENERAL CORPORATION
		CONTRACT NO. 4.0-15-RJA-008 TEST NO. 4.0-15-RJA-008 TEST STAGE 1 PREPARED BY JH CHECKED BY JH APPROVED BY JH TEST DIR. (gag) ARMY GENERAL CORPORATION	FILE # 2 TEST DATE 1-15-58 DATE OF 1-1-58 DATE 1-1-58 DATE	USE GENERATOR DATA IN THE COMMENTS: YES OR NO YES SECTION 107 ARMY GENERAL CORPORATION

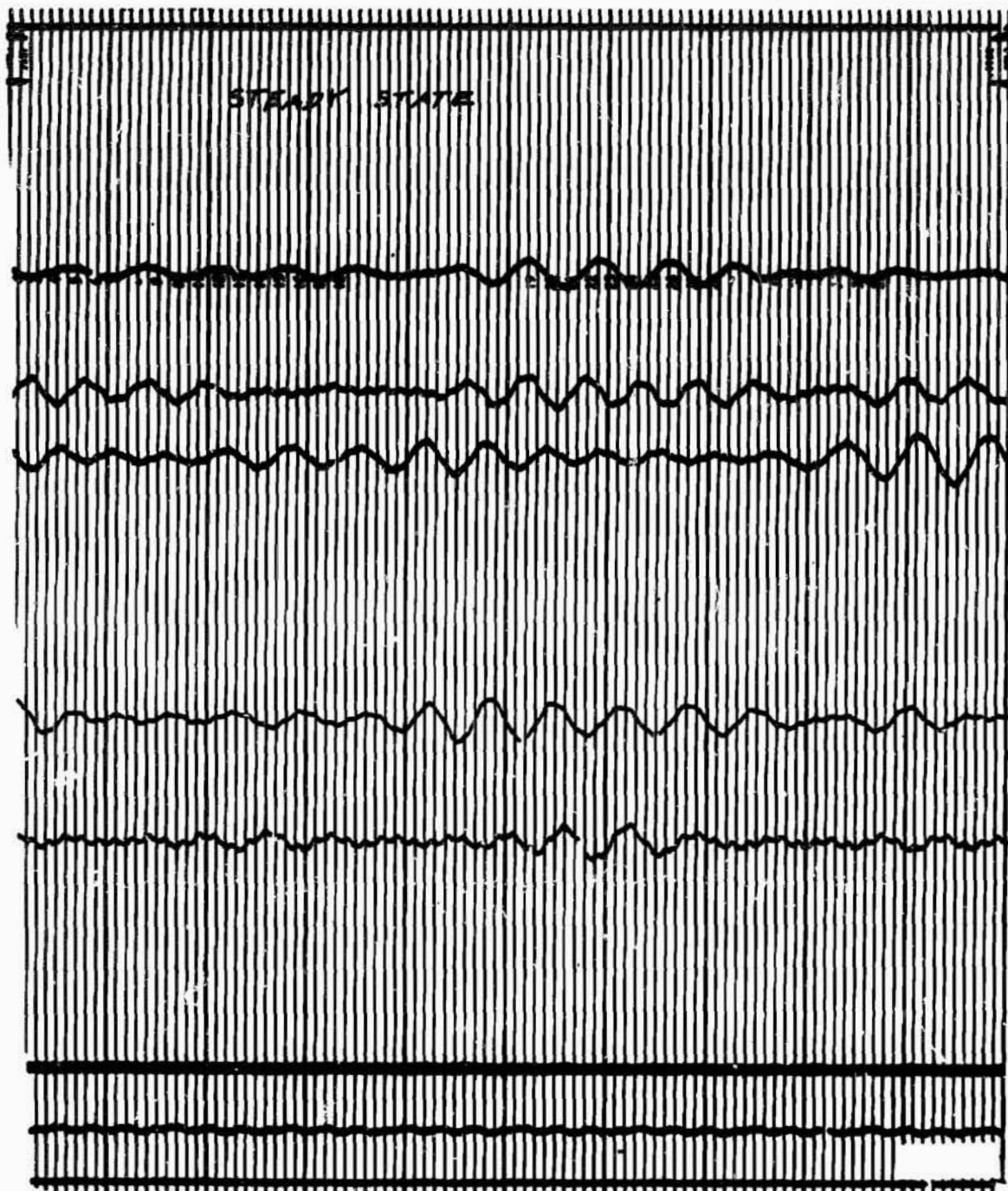
Test 4.0-15-RJA-008--Plot C, Gas-Generator Data vs Time

Report BSD-TR-65-54



Test 4.0-15-RJA-005 Engine Parameters, Narrow Band--Data Sample Prior to FS1

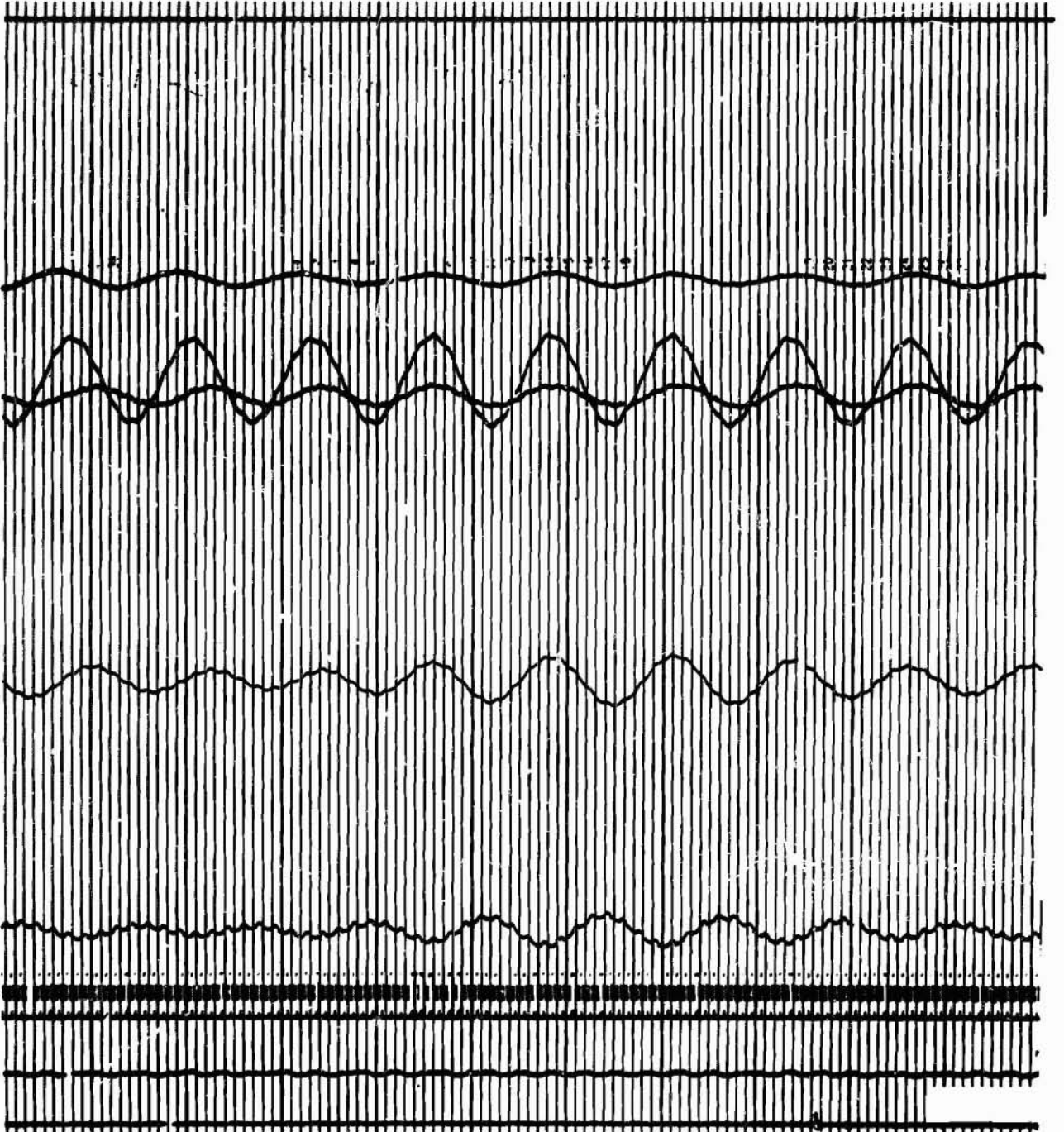
Report BSD-TR-65-54



Test 4.0-15-RJA Engine Parameters, Narrow Band--Data Sample after FS1 without Operation of Pulse Generators

Figure 41

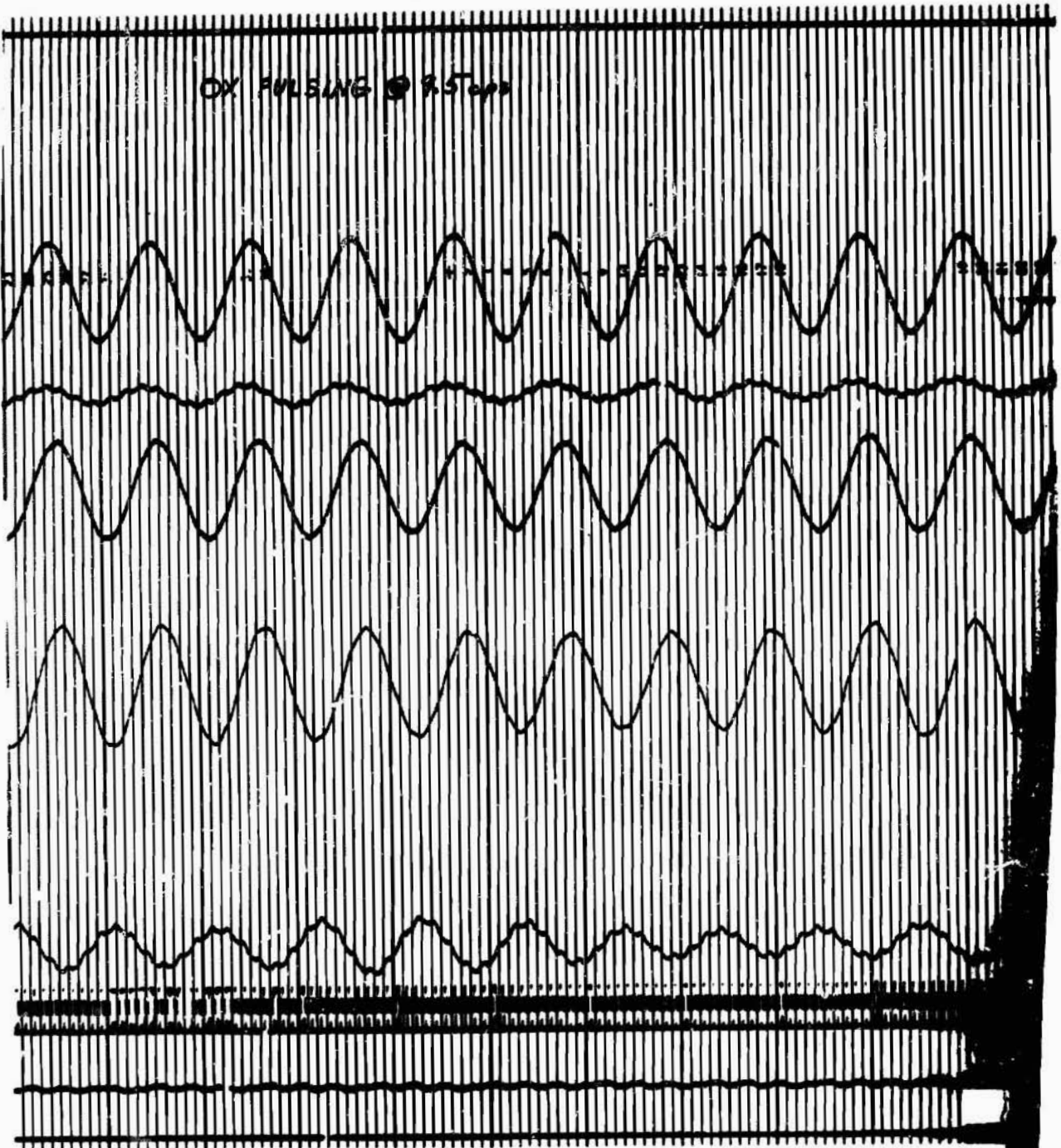
Report BSD-TR-65-54



Test 4.0-15-RJA Engine Parameters, Narrow Band--Data Sample during Operation of Oxidizer System Pulse Generator at 8.0 cps

Figure 42

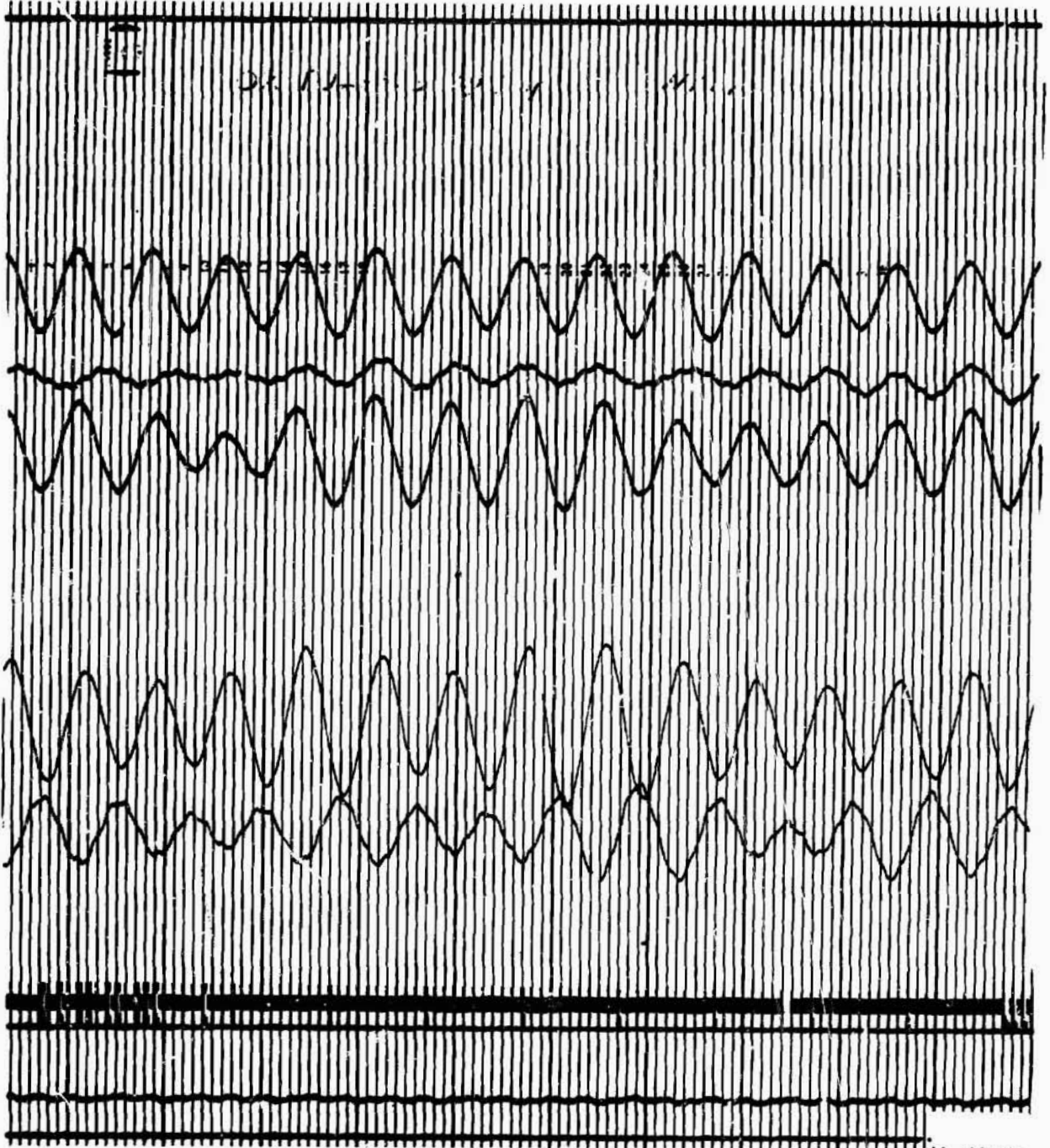
Report WSD-TR-65-54



Test 4.0-15-RJA-005 Engine Parameters, Narrow Band--Data Sample during Operation of Oxidizer System Pulse Generator at 9.5 cps

Figure 43

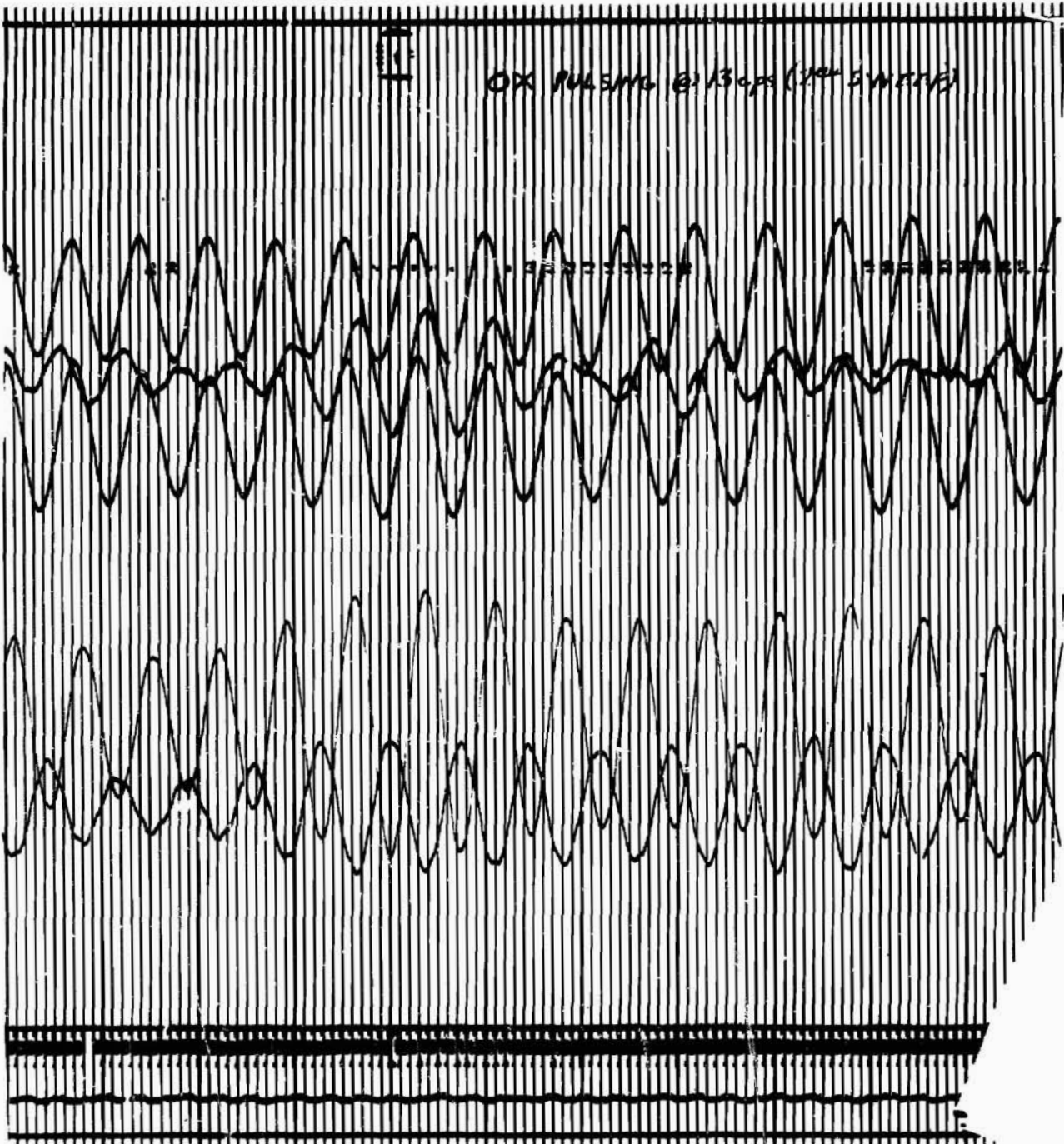
Report BSD-TR-65-54



Test 4.0-15-RJA-005 Engine Parameters, Narrow Band--Data Sample during Operation of Oxidizer System Pulse Generator at 11.0 cps

Figure 44

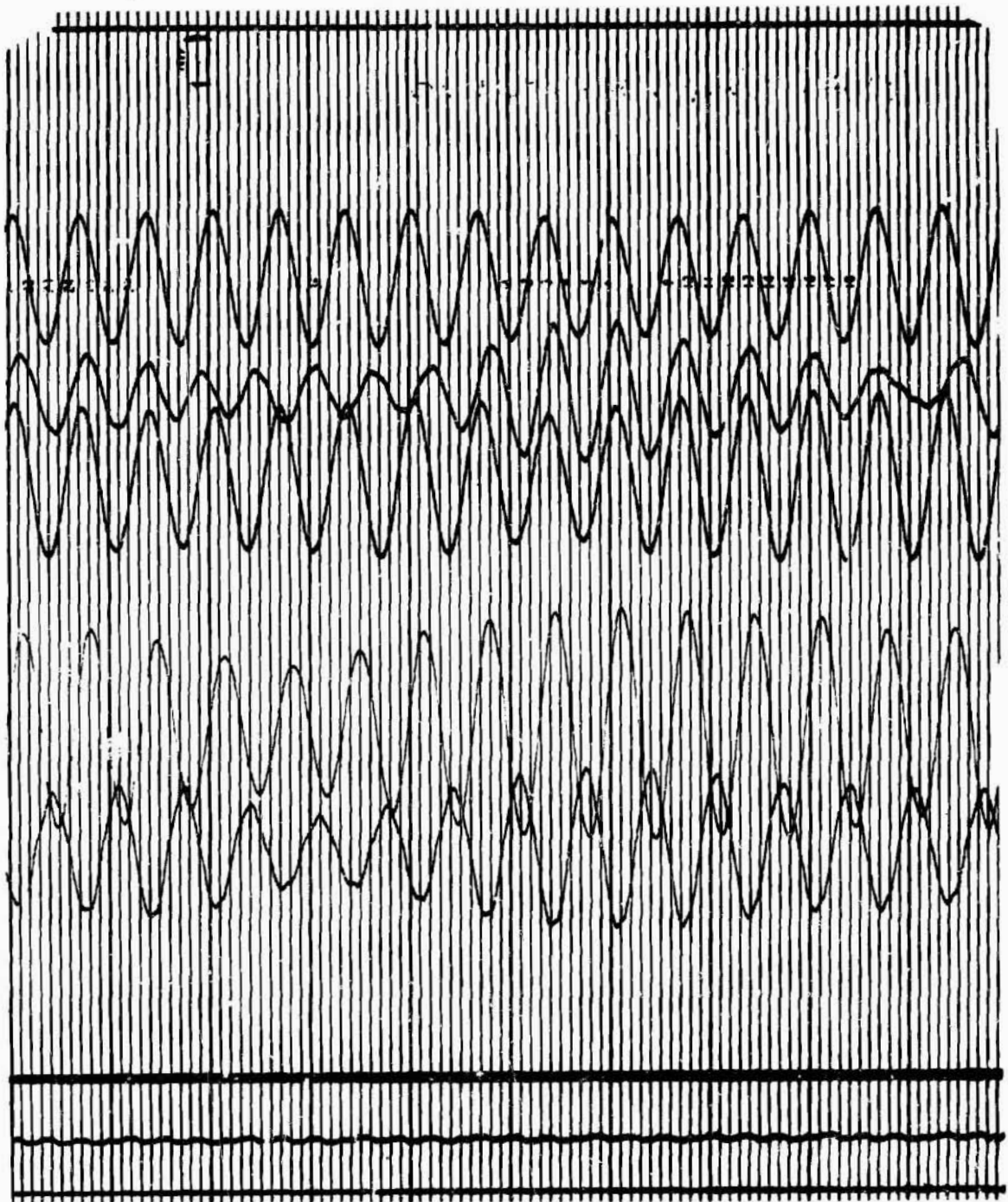
Report RSD-TR-65-54



Test 4.0-15-RJA-005 Engine Parameters, Narrow Band--Data Sample during Operation of Oxidizer-System Pulse Generator at 13.0 cps

Figure 45

Report BSD-TR-65-54



Test 4.0-15-RJA-005 Engine Parameters, Narrow Band--Data Sample during Operation of Oxidizer-System Pulse Generator at 13.0 cps

Figure 46

AMDR 9635-037, APPENDIX I

COPIES

RECIPIENT

NASA Headquarters
Washington, D.C. 20546

1 Chief, Liquid Propulsion Technology, RPL
1 Mr. E. Z. Gray
Chief, Advanced Manned Missions, MT
1 Mr. Vincent L. Johnson
Director, Launch Vehicles and Propulsion, SV
Office of Space Science and Applications

NASA Marshall Space Flight Center
Huntsville, Alabama 35805

1 Attn: Lawrence Garrison, PR-SC
1 Office of Technical Information, MS-IPC
1 Technology Utilization Office, MS-T
1 S. Morea, I-E-F
1 T. Smith, I-E-H
1 M. Urlaub, I-V-SIC
1 A. Thompson, I-V-SIB
1 O. Goetz, R-TEST-C
1 R. Stone, R-TEST-CTM
1 H. Johnstone, R-TEST-SP
1 J. Jones, R-COMP-RRV
1 N. Showers, R-P&VE-SL
2 T. Bullock, R-P&VE-SLR
1 H. Paul, R-P&VE-P
1 J. Thomson, R-P&VE-PA
1 C. Smith, R-P&VE-PAB
2 D. Davis, R-P&VE-PAB
1 L. Gross, R-P&VE-PAC
1 C. C. Wood, R-P&VE-PT
3 A. L. Worlund, R-P&VE-PTF

END

DATE

FILMED

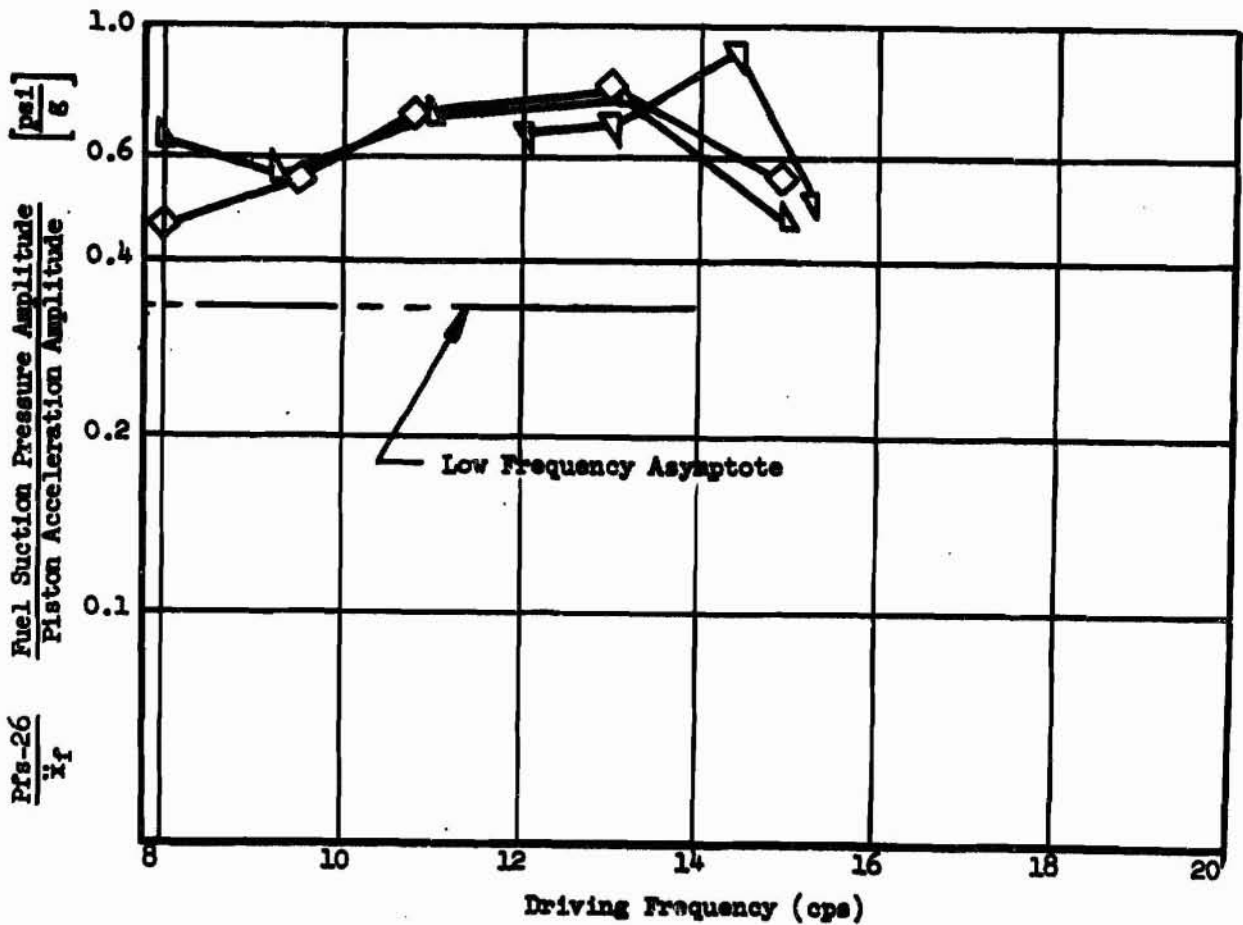
JUL 20 1967

Report BSD-TR-65-54

NOTES:

- 1) Narrow band passed data
- 2) Identification of data points

Symbol	Run	$\overline{Pfs-0}$ (psia)
◇	002 (2)	22
◊	004 (3)	24
◀	006 (2)	26



Fuel Suction Time, $Pfs-26/X_f$ vs Driving Frequency with $\overline{Pfs-0}$ at 24 ± 2 psia

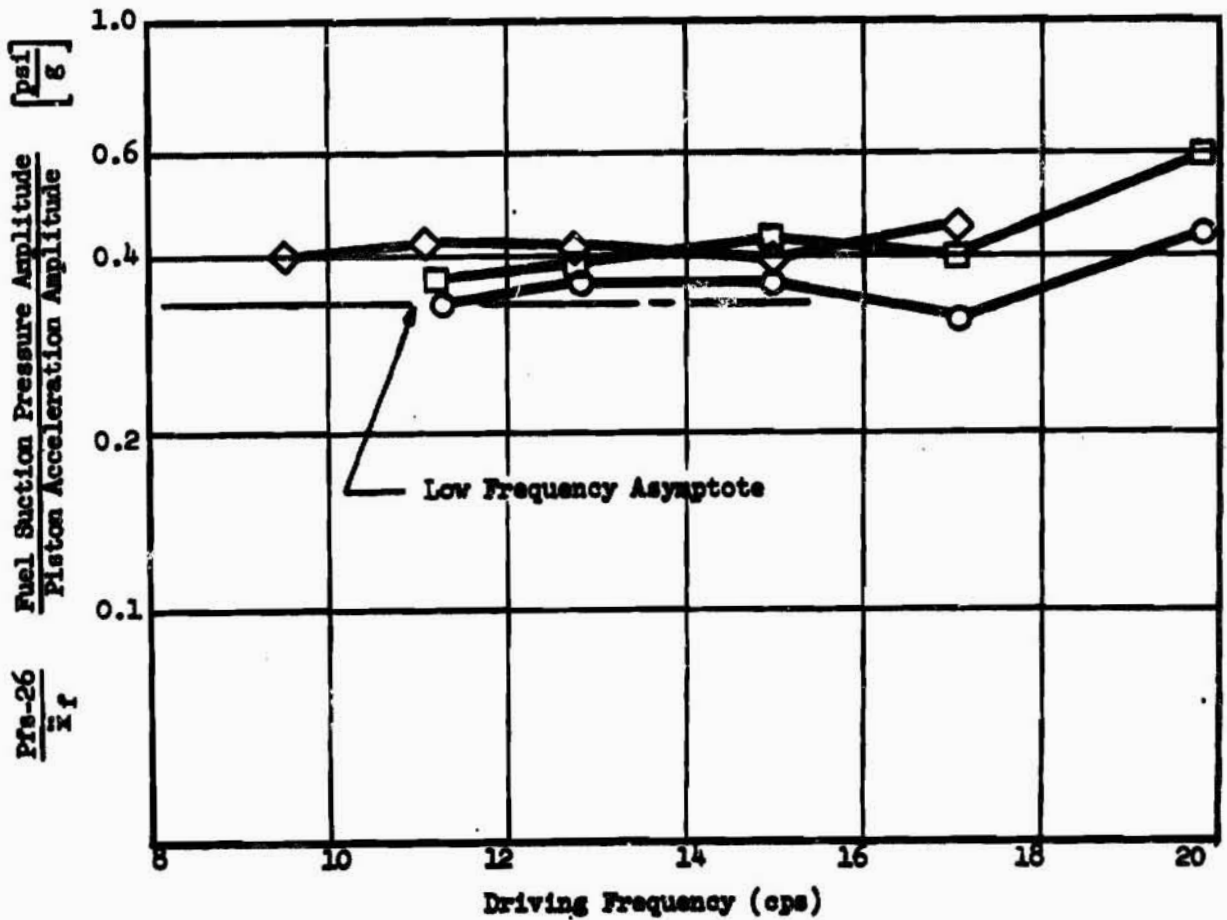
Figure III D-4

Report BSD-TR-65-54

NOTES:

- 1) Narrow band passed data
- 2) Identification of data points

Symbol	Run	$\overline{Pfs-O}$ (psia)
○	008 (1)	36
□	008 (2)	30
◇	008 (3)	25



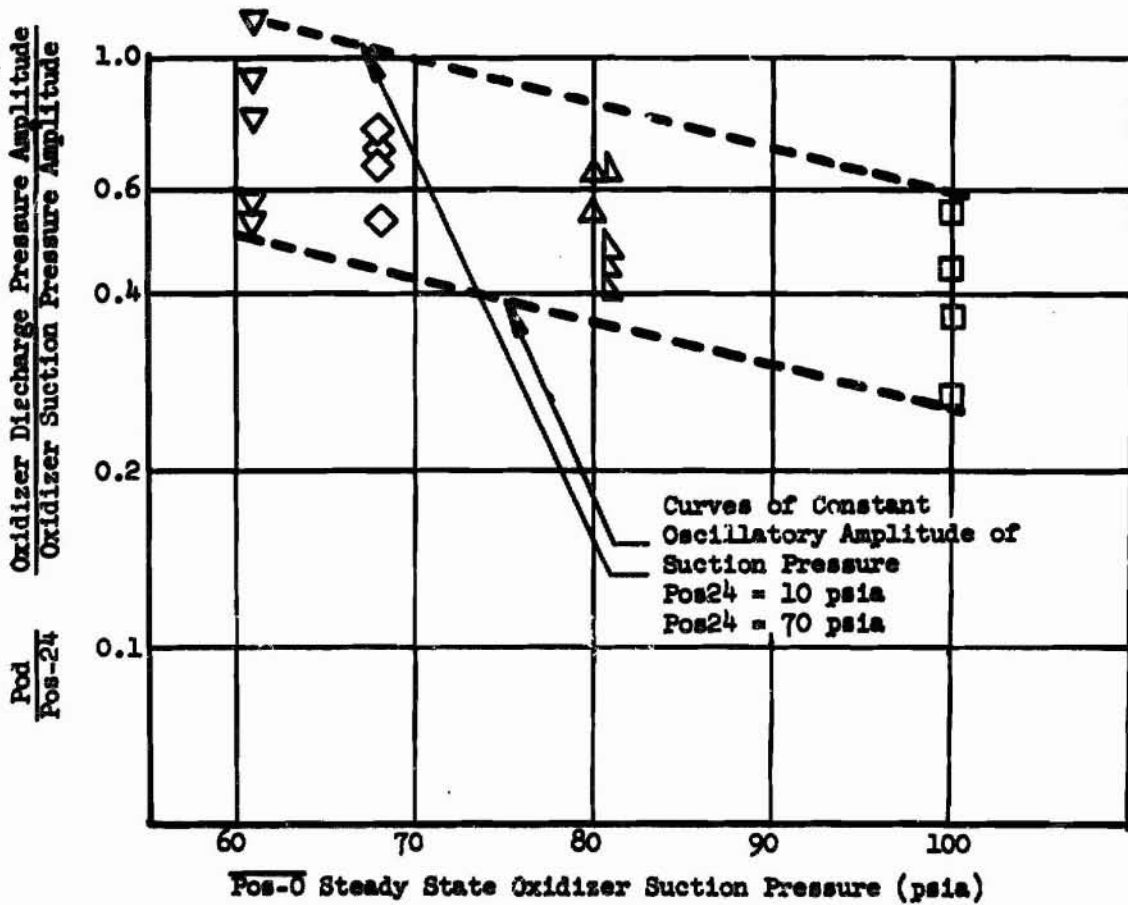
Fuel Suction Time, $Pfs-26/Xf$ vs Driving Frequency for Test Run 4,0-15-3JA-008 with P/N 289660 Fuel Impeller

NOTES:

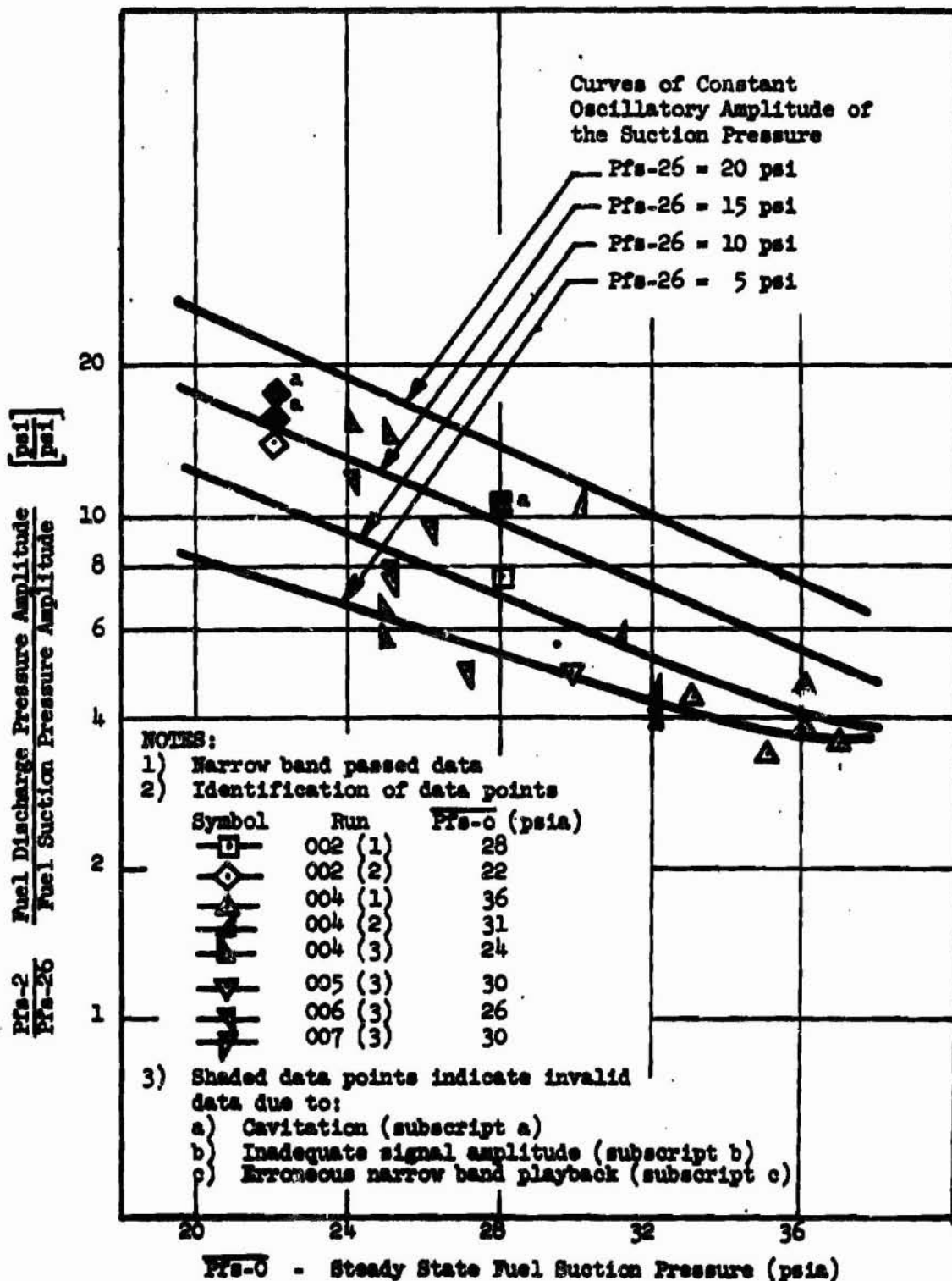
- 1) Narrow band passed data
- 2) Identification of data points

Symbol	Run	Pos-0 (psia)
○	001 (1)	61
×	002 (3)	65
□	003 (1)	100
◇	003 (2)	68
△	005 (1)	80
▽	005 (2)	61
▲	006 (1)	100
▾	007 (1)	81

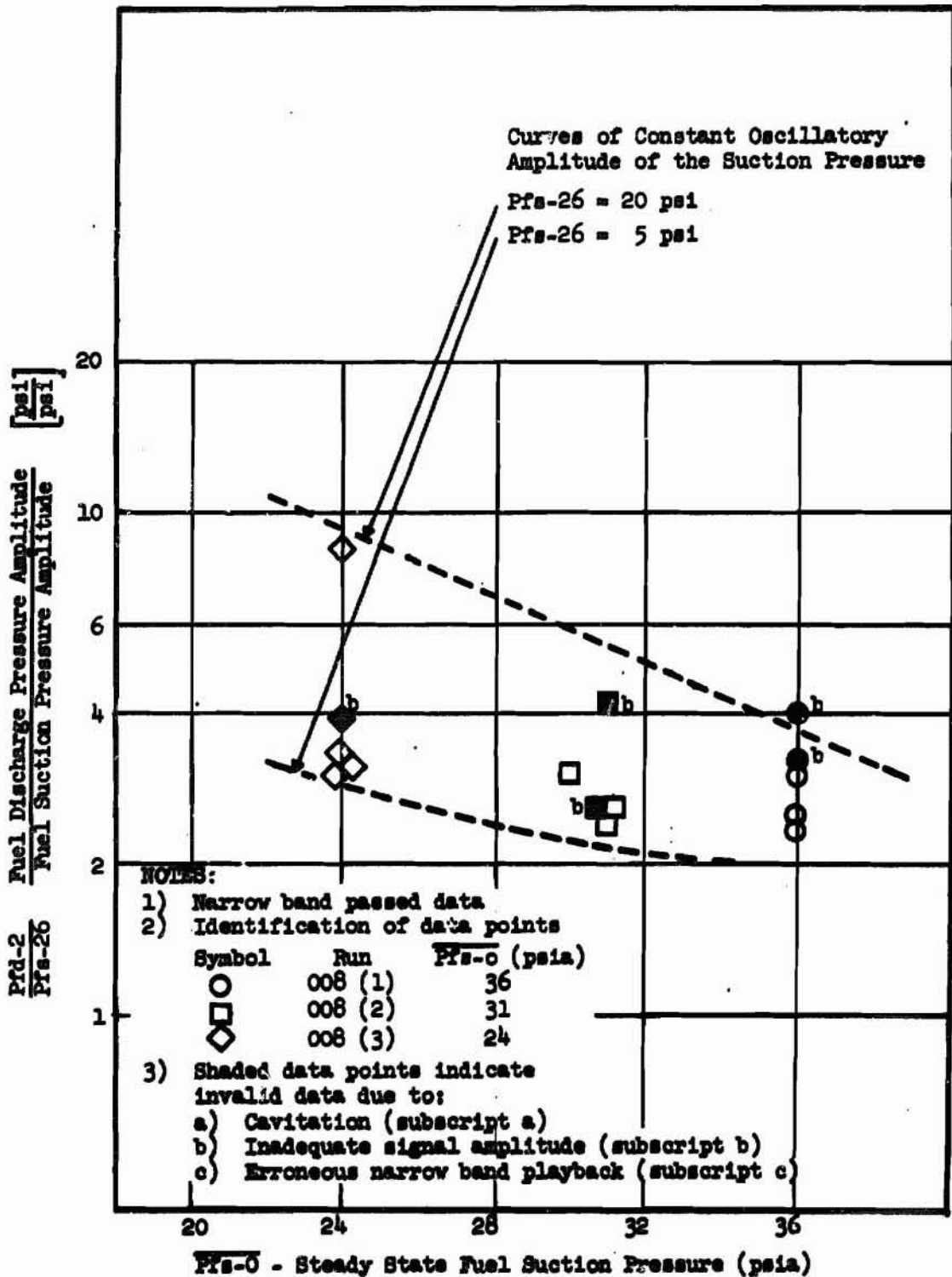
$\left[\frac{\text{psi}}{\text{psi}} \right]$



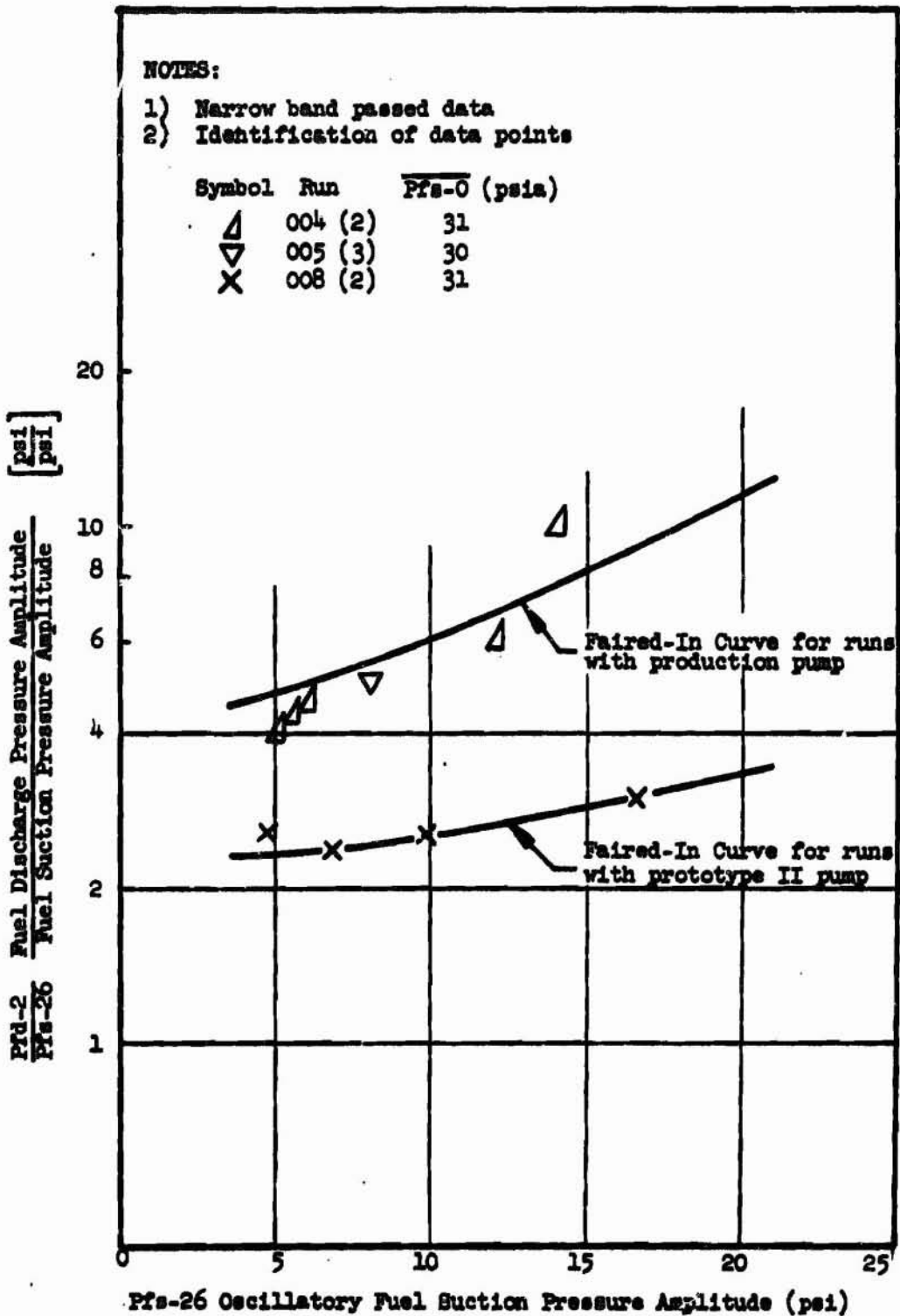
Oxidizer Pump Amplification, Pod/Pos-24 vs Pos-0 with P/N 246647 Fuel Impeller



Fuel Pump Amplification, Pfd-2/Pfs-26 vs Pfs-0 with P/N 246647 Fuel Impeller



Fuel Pump Amplification, Pfd-2/Pfs-26 vs $\overline{\text{Pfs-0}}$ with P/N 289660 Fuel Impeller



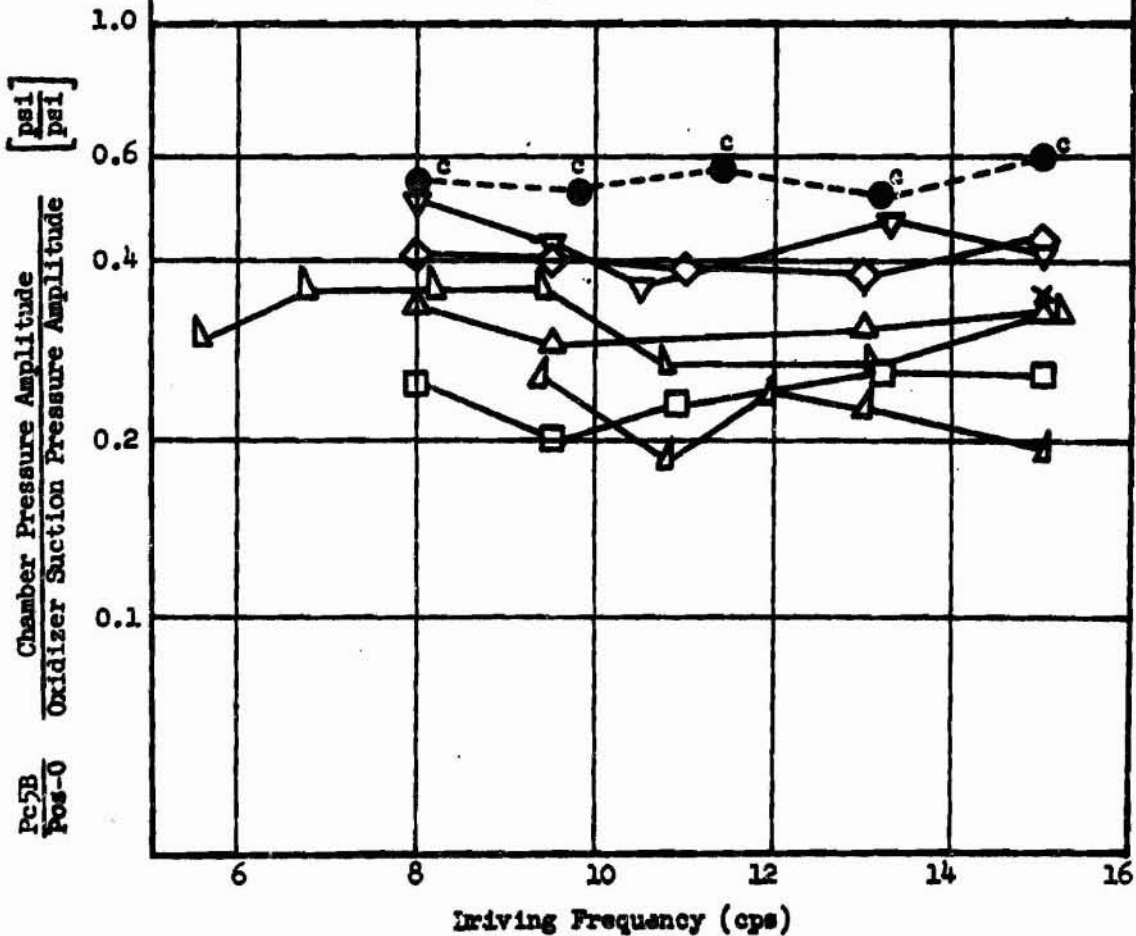
Fuel Pump Amplification, $Pfd-2/Pfs-26$ vs $Pfs-26$ with $\overline{Pfs-0}$ Constant

NOTES:

- 1) Narrow band passed data
- 2) Identification of data points

Symbol	Run	$\overline{P_{os-0}}$ (psia)
○	001 (1)	61
✕	002 (3)	65
□	003 (1)	100
◇	003 (2)	68
△	005 (1)	80
▽	005 (2)	61
▲	006 (1)	100
▾	007 (1)	81

- 3) Shaded points indicate invalid data due to:
 - a) Cavitation (subscript a)
 - b) Inadequate signal amplitude (subscript b)
 - c) Erroneous narrow band playback (subscript c)

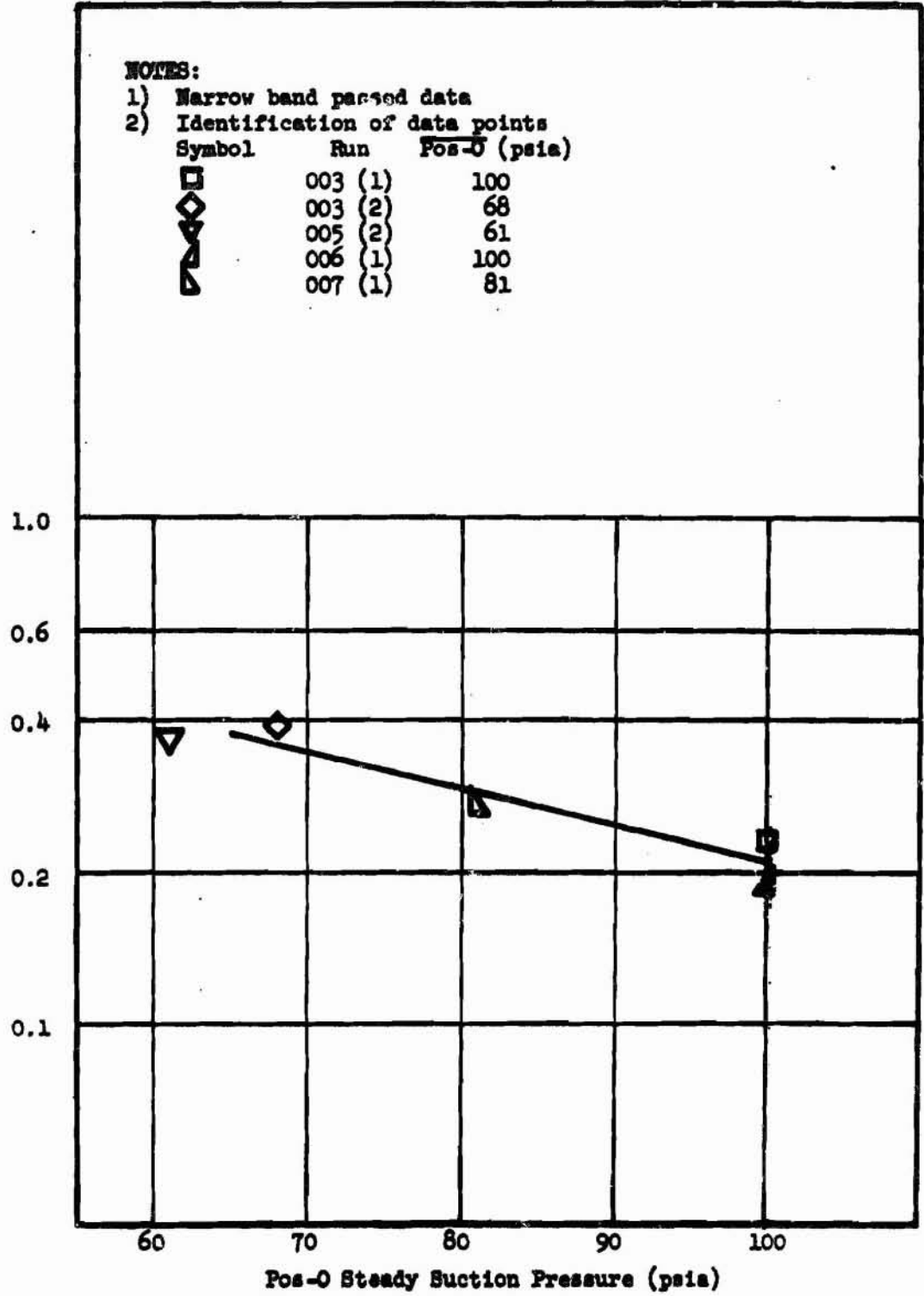


Engine Function P_{c5B}/P_{os-24} vs Driving Frequency

[$\frac{\text{psi}}{\text{psi}}$]

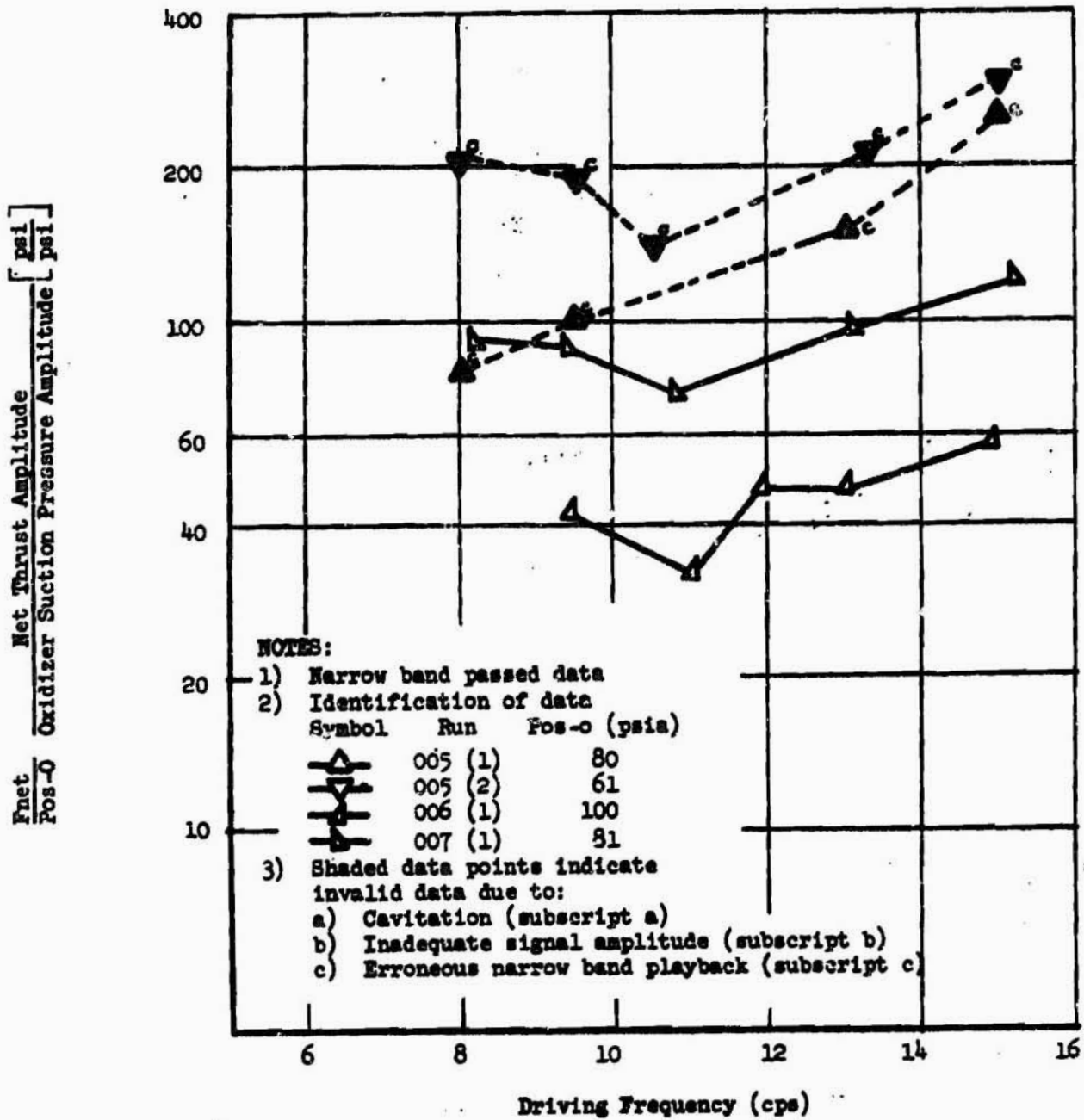
$\frac{\text{Chamber Pressure Amplitude}}{\text{Oxidizer Suction Pressure Amplitude}}$

$\frac{Pc5B}{Pos-0}$



Engine Function Pc5B/Pos-24 vs Pos-0 at Constant Pulse Generator Frequency of 11 cps

Report BSD-TR-65-54

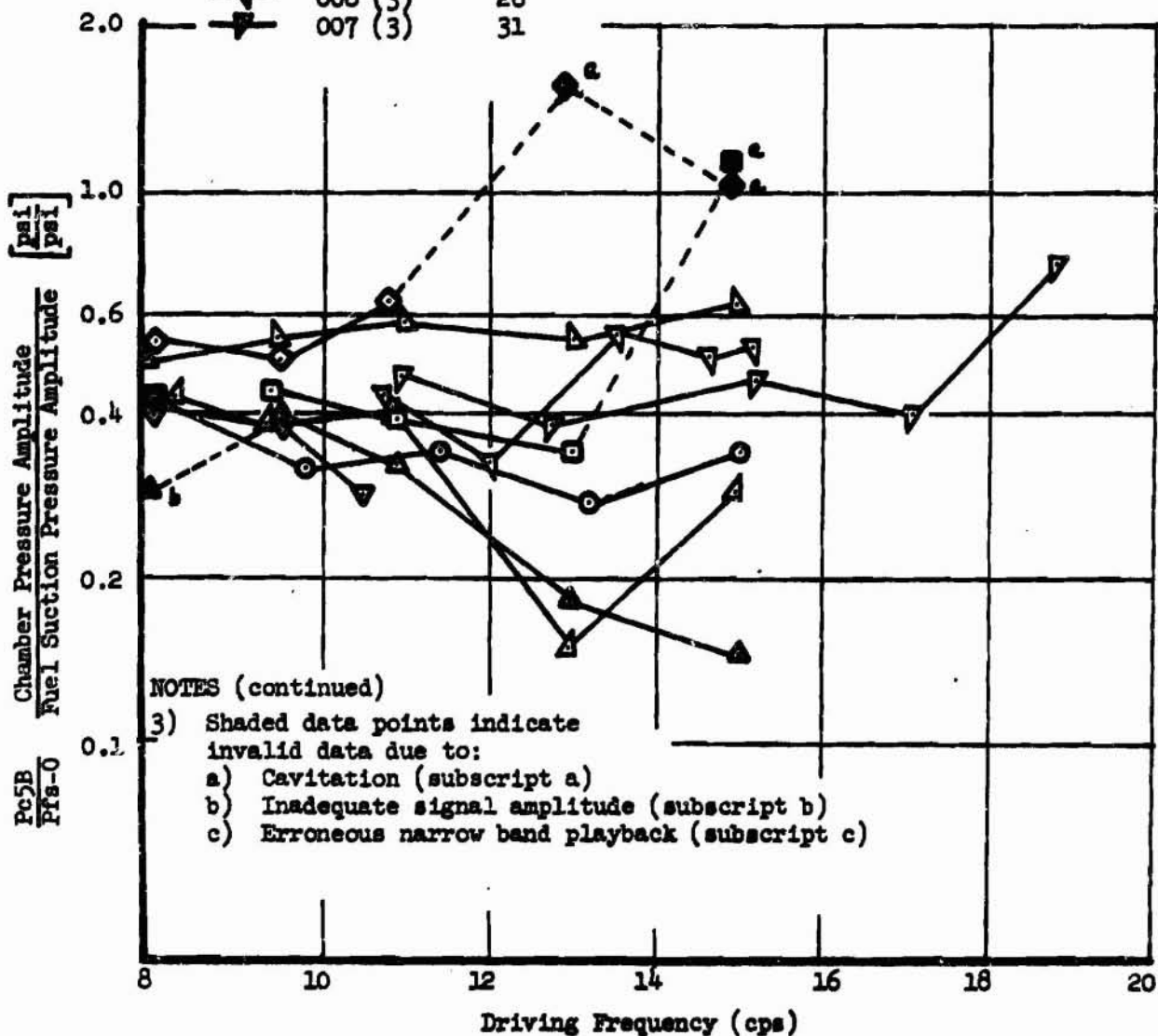


Engine Function Fnet/Pos-24 vs Driving Frequency

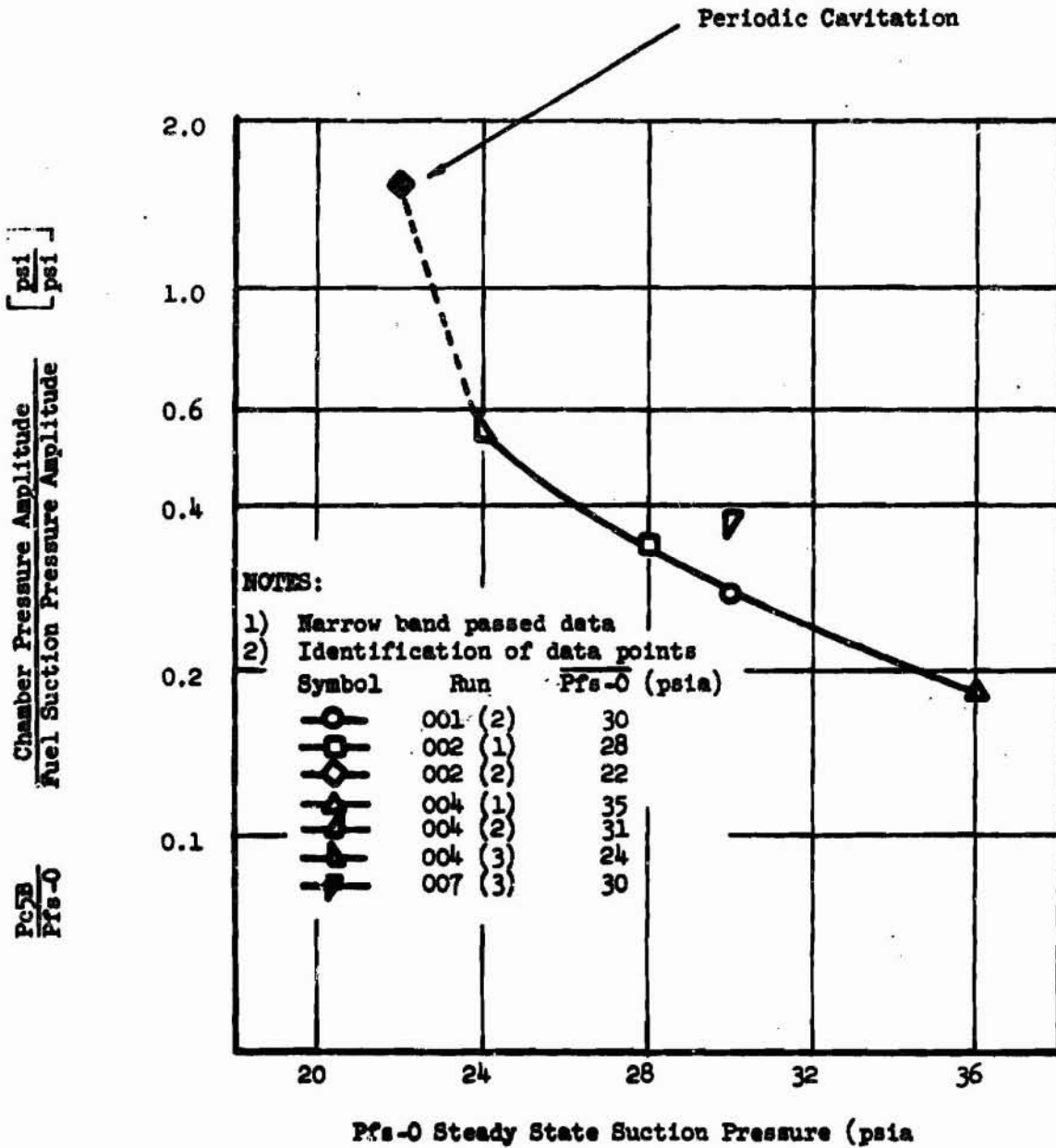
NOTES:

- 1) Narrow band passed data
- 2) Identification of data points

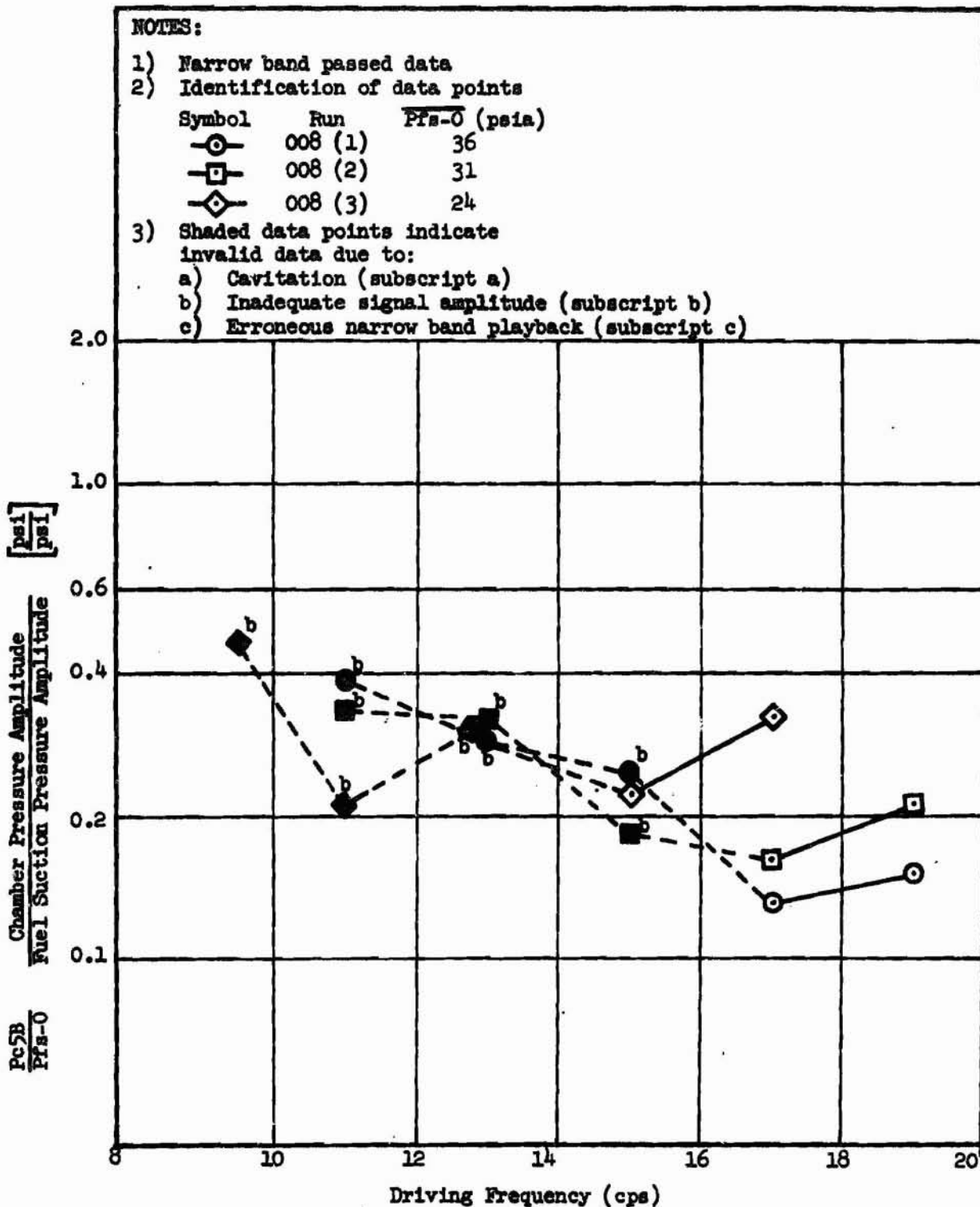
Symbol	Run	$\overline{P_{fs-0}}$ (psia)
○	001 (2)	30
□	002 (1)	28
◇	002 (2)	22
△	004 (1)	35
▲	004 (2)	31
▴	004 (3)	24
▾	005 (3)	30
▽	006 (3)	26
◀	007 (3)	31



Engine Function P_{c5B}/P_{fs-0} vs Driving Frequency



Engine Function P_{c5B}/P_{fs-0} vs P_{fs-0} at Constant Pulse Generator Frequency of 13 cps



Engine Function Pc5B/Pfs-0 vs Driving Frequency with Fuel Impeller
P/N 289660

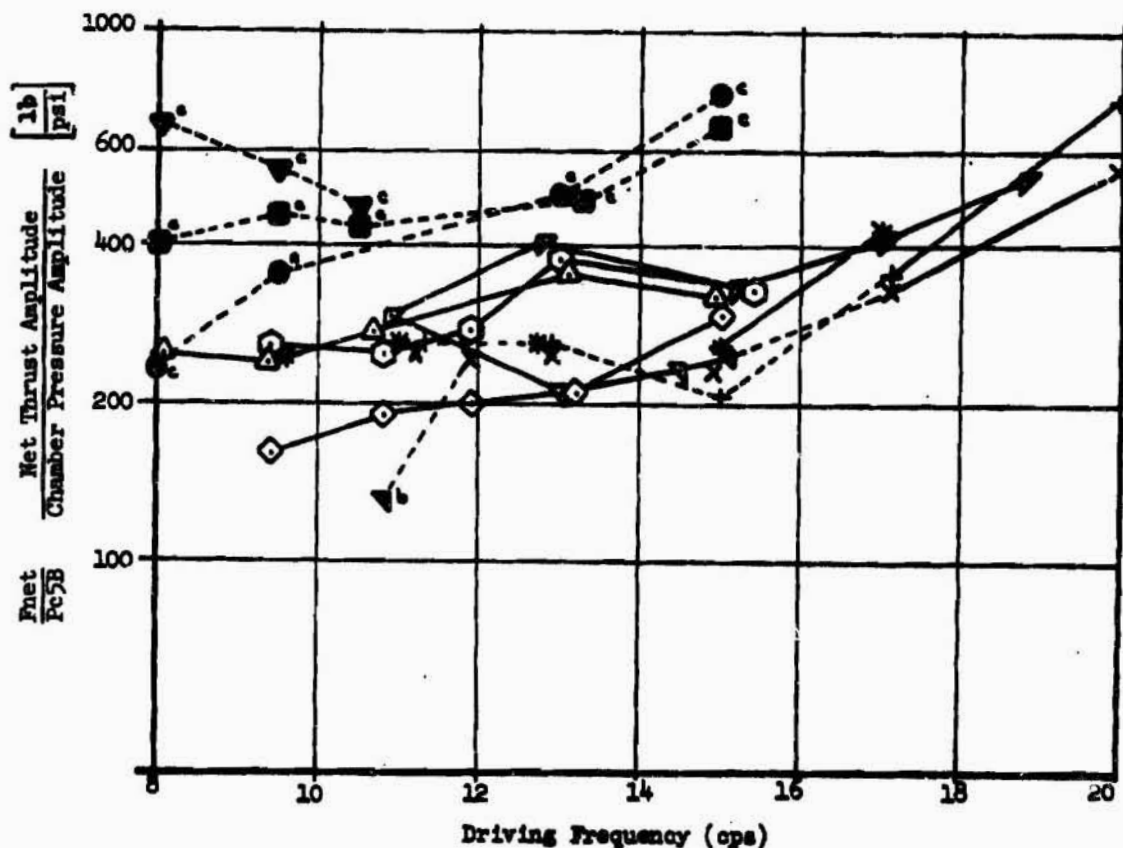
Report BSD-TR-65-54

NOTES:

- 1) Narrow band passed data
- 2) Identification of data points

Symbol	Run	Pulsing
○	005 (1)	Ox
◻	005 (2)	Ox
◊	005 (3)	Fuel
△	006 (1)	Ox
▽	006 (3)	Fuel
◐	007 (1)	Ox
◑	007 (2)	Ox & Fuel
◒	007 (3)	Fuel
-+-	008 (1)	Fuel
-*-	008 (2)	Fuel
-#-	008 (3)	Fuel

- 3) Shaded data points indicate invalid data due to:
 - a) Cavitation (subscript a)
 - b) Inadequate signal amplitude (subscript b)
 - c) Erroneous narrow band playback (subscript c)



Engine Function F_{net}/P_{c5B} vs Driving Frequency

Figure III D-16

Report BSD-TR-65-54

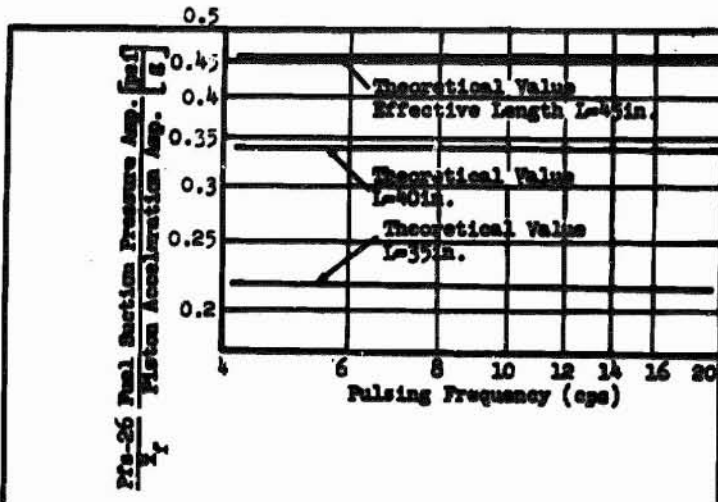


Figure III D-19. Function Pfs-26/Xf vs Driving Frequency for Fuel Section Line Effective Lengths of 35, 40, and 45 in.

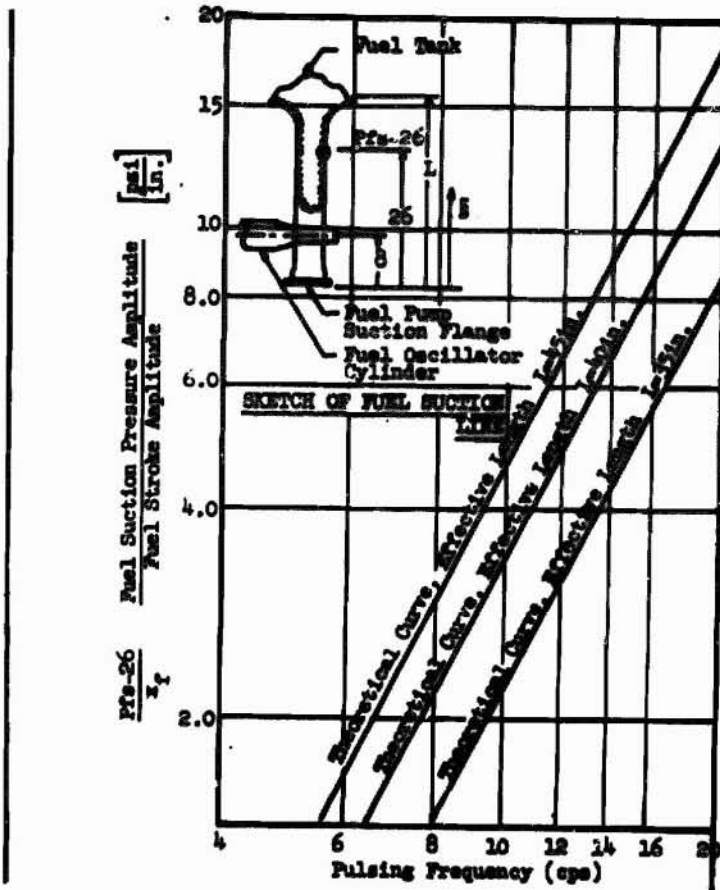
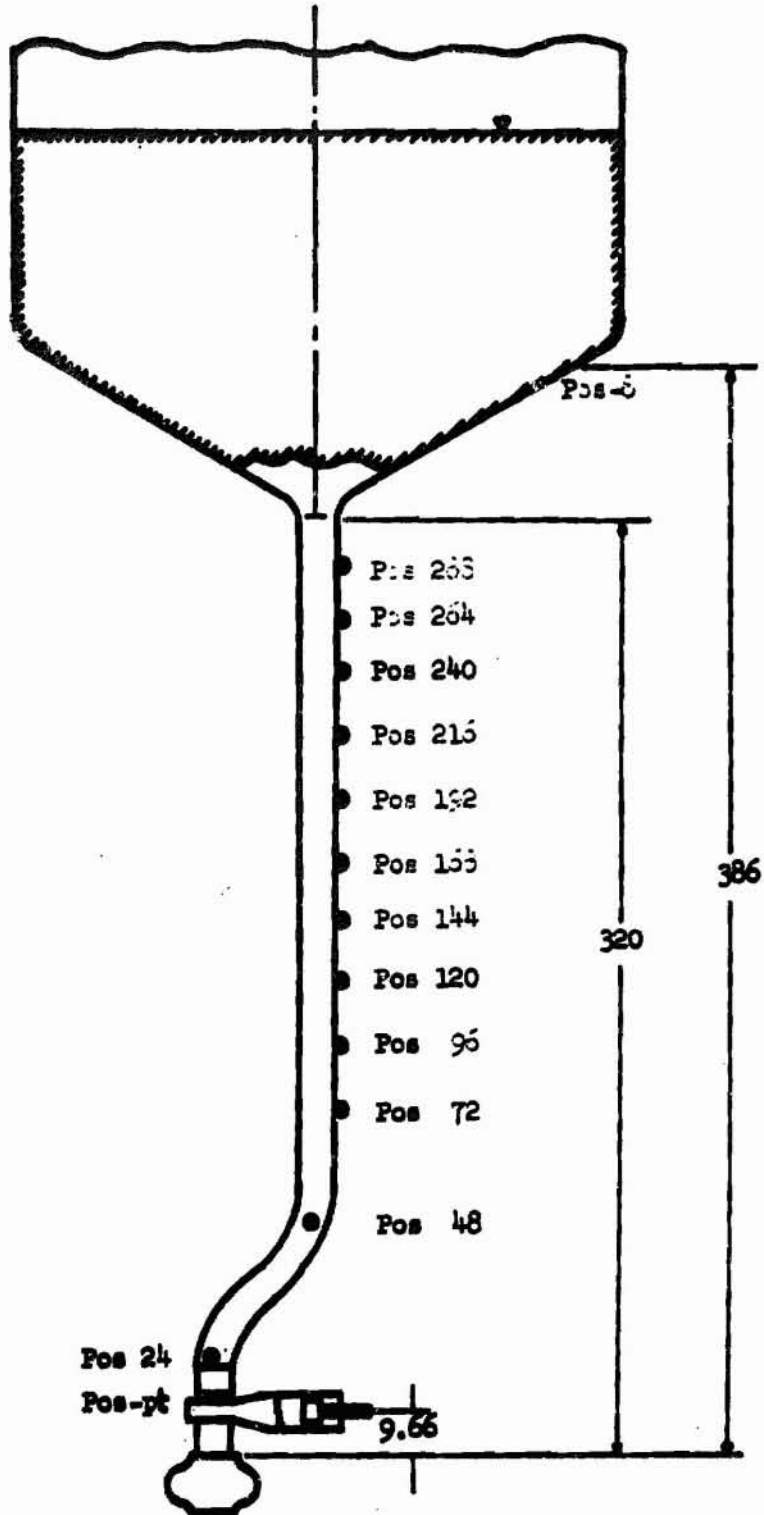


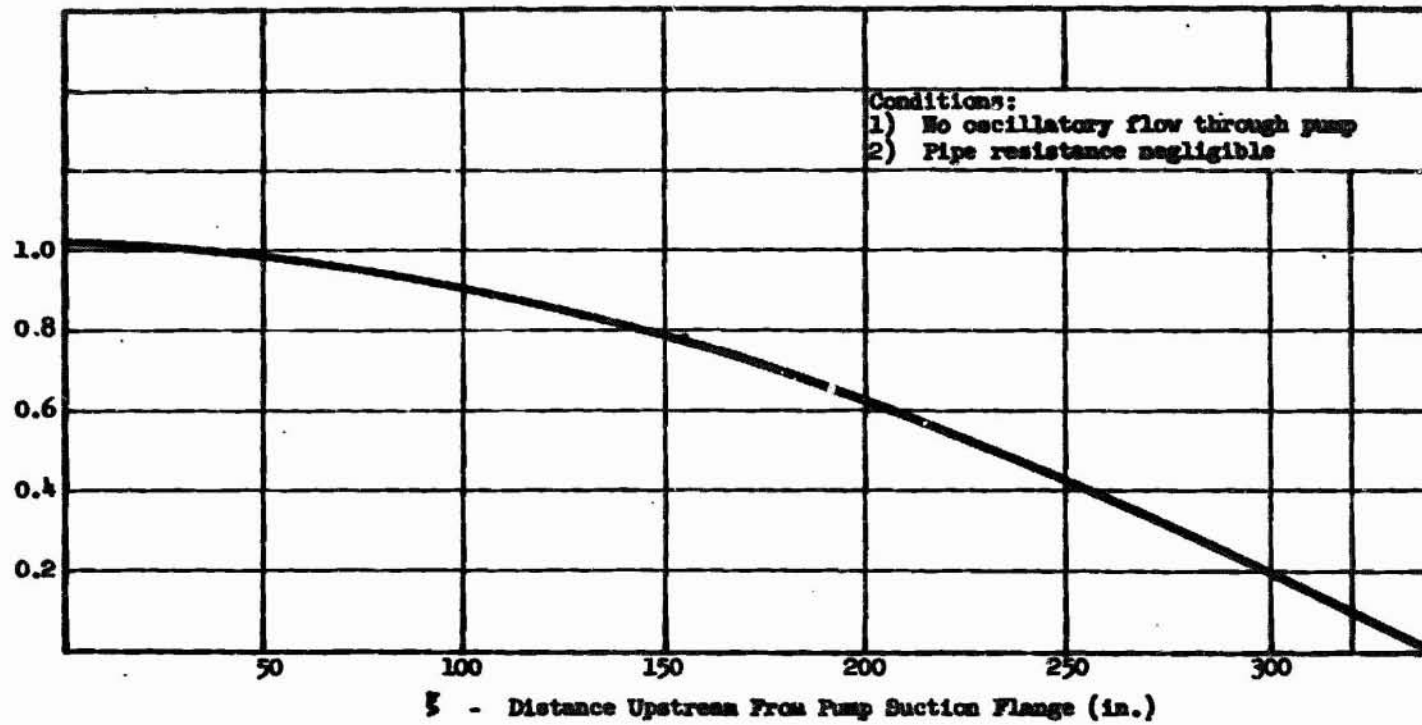
Figure III D-20. Function Pfs-26/Xf vs Driving Frequency for Fuel Section Line Effective Lengths of 35, 40, and 45 in.

Figure III D-19 and Figure III D-20

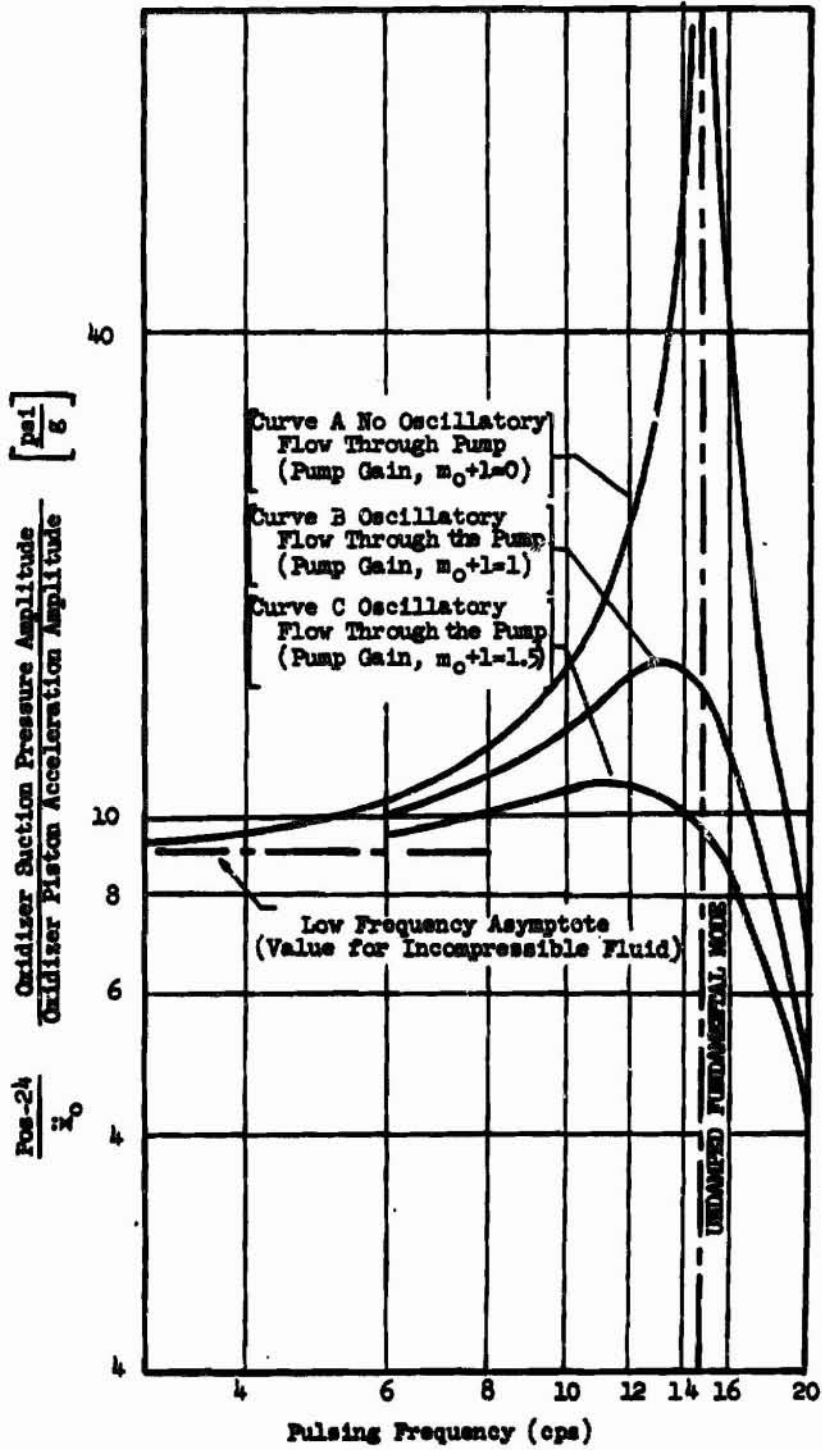


Sketch of Oxidizer Suction Line and Pump

Pos-4
42-502
Suction Pressure at Station
Suction Pressure at $x = 24$ in.



Plot of Oscillatory Pressure Distribution in the Oxidizer Suction Line



Function Pos-24/ x_0 vs Driving Frequency

Figure III D-23

Report BSD-TR-55-54

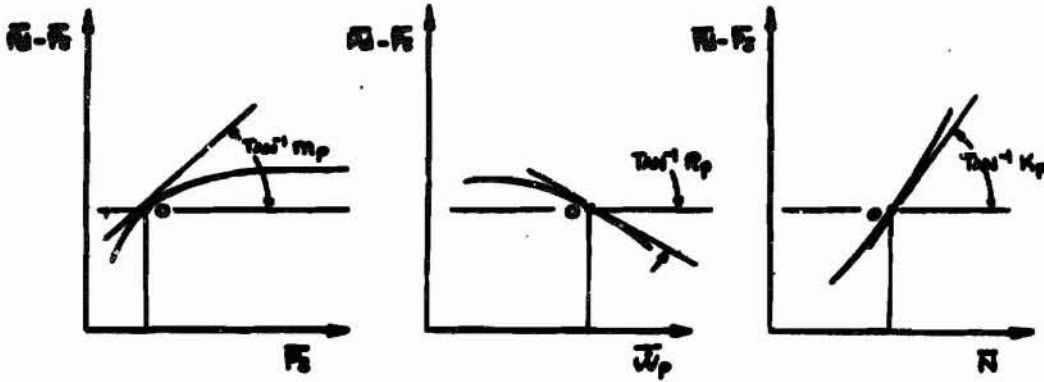


Figure III D-24. Plot of Average Oscillatory Head Rise vs P_s , vs W_p , and vs \bar{N}

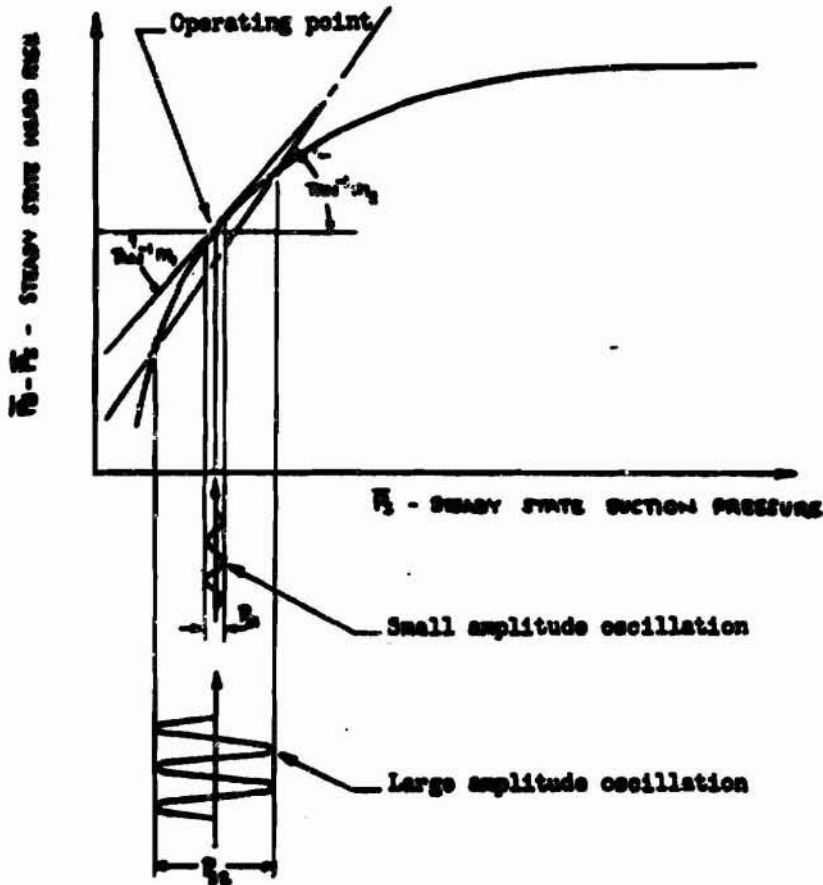
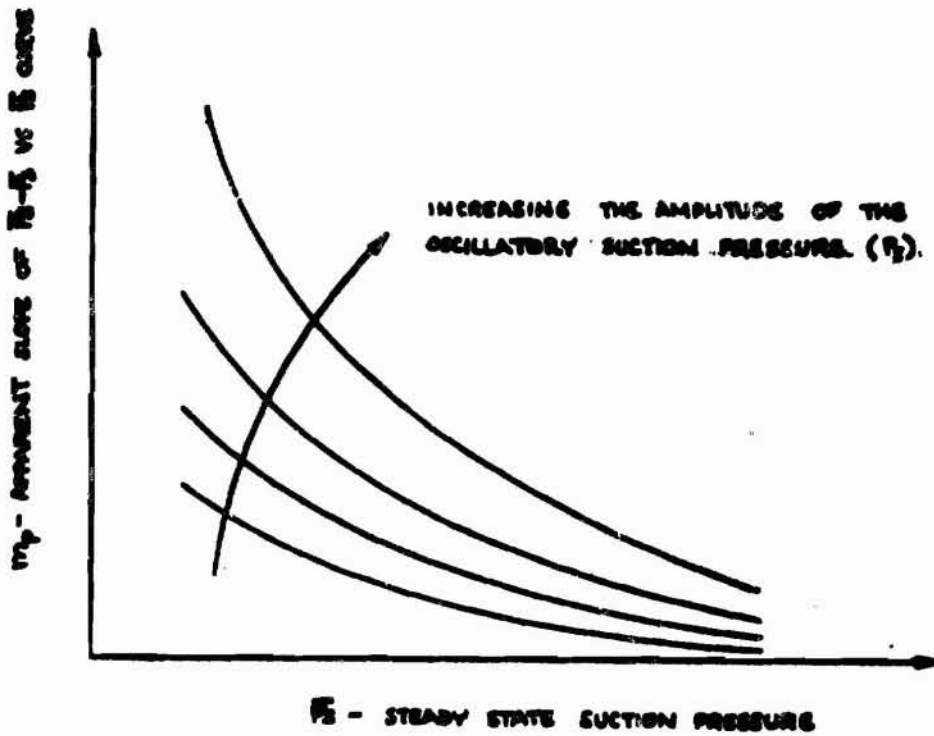


Figure III D-25. Plot of the Effect of Amplitude of Suction Pressure Oscillation on Curve Slope of Oscillatory Head Rise vs P_s Curve

Figure III D-24 and Figure III D-25

Report BSD-TR-65-54



Plot of Pump Gain Showing Nonlinear Effect of \bar{P}_s and P_s

AFSC Technical Report ESD-TR-65-54

APPENDIX A

SYMBOLS USED IN REPORT

PRECEDING PAGE BLANK NOT FILMED.

AFSC Technical Report BSD-TR-65-54, Appendix A

F_{net}	Oscillatory engine thrust amplitude
P_c	Oscillatory thrust chamber pressure amplitude
P_{od}	Oscillatory oxidizer pump discharge pressure amplitude
P_{fd}	Oscillatory fuel pump discharge pressure amplitude
P_{os-0}	Oscillatory oxidizer pump suction pressure amplitude
P_{fs-0}	Oscillatory fuel pump suction pressure amplitude
$\overline{P_{os-0}}$	Nominal oxidizer pump suction pressure
$\overline{P_{fs-0}}$	Nominal fuel pump suction pressure
x_o	Oxidizer piston displacement amplitude
x_f	Fuel piston displacement amplitude
\dot{x}_o	Oxidizer piston velocity amplitude
\dot{x}_f	Fuel piston velocity amplitude
\ddot{x}_o	Oxidizer pulse generator piston acceleration amplitude
\ddot{x}_f	Fuel pulse generator piston acceleration amplitude
\dot{x}_g	Vehicle vibratory acceleration at turbopump assemblies
\dot{m}	Instantaneous oscillatory mass flow
\dot{y}	Instantaneous oscillatory fluid velocity
p	Instantaneous oscillatory pressure
g	Gravitational constant
ρ	Mass density of fluid
m	Mass of fluid
β	Bulk modulus of fluid
d	Diameter of pipe line
t	Thickness of pipe line
P_{CG}	Gas Generator Chamber pressure

AFRC Technical Report ASD-TR-65-54, Appendix A

P_{te}	Turbine exhaust pressure
FOS_{pt}	Oxidiser suction line torus pressure
Pfs_{pt}	Fuel suction line torus pressure
F_{GB-1}	Engine dynamic thrust measured at gimbal block load cell
F_{GB-2}	Engine dynamic thrust measured at gimbal block load cell
LOP	Oxidiser pulse generator piston position
LFP	Fuel pulse generator piston position
P_{fJ}	Thrust chamber fuel injector manifold pressure
P_{oJ}	Thrust chamber oxidiser injector manifold pressure
E	Elastic modulus of pipe line
a	Acoustic velocity of sinusoidal wave within fluid filled pipe line
f	Frequency (cycles/sec)
ω	Circular frequency (radians/sec)
m	Slope of the head-rise versus suction pressure curve
n+1	Pump gain
R_p	Pump resistance (slope of the head-rise versus pump flow curve)
K_p	Pump speed fluctuation constant (slope of the head-rise versus impeller speed curve)
R_d	Hydraulic flow resistance of propellant injector
L_d	Inertance of fluid in pump discharge line
c^*	Characteristic velocity of thrust chamber
A_t	Area of thrust chamber throat
j	$\sqrt{-1}$
s	Laplacian operator
\dot{W}_d	Oscillatory flow in pump discharge line

AFSC Technical Report BDD-TR-65-54, Appendix A

τ_c	Combustion time delay
\approx	is approximately
$<$	is less than
\sim	cycles/sec
Ω	ohms
P_{OT}	Oxidizer tank pressure, psig
P_{FT}	Fuel tank pressure, psig
FS_1	Fire switch one
FS_2	Fire switch two
T_{OT}	Oxidizer tank temperature, °F
T_{OS}	Oxidizer suction line temperature, °F
N_{TS}	Turbopump shaft speed, rpm
T_{FT}	Fuel tank temperature, °F
P_{fJGG}	Gas generator fuel injector manifold pressure
P_{oJGG}	Gas generator oxidizer injector manifold pressure
P_{T1}	Turbine inlet pressure, psi
N_{oFCS}	Fuel piston frequency, cps
N_{oOCS}	Oxidizer piston frequency, cps
\overline{F}_{net}	Nominal subassembly thrust, lb
\overline{P}_c	Nominal chamber pressure, psig
\angle	Phase angle
GTPA	Acceleration, turbopump assembly
GTCB	Acceleration, thrust chamber dome
GEF-5V	Acceleration, fifth point, vertical
GQ4-V	Acceleration, Quad Point 4, Vertical

AFSC Technical Report DSD-TR-65-54, Appendix A

P_{TE}	Turbine hot gas exhaust pressure
P_{CGG}	Gas generator chamber pressure
P_{OBTV}	Oxidizer bootstrap thrust venturi pressure
P_{FBTV}	Fuel bootstrap thrust venturi pressure
G_{TSV}	Acceleration, tank support, vertical
G_{OFL}	Acceleration, oscillator frame, longitudinal
G_{UTR}	Acceleration, upper tank, radial
G_{FLL}	Acceleration, fuel line, longitudinal
G_{MTR}	Acceleration, mid tank, radial
G_{OLL}	Acceleration, oxidizer line, longitudinal
GE-5TSV	Acceleration, tank support, test stand E-5, vertical
GEF5H	Acceleration, fifth point, horizontal
LOPV	Oxidizer pre-valve gate position
LFPV	Fuel pre-valve gate position

AFSC Technical Report ESD-TR-67-54

APPENDIX B

FILTERING METHOD FOR ENGINE TRANSFER FUNCTION DATA

BLANK PAGE

AFSC Technical Report BSD-TR-65-54, Appendix B

1. Wide Band (2-30 cps)

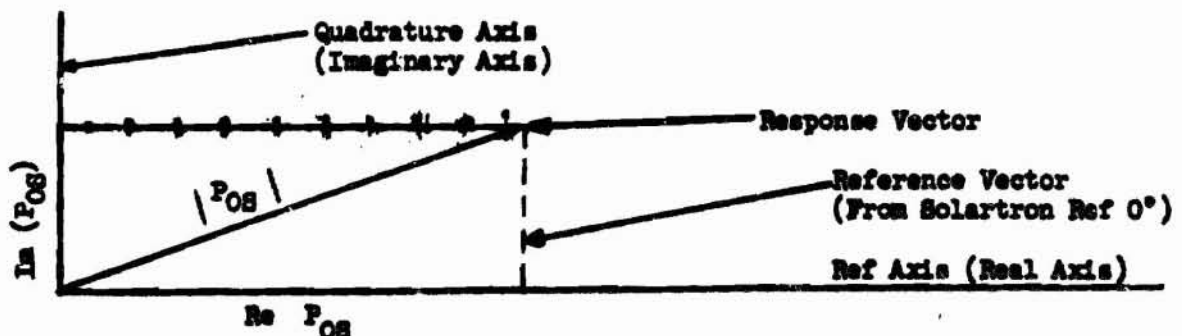
With the exception of accelerometer data, all dynamic data was filtered during POGO testing through a wide-band filter. This filter excluded all frequencies outside of the 2 to 30 cps band. Since the pulse generator frequencies range from 8 to 15 cps, they are included within this band width. Even though the oscillations of suction pressures and related parameters had a component with a relatively large amplitude at the driving frequency, there were also components at other frequencies because of engine operation. Many of these additional components were also within the 2 to 30 cps band width, thus resulting in a complex wave form of the trace for each parameter. This complex wave form had a varying amplitude as a result of the random nature of the noise of the engine system.

2. Narrow Band (less than 5 cps)

After each test, tapes of the parameters recorded for the transfer functions (P_{OG} , F_{Pg} , P_c , and F_{net}) were played through a narrow-band filter of less than 5 cps band width. The center frequency of this band was set at the pulse frequency for each parameter. Since there were five pulse frequencies, there were five settings of center frequency for each playback. Because all extraneous frequencies outside of the pulse frequency were excluded, these transfer function traces more accurately depict the effect of the pulse on the functions than do the wide band traces. Thus, the amplitudes of the transfer functions can be estimated from the narrow-band playback. The phase angle can not be estimated because the narrow band filters were not phase calibrated.

3. Solartron Resolved Component Indicator

The same functions that were analyzed by means of the narrow band filters (P_{OG} , F_{Pg} , P_c , and F_{net}) were finally played back, individually, through the Solartron "Resolved Component Indicator." The signal of each function was electronically compared to the Solartron reference signal (piston frequency). Only that portion of the signal that was at the same frequency as the reference signal was analyzed by the Solartron. The Solartron data was recorded from values indicated by two Solartron dials which provided the "reference" and "quadrature" components of the amplitude of the transfer function oscillation. Thus, the Solartron gives the "in-phase" (actual) and "90° phase-shifted" (imaginary) vectors which, when added vectorally, give the absolute magnitude of the response vector. This relationship is illustrated for P_{OG} below:



AFSC Technical Report BSD-TR-65-54, Appendix B

Thus we see that the amplitude is $|P_{OS}| = \sqrt{Im^2 + Re^2}$

And the phase angle is $\psi = \tan^{-1} \frac{Im}{Re}$

Because there were five discrete frequencies, there were five values of amplitude and of phase angle for each transfer function.

In summary, the Solartron has two advantages over narrow band data: (1) the Phase angle between the selected functions can be determined; (2) the transfer function amplitude is more accurately measured since only that portion of the signal which is at the exact pulse frequency is analyzed. All other signals which would be included within a band width by a band filter are eliminated.

AFSC Technical Report BMD-TR-65-54

APPENDIX C

FOGO INSTRUMENTATION LIST

BLANK PAGE

AFSC Technical Report DSD-TR-65-54, Appendix C

Function	Transducer Type	Gage Range	Calibration Range	AGC Range 1	AGC Range 2	Dib Tests						Runs Used								
						1	2	3	4	5	6	7	8	9	10	11	12			
Ref 0°	Solartron	-----	-----	X	X							X	X	X	X	X	X	X	X	X
Ref 90°	Solartron	-----	-----	X	X							X	X	X	X	X	X	X	X	X
Ref 180°	Solartron	-----	-----	X	X							X	X	X	X	X	X	X	X	X
Ref 270°	Solartron	-----	-----	X	X							X	X	X	X	X	X	X	X	X
FGB-1	Electro Optical	240K lb	20K lb P-P	X	X				X			X	X	X	X	X	X	X	X	X
FGB-2	Electro Optical	240K lb	20K lb P-P	X	X				X			X	X	X	X	X	X	X	X	X
F _{net}	-----	240K lb	20K lb P-P	X	X		X	X	X		X	X	X	X	X	X	X	X	X	X
Pos-48	Micro	100 psi	50 psi P-P		X				X			X	X	X	X					
Pos-96	Micro	100 psi	50 psi P-P		X				X			X	X	X	X	X	X	X	X	X
Pos-144	Micro	100 psi	50 psi P-P		X				X			X	X	X	X	X	X	X	X	X
Pos-192	Micro	100 psi	50 psi P-P		X				X			X	X	X	X	X	X	X	X	X
Pos-240	Micro	100 psi	50 psi P-P		X				X			X	X	X	X	X	X	X	X	X
Pos-288	Micro	100 psi	50 psi P-P		X				X			X	X	X	X	X	X	X	X	X
PTE	Micro	100 psi	(Note 15)		X				X			X	X	X	X	X	X	X	X	X
POGG	Micro	1500 psi	250 psi P-P		X				X			X	X	X	X	X	X	X	X	X
POBTV	Micro	1500 psi	250 psi P-P		X				X			X	X	X	X	X	X	X	X	X
POSTV	Micro	1500 psi	250 psi P-P		X				X			X	X	X	X	X	X	X	X	X
POTS	-----	30K rpm	2000 rpm P-P		X				X			X	X	X	X	X	X	X	X	X
PTSV	S/G ACC	± 5g	2g P-P		X							X	X	X	X	X	X	X	X	X
GMTR-Y	S/G ACC	(Note 20)	2g P-P		X							X	X	X	X	X	X	X	X	X
GMTR-X	S/G ACC	(Note 24)	2g P-P		X							X	X	X	X	X	X	X	X	X
GMTR-Y	S/G ACC	(Note 17)	2g P-P		X							X	X	X	X	X	X	X	X	X
GMTR-X	S/G ACC	± 5g	2g P-P		X							X	X							

AFSC Technical Report DSD-TR-63-54, Appendix C

NOTES (cont.)

- 14. \pm 5g Runs 2, 3; \pm 10g Runs 3, 4, 5, 6; \pm 15g Runs 7, 8
- 15. 50 psi F-P Runs 1, 2, 3; 25 psi F-P Runs 4, 5, 6, 7, 8
- 16. \pm 5g Runs 1, 2, 3, 4; \pm 10g Run 5; \pm 5g Run 6; \pm 15g Runs 7, 8
- 17. \pm 5g Runs 1, 2, 3, 4; \pm 10g Runs 5, 6; \pm 5g Runs 7, 8
- 18. \pm 5g Runs 1, 2, 3, 4; \pm 10g Runs 5, 6; \pm 5g Run 7; \pm 10g Run 8
- 19. \pm 2g F-P Runs 1, 2, 3, 4; \pm 5g F-P Runs 5, 6, 7, 8
- 20. \pm 5g Runs 1, 2, 3, 4, 5; \pm 10g Runs 6, 7, 8
- 21. 2g F-P Runs 1, 2, 3, 4, 5, 6; 5g F-P Runs 7, 8-
- 22. 2g F-P Runs 1, 2, 3, 4, 5, 6, 7; 5g F-P Run 8
- 23. \pm 5g Runs 1, 2, 3, 4, 5, 6, 7; \pm 10g Run 8
- 24. \pm 5g Runs 1, 2, 3, 4, 5, 6, 7; \pm 10g Run 8

AFSC Technical Report DSD-TR-65-54, Appendix C

QEC 4-202

STRAIN GAGE ACCELEROMETER

Cross axis sensitivity	< 0.01 g/g full 3 times gage range
Input Z	≈ 390
Output voltage	32-40mv full scale
Linearity & hysteresis	< 0.75% full range
Damping	0.7 ± 0.1
Output Z	≈ 350 Ω
Natural frequency	
+ 5g	300
+ 10g	400
+ 15g	530
Temperature range	-70°F to +300°F
Thermal zero shift	< 0.01% full range/°F
Thermal sensitivity	< 0.01% full range/°F

MICRO PT 3J-2C

Linearity & hysteresis & temperature	± 0.5%
Bridge resistance	500 Ω (nominal)
Output voltage	500 mv ± 3.5 mv

SANGAMO TAPE RECORDER

Input Z	20K Ω
Output Z	< 50 Ω
Output current	± 10 ma
Frequency response	DC-5KC, ± 1/2 dB at 30 IPS
Center frequency	2.7KC @ 30 ips
SN ratio	≈ 48db

AFSC Technical Report BSD-TR-65-54, Appendix C

DC drift	< 1% full scale per 10°F
DC linearity	< 1% full scale
Distortion	< 1% total harmonic distortion

EQUIPMENT SPECIFICATIONS

KAYLAB 110DC AMPLIFIER

Gain accuracy	± 1% dc
Input Z	100,000 Ω
Output Z	< 1 Ω
Output capability at dc	0 to + 25V, 0 to + 25 ma (with Load < 1000 Ω)
Linearity	< 0.1% to 2Kc
Frequency response	+ 3% dc to 10Kc; < 3dB Down at 30Kc
Phase shift	< 5° to 2Kc

KAYLAB 111 DC AMPLIFIER

Gain accuracy	± 1% dc to 2Kc
Input Z	100,000 Ω
Output Z	< 1 Ω
Output capability dc	0 to ± 35V (Load < 1000 Ω)
Linearity	< 0.1% dc to 2Kc
Frequency response	+ 3% dc to 10 Kc; < 3dB Down at 40Kc
Phase shift	< 5° to 2Kc

AFSC Technical Report BSD-TR-65-54, Appendix C

DYTRONICS 722 FILTER

Accuracy of cutoff frequency	$\pm 3\%$
Rate of attenuation	36db/octave or 72 db/Octave when cascaded
Attenuation in passband	$\approx 2DB$
Maximum output voltage (Load Z 10K)	10VP-P, 0.1% Dist. 20VP-P, 0.2% Dist. 40VP-P, 1% Dist. 65VP-P, 1.5% Dist.
Maximum peak input voltage	200v
Output current	± 5 ma
Input Z	1 meg Ω
Output Z	High Pass 650 Ω Low Pass 1100 Ω

AEROJET HIGH-PASS FILTER

Cut-off frequency	3db down at 1.5 cps with Z > 10K Ω
Rate of attenuation	6db/octave AVERAGE
Attenuation in passband	< 6DB with Z > 10K Ω
Maximum input voltage	100v P-P
Maximum output voltage	> 30V P-P at > 2cps
Input Z	$\approx 15K \Omega$
Output Z	$\approx 500 \Omega$
Phase shift	< 9° at > 1.5 cps

AFSC Technical Report DSD-TR-65-54, Appendix C

SOLARTRON RESOLVED COMPONENTS INDICATOR

Frequency range	0.1 cps - 1K cps
Input Z	10 meg Ω
Accuracy	\pm 3% full-scale deflection
Harmonic rejection	> 40 db

SOLARTRON L. F. DECADE OSCILLATOR

Frequency range	0.01 cps to 11.1 kc
Accuracy	$<$ \pm 2%
Output Z (0° & 180°)	$<$ 10 Ω
Harmonic distortion	$<$ 2%
Amplitude stability	\pm 5%

SOLARTRON REFERENCE GEN.

Speed range	0 to 6000 rpm
Phase errors	$<$ 1°
Residual noise	$<$ 2%
Output	4 Phases, 10v/phase
Amplitude stability	\pm 1%

MICROSYSTEMS FG6-C1 LOAD CELL

Range	0 to 240,000 lb
Combined inaccuracies & thermal shift	\approx \pm 0.6%
Thermal shift	0.01% per F°
Repeatability	$<$ \pm 0.25%
Bridge resistance	500 Ω nominal

AFSC Technical Report 225-TR-65-54

APPENDIX D

METHOD OF CALCULATION OF PUMP INLET PRESSURES
FROM TANK BOTTOM PRESSURES

BLANK PAGE

AFSC Technical Report ASD-TR-65-54, Appendix D

1. General

Adjustment and control of nominal pressures in the engine parameters is difficult because any pressure monitored in the suction lines has a large amplitude oscillation during pulsing. Therefore, it was decided to monitor and maintain the required nominal suction pressures (pump inlet) at some location where the pulsations would be dampened. The locations selected were the bottom pressure taps of the two tanks (oxidizer and fuel). Pressures monitored at these taps would not be affected by the pulsing system, because the pressure oscillations induced in the suction lines would dissipate upon entering the large volume of their respective tanks.

2. Terminology

P_{ft-B}	= fuel tank bottom pressure (psia)
P_{ot-B}	= oxidizer tank bottom pressure (psia)
P_{fs-O}	= fuel pump inlet nominal pressure (psia)
P_{os-O}	= oxidizer pump inlet nominal pressure (psia)
P_L	= respective (oxidizer or fuel) pressure drop in suction line (psi)
P_{valve}	= respective pressure drop across pre-valve (psi)
P_{vel}	= respective static pressure drop due to velocity head (ft/sec)
P_{gh}	= respective pressure gain due to gravity head (psi)
\dot{W}	= propellant flow rate (lb/sec)
D	= diameter of respective suction line (in.)
h	= height of tank bottom tap above its respective pump inlet (in.)
σ	= respective propellant specific gravity

AFSC Technical Report B&D-TR-65-54, Appendix D

3. Fuel System

a. Known Values

- P_L = 0.2 psi (supplied by Martin Co.)
 P_{valve} = 2.6 psi (supplied by Martin Co.)
 \dot{W} = 282 lb/sec (no flowmeters; calculated from pressure drops and nominal system resistances)
 \dot{W} = 0.901
 D = 6 in.
 h = 52.5 in.

b. Calculations

- (1) $P_{gh} = .0361 \sigma h$
 $P_{gh} = .0361 (.901) (52.5)$
 $P_{gh} = 1.7 \text{ psi}$
 (2) $P_{\text{vel}} = .05811 W^2 / \sigma (D)^4$
 $P_{\text{vel}} = .05811 (282)^2 / (.901) (6)^4$
 $P_{\text{vel}} = 4.3 \text{ psi}$
 (3) $P_{\text{ft-B}} = (P_{\text{fs-O}}) + P_L + P_{\text{valve}} + P_{\text{vel}} - P_{gh}$
 $P_{\text{ft-B}} = (P_{\text{fs-O}}) + 0.2 + 2.6 + 4.3 - 1.7$
 $P_{\text{ft-B}} = (P_{\text{fs-O}}) + 5.4 \text{ psi}$

4. Oxidizer System

a. Known Values

- P_L = 3.5 psi (supplied by Martin Co.)
 P_{valve} = 2.4 psi (supplied by Martin Co.)
 \dot{W} = 546 lb/sec (no flowmeters; calculated from pressure drops and nominal system resistances)
 \dot{W} = 1.439
 D = 7 in.
 h = 362.5 in.

AFSC Technical Report DD-TR-65-54, Appendix D

b. Calculations

$$(1) P_{gh} = .0361 \sigma h$$

$$P_{gh} = (.0361) (2.439) (362.5)$$

$$P_{gh} = 18.84 \text{ psi}$$

$$(2) P_{vel} = .05811 W^2 / \sigma (D)^4$$

$$P_{val} = (.05811) (546)^2 / (1.439) (7)^4$$

$$P_{vel} = 5.02 \text{ psi}$$

$$(3) P_{ot-B} = (P_{os-O}) + P_L + P_{valve} + P_{vel} - P_{gh}$$

$$P_{ot-B} = (P_{os-O}) + 3.5 + 2.4 + 5.02 - 18.84$$

$$P_{ot-B} = (P_{os-O}) - 7.9 \text{ psi}$$

AFSC Technical Report DSD-TR-63-54

APPENDIX E

**LIST OF SPECIAL ENGINE HARDWARE USED
DURING TESTING**

*RECORDING PAGE BLANK - NOT FILMED.

AFSC Technical Report BMD-TR-65-54, Appendix E

<u>PN</u>	<u>Description</u>
298332	Modification Kit
265382-9	Oxidizer Discharge Line
286981-1	Boss
286993-1	Boss
287035-19	Injector
287050-1	Dome
298333-9	Fuel Suction Line
298334-9	Oxidizer Suction Line
298335-9	Oxidizer Discharge Line
298336-9	Fuel Suction Line
298337-1	Clevis, Mounting
298338-1	Clevis, Mounting
298339-9	Bracket, Support
298340-1	Bracket, Support
298341-1	Bracket, Angle
298342-9	Oxidizer Torus
298343-9	Fuel Torus
298344-1	Body Connecting Link
298344-3	Body Connecting Link
298345-1	Closure Torus
248467	Load Cell Gimbal Block (Not part of Mod Kit 298332)

Note: The above hardware was added or installed in accordance with the basic engine configuration shown in PN 277640-29. Only SAI was mounted on engine frame.

REPRODUCIBILITY OF THE ORIGINAL PAGE IS POOR

AFSC Technical Report DDC-TR-65-54

APPENDIX F
COMPARISON DATA

NO COPY PAGE SEAM-NOX-FILMED.

AFSC Technical Report ASD-TR-65-54, Appendix F

The Solartron data summary for Tests 4.0-15, RJA-002, -003, -004, -006, -007, and -008 is provided in the following tables. Each test is assigned one or more sweep numbers which identify the various frequency sweeps conducted during the tests. The frequency sweeps are distinguished in accordance with the fuel and oxidizer suction pressures which were maintained during each sweep and in accordance with the value in cycles per second assigned to each frequency step.

Various frequency response functions (expressed as ratios) are listed in the "function" column of the tables. A frequency response function is defined, for any function in the engine system, as the complex ratio of oscillatory output to the oscillatory input. For example, a specific frequency-response function would be the complex ratio of oscillatory thrust chamber pressure to the oscillatory fuel pump suction pressure. During engine testing, data on the oscillatory amplitudes of the two engine parameters for each frequency response function were obtained for all the frequency steps of pulse generator operation. The ratios of the absolute amplitudes were then tabulated as shown for each frequency level.

Following the entry for each frequency response function amplitude in the table is the corresponding data on the phase angle between the oscillations of the two frequency-response function parameters (designated \angle) that were obtained for each frequency step. The phase angle of the frequency response function is given as the number of degrees in rotation that the phase of the output parameter oscillation is advanced (when positive) or retarded (when negative) from that of the input parameter oscillation.

Further details concerning Solartron resolved component data are discussed in Appendix B, Part 3 and in Section III, B, 4, Data Reduction.

REPRODUCIBILITY OF THE ORIGINAL PAGE IS POOR

BLANK PAGE

Report BSD-TR-65-54

TABLE 2

TEST 4.0-15-RJA-003 SOLARTRON DATA SUMMARY

SUBJECT		DATE
POGO SOLARTRON DATA SUMMARY		WORK ORDER
FOR RUN NO. 4.0-15-RJA-003		DATE
BY	CHK BY	DATE
MEISENHOLDER	M'CALISTER	10 JAN 64

A. TEST SCHEDULE

TIME FROM PS-1 T (SEC)	MINIMAL OIL SECTION PRESS. POS (MG)	MINIMAL FUEL SECTION PRESS. FPS (MG)	REMARKS

B. TABULATION OF THE AMPLITUDE & PHASE OF THE DYNAMIC DATA AS A FUNCTION OF THE DRIVING FREQUENCY (SOLARTRON DATA)

FUNCTION	DRIVING FREQUENCY (CPS) REGO = 100 PMA					DRIVING FREQUENCY (CPS) REGO = 68 PMA					DRIVING FREQUENCY (CPS)	REMARKS
	16	18	11	9.5	8	18	11	9.5	8			
	AMPLITUDE (P-P)					AMPLITUDE (P-P)					AMPLITUDE (P-P)	
PS-1 FOR 1	.248	.261	.244	.208	.267	.293	.279	.275	.287	.297		
∠	-9	-5	-1	+2	-1	-10	-3	-2	-1	-4		
PS-1 FOR 2												
∠												
PS-1 FOR 3	.458	.54	.525	.52	.577	.496	.495	.521	.546	.599		
∠	-45	-35	-33	-30	-32	-46	-38	-30	-26	-15		
PS-1 FOR 4	.152	.278	.284	.178	.188	.272	.204	.398	.581	.316		
∠	-47	-89	-37	12	-34	-58	-47	-46	-34	-22		
PS-1 FOR 5	.204	.21	.206	.182	.206	.316	.328	.348	.359	.334		
∠	-37	-31	-31	-21	-22	-54	-36	-32	-25	-11		
PS-1 FOR 6	.332	.516	.54	.393	.325	.546	.614	.647	.604	.579		
∠	-2	-3	-4	42	-2	-12	-9	-16	-8	-7		
PS-1 FOR 7	.446	.387	.392	.349	.398	.634	.688	.657	.656	.609		
∠	8	4	2	9	10	-8	2	-2	1	4		
PS-1 FOR 8	7.6	14.1	14.1	12.5	10	3.7	3.5	7.1	9.7	10.1		
∠	116	151	182	200	205	114	118	182	185	162		ALL DATA RELAYED TO BE CRUCIAL
PS-1 FOR 9	1.341	.754	.724	1.018	1.07	1.16	1.12	1.013	1.088	1.06		
∠	10	7	6	-33	12	4	11	14	9	11		

Table 2

Report BSD-TR-65-54

TABLE 3 (cont.)

SUBJECT		DATE
POGO SOLARTRON DATA SUMMARY		WORK ORDER
FOR RUN NO. <u>40-15-RJA-006</u>		DATE
BY	CHK. BY	DATE
<u>MCCALISTER</u>		

A. TEST SCHEDULE

TIME FROM PE-1 T (SEC)	NOMINAL DR. SECTION FREQ. FPS (Hz)	GENERAL FREQ. SECTION FREQ. FPS (Hz)	REMARKS

B. TABULATION OF THE AMPLITUDE & PHASE OF THE DYNAMIC DATA AS A FUNCTION OF THE DRIVING FREQUENCY (SOLARTRON DATA)

FUNCTION	DRIVING FREQUENCY (CPS)					DRIVING FREQUENCY (CPS)					DRIVING FREQUENCY (CPS)					REMARKS
	15	13	10.5	9.4	8	15										
	AMPLITUDE (P-P)					AMPLITUDE (P-P)					AMPLITUDE (P-P)					
<u>PE-1</u>																
<u>PE-2</u>																
<u>PE-3</u>																
<u>PE-4</u>																
<u>PE-5</u>																
<u>PE-6</u>																
<u>PE-7</u>																
<u>PE-8</u>																
<u>PE-9</u>																
<u>PE-10</u>																
<u>PE-11</u>																
<u>PE-12</u>																
<u>PE-13</u>																
<u>PE-14</u>																
<u>PE-15</u>																
<u>PE-16</u>																
<u>PE-17</u>																
<u>PE-18</u>																
<u>PE-19</u>																
<u>PE-20</u>																
<u>PE-21</u>																
<u>PE-22</u>																
<u>PE-23</u>																
<u>PE-24</u>																
<u>PE-25</u>																
<u>PE-26</u>																
<u>PE-27</u>																
<u>PE-28</u>																
<u>PE-29</u>																
<u>PE-30</u>																
<u>PE-31</u>																
<u>PE-32</u>																
<u>PE-33</u>																
<u>PE-34</u>																
<u>PE-35</u>																
<u>PE-36</u>																
<u>PE-37</u>																
<u>PE-38</u>																
<u>PE-39</u>																
<u>PE-40</u>																
<u>PE-41</u>																
<u>PE-42</u>																
<u>PE-43</u>																
<u>PE-44</u>																
<u>PE-45</u>																
<u>PE-46</u>																
<u>PE-47</u>																
<u>PE-48</u>																
<u>PE-49</u>																
<u>PE-50</u>																
<u>PE-51</u>																
<u>PE-52</u>																
<u>PE-53</u>																
<u>PE-54</u>																
<u>PE-55</u>																
<u>PE-56</u>																
<u>PE-57</u>																
<u>PE-58</u>																
<u>PE-59</u>																
<u>PE-60</u>																
<u>PE-61</u>																
<u>PE-62</u>																
<u>PE-63</u>																
<u>PE-64</u>																
<u>PE-65</u>																
<u>PE-66</u>																
<u>PE-67</u>																
<u>PE-68</u>																
<u>PE-69</u>																
<u>PE-70</u>																
<u>PE-71</u>																
<u>PE-72</u>																
<u>PE-73</u>																
<u>PE-74</u>																
<u>PE-75</u>																
<u>PE-76</u>																
<u>PE-77</u>																
<u>PE-78</u>																
<u>PE-79</u>																
<u>PE-80</u>																
<u>PE-81</u>																
<u>PE-82</u>																
<u>PE-83</u>																
<u>PE-84</u>																
<u>PE-85</u>																
<u>PE-86</u>																
<u>PE-87</u>																
<u>PE-88</u>																
<u>PE-89</u>																
<u>PE-90</u>																
<u>PE-91</u>																
<u>PE-92</u>																
<u>PE-93</u>																
<u>PE-94</u>																
<u>PE-95</u>																
<u>PE-96</u>																
<u>PE-97</u>																
<u>PE-98</u>																
<u>PE-99</u>																
<u>PE-100</u>																

Report BSD-TR-65-54

TABLE 4

TEST 4.0-15-RJA-006 SOLARTRON DATA SUMMARY

P060 SOLARTRON DATA SUMMARY FOR RUN NO. <u>40-15-RJA-006</u>		DATE <u>7 FEB 65</u>
BY <u>MEISENHOLDER</u>	CHK. BY	DATE

A. TEST SCHEDULE

TIME FROM FS - 1 T (SEC)	APPROXIMATE DEFLECTION PERCENT PDS (M)	APPROXIMATE DEFLECTION PERCENT PFS (M)	REMARKS

B. TABULATION OF THE AMPLITUDE | PHASE OF THE DYNAMIC DATA AS A FUNCTION OF THE DRIVING FREQUENCY (SOLARTRON DATA)

FUNCTION	DRIVING FREQUENCY (CPD) PFS = 26 PMA / PDS = 70 PMA					DRIVING FREQUENCY (CPD)					DRIVING FREQUENCY (CPD)					REMARKS
	5.0	14.6	13	12	10.8											
	AMPLITUDE (P-P)					AMPLITUDE (P-P)					AMPLITUDE (P-P)					
FS - 1	.170	.286	.120	.256	.227											
L	+51	+45	+56	+81	+63											
FS - 2	.397	.602	.362	.401	-											
L	+12	-28	+17	+11	-											
FS - 3	.286	.325	.291	.368	.250											
L	+2	-6	+14	-12	-10											
FS - 4	.098	.125	.087	.137	.157											
L	-17	-46	-26	-13	-36											
FS - 5	.295	.280	.325	.350	.291											
L	-40	-43	-30	-33	-31											
FS - 6	1.30	1.45	.97	1.0	.88											
L	-36	-39	-14	-25	-26											
FS - 7	4.63	4.20	3.75	3.56	1.49											
L	+7	-3	-4	+10	+5											
FS - 8	11.2	11.5	11.1	7.3	5.6											
L	+11	+7	+12	+18	+10											
FS - 9																
L																
FS - 10	2.85	2.74	2.27	2.86	3.75											
L	+4	+10	+16	+8	+5											

Table 4

Report BSD-TR-65-54

TABLE 5 (cont.)

PD&O SOLARTRON DATA SUMMARY FOR RUN NO. <u>40-15-RTA-007</u>		DATE <u>8 FEB 64</u>
BY	<u>HEISSHOLDER</u>	DATE <u>8 FEB 64</u>

A. TEST SCHEDULE

TIME FROM PE -1 T (SEC)	GENERAL DEL. SECTION FREQ. FDS (Hz)	GENERAL DEL. SECTION FREQ. FPS (Hz)	REMARKS

B. TABULATION OF THE AMPLITUDE & PHASE OF THE DYNAMIC DATA AS A FUNCTION OF THE DRIVING FREQUENCY (SOLARTRON DATA)

FUNCTION	DRIVING FREQUENCY (CPD)					DRIVING FREQUENCY (CPD)					DRIVING FREQUENCY (CPD)					REMARKS
	15.2	12.8	10.9	9.4	8.2	14.9	13.1	10.8	9.4	8.2	6.75	5.6				
	AMPLITUDE (P-P)					AMPLITUDE (P-P)					AMPLITUDE (P-P)					
PC-1	.256	.291	.259	.274	.265	.256	.282	.257	.184	.222	.199	.267				
∠	-22	-7	-3	+2	+3	-10	+3	-6	-25	-11	-8	+9				
PC-2	1.22	.96	.95	1.09	1.01	1.03	1.04	1.04	.70	1.0	.81	1.05				
∠	+22	-6	+1	+5	+1	-10	+4	-1	-24	-10	-13	+12				
PC-3	.672	.510	.602	.625	.617	.700	.641	.646	.597	.280	.785	.842				
∠	-32	-2	+1	0	-5	-7	-5	0	-9	-8	+2	0				
PC-4	.846	.303	.412	.429	.405	.557	.445	.547	.492	.302	.480	.912				
∠	-53	-36	-28	-21	-24	-41	-38	-21	-20	-16	-9	+19				
PC-5	.249	.212	.302	.280	.254	.307	.234	.274	.267	.297	.280	.281				
∠	-52	-37	0	-29	-26	-57	-50	-30	-39	-48	-28	41				
PC-6	.272	.231	.276	.322	.290	.260	.400	.345	.288	.377	.266	.278				
∠	-48	-31	-24	-21	-15	-71	-47	-28	-33	-26	-14	+6				
PC-7	.788	.70	1.24	.65	.62	.55	.57	.67	.62	.58	.65	.26				
∠	+1	-1	-128	-8	-2	-16	-12	-9	-11	-32	-19	-20				
PC-8	.862	.77	.74	.75	.71	.47	.90	.84	.67	.75	.59	.30				
∠	+5	+5	+4	0	+9	-30	-9	-7	-5	-10	-5	-13				
PC-9	3.68	7.53	14.5	13.9	14.0	4.3	5.5	11.0	14.8	14.1	14.7	10.7				
∠	-140	-133	-113	-80	-59	-126	-132	-119	-82	-60	-31	-19				
PC-10	1.12	1.09	.59	1.15	1.14	.85	1.57	1.26	1.08	1.27	1.03	1.13				
∠	+4	+6	-24	+8	+11	-14	+3	+2	+6	+22	+14	+7				

Report ESD-TR-65-54

TABLE 6

TEST 4.0-15-RJA-008 SOLARTRON DATA SUMMARY

P060 SOLARTRON DATA SUMMARY FOR RUN NO. 4.0-15-RJA-008		FORM 0008
BY MEISENHOLDER	DATE BY	DATE 18 JAN 65

A. TEST REQUIRE

TIME FROM P0-1 T (SEC)	ADDITIONAL OR- BETION FREQ F06 (Hz)	GENERAL PUL- SATION FREQ F05 (Hz)	REMARKS

B. TABULATION OF THE AMPLITUDE & PHASE OF THE RESPONSE DATA AS A
FUNCTION OF THE DRIVING FREQUENCY (SOLARTRON DATA)

FUNCTION	PART 1 DRIVING FREQUENCY (CFP) F05 = 26.821A					PART 2 DRIVING FREQUENCY (CFP) F05 = 31.821A					PART 3 DRIVING FREQUENCY (CFP) F05 = 24.821A					REMARKS
	20	17.1	15.0	12.8	11.8	20	17.1	15.0	12.8	11.2	17.1	15.0	12.8	11.1	9.5	
	AMPLITUDE (P-P)					AMPLITUDE (P-P)					AMPLITUDE (P-P)					
F05	.08	.26	.34	.14	.23	.67	.20	.20	.15	.27	.27	.12	.18	.15	.22	
∠	-2	-12	+23	+7	+7	+12	+12	+63	+16	+17	+2	+18	+14	+11	+28	
F06	1.1	1.8	.80	1.1	.9	.34	.48	.21	1.0	.79	1.0	.99	.71	.74	.82	
∠	-2	+22	+6	+26	-11	+4	+28	+18	-2	+22	-2	+27	+7	0	+28	
F07	.50	.28	.28	.64	.78	.48	.28	.28	.79	.34	.28	.48	.45	.28	.22	
∠	+16	+45	-19	+19	+4	+12	+18	-45	-1	-18	0	-18	-15	0	0	
F08	.15	.070	.104	.177	.220	.14	.070	.087	.29	.16	.12	.12	.16	.18	.22	
∠	-48	-15	-70	-53	-63	-34	-38	-117	-66	-25	-45	-24	-60	-45	-27	
F09	.20	.075	.11	.18	.16	.26	.18	.18	.48	.27	.35	.48	.28	.28	.22	
∠	-49	-9	-51	-23	-18	-72	-44	-114	-62	-23	-30	-2	-55	-35	-45	
F10	.39	.16	.20	.35	.28	.48	.22	.22	.67	.37	.408	.41	.50	.50	.48	
∠	-52	-18	-66	-44	-36	-67	-41	-107	-52	-28	-78	-73	-45	-22	-22	
F11	1.21	1.06	1.02	.85	.70	1.89	1.59	1.48	1.65	1.66	4.25	2.98	2.10	1.85	1.72	
∠	-1	+6	+18	+30	+45	-18	-6	+2	+4	+26	-45	+23	+5	+10	-8	
F12	2.52	2.25	2.28	2.0	1.5	3.2	3.1	2.5	2.3	2.3	3.2	3.5	3.2	2.0	2.2	
∠	-4	-3	+4	+9	+27	-13	-2	+10	+18	+27	-32	+1	+15	+28	+11	
F13	.40	.42	.39	.40	.33	.48	.42	.40	.40	.40	.45	.48	.44	.44	.42	
∠	-24	-19	-16	-18	-18	-25	-17	-20	-8	-18	-28	-24	-24	-27	-20	
F14	1.92	2.08	2.13	2.34	2.14	1.68	1.65	1.65	1.40	1.87	1.35	1.67	1.52	1.89	1.28	
∠	-3	-9	-15	-21	-18	+5	-3	+7	+9	+1	+12	-22	+18	+13	+19	

Table 6

REPRODUCIBILITY OF THE ORIGINAL PAGE IS POOR

AFSC Technical Report E&D-TR-65-34

APPENDIX G

FIGURES

B. (cont.)

If this equation is written as a set of linear equations, the direct method for the measurement of the matrix $\bar{Y}(\omega)$ should become obvious

$$\left\{ \begin{array}{l} \dot{V}_1^s(\omega) = Y_{11}(\omega)P_1(\omega) + Y_{12}(\omega)P_2(\omega) + \dots + Y_{1n}(\omega)P_n(\omega) \\ \vdots \\ \dot{V}_j^s(\omega) = Y_{j1}(\omega)P_1(\omega) + \dots + Y_{jk}(\omega)P_k(\omega) + \dots + Y_{jn}(\omega)P_n(\omega) \\ \vdots \\ \dot{V}_n^s(\omega) = Y_{n1}(\omega)P_1(\omega) + \dots + Y_{nn}(\omega)P_n(\omega) \end{array} \right. \quad (2)$$

where $\dot{V}_j^s(\omega)$ = complex amplitude of oscillatory flow into the j^{th} port
 $P_k(\omega)$ = complex amplitude of oscillatory pressure at k^{th} port
 $Y_{jk}(\omega)$ = admittance matrix coefficient.

From eq (2) it is seen that the definition of each admittance coefficient is obtained by setting all but the k^{th} oscillatory pressure to zero:

$$Y_{jk}(\omega) = \frac{\dot{V}_j^s(\omega)}{P_k(\omega)} \Big|_{\text{only } P_k(\omega) \neq 0} \quad (3)$$

Physically, the direct measurement of the k^{th} column of the admittance matrix may be achieved by applying an oscillatory pressure at the k^{th} port while measuring the oscillatory flow at each of the other ports. By consecutively pulsing all n ports, the entire admittance matrix may be defined. These ports must be short-circuited by connecting them to zero load impedances so that all

B. (cont.)

oscillatory pressures except the source pressure are zero. In other words, the total pressures (oscillatory plus mean) must be kept constant at these ports. This short-circuiting might be done by inserting sidebranch resonators or large capacitance accumulators at all ports of the element. If resonators were used, then they would be "tuned" to obtain a very small impedance at the pulsing frequency. Tuning would be achieved while the pulser is operating at a constant frequency by varying the volume of gas in the resonator cavity until the oscillatory pressure amplitude in the gas cavity is maximized. However, this method of directly measuring the admittance matrix is not recommended because of the laborious resonator tuning procedure.

The use of accumulators to establish the proper boundary conditions for admittance measurement has recently been attempted by investigators of fluidic (fluid amplifier) devices. The measurement technique, which is reported in bibliography entries H.2 and H.3, requires that each port other than the source port be terminated by an accumulator with very large capacitance. By use of expansion chambers with cross sectional areas much larger than each port, the investigators were quite successful in measuring the admittance matrix of a fluidic amplifier at low frequencies. However, this procedure is only applicable to a laboratory experiment since it requires the time-consuming removal and reinstallation of certain pulsers and accumulators prior to each pulsing condition. Therefore, since both methods of directly measuring the admittance matrix of an n-port hydraulic element are impractical for industrial use, an indirect method must be derived.

G. INDIRECT ADMITTANCE MEASUREMENT

The establishment of the ideally free conditions at each port in an n-port network is often so difficult as to preclude the direct measurement of the admittance matrix. Therefore, it is desirable to develop an indirect measurement technique to allow admittance measurement when some or all of the ports are dynamically constrained by some non-zero load impedance. This method, which is equivalent to that derived in bibliography entry H.17 for structural systems, will allow the dynamic loading effect of the constraining network to be analytically removed from the pulse test data.

Consider the constrained n-port hydraulic network illustrated in Figure 2. If the parallel combination of the test element and load element is called the constrained element, then a "constrained impedance matrix" describes the pressures at all ports as a function of the total source flow into the constrained network. Therefore this network is described by the equation

$$P(\omega) = Z_c(\omega) \dot{V}_s(\omega) \quad (4)$$

where $Z_c(\omega) = [Z_{jk}^c(\omega)] =$ constrained impedance matrix

The constrained impedance matrix may be measured by sequentially pulsing each port with the other pulsers blocked (zero oscillatory source flow):

$$Z_{jk}^c(\omega) = \left. \frac{P_j(\omega)}{\dot{V}_k^s(\omega)} \right|_{\text{only } \dot{V}_k^s \neq 0} = \text{element of the constrained impedance matrix} \quad (5)$$

Once the constrained impedance matrix $Z_c(\omega)$ has been measured by use of eq (5),

AMDR 9635-037, APPENDIX G

C. (cont.)

the unknown admittance matrix of the test element $Y(\omega)$ may be found by use of the following simple relationship:

$$Y(\omega) = Z_c^{-1}(\omega) - Y_L(\omega) \quad (6)$$

where $Z_c^{-1}(\omega)$ = inverse of the constrained impedance matrix

$Y_L(\omega)$ = load admittance matrix

In order to use this equation, one must be able to measure or accurately predict the load admittance matrix of the constraining network. If it is assumed that the load network is non-interacting, so that there is no transmission of oscillations through the load from one port to another, then the load admittance matrix $Y_L(\omega)$ is diagonal and may be measured at the same time as $Z_c(\omega)$. The following equation defines the load admittance matrix:

$$Y_L(\omega) = \begin{cases} \frac{V_j(\omega)}{V_k(\omega)}, & j=k \\ 0, & j \neq k \end{cases} = \text{Non interacting load admittance matrix} \quad (7)$$

Note that this matrix requires measurement of the oscillatory flows into the load at each port but is independent of the source location. However as a check on the assumption of linearity and non-interacting load transmission paths, this matrix should be computed for each of the n pulsing conditions.

D. EXAMPLE: TURBOPUMP ADMITTANCE MEASUREMENT

As an example of the application of the constrained impedance method to the measurement of the admittance matrix of a two-port hydraulic network, a hypothetical pulse test of a rocket engine turbopump and associated flow facility will be considered. A pump "cold-flow" test facility and pulsing apparatus, as shown in Figure 3, is typical of dynamic test equipment used by "Pogo" investigators to empirically determine the dynamic characteristics of the turbopump.

The procedure for the pulse testing of a turbopump is to pulse the flow at the pump inlet with the outlet pulser locked and then pulse the output with the inlet pulser locked. Of course, both modes of pulsing should be performed at the same steady state operating point, so that the effect of operating conditions upon the admittance matrix may be determined. The oscillatory pressures and flows shown in Figure 3 should be measured with flush mounted pressure transducers and transient flowmeters and should be recorded on magnetic tape. The tape recording of all dynamic response data is essential since a digital computer is usually required to 1) transform the original data from the time domain to frequency domain, and 2) manipulate the resulting frequency response information to obtain the admittance matrix. Normally, the frequency response information is obtained by means of 1) a cross spectral analysis program in the case of random or noisy periodic data, or 2) a Fourier analysis program in the case of aperiodic (transient) or periodic data.

If the transient flows are not measured, they can be inferred from the three flush mounted pressure measurements provided at each port. The oscillatory flow passing through each branch may be computed from the oscillatory differential

AMDR 9635-037, APPENDIX G

D. (cont.)

pressure since the impedance between the pressures is known. It will be assumed in the following discussion that the fluctuating component of flow is not measured.

Since the turbopump shown in Figure 3 is a two-port system, eq (6) may be written

$$\begin{bmatrix} Y_{11}(\omega) & Y_{12}(\omega) \\ Y_{21}(\omega) & Y_{22}(\omega) \end{bmatrix} = \begin{bmatrix} Z_{11}^c(\omega) & Z_{12}^c(\omega) \\ Z_{21}^c(\omega) & Z_{22}^c(\omega) \end{bmatrix}^{-1} \begin{bmatrix} Y_{11}^l(\omega) & 0 \\ 0 & Y_{22}^l(\omega) \end{bmatrix} \quad (8)$$

Recalling the definition for the inverse of a matrix, eq (8) may be written explicitly in terms of the unknown elements $Y_{jk}^{(c)}$ of the pump admittance matrix:

$$Y_{11}(\omega) = \frac{Z_{22}^c(\omega)}{\det Z_c(\omega)} - Y_{11}^l(\omega) \quad (9)$$

$$Y_{12}(\omega) = - \frac{Z_{12}^c(\omega)}{\det Z_c(\omega)} \quad (10)$$

$$Y_{21}(\omega) = - \frac{Z_{21}^c(\omega)}{\det Z_c(\omega)} \quad (11)$$

$$Y_{22}(\omega) = \frac{Z_{11}^c(\omega)}{\det Z_c(\omega)} - Y_{22}^l(\omega) \quad (12)$$

AMDR 9635-037, APPENDIX G

D. (cont.)

where $\det Z_c(\omega)$ is the determinant of the constrained impedance matrix. Since it is assumed that oscillatory flow is not measured, the following definitions of the constrained impedance coefficients and load admittance coefficients must be used:

$$Z_{jk}^c(\omega) = \frac{Z_k^s(\omega) P_j(\omega)}{P_k^s(\omega) - P_k^l(\omega)} \Big|_{\text{only } (P_k^s(\omega) - P_k^l(\omega)) \neq 0} \quad (13)$$

$$Y_{kk}^l(\omega) = \frac{P_k^l(\omega) - P_k^s(\omega)}{Z_k^l(\omega) P_k(\omega)} \quad (14)$$

where $Z_k^s(\omega)$ = impedance of source branch at k^{th} port
 $Z_k^l(\omega)$ = impedance of load branch at k^{th} port.

Equations (9) through (14) are sufficient to completely define the admittance matrix of the pump from the six measured pressure responses ($P_1(\omega)$, $P_1^l(\omega)$, $P_1^s(\omega)$, $P_2(\omega)$, $P_2^l(\omega)$, $P_2^s(\omega)$) and for the four known branch impedances ($Z_1^l(\omega)$, $Z_1^s(\omega)$, $Z_2^l(\omega)$, $Z_2^s(\omega)$). These equations may be easily programmed to compute the admittance matrix coefficients at each frequency from the input spectral pressure data.

APPENDIX G

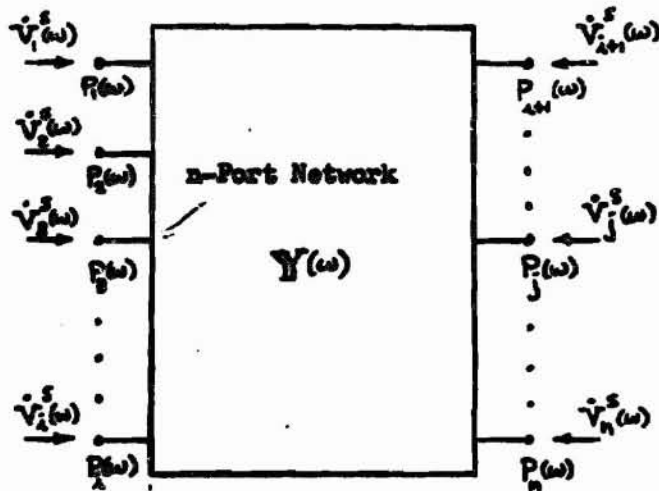


FIGURE 1 GENERAL N-PORT NETWORK

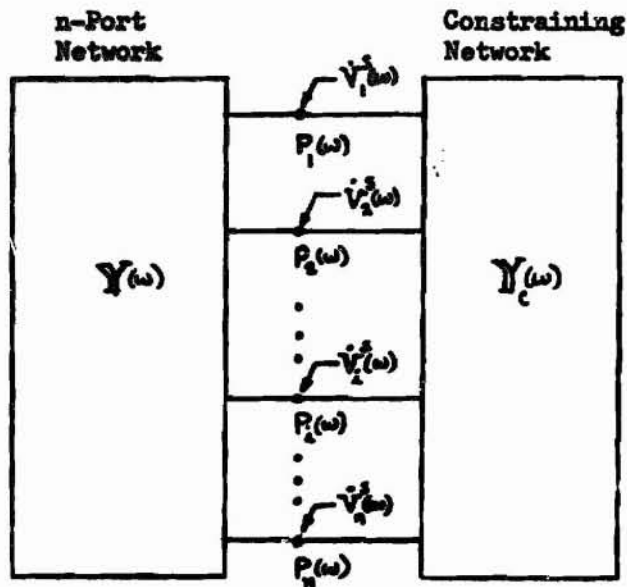


FIGURE 2 CONSTRAINED N-PORT NETWORK

APPENDIX G

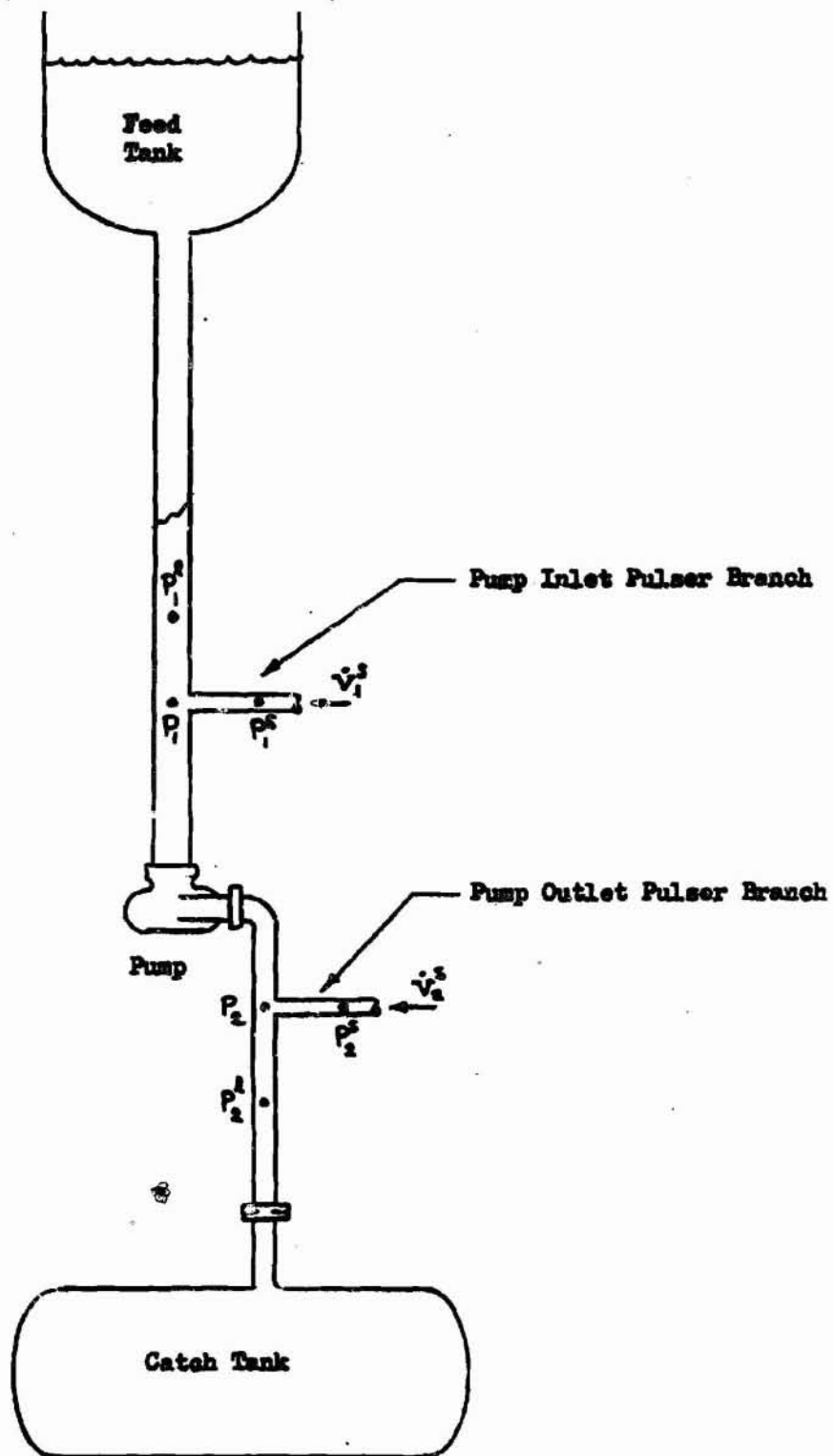


FIGURE 3 PUMP PULSE TEST FACILITY

AMDR 9635-037

APPENDIX H

INVESTIGATION OF THE TRANSFER OF OSCILLATIONS
THROUGH THE YLR87-AJ-5 ENGINE SYSTEM
(AFSC Technical Report BSD TR 65-54)

BLANK PAGE

AFSC Technical Report BSD-TR-65-54

FOREWORD

The information presented herein documents the program conducted at Aerojet-General in Sacramento, California, to investigate, through means of a test program and related test data analysis, the transfer of oscillations through the YLR87-AJ-5 engine system to verify and, if needed, modify the transfer ratios assigned to the oscillations in the analytical model of the Titan II missile. Contractual authority for Aerojet-General to conduct this program was authorized under Contract Change Notice (CCN) 102, dated 16 April 1963, to Contract AF 04(647)-521. CCN 102 was incorporated into this contract by Supplemental Agreement 67. Effort on this program was started 24 August 1963, and is considered complete with submittal of this report to Ballistic Systems Division (BSD).

Air Force monitoring of this program was provided by the BSUPT office of BSD at Norton Air Force Base, San Bernardino, California. Personnel at Aerojet-General responsible for the writing of this report were Messrs. D. B. O'Connell, S. G. Meisenholder, and H. K. Fong. This report was prepared in accordance with AFSC Regulation 80-20A, dated 25 September 1964.

Publication of this report does not constitute Air Force approval of the report's findings or conclusions. It is published only for the exchange and stimulation of ideas.

AFSC Technical Report BSD-TR-65-54

ABSTRACT

Longitudinal oscillations, referred to as POGO oscillations, have been noted in the first-stage engine system of the Titan II ICBM during missile flight testing. As a result of this problem, theoretical equations of the propellant feed systems were devised to analyze the transfer of these oscillations through the first-stage engine. However, further data from engine tests were required to verify or modify the theoretical equations. Consequently, Ballistics Systems Division (BSD) issued CCN 102 to Aerojet-General to conduct special engine tests to obtain data to verify these equations and to provide these data to Space Technology Laboratories and BSD.

Static engine testing at Aerojet-General for the investigation of the transfer of oscillations through the YLR87-AJ-5 engine system was commenced 24 August 1963 and completed 13 November 1963. The test program included eight engine tests during which oscillations were mechanically induced in the pump suction lines.

In accordance with requirements of BSD and Space Technology Laboratories (technical adviser to BSD), six no-flow tests were performed, in addition to the eight engine tests, to obtain information necessary for conducting the engine tests. The no-flow tests provided information on the effects that length of piston stroke, frequency values, and turbopump frame vertical oscillations have on the dynamic response of the propellant system. These tests were performed without test-firing the engine by inducing oscillations in the propellant-filled engine with the thrust-chamber valves being closed. Analysis of the no-flow test data is not included in this report because the test results in no way affected data from the engine tests.

The frequency of the oscillations induced during engine testing ranged from 5.6 to 19 cps. The nominal suction pressure for the oxidizer pump was varied from 68 to 100 psia. The nominal suction pressure for the fuel pump was varied from 22 to 36 psia. The amplitude of the oxidizer circuit oscillations was varied by changing the length of the oxidizer pulse generator piston stroke; the stroke length, set prior to each test, ranged from 0.15 to 0.5 in. The resultant peak-to-peak amplitudes in the oxidizer suction line varied from 2 to 73 psig, for narrow-band data. The amplitude of the fuel circuit oscillations was similarly varied; the fuel-pulse-generator piston-stroke length was set at values ranging from 0.5 to 2.0 in. The resultant peak-to-peak amplitudes in the fuel suction line varied from 1.8 to 18.1 psig, for narrow-band data.

Only one subassembly (SA) of the first-stage engine, SA 1, was installed during the eight engine tests. Subassembly 2 was deleted not only to conserve propellants, but also to allow extension of engine test time from 165 sec to 200 sec. (Engine firing time could not be extended further because the YLR87-AJ-5 turbopump gearbox is limited to operation for 200 sec per test-firing.)

AFSC Technical Report DSD-TR-65-54

ABSTRACT (cont.)

Evaluation of test results is based on the analysis of wide-band and narrow-band data rather than on the Solartron data, discussed in Appendix F. Although further analysis based on the Solartron data would provide a more refined accuracy than that based on band-pass data, the general trends and relationships discussed in this report would remain unchanged. Evaluation of the Solartron data has been omitted because at the time the analysis was conducted, this data was not available. Significant results of the testing are delineated below.

A. OXIDIZER SYSTEM

1. Resonant frequency of the oxidizer pump suction fluid column is less than that predicted, and is in the general range of vehicle resonant frequency during first-stage flight.
2. An increase in nominal suction pressure results in a decrease in the system transfer function,

$$F_{net}/F_{os} \left(\frac{\text{oscillatory thrust}}{\text{oscillatory oxidizer pump suction pressure}} \right)$$

3. An increase in the nominal value of the oxidizer-pump suction pressure results in an increase in the resonant frequency of the fluid column in the pump suction line.
4. An increase in nominal suction pressure at a constant piston acceleration, amplitude, and frequency results in an increase in the dynamic suction pressure amplitude.
5. The overall oxidizer system results exhibited a good correlation with the Aerojet-General theoretical equations.

B. FUEL SYSTEM

1. Natural frequency of the fuel suction fluid column is approximately 1/20 of the predicted value, which puts it in the general range of the vehicle resonant frequency during first-stage flight.
2. An increase in the nominal fuel suction pressure results in a decrease in the system transfer function, F_{net}/F_{FS} , within the fundamental resonant frequency range of the vehicle during first-stage flight.
3. An increase in the nominal fuel suction pressure results in an increase in the fundamental resonant frequency of the fuel pump suction fluid column.

AFSC Technical Report HED-TR-65-54

ABSTRACT (cont.)

4. An increase in nominal fuel suction pressure at a constant piston acceleration amplitude results in a decrease of dynamic fuel suction pressure amplitude.

C. REDESIGNED FUEL-PUMP IMPELLER CHARACTERISTICS

1. During engine operation with a redesigned fuel-pump impeller (PN 809660), the resonant frequency of the fuel suction column is approximately 20% higher for a particular suction pressure than the resonant frequency of the column with a production configuration fuel impeller, PN 246627.

2. The transfer function across the pump with the redesigned fuel-pump impeller is decreased by approximately 50% for a particular suction pressure from that obtained during pump operation with the production configuration fuel impeller.

3. The above two findings are based on the limited data of one test.

In general, the overall test results showed that the Aerojet-General theoretical equations were correct. Also, the test data provided means for further refinement of the analytical model.

AFSC Technical Report DSD-TR-65-54

TABLE OF CONTENTS

	<u>Page</u>
I. Introduction	1
II. Conclusions	2
III. Technical Discussion	3
A. General	3
B. Test Equipment, Instrumentation, and Data Reduction	4
C. Test Conditions	10
D. Analysis of Results	19

APPENDICES

	<u>Appendix</u>
Symbols Used in Report	A
Filtering Method	B
FOGO Instrumentation List	C
Method of Calculating Pump Inlet Pressure	D
Special Engine Hardware Used During Testing	E
Solartron Data	F
Figures	G

AFSC Technical Report DHD-TR-65-54

TABLE LIST

	<u>Table</u>
Test 4.0-15-RJA-002 Solartron Data Summary	1
Test 4.0-15-RJA-003 Solartron Data Summary	2
Test 4.0-15-RJA-004 Solartron Data Summary	3
Test 4.0-15-RJA-006 Solartron Data Summary	4
Test 4.0-15-RJA-007 Solartron Data Summary	5
Test 4.0-15-RJA-008 Solartron Data Summary	6

Tables 1 through 6 included in Appendix F

AFSC Technical Report BSD-TR-65-54

FIGURE LIST

	<u>Figure</u>
Oxidizer Suction Time, Pos-24/ $\frac{1}{2}$ vs Driving Frequency for all Oxidizer Pulsing Runs	III D-1
Fuel Suction Time, Pfs-26/ $\frac{1}{2}$ vs Driving Frequency with $\overline{\text{Pfs-0}}$ at 34 ± 2 psia	III D-2
Fuel Suction Time, Pfs-26/ $\frac{1}{2}$ vs Driving Frequency with $\overline{\text{Pfs-0}}$ at 30 ± 2 psia	III D-3
Fuel Suction Time, Pfs-26/ $\frac{1}{2}$ vs Driving Frequency with $\overline{\text{Pfs-0}}$ at 24 ± 2 psia	III D-4
Fuel Suction Time, Pfs-26/ $\frac{1}{2}$ vs Driving Frequency for Test Run 4.0-15-RJA-008 with P/N 289660 Fuel Impeller	III D-5
Oxidizer Pump Amplification, Pod/Pos-24 vs $\overline{\text{Pos-0}}$ with P/N 246647 Fuel Impeller	III D-6
Fuel Pump Amplification, Pfd-2/Pfs-26 vs $\overline{\text{Pfs-0}}$ with P/N 246647 Fuel Impeller	III D-7
Fuel Pump Amplification, Pfd-2/Pfs-26 vs $\overline{\text{Pfs-0}}$ with P/N 289660 Fuel Impeller	III D-8
Fuel Pump Amplification, Pfd-2/Pfs-26 vs Pfs-26 with $\overline{\text{Pfs-0}}$ Constant	III D-9
Engine Function Pc5B/Pos-24 vs Driving Frequency	III D-10
Engine Function Pc5B/Pos-24 vs $\overline{\text{Pos-0}}$ at Constant Pulse Generator Frequency of 11 cps	III D-11
Engine Function Fnet/Pos-24 vs Driving Frequency	III D-12
Engine Function Pc5B/Pfs-0 vs Driving Frequency	III D-13
Engine Function Pc5B/Pfs-0 vs $\overline{\text{Pfs-0}}$ at Constant Pulse Generator Frequency of 13 cps	III D-14
Engine Function Pc5B/Pfs-0 vs Driving Frequency with Fuel Impeller P/N 289660	III D-15
Engine Function Fnet/Pc5B vs Driving Frequency	III D-16
Sketch of Fuel Circuit and Oscillatory Fluid Particle Motion	III D-17

AFSC Technical Report DSD-TR-65-54

FIGURE LIST (cont.)

	<u>Figure</u>
Plot of Oscillatory Pressure Distribution In the Fuel Suction Line	III D-18
Function $P_{fs}-26/X_f$ vs Driving Frequency for Fuel Suction Line Effective Lengths of 35, 40, and 45 in.	III D-19
Function $P_{os}-26/X_o$ vs Driving Frequency for Fuel Suction Line Effective Lengths of 35, 40, and 45 in.	III D-20
Sketch of Oxidizer Suction Line and Pump	III D-21
Plot of Oscillatory Pressure Distribution in the Oxidizer Suction Line	III D-22
Function $P_{os}-24/X_o$ vs Driving Frequency	III D-23
Plot of Average Oscillatory Head Rise vs \bar{P}_s , vs \bar{W}_s , and vs \bar{H}	III D-24
Plot of the Effect of Amplitude of Suction Pressure Oscillation on Curve Slope of Oscillatory Head Rise vs \bar{P}_s Curve	III D-25
Plot of Pump Gain Showing Nonlinear Effect of \bar{P}_s and P_s	III D-26 *
Closed-Loop Flow Diagram for Engine-Vehicle System in Flight	1
Open-Loop Flow Diagram for Engine-Transfer Function-Test Program	2
Schematic Diagram of Engine-Transfer Function-Test Apparatus	3
E-6 "POGO" Test Stand	4
E-6 Stand, Fuel-System Pulsing Assembly	5
E-6 Stand, Oxidizer-System Pulsing Assembly	6
E-6 Stand, Fuel-System Slave Motor and Pulsing Assembly	7
E-6 Stand, Oxidizer System Slave Motor and Pulsing Assembly	8
Test Stand and Test Hardware Accelerometer Locations	9
Oxidizer Suction-Line Transducers	10
Fuel and Oxidizer Suction-Line Toruses and Transducers	11

*Figures 1 through 46 included in Appendix G

AFSC Technical Report BED-TR-65-54

FIGURE LIST (cont.)

	<u>Figure</u>
Engine Parameter Instrumentation	12
E-6 Stand, Flush-Mounted Transducer on Oxidiser Torus	13
Test 4.0-15-RJA-001	
Plot A, Tank Pressure Data vs Time	14
Plot B, Oxidiser Circuit Data vs Time	15
Plot C, Fuel Circuit Data vs Time	16
Plot D, Gas Generator Data vs Time	17
Test 4.0-15-RJA-002	
Plot A, Tank-Pressure Data vs Time	18
Plot B, Oxidiser-Circuit Data vs Time	19
Plot C, Fuel-Circuit Data vs Time	20
Plot D, Gas-Generator Data vs Time	21
Test 4.0-15-RJA-003	
Plot A, Oxidiser-Circuit Data vs Time	22
Plot B, Fuel-Circuit Data vs Time	23
Plot C, Gas-Generator Data vs Time	24
Test 4.0-15-RJA-004	
Plot A, Oxidiser-Circuit Data vs Time	25
Plot B, Fuel-Circuit Data vs Time	26
Plot C, Gas-Generator Data vs Time	27
Test 4.0-15-RJA-005	
Plot A, Oxidiser-Circuit Data vs Time	28
Plot B, Gas-Generator Data vs Time	29
Plot C, Fuel-Circuit Data vs Time	30
Test 4.0-15-RJA-006	
Plot A, Oxidiser Circuit Data vs Time	31
Plot B, Fuel-Circuit Data vs Time	32
Plot C, Gas-Generator Data vs Time	33

AFSC Technical Report BSD-TR-65-54

FIGURE LIST (cont.)

	<u>Figure</u>
Test 4.0-15-RJA-007	
Plot A, Oxidizer-Circuit Data vs Time	34
Plot B, Fuel-Circuit Data vs Time	35
Plot C, Gas-Generator Data vs Time	36
Test 4.0-15-RJA-008	
Plot A, Oxidizer-Circuit Data vs Time	37
Plot B, Fuel-Circuit Data vs Time	38
Plot C, Gas-Generator Data vs Time	39
Test 4.0-15-RJA-005 Engine Parameters, Narrow Band Data	
Data Sample Prior to FSI	40
Data Sample After FSI without Operation of Pulse Generators	41
Data Sample During Operation of Oxidizer System Pulse Generator at 8.0 cps	42
Data Sample During Operation of Oxidizer System Pulse Generator at 9.5 cps	43
Data Sample During Operation of Oxidizer System Pulse Generator at 11.0 cps	44
Data Sample During Operation of Oxidizer-System Pulse Generator at 13.0 cps	45
Data Sample During Operation of Oxidizer-System Pulse Generator at 15.0 cps	46

AFSC Technical Report MED-TR-65-54

I

INTRODUCTION

Longitudinal oscillations of significant amplitude have been measured in the YLR07-AJ-5 engine system during the Stage I portion of Titan II missile flights. As a result of this problem, theoretical equations of the Stage I missile propellant feed systems were devised to aid in analyzing the transfer of these oscillations. Since these equations employed relationships substantiated by limited flight data, data from static engine tests where oscillations were introduced into the propellant feed systems were required to allow verification or modification of the equations for the propellant feed systems. The Aerojet-General proposal LR-63558, dated 13 June 1963, proposed the performance of a test program to obtain data to verify the engine transfer functions as represented by the theoretical equations. The tests were to be conducted while oscillations were induced mechanically in the pump suction lines during engine subassembly firings.

Contract Change Notification (CCN) 102 and Supplemental Agreement 67 to Contract AF 04(647)-521 authorized the Aerojet-General Corporation to conduct a test program to obtain the necessary data. Among the requirements of the program were included the design and procurement of special test equipment, the modification of engine hardware, and the procurement and installation of special POGO instrumentation. (The term "POGO" refers, by analogy with the motion involved, to longitudinal missile oscillations.) Requirements for engine static testing included simulation of the POGO oscillation frequencies and amplitudes and of the pump suction pressures observed during past Titan II missile flights. A final requirement was to provide data from the testing discussed above to Space Technology Laboratory for verification or modification of the theoretical equations used to express the propellant feed systems algebraically. This report describes the test program, its significant results, an analysis of these results, and conclusions.

BLANK PAGE

AFSC Technical Report BMD-TR-65-54

II

CONCLUSIONS

The primary objective of the engine transfer function test (ETFT) program was to provide data required for the verification or modification of the Aerojet-General theoretical equations used to express the engine transfer functions algebraically. In general, it was concluded that the overall test results showed that the equations were correct. Also, it was concluded that the test data would provide the means of further refinement of the analytical model.

All test data required by CCN 102 were successfully acquired, processed, and transmitted to representatives of Space Technology Laboratories. The data provided extensive information on the effects of the primary, independent variables on the frequency response of the engine feed system.

Further, it was concluded that the special POGO instrumentation installed operated satisfactorily to provide valid data on the dynamic response of the first-stage engine propellant systems.

It was concluded from test results that the first-stage POGO oscillation frequencies, amplitudes, and pump suction pressures observed during Titan II "closed-loop" missile flights were satisfactorily simulated by operation of the pulse generators and other special test equipment used in conjunction with the CCN 102 "open-loop" engine tests. Moreover, with respect to overall test objectives, all 8 tests conducted were classified by representatives of BMD and Space Technology Laboratories as satisfactory.

However, with regard to static test simulation of the missile longitudinal oscillations, the following qualifications should be considered. Although special hardware design and test conditions were arranged to simulate, as accurately as possible, the oscillatory conditions observed in the Titan II flight test vehicles, two primary deviations still existed. In the first instance, flow oscillations in the suction lines of the flight vehicles were longitudinally induced, whereas, in the simulated system, the flow oscillations were induced radially into the suction line through a 360° torus. With respect to the second qualification, the structural acceleration of the vehicles (measured at the Stage I engine) was approximately 3 gs, which corresponds to a 0.25-in. fuel pulse generator piston stroke in the simulated system. However, the fuel piston stroke employed during the ETFT program ranged from 0.5 in. to 2.0 in. to minimize the effect of extraneous engine vibrations (noise) on the test results. The exact effect, if any, of these two deviations cannot be accurately ascertained. Transmission of the lateral oscillations introduced at the special pump-suction-line torus may not entirely duplicate the normal transmission of the longitudinal oscillations in the missile. Furthermore, both of these deviations may cause a degree of pump cavitation that does not occur in the vehicles.

AFSC Technical Report BSD-TR-65-54

III

TECHNICAL DISCUSSION

A. GENERAL

The purpose of the Engine Transfer Function Test (ETFT) Program was to obtain static-test data to verify the theoretical engine system transfer functions that are used in the engine transfer analytical model. Figures 1 and 2 are simplified flow diagrams of the first-stage engine which describe the primary transfer functions in the engine-missile system and in the static-test engine, respectively. In flight, the vehicle-engine system is a "closed-loop" system in which thrust oscillations (F_n) feed back through a dynamic transfer function in the missile structure, resulting in vehicle axial vibratory acceleration (X_s). This structural acceleration causes oscillations in the propellant suction pressures and flow rates which are transferred through the engine, resulting in thrust oscillations. By analogy with the motion involved, the axial accelerations are called "JOGO."

During the ETFT Program, the engine was dynamically tested on an "open loop" system (engine without vehicle oscillation transfer) with negligible structural feedback. Missile oscillations were simulated on these tests traversing the nominal range of frequencies, amplitudes and pump suction pressures encountered during the past Titan II missile flights. The oscillations were induced in the pump suction propellant system by means of a piston-drive pulse generator of the volume-displacement type. A simplified flow diagram of the engine feed system is shown in Figure 2. The figure shows that the excitation or input to the system is composed of two separate oscillatory accelerations (X_o , X_f), which individually create suction pressure oscillations (P_{os} , P_{fs}). The oscillatory response of the engine to these suction pressure perturbations is determined by measurement of those oscillatory components of the oscillations in the chamber pressure (P_c) and thrust (F_n) which occur at the same frequency as the pulse generator input. Appendix B describes the three methods employed for frequency filtering. This report presents only the plots of the frequency response with respect to oscillation amplitude which, for any system, is defined as the ratio of the amplitude of the oscillatory output to the amplitude of the oscillatory input.

It should be noted that six "no-flow" tests were performed in addition to the eight engine tests conducted during this program. Data from the "no-flow" tests are not presented or analyzed in this report since the test results in no way affected data from the engine tests. The tests were conducted to provide interim information to aid in conducting the engine test program. Information was acquired on the effects of piston stroke length, frequency values, and turbopump frame vertical oscillations on the dynamic response of the propellant system. These tests were performed with propellants in the engine, with thrust-chamber valves closed, and with suction-line precheck valves open. The two pulse generators were then individually operated at specified stroke lengths, frequencies, and pump nominal suction pressures. The no-flow tests were conducted at various intervals throughout the engine test program: Two before Test -001 and the others between engine tests. The final no-flow test followed test -007.

AFSC Technical Report, BSD-TR-65-54

.III, Technical Discussion (cont.)

B. TEST EQUIPMENT, INSTRUMENTATION, AND DATA REDUCTION

1. Test Equipment

The tests were conducted on Test Stand E-6 on Subassembly Number 1 of R&D Engine YLR87-AJ-7, SN GR 2-87. For these tests, a special 7-in.-oxidizer suction line installed between the test stand tanks and the engine interface was used to simulate the dynamics of the missile propellant system with which a single subassembly was operated. Subassembly No. 2 was not installed on the engine assembly. Oscillation in pump suction pressures was induced by a mechanical pulse generator system. Special fuel and oxidizer suction line assemblies were installed to incorporate a torus-manifold which interfaced with the pulse generator system. A schematic diagram of this system is shown in Figure 3.

Both fuel and oxidizer circuits incorporated separate piston mechanisms of identical design. A variable-speed motor was also installed to provide the various frequency levels required during the test. The variable speed motor was connected to a slave motor which operated the piston by a crank mechanism. The slave motor with the operating mechanism was mounted on a platform supported from the test-stand structure as shown in Figures 4, 5, 6, 7, and 8. This motor-drive system was designed to pulsate either the fuel or oxidizer system separately or simultaneously by a system of clutches.

2. Engine Hardware

The Gemini R&D engine SN GR 2-87 was modified for these tests by incorporating the 2BIE-38 pattern injector (PN 287035 modified by special instrumentation bosses) and the new contour nozzle combustion chamber, PN 269400. Gears of 4360 alloy steel were installed in the turbopump gearbox. The turbine manifold assembly, PN 261244, was of the nonslip vane type for Test Runs -001 through -007. On Test Run -008, the existing SN 098 turbopump assembly, incorporating the production fuel impeller PN 246627, was removed and another unit, TPA SN 1235, was installed incorporating the redesigned fuel impeller (CCN 104/112/114) PN 289660 and a slip-vane type turbine manifold, PN 263013..

The engine assembly was further modified, as discussed in Section II,B,1, by the incorporation of special fuel and oxidizer suction line assemblies having torus manifolds connecting to the pulse generators, by the addition of bosses for flush-mounted pressure transducers in the suction discharge lines and in the injector, and by the deletion of Subassembly No. 2. Subassembly No. 2 was deleted both to conserve propellants and to extend engine test duration. Aerojet-General, BSD, and Space Technology Laboratories agreed that a single subassembly would provide adequate data.

AFSC Technical Report ESD-TR-65-54

III, B, Test Equipment, Instrumentation, and Data Reduction (cont.)

The torus-type manifolds which interfaced with the pulse generator system were designed with equally spaced ports located circumferentially along the suction line wall, thus providing a uniform entry of the pulsating flow into the suction line flow stream. Also, a special load cell was installed in place of the gimbal block assembly for the thrust measurement.

The engine was assembled in accordance with the configuration for FX 277640-29. A list of the special hardware is included in Appendix E.

3. Instrumentation

a. General

In addition to the standard instrumentation used on these tests, special FOGO instrumentation required for the engine transfer function data was included. This special instrumentation is listed in Appendix C and discussed in the following paragraphs. Figures 9, 10, 11 and 12 of Appendix G describe the overall system and location of the FOGO instrumentation.

b. Pressure Measurement

All of the system pressures monitored in determination of dynamic performance were measured by solid-state, strain-gage transducers. The transducer selected was the Model PT3J-62 transducer manufactured by Microsystems Inc., San Gabriel, California; this unit has excellent characteristics for dynamic measurements. The transducer is standardized at a 500-millivolt output for full-scale gage pressure, permitting a 25-decibel increase in the signal-to-noise ratio over that obtained with a standard strain-gage unit of 30 millivolt output. In addition, the high gage factor of semi-conductor strain-gages permits a very stiff transducer construction resulting in a diaphragm with a high resonant frequencies, which produces a minimum disturbance of the oscillations under investigation in the frequency of 5 to 20 cps.

For pressure measurements, special instrumentation bosses for the transducers were installed whenever possible throughout the system so that the transducer diaphragms were mounted flush with the walls of the fluid conduits under investigation. A typical installation of a flush-mounted pressure transducer is shown in Figure 13. Differently designed transducer mountings were installed for the hot-gas system parameters, P_{05B}, P_{agg} and P_{te} (refer to Appendix A for symbols). The instrumentation system for these conduits utilized a short length of tubing which coupled the boss to the transducer. The tubing was water cooled to maintain transducer diaphragm temperatures below 130°F. The use of the short impulse lines connected to these conduits does not lead to any resonant amplification phenomena within the frequency range investigated since the medium is all gaseous. If the transducer is connected with an impulse line less than 12 in. long, resonances at FOGO frequencies are a significant problem only with a two-phase transducer designed for combined conditions of liquid or gaseous pressure or with a liquid-coupled transducer with relatively high compliance.

AFSC Technical Report BSD-TR-65-54

III, B, Test Equipment, Instrumentation, and Data Reduction (cont.)

Microsystems transducers were used in three full-scale values for the test series. All suction pressures except the piston torus pressures, $P_{os_{pt}}$ and $P_{fs_{pt}}$, were instrumented with 0- to 100-psi range full-scale transducers. The two piston torus pressures were instrumented with 0- to 500-psi range transducers, and all measurements on the downstream side of the pumps utilized 0- to 1,500-psi range transducers.

c. Acceleration Measurement

Vibration accelerations were monitored with Model 4-202 strain-gage accelerometers manufactured by the Consolidated Electrodynamics Corporation. Strain-gage accelerometers were selected in preference to those of the piezoelectric type in view of the low frequency range investigated. Some difficulty was experienced early in the test program in bonding accelerometer pads to the hardware. The difficulty was eliminated by roughening the surfaces before bonding and by using a high temperature, quick-setting epoxy resin as the bonding agent.

d. Thrust Measurement

Thrust measurement was obtained by means of a special load cell replacing the gimbal block on Subassembly no. 1. This cell utilized semiconductor strain-gage as sensing elements. The actual subassembly dynamic thrust was determined by correcting the load cell force signal for the inertia of the thrust-chamber assembly (TCA). This was done electrically by summing the load cell output with the thrust chamber longitudinal accelerometer signal after the latter had been adjusted to have the same force sensitivity as the load-cell channel. The proportionality factor by which the acceleration signal was multiplied before summing with the load cell force signal is given by the following relationship:

$$K = \frac{\text{force sensitivity of system in millivolts/lb}}{\text{acceleration sensitivity of system in millivolts/g}} \times \text{TCA weight in lb}$$

The actual test data indicated little difference between this corrected thrust, F_{net} , and the raw load cell outputs F_{GB-1} and F_{GB-2} .

e. Piston Position Measurement

The positions of the pulsing pistons relative to their respective cylinders were measured with linear potentiometers with a 2-in. maximum displacement capability. Considerable difficulty was experienced with the mechanical linkage connecting these potentiometers to the pulse generator piston shaft. The crank mechanism of the pulse generator allows radial turning of the shaft about its longitudinal axis. This radial turning made possible the transmission of lateral force through the vertical arm connecting the shaft to the potentiometer, which could have resulted in binding of the potentiometer. The difficulty was accentuated

AFSC Technical Report ASD-TR-65-74

III, B, Test Equipment, Instrumentation, and Data Reduction (cont.)

on the oxidizer side because of the smaller piston strokes. The problem was corrected by fabricating precision connecting mechanisms utilizing ball bearings. These permitted shaft rotation with minimum linear play of the vertical arm in the direction of the piston stroke and prevented lateral forces from acting on the potentiometer.

f. Prevalve Blade Flutter Measurement

Supplemental Agreement 65, which incorporated CCN 114 in the AF O4(647)-521 contract, included an additional contractual requirement to monitor blade (valve gate) flutter of the test stand prevalves during the EFT program. The prevalves are situated in the propellant lines leading from the fuel and oxidizer tanks to the turbopump inlets. The purpose of monitoring blade flutter was to determine if the pressure oscillations induced in the pump suction lines downstream from the valves could, in turn, induce movement of the pre- valve blades. Such blade movement could result in secondary pressure fluctuations in both fuel and oxidizer feed circuits.

The instrumentation provided to measure blade flutter consisted of two rotary potentiometers LOPV and LFPV installed on the prevalves of the oxidizer line and the fuel line, respectively. The LOPV potentiometer was installed on the oxidizer pre- valve during all of the eight engine tests conducted. The LFPV potentiometer, however, was not installed for Tests -001 through -005. The potentiometer could not be installed for the first six tests because a boss on the existing fuel pre- valve made installation impossible. After Test -006, the existing pre- valve was removed and replaced with another valve to mate with the potentiometer. Accordingly, the potentiometer was installed during Tests -007 and -008.

No discernible blade flutter was recorded from LOPV or LFPV throughout the test program. Because of the lack of a secondary perturbational effect from the pre- valve blades, no analysis of the LOPV or LFPV data is included in Section III, D, 1, Analysis of Dynamic Data.

g. Signal Conditioning and Recording

The outputs of the transducers were amplified to suitable levels by Kaylab Model III amplifiers. The frequency response characteristic of these amplifiers is flat within ± 0.3 d.b. from 0 cps to 10 kilocycles (kc) per sec. These amplifiers exhibit less than 5° of phase shift at 2 kc. The effect of amplifier distortion on the test data signals is therefore negligible in the 0- to 20-cps range of oscillations measured. After amplification, the direct current components of the data were removed by simple resistance-capacitance high-pass filters with corner frequencies of 2 cps. The signals were then attenuated to the correct levels to modulate the carriers of the FM tape recorder channels at $\pm 40\%$ for the desired data variations, e.g., 50 psi peak-to-peak.

AFSC Technical Report BSD-TR-65-54

II, B, Test Equipment, Instrumentation, and Data Reduction (cont.)

The tape recorders used for primary data acquisition in this test series were Model 451RB machines manufactured by Sangamo Electrical Co. Springfield, Ill. All channels were recorded in the FM mode at a center frequency of 27 k.c. and a tape speed of 30-in./sec. Both of these machines were checked and aligned prior to each test in the series to minimize the possibility of losing data from head misalignment.

The two master tapes each contained 32 channels of data; they were subsequently used to produce the tape copies and the oscillographic data furnished to Sapce Technology Laboratories and to the Aerospace Corp. after each test.

h. Calibrations

All data channels, with the exception of the linear potentiometers, were calibrated by comparison of the recorded parameter oscillations with oscillations from a standard alternating current signal. The calibration ac signal was set at a voltage equivalent to the amplitude of a given data signal and was then substituted for the data channel signal at the output of the Kaylab amplifier. The gain accuracy of $\pm 1\%$ of the amplifier permits the use of this technique. The calibrations compensated for the effect of the high-pass resistance-capacitance filters so that no data correction was necessary as a result of using these devices. The piston-position potentiometers, LOP and LFP, were calibrated by setting the pistons to the desired length of stroke with a dial indicator and then physically operating the pulsing mechanism at low speed and recording the signals on tape. Direct-coupled Sanborn recordings of the piston position channels verified that there was negligible difference between the value of the pre-set stroke and the low-speed, peak-to-peak value recorded as the calibration. This calibration also served as a checkout for the Solartron reference system.

4. Data Reduction

Because of the 14-track limitation for the dub tapes and the 12-channel limitation for the oscillograph playbacks, the data were divided into 6 groups limited to 12 parameters each as shown in the POGO Instrumentation List, Appendix C. Each of these groupings was played back into an Ampex CF100 tape recorder, and a tape copy was made at 30-in./sec tape recording speed using a center frequency of 54 kc. These copies were made without signal conditioning or filtering between reproducer and recorder. In addition, an oscillograph playback was made of each of the groupings which was band-passed from 2 to 30 cps using Dytronics Model 722 filters. Narrow band playbacks were made of Pos²⁴, Pfs²⁶, Pos-2, Pfd-2, Pc5B, and F_{net} using 2 cascaded Dytronics filters on each channel. All of the filter sections were set at the frequency of pulsation. Two of the sections were set for low pass, and two were set for high pass. To compensate for the variation in signal produced by attenuation from the cascaded filters as the center frequency was changed, it was necessary to translate the calibrations on the master tapes to the frequencies of pulsation by reading the tape-calibration levels and substituting signals of matching amplitude at the new frequencies.

AFSC Technical Report ASD-TR-65-74

III, B, Test Equipment, Instrumentation, and Data Reduction (cont.)

Data processing was also accomplished using Solartron transfer function monitoring equipment. Phase-reference signals for this system were generated by a synchro-generator driven from the shaft of the pulsing mechanism. The outputs of this synchro-generator are 2-kc carriers with amplitude modulation according to the sine and cosine of the angular position of the shaft. These outputs were converted by the Solartron J1603 Reference Generator into four constant-amplitude, phase-reference signals 90° apart at the driving frequency. These four signals were recorded on both tape transports to serve as the fundamental Solartron data processing references.

The reduction of the taped data was accomplished by means of a Solartron Resolved Components Indicator Model VPE33.2. This instrument utilized the four constant-amplitude reference signals recorded on the tape during the test and resolved a selected data signal into one component which is in phase with and one component which is 90° out of phase with the 0° reference signal. The component magnitudes are read as voltages, tabulated at each pulsation frequency, and are subsequently converted by calculation to oscillatory amplitude and phase angle. Inter-parameter transfer functions were determined by graphical means from vector plots of the component magnitudes.

AFSC Technical Report BSD-TR-65-54

.II, Technical Discussion (cont.)

C. TEST CONDITIONS

The method of inducing pressure oscillations in the suction lines has been discussed in Paragraph III,B,1. In general, the variables in each test consisted of the value in cps selected for each driving frequency level, the length selected for the pulse generator piston stroke, and the average suction pressures at the pump inlet. All of these variables have an effect on the dynamic response of the test stand and engine propellant systems. With the exception of the pump nominal suction pressures, all of the test conditions were mechanically set prior to each test. The pump nominal suction pressures were controlled during the tests by means of manually controlling the tank ullage pressures. With the pressure oscillations being induced in the pump suction lines during the tests, it would be extremely difficult to accurately determine that the required pump nominal suction pressures were being achieved by the visual monitoring of pump suction pressures or of pressure in the pump suction lines. Instead, propellant tank bottom pressures were visually monitored during the test and were adjusted to obtain the desired pump average suction pressures. The tank bottom pressures required to obtain desired nominal pump inlet pressures were calculated by the method described in Appendix D. The maximum allowable duration of each test was 200 sec, the turbopump gearbox being the limiting factor.

The following subparagraphs present a discussion of each test. Individual plots of pertinent parameters versus test duration (Appendix G) are referenced to clarify the discussion of special program requirements and general engine performance. It should be noted that any dynamic conditions resulting from the pulsing are not accurately reflected on these plots since the plots are only traces connecting individual data points at intervals of one second, whereas the induced oscillations range from 5 cps to 20 cps. Immediately after each test, a technical meeting was held at Aerojet-General, Sacramento, to review the data, discuss the results, and confirm the conditions for the next test. In this manner the latest knowledge gained was utilized in establishing the conditions for each test. Representatives from the Ballistic Systems Division, Space Technology Laboratories, Martin Marietta Co., Aerojet-General Corp., and the Committee for Investigation of Missile Oscillations were invited to these meetings.

1. Test 4.0-15-RJA-001

The first engine test was a reference checkout test. Its purpose was to check the dynamic response of the test stand during pulsing, to verify engine steady-state performance, to obtain empirical data for verifying the theoretical relationship of driving frequency and piston stroke to the amplitude of the resulting pump suction pressure oscillation, and to obtain engine transfer function data. Both the oxidizer system and the fuel system were pulsed.

AFSC Technical Report BMD-TR-65-54

III, C, Test Conditions (cont.)

The check of the dynamic response of the test stand was considered vital since there was some concern pertaining to the testing hazard resulting from the resonant frequency of the test stand. If its resonant frequency were within the range of the driving frequency (5 cps to 20 cps), serious damage to the test stand could result. Accelerometers were mounted on the test stand, one of them being monitored for hazardous accelerations during the testing as a safety criterion for engine shutdown.

The steady-state performance verification was required to ensure that mixture ratio, thrust, etc., were within the nominal operating range.

Since all existing curves of piston stroke and frequency (of the pulse generator system) vs the resultant amplitude of pump suction pressure oscillations were theoretical, it was necessary to obtain empirical verification of the basic theory. An accurate knowledge of this relationship was mandatory since a large unexpected pump suction pressure oscillation at a relatively low average pump suction pressure could result in operation below minimum net positive suction head and could endanger the engine and test stand.

Two consecutive frequency sweeps were conducted during this test, one on each propellant system. The frequency steps of each sweep were 15 cps, 13 cps, 11 cps, 9.7 cps, and 8 cps. The scheduled nominal suction pressures were 70 + 2 psia and 34 + psia for POB-0 and PFB-0, respectively; however, the values achieved on the test averaged approximately 60 psia and 30 psia, respectively. This is illustrated in Figure 14, where the oxidizer and fuel-tank bottom pressures averaged approximately 38 psig and 21 psig, respectively, instead of the required 48 psig and 25 psig, respectively. The oxidizer and fuel piston strokes were 0.15 in. and 1.125 in., respectively.

At the start of the test, the gaseous-nitrogen start valve remained open approximately 5 sec instead of the normal time of 1 sec, which caused a 27,300 rpm turbine speed and a chamber pressure of 890 psia (scheduled chamber pressure was 775 psia). This anomaly is shown in Figures 15, 16, and 17. All other related engine parameters showed similar overshoots. However, this anomaly had no detrimental effect on the objectives of the test. The nitrogen start valve was removed and replaced with a new valve prior to Test -002. Even though the plotted pump suction pressures are not an accurate reflection of the dynamic conditions, there was an obvious increase in the dynamic amplitude of PFB-20 at FSI + 100 sec (Figure 16). The increase in amplitude of the oscillations at PFB-20 resulted from the effects of the 15-cps frequency step on the fuel system; the higher frequency of this step produced greater pressure oscillation amplitudes. Significant variations of POB-B and PFB-B during the first 10 sec of the test are a result of delay due to human reaction time in manually maintaining the required tank pressures. These pressures were relatively constant throughout the pulsing portion of the test and had no effect on the test objectives. All test objectives were met and no problem of resonance occurred with the test stand.

AFSC Technical Report DSD-TR-65-54

III, C, Test Conditions (cont.)

2. Test 4.0-15-RJA-002

The primary objective of this test was to acquire transfer function data of the fuel system at various predetermined frequencies and at two different fuel pump suction pressures. A secondary objective was to obtain further data on oxidizer system characteristics during pulsation of the system with an oxidizer pulse generator piston stroke of 0.3 in. at 15 cps. The additional reference data was necessary in order to more accurately specify the conditions of piston stroke length and tank bottom pressures for Test 4.0-15-RJA-003, during which pressure oscillations were to be induced in the oxidizer system (Figures 18 through 21).

Each of two frequency sweeps on the fuel system was conducted at five frequency steps as follows: 15 cps, 13 cps, 11 cps, 9.5 cps, and 8.0 cps. The fuel piston stroke was 1.3 in. The tank bottom pressures for the two sweeps were scheduled to be 48 ± 10 psig and 25 ± 3 psig for POT-B and PFT-B, respectively, during the first sweep, and 48 ± 10 psig and 21 ± 3 psig for POT-B and PFT-B, respectively, during the second sweep. However, POT-B averaged approximately 43 psig during both frequency sweeps, and PFT-B was 19 psig and 13 psig for the first and second sweeps, respectively. These tank bottom pressures are shown in Figure 18. As indicated in this figure, it took approximately 25 sec (FS1 + 95 sec to FS1 + 120 sec) to reduce PFT-B between frequency sweeps to the pressure level required for the second sweep. The frequency steps of the two sweeps and the test times at which they were conducted are as follows: first sweep (fuel), 15 cps from FS1 + 55 to FS1 + 61.5 sec, 13 cps from FS1 + 63.5 to FS1 + 70 sec, 11 cps from FS1 + 72.5 to FS1 + 79 sec, 9.5 cps from FS1 + 81 to FS1 + 87 sec, and 8.0 cps from FS1 + 90 to FS1 + 96.5 sec; second sweep (fuel), 15 cps from FS1 + 119 to FS1 + 125 sec, 13 cps from FS1 + 127 to FS1 + 133 sec, 11 cps from FS1 + 136 to FS1 + 142.5 sec, 9.5 cps from FS1 + 153 to FS1 + 157 sec, and 8.0 cps from FS1 + 159.5 to FS1 + 168 sec.

After these two fuel system frequency sweeps, the oxidizer system was pulsed, maintaining POT-B at 43 psig and PFT-B at 13 psig. The oxidizer pulse generator piston stroke was 0.3 in. At FS1 + 173 sec, pulsing was initiated in the oxidizer system at 9.2 cps, and the frequency was increased at a rate of 1.2 cps until FS1 + 180 sec, when it reached the required frequency of 15 cps. This frequency was maintained until FS1 + 189 sec, when the pulsing was terminated. Test duration was 194.7 sec.

As shown in Figures 19 and 20, the large amplitudes in pressure oscillations in PFD, PFJ, PFS, Pc5, POJ, POD and POS (see Appendix A for symbols) that occur at approximately FS1 + 40 sec and at FS1 + 120 sec are a result of the 15-cps frequency step of the two fuel system sweeps as explained in the discussion of Test -001. As stated previously, these erratic oscillations are not an accurate reflection of conditions in engine parameters because the graphs are plotted with data points at intervals of 1 sec, whereas the induced oscillations range from 5 to 20 cps. The large increase and decrease of POS and PFS during the initial

AFSC Technical Report ASD-TR-65-54

III, C, Test Conditions (cont.)

40 sec of the test are also reflected in POT-B and PFT-B and are a result of human error in manually controlling the tank ullage pressures. The primary and secondary objectives of this test were accomplished satisfactorily.

3. Test 4.0-15-RJA-003

The primary objective of this test was to acquire transfer function data of the oxidizer system at various predetermined frequencies and at two different oxidizer tank bottom pressures. Only the oxidizer system was pulsed. The scheduled tank bottom pressures were POT-B at 78 ± 2 psig and 48 ± 2 psig for the first and second frequency sweeps, respectively, and PFT-B at 21 ± 2 psig for both sweeps. The actual running pressures were within the tolerances established for the "target" values. As shown in Figure 22, POT-B was 78 psig until FB1 + 89 sec at which time reduction to 48 psig was initiated. This value of 48 psig was reached at FB1 + 128 sec, and POT-B averaged approximately 46 psig for the remainder of the test. PFT-B (Figure 23) remained fairly constant throughout the test; PFT-B ranged between 21 and 22 psig. The oxidizer pulse-generator piston stroke was 0.33 in. Frequency steps for each sweep were 15, 13, 11, 9.5, and 8.0 cps. The duration of each step was as follows: first sweep (oxidizer), 15 cps from FB1 + 38 to FB1 + 45 sec, 13 cps from FB1 + 48 to FB1 + 54.5 sec, 11 cps from FB1 + 57 to FB1 + 63.5 sec, 9.5 cps from FB1 + 65 to FB1 + 72 sec, and 8.0 cps from FB1 + 74.5 to FB1 + 82 sec; second sweep (oxidizer), 15 cps from FB1 + 143 to FB1 + 149.5 sec, 13 cps from FB1 + 152 to FB1 + 159 sec, 11 cps from FB1 + 162 to FB1 + 167.5 sec, 9.5 cps from FB1 + 170 to FB1 + 176 sec, and 8.0 cps from FB1 + 179 to FB1 + 185.5 sec. Test duration was 200.45 sec.

In Figure 22, Pc5 data shows indications of various single data point pressure spikes; however, there is no evidence of this in the dynamic data. These individual data points are considered erroneous. The POS-14 trace is also unreliable due to a malfunctioning pressure transducer. The POS-14 transducer was replaced prior to Test -004.

A secondary objective of pulsing the fuel system was deleted prior to the test due to a leak between the fuel piston shaft and the chevron packing. The fuel system pulse generator was repaired by installing a new chevron packing prior to Test -004.

4. Test 4.0-15-RJA-004

The primary objective of this test was to acquire further transfer function data of the fuel system at various predetermined frequencies and at two different tank bottom pressures. Since the actual tank bottom pressures for Test 4.0-15-RJA-002 ran well below the scheduled values, the scheduled tank bottom pressures for Test -004 were the same as those for Test -002 with PFT-B at 26 ± 2 psig and 22 ± 2 psig for the first and second frequency sweeps, respectively, and POT-B at 48 psig for both frequency sweeps. Both tank bottom pressures were maintained at the scheduled values as shown in Figures 25 and 26. Originally,

AFSC Technical Report BSD-TR-65-54

III, C, Test Conditions (cont.)

pulsation of both the fuel system and the oxidizer system was planned; but, due to binding of an O-ring in the oxidizer pulse generator cylinder, the oxidizer system pulsation was deleted. A third pulsation of the fuel system was conducted instead.

At FS1 + 76 sec, reduction of PFT-B from the first frequency sweep pressure of 28 psig to the second frequency sweep pressure of 21 psig was initiated. PFT-B was reduced to this lower pressure at FS1 + 90 sec. The frequency steps of both frequency sweeps were 15, 13, 11, 9.5, and 8.0 cps (identical with that of Test -002). The durations for which these frequency steps extended are as follows (shown in Figure 27): first sweep (fuel oscillations induced in fuel system), 15 cps from FS1 + 28 to FS1 + 35 sec, 13 cps from FS1 + 37 to FS1 + 44 sec, 11 cps from FS1 + 46 to FS1 + 53.5 sec, 9.5 cps from FS1 + 56.5 to FS1 + 62.5 sec, and 8.0 cps from FS1 + 65 to FS1 + 72.5 sec; second sweep (fuel), 15 cps from FS1 + 97.5 to FS1 + 104 sec, 13 cps from FS1 + 105.5 to FS1 + 112 sec, 11 cps from FS1 + 114.5 to FS1 + 120.5 sec, 9.5 cps from FS1 + 122.5 to FS1 + 128 sec, and 8.0 cps from FS1 + 130 to FS1 + 136.5 sec. The fuel piston stroke for this test was 1.5 in.

A secondary objective of pulsing the oxidizer system was deleted because of an O-ring binding in the oxidizer-pulse-generator cylinder. A third fuel-system frequency sweep was conducted instead, maintaining POT-B at 48 psig, and lowering PFT-B to 16 + 2 psig. This pressure reduction was initiated at FS1 + 138 sec, and PFT-B entered the "target" range (16 + 2 psig) at FS1 + 151 sec. Test times of the frequency steps were as follows: 15 cps from FS1 + 160 to FS1 + 167.5 sec, 13 cps from FS1 + 167.5 to FS1 + 174 sec, 11 cps from FS1 + 174 to FS1 + 183 sec, 9.5 cps from FS1 + 183 to FS1 + 191 sec, and 8.0 cps from FS1 + 191 to FS1 + 198.5 sec. Test duration was 201.2 sec.

The nitrogen start valve remained open 15 sec after the start of the test, causing a 27,100 rpm turbine speed (NT) and a 905-psia combustion-chamber pressure (Pc5C-2) during this period (Figures 25, 26, and 27). All related parameters (Pfd-1, PfJ, Pod, PoJ, PTi, PoJGG and PfJGG--reference Appendix A for symbols) showed similar "overshoots"; however, pulsing of the fuel system did not begin until after normal operating conditions were achieved at FS1 + 28 sec. The nitrogen start valve was removed and replaced with a new valve prior to Test -005.

5. Test 4.0-15-RJA-005

The primary objective of this test was to acquire further transfer function data on the oxidizer system at various predetermined frequencies and at two different oxidizer tank bottom pressures. These objectives were identical to the previous oxidizer system test (-003) with the exception of the target oxidizer-tank bottom pressures. However, in Test -003, only the oxidizer system was pulsed; in Test -005, both fuel and oxidizer systems were pulsed. The tank bottom pressures were maintained within the "target" tolerance of 58 + 2 psig and 37 + 2 psig for POT-B during the first and second frequency sweeps, respectively, and 21 + 2 psig for PFT-B during both sweeps. As shown in Figure 28, after the first frequency

AFSC Technical Report ASD-TR-65-54

III, C, Test Conditions (cont.)

sweep, the reduction of POT-B occurred between the times of FSI + 80 sec and FSI + 90 sec. The scheduled frequency steps for both sweeps were 15, 13, 11, 9.5, and 8.0 cps. All steps were accomplished except for the 11-cps step of the first sweep, which was inadvertently omitted. The test times of these steps were as follows (Figure 29): first sweep (oxidizer), 15 cps from FSI + 42.5 to FSI + 48 sec, 13 cps from FSI + 49.5 to FSI + 57.5 sec, 9.5 cps from FSI + 61.5 to FSI + 68 sec, and 8.0 cps from FSI + 69.5 to FSI + 77.5 sec; second sweep (oxidizer), 15 cps from FSI + 103 to FSI + 108.5 sec, 13 cps from FSI + 109 to FSI + 121 sec, 10.5 cps from FSI + 129.5 to FSI + 133.5 sec, 9.5 cps from FSI + 135 to FSI + 141.5 sec, and 8.0 cps from FSI + 143 to FSI + 152 sec. The oxidizer piston stroke was 0.5 in.

A secondary objective of pulsing the fuel system (deleted in Test -003) was also accomplished. Pressures for POT-B at 37 + 2 psig and for FFT-B at 21 + 2 psig were maintained within tolerance for this fuel sweep, and frequency steps of 10.5 cps, 9.5 cps, and 8.0 cps were made. The 15- and 13-cps steps were not conducted in this sweep since a long fuel-piston stroke of 2.0 in. was employed; this longer stroke, in conjunction with the higher frequencies, would have caused dangerously large oscillatory amplitudes in fuel suction pressure. Since the fuel sweep included only the lower frequencies, the 2-in. fuel-piston stroke was used to increase the oscillatory amplitudes at these frequencies. As explained in the discussion of Test -001, pulsation at the lower frequencies normally produces engine parameter oscillation of less amplitude than does pulsation at higher frequencies of 13 to 15 cps. The increased oscillatory amplitude at the lower frequencies was needed to produce data which could be readily distinguished from random oscillations due to engine noise. The test times of these steps were as follows: 10.5 cps from FSI + 160 to FSI + 166.5 sec, 9.5 cps from FSI + 168 to FSI + 172 sec, and 8.0 cps from FSI + 176 to FSI + 184 sec. Test duration was 197.9 sec.

The oscillations of POS-14 (Figure 28), during the two oxidizer pulsing phases of this test, showed a much greater amplitude than experienced on previous tests. This was a result of the 0.5-in. oxidizer piston stroke, the largest that had been used thus far. Another trace in Figure 30, TPT (Tank Fuel Temperature), also showed erratic performance; however, this was an unreliable trace due to a discrepant thermocouple. The thermocouple was replaced after Test -005.

No other anomalies were apparent in the test records; however, post-fire inspection revealed that the turbine first- and second-stage nozzles were damaged. The nozzle bucket brase had begun to separate, allowing the buckets to lower and contact the turbine rotor. The turbine manifold, PN 261244-19, SN 000252, was replaced prior to Test 4.0-15-RJA-006 with turbine manifold PN 261244-19, SN 000276. At the time of failure, manifold SN 000252 had accumulated 1050.7 sec total run time; the design run time of this manifold is 800 sec.

AFSC Technical Report ASD-TR-65-54

III, C, Test Conditions (cont.)

6. Test 4.0-15-RJA-006

The primary objective of this test was to investigate resonance of the fluid column in both oxidizer and fuel pump propellant suction lines. The first frequency sweep was conducted on the oxidizer system with frequency steps of 15, 13, 12, 11, and 9.5 cps. The tank bottom pressures were maintained, except for a few short intervals, within the target tolerance of 78 ± 2 psig and 21 ± 2 psig for POT-B and FFT-B, respectively (Figures 31 and 32). Test times of the frequency steps for the first sweep, as shown in Figure 33, were as follows: 15 cps from FSI + 21 to FSI + 27 sec, 13 cps from FSI + 29 to FSI + 35 sec, 11 cps from FSI + 36 to FSI + 41 sec, 9.5 cps from FSI + 42 to FSI + 47 sec, and 8.0 cps from FSI + 49 to FSI + 53.5 sec. The oxidizer pulse generator piston stroke was 0.15 in.

On completion of the oxidizer system frequency sweep, POT-B and FFT-B were lowered to 48 ± 2 psig and 15 ± 2 psig, respectively. Both during and after this pressure reduction the oxidizer system was pulsed at 15 cps for a period of 60 sec beginning at FSI + 71 sec. The reduction of POT-B was effected in approximately 17 sec. Pulsing was terminated at FSI + 122 sec. This procedure, combining pulsing with reduction in oxidizer tank pressure, was performed in order to gain further insight into the individual effect of variation in suction pressure on the dynamic response of the oxidizer system during pulsation.

A fuel-system frequency sweep was then conducted at these reduced tank bottom pressures, and at frequency steps of 15, 14.6, 13, 12, and 11 cps (the 14.6 cps step slightly exceeded the programed value of 14.0 cps). The fuel-pulse-generator piston stroke was 0.60. Test times of the frequency steps of this sweep were as follows: 15 cps from FSI + 141.5 to FSI + 153 sec, 13.6 cps from FSI + 153.5 to FSI + 164 sec, 11 cps from FSI + 165.5 to FSI + 171 sec, 9.5 cps from FSI + 173 to FSI + 178 sec, and 8.0 cps from FSI + 179 to FSI + 189 sec. Test duration was 200.1 sec.

All the traces in Figures 31 through 33 were normal except TTT, which was erroneous due to a discrepant thermocouple. The thermocouple was replaced prior to Test -007.

7. Test 4.0-15-RJA-007

The primary objective of this test was to acquire transfer function data when pressure oscillations were induced simultaneously in both propellant systems. To ensure that the fuel and oxidizer pistons would pulse in phase with each other, the pistons were put in phase with one another and engaged with the "vari-drive" motor prior to starting the varidrive motor and the engine test. Since both pulse mechanisms were already engaged, the motor was not started until after steady-state operation was achieved to preclude any interference with the start transient. Pulse generator piston strokes were 0.7 in. for fuel and 0.5 in. for

AFSC Technical Report BGD-TR-65-54

III, C, Test Conditions (cont.)

oxidizer. The tank bottom pressures, which were maintained within the target tolerance throughout the test, were 58 ± 2 psig and 21 ± 2 psig for POT-B and FFT-B, respectively, as evidenced in Figures 34 and 35. Frequency steps for this sweep were 15 cps, 13 cps, 11 cps, 9.5 cps and 8.0 cps. The test duration of each frequency step was as follows (Figure 36): 15 cps from FSI + 20 to FSI + 25 sec, 13 cps from FSI + 27 to FSI + 32 sec, 11 cps from FSI + 33.5 to FSI + 39 sec, 9.5 cps from FSI + 40 to FSI + 46 sec, and 8.0 cps from FSI + 47.5 to FSI + 55 sec. No problems were encountered during this dual frequency sweep.

A secondary objective of this test was to further investigate the fluid-column resonance in both pump propellant suction lines. This investigation consisted of an individual frequency sweep of each propellant system. The oxidizer system was pulsed first at steps of 15, 13, 11, 9.5, 8.0, 6.5, and 5.0 cps. During the first five steps of this oxidizer sweep the fuel pulsing system coasted (the flywheel was not adequately braked after the dual frequency sweep) resulting in the inducement of oscillations in the fuel system at a maximum frequency of 2.5 cps. However, the frequency (and therefore amplitude) of the fuel-pressure oscillations was not of a sufficient magnitude to have any consequence on the data obtained from the oxidizer frequency sweep. The test duration of each frequency step during this oxidizer-system frequency sweep was as follows: 15 cps from FSI + 67 to FSI + 72 sec, 13 cps from FSI + 74 to FSI + 79 sec, 11 cps from FSI + 80 to FSI + 86 sec, 9.5 cps from FSI + 87.5 to FSI + 92 sec, 8.0 cps from FSI + 93 to FSI + 98 sec, 6.5 cps from FSI + 100 to FSI + 105.5 sec, and 5.0 cps from FSI + 108.5 to FSI + 114 sec.

After the oxidizer system was pulsed, the fuel system was pulsed at frequency steps of 11, 13, 15, 17 and 19 cps. Since some of these frequencies were higher than those at which the pulse generator had been previously operated, the sweep progressed inversely from low to high frequencies. In this manner, if the amplitude of the pump-suction-pressure oscillations had become excessive at the higher frequencies and had necessitated termination of the frequency sweep, the data at the lower frequencies would already have been acquired. All frequency steps were accomplished, however, without excessive pressure-oscillation amplitude. There was some difficulty in achieving the scheduled test duration for the last two frequencies due to mechanical slippage in the pulsing system; however, sufficient duration was obtained at these required frequencies to provide data for engineering evaluation. The test duration of each frequency step during this fuel-system frequency sweep was as follows: 11 cps from FSI + 132 to FSI + 137.5 sec, 13 cps from FSI + 139 to FSI + 143 sec, 15 cps from FSI + 145.5 to FSI + 150 sec, 17 cps from FSI + 156.5 to FSI + 161 sec, and 19 cps from FSI + 177.5 to FSI + 184 sec. Test duration was 190.9 sec.

8. Test 4.0-15-RJA-008

The primary objective of this test was to acquire transfer function data on the redesigned POGO fuel impeller (FN 289660) for comparison with the data gained from testing the existing production impeller (FN 246627) during the previous seven tests. Three frequency sweeps were conducted on the fuel system. Tank

AFSC Technical Report ASD-TR-65-54

III, C, Test Conditions (cont.)

bottom pressures (Figures 37 and 28), which were maintained within the target tolerance, were 48 ± 2 psig for POT-B throughout the test and, for PFI-B, 27 ± 2 psig (FS1 + 10 to FS1 + 51 seconds), 21 ± 2 psig (FS1 + 57 to FS1 + 90 sec), and 15 ± 2 psig (FS1 + 95 sec to FS2) during the three sweeps, respectively. These pressures were selected because they were the same pressures used in Test 4.0-15-RJA-004, and therefore would provide a direct comparison of data. The frequency steps conducted were 20, 17, 15, 13, and 11 cps for both the first and second frequency sweeps, and 17, 15, 13, 11, and 9.5 cps for the third sweep. The test durations for the three frequency sweeps were as follows (Figure 39): first sweep, 20 cps from FS1 + 12.5 to FS1 + 21 sec, 17 cps from FS1 + 23 to FS1 + 25.5 sec, 15 cps from FS1 + 27.5 to FS1 + 31.5 sec, 13 cps from FS1 + 33 to FS1 + 37 sec, and 11 cps from FS1 + 39 to FS1 + 45 sec; second sweep, 20 cps from FS1 + 60 to FS1 + 64 sec, 17 cps from FS1 + 67 to FS1 + 70 sec, 15 cps from FS1 + 71.5 to FS1 + 75.5 sec, 13 cps from FS1 + 77.5 to FS1 + 81.5 sec, and 11 cps from FS1 + 83 to FS1 + 88 sec; third sweep, 17 cps from FS1 + 106 to FS1 + 111 sec, 15 cps from FS1 + 112.5 to FS1 + 117 sec, 13 cps from FS1 + 119 to FS1 + 123 sec, 11 cps from FS1 + 125 to FS1 + 129.5 sec, and 9.5 cps from FS1 + 131 to FS1 + 135.5 sec. The fuel pulse generator piston stroke was 0.75 inch. Test duration was 136.9 seconds.

AFSC Technical Report DMD-TR-65-54

III, Technical Discussion (cont.)

D. ANALYSIS OF RESULTS

1. Analysis of Dynamic Data

a. General

The pulsing system used to induce pressure oscillations in the pump suction lines is discussed in Paragraph III,B,1. It should be noted that during these tests, the feed system pressure oscillations were generated by a constant-stroke piston device. Therefore, the oscillatory pressure amplitudes generated are proportional to the square of the driving frequency (for incompressible fluids). Since frequency was varied during a given test, the driving amplitude was also varying correspondingly. This effect is of no consequence in experimental investigations of linear systems; however, the Titan II engine-feed system displays strong nonlinearities with respect to oscillation frequency and amplitude. All response data presented herein should be viewed in the light of the above observation. The discussion of the data analysis will be presented under three categories: (1) missile-to-engine pump suction line dynamics, (2) turbopump characteristics, and (3) overall engine frequency response.

Due to delays in data reduction, the Solartron data were initially not available for the analysis; only results from the wide band and narrow band data are discussed in this report. The Solartron data were subsequently provided and are presented in Appendix F for information only, no analysis having been conducted on these data. Descriptions of Solartron-filtered data are provided in Appendix B, Appendix F, and in Section III,B,4, Data Reduction.

b. Results

(1) Missile-to-engine Pump Suction Line Dynamic Characteristics

The dynamic response characteristics of the missile-to-engine pump suction lines are best described by plots of frequency versus the ratios of amplitude of the dynamic suction pressures (P_{os} , P_{fs}) to the pulse generator piston accelerations (\ddot{X}_o , \ddot{X}_f). The suction line frequency response functions for the ground test (P_{os}/\ddot{X}_o , P_{fs}/\ddot{X}_f) are not the same as those corresponding to flight response functions (P_{os}/\ddot{X}_s , P_{fs}/\ddot{X}_s) but should display similar response characteristics.

The oscillatory response of oxidizer dynamic suction pressure to a vibratory acceleration is illustrated in Figure III D-1. The function P_{os-24}/\ddot{X}_o is plotted versus frequency (P_{os-24} refers to the oxidizer nominal suction pressure measured 24 in. above the turbopump flange). The figure shows that increasing the nominal suction pressure (P_{os-0}) results in an increase in the amplitude of P_{os-24}/\ddot{X}_o (at constant frequency). The peaking of the curves, which is most evident for the case in which the nominal suction pressure is 100 psia, indicates a resonant condition in the oxidizer suction line and correlates with the predicted values discussed in Section III,D,2,a,(2). Narrow-band phase-shift data indicate that the suction pressure oscillation lags behind the piston stroke by a phase angle of approximately 90° at the

AFSC Technical Report MSD-TR-65-54

III, D, Analysis of Results (cont.)

frequency of the peak amplitude response, which is a more positive indication of resonance. These preliminary results show that the resonant frequency is a function of the nominal suction pressure. The curves of Figure III D-1 indicate that the resonant frequency of the oxidiser suction line is approximately 11 cps when the average oscillatory suction pressure (P_{fs-0}) is 100 psia and that this resonant frequency is decreased as the nominal suction pressure is reduced. This dependency of the resonant frequency on the nominal suction pressure is explained in Section III,D,2,a,(2), in which the shift in the acoustic resonance is attributed to a change in the pump impedance.

However, the results show that the fundamental resonant frequency in the oxidiser suction line as determined from test data is significantly less than that predicted by the analytical model. A possible explanation of this phenomenon is that a frequency coupling of the fundamental acoustic resonant frequency of the oxidiser suction line and the resonant frequency of a spring-mass system within the circuit is occurring, which effectively lowers the resonant frequency of the circuit. Theoretically, the rigid mass of the spring-mass system consists of an incompressible column of oxidiser in the oxidiser suction line. The oxidiser column is believed to resonate by means of a localized mechanical compliance which operates as an unidirectional spring. Within the oxidiser circuit, there are two possible sources of this mechanical compliance: either a gas bubble of nitrogen and nitrogen-tetroxide vapor formed in the flow vortex at the pump suction inlet or a mechanical compliance provided by the elasticity of the turbopump frame upon which the column of oxidiser in the circuit is supported.

Figures III D-2 through III D-4 are plots of the fuel suction line frequency response function (P_{fs-26}/X_f) versus frequency for nominal suction pressures (P_{fs-0}) of 35, 30, and 23 psia, respectively, (P_{fs-26} is the dynamic pressure measured in the fuel line at a location 26 in. above the pump flange). Figure III D-2 shows that the amplitude response function with P_{fs-0} at 35 psia is constant with respect to frequency (within experimental accuracy); this behavior is characteristic of incompressible flow conditions. If the value for P_{fs-26}/X_f of 0.33 psi/g obtained from test data is compared to the theoretical values shown in Figure III D-19, the theoretical curve corresponding to an effective fluid column length of 40 in. exhibits the best correlation with the test data. On the basis of this data, the effective length of the fuel suction line is assumed to be approximately 40 in. As noted in Section III,D,2,a,(1), the oscillatory pressure distribution in a line of this length is such that the oscillatory amplitude at the suction flange (P_{fs-0}) is greater than that at a station 26 in. further upstream (P_{fs-26}) by the factor of 2.2.

Figure III D-3 shows that, as P_{fs-0} is reduced to 30 ± 2 psia, the response function amplitude P_{fs-26}/X_f is no longer constant with respect to frequency. This variation, with respect to frequency, is also indicated in Figure III D-4. The trends shown in Figures III D-3 and III D-4 indicate a resonant phenomenon similar to the resonance in the oxidiser suction line. The observed resonant frequency is approximately 16 cps with P_{fs-0} at 30 psia and 13 cps with P_{fs-0} at 23 psia. The resonance in the fuel suction line may be accounted for by the theory that the essentially incompressible column of fuel resonates on a gas-bubble spring. This gas-bubble theory explains the observed reduction of the resonant

AFSC Technical Report ASD-TR-65-54

III, D, Analysis of Results (cont.)

frequency with decrease of nominal suction pressure. Since the stiffness of the gas spring is proportional to the pressure and inversely proportional to the volume of gas, a lowering in pressure will produce more gas vapor, a more compliant spring, and thus a lower fundamental resonant frequency.

For Test 4.0-15-RJA-008, TPA SN 1235, which incorporated the redesigned POGO fuel pump impeller, PN 289660, was installed in the engine. The oscillatory pressure response of the fuel suction line during Test 4.0-15-RJA-008 is shown in Figure III D-5. Not only the curves showing the amplitude response, but also the narrow-band phase shift data indicate that the resonant frequency for each value of nominal suction pressure (36, 31, and 25 psia) obtained with the POGO impeller has been apparently increased over that of the fuel pump with the original production impeller, PN 246647, by at least 20%. For example, the narrow-band phase-shift data show that use of the redesigned fuel pump results in a 17-cps fuel-suction-line fundamental frequency for a nominal suction pressure (PFS-0) of 25 psia. This represents a 3½cps increase when compared to the 14-cps resonance obtained with the original production configuration pump for the same value of suction pressure. Since the resonant frequency of a resonating system with unidirectional compliance is inversely proportional to both the mass and the compliance of the system, it follows that the use of the redesigned fuel pump has resulted in a change of the compliance and/or the mass of the column of fuel in the suction line.

Comparison of Figure III D-5 with Figures III D-2 through III D-4 shows that the value of $Pfs-26/Xf$ at low frequencies with the PN 289660 impeller is not significantly changed from the value that was obtained using the original production configuration pump impeller. Since the value of $Pfs-26/Xf$ at low frequencies is proportional to the effective length of the fluid column above the Pfs-26 transducer, the effective length of the column of fuel in the suction line is the same for both the production and redesigned fuel pumps. This fact eliminates the possibility that the fuel line frequency shift is due to a change in mass characteristics of the fluid column. Therefore, the cause of the increased natural frequency with the redesigned fuel impeller is due to the reduction of compliance in the system. With respect to the aforementioned gas-bubble theory, the reduction in compliance may be explained by the decrease in volume of gas at the pump suction inlet due to the improved cavitation performance (at nominal suction pressures) of the redesigned pump.

(2) Turbopump Dynamic Characteristics

Test data on oscillatory performance of both the fuel and oxidizer turbopumps were compared to the theoretical values. The propellant turbopumps are evaluated with respect to the amount of amplification or attenuation of the induced oscillations in suction pressure supplied at the pump inlet. The measure of the pump dynamic amplification is called the "pump pressure amplification factor" which is defined as the ratio of the oscillatory discharge pressure amplitude to the oscillatory suction pressure amplitude. The oxidizer pump pressure amplification factor ($Pod/Pos-24$) is plotted with respect to the nominal suction pressure in Figure III D-6. $Pod/Pos-24$ (which is approximately equal to $Pod/Pos-0$) increases as

AFEC Technical Report B6D-TR-65-54

III, D, Analysis of Results (cont.)

the nominal suction pressure is decreased. This increase is due to the existence of a greater value of pump gain when the suction pressure is reduced, as explained in Section III,D,2,b (indicated by the slope of the head rise versus suction pressure curve in Figure III D-25). The theory that is presented in Section III,D,2,b includes a prediction that the pump amplification factor is also a function of oscillatory suction pressure amplitude. However, accurate comparison of these oscillatory amplitudes recorded on the wide-band data is difficult because the parameter trace is a complex waveform including several random oscillations normal to engine operation. Therefore, no attempt has yet been made to correlate the oxidizer pump amplification to the amplitude of the suction pressure oscillations.

Figure III D-7 is a plot of the fuel pump pressure amplification factor as a function of nominal fuel suction pressure (P_{fs-0}). The ordinate used was P_{fd}/P_{fs-26} , which is proportional to P_{fd}/P_{fs-0} . From Section III,D,2,a,(1), it was found that $P_{fs-0} = 2.2(P_{fs-26})$ due to the oscillatory pressure distribution in the suction line. Thus, the values of P_{fd}/P_{fs-26} must be divided by 2.2 to obtain P_{fd}/P_{fs-0} . Figure III D-7 provides an indication of the effect of variation of both the average values and the oscillatory amplitudes of the suction pressure on the oscillatory pump performance. It is seen that the pressure-amplification factor increases as the nominal suction pressure is decreased and as the oscillatory suction pressure amplitude is increased. The increase of the amplification factor with increase of the oscillatory amplitude of the suction pressure indicates that, with respect to oscillatory performance, the pump is a nonlinear device. Fuel suction pressure oscillations of large amplitude were found to produce periodic cavitation in the fuel pump. It is also shown in Figure III D-7 that the effect of this periodic cavitation on the fuel pump amplification factor is negligible. The shaded data points were obtained from a test where the suction pressure oscillations were of such an amplitude as to cause periodic cavitation at the pump suction inlet. These data show a good correlation with data obtained without cavitation.

The difference in pump amplification factor between the redesigned and production fuel pumps may be observed by comparison of Figures III D-7 and III D-8. The redesigned fuel pump in TPA SN 1235 displays values of P_{fd-2}/P_{fs-26} which are 25% to 50% lower than those exhibited by the production configuration fuel pump in TPA SN 098.

The function P_{fd-2}/P_{fs-26} is plotted versus oscillatory amplitude of the fuel suction pressure for both the redesigned and production configuration fuel pumps in Figure III D-9. The increase of pump amplification factor with increase of pulsing amplitude (at a constant nominal fuel suction pressure) clearly displays the nonlinear characteristics of the pump. This topic is covered in detail in Section III,D,2,b (see Figure III D-23).

(3) Overall Frequency Response of the Engine

The function P_o/P_{os-0} , which indicates the relative oscillatory thrust chamber pressure amplitude to the oscillatory oxidizer suction pressure amplitude, is plotted versus frequency in Figure III D-10. Figure III D-10

AFSC Technical Report ASD-TR-65-54

III, D, Analysis of Results (cont.)

shows that the amplitude of the engine function P_c/P_{os-0} is not strongly sensitive to frequency variations; there are no resonance-like characteristics observed. With respect to the amplitude of thrust-chamber oscillations, the engine response appears to be more strongly a function of nominal suction pressure than of oscillatory oxidizer suction pressure amplitude or frequency. When P_c/P_{os-0} is plotted against suction pressure for a constant frequency, as in Figure III D-11, this effect is shown more clearly. The effect of reducing the nominal suction pressure is to increase the value of P_c/P_{os-0} . The dependency of this function upon suction pressure must be due to the increase of pump gain (and pump amplification factor) as the nominal suction pressure is reduced, as indicated in Figure III D-6.

With respect to oscillatory engine thrust amplitude, response of the engine subassembly to an oxidizer suction pressure oscillation is indicated by the function F_{net}/P_{os-0} . The narrow-band results presented in Figure III D-12, which is a plot of this function versus frequency, are inconclusive. Following the completion of this analysis, the reduction of the Solartron data was completed and is provided in Appendix F. Descriptions of Solartron data are provided in Appendix B, Appendix F, and in Section III, B, 4, Data Reduction. It is believed that analysis of the Solartron data will yield plots of F_{net}/P_{os-0} versus frequency which will display the same characteristics as those for P_c/P_{os-0} . This conclusion is based on the wide-band and narrow-band data analysis, in which the oscillatory thrust amplitude is found to be approximately proportional to the oscillatory chamber pressure amplitude.

Figure III D-13 presents curves expressing the ratio of the amplitude of the oscillations in thrust-chamber pressure to the oscillatory fuel suction pressure amplitude (P_c/P_{fs-0}) plotted as a function of the driving frequency. Partly as a result of some invalid data points, the curves of P_c/P_{fs-0} versus frequency do not entirely correspond to the curves of P_c/P_{os-0} versus frequency shown in Figure III D-10. If the invalid data points (invalid due to poor signal-to-noise ratio or cavitation at the pump) are disregarded, the results are more consistent. As in the oxidizer circuit, the amplitude of the transfer function increases as the nominal fuel suction pressure is reduced. The effect of increased amplitude of P_c/P_{fs-0} associated with reduced nominal fuel suction pressure is caused by the corresponding increase in pump gain. Theoretically, assuming a linear system, the oscillatory chamber pressure amplitude should be proportional to the amplitude of the discharge pressure oscillations (at POGO frequencies). Under these conditions, an increase in P_{fd}/P_{fs-0} must cause an increase in P_c/P_{fs-0} .

The effect of periodic cavitation at the fuel pump is indicated in both Figures III D-13 and III D-14. When a suction pressure oscillation of large amplitude causes periodic cavitation at the pump inlet, the amplitude of P_c/P_{fs-0} is increased. On the other hand, it was shown in Section III, D, 1, b, (2) that pump cavitation induced by the pulse generator system did not cause an increase in the pump amplification factor P_{fd}/P_{fs-0} . Therefore, cavitation is seen to change the response characteristics of the hydraulic system and thrust chamber downstream of the fuel pump, but not those of the pump.

AFSC Technical Report ASD-TR-65-54

III, D, Analysis of Results (cont.)

The effect of the oscillatory suction pressure amplitude upon the response function P_c/P_{fs-0} is indicated in Figure III D-13. The nature of the test apparatus is such that the amplitude of the suction pressure oscillations is approximately proportional to the driving frequency squared. This increase of the oscillatory suction pressure amplitude with increasing frequency will cause a corresponding increase of the fuel pump amplification factor (P_{fd}/P_{fs-26}), as was predicted in Section III, D, 1, b, (2). However, the results given in Figure III D-13 do not display a corresponding increase in the amplitude of the function P_c/P_{fs-0} with increasing frequency. Rather, the wide-band data indicates that the amplitude of P_c/P_{fs-0} at a constant value of P_{fs-0} either remains constant or decreases with increasing frequency. This fact indicates a nonlinear behavior of the engine system downstream of the fuel pump.

Figure III D-15 shows the effect of the redesigned fuel pump in TPA SN 1235 on the amplitude of the transfer function P_c/P_{fs-0} . The values of P_c/P_{fs-0} at the lower frequencies of pulse generator operation (8 to 13 cps) are invalid and should be disregarded because of the low signal-to-noise ratio of P_c at those frequencies. The higher frequency data for the redesigned pump, when compared to that for the production configuration pump, show a significant reduction in the amplitude of P_c/P_{fs-0} at a constant value of P_{fs-0} (compare Figures III D-13 and III D-15).

The plot of the thrust transfer function (F_{net}/P_c) versus frequency is presented in Figure III D-16. At low frequency (8 to 11 cps) the valid dynamic data (F_{net}/P_c) corresponds to the predicted nominal value of F_{net}/P_c (the ratio of the nominal subassembly thrust to the nominal chamber pressure). However, the higher frequency data indicates that the dynamic values of F_{net}/P_c may be somewhat greater than those predicted for the nominal value. In general, the spread of the data is more than would be expected; analysis of the Solartron data, the data shown in Appendix F, should show more consistent results.

2. Method of Analysis and Equations

This section presents the simplified equations that describe the oscillatory response of the Titan II engine and propellant supply system to an oscillatory acceleration from the pulse generator. The dynamic equations are simplified in that they are linearized and consider only the major propellant flow paths of the engine. Included are missile-to-engine suction line dynamics, pump dynamics, and the dynamics of the pump discharge lines and the thrust chamber assembly.

AFSC Technical Report DED-TR-69-54

III, D, Analysis of Results (cont.)

a. Missile-to-Engine Suction Line Dynamic Characteristics

The dynamic characteristics of the suction lines were analyzed in order to determine the magnitude of suction pressure oscillatory pressure amplitudes at the various transducer locations. It was assumed that the oscillatory type of propellant flow in the fuel pump suction circuit can be treated as incompressible. This assumption is justified because the fuel suction line is much shorter than the acoustic wave length of pressure oscillations in the POGO frequency range. However, the effect of the distributed compressibility of the fluid in the oxidizer suction line cannot be neglected, since its quarter-wave-length resonant frequency is in the POGO frequency range. The following analysis is broken into two parts: Part 1 deals with the fuel circuit and Part 2 deals with the oxidizer circuit. The analysis predicts the frequency response and oscillatory pressure distribution in both suction lines.

(1) Fuel Circuit

The basic geometry of the fuel suction line circuit is given in Figure III D-17. Certain critical pressure transducer locations are designated. Since Pfs-26 monitors all oscillatory suction pressure measurements, it is extremely important to investigate the nature of the instantaneous pressure distribution between this transducer and the pump suction flange. A conversion factor is necessary to convert the oscillatory suction pressure amplitude at Pfs-26 to the amplitude at the pump suction flange (Pfs-0). The following analysis calculates the theoretical value for this factor (Pfs-0/Pfs-26) and also predicts the frequency response of the fuel suction line.

Figure III D-17 shows that the pulse generator is a constant displacement, reciprocating piston device which produces an oscillatory flow both upstream and downstream of the fuel suction line torus. Therefore, using the law of continuity, the oscillatory flow relationship may be found.

$$\dot{m}_t = \dot{m}_1 + \dot{m}_2 \quad (\text{Eq 1})$$

$$A_{ps} \dot{x} = A_{sp} [\dot{y}_1 + \dot{y}_2] \quad (\text{Eq 2})$$

$$\dot{x} = \frac{A_s}{A_p} [\dot{y}_1 + \dot{y}_2] \quad (\text{Eq 3})$$

where

\dot{m}_t = oscillatory mass flow in oscillator ($\frac{\text{lb sec}}{\text{in.}}$)

\dot{m}_1 = oscillatory mass flow upstream ($\frac{\text{lb sec}}{\text{in.}}$)

\dot{m}_2 = oscillatory mass flow downstream ($\frac{\text{lb sec}}{\text{in.}}$)

\dot{y}_1 = oscillatory fluid velocity upstream (in./sec)

\dot{y}_2 = oscillatory fluid velocity downstream (in./sec)

\dot{x} = piston velocity (in./sec)

A_s = suction pipe area (in.²)

AFSC Technical Report DSD-TR-67-54

III, D, Analysis of Results (cont.)

$$A_p = \text{piston area (in.}^2\text{)}$$

$$\rho = \text{propellant mass density (lb sec}^2\text{/in.}^4\text{)}$$

If the downstream impedance is assumed to be much greater than the upstream impedance, the downstream oscillatory flow will be negligible.

$$y_2 = \frac{m_2}{\rho A_s} = 0 \quad (\text{Eq 4})$$

Equation 3 becomes:

$$\ddot{x} = \frac{A_s}{A_p} \ddot{y}_1 \quad (\text{Eq 5})$$

The oscillatory pressure (at a distance ξ from the pump suction flange) is related to the fluid motion as expressed by Newton's Third Law.

$$F(\xi) = m(\xi) \ddot{y} - \rho A_s [L - \xi] \ddot{y} \quad (\text{Eq 6})$$

$$P(\xi) = \frac{F(\xi)}{A_s} = \rho [L - \xi] \ddot{y} \quad (\text{Eq 7})$$

where

$P(\xi)$ = oscillatory pressure at station ξ (psi)

\ddot{y} = oscillatory acceleration of column of fluid (in./sec²)

ξ = height of station above pump suction flange (in.)

L = total effective height of column of fluid (in.)

$F(\xi)$ = force at station ξ (lb)

Assuming that the density of the propellant is constant, the oscillatory pressure at any station above the oscillator is seen to be proportional to the distance from the effective tank bottom. This distance may be designated as h ($h = L - \xi$). Then

$$P(\xi) \rho = \rho \ddot{y} h \quad (\text{Eq 8})$$

Now, the substitution of the time derivative of Equation 5 into Equation 8 yields

$$P(\xi) = \frac{A_p}{A_s} \rho \ddot{x} h \quad (\text{Eq 9})$$

AFSC Technical Report DSD-TR-65-54

III, D, Analysis of Results (cont.)

where $P(\xi)$ = oscillatory pressure at station ξ (psi)
 X = acceleration of piston (in./sec²)
 h = height of fluid from station to the effective bottom of the tank (in.)

Rewriting Equation 9 for sinusoidal flow:

$$|P(\xi)| \sin \omega t = \frac{A_p}{A_s} \rho h |X| \sin \omega t \quad (\text{Eq. 10})$$

where $|P(\xi)|$ = absolute amplitude of oscillatory pressure (psi)
 $|X|$ = absolute amplitude of oscillatory piston acceleration (in./sec²)
 ω = circular frequency (radians/sec)
 t = time (sec)

Equation 9 results in an instantaneous pressure distribution which has a linear variation from zero at the effective end of the column of fluid to maximum at the top of the ports in the fuel "torus." Since the suction line is gradually faired into the fuel tank as shown in Figure III D-17, the exact length of the column of fluid (L) is not known, but is assumed to be greater than 35 inches and less than 45 inches. The oscillatory pressure distribution for effective lengths of 35, 40, and 45 inches, normalized to the station $\xi = 26$ in., is shown in Figure III D-18. The conversion factor P_{fs-0}/P_{fs-26} is given as 2.89 for $L = 35$ in., 2.22 for $L = 40$ in., and 1.90 for $L = 45$ in.

Equation 10 may be rewritten to show that the response of the suction pressure to a sinusoidal acceleration is independent of frequency:

$$\frac{|P(\xi)|}{X} = \frac{A_p}{A_s} \rho h \quad (\text{Eq. 11})$$

This function (with $\xi = 26$ in.) is plotted in Figure III D-19 for three different values of effective column length, $L = 35, 40,$ and 45 in. By applying the Laplace transformation to Equation 9 and substituting $s = j\omega$, the expression for the suction pressure response to a constant displacement excitation is obtained.

$$\frac{P(\xi)}{X} = \frac{A_p}{A_s} \rho h \omega^2 \quad (\text{Eq. 12})$$

AFSC Technical Report BSD-TR-65-54

III, D, Analysis of Results (cont.)

Equation 12 is solved for $\xi = 26$ in. and $L = 35, 40,$ and 45 in., and is plotted in Figure III D-20. It may be seen from this figure that, for an oscillation produced by a constant pulse generator piston stroke, the oscillatory pressure amplitude increases as the square of the frequency.

It should be realized that the above relationships neglect the compressibility of the fuel. This assumption is valid if the "organ pipe" acoustic resonant frequency of the fuel line is much greater than the frequencies of interest. The fundamental acoustic resonant frequency of the fuel suction line may be calculated from the formula

$$f_{1/4} = \frac{a}{4L} \quad (\text{Eq. 13})$$

where

$f_{1/4}$ = quarter wave length frequency

a = acoustic velocity

L = effective axial length of the pipe

Substituting $a = 5200$ fps and $L = 40$ in., it is found that the fundamental acoustic frequency is 390 cps. Therefore, the assumption that this frequency is much larger than the frequency of interest (5 - 20 cps) is certainly valid.

(2) Oxidizer Circuit

The approximate geometry of the oxidizer suction line and tank and the locations of the suction pressure transducers are given in Figure III D-21. As mentioned earlier, the length of the oxidizer suction line is greater than one-sixth of an acoustic wave length in the POGO frequency range, so consideration must be given to the compressibility of the fluid. This may be done for the case assuming no loss by solving the one-dimensional wave equation:

$$\frac{\partial^2 y(\xi)}{\partial t^2} = a^2 \frac{\partial^2 y(\xi)}{\partial \xi^2} \quad (\text{Eq. 14})$$

where

a = acoustic velocity of waves in the oxidizer circuit

$y(\xi)$ = fluid particle displacement at station

ξ = length from pump suction flange

t = time

AFSC Technical Report DSD-TR-65-54

III, D, Analysis of Results (cont.)

The acoustic wave velocity in a pipe with radial compliance is

$$a = \sqrt{\frac{1}{\rho \left(\frac{1}{\beta} + \frac{d}{Et} \right)}} \quad (\text{Eq 15})$$

where

ρ = mass density $\left(\frac{\text{lb. sec}^2}{\text{in.}^4} \right)$

β = bulk modulus (psi)

d = pipe diameter (in.)

t = pipe wall thickness (in.)

E = pipe elastic modulus (psi)

For a first approximation, it is assumed that the oscillatory flow through the pump is negligible compared to the oscillatory flow upstream from the pump, as in the fuel circuit analysis. Because of the high impedance at the pump and the low impedance at the fuel tank, the suction line is dynamically very similar to an organ pipe with one open end. The pressure distribution (mode shape) for the fundamental mode of an organ pipe, normalized to Pos-24, is shown in Figure III D-22. This fundamental mode, called the quarter-wave-length mode, may be calculated knowing the pipe length and the acoustic wave velocity from Equation 13.

The frequency response of the suction line to a pulse generator sinusoidal acceleration, using the above simplified mathematical model, is plotted as Curve A in Figure III D-23. Curves B and C in the same figure result from a more sophisticated analysis which accounts for oscillatory flow through the pump. The oscillatory flow has the effect of adding damping to the system. The result of damping is to lower the resonant frequency and reduce the peak amplitudes. The resonant frequency is reduced from 14.7 cps to 13.2 cps for a pump gain of 1.0 and to 11.5 cps for a pump gain of 1.5. The pump gain that is referred to is the slope of the discharge-pressure-versus-suction-pressure curve $\left[\frac{\partial (p_{od})}{\partial (P_{os})} \right]$, as explained in Section III, D, 2, b.

b. Turbopump Dynamic Characteristics

The dynamic equations that have been used to predict the oscillatory performance of the turbopump are obtained from the nominal or steady-state values in pump discharge pressure, in pump suction pressure, and in pump flow rate. The forms of the characteristic curves are shown in Figure III D-24 as plots of the pump head rise $(P_d - P_s)$ versus each of the three independent pump variables: suction

AFSC Technical Report DSD-TR-65-54

III, D, Analysis of Results (cont.)

pressure (\bar{P}_s), flow (\bar{W}_p), and impeller shaft speed (\bar{N}). Figure III D-24 shows that, if only small perturbations about the operating point "o" are considered, the plots may be treated as being linear in the region of the operating point. Thus, the slopes of the characteristic curves are described as the partial derivatives:

$$m = \left| \frac{\partial(\bar{P}_d - \bar{P}_s)}{\partial \bar{P}_s} \right| \text{ constant } \bar{W}_p, \bar{N} \quad (\text{Eq 16})$$

$$-R_p = \left| \frac{\partial(\bar{P}_d - \bar{P}_s)}{\partial \bar{W}} \right| \text{ constant } \bar{P}_s, \bar{N} \quad (\text{Eq 17})$$

$$K_p = \left| \frac{\partial(\bar{P}_d - \bar{P}_s)}{\partial \bar{N}} \right| \text{ constant } \bar{P}_s, \bar{W}_p \quad (\text{Eq 18})$$

where

- \bar{P}_d = nominal pump discharge pressure
- \bar{P}_s = nominal pump suction pressure
- \bar{W} = nominal flow through pump
- \bar{N} = nominal pump impeller speed

Therefore, the linearized oscillatory performance of the pump is governed by these "slopes" or derivatives and is given, in terms of small perturbational quantities, by the following equation:

$$P_d - P_s = m P_s - R_p \dot{W}_p + K_p \dot{N} \quad (\text{Eq 19})$$

where

- P_d = oscillatory component of pump discharge pressure
- P_s = oscillatory component of pump suction pressure
- \dot{W}_p = oscillatory component of pump flow
- \dot{N} = oscillatory component of pump impeller speed

Rearranging Equation 19:

$$P_d = (m + 1) P_s - R_p \dot{W}_p + K_p \dot{N} \quad (\text{Eq 20})$$

where, the constants may be defined:

- $m + 1$ = pump gain
- R_p = pump resistance
- K_p = speed fluctuation constant

AFEC Technical Report DSD-TR-65-54

III, D, Analysis of Results (cont.)

Dividing Equation 20 by the oscillatory suction pressure amplitude, the amount of amplification of a suction pressure perturbation may be investigated:

$$\frac{P_d}{P_s} = (m + 1) - K_p \frac{\dot{W}_p}{P_s} + K_p \frac{N}{P_s} \quad (\text{Eq 21})$$

Equation 21 is the final form of the oscillatory pump equation and indicates that the pump amplification is dependent on the oscillatory components of suction pressure, pump flow, and impeller speed. The terms are vector quantities and must be added or subtracted vectorially.

Oscillatory data from the Titan II flight analyses show that the fluctuation of the pump impeller speed is small in the POGO frequency range so that the term involving impeller speed may be neglected. Thus the simplified expression for the pump amplification factor is:

$$\frac{P_d}{P_s} = (m + 1) - K_p \frac{\dot{W}_p}{P_s} \quad (\text{Eq 22})$$

The effect of suction pressure on the pump gain term is shown in Figure III D-25. The effect of decreasing the nominal suction pressure (\bar{P}_s) or of increasing the oscillatory suction pressure amplitude (P_s) is to increase the apparent slope (m) of the head-rise-versus-suction-pressure curve. From Equation 22, it is seen that an increase in the pump gain will cause a corresponding increase in the pump amplification factor P_d/P_s . To summarize, the curve of P_d/P_s versus suction pressure should display the same characteristics as Figure III D-25, since a reduction in \bar{P}_s or an increase in P_s both result in a greater value of $m + 1$, which should increase P_d/P_s .

c. Dynamic Characteristics of Propellant Discharge Lines and Thrust Chamber Assembly

The oscillatory performance of the engine-feed system downstream of the pump may be described by two equations which govern the dynamic characteristics of the propellant discharge lines and thrust chamber assembly. Using a "lumped" parameter model, which characterizes incompressible flow, the dynamic equation which governs the frequency response of the pump discharge system is:

$$P_d - P_c = (R_d + j L_d \omega) \dot{W}_d \quad (\text{Eq 23})$$

where

P_d = oscillatory component of pump discharge pressure

P_c = oscillatory component of thrust chamber pressure

\dot{W}_d = oscillatory component of pump discharge line flow

AFSC Technical Report DOD-TR-65-54

III, D, Analysis of Results (cont.)

R_d = hydraulic flow resistance of propellant injector

L_d = inertance of fluid in pump discharge line

ω = circular frequency

$$j = \sqrt{-1}$$

The oscillatory performance of the thrust chamber is given by the expression:

$$\dot{W}_{od} + \dot{W}_{fd} = \frac{A_t g}{C^*} (\tau_c \dot{P}_c + P_c) \quad (\text{Eq 24})$$

where

\dot{W}_{od} = oscillatory oxidizer pump discharge line flow

\dot{W}_{fd} = oscillatory fuel pump discharge line flow

C^* = characteristic velocity

A_t = area of thrust chamber (sonic) throat

g = gravitational constant

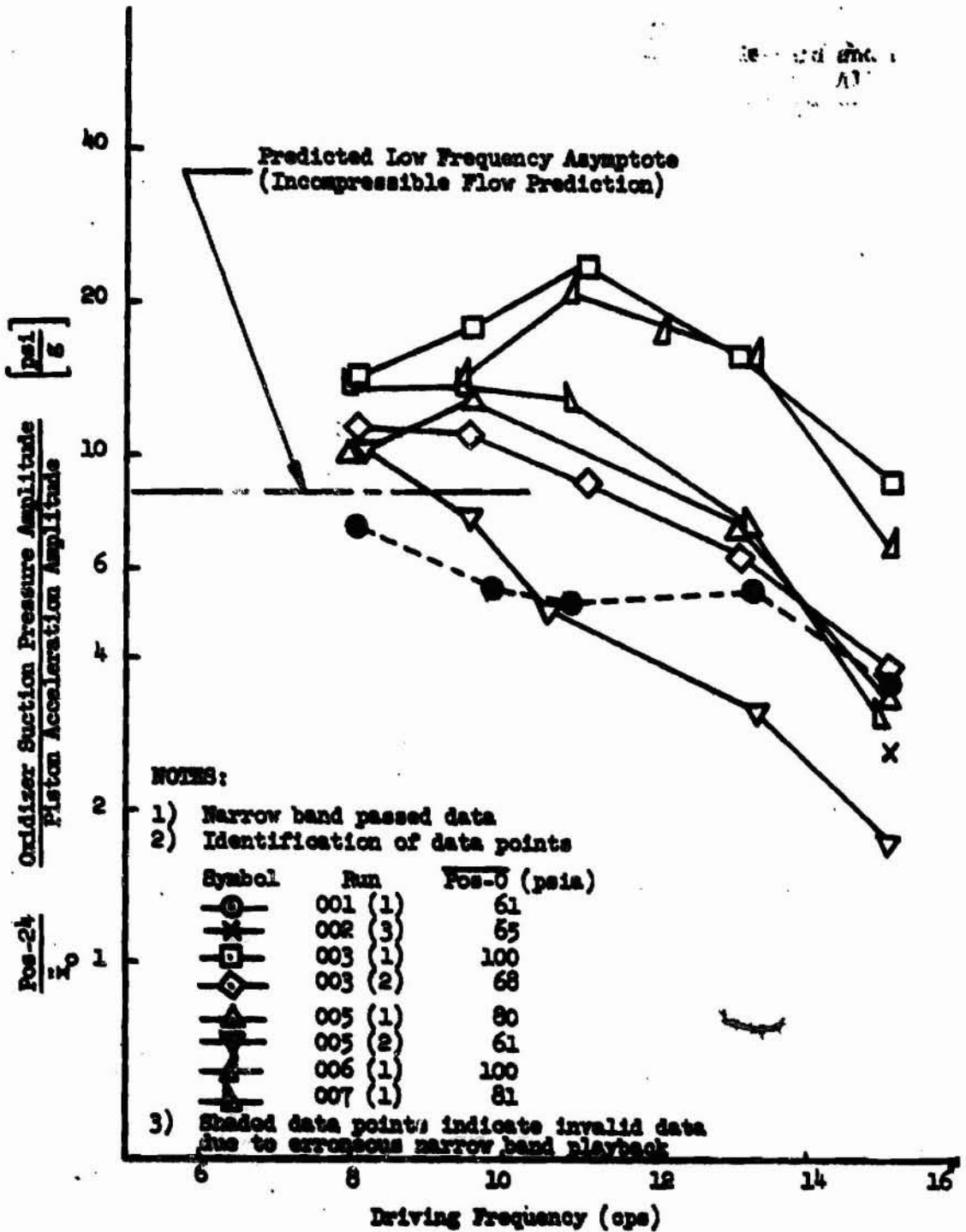
τ_c = combustion time delay

\dot{P}_c = rate of the oscillatory thrust chamber pressure

P_c = oscillatory thrust chamber pressure

Equation 24 indicates that the thrust chamber pressure is proportional to the vector sum of the oxidizer and fuel flow rate. For example, if there is only oscillatory fuel flow (\dot{W}_{fd}), then the oscillatory thrust chamber pressure (P_c) is directly proportional to this flow. From Equation 23, it is seen that the oscillatory flow in the fuel discharge line (\dot{W}_{fd}) is proportional to the oscillatory pressure difference ($P_{fd} - P_c$) across the discharge line and injector. Thus the effect of increasing the oscillatory discharge pressure amplitude (P_{fd}) is to increase the oscillatory flow (\dot{W}_{fd}) and therefore to increase the oscillatory chamber pressure amplitude (P_c).

BLANK PAGE



Oxidizer Suction Time, Pos-24/X₀ vs Driving Frequency for all Oxidizer Pulsing Runs

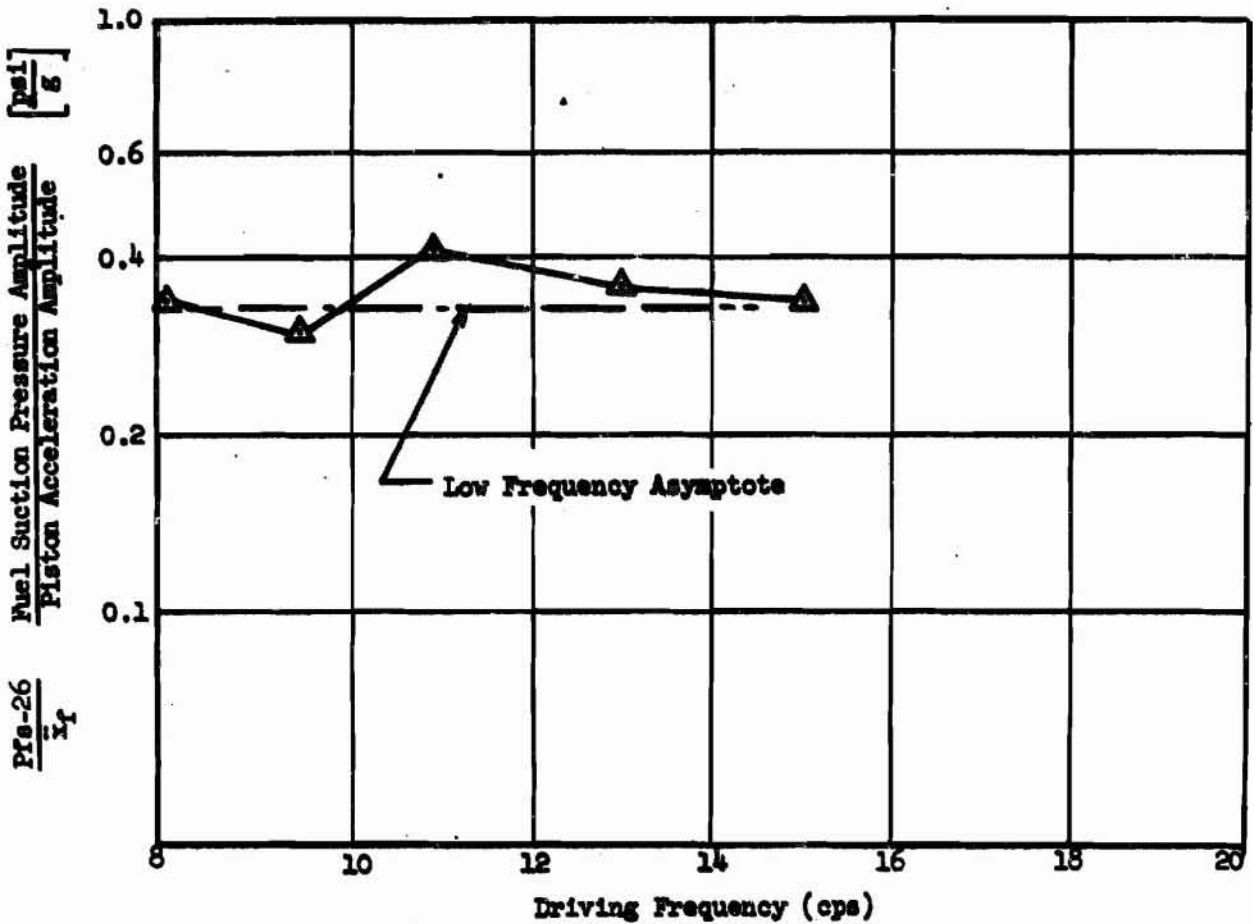
Figure III D-1

Report ESD-TR-65-54

NOTES:

- 1) Narrow band passed data
- 2) Identification of data points

Symbol	Run	$\overline{Pfs-0}$ (psia)
—▲—	004	36



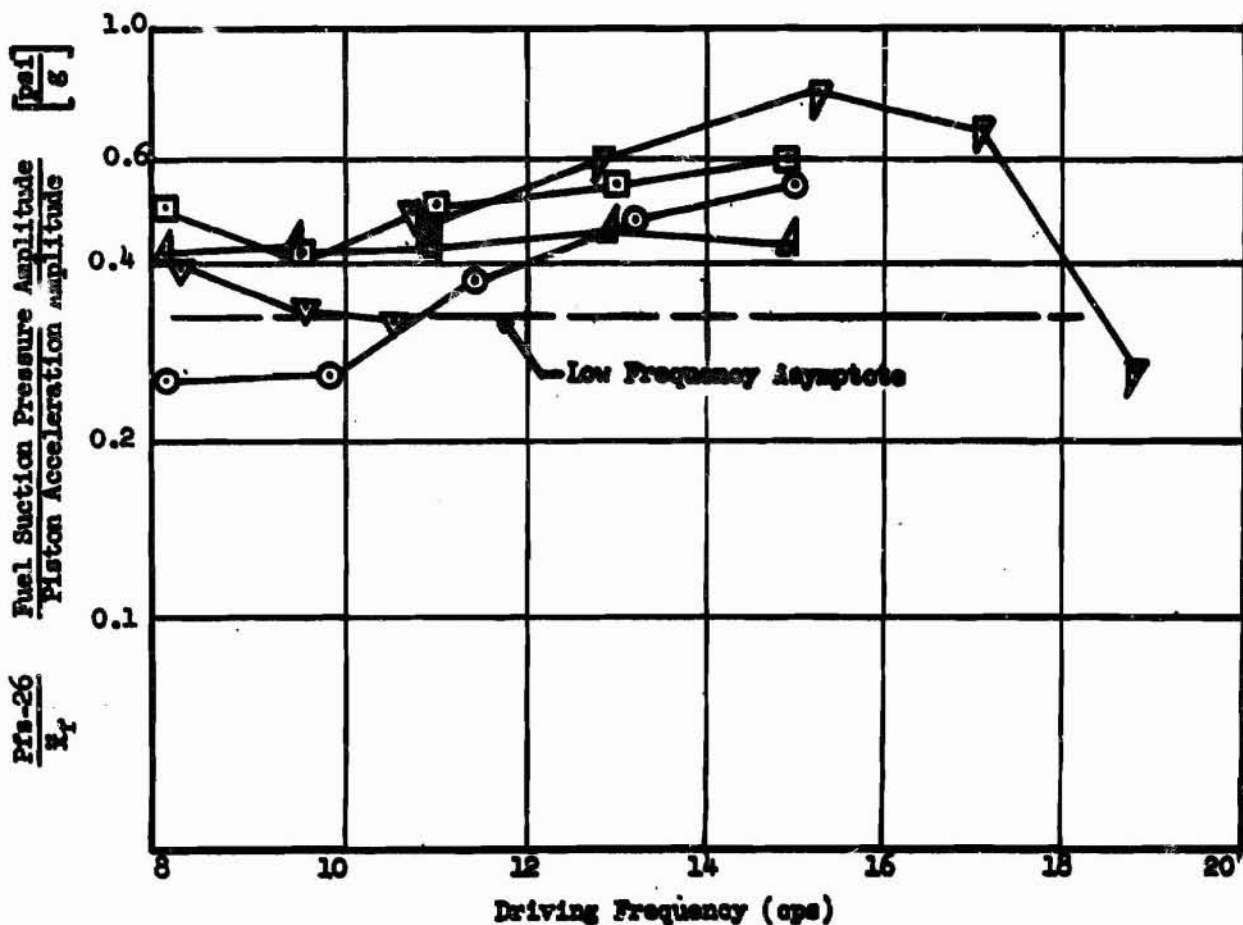
Fuel Suction Time, $Pfs-26/Xf$ vs Driving Frequency with $\overline{Pfs-0}$ at 34 ± 2 psia

Figure III D-2

NOTES:

- 1) Narrow band passed data
- 2) Identification of data points

Symbol	Run	$\overline{Pfs-0}$ (psia)
○	001 (2)	30
□	002 (1)	28
△	004 (2)	31
▽	007 (3)	30



Fuel Suction Time, $Pfs-26/K_f$ vs Driving Frequency with $\overline{Pfs-0}$ at 30 ± 2 psia

Figure III D-3

C, Resonance and Antiresonance in a Hydraulic Transmission Line (cont.)

value of impedance:

$$\left| \frac{Z_{\text{antires}}}{Z_c} \right| = \left| \frac{Z_{\text{res}}}{Z_c} \right|^{-1} = \frac{(2n-1)\pi\alpha l}{2\beta r_{\text{res}}} = \alpha' l \quad (64)$$

In conclusion, Eq (59) and (62) may be used in conjunction with the dimensionless curves presented in Figures 2 through 11 to hand-calculate the resonant frequency and the resonant value of the impedance of the uniform absorbent line with open-closed ends. For lines of more complex geometry and/or end conditions, the exact equations such as Eq (41) should be used to compute the frequency response characteristics of the transmission line.

AMDR 9635-037, APPENDIX D

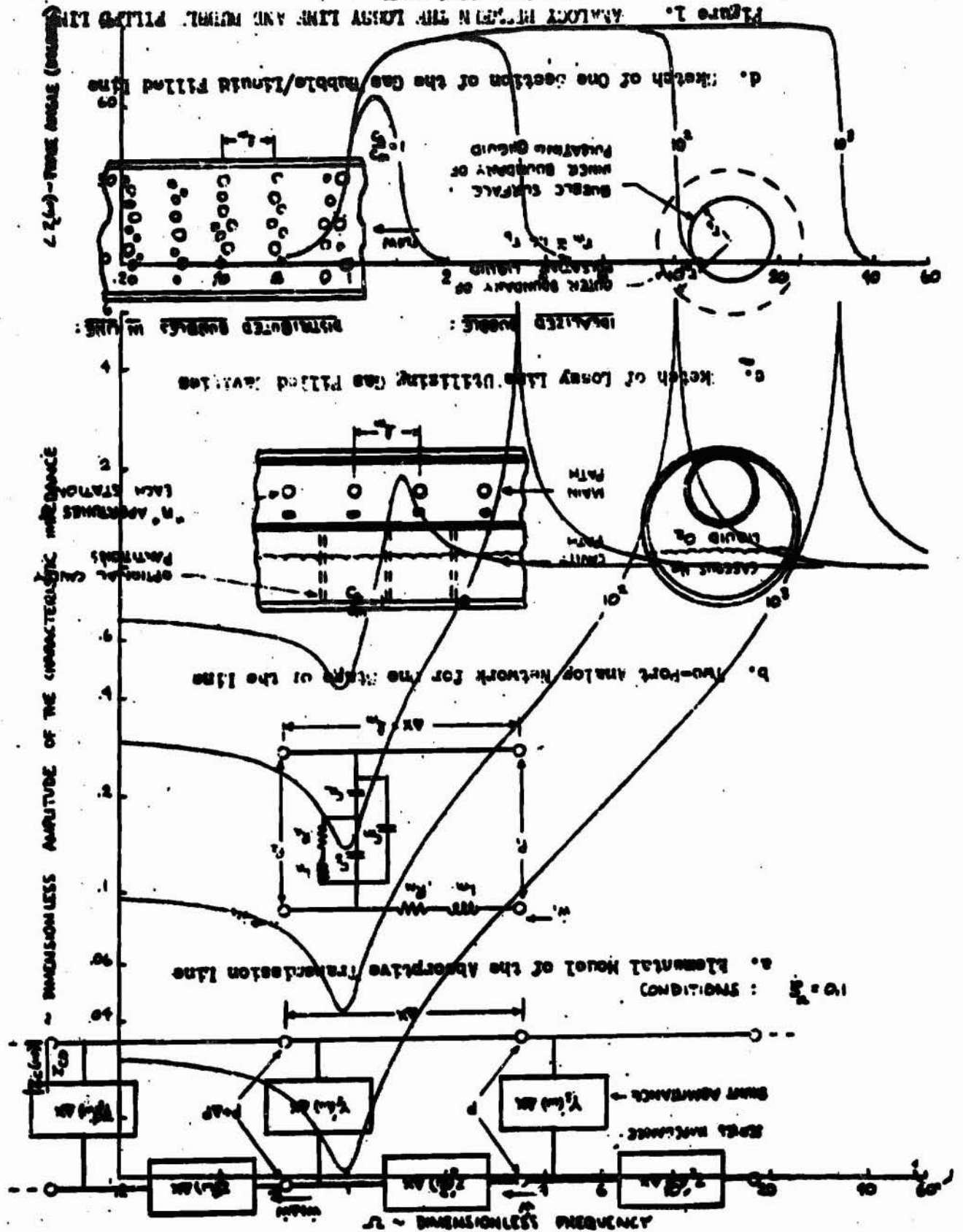


FIGURE 2. CHARACTERISTIC IMPEDANCE OF THE ABSORPTIVE LINE

BLANK PAGE

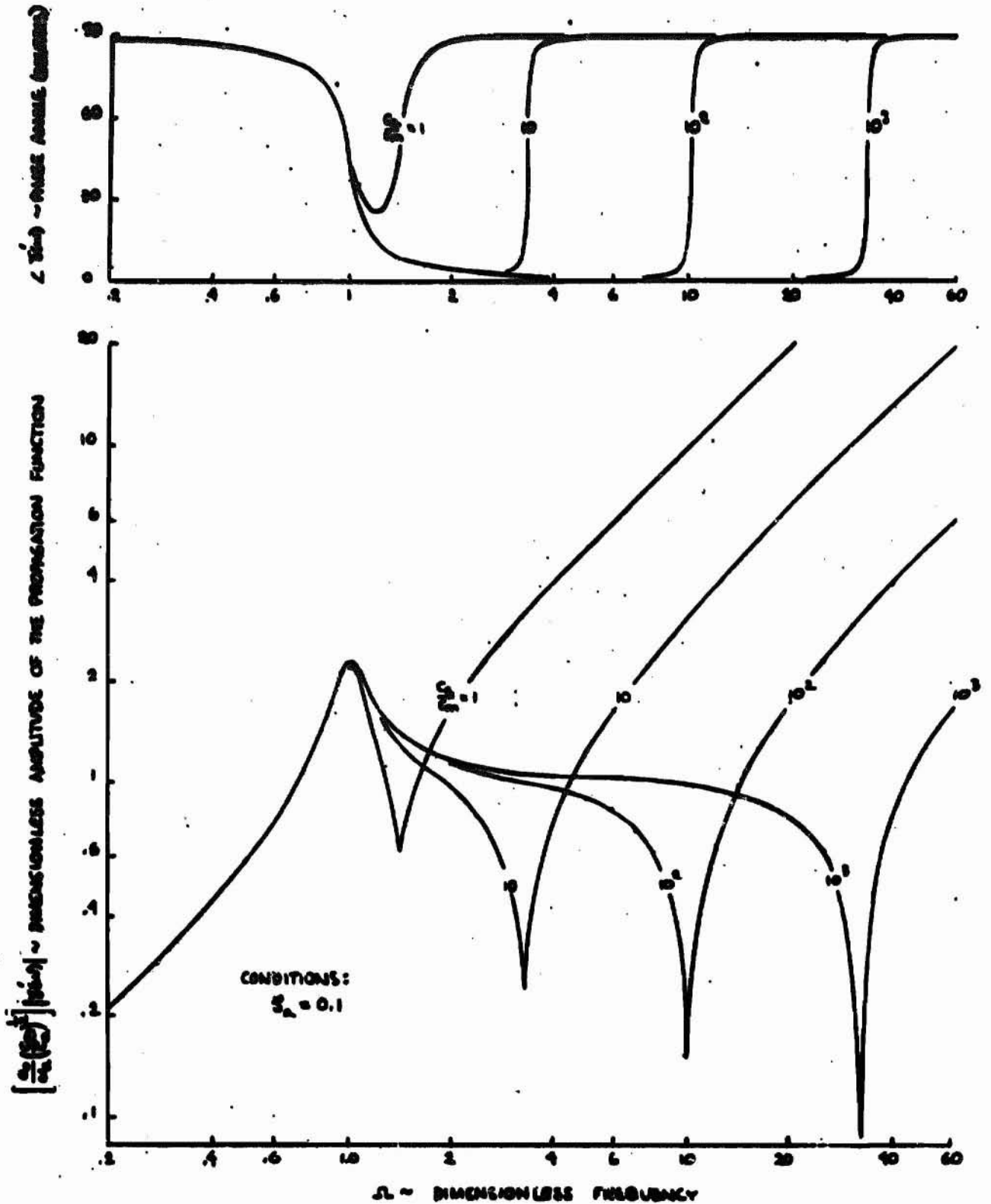


FIGURE 3. PROPAGATION FUNCTION OF THE ABSORPTIVE LINE

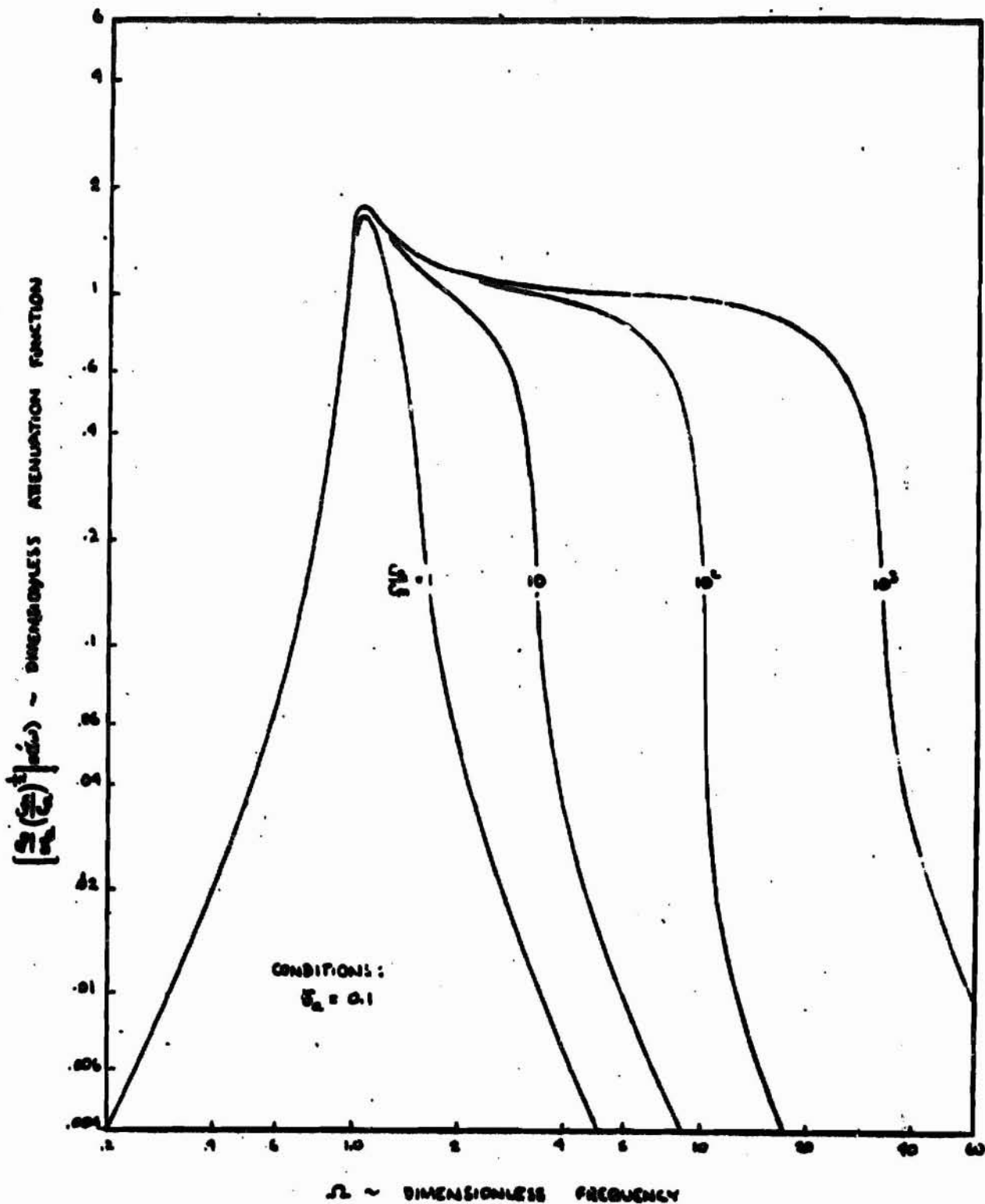


FIGURE 4. ATTENUATION FUNCTION OF THE ABSORPTIVE LINE

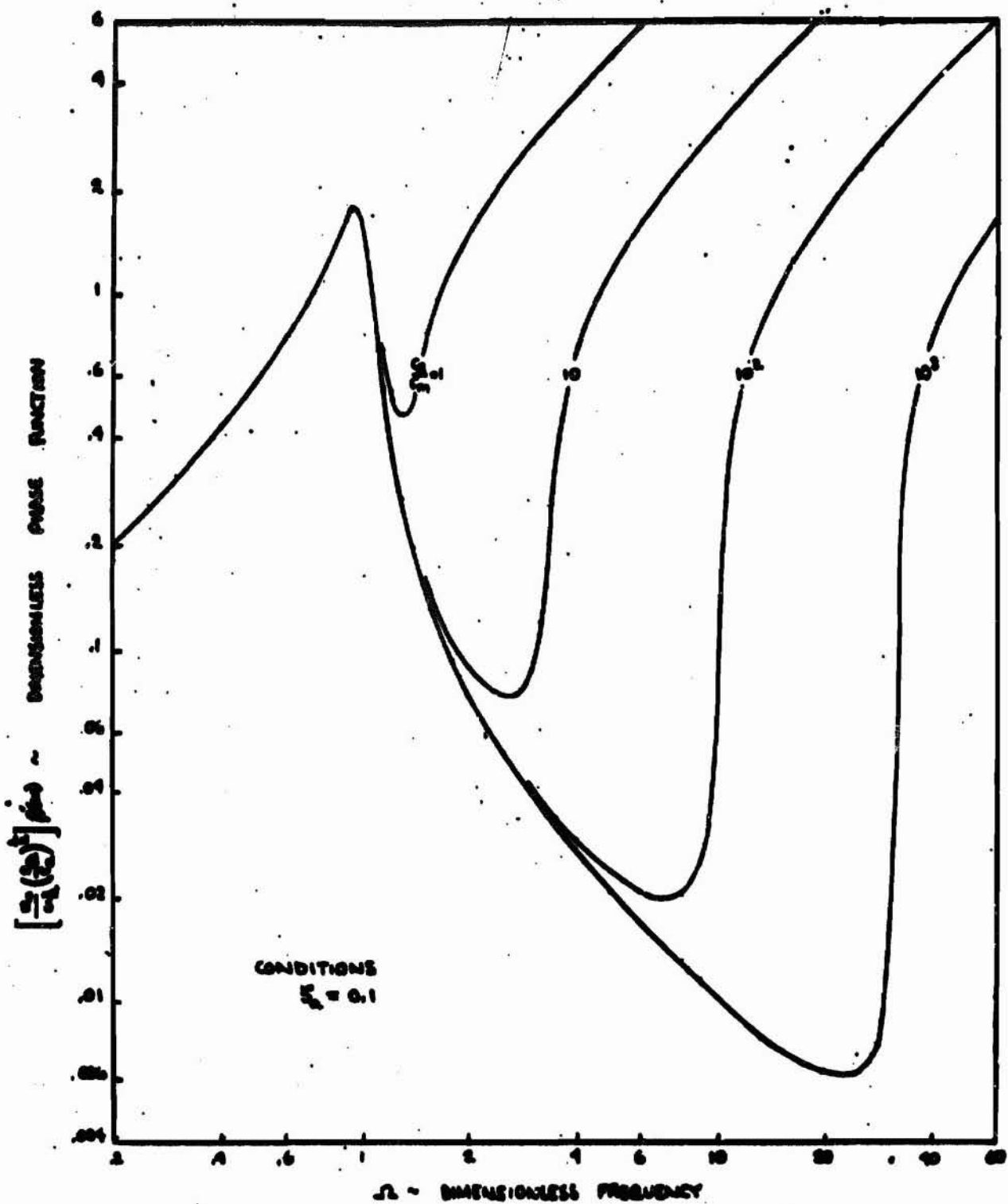


FIGURE 5.

PHASE FUNCTION OF THE ABSORPTIVE LINE

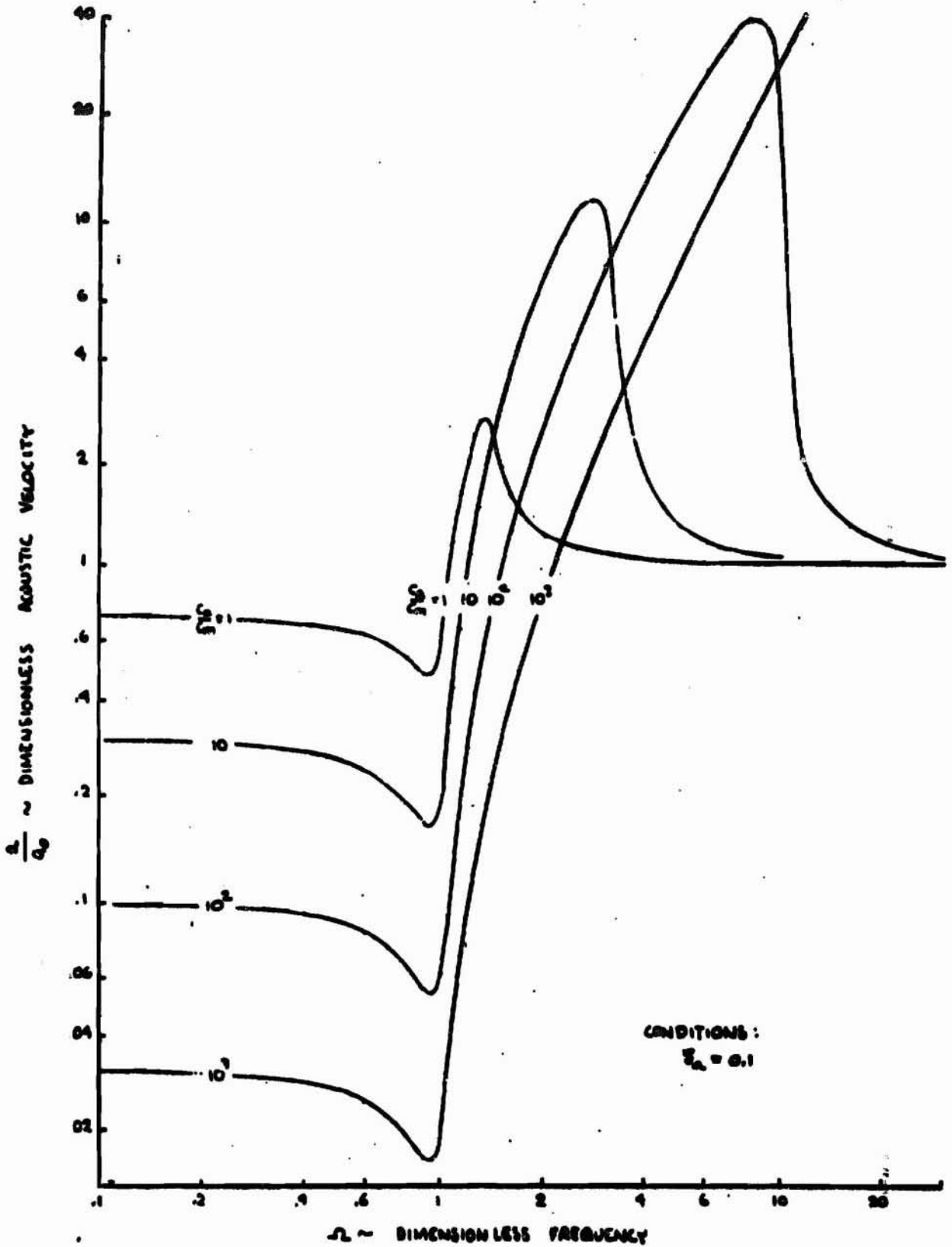


FIGURE 6. ACOUSTIC VELOCITY OF THE ABSORPTIVE LINE

ANDR 9635-037, APPENDIX D

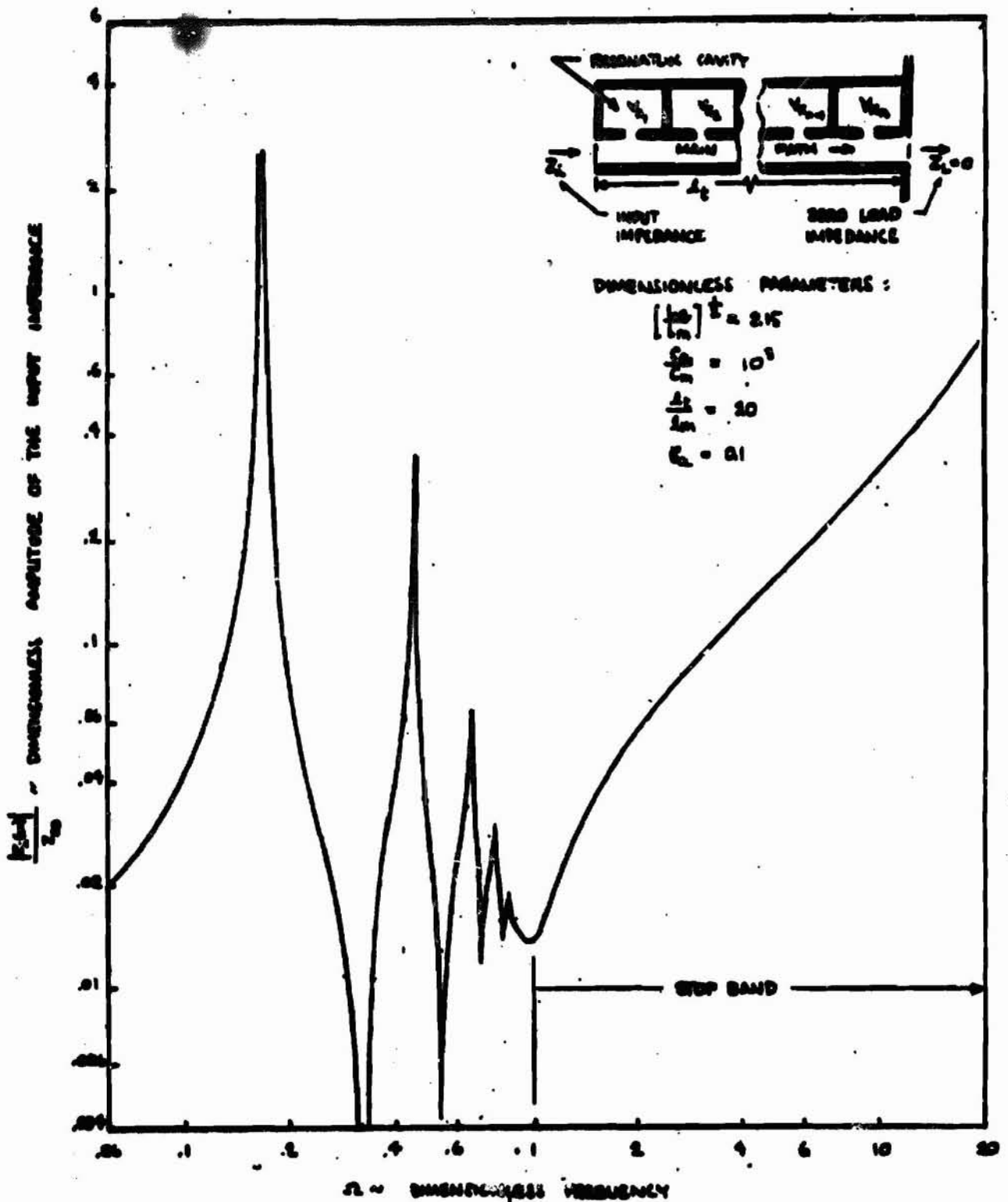


FIGURE 7. INPUT IMPEDANCE OF AN OPEN-ENDED LOSSY LINE WITH $\epsilon_r = 0.1$

AMDR 9635-037, APPENDIX D

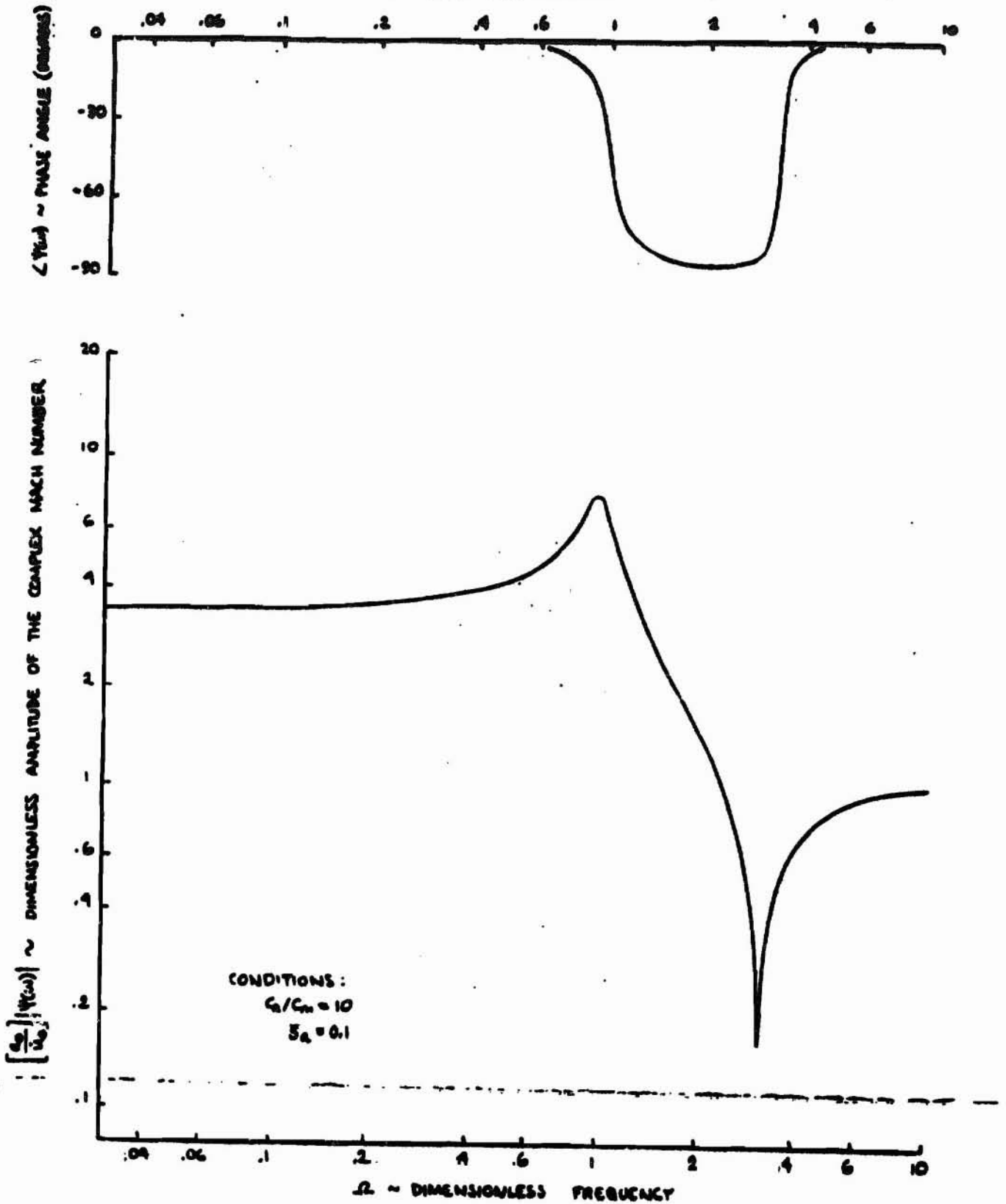


FIGURE 8. COMPLEX MACH NUMBER OF AN ABSORPTIVE LINE WITH FLOW

AMSR 9635-037, APPENDIX D

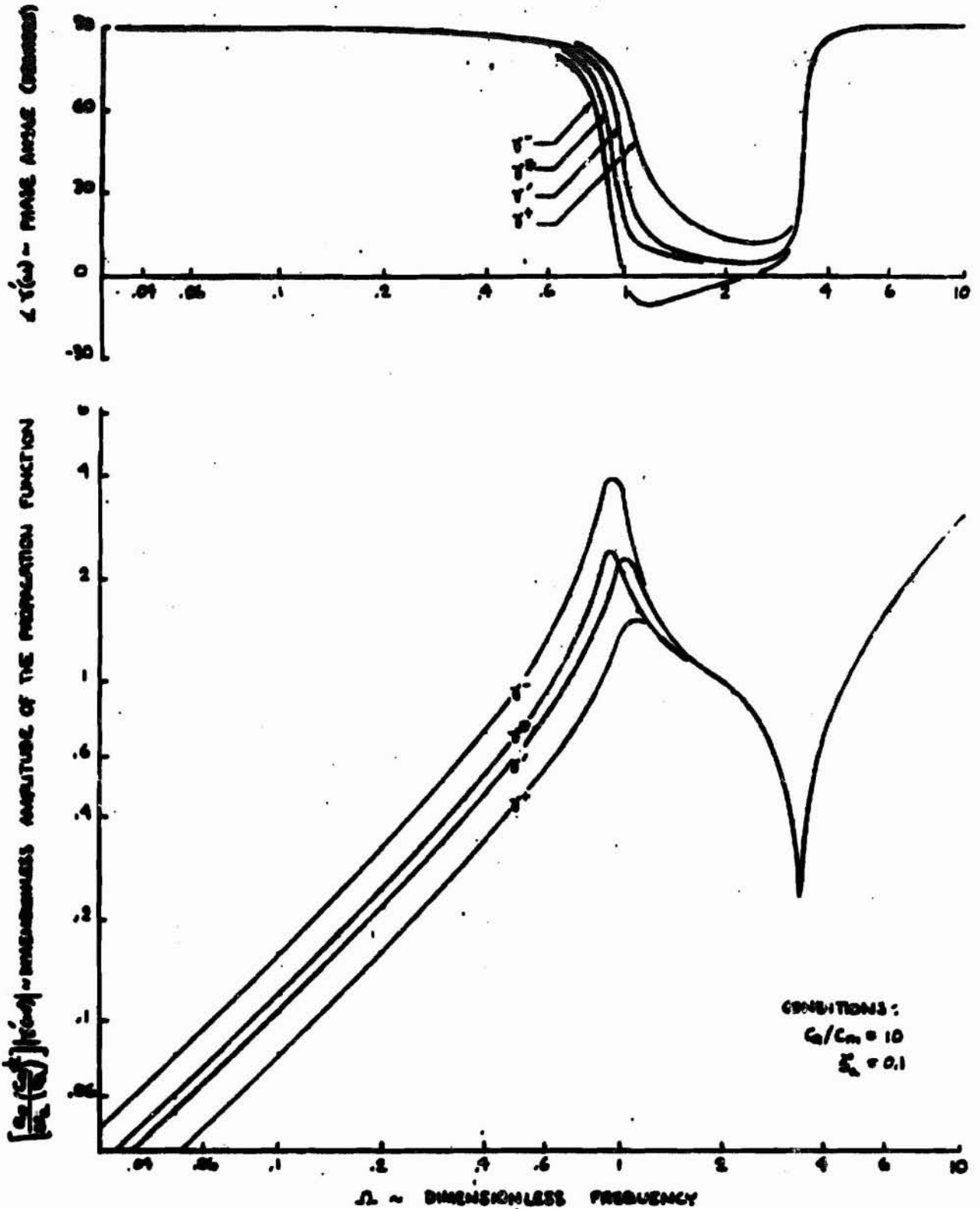


FIGURE 9. PROPAGATION FUNCTIONS OF AN ABSORPTIVE LINE WITH FLOW

AMDR 9635-037, APPENDIX D

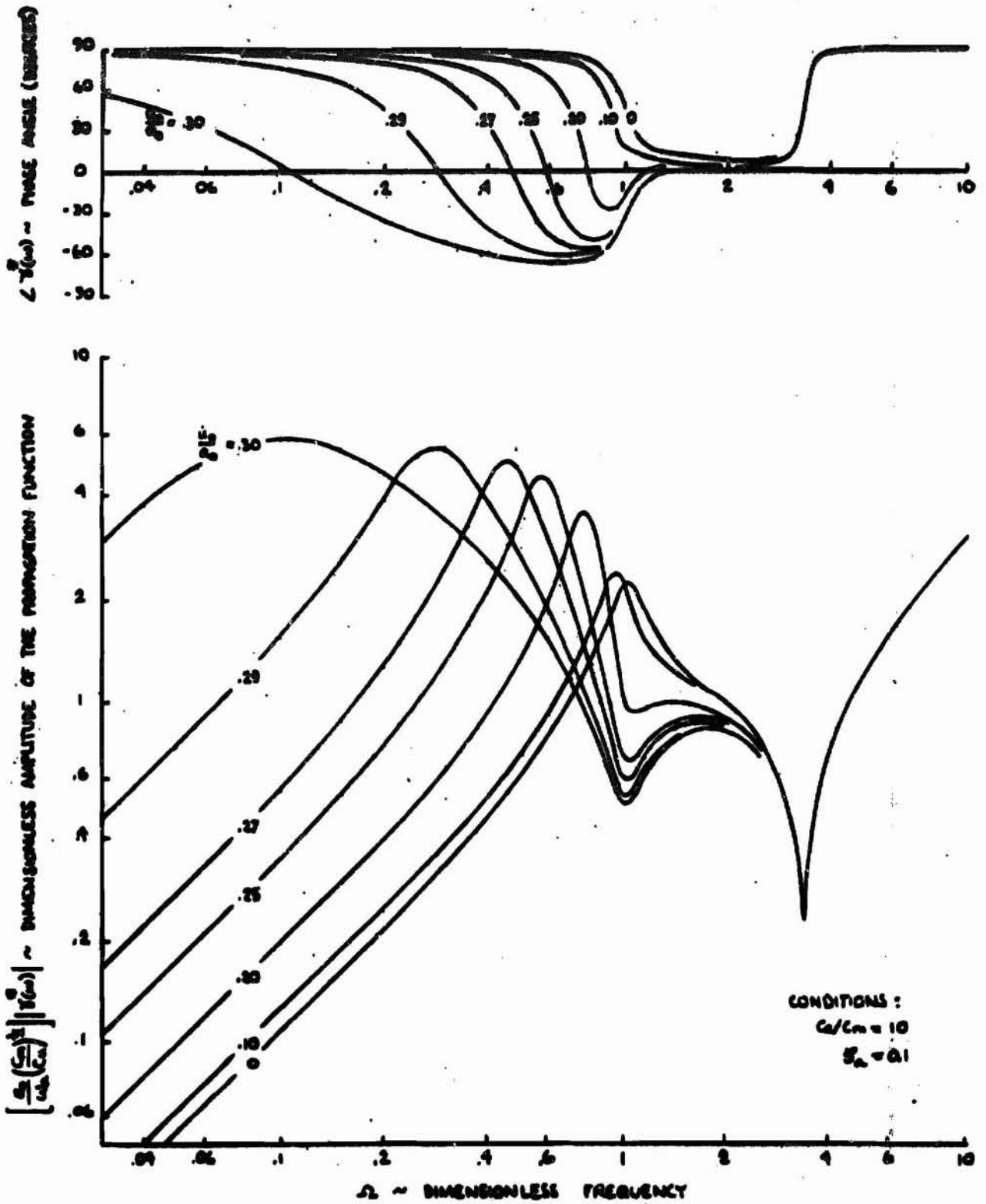


FIGURE 10. EFFECTIVE PROPAGATION FUNCTION OF AN ABSORPTIVE LINE WITH FLOW

AMSR 9635-037, APPENDIX D

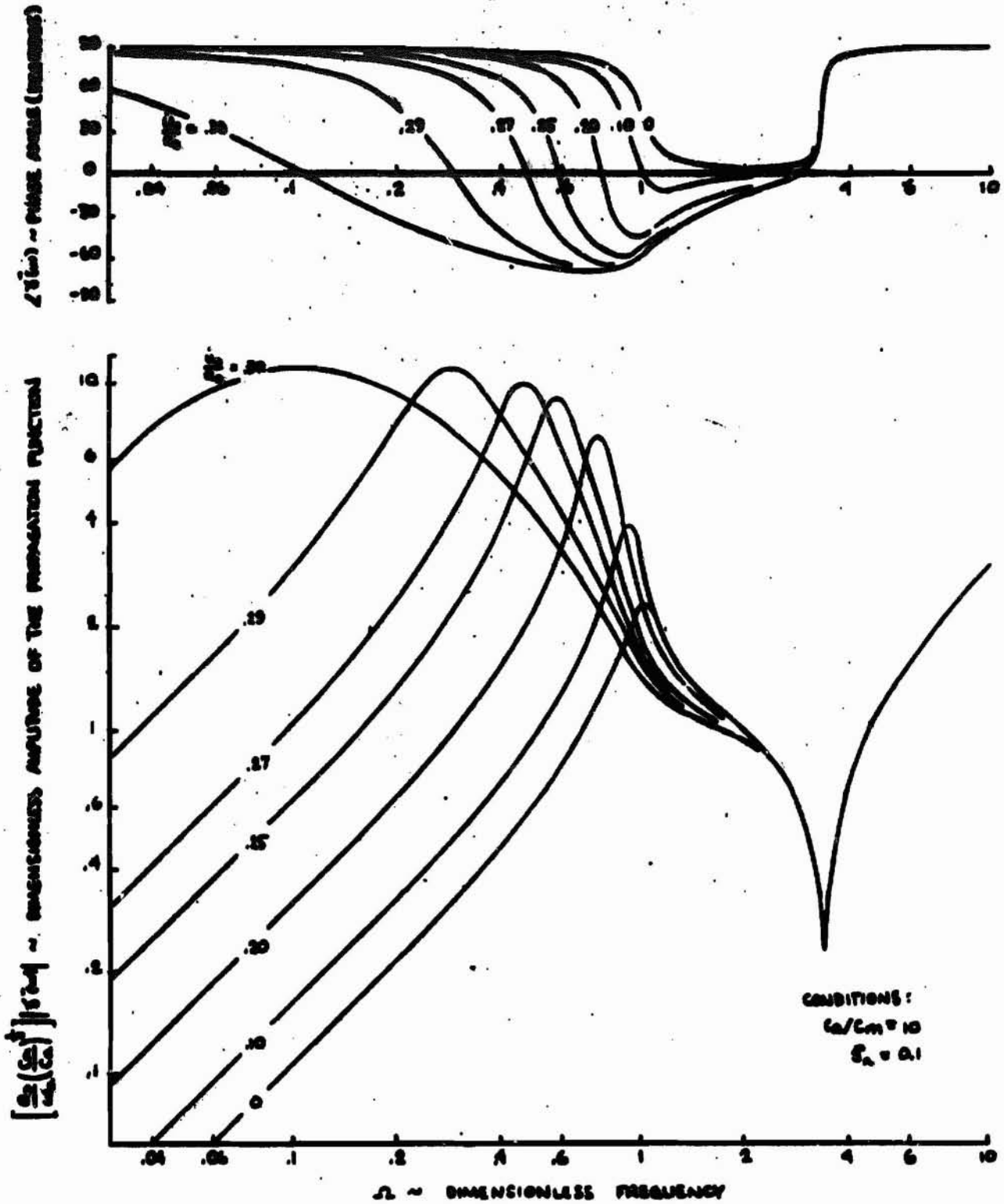
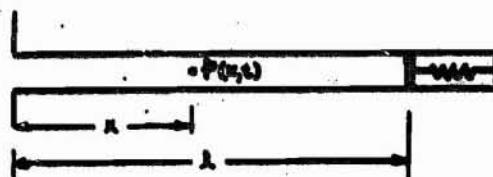
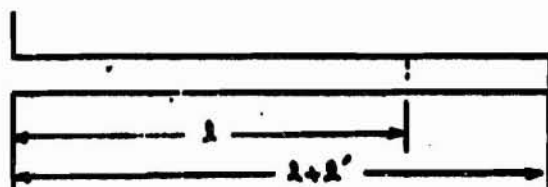


FIGURE 11. UPSTREAM PROPAGATION FUNCTION OF AN ABSORPTIVE LINE WITH FLOW

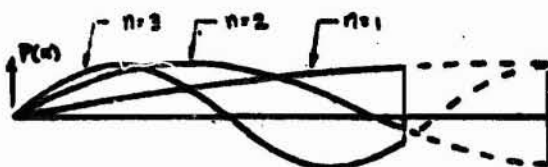
AMDR 9635-037, APPENDIX D



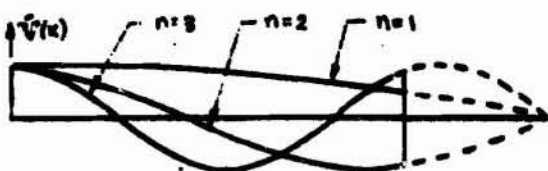
a. Line with Compliance at One End



b. Equivalent Closed-Open End "Organ Pipe"



c. Pressure Mode Shapes for Lossless Line



d. Flow Mode Shape for Lossless Line

FIGURE 12. ACOUSTIC MODE SHAPES FOR A LOSSLESS LINE

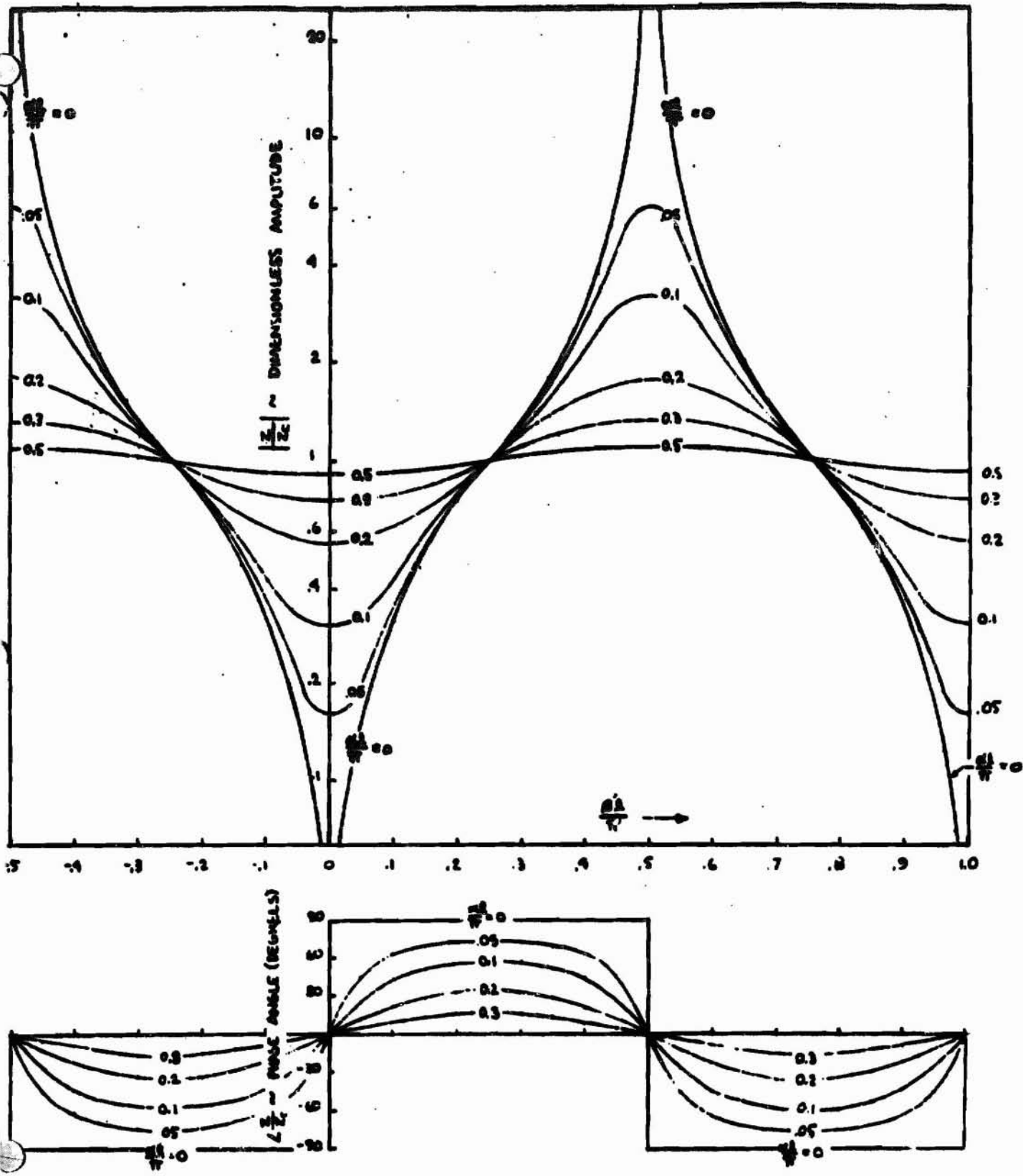


FIGURE 13. PLOT OF $|Z_c| = \text{Tanh}(\alpha'z + j\beta'z)$

APPENDIX E

**BUBBLE DYNAMICS AND WAVES
PROPAGATION THROUGH A BUBBLY MIXTURE**

PRECEDING PAGE BLANK NOT FILMED.

AMDR 9635-037, APPENDIX E

A. INTRODUCTION

The objective of this appendix is to present expressions for the acoustic properties of a gas bubble in a liquid and to show how the generalized absorptive line analysis may be applied to the case of wave propagation through a mixture of liquid and uniformly distributed gas bubbles. The analysis accounts for the effect of the damping or energy dissipation of the bubbles as well as their compliance. Obviously, the increase of the distributed capacitance due to the presence of bubbles will lower the propagation velocity of acoustic waves which travel through the mixture. A secondary effect of the pulsating bubbles is to cause attenuation of the acoustic waves due to bubble damping. The bubble damping is predominantly caused by thermal effects, such as irreversible heat transfer across the bubble walls. This thermal damping is maximum at intermediate frequencies since there is little energy dissipation at very low frequencies when the pulsations are isothermal and at very high frequencies when the pulsations are adiabatic.

B. ACOUSTIC VELOCITY FOR ISOTHERMAL BUBBLES

At frequencies well below the resonant frequency of the bubbles, the acoustic velocity of the mixture may be accurately predicted by the assumption of isothermal bubble pulsations. The analysis was first applied to the case of air bubbles in water by Wood in bibliography entry C.19. Wood's respective expressions for the density, bulk modulus, and acoustic velocity of the mixture

B. (cont.)

may be written

$$\rho_m = \chi \rho_g + (1-\chi) \rho_l \quad (1)$$

$$\frac{1}{B_m} = \frac{\chi}{B_g} + \frac{1-\chi}{B_l} \quad (2)$$

$$a_m = a_l \left[(1-\chi + \chi B_l / B_g)(1-\chi + \chi B_g / B_l) \right]^{-1/2} \quad (3)$$

where

$$\chi = \frac{v}{1+v} = \frac{\text{Gas Volume}}{\text{Mixture Volume}}$$

$$v = \frac{\text{Gas Volume}}{\text{Liquid Volume}}$$

Although these results were obtained for a mixture at rest, bibliography entry C.11 states that they are applicable to two phase flow if the slip ratio between the two phases is small. For the small gas/vapor concentrations that are considered in this report the flow velocities of both phases are equal. Therefore the density, bulk modulus, and low frequency acoustic velocity of the flowing mixture illustrated in Figure 1a may be determined once the expression for the gas concentration is known. In the case of a non-reacting gas injected into a liquid with no evaporation, such as an air/water mixture, the gas volume ratio is written

$$v = \frac{\bar{m}_g}{\bar{m}_l} \frac{R_g T_b}{P_b} w_l \quad (4)$$

B. (cont.)

where

$$\frac{\bar{m}_g}{\bar{m}_l} = \frac{\text{gas injectant mass flow}}{\text{liquid mass flow}}$$

$$R_g = \text{gas constant for injectant}$$

$$T_b = \text{bubble temperature}$$

$$\bar{P}_b = \text{bubble static pressure}$$

$$w_l = \text{weight density of liquid}$$

For the case of a non-reacting gas injected into a liquid with a large vapor pressure, evaporation of the liquid will occur so that the volume of gas/vapor will be larger than that predicted by eq (4). Analysis of this condition by Glasgow and Worlund (bibliography entry C.10, 20), has shown that, if the gas bubble is totally saturated by the vapor, the resulting gas/vapor volume ratio is

$$\mathcal{V} = \frac{\bar{m}_g}{\bar{m}_l} \frac{R_g T_b}{\bar{P}_b - P_v} w_l \quad (5)$$

where P_v is the vapor pressure of the vapor. Although this is a good approximation for the isothermal injection of gaseous helium into the Saturn propellants, it does not hold when the initial gas temperature is substantially different than the liquid temperature. For this case, \mathcal{V} may be predicted by use of thermodynamic source theory as discussed by Yang and Clark (bibliography entry D.12).

The isothermal acoustic velocity for an air/water mixture, as obtained by eq (3) is plotted in Figure 2. Note that the minimum velocity of sound is extremely low (55 fps) and occurs at a volume ratio of $\chi = 0.5$. For small

B. (cont.)

gas concentrations, the mixture density is nearly equal to the liquid density and the expression for the acoustic velocity may be reduced

$$c_m = c_2 [1 + k \chi_0 \nu]^{-\frac{1}{2}} \quad (6)$$

where

$$k = \frac{c_p}{c_v} = \text{specific heat ratio for gas}$$

$$\chi_0 = \frac{B_0}{k P_0} = \text{adiabatic compressibility ratio for the gas}$$

This expression is analogous to equation 31 in Appendix D, which gives the low frequency acoustic velocity for the generalized absorptive line.

G. BUBBLE CAPACITANCE AND CONDUCTANCE

The assumption that bubbles pulsate isothermally is valid only at zero frequency since the heat flow across the bubble wall is reversible only for a quasi-static compression-expansion process. Therefore the analysis of bubble dynamics must account for the thermal damping induced by the polytropic pulsations of the bubble. Additional damping is caused by acoustical reradiation of sound energy from the bubbles and viscous damping at the boundary of the bubble. However, it will be shown that at frequencies below the fundamental vibrational mode of the bubble, the thermal damping is dominant.

The objective of the following analysis is to determine the acoustical capacitance and conductance relative to thermally coupled oscillations of a bubble. It is assumed that any growth of the bubble is slow so that the small amplitude pulsations occur about an equilibrium bubble radius. The bubbles are

AMDR 9635-037, APPENDIX E

C. (cont.)

assumed to be spherical with a radius much smaller than an acoustic wave length. According to bibliography entry C.18, non-spherical bubbles behave as spherical bubbles of the same volume.

In order to determine the capacitance and thermal conductance of a bubble, consider the differential equation governing the temperature and volume fluctuations of the bubble shown in Figure 1b.

$$\frac{D_g}{r} \cdot \frac{\partial^2}{\partial r^2}(r\hat{T}) - \frac{1}{r} \frac{\partial}{\partial t}(r\hat{T}) = \frac{1}{\rho_g c_p v} \frac{\partial v}{\partial t} \cdot P_s \quad (7)$$

D_g = thermal diffusivity of gas

r = radial distance

$P_s = \hat{P}_s(t)$ = instantaneous pressure at bubble surface

$\hat{T} = \hat{T}(r,t)$ = instantaneous temperature at radius

$v = v(r,t)$ = instantaneous volume change at radius

It is shown in bibliography entry C.6 that for sinusoidal pressure and temperature oscillations eq (7) reduces to

$$D_g \frac{\partial^2}{\partial r^2}[rT(r,\omega)] - j\omega [rT(r,\omega)] = \frac{j\omega r}{\rho_g c_p} P_s(\omega) \quad (8)$$

where

$T(r,\omega)$ = complex amplitude of $\hat{T}(r,t)$

$P_s(\omega)$ = complex amplitude of $\hat{P}_s(t)$

The solution to eq (8) in terms of the oscillatory volume flow $\hat{V}_s(\omega)$, and pressure $P_s(\omega)$ at the bubble surface is given in bibliography entry C.17 as

$$\hat{V}_s(\omega) = Y_{sb}(\omega) P_s(\omega) = j\omega C_0 (\epsilon - j\delta) P_s(\omega) \quad (9)$$

AMDR 9635-037, APPENDIX E

G. (cont.)

where

- Y_{sb} = admittance of bubble at surface
- C_0 = adiabatic bubble capacitance
- ϵ = dimensionless bubble capacitance
- δ = dimensionless bubble conductance

The exact expressions for the parameters C_0 , ϵ , and δ are

$$C_0 \triangleq \left. \frac{\partial \bar{V}_s}{\partial \bar{P}_s} \right|_s = \frac{\bar{V}_b}{k \bar{P}_b} \quad (10)$$

$$\epsilon \triangleq \frac{C_b(\omega)}{C_0} = 1 + \frac{3(k-1)}{\bar{\Phi}} \frac{\sinh \bar{\Phi} - \sin \bar{\Phi}}{\cosh \bar{\Phi} - \cos \bar{\Phi}} \quad (11)$$

$$\delta \triangleq \frac{G_b(\omega)}{\omega C_0} = \frac{3(k-1)}{\bar{\Phi}} \left[\frac{\sinh \bar{\Phi} + \sin \bar{\Phi}}{\cosh \bar{\Phi} - \cos \bar{\Phi}} - \frac{2}{\bar{\Phi}} \right] \quad (12)$$

$$\bar{\Phi} \triangleq \left[\frac{2r_b^2 \omega}{D_g} \right]^{\frac{1}{2}} \quad (13)$$

It should be noted that the bubble capacitance and conductance are dependent on frequency since $\bar{\Phi}$ is proportional to $\omega^{\frac{1}{2}}$. These parameters are plotted versus $\bar{\Phi}$ in Figure 3 for air and helium. Investigation of the transcendental functions that define ϵ and δ reveals that they are ill behaved for small arguments $\bar{\Phi}$. Therefore, the following approximations must be used for $\bar{\Phi}$ less than .5

$$\epsilon = k \quad 0 \leq \bar{\Phi} \leq 0.5 \quad (14)$$

$$\delta = 3.15 \cdot 10^{-2} (k-1) \bar{\Phi}^2 \quad 0 \leq \bar{\Phi} \leq 0.5 \quad (15)$$

C. (cont.)

For Φ greater than .5 the exact expressions given in eqs (11) and (12) may be used. However, if simpler expressions are desired, ϵ and δ may be approximated by the expressions

$$\epsilon = 1 + \frac{3(k-1)}{\Phi} \quad , \quad \Phi \geq 5.0 \quad (16)$$

$$\delta = \frac{3(k-1)}{\Phi} \left[1 - \frac{2}{\Phi} \right] \quad \Phi \geq 5.0 \quad (17)$$

For a small concentration ($\nu < .05$) of gas bubbles in a liquid the ratio of the gas compressibility to the liquid compressibility is

$$\chi = \frac{B_g}{k P_b} \epsilon = \chi_0 \epsilon \quad (18)$$

Note that for low frequencies or small bubbles, the dimensionless capacitance is $\epsilon = k$ so that the gas compressibility ratio is indeed isothermal as assumed in the previous section. Referring to Figure 3, it is seen that the dimensionless conductance, which is a measure of thermal dissipation, vanishes for the isothermal case. Dissipation is also small for the adiabatic case which corresponds to large bubbles or high frequencies. However, there is a transition region, corresponding to polytropic bubble pulsations, when the thermal dissipation is maximized.

AMDR 9635-037, APPENDIX E

D. BUBBLE RESONANCE AND DAMPING

The Fourier transformed equation of motion of the bubble, accounting for thermal, acoustical radiation and viscous damping may be written

$$Z_b(\omega) \dot{V}_b(\omega) = [j\omega L_b + R_{rad} + R_{vis} + \frac{1}{G_b + j\omega C_b}] \dot{V}_b(\omega) = P_m(\omega) \quad (19)$$

where

- $Z_b(\omega)$ = impedance of the bubble
- L_b = inertance due to virtual mass of liquid
- R_{rad} = resistance due to radiation loss
- R_{vis} = resistance due to viscous loss
- G_b = conductance due to thermal loss
- C_b = capacitance of bubble

Using the previously derived expressions for G_b and C_b , the impedance expression may be written

$$Z_b(\omega) = j\omega L_b + \frac{\delta}{\omega C_0 (\delta^2 + \epsilon^2)} + R_{rad} + R_{vis} + \frac{\epsilon}{j\omega C_0 (\delta^2 + \epsilon^2)} \quad (20)$$

Noting that $\epsilon^2 \gg \delta^2$ from Figure 3, we may simplify and summarize the expressions for the acoustic parameters

$$Z_b(\omega) = j\omega L_b + R_{th} + R_{rad} + R_{vis} + \frac{1}{j\omega C_0} \quad (21)$$

where

$$\begin{aligned} L_b &= \frac{\rho l}{4\pi r_b} \\ R_{th} &= \frac{1}{\omega C_0} \frac{\delta}{\epsilon^2} \\ R_{rad} &= \frac{\rho \omega^2}{4\pi a^2} \\ R_{vis} &= \frac{\eta l}{\pi r_b^3} \\ C_0 &= \frac{V_b}{k P_b} = \frac{4\pi r_b^3}{3k P_b} \end{aligned}$$

AMDR 9635-037, APPENDIX E

D. (cont.)

The resonant frequency of the bubble is obtained from eq (21) by determining ω such that the bubble reactance ($\text{Im } Z_b$) vanishes:

$$\omega_a = \left[\frac{1}{L_b C_b} \right]^{\frac{1}{2}} = \frac{1}{r_b} \left[\frac{3k \bar{P}_b}{\rho_l \epsilon} \right]^{\frac{1}{2}} \quad (22)$$

This is the "breathing mode" frequency of the bubble, which may be predicted more accurately for very small bubbles by accounting for effect of surface tension on the bubble stiffness. By including this effect, the exact expression for the breathing mode frequency is given in bibliography entry C.6 as

$$\omega_a = \left(\frac{\tau}{\epsilon} \right)^{\frac{1}{2}} \omega_0 \quad (23)$$

where the adiabatic breathing mode frequency and the surface tension factor are defined as

$$\omega_0 \triangleq \frac{1}{r_b} \left[\frac{3k \bar{P}_b}{\rho_l} \right]^{\frac{1}{2}} = \text{adiabatic breathing mode frequency} \quad (24)$$

$$\tau \triangleq 1 + \frac{2\sigma}{\bar{P}_b r_b} \left[1 - \frac{\epsilon}{3k} \right] = \text{surface tension factor} \quad (25)$$

With these definitions, the dimensionless bubble impedance is

$$Z_b(j\omega C_0) = (1 - \Omega^2) + j 2\zeta_a \Omega \quad (26)$$

where

$$\Omega_a = \omega / \omega_a = \text{dimensionless frequency}$$

$$\zeta_a = \frac{1}{2} \omega_a C_0 (\Sigma R) = \text{total damping factor}$$

AMDR 9635-037, APPENDIX E

D. (cont.)

The dimensionless frequency is easily found in terms of the adiabatic breathing mode frequency:

$$\Omega = \left(\frac{\epsilon}{\tau}\right)^{\frac{1}{2}} \cdot \frac{\omega}{\omega_0} = \left(\frac{\epsilon}{\tau}\right)^{\frac{1}{2}} \Omega_0 \quad (27)$$

The bubble damping factor may be derived by use of the resistance expressions accompanying eq (21). The effective capacitance may be adjusted by the factor τ to account for surface tension.

$$\delta_a = \delta_{th} + \delta_{rad} + \delta_{vis} \quad (28)$$

where
$$\delta_{th} = \frac{1}{2} \frac{\tau \delta}{\epsilon \Omega} = \text{thermal damping factor}$$

$$\delta_{rad} = \Theta_2 \left(\frac{\tau}{\epsilon}\right)^{\frac{1}{2}} \Omega^2 = \text{radiative damping factor}$$

$$\delta_{vis} = \Theta_3 \left(\frac{\epsilon}{\tau}\right)^{\frac{1}{2}} = \text{viscous damping factor}$$

Thus the damping factors are all functionally dependent upon the dimensionless conductance and/or capacitance, which may be expressed in terms of the dimensionless frequency:

$$\epsilon = \begin{cases} 1 + \frac{3(k-1)}{\Theta_1 \Omega_0^{k/2}} \frac{\sinh \Theta_1 \Omega_0^{k/2} - \sin \Theta_1 \Omega_0^{k/2}}{\cosh \Theta_1 \Omega_0^{k/2} - \cos \Theta_1 \Omega_0^{k/2}}, & \Theta_1 \Omega_0^{k/2} \geq 0.5 \\ k, & \Theta_1 \Omega_0^{k/2} < 0.5 \end{cases} \quad (29)$$

$$\delta = \begin{cases} \frac{3(k-1)}{\Theta_1 \Omega_0^{k/2}} \left[\frac{\sinh \Theta_1 \Omega_0^{k/2} + \sin \Theta_1 \Omega_0^{k/2}}{\cosh \Theta_1 \Omega_0^{k/2} - \cos \Theta_1 \Omega_0^{k/2}} - \frac{2}{\Theta_1 \Omega_0^{k/2}} \right], & \Theta_1 \Omega_0^{k/2} \geq 0.5 \\ 3.15 \cdot 10^{-2} (k-1) \Theta_1^2 \Omega_0, & \Theta_1 \Omega_0^{k/2} < 0.5 \end{cases} \quad (30)$$

AMDR 9635-037, APPENDIX E

D. (cont.)

The constants \mathbb{Q}_1 , \mathbb{Q}_2 , and \mathbb{Q}_3 may be called the thermal, radiative, and viscous damping parameters, respectively. These parameters are defined by the equations

$$\mathbb{Q}_1 = \left[\frac{2r_b^2 \omega_0}{D_g} \right]^{\frac{1}{2}} = \left[\frac{2r_b}{D_g} \right]^{\frac{1}{2}} \left[\frac{3k\bar{P}_b}{\rho_L} \right]^{\frac{1}{4}} \quad (31)$$

$$\mathbb{Q}_2 = \frac{r_b \omega_0}{2a_L} = \left[\frac{3k\bar{P}_b}{4B_L} \right]^{\frac{1}{2}} = \left[\frac{3}{4} \frac{1}{\chi_o} \right]^{\frac{1}{2}} \quad (32)$$

$$\mathbb{Q}_3 = \frac{2\eta_L}{r_b^2 \omega_0} = \frac{2\eta_L}{r_b} \left[\frac{\rho_L}{3k\bar{P}_b} \right]^{\frac{1}{2}} \quad (33)$$

By the use of the above constants for a given gas/liquid mixture, and the equations for the desired bubble oscillation characteristics such as ω_0 , χ_o , and ξ_L , the dynamic behavior of a bubble may be completely specified. For example, a plot of the adiabatic breathing mode frequency of helium bubbles in the Saturn propellants is shown in Figure 4.

E. APPLICATION OF THE ABSORPTIVE LINE ANALYSIS

The application of the generalized absorptive transmission line to the case of wave propagation through a homogenous mixture of liquid and gas bubbles is easily accomplished by use of the bubble oscillatory representation derived in the preceding sections of this appendix. Consider eqs (16) and (24) from Appendix D, which describe the characteristic impedance and propagation function, respectively:

AMDR 9635-037, APPENDIX E

E. (cont.)

$$Z_c(\omega) = Z_{co} \left[\frac{(1-\Omega^2)^2 - \left(\frac{C_a}{C_m} - 4\delta_a\right)\Omega^2 + \frac{C_a}{C_m} + j2\delta_a\Omega \frac{C_a}{C_m}}{(1-\Omega^2 + \frac{C_a}{C_m})^2 + 4\delta_a^2\Omega^2} \right]^{\frac{1}{2}} \quad (34)$$

$$\delta'(\omega) = j\omega L_m / Z_c(\omega) \quad (35)$$

Recall that in the original absorptive line analysis, the parameters C_a/C_m , ω_a , and δ_a were independent of frequency and were thus input variables. In the case of wave propagation through a bubbly mixture, it has been shown that these frequency dependent functions are defined as follows:

$$\frac{C_a}{C_m} = \epsilon(\omega) \frac{C_0}{C_m} \quad (36)$$

$$\omega_a = \left[\frac{\tau(\omega)}{\epsilon(\omega)} \right]^{\frac{1}{2}} \omega_0 \quad (37)$$

$$\Omega = \left[\frac{\epsilon(\omega)}{\tau(\omega)} \right]^{\frac{1}{2}} \Omega_0 \quad (38)$$

$$\begin{aligned} \delta_a &= \delta_{th} + \delta_{rad} + \delta_{vis} \\ &= \frac{1}{2} \frac{\tau(\omega) \delta(\omega)}{\epsilon(\omega) \Omega} + \mathbb{Q}_2 \left[\frac{\tau(\omega)}{\epsilon(\omega)} \right]^{\frac{1}{2}} \Omega^2 + \mathbb{Q}_3 \left[\frac{\epsilon(\omega)}{\tau(\omega)} \right]^{\frac{1}{2}} \end{aligned} \quad (39)$$

where $\tau(\omega)$, $\epsilon(\omega)$, and $\delta(\omega)$ are defined by eqs (25), (29), and (30), respectively. The input variables required by these equations are now ω_0 , C_0/C_m , \mathbb{Q}_1 , \mathbb{Q}_2 , and \mathbb{Q}_3 . These constants may be evaluated by the graphs presented in this appendix.

Both the bubble adiabatic breathing mode frequency and capacitance ratio are strongly dependent on gas pressure. The prediction of the breathing mode frequency for helium bubbles in LO_2 or RP-1 may be accomplished by use of Figure 4. For

AMDR 9635-037, APPENDIX E

E. (cont.)

small gas concentrations, the adiabatic capacitance ratio is given by the expression

$$\frac{C_o}{C_m} = \chi_o \psi = \frac{B_\lambda}{k P_b} \quad (40)$$

where ψ is obtained by use of eq (4), eq (5) or an exact bubble growth analysis employing thermodynamic source theory. For the case of negligible propellant vaporization and isothermal He injection, C_o/C_m may be estimated from Figure 5, which is a plot of eq (40) combined with eq (4). The effect of the propellant line structural elasticity has been included by use of the following equation for the effective liquid bulk modulus:

$$B_\lambda = B_\infty \left[1 + \frac{B_\infty d}{E h} \right]^{-1} \quad (41)$$

where

B_λ = bulk modulus of liquid and elastic line

B_∞ = bulk modulus of liquid only

E = elastic modulus of wall material

h = line wall thickness

d = line diameter

It is seen from Figure 5 that the effect of reducing the dimensionless wall thickness is to lower the capacitance ratio by means of increasing the effective liquid compressibility.

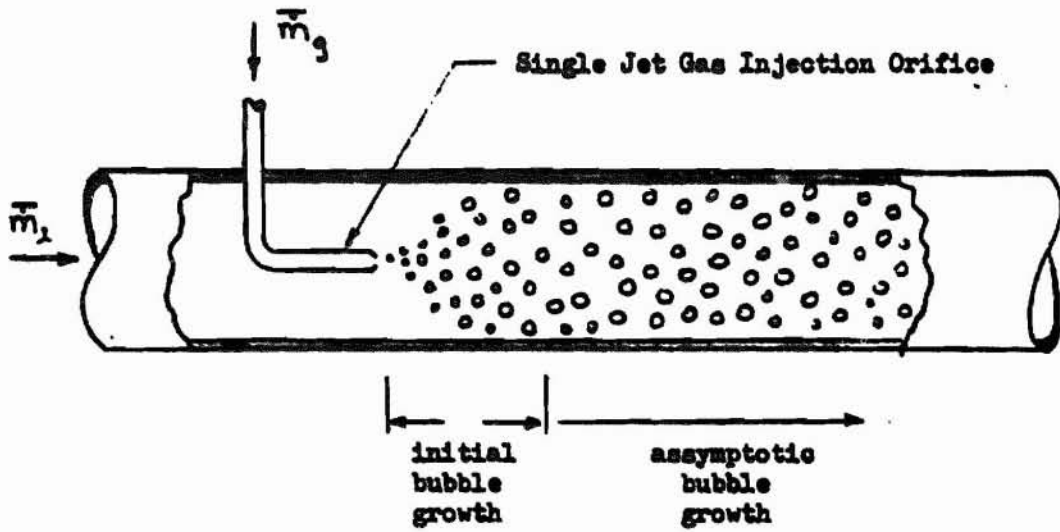
The effect of oxygen vaporization on the capacitance ratio for isothermal injection of helium in LO_2 is shown in Figure 6. This plot of eqs (4), (5), and (40) illustrates that the capacitance ratio at low pressures is considerably

E. (cont.)

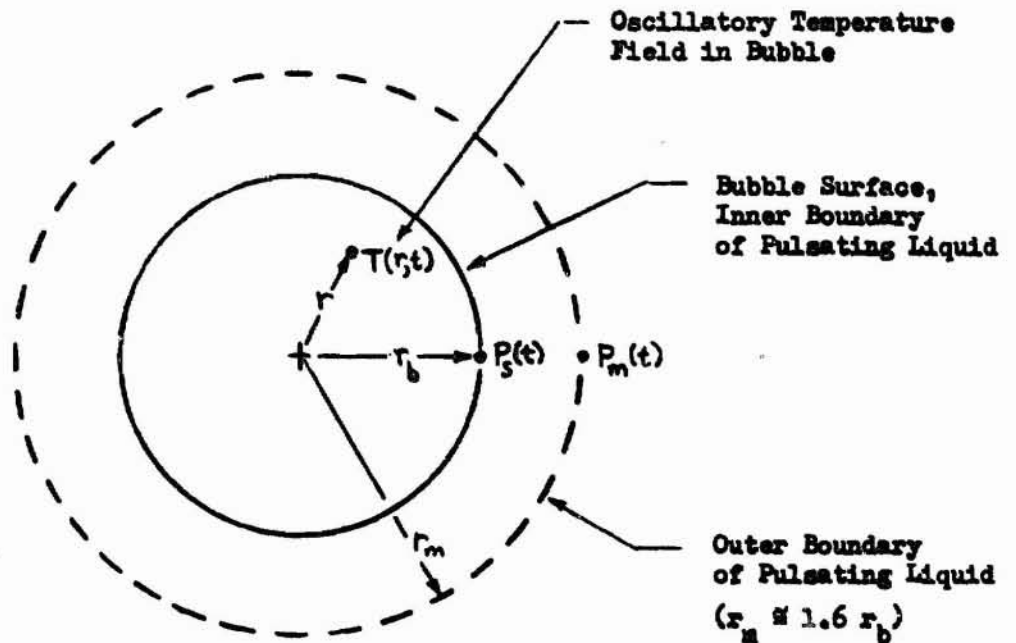
increased by the effect of vaporization. Therefore, it is seen that Figure 6 should be used for the evaluation of isothermal gas injection in LO_2 whereas Figure 5 is adequate for RP-1.

Finally, the bubble damping parameters may be estimated from eqs (31), (32), and (33). The thermal damping parameter \mathcal{Q}_1 , is of particular importance since the thermal damping is dominant at the frequencies of interest. This parameter is a function of the gas thermal diffusivity which is plotted in Figures 7 and 8 for helium and air. Figure 9, which results from Figure 8 and eq (31), allows the determination of \mathcal{Q}_1 , as a function of the bubble temperature, pressure and radius.

APPENDIX E



a) Suction Line Section with Gas Bubble Injection



b) Coordinate System for Bubble Dynamic Model

FIGURE 1 SKETCH OF GAS INJECTION AND BUBBLE MODELS

APPENDIX E

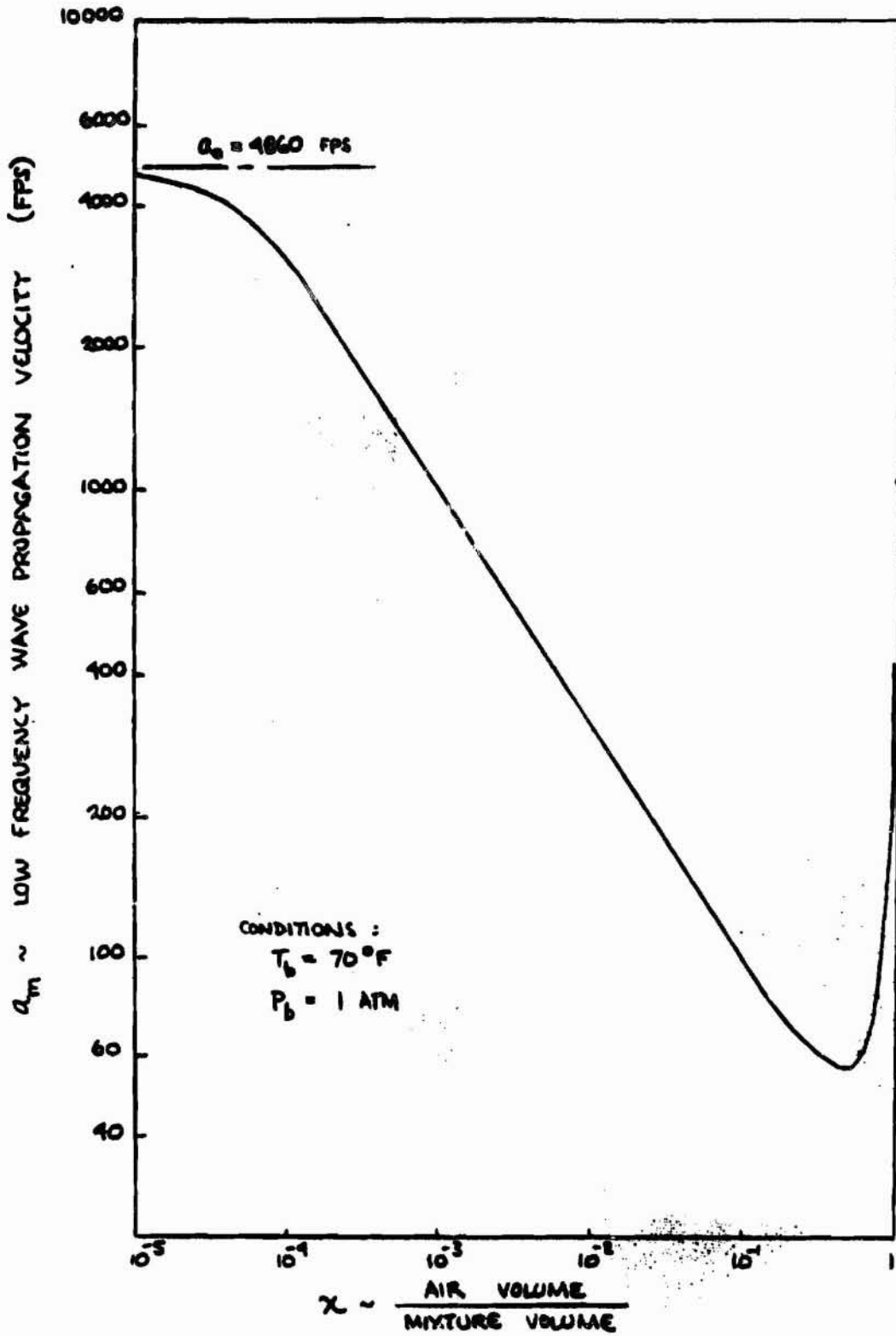


FIGURE 2 ACOUSTIC VELOCITY FOR AN AIR-WATER MIXTURE

APPENDIX B

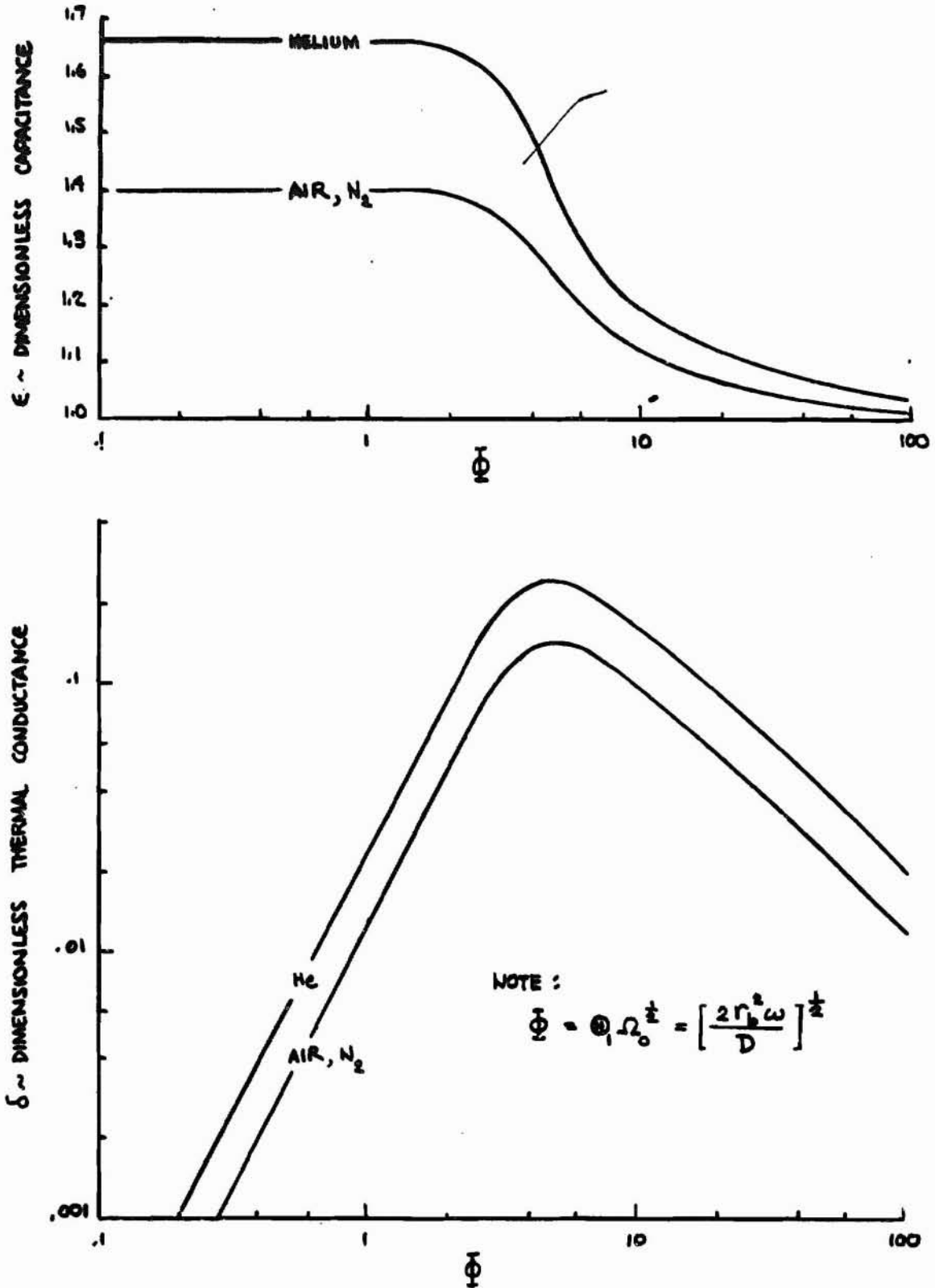


FIGURE 3 THERMAL CAPACITANCE AND CONDUCTANCE OF A GAS BUBBLE

APPENDIX E

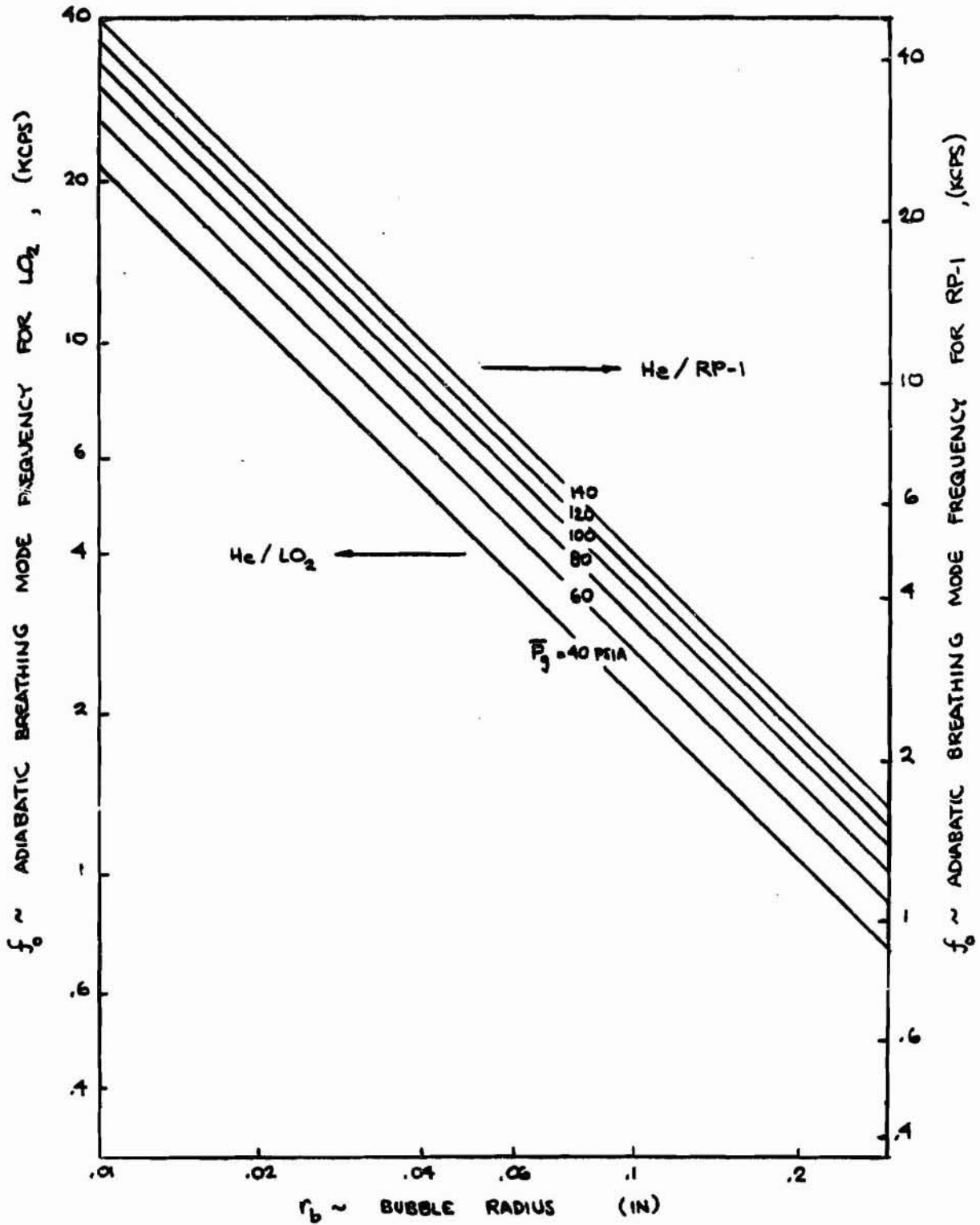


FIGURE 4 ADIABATIC BREATHING MODE FREQUENCY FOR HELIUM BUBBLES

APPENDIX B

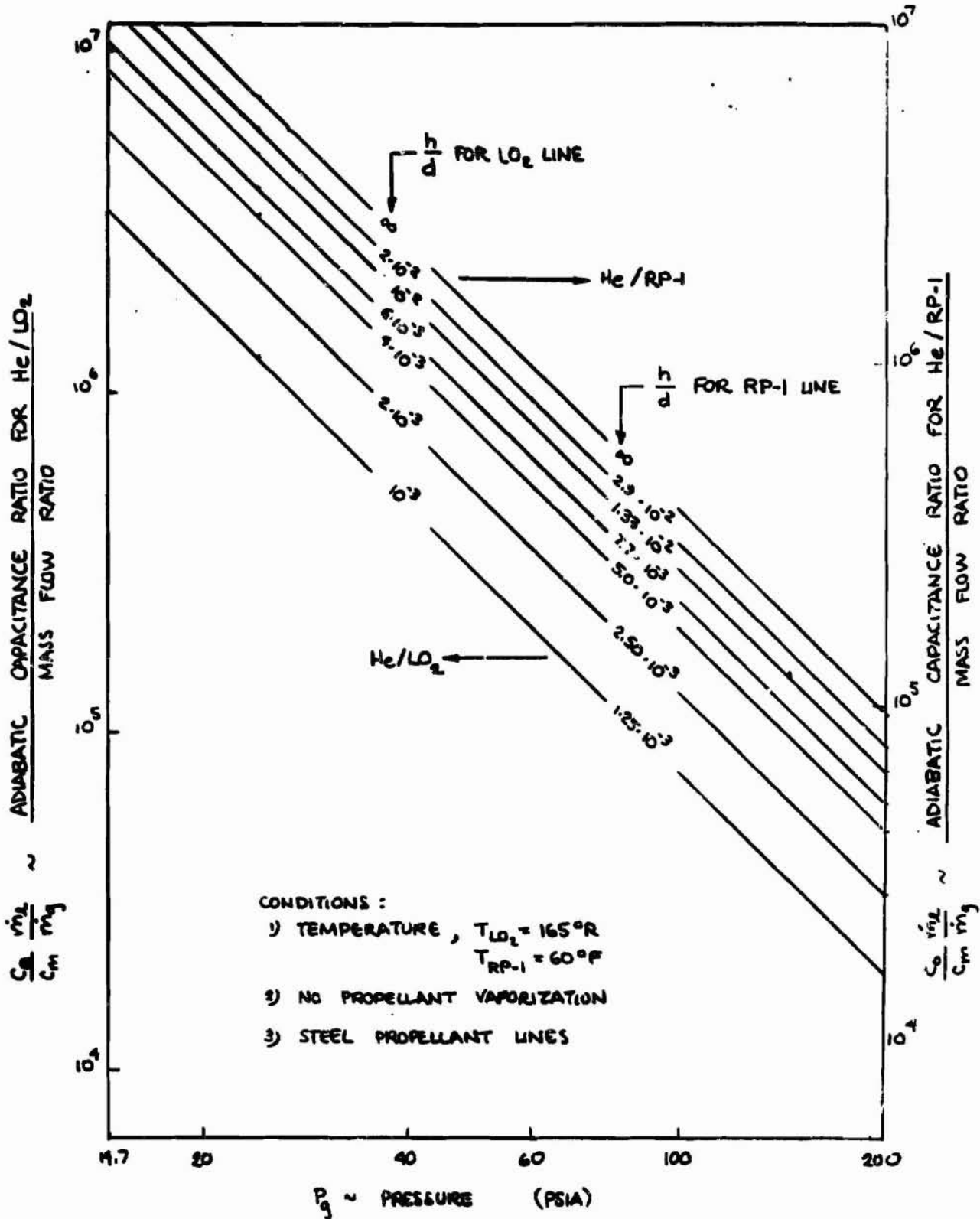


FIGURE 5 HELIUM CAPACITANCE RATIO FOR NO PROPELLANT VAPORIZATION

APPENDIX E

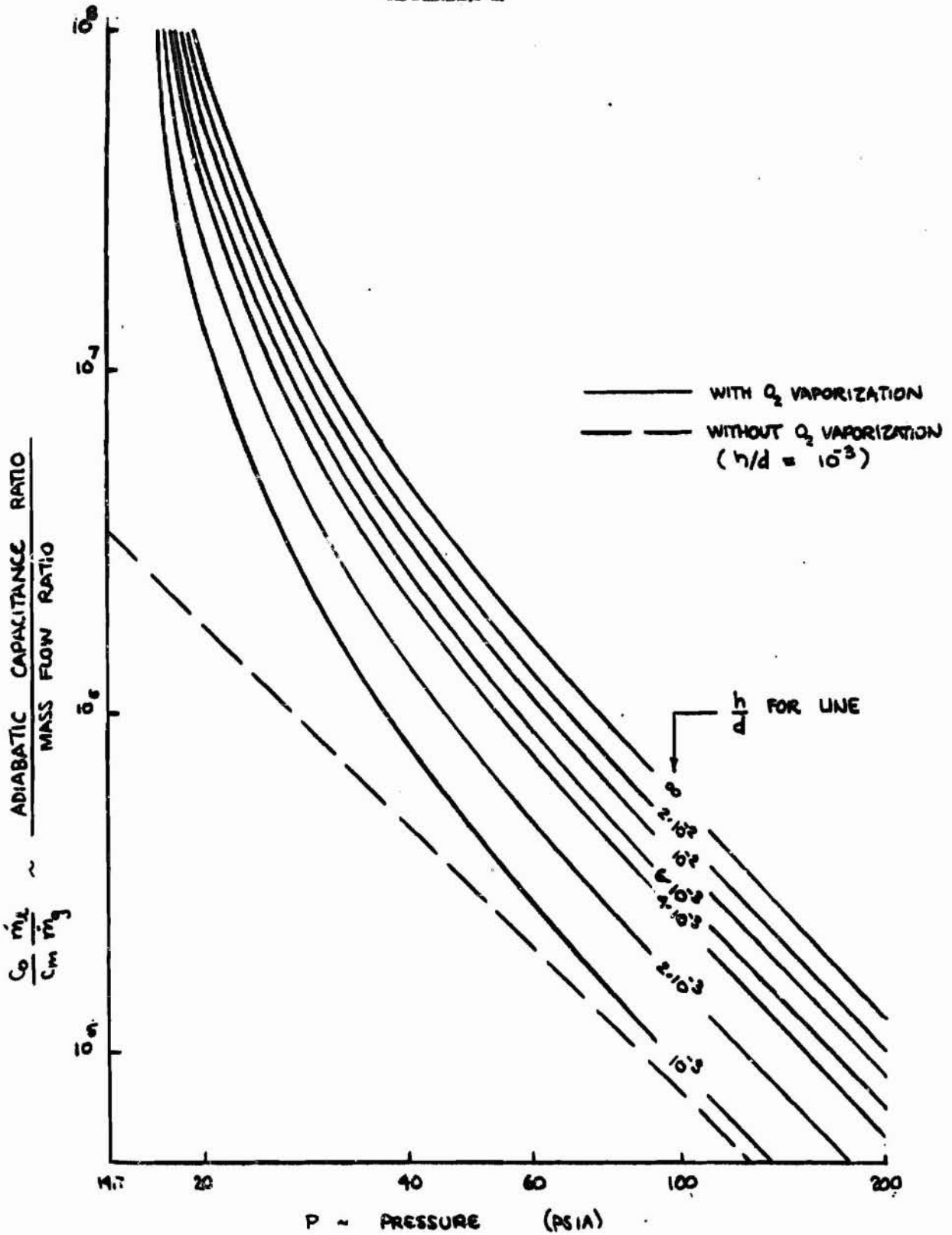


FIGURE 6 CAPACITANCE RATIO FOR ISOTHERMAL HELIUM INJECTION IN LO₂

APPENDIX B

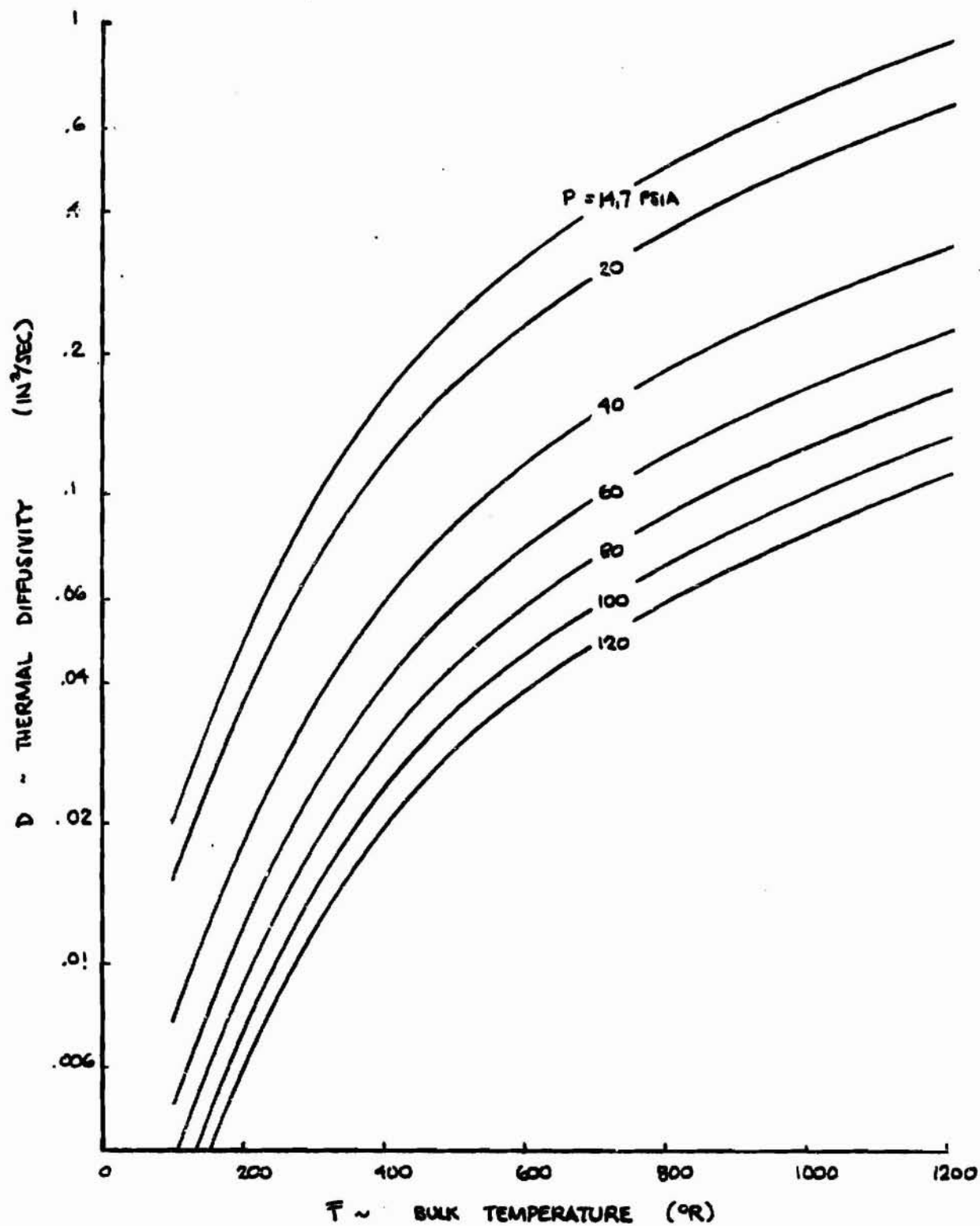


FIGURE 7 THERMAL DIFFUSIVITY OF HELIUM VERSUS TEMPERATURE

APPENDIX B

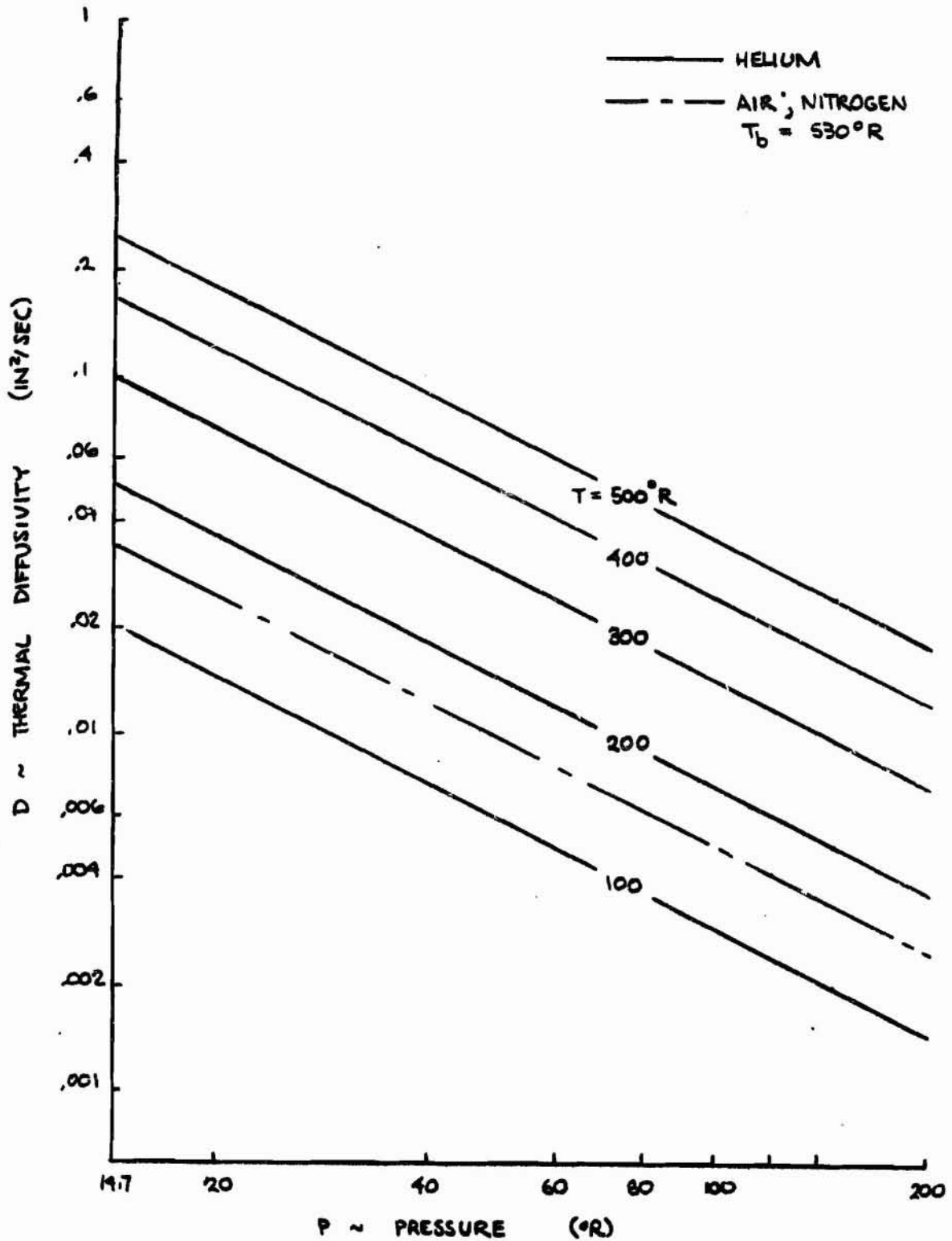


FIGURE 8 THERMAL DIFFUSIVITY OF AIR AND HELIUM

APPENDIX E

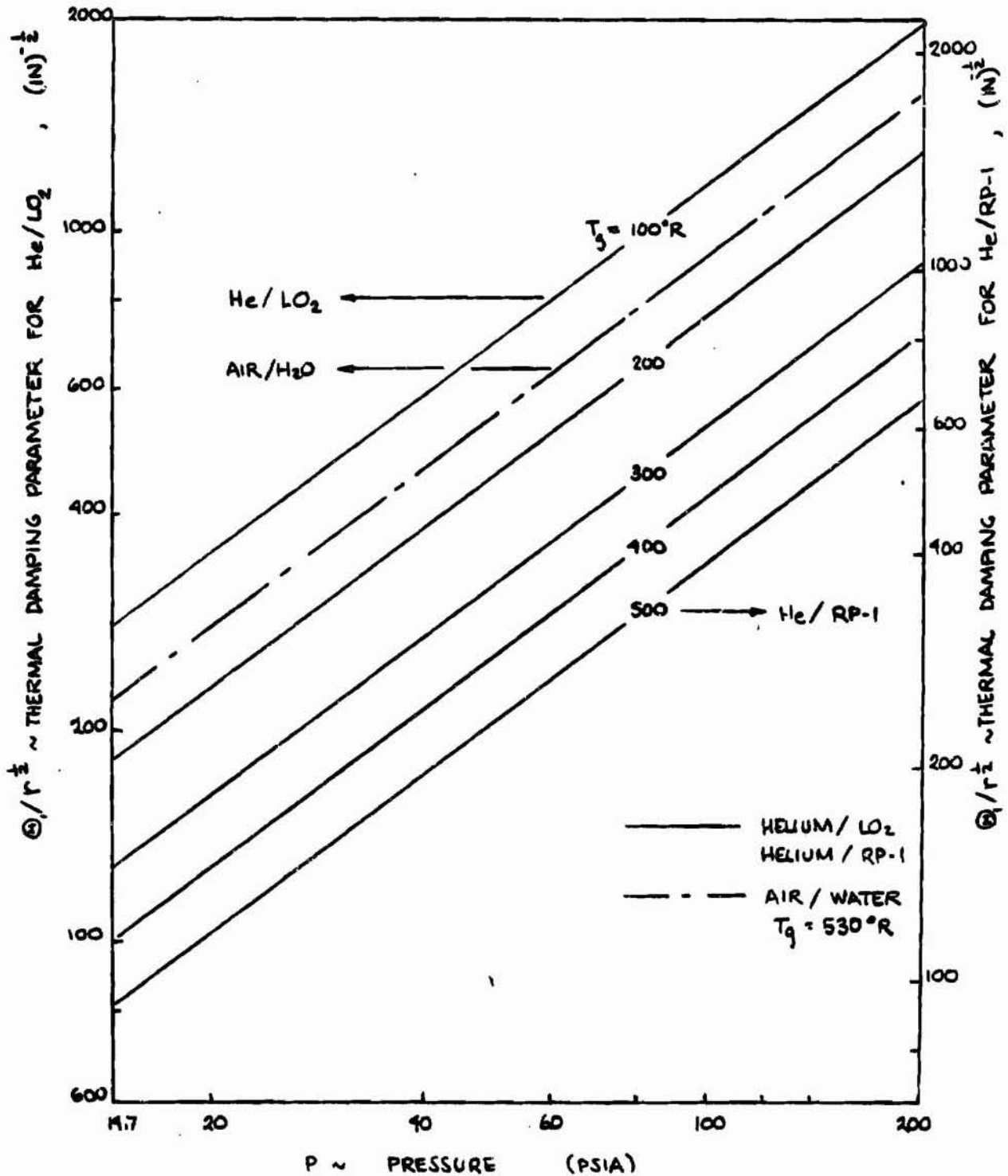


FIGURE 9 THERMAL DAMPING PARAMETER FOR HELIUM BUBBLES

AMDR 9635-037

APPENDIX F

ANALYTICAL MODELS OF THE PROPELLANT FEED SYSTEM

PRECEDING PAGE BLANK NOT FILMED.

APPENDIX F

A. APPLICATION OF THE ANALYTICAL MODELS

The analytical models developed for the frequency response analysis of the Saturn IB and Saturn IC feed systems are presented in this appendix. Both the preliminary model used in Part I and the final model used in Part II are discussed. The preliminary model was used for the study of the response characteristics of the nominal feed system, as well as an initial evaluation of candidate stabilizing devices. This model is sketched in Figure 1. The final analytical model, shown in Figure 2, was developed to allow a more complete evaluation of the various feed system stabilizing devices. Both models were used to represent four Saturn feed system configurations; which were the Saturn IB outboard engine LO_2 system, the Saturn IB outboard engine fuel system, the Saturn IC outboard engine LO_2 system, and the Saturn IC outboard engine fuel system. Because of the very close similarity between the inboard engine feed system and the outboard engine feed system, the results of these studies are generally applicable to either system.

A digital computer program has been devised for each model to compute the various transfer functions and impedances which describe the response of the feed system as a function of frequency. Both programs utilize matrix methods to couple the various elements, such as stabilizing devices, suction lines, pump cavitation compliance, pump resistance, discharge impedance, and thrust chamber impedance. The results of the analysis may be presented as Bode (frequency response) plots of pertinent propulsion system transfer functions. In addition, the complex coefficients of the characteristic matrices that describe each feed system element may be printed out. Once the frequency response of these elements is determined, in terms of a characteristic matrix, this matrix may be approximated as a function of the Laplacian variable s , by numerical methods. Thus the analytical models may be used to investigate the dynamic characteristics of the entire propulsion system or any of its major components.

AMDR 9635-037, APPENDIX F

B. ANALYTICAL MODEL FOR PART I

1. Matrix Operations and Resultant Transfer Functions

The initial analytical model makes extensive use of the transmission matrix theory discussed in Appendix B. Consider the transmission matrix of the entire propulsion system circuit shown in Figure 1:

$$\dot{\Psi}_1(\omega) = \bar{A}_t(\omega) \dot{\Psi}_g(\omega) \quad (1)$$

where

$$\bar{A}_t(\omega) = [a_{ij}^t(\omega)] = \text{forward transmission matrix of the entire circuit}$$

$$\dot{\Psi}_1(\omega) = [P_1(\omega) \dot{V}_1(\omega)]^t = \text{input state vector}$$

$$\dot{\Psi}_g(\omega) = [P_g(\omega) \dot{V}_g(\omega)]^t = \text{output state vector}$$

The matrix $\bar{A}_t(\omega)$ may be obtained by multiplying the transmission matrices of the individual elements:

$$\bar{A}_t(\omega) = \bar{A}_1(\omega) \bar{A}_2(\omega) \cdots \bar{A}_k(\omega) \cdots \bar{A}_7(\omega) \quad (2)$$

where

$$\bar{A}_k(\omega) = [a_{ij}^k(\omega)] = \text{forward transmission matrix of the } k^{\text{th}} \text{ element}$$

From the circuit of Figure 1, it is immediately seen that P_1 and \dot{V}_1 are the oscillatory amplitudes of the pressure and volume flow at the tank-suction line interface, respectively. Obviously, P_g is the oscillatory amplitude of the suction pressure. However, it is not so obvious that \dot{V}_g is the oscillatory flow modulation due to the vertical oscillatory motion of the pump.

Recall that the forward transmission matrix of a 2-port network can be easily transformed to an admittance or impedance matrix by use of Table 1 in Appendix B. Therefore, alternate expressions for the response of the entire circuit may be written in terms of its admittance matrix $\dot{Y}_t(\omega)$ or impedance matrix $Z_t(\omega)$

$$\dot{V}_t^s(\omega) = Y_t(\omega) P_t(\omega) \quad (3)$$

AMDR 9635-037, APPENDIX F

B.1, Matrix Operations and Resultant Transfer Functions (cont.)

$$\mathbb{P}_t(\omega) = \mathbb{Z}_t(\omega) \mathbb{V}_t^s(\omega) \quad (4)$$

where

$$\mathbb{P}_t(\omega) = [P_1(\omega) \ P_8(\omega)]^t = \text{"external" pressure vector}$$

$$\mathbb{V}_t^s(\omega) = [V_1^s(\omega) \ V_8^s(\omega)]^t = \text{"external" source flow vector}$$

The matrix $\mathbb{Y}_t(\omega)$ and its inverse $\mathbb{Z}_t(\omega)$ may be used to derive the desired system transfer functions. We wish to derive transfer functions that relate the oscillatory suction pressure oscillations ($P_8(\omega)$) to the major "Pogo" oscillatory inputs, oscillatory pump motion and oscillatory tank bottom pressure. First, we consider the input impedance of the pump inlet by designating $V_8^s(\omega)$ as the input and setting the tank pressure $P_1(\omega)$ to zero:

$$Z_{ip}(\omega) \triangleq \left. \frac{P_8(\omega)}{V_8^s(\omega)} \right|_{P_1(\omega)=0} \quad (5)$$

Inspecting eq (5) it is seen that this defines the reciprocal of the input admittance at port 8 (the pump inlet):

$$Z_{ip}(\omega) = [Y_{11}^t(\omega)]^{-1} \quad (6)$$

The impedance $Z_{ip}(\omega)$ may be used to obtain the transfer function $H_p(\omega)$ which relates the oscillatory suction pressure, $P_8(\omega)$, to the longitudinal pump acceleration, $\ddot{x}_p(\omega)$:

$$H_{ps}(\omega) \triangleq \left. \frac{P_8(\omega)}{\ddot{x}_p(\omega)} \right|_{P_1(\omega)=0} = \frac{A_p Z_{ip}(\omega)}{j\omega} \quad (7)$$

where A_p = cross-sectional area of pump inlet

This transfer function defines the sensitivity of the feed system to pump vibratory motion with zero tank bottom oscillatory pressure. An additional feed system transfer function may be derived to express the effect

AMDR 9635-037, APPENDIX F

B.1, Matrix Operations and Resultant Transfer Functions (cont.)

of the feed system in the case that longitudinal tank vibration causes the tank bottom pressure P_1 to be non-zero. For the case of a "blocked" pump structure ($\ddot{x}_p = 0$), this transfer function, $H_{ts}(\omega)$, expresses the oscillatory suction pressure P_8 as a function of the oscillatory tank pressure P_1 :

$$H_{ts}(\omega) \triangleq \left. \frac{P_8(\omega)}{P_1(\omega)} \right|_{\ddot{x}_p=0} = \frac{Z_{21}^t(\omega)}{Z_{11}^t(\omega)} \quad (8)$$

where Z_{12}^t and Z_{22}^t are elements of the impedance matrix defined by eq (4).

2. Transmission Matrices for Each Circuit Elementa. Suction Line Elements: Z_1 , Z_2 , and Z_3

It is seen from Figure 1 that the suction line is represented as three distinct uniform transmission line elements. This has been done to account for the variation of such parameters as the cross-sectional area (A_m), acoustic velocity (a_o), resonator capacitance ratio (C_m/C_m), resonator natural frequency (ω_a), and resonator damping constant (ζ_a) along the axis of the line. These variables may be computed for each of the three lengths of suction line.

The three suction line elements may each be described by the transmission matrix of the generalized absorptive line as derived in Appendix D. When steady state flow effects are included, this matrix is given by eq (39) of Appendix D. Of course, the following matrix equation for the suction line element applies to the "lossless" case as well as the "lossy" case.

$$\begin{bmatrix} P_1(\omega) \\ \dot{V}_1(\omega) \end{bmatrix} = \begin{bmatrix} a_{11}^i(\omega) & a_{12}^i(\omega) \\ a_{21}^i(\omega) & a_{22}^i(\omega) \end{bmatrix} \begin{bmatrix} P_2(\omega) \\ \dot{V}_2(\omega) \end{bmatrix} \iff \Psi_1(\omega) = \bar{A}(\omega) \Psi_2(\omega) \quad (9)$$

AMDR 9635-037, APPENDIX F

B,2,a, Suction Line Elements: Z_1 , Z_2 , and Z_3

where

$$\mathbf{A}(\omega) = \begin{bmatrix} e^{-\psi_1 \delta_1^* \lambda_1} \cosh \delta_1^* \lambda_1 & e^{-\psi_1 \delta_1^* \lambda_1} Z_c \sinh \delta_1^* \lambda_1 \\ \frac{e^{-\psi_1 \delta_1^* \lambda_1}}{Z_c} \sinh \delta_1^* \lambda_1 & e^{-\psi_1 \delta_1^* \lambda_1} \cosh \delta_1^* \lambda_1 \end{bmatrix} \quad (10)$$

and

$$\psi_1 = \psi_1(\omega) = \frac{\dot{u}_{01} \delta_1'(\omega)}{j\omega} = \text{complex Mach number}$$

$$\delta_1^* = \delta_1^*(\omega) = \frac{\delta_1'(\omega)}{1 - \psi_1^*(\omega)} = \text{effective propagation function}$$

$$\delta_1' = \delta_1'(\omega) = \text{propagation function defined by eq (24), Appendix D}$$

$$Z_c = Z_c(\omega) = \text{characteristic impedance defined by eq (16), Appendix D}$$

$$\dot{u}_{01} = \text{nominal flow velocity in line \#1}$$

$$\lambda_1 = \text{length of line \#1}$$

The transmission matrices of elements Z_2 and Z_3 may be obtained by replacing the subscript "1" by "2" and "3", respectively.

b. Sidebranch Element: Z_4

Element Z_4 represents a second order resonator such as a surge chamber, accumulator, or standpipe, and may be used to alter the feed system frequency response. For the purpose of the preliminary analysis, the effect of vehicle oscillatory motion upon the dynamic performance of this device has been ignored. Hence the transmission matrix for this device is simply a function of the input admittance Y_4 :

$$\mathbf{A}_4(\omega) = \begin{bmatrix} 1 & 0 \\ Y_4(\omega) & 1 \end{bmatrix} \quad (11)$$

The input admittance of the sidebranch resonator is given by the expression

$$Y_4(\omega) = j\omega C_4 \left[1 - \left(\frac{\omega}{\omega_4}\right)^2 + j 2\zeta_4 \left(\frac{\omega}{\omega_4}\right) \right]^{-1} \quad (12)$$

AMDR 9635-037, APPENDIX F

B,2,b, Sidebranch Element: Z_4 (cont.)

where C_4 = branch device capacitance
 ξ_4 = generalized damping factor of the device
 ω_4 = resonant frequency of the device

c. Series Impedance Element: Z_5

Element Z_5 represents the short length of suction line between the conceptual branch device and the pump inlet. Since the length of this element is much shorter than a wavelength at the frequencies of interest, a lumped parameter representation may be used. Thus the transmission matrix of this element is given by the equation

$$A_5(\omega) = \begin{bmatrix} 1 & Z_5(\omega) \\ 0 & 1 \end{bmatrix} \quad (13)$$

The series impedance is simply

$$Z_5(\omega) = j\omega L_5 + R_5 \quad (14)$$

where L_5 = line inertance
 R_5 = line resistance.

d. Pump Cavitation Compliance Element: Z_6

Element Z_6 accounts for compliance of the cavitation bubbles that exist at the pump inlet. The transmission matrix for this shunt element is similar to that of the sidebranch device.

$$A_6(\omega) = \begin{bmatrix} 1 & 0 \\ Y_6(\omega) & 1 \end{bmatrix} \quad (15)$$

AMDR 9635-037, APPENDIX F

B.2.d, Pump Cavitation Compliance Element: Z_6

The complex admittance, Y_6 , of the cavitation bubble is generally composed of an imaginary part caused by the compliance of the gas bubbles and a real part caused by the polytropic volume oscillation of the bubbles.

$$Y_6(\omega) = j\omega C_6 + G_6 \quad (16)$$

where C_6 = cavitation bubble capacitance
 G_6 = cavitation bubble conductance.

e. Engine Impedance Element: Z_7

The impedance of the engine includes the pump, discharge line, injector, and combustion process, and may be represented by this element. This impedance representation of the engine, including the pump, is possible only because the pump oscillatory pressure gain in unity for nominal operating conditions of both the H-1 and F-1 turbopumps. This element accounts for the load impedance caused by the engine, but ignores the cross-coupling effect of the opposite propellant feed system. It is seen that the opposite feed system circuit is coupled through the common pressure in the thrust chamber.

The transmission matrix of the engine impedance element is expressed by the equation

$$\bar{A}_7(\omega) = \begin{bmatrix} 1 & 0 \\ \frac{1}{Z_7(\omega)} & 1 \end{bmatrix} \quad (17)$$

The input impedance of the engine is given as

$$Z_7(\omega) = j\omega L_7 + R_7 \quad (18)$$

where L_7 = inertance of the discharge lines
 R_7 = resistance of the pump, discharge lines, and thrust chamber.

C. ANALYTICAL MODEL FOR PART II

1. Matrix Operations and Resultant Transfer Functions

The transmission matrix model used in Part I is not well suited to the consideration of the oscillatory pressure response at more than two nodes in the feed system network. Therefore, the mathematical model for Part II utilizes a different technique, called the nodal admittance matrix method, to predict the pressure responses at multiple locations in the feed system. As in the case of the transmission matrix model, the admittance matrix model uses the "building block" approach where the matrix representing the entire circuit is constructed from the matrices of the individual circuit elements.

The admittance matrix $\dot{Y}_n(\omega)$ of the entire circuit shown in Figure 2 is defined by the equation

$$\dot{V}_n^s(\omega) = \dot{Y}_n(\omega) \dot{P}_n(\omega) \quad (19)$$

where

$$\dot{V}_n^s(\omega) = [\dot{V}_1^s(\omega) \dot{V}_2^s(\omega) \dots \dot{V}_n^s(\omega)] = \text{Nodal Oscillatory Shunt Flow Vector}$$

$$\dot{P}_n(\omega) = [P_1(\omega) P_2(\omega) \dots P_n(\omega)] = \text{Nodal Oscillatory Pressure Vector}$$

The 9 x 9 matrix $\dot{Y}_n(\omega)$ may be formed by use of the equation

$$\dot{Y}_n(\omega) = \dot{Y}_1'(\omega) + \dot{Y}_2'(\omega) + \dots + \dot{Y}_k'(\omega) + \dots + \dot{Y}_9'(\omega) \quad (20)$$

where $\dot{Y}_k'(\omega)$ is a modified 9 x 9 admittance matrix formed from the 2 x 2 admittance matrix $\dot{Y}_k(\omega)$ which represents the kth element. The following equations describe the formation of these modified admittance matrices for each of the individual elements:

$$\dot{Y}_1'(\omega) = \begin{bmatrix} \dot{Y}_1(\omega) & 0 & \dots & 0 \\ 0 & 0 & \dots & 0 \\ \vdots & \vdots & \text{O} & \vdots \\ 0 & 0 & \dots & 7 \times 7 \end{bmatrix} \quad (21)$$

AMDR 9635-037, APPENDIX F

G.1, Matrix Operations and Resultant Transfer Functions (cont.)

$$H_{pd}(\omega) = \frac{P_8(\omega)}{\dot{X}_p(\omega)} \Big|_{\substack{\text{with } P_1(\omega) = 0 \\ \text{only } \dot{V}_7^E(\omega) \neq 0}} = \frac{\Delta_{11,78}(\omega)}{j\omega A_p \Delta_{11}(\omega)} = \text{pump to discharge pressure transfer function} \quad (34)$$

$$H_{pe}(\omega) = \frac{P_9(\omega)}{\dot{X}_p(\omega)} \Big|_{\substack{\text{with } P_1(\omega) = 0 \\ \text{only } \dot{V}_7^E(\omega) \neq 0}} = \frac{\Delta_{11,79}(\omega)}{j\omega A_p \Delta_{11}(\omega)} = \text{pump to chamber pressure transfer function} \quad (35)$$

$$H_{ts}(\omega) = \frac{P_7(\omega)}{P_1(\omega)} \Big|_{\text{only } \dot{V}_1^E(\omega) \neq 0} = \frac{\Delta_{17}(\omega)}{\Delta_{11}(\omega)} = \text{tank to suction pressure transfer function} \quad (36)$$

$$H_{td}(\omega) = \frac{P_8(\omega)}{P_1(\omega)} \Big|_{\text{only } \dot{V}_1^E(\omega) \neq 0} = \frac{\Delta_{18}(\omega)}{\Delta_{11}(\omega)} = \text{tank to discharge pressure transfer function} \quad (37)$$

$$H_{te}(\omega) = \frac{P_9(\omega)}{P_1(\omega)} \Big|_{\text{only } \dot{V}_1^E(\omega) \neq 0} = \frac{\Delta_{19}(\omega)}{\Delta_{11}(\omega)} = \text{tank to chamber pressure transfer function} \quad (38)$$

As in Part I, A_p refers to the cross sectional area of the pump inlet. Note that eqs (36), (37) and (38) are special cases of eq (31). Eqs (31) and (32) allow the prediction of the distribution of oscillatory pressure response to a particular input. Equations (33) and (36) correspond to eqs (7) and (8) in Part I.

AMDR 9635-037, APPENDIX F

C, Analytical Model for Part II (cont.)

2. Admittance Matrices for Each Circuit Element

a. Suction Line Elements: Z_1 through Z_5

The purpose of representing the suction line by six transmission line elements, as shown in Figure 2, is to provide a better approximation of the axial variation of the gas injection parameters, such as gas capacitance ratio, bubble resonant frequency and bubble damping parameters.

The admittance matrix of the k^{th} suction line element ($k = 1, 2, \dots, 5$) is obtained by transforming eq (10) of this appendix by means of the equation given in Table 2 of Appendix B,

$$Y_k(\omega) = \frac{1}{Z_{ck}} \begin{bmatrix} C \tanh \gamma_k^* & -e^{-\gamma_k^*} C \operatorname{sch} \gamma_k^* \\ -e^{\gamma_k^*} C \operatorname{sch} \gamma_k^* & C \tanh \gamma_k^* \end{bmatrix} \quad (39)$$

where the characteristic impedance (Z_{ck}) and propagation function (γ_k^*) are still defined by the expressions accompanying eq (10). In order to represent the case of gas injection, the following expressions for the suction line distributed parameters are used in evaluating Z_{ck} and γ_k^*

$$\left(\frac{C_a}{C_m}\right)_k = \epsilon_k(\omega) \left(\frac{C_0}{C_m}\right)_k \quad (40)$$

$$\Omega_{ak} = (\epsilon_k(\omega))^{\frac{1}{2}} \left(\frac{\omega}{\omega_{bk}}\right) \quad (41)$$

$$(\xi_a)_k = \xi_{0k} + (\xi_{tw})_k + (\xi_{rad})_k + (\xi_{vis})_k \quad (42)$$

where

$\left(\frac{C_0}{C_m}\right)_k$ = adiabatic capacitance ratio for k^{th} line

ω_{bk} = adiabatic breathing mode frequency for k^{th} line

ξ_{0k} = distributed viscous damping factor for k^{th} line

AMDR 9635-037, APPENDIX F

C,2,a, Suction Line Elements: Z_1 through Z_5 (cont.)

$(\xi_{th})_k$ = bubble thermal damping factor

$(\xi_{rad})_k$ = bubble radiative damping factor

$(\xi_{vis})_k$ = bubble viscous damping factor

Note that eqs (40), (41) and (42) correspond to eqs (37), (38) and (39) in Appendix E, respectively. The various bubble dynamic variables, such as $(C_0/C_m)_k$, ω_{0k} , Θ_{1k} , Θ_{2k} , ϵ_1 , Θ_{3k} may be evaluated from the results of Appendix E for each segment of the suction line.

b. Combined Side Branch Device and Suction Line Element: Z_6

The admittance matrix of this two port element can be easily obtained by modifying the admittance matrix for a single transmission line element, as given by eq (39):

$$Y_6(\omega) = \frac{1}{Z_{c6}} \begin{bmatrix} Y_6 Z_{c6} + \text{Ctnh } \delta_6^* l_6 & -e^{\delta_6^* l_6} \text{Csch } \delta_6^* l_6 \\ -e^{-\delta_6^* l_6} \text{Csch } \delta_6^* l_6 & \text{Ctnh } \delta_6^* l_6 \end{bmatrix} \quad (43)$$

where

$$Y_6 = Y_6(\omega) = j\omega C_6 \left[1 - \left(\frac{\omega}{\omega_0}\right)^2 + j2\xi_6 \left(\frac{\omega}{\omega_0}\right) \right]^{-1} \quad (44)$$

Note that eq (43) is obtained by simply adding the input admittance of the sidebranch device to the Y_{11} element of the admittance matrix of the suction line.

AMDR 9635-037, APPENDIX F

C.2, Admittance Matrices for Each Circuit Element (cont.)

c. Turbopump with Cavitation Compliance: Z_7

The development of the turbopump dynamic equations to obtain the admittance matrix of the pump is presented in Appendix A. The admittance matrix is given as:

$$\underline{Y}_7(\omega) = \frac{1}{Z_7(\omega)} \begin{bmatrix} \mu_7 + Y_7(\omega)Z_7(\omega) & -1 \\ -\mu_7 & 1 \end{bmatrix} \quad (45)$$

where

$$Z_7(\omega) = j\omega L_7 + R_7 = \text{pump series impedance}$$

$$Y_7(\omega) = j\omega C_7 + G_7 = \text{pump shunt admittance}$$

$$\mu_7 = \text{pump forward gain}$$

Note that the pump is non-reciprocal when the pump gain is non unity ($Y_{12} \neq Y_{21}$).

d. Combined Sidebranch Device, Discharge Line and Combustion Chamber: Z_8

As shown in Figure 2, entire feed system downstream of the pump is represented by the element Z_8 . This circuit consists of the sidebranch resonator at the pump outlet, the lumped parameter discharge line, the injector, and the combustion dynamics of the chamber. The admittance matrix of this circuit may be written by inspection:

$$\underline{Y}_8(\omega) = \begin{bmatrix} Y_{rs} + Y_{ds} & -Y_{ds} \\ -Y_{ds} & Y_{ks} + Y_{ds} \end{bmatrix} \quad (46)$$

AMDR 9635-037, APPENDIX F

C,2,d, Combined Sidebranch Device, Discharge Line & Combustion Chamber: Z_8 (cont.)

where

Y_{r8} = input admittance of the sidebranch device

Y_{d8} = input admittance of the discharge line/injector

Y_{k8} = input admittance of the combustion process

The admittances Y_{r8} , Y_{d8} , and Y_{k8} are defined by the following equations:

$$Y_{r8}(\omega) = j\omega C_8 \left[1 - \left(\frac{\omega}{\omega_8}\right)^2 + j 2\zeta_8 \left(\frac{\omega}{\omega_8}\right) \right] \quad (47)$$

$$Y_{d8}(\omega) = j\omega L_{d8} + R_{d8} \quad (48)$$

$$Y_{k8}(\omega) = \left[K \frac{c^*}{A_t g} \frac{e^{-j\omega\tau_1}}{1+j\omega\tau_2} \right]^{-1} \quad (49)$$

The equation for the admittance of the combustion process has been adapted from eq (18) in Appendix A by use of the assumption that there is no coupling between the two propellant feed systems.

AMDR 9635-037, APPENDIX F

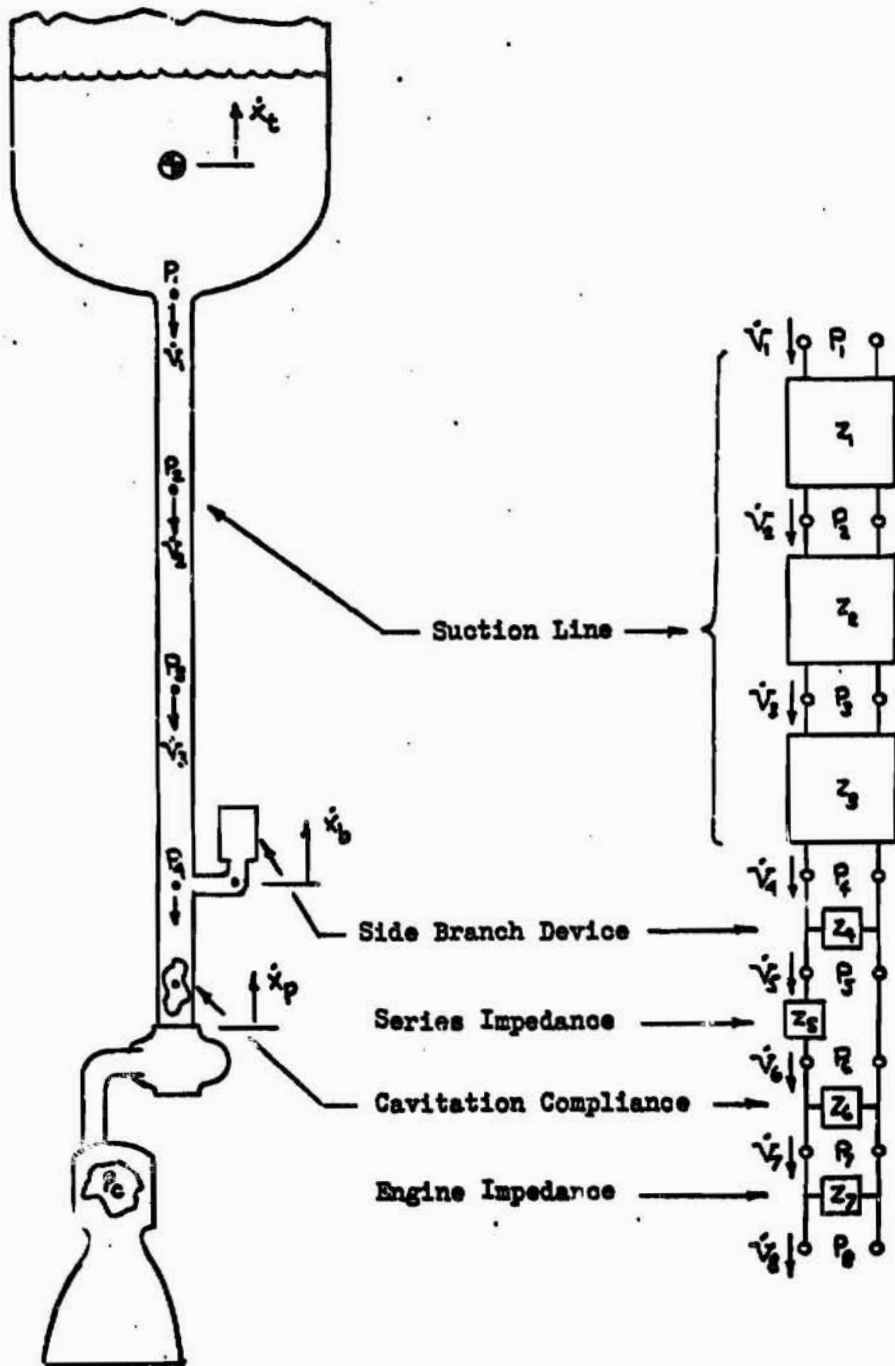


FIGURE 1. SKETCH OF THE PROPELLANT FEED SYSTEM MODEL FOR PART I

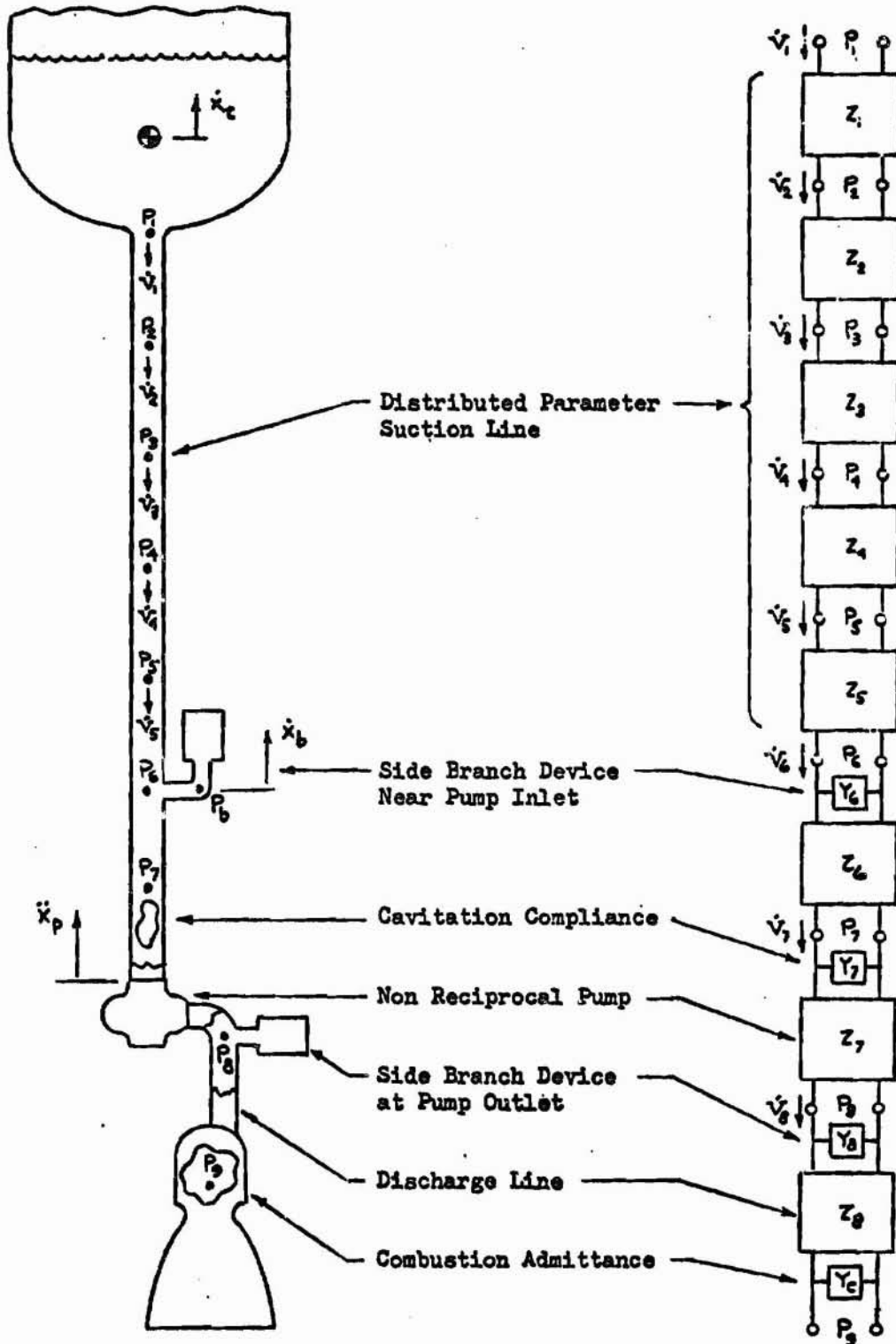


FIGURE 2 PROPULSION SYSTEM MODEL USED IN PART II

APPENDIX G

MEASUREMENT OF AN ACOUSTICAL ADMITTANCE MATRIX

PRECEDING PAGE BLANK NOT FILMED.

AMDR 9635-037, APPENDIX G

A. INTRODUCTION

This appendix presents the theoretical basis for a new method of empirically determining the dynamic characteristics of a hydraulic element. This method allows the measurement of the acoustical admittance matrix which completely characterizes the linear transmission of oscillations through an arbitrary element, as a function of frequency and operation condition. As explained in Appendix B, the admittance matrix is linearly related to other matrices which describe the oscillatory performance of an individual circuit element, such as the transmission matrix. Since the matrices of each circuit element must be combined to arrive at the frequency domain model of the overall system response and stability characteristics, the admittance matrices of the critical elements must be measured to improve the accuracy of the system analysis. The admittance measurement method which is described in this appendix allows the dynamic characteristics of these critical elements to be experimentally defined by relatively inexpensive pulse tests, with little or no a priori knowledge of the dynamic behavior of the test element or facility.

B. DIRECT ADMITTANCE MEASUREMENT

The direct admittance measurement method is easily found by consideration of the defining equation for the admittance matrix of an n-port network.

$$\dot{V}_s(\omega) = Y(\omega) F(\omega) \quad (1)$$

where

$$Y(\omega) = \begin{bmatrix} Y_{11}(\omega) & \dots & Y_{1n}(\omega) \\ \vdots & \ddots & \vdots \\ Y_{n1}(\omega) & \dots & Y_{nn}(\omega) \end{bmatrix} = \text{admittance matrix.}$$

The n-port network described by this equation is shown in Figure 1.

APPENDIX A

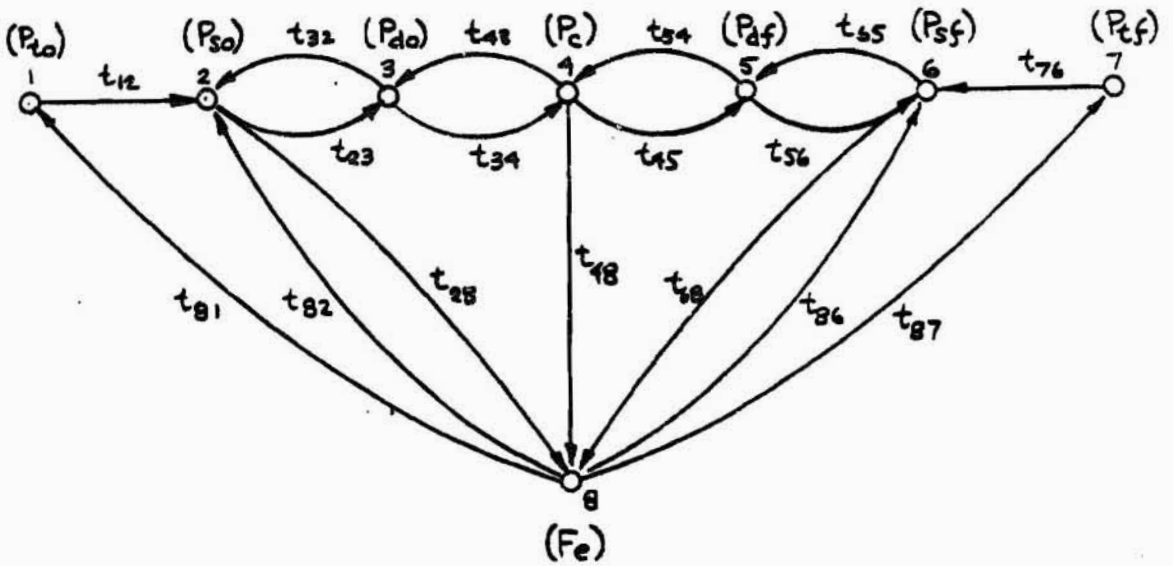


FIGURE 6 "POGO" SYSTEM SIGNAL FLOW GRAPH

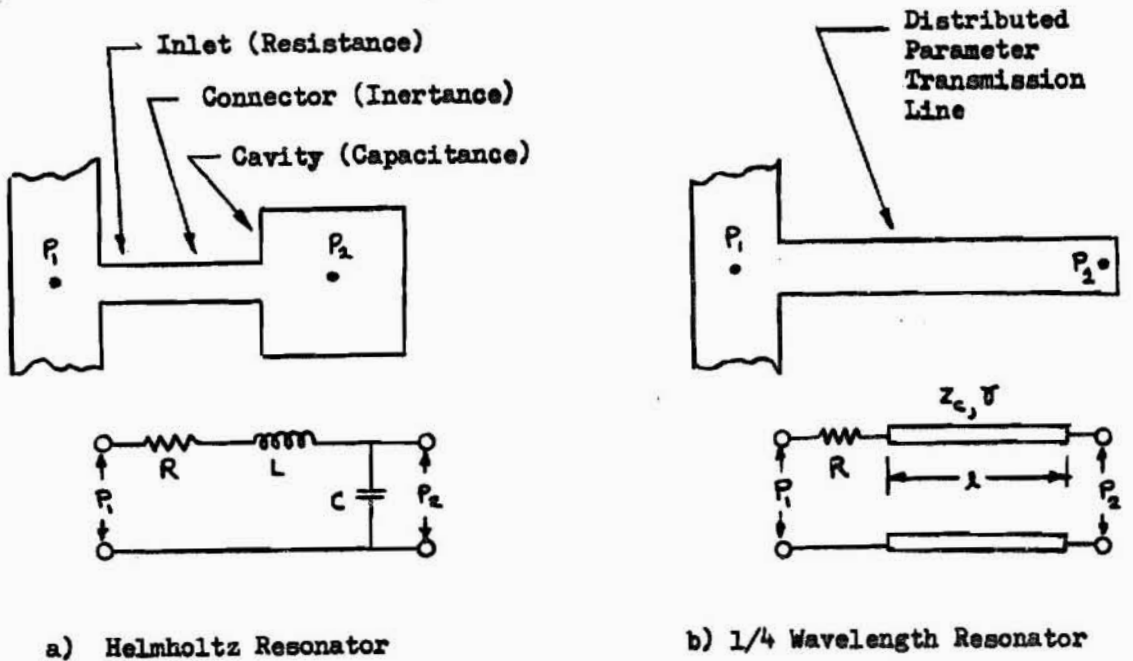


FIGURE 7 TYPICAL FEED SYSTEM COMPENSATING DEVICES

APPENDIX A

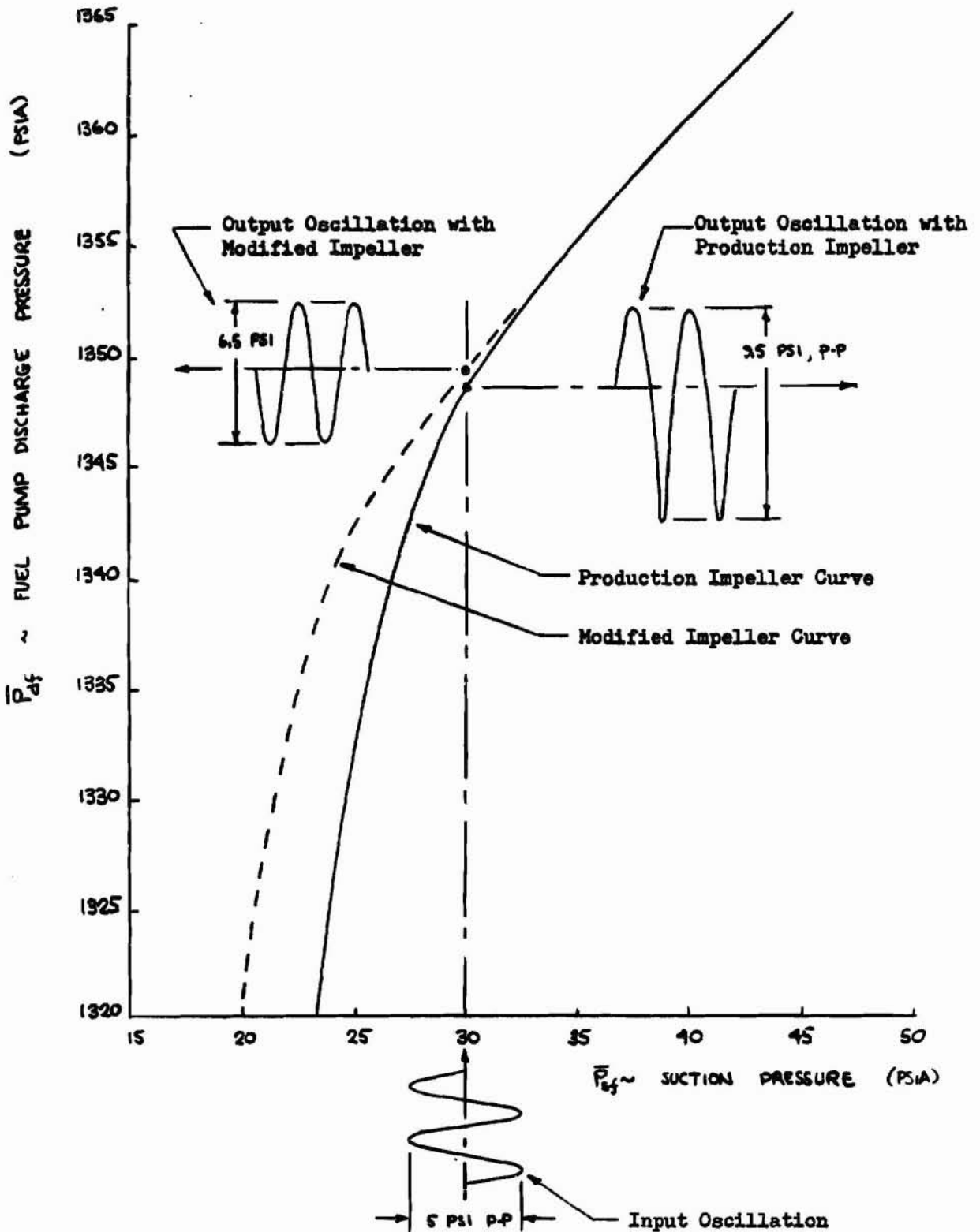


FIGURE 8 EFFECT OF THE MODIFIED FUEL PUMP IMPELLER ON CAVITATION PERFORMANCE AND PUMP GAIN

AMDR 9635-037

APPENDIX B

MATRIX METHODS APPLIED TO THE
FREQUENCY DOMAIN ANALYSIS OF A FLUID FEED SYSTEM

PRECEDING PAGE BLANK NOT FILMED.

AMDR 9635-037, APPENDIX B

A. INTRODUCTION

The purpose of this appendix is to introduce the reader to the use of matrix methods in the analysis of the frequency response characteristics of the complex fluid feed systems commonly found in rocket propulsion systems. This frequency domain analysis utilizes the linearized equations of motion for each element in the system, which describe its response to small perturbations about a given operating point. When these linear simultaneous differential equations are Fourier transformed, the resulting equations, with frequency as the independent variable, can be used to determine the steady state frequency response of the coupled system.

The use of matrices permits one to express the large sets of frequency response equations in symbolic form, which facilitates the algebraic manipulation necessary to obtain the desired system transfer functions. Thus the numerical calculations may be delayed until the complete mathematical model is formulated, at which time the matrix representation may be efficiently programmed for a digital computer.

B. ACOUSTICAL IMPEDANCE AND ADMITTANCE

1. Impedance and Admittance Concepts

The pressure and weight flow fluctuations at a station or "port" within a fluid feed system are related by the frequency response characteristics of that system. If these fluctuations are assumed to be sinusoidal, then the variables may be written in terms of their complex amplitudes. Thus, the pressure $p(t)$ as a function of time may be written

$$p(t) = \text{Re} [P(\omega) e^{j\omega t}] = P(\omega) \cos \omega t \quad (1)$$

AMDR 9635-037, APPENDIX B

B.1, Impedance and Admittance Concepts (cont.)

where

$P(\omega)$ = amplitude of the pressure oscillation

ω = circular frequency

t = time

j = $\sqrt{-1}$

The oscillation amplitude $P(\omega)$ is a complex valued function of frequency and may be written

$$P(\omega) = \text{Re} [P(\omega)] + j \text{Im} [P(\omega)] \quad (2)$$

$$P(\omega) = |P(\omega)| e^{j\angle P(\omega)} = |P(\omega)| [\cos \angle P(\omega) + j \sin \angle P(\omega)] \quad (3)$$

where

$\text{Re} [P(\omega)]$ = real part of $P(\omega)$

$\text{Im} [P(\omega)]$ = imaginary part of $P(\omega)$

$|P(\omega)|$ = absolute magnitude of $P(\omega)$

$\angle P(\omega)$ = phase angle of $P(\omega)$

In the same fashion, a sinusoidal volume flow fluctuation may be written as:

$$\dot{V}(\omega) = |\dot{V}(\omega)| e^{j\angle \dot{V}(\omega)} = |\dot{V}(\omega)| [\cos \angle \dot{V}(\omega) + j \sin \angle \dot{V}(\omega)] \quad (4)$$

Using the complex variable notation, the concept of acoustical impedance may be introduced. Impedance is defined as the ratio of oscillatory pressure to an oscillatory volume flow. Thus, in the simple circuit shown in

AMDR 9635-037, APPENDIX B

B.1, Impedance and Admittance Concepts (cont.)

Figure 1, pressure and flow are related by the impedance $Z(\omega)$.

$$Z_i(\omega) \triangleq \frac{P_i(\omega)}{\dot{V}_i(\omega)} = \frac{|P_i(\omega)|}{|\dot{V}_i(\omega)|} e^{j(\angle P_i(\omega) - \angle \dot{V}_i(\omega))} = |Z_i(\omega)| e^{j\angle Z_i(\omega)} \quad (5)$$

where $|Z_i(\omega)|$ = absolute amplitude of $Z_i(\omega)$
 $\angle Z_i(\omega)$ = phase angle of $Z_i(\omega)$

For the circuit of Figure 1 the reciprocal of impedance is the hydraulic admittance:

$$Y_i(\omega) \triangleq \frac{1}{Z_i(\omega)} = \frac{1}{|Z_i(\omega)|} e^{-\angle Z_i(\omega)} = |Y_i(\omega)| e^{-\angle Y_i(\omega)} \quad (6)$$

where $|Y_i(\omega)|$ = absolute amplitude of $Y_i(\omega)$
 $\angle Y_i(\omega)$ = phase angle of $Y_i(\omega)$

The following discussion will delineate the use of these "impittance" (impedance or admittance) concepts and matrix methods to characterize the frequency response of the system. If the system is linear, then the restriction of these methods to the frequency domain is not a serious limitation since the inverse Fourier transform may be taken to obtain the response to an arbitrary transient.

2. The Impedance Matrix

For the linear n-port network shown in Figure 2, the oscillatory pressure response at any port may be found by the principle of superposition.

AMDR 9635-037, APPENDIX B

B.2, The Impedance Matrix (cont.)

The total pressure response at the i^{th} port is thus equal to the summation of the individual responses at that port due to each of the oscillatory flow sources at the n ports:

$$P_i(\omega) = \sum_{j=1}^n Z_{ij}(\omega) \dot{V}_j^s(\omega) \quad (7)$$

where

$Z_{ij}(\omega)$ = transfer impedance

$P_i(\omega)$ = oscillatory pressure at i^{th} port

$\dot{V}_j^s(\omega)$ = oscillatory flow from source into the j^{th} port

Rewriting eq (7) in matrix form, the defining equation for the impedance matrix of an n port network is obtained

$$P(\omega) = Z(\omega) \dot{V}_s(\omega) \quad (8)$$

where

$Z(\omega) = [Z_{ij}(\omega)]$ = impedance matrix

$P(\omega) = [P_1(\omega) \dots P_n(\omega)]^t$ = oscillatory pressure vector

$\dot{V}_s(\omega) = [\dot{V}_1^s(\omega) \dots \dot{V}_n^s(\omega)]^t$ = oscillatory source flow vector

It is seen that the impedance matrix expresses the pressures as explicit functions of the flow into the network from the sources. This equation yields the definition of the impedance matrix elements:

$$Z_{ij}(\omega) = \left. \frac{P_i(\omega)}{\dot{V}_j^s(\omega)} \right|_{\text{only } \dot{V}_j^s(\omega) \neq 0} \quad (9)$$

AMDR 9635-037, APPENDIX B

B,2, The Impedance Matrix (cont.)

The elements of the impedance matrix are generally complex valued functions of frequency. The diagonal elements of the matrix ($Z_{ii}(\omega)$) are usually called driving point impedances whereas the off-diagonal elements ($Z_{ij}(\omega), i \neq j$) are called transfer impedances. If the impedance matrix is symmetric, so that it equals its own transpose, then the network is said to be reciprocal.

$$Z_{ij}(\omega) = Z_{ji}(\omega) \iff \text{reciprocal network} \quad (10)$$

3. Admittance Matrix

The admittance matrix is used to relate the oscillatory flow responses to the applied oscillatory pressures. Again employing the superposition principle, the oscillatory "shunt" flow directed into the i^{th} port equals the sum of the flow responses due to each of the applied pressures:

$$\dot{V}_i^s(\omega) = \sum_{j=1}^n Y_{ij}(\omega) P_j(\omega) \quad (11)$$

which may be expressed in matrix form as

$$\dot{\mathbf{V}}_s(\omega) = \mathbf{Y}(\omega) \mathbf{P}(\omega) \quad (12)$$

where

$$\mathbf{Y}(\omega) = [Y_{ij}(\omega)] = \text{admittance matrix}$$

$$\dot{\mathbf{V}}_s(\omega) = [\dot{V}_1^s(\omega) \dots \dot{V}_n^s(\omega)]^t = \text{oscillatory shunt flow vector}$$

AMDR 9635-037, APPENDIX B

B,3, Admittance Matrix (cont.)

The definition of the admittance matrix element results from eq (11) with only one pressure source considered:

$$Y_{ij}(\omega) = \frac{V_i^s(\omega)}{P_j(\omega)} \Big|_{\text{only } P_j(\omega) \neq 0} \quad (13)$$

Comparison of eqs (8) and (12) reveals that the impedance matrix is equal to the inverse of the admittance matrix

$$Z(\omega) = Y(\omega)^{-1} \quad (14)$$

The elements of the impedance matrix can thus be determined from the first order cofactors and determinant of the admittance matrix

$$Z_{ij}(\omega) = \frac{\Delta_{ji}(\omega)}{\Delta(\omega)} \quad (15)$$

where

$$\Delta(\omega) = \det Y(\omega) = \text{determinant of matrix } Y(\omega)$$

$$\Delta_{ji} = \begin{vmatrix} Y_{11} & \dots & Y_{1i} & \dots & Y_{1n} \\ \vdots & & \vdots & & \vdots \\ Y_{j1} & \dots & Y_{ji} & \dots & Y_{jn} \\ \vdots & & \vdots & & \vdots \\ Y_{n1} & \dots & Y_{ni} & \dots & Y_{nn} \end{vmatrix} = \text{determinant of matrix } Y(\omega) \text{ with } i^{\text{th}} \text{ column and } j^{\text{th}} \text{ row removed}$$

It is seen from eq (15) that, if the impedance matrix is symmetric, then the admittance matrix will also be symmetric. Thus the requirements for reciprocity of a network may be stated in terms of either its impedance matrix or admittance matrix.

AMDR 9635-037, APPENDIX B

B, Acoustical Impedance & Admittance (cont.)

4. Reduction of an Impedance or Admittance Matrix

The order of an impedance or admittance matrix may be reduced by simply eliminating the rows and columns which correspond to pressures or flows that are identically equal to zero in the network. For example, if the oscillatory flow at the i^{th} port is zero, then a new impedance matrix, $\mathbb{Z}'(\omega)$, may be constructed by removing the i^{th} row and the i^{th} column from the original matrix.

$$\begin{bmatrix} P_1(\omega) \\ \vdots \\ P_{i-1}(\omega) \\ P_{i+1}(\omega) \\ \vdots \\ P_n(\omega) \end{bmatrix} = \begin{bmatrix} Z_{11}(\omega) & \dots & Z_{1,i-1}(\omega) & Z_{1,i+1}(\omega) & \dots & Z_{1n}(\omega) \\ \vdots & & \vdots & \vdots & & \vdots \\ Z_{i-1,1}(\omega) & \dots & Z_{i-1,i-1}(\omega) & Z_{i-1,i+1}(\omega) & \dots & Z_{i-1,n}(\omega) \\ Z_{i+1,1}(\omega) & \dots & Z_{i+1,i-1}(\omega) & Z_{i+1,i+1}(\omega) & \dots & Z_{i+1,n}(\omega) \\ \vdots & & \vdots & \vdots & & \vdots \\ Z_{n1}(\omega) & \dots & Z_{n,i-1}(\omega) & Z_{n,i+1}(\omega) & \dots & Z_{nn}(\omega) \end{bmatrix} \begin{bmatrix} \dot{V}_1^s(\omega) \\ \vdots \\ \dot{V}_{i-1}^s(\omega) \\ \dot{V}_{i+1}^s(\omega) \\ \vdots \\ \dot{V}_n^s(\omega) \end{bmatrix} \quad (16)$$

$\underbrace{\hspace{15em}}_{\mathbb{Z}'(\omega)}$

If the only non-zero flows occur at the k^{th} and the l^{th} ports then all other rows and columns of the impedance matrix can be eliminated, resulting in an impedance matrix of order 2.

$$\begin{bmatrix} P_k(\omega) \\ P_l(\omega) \end{bmatrix} = \begin{bmatrix} Z_{kk}(\omega) & Z_{kl}(\omega) \\ Z_{lk}(\omega) & Z_{ll}(\omega) \end{bmatrix} \begin{bmatrix} \dot{V}_k^s(\omega) \\ \dot{V}_l^s(\omega) \end{bmatrix} \quad (17)$$

AMDR 9635-037, APPENDIX B

B.4, Reduction of an Impedance or Admittance Matrix (cont.)

The admittance matrix of an n-port network may be reduced by eliminating the rows and columns which correspond to a port with zero pressure. Therefore, if the i^{th} pressure is zero, the following modified admittance equation can be written:

$$\begin{bmatrix} \hat{V}_1^s(\omega) \\ \vdots \\ \hat{V}_{i-1}^s(\omega) \\ \hat{V}_{i+1}^s(\omega) \\ \vdots \\ \hat{V}_n^s(\omega) \end{bmatrix} = \underbrace{\begin{bmatrix} Y_{11}(\omega) & \dots & Y_{1,i-1}(\omega) & Y_{1,i+1}(\omega) & \dots & Y_{1n}(\omega) \\ \vdots & & \vdots & \vdots & & \vdots \\ Y_{i-1,1}(\omega) & \dots & Y_{i-1,i-1}(\omega) & Y_{i-1,i+1}(\omega) & \dots & Y_{i-1,n}(\omega) \\ Y_{i+1,1}(\omega) & \dots & Y_{i+1,i-1}(\omega) & Y_{i+1,i+1}(\omega) & \dots & Y_{i+1,n}(\omega) \\ \vdots & & \vdots & \vdots & & \vdots \\ Y_{n1}(\omega) & \dots & Y_{n,i-1}(\omega) & Y_{n,i+1}(\omega) & \dots & Y_{nn}(\omega) \end{bmatrix}}_{\hat{Y}(\omega)} \begin{bmatrix} P_1(\omega) \\ \vdots \\ P_{i-1}(\omega) \\ P_{i+1}(\omega) \\ \vdots \\ P_n(\omega) \end{bmatrix} \quad (18)$$

Consider the definition of the impedance matrix element for this modified circuit:

$$Z'_{jk}(\omega) = \left. \frac{P_j(\omega)}{\hat{V}_k^s(\omega)} \right|_{\substack{\text{with } P_i(\omega) = 0 \\ \text{only } \hat{V}_k^s \neq 0}} \quad (19)$$

This impedance can be obtained from the reduced admittance matrix $\hat{Y}(\omega)$ by inversion or from the original admittance matrix $Y(\omega)$ by use of the expression,

$$Z'_{jk}(\omega) = \frac{\Delta_{ii,kj}(\omega)}{\Delta_{ii}(\omega)} \quad (20)$$

B.4, Reduction of an Impedance or Admittance Matrix (cont.)

where

$\Delta_{ii}(\omega)$ = first order cofactor of $Y(\omega)$ formed by eliminating the i^{th} row and i^{th} column

$\Delta_{ij, kj}(\omega)$ = second order cofactor of $Y(\omega)$ formed by eliminating the i^{th} and k^{th} rows, and the i^{th} and j^{th} columns.

C. TRANSMISSION MATRICES

1. General

The use of a transmission matrix to describe the frequency response characteristics of a hydraulic network is particularly useful when the network is composed of one or more tandem arrays of n-port sub networks. Referring to Figure 3, the typical n-port network may be represented by a transmission matrix which relates the oscillatory pressures and flows at the "output" ports in terms of the pressures and flows at the "input" ports. The designation of each port as either "input" or "output" is quite arbitrary but normally follows the convention shown in Figure 3, which applies to a system with an even number of ports. The assumption of an even number of ports is not overly restrictive since an additional "dummy" port or node can usually be added to a network with an odd number of ports. Therefore, this report will not deal with transmission systems where the number of inputs and outputs are not equal. Such systems, which are discussed in Bibliography H.17, lead to rectangular transmission matrices.

2. Forward Transmission Matrix

For the n-port network shown in Figure 3, the oscillatory pressures and flows at the input port set are related to the pressures and flows at the

AMDR 9635-037, APPENDIX B

C,2, Forward Transmission Matrix (cont.)

output port set by the following system of equations:

$$P_k^1(\omega) = \sum_{j=1}^{n/2} a_{kj}^1(\omega) P_j^2(\omega) + \sum_{j=1}^{n/2} a_{kj}^2(\omega) \dot{V}_j^2(\omega) \quad (21)$$

$$\dot{V}_k^1(\omega) = \sum_{j=1}^{n/2} a_{kj}^3(\omega) P_j^2(\omega) + \sum_{j=1}^{n/2} a_{kj}^4(\omega) \dot{V}_j^2(\omega) \quad (22)$$

where

- $P_k^1(\omega)$ = oscillatory pressure at the k^{th} input port
- $P_j^2(\omega)$ = oscillatory pressure at the j^{th} output port
- $\dot{V}_k^1(\omega)$ = oscillatory flow at the k^{th} input port
- $\dot{V}_j^2(\omega)$ = oscillatory flow at the j^{th} output port

Writing these equations in matrix form yields the expression,

$$\begin{cases} P_1(\omega) = A_1(\omega) P_2(\omega) + A_2(\omega) \dot{V}_2(\omega) \\ \dot{V}_1(\omega) = A_3(\omega) P_2(\omega) + A_4(\omega) \dot{V}_2(\omega) \end{cases} \quad (23)$$

where

- $P_1(\omega) = [P_1^1(\omega) \dots P_m^1(\omega)]^t$ = input pressure vector
- $P_2(\omega) = [P_1^2(\omega) \dots P_m^2(\omega)]^t$ = output pressure vector
- $\dot{V}_1(\omega) = [\dot{V}_1^1(\omega) \dots \dot{V}_m^1(\omega)]^t$ = input flow vector
- $\dot{V}_2(\omega) = [\dot{V}_1^2(\omega) \dots \dot{V}_m^2(\omega)]^t$ = output flow vector
- $m \triangleq n/2$

AMDR 9635-037, APPENDIX B

C,2, Forward Transmission Matrix (cont.)

When written in more compact form, eq (23) defines the forward transmission matrix:

$$\Psi_1(\omega) = \bar{A}(\omega) \Psi_2(\omega) \quad (24)$$

where

$$\bar{A}(\omega) = \begin{bmatrix} \bar{A}_1(\omega) & \bar{A}_2(\omega) \\ \bar{A}_3(\omega) & \bar{A}_4(\omega) \end{bmatrix} = \text{forward transmission matrix}$$

$$\Psi_1(\omega) = \begin{bmatrix} P_1^t(\omega) \\ V_1^t(\omega) \end{bmatrix}^t = \text{input state vector}$$

$$\Psi_2(\omega) = \begin{bmatrix} P_2^t(\omega) \\ V_2^t(\omega) \end{bmatrix}^t = \text{output state vector}$$

$\bar{A}(\omega)$ is called the forward transmission matrix because of the manner in which the matrix of each successive element in a tandem chain is post-multiplied onto the matrix of the preceding element.

$$\Psi_1(\omega) = \bar{A}_k(\omega) \Psi_k(\omega) = [\bar{A}_1(\omega) \bar{A}_2(\omega) \dots \bar{A}_{k-1}(\omega)] \Psi_k(\omega) \quad (25)$$

3. Rearward Transmission Matrix

The rearward transmission matrix is defined by the matrix expression,

$$\begin{cases} P_2(\omega) = B_1(\omega) P_1(\omega) + B_2(\omega) \dot{V}_1(\omega) \\ \dot{V}_2(\omega) = B_3(\omega) P_1(\omega) + B_4(\omega) \dot{V}_1(\omega) \end{cases} \quad (26)$$

AMDR 9635-037, APPENDIX B

C,3, Rearward Transmission Matrix (cont.)

which can be written as

$$\Psi_2(\omega) = \mathbb{B}(\omega) \Psi_1(\omega) \quad (27)$$

where

$$\mathbb{B}(\omega) = \left[\begin{array}{c|c} \mathbb{B}_1(\omega) & \mathbb{B}_2(\omega) \\ \hline \mathbb{B}_3(\omega) & \mathbb{B}_4(\omega) \end{array} \right] = \text{rearward transmission matrix.}$$

Comparison of eq (24) with eq (27) reveals that the rearward transmission matrix is the inverse of the forward transmission matrix.

$$\mathbb{B}(\omega) = \mathbb{A}^{-1}(\omega) \quad (28)$$

Considering a tandem connection of elements, it is seen that the rearward transmission matrix of each element is pre-multiplied onto the matrix of the preceding element.

$$\Psi_k(\omega) = \mathbb{B}_k(\omega) \Psi_1(\omega) = \left[\mathbb{B}_{k-1}(\omega) \mathbb{B}_{k-2}(\omega) \cdots \mathbb{B}_2(\omega) \mathbb{B}_1(\omega) \right] \Psi_1(\omega) \quad (29)$$

D. RELATIONSHIPS BETWEEN THE MATRICES

It has been shown that the linear frequency response of an n -port network where n is an even integer may be described by either of the $n \times n$ matrices, $\mathbb{Z}(\omega)$, $\mathbb{Y}(\omega)$, $\mathbb{A}(\omega)$, and $\mathbb{B}(\omega)$. Since each of these matrices represents a different algebraic description of the same physical system, it is obvious that they are linearly related. The objective of this section is to present these relationships so that the analyst can always obtain the most convenient matrix when given the system dynamic equations in an arbitrary form.

D, Relationships Between the Matrices (cont.)

The algebraic relationships which permit transformations of the characteristic matrices are easily derived if the defining eq (8), (12), (24), and (27) are first partitioned such that the nxn matrices are divided into four n/2 x n/2 submatrices:

$$\begin{bmatrix} \mathbf{P}_1(\omega) \\ \mathbf{P}_2(\omega) \end{bmatrix} = \begin{bmatrix} \mathbf{Z}_1(\omega) & \mathbf{Z}_2(\omega) \\ \mathbf{Z}_3(\omega) & \mathbf{Z}_4(\omega) \end{bmatrix} \begin{bmatrix} \dot{\mathbf{V}}_1(\omega) \\ \dot{\mathbf{V}}_2(\omega) \end{bmatrix} \quad (30)$$

$$\begin{bmatrix} \dot{\mathbf{V}}_1(\omega) \\ \dot{\mathbf{V}}_2(\omega) \end{bmatrix} = \begin{bmatrix} \mathbf{Y}_1(\omega) & \mathbf{Y}_2(\omega) \\ \mathbf{Y}_3(\omega) & \mathbf{Y}_4(\omega) \end{bmatrix} \begin{bmatrix} \mathbf{P}_1(\omega) \\ \mathbf{P}_2(\omega) \end{bmatrix} \quad (31)$$

$$\begin{bmatrix} \mathbf{P}_1(\omega) \\ \dot{\mathbf{V}}_1(\omega) \end{bmatrix} = \begin{bmatrix} \mathbf{A}_1(\omega) & \mathbf{A}_2(\omega) \\ \mathbf{A}_3(\omega) & \mathbf{A}_4(\omega) \end{bmatrix} \begin{bmatrix} \mathbf{P}_2(\omega) \\ \dot{\mathbf{V}}_2(\omega) \end{bmatrix} \quad (32)$$

$$\begin{bmatrix} \mathbf{P}_2(\omega) \\ \dot{\mathbf{V}}_2(\omega) \end{bmatrix} = \begin{bmatrix} \mathbf{B}_1(\omega) & \mathbf{B}_2(\omega) \\ \mathbf{B}_3(\omega) & \mathbf{B}_4(\omega) \end{bmatrix} \begin{bmatrix} \mathbf{P}_1(\omega) \\ \dot{\mathbf{V}}_1(\omega) \end{bmatrix} \quad (33)$$

As before, the subscript "1" denotes input ports and the subscript "2" denotes output ports. The linear relationships between the various submatrices, which are easily obtained by suitable manipulation of these equations, are presented in Table I of this appendix.

TABLE I. RELATIONSHIPS BETWEEN THE CHARACTERISTIC MATRICES OF AN N-PORT NETWORK

FROM TO ↓	Z	Y	A	B
Z	$\begin{bmatrix} Z_1 & Z_2 \\ Z_3 & Z_4 \end{bmatrix}$	$\begin{bmatrix} Y_1 & -Z_1 Y_2 Y_4^{-1} \\ -Y_4^{-1} Y_3 Z_1 & (Y_4 - Y_3 Y_1^{-1} Y_2)^{-1} \end{bmatrix}$ WHERE $Z_1 = (Y_1 - Y_2 Y_4^{-1} Y_3)^{-1}$	$\begin{bmatrix} A_1 A_3^{-1} & (A_1 A_3^{-1} A_4 - A_2) \\ A_3^{-1} & A_3^{-1} A_4 \end{bmatrix}$	$\begin{bmatrix} -B_3^{-1} B_4 & -B_3^{-1} \\ (B_2 - B_1 B_3^{-1} B_4) & -B_1 B_3^{-1} \end{bmatrix}$
Y	$\begin{bmatrix} Y_1 & -Y_1 Z_2 Z_4^{-1} \\ -Z_4^{-1} Z_3 Y_1 & (Z_4 - Z_3 Z_1^{-1} Z_2)^{-1} \end{bmatrix}$ WHERE $Y_1 = (Z_1 - Z_3 Z_4^{-1} Z_3)^{-1}$	$\begin{bmatrix} Y_1 & Y_2 \\ Y_3 & Y_4 \end{bmatrix}$	$\begin{bmatrix} A_1 A_2^{-1} & (A_3 - A_1 A_2^{-1} A_1) \\ -A_2^{-1} & A_2^{-1} A_1 \end{bmatrix}$	$\begin{bmatrix} -B_2^{-1} B_1 & B_2^{-1} \\ (B_4 B_2^{-1} B_1 - B_3) & -B_4 B_2^{-1} \end{bmatrix}$
A	$\begin{bmatrix} Z_1 Z_3^{-1} & (Z_1 Z_3^{-1} Z_4 - Z_2) \\ Z_3^{-1} & Z_3^{-1} Z_4 \end{bmatrix}$	$\begin{bmatrix} -Y_3^{-1} Y_4 & -Y_3^{-1} \\ (Y_2 - Y_1 Y_3^{-1} Y_4) & -Y_1 Y_3^{-1} \end{bmatrix}$	$\begin{bmatrix} A_1 & A_2 \\ A_3 & A_4 \end{bmatrix}$	$\begin{bmatrix} A_1 & -A_1 B_1 B_4^{-1} \\ -B_4^{-1} B_3 A_1 & (B_4 - B_3 B_1^{-1} B_2)^{-1} \end{bmatrix}$ WHERE $A_1 = (B_1 - B_3 B_4^{-1} B_2)^{-1}$
B	$\begin{bmatrix} Z_4 Z_2^{-1} & (Z_3 - Z_4 Z_2^{-1} Z_1) \\ -Z_2^{-1} & Z_2^{-1} Z_1 \end{bmatrix}$	$\begin{bmatrix} -Y_2^{-1} Y_1 & Y_2^{-1} \\ (Y_4 Y_2^{-1} Y_1 - Y_3) & -Y_4 Y_2^{-1} \end{bmatrix}$	$\begin{bmatrix} B_1 & -B_1 A_2 A_4^{-1} \\ -A_4 A_3 B_1 & (A_4 - A_3 A_1^{-1} A_2)^{-1} \end{bmatrix}$ WHERE $B_1 = (A_1 - A_2 A_4^{-1} A_3)^{-1}$	$\begin{bmatrix} B_1 & B_2 \\ B_3 & B_4 \end{bmatrix}$

AMDR 9635-037, APPENDIX B

REPRODUCIBILITY OF THE ORIGINAL PAGE IS POOR

AMDR 9635-037, APPENDIX B

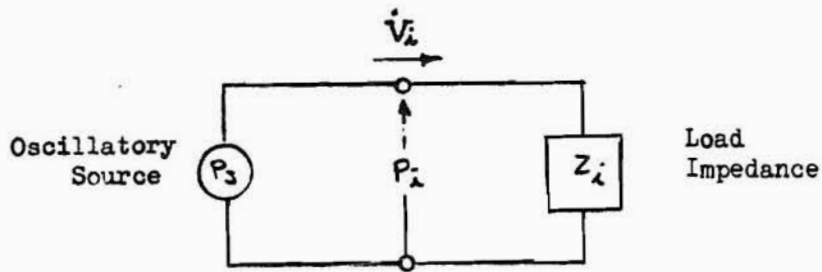


FIGURE 1. SIMPLE ONE-PORT NETWORK

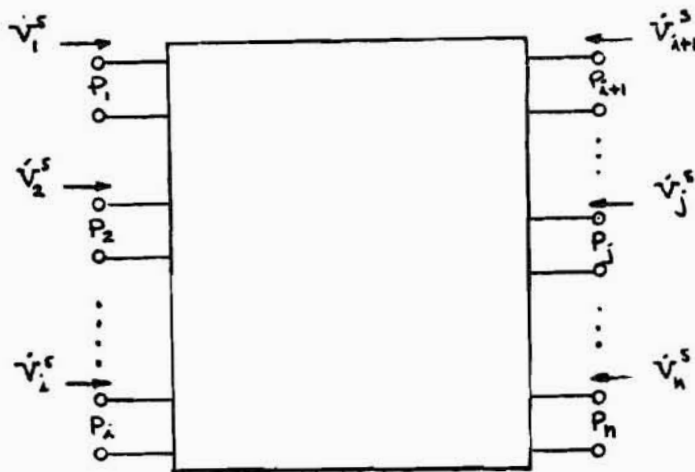


FIGURE 2. GENERAL n-PORT NETWORK

AMDR 9635-037, APPENDIX B

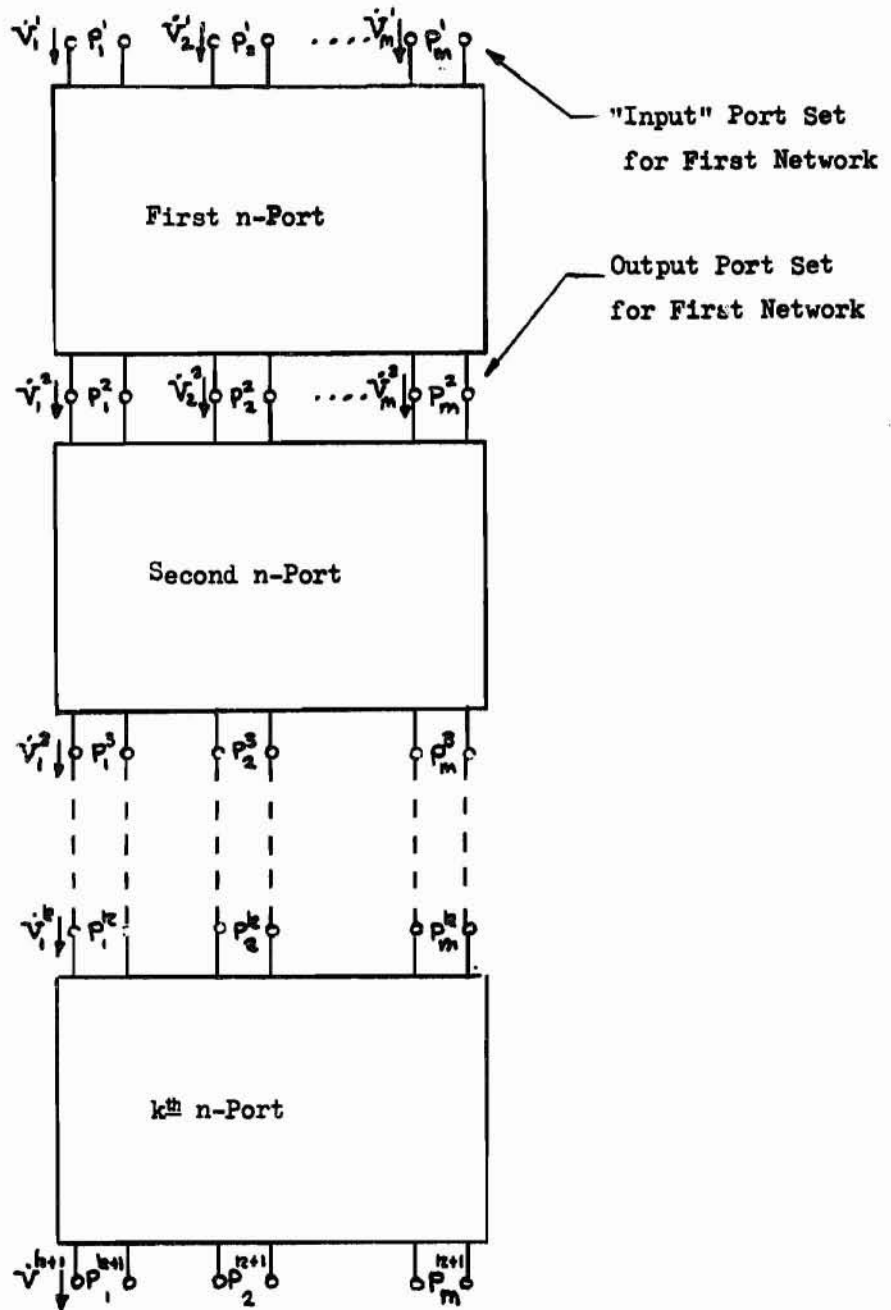


FIGURE 3. TANDEM ARRAY OF N-PORT NETWORKS

AMDR 9635-037

APPENDIX C

DIGITAL COMPUTER PROGRAM FOR
ENGINE-FEED SYSTEM FREQUENCY RESPONSE

BLANK PAGE

AMDR 9635-037, APPENDIX C

I. DIGITAL COMPUTER PROGRAM FOR ENGINE-FEED SYSTEM FREQUENCY RESPONSEA. COMPUTER PROGRAM APPLICATION

The digital computer program which is used to determine the engine-feed system frequency response is contained in this appendix. The program consists of a series of subroutines whose operation can best be understood by their application to the following gas generator assembly (GGA) low frequency combustion stability problem. In this problem, the input impedance frequency response from 0 to 1000 cps is required for the oxidizer and fuel feed systems on Test Stand E-3 whose schematic is shown in Fig 1. A printout at 1 cps intervals shall include the line load impedances, the injector coupling matrix elements, the combined feed system impedance, and the coupling matrix determinant. In addition, it is necessary to compute the magnitude and phase of the open loop transfer function (OLTF) for the GGA on Test Stand E-3 over a 100 to 300 cps frequency range for every 1 cps where

$$OLTF = \frac{c^*}{A_t g} \frac{e^{-\tau_1 s}}{1 + \tau_1 s} \left[\frac{K_o}{Z_o} + \frac{K_f}{Z_f} \right]$$

The detailed subroutines, which are listed in Section B of this appendix, are applied to the GGA problem in the following manner.

1. Fuel Feed Line (See Fig 1)

a. Compute sending end impedance for element (1), given zero receiving end impedance, by Subroutine ZFUNC.

b. Compute sending end impedance for element (2), given infinite receiving end impedance, by Subroutine ZFUNC.

c. Combine these two sending end impedances (which are in parallel) to yield the receiving end impedance for element (3).

d. Compute sending end impedance for element (3) by Subroutine ZFUNC to yield receiving end impedance for element (4).

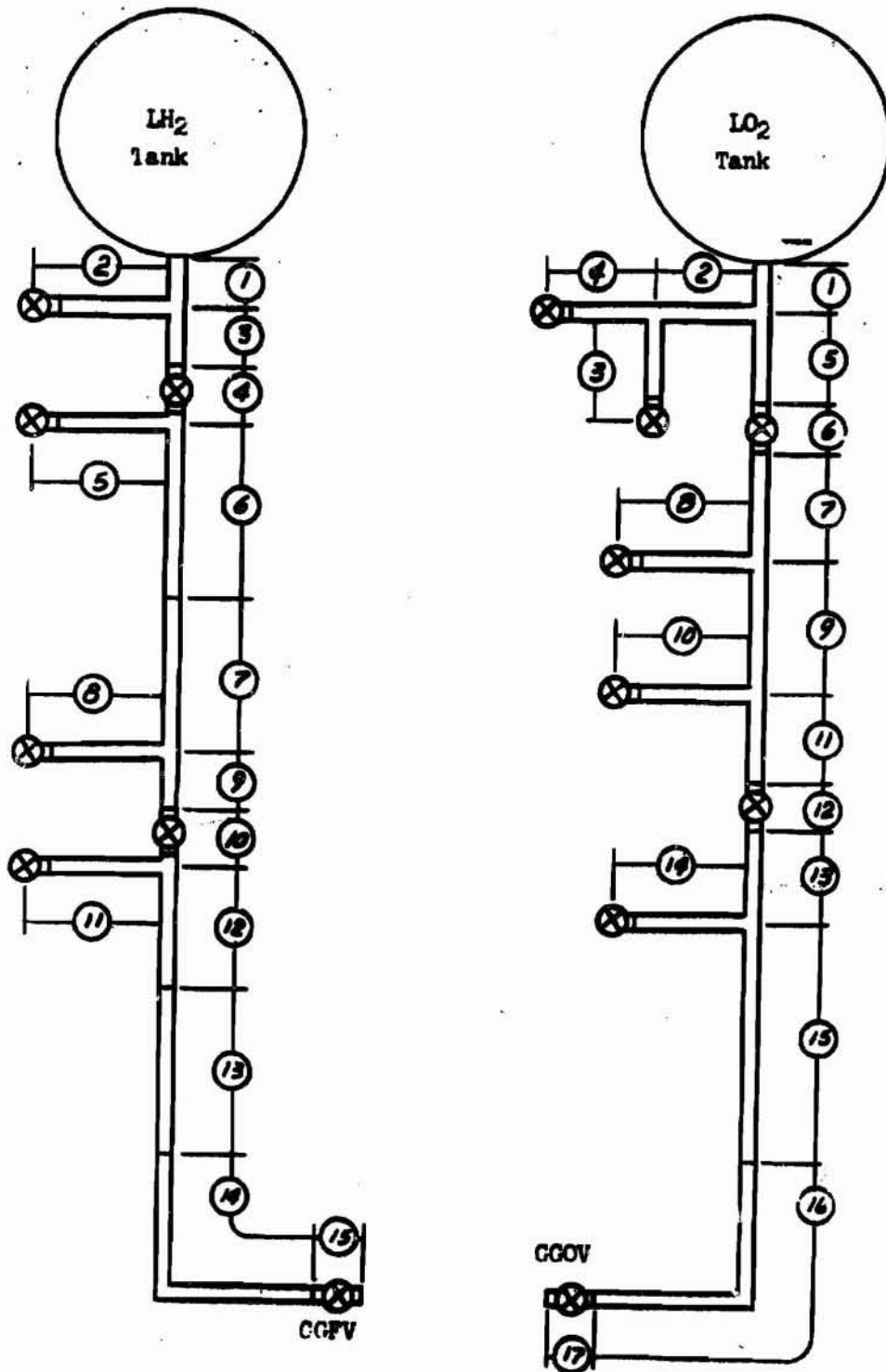


Figure 1 GGA PROPELLANT FEED SYSTEM SCHEMATIC

I,A, Computer Program Application (cont.)

- e. Compute sending end impedance for element (4) by Subroutine ZFUNC.
- f. Compute sending end impedance for element (5), given infinite receiving end impedance, by Subroutine ZFUNC.
- g. Combine these last two sending end impedances, which are in parallel, to yield the receiving end impedance for element (6).
- h. Continue with elements (6), (9), and (12) treated as has been element (3); elements (7), (10), and (13) as has been element (4); and elements (8) and (11) as has been element (5).
- i. Elements (14) and (15) are treated serially, with the sending end impedance of (14) being the receiving end impedance of (15), for use by Subroutine ZFUNC.
- j. The sending end impedance of element (15) is finally obtained and can be regarded as the fuel feed line impedance, Z_{FL} .

2. Oxidiser Feed Line (See Fig 1)

- a. The sending end impedance of element (17) is obtained by the same approach as used in 1. and can be regarded as the oxidiser feed line impedance, Z_{OL} . Note that both elements (3) and (4) are "dead-ends," thus have infinite receiving end impedance, and have their sending end impedances in parallel, the combination of which is the receiving end impedance of element (2).

3. Oxidiser Injector (See Fig 2)

- a. The oxidiser injector follows oxidiser element (17), and the coupling (2 x 2) matrix for the injector must be obtained. The coupling matrices for Z_{OR3} , Z_{t2} , Z_{t1} , and Z_1 are obtained by suitable use of Subroutine ALVAL.
- b. The admittance matrices (2 x 2) of Z_{OR1} and Z_{OR2} are obtained

AMDR 9635-037, APPENDIX C

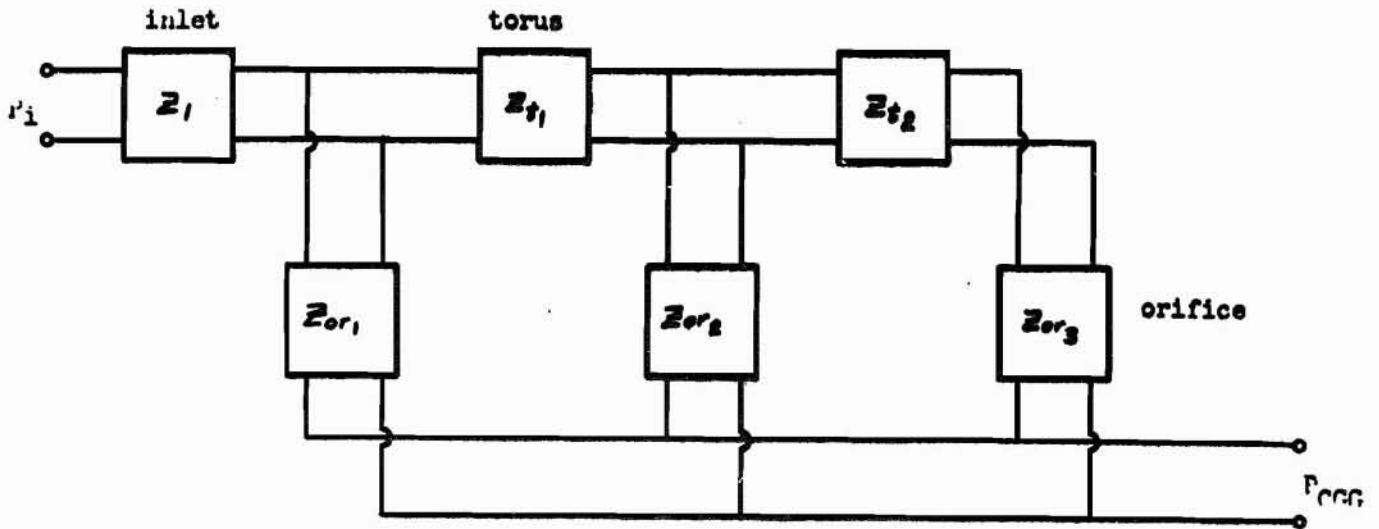


Figure 2 ANALOG CIRCUIT GGA OXIDIZER INJECTOR

AMDR 9635-037, APPENDIX C

I,A, Computer Program Application (cont.)

by using Subroutine ALVAL to get their respective coupling matrices and converting each to its respective admittance matrix by Subroutine ALTOY.

c. The combined coupling matrix of Z_{t2} and Z_{OR3} is obtained by premultiplying Z_{OR3} 's coupling matrix onto that of Z_{t2} through use of Subroutine MAGMUL.

d. This combined coupling matrix is converted to an admittance matrix by Subroutine ALTOY and then added to the admittance matrix of Z_{OR2} by Subroutine MAGADS to yield the combined admittance matrix of these elements. This matrix is converted back to a coupling matrix by Subroutine YTOAL.

e. Z_{t1} is now treated as was Z_{t2} , Z_{OR1} as was Z_{OR2} , and the new combined coupling matrix as was Z_{OR3} to yield the combined coupling matrix of all these elements.

f. The injector coupling matrix is obtained by premultiplying the coupling matrix of Z_1 by that of the combined other elements.

g. Overall fuel impedance of Z_{OX} is obtained by the formula

$$Z_{OX} = \frac{\kappa_{11} Z_{t1} + \kappa_{12}}{\kappa_{21} Z_{t1} + \kappa_{22}}$$

where the κ_{ij} terms are the elements of the oxidiser injector coupling matrix.

4. Fuel Injector (See Fig 3)

a. The fuel injector follows fuel element (15), and the coupling (6 x 6) matrix for the injector (other than inlet element Z_1) must first be obtained. The coupling matrices (2 x 2) for Z_{t1} , Z_{t2} , Z_{t3} , Z_{k1} , Z_{k2} , Z_{k3} , and Z_1 are obtained by suitable use of Subroutine ALVAL.

b. The admittance matrices (2 x 2) of Z_{s1} , Z_{s2} , Z_{s3} , Z_{s4} , Z_{OR1} , Z_{OR2} , Z_{OR3} , and Z_{OR4} are obtained by using Subroutine ALTOY.

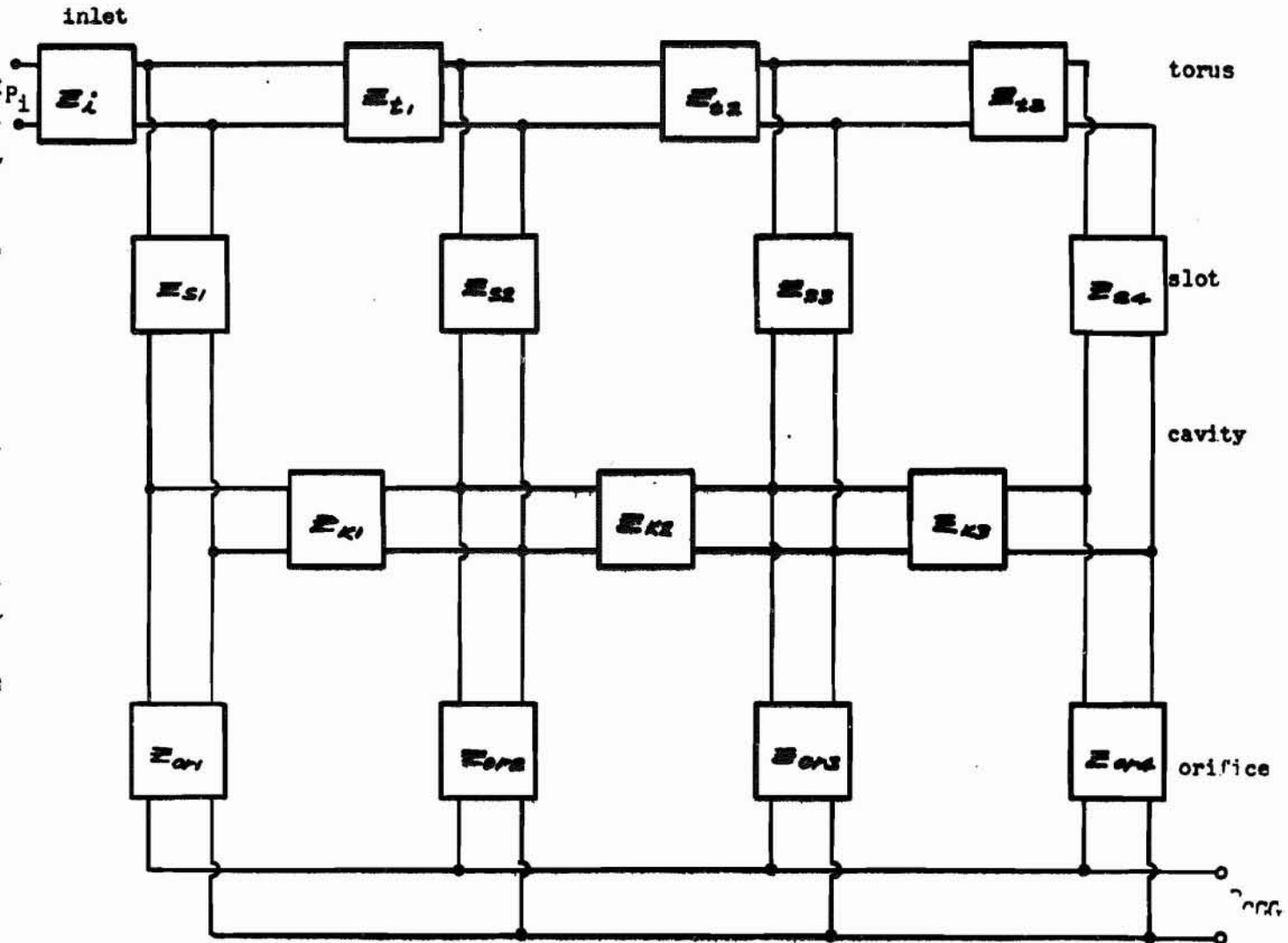


Figure 3 ANALOG CIRCUIT GGA FUEL INJECTOR

AMDR 9635-037, APPENDIX C

I,A, Computer Program Application (cont.)

c. The 6 x 6 coupling matrix of Z_{s4} and Z_{OR4} is computed by input of their admittance matrices to Subroutine KIPMAT (with NF = 1).

d. The 6 x 6 coupling matrix of Z_{t3} and Z_{k3} is computed by input of their coupling matrices and the unit 2 x 2 matrix (for the bottom horizontal path) to Subroutine KIPMAT (with NF = 1).

e. The Z_{t3} , Z_{k3} coupling matrix is premultiplied by the Z_{s4} , Z_{OR4} coupling matrix by Subroutine MAGMUL to yield the combined coupling matrix.

f. The Z_{s3} , Z_{OR3} coupling matrix is computed as in (c.) and postmultiplied onto the combined coupling matrix from (e.).

g. The Z_{t2} , Z_{k2} coupling matrix is computed as in (d.) and postmultiplied onto the combined coupling matrix resulting from (f.).

h. Similarly, we treat the remainder of the six-port network elements to obtain its combined coupling matrix. The equivalent six-port impedance matrix is then obtained by Subroutine GALTOY (with NF = 1).

i. The equivalent 2 x 2 coupling matrix of the six-port network is now obtained by the conversion of the Z_{33} , Z_{34} , Z_{43} , Z_{44} square array of impedance elements to its equivalent coupling matrix by the equations:

$$\alpha_{11} = \frac{Z_{33}}{Z_{44}}, \quad \alpha_{12} = \frac{Z_{34}Z_{43} - Z_{33}Z_{44}}{Z_{44}}, \quad \alpha_{21} = \frac{1}{Z_{44}}, \quad \alpha_{22} = \frac{Z_{43}}{Z_{44}}$$

j. The above coupling matrix is postmultiplied by the Z_1 coupling matrix to yield the overall 2 x 2 coupling matrix of the fuel injector.

k. Overall fuel impedance Z_f is obtained by the formula

$$Z_f = \frac{\alpha_{11}Z_{f1} + \alpha_{12}}{\alpha_{21}Z_{f1} + \alpha_{22}}$$

where the α_{ij} terms are the elements of the fuel injector coupling matrix.

I,A, Computer Program Application (cont.)

5. Open Loop Transfer Function (F)

This final result is now obtained by

$$F = \frac{C^*}{A_t g} \left(\frac{e^{j\omega\tau_1}}{1 + j\omega\tau_2} \right) \left(\frac{K_{ss}}{Z_{ss}} + \frac{K_p}{Z_p} \right)$$

6. Output Display

Those variables to be printed out are first converted to their respective magnitudes and phases by Subroutine COMREC.

B. FEED LINE ANALYSIS COMPLEX ARITHMETIC SUBROUTINE LIST

Deck Name	Subroutine Name
S1	MAGMUL
S3	ZFUNC
S4	YTOAL
S5	ALTOY
S6	ALVAL
S7	COMREC
S8	EXPMAT
S9	GALTOY
S10	MATINV
S11	MAGADS
S13	ALVAZ

1. Name: MAGMUL

Argument List: (A, B, C, N) - A, B, and C are each a square matrix array of complex elements, each matrix being of order N(2 ≤ N ≤ 6).

AMDR 9635-037, APPENDIX C

I,B, Feed Line Analysis Complex Arithmetic Subroutine List (cont.)

Purpose: $[C_{1j}] = [A_{1j}] [B_{1j}]$ - matrix multiplication of A onto B to yield C.

2. Name: ZFUNC

Argument List: (N, ZIF, ZRI, ZRO)

ZRI = receiving end impedance of a transmission line type lumped parameter feed line element.

ZRO = sending end impedance of this element.

N = index number of referenced element.

Purpose:

$$ZRO = Z_0 \frac{ZRI + Z_0 [\tanh(\sqrt{L})]}{Z_0 + ZRI [\tanh(\sqrt{L})]}$$

where

$$Z_0 = \sqrt{\frac{R + j\omega L}{j\omega C}}, \quad \sqrt{L} = \sqrt{(R + j\omega L)(j\omega C)},$$

$$R = RA(N), \quad L = XLA(N), \quad C = CA(N)$$

RA(I), XLA(I), and CA(I) are single variable arrays of the parameters of the transmission line elements considered which are placed on COMMON by the main program, along with frequency ω (rad/sec).

If ZIF \geq 0., the above formula is applied. If ZRI is infinite, ZIF is made negative and we have

$$ZRO = Z_0 \operatorname{ceth}(\sqrt{L})$$

If $\omega C = 0$, we then have

$$ZRO = ZRI + R + j\omega L$$

AMDR 9635-037, APPENDIX C

I,B, Feed Line Analysis Complex Arithmetic Subroutine List (cont.)

3. Name: YTOAL

Argument List: (Y, AL) - Both Y and AL are 2 x 2 matrices with complex elements.

Purpose: To convert a 2 x 2 complex admittance matrix into a 2 x 2 complex coupling matrix by the relations:

$$\alpha_{11} = -Y_{22}/Y_{21}$$

$$\alpha_{12} = -1/Y_{21}$$

$$\alpha_{21} = -|Y_{13}|/Y_{21}$$

$$\alpha_{22} = -Y_{11}/Y_{21}$$

4. Name: ALTOY

Argument List: (AL, Y) - Both AL and Y are 2 x 2 matrices with complex elements.

Purpose: To convert a 2 x 2 complex coupling matrix into a 2 x 2 complex admittance matrix by the relations:

$$Y_{11} = \alpha_{22}/\alpha_{12}$$

$$Y_{12} = -|\alpha_{13}|/\alpha_{12}$$

$$Y_{21} = -1/\alpha_{12}$$

$$Y_{22} = \alpha_{11}/\alpha_{12}$$

5. Name: ALVAL

Argument List: (R, L, C, NF, AL, ω) - AL is a 2 x 2 array

AMDR 9635-037, APPENDIX C

I, B, Feed Line Analysis Complex Arithmetic Subroutine List (cont.)

of complex quantities which is the coupling matrix of a two-part feed line element. R, L, and C are the lumped parameters of the element, and ω is the frequency (rad/sec) for which the impedances are being evaluated.

Purpose: As NF is set to various values, different forms of the coupling matrix are obtained, as indicated below:

$$a. \quad NF = -1: \quad AL = [a_{ij}] = \begin{bmatrix} 1 & \frac{1}{j\omega C} \\ 0 & 1 \end{bmatrix}$$

$$b. \quad NF = 0: \quad AL = [a_{ij}] = \begin{bmatrix} 1 & R + j\omega L \\ 0 & 1 \end{bmatrix}$$

$$c. \quad NF = 1: \quad AL = [a_{ij}] = \begin{bmatrix} 1 + (R + j\omega L)(j\omega C) & R + j\omega L \\ j\omega C [2 + (R + j\omega L)(j\omega C)] & 1 + (R + j\omega L)(j\omega C) \end{bmatrix}$$

$$d. \quad NF = 2: \quad AL = [a_{ij}] = \begin{bmatrix} \cosh(\gamma L) & Z_0 \sinh(\gamma L) \\ \frac{1}{Z_0} \sinh(\gamma L) & \cosh(\gamma L) \end{bmatrix}$$

where $Z_0 = \sqrt{\frac{R + j\omega L}{j\omega C}}$, $\gamma L = \sqrt{(R + j\omega L)(j\omega C)}$

$$e. \quad NF = 3: \quad AL = [a_{ij}] = \begin{bmatrix} 1 & R + j\omega L \\ j\omega C & 1 + (R + j\omega L)(j\omega C) \end{bmatrix}$$

$$f. \quad NF = 4: \quad AL = [a_{ij}] = \begin{bmatrix} 1 + (R + j\omega L)(j\omega C) & R + j\omega L \\ j\omega C & 1 \end{bmatrix}$$

AMDR 9635-037, APPENDIX C

I,B, Feed Line Analysis Complex Arithmetic Subroutine List (cont.)

6. Name: COMREC

Argument List: (Z, XM, PH) - Z is a complex number.

Purpose:

$$XM = |Z| = \text{magnitude of } Z$$

$$PH = \angle Z(^{\circ}) = \text{phase in degrees } (-180^{\circ} \leq PH \leq 180^{\circ})$$

7. Name: EXPMAT

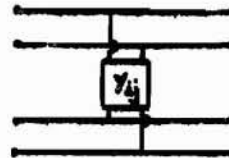
Argument List: (A1, A2, A3, NF, N, A) - A1, A2, and A3 are each a 2 x 2 matrix array of complex elements, and A is an N x N matrix array of complex elements.

Purpose: To generate either a four- or six-port coupling matrix from its component two-port matrices (admittance or coupling) for either the interacting or non-interacting configuration, as indicated below:

a. Four-Port Interacting Network: NF = -1

$$N = 4$$

$$A = \begin{bmatrix} 1 & 0 & 0 & 0 \\ 0 & 1 & 0 & 0 \\ Y_{11} & Y_{12} & 1 & 0 \\ Y_{21} & Y_{22} & 0 & 1 \end{bmatrix}$$



$$A1 = \begin{bmatrix} Y_{11} & Y_{12} \\ Y_{21} & Y_{22} \end{bmatrix} = \text{admittance matrix of interacting two-port element}$$

b. Four-Port Non-Interacting Network: NF = 1

$$N = 4$$



AMDR 9635-037, APPENDIX C

I,B, Feed Line Analysis Complex Arithmetic Subroutine List (cont.)

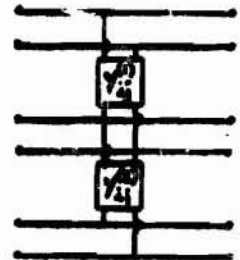
$$A = \begin{bmatrix} x_{11}^{(1)} & 0 & x_{12}^{(1)} & 0 \\ 0 & x_{11}^{(2)} & 0 & x_{12}^{(2)} \\ x_{21}^{(1)} & 0 & x_{22}^{(1)} & 0 \\ 0 & x_{21}^{(2)} & 0 & x_{22}^{(2)} \end{bmatrix}$$

$$A1 = \begin{bmatrix} x_{11}^{(1)} & x_{12}^{(1)} \\ x_{21}^{(1)} & x_{22}^{(1)} \end{bmatrix} \quad \text{and} \quad A2 = \begin{bmatrix} x_{11}^{(2)} & x_{12}^{(2)} \\ x_{21}^{(2)} & x_{22}^{(2)} \end{bmatrix}$$

which are the respective coupling matrices of the two non-interacting two-port elements.

- c. Six-Port Interacting Network: $NF = -1$
 $N = 6$

$$A = \begin{bmatrix} 1 & 0 & 0 & 0 & 0 & 0 \\ 0 & 1 & 0 & 0 & 0 & 0 \\ 0 & 0 & 1 & 0 & 0 & 0 \\ y_{11}^{(1)} & y_{12}^{(1)} & 0 & 1 & 0 & 0 \\ y_{21}^{(1)} & y_{22}^{(1)} + y_{11}^{(2)} & y_{12}^{(2)} & 0 & 1 & 0 \\ 0 & y_{21}^{(2)} & y_{22}^{(2)} & 0 & 0 & 1 \end{bmatrix}$$



$$A1 = \begin{bmatrix} y_{11}^{(1)} & y_{12}^{(1)} \\ y_{21}^{(1)} & y_{22}^{(1)} \end{bmatrix} \quad \text{and} \quad A2 = \begin{bmatrix} y_{11}^{(2)} & y_{12}^{(2)} \\ y_{21}^{(2)} & y_{22}^{(2)} \end{bmatrix}$$

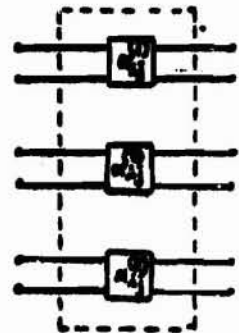
which are the respective admittance matrices of the interacting two-port elements.

AMDR 9635-037, APPENDIX C

I,B,Feed Line Analysis Complex Arithmetic Subroutine List (cont.)

- d. Six-Port Non-Interacting Network: NF = 1
N = 6

$$A = \begin{bmatrix} a_{11}^{(1)} & 0 & 0 & a_{14}^{(1)} & 0 & 0 \\ 0 & a_{11}^{(2)} & 0 & 0 & a_{12}^{(2)} & 0 \\ 0 & 0 & a_{11}^{(3)} & 0 & 0 & a_{12}^{(3)} \\ a_{21}^{(1)} & 0 & 0 & a_{24}^{(1)} & 0 & 0 \\ 0 & a_{21}^{(2)} & 0 & 0 & a_{22}^{(2)} & 0 \\ 0 & 0 & a_{21}^{(3)} & 0 & 0 & a_{22}^{(3)} \end{bmatrix}$$



$$A_1 = \begin{bmatrix} a_{11}^{(1)} & a_{12}^{(1)} \\ a_{21}^{(1)} & a_{22}^{(1)} \end{bmatrix}$$

$$A_2 = \begin{bmatrix} a_{11}^{(2)} & a_{12}^{(2)} \\ a_{21}^{(2)} & a_{22}^{(2)} \end{bmatrix}$$

$$A_3 = \begin{bmatrix} a_{11}^{(3)} & a_{12}^{(3)} \\ a_{21}^{(3)} & a_{22}^{(3)} \end{bmatrix}$$

which are the respective coupling matrices of the three non-interacting two-port elements.

8. Name: GALTOY

Argument List: (A, B, N, NF) - A is a 2N x 2N coupling matrix of complex elements. B is the equivalent 2N x 2N impedance matrix if NF = 1, or the equivalent 2N x 2N admittance matrix if NF = -1.

Purpose: Transformation of a 4 x 4 or 6 x 6 coupling matrix to either its equivalent impedance matrix or admittance matrix. Let A be partitioned as follows:

$$A = \begin{bmatrix} a_{ij} & b_{ij} \\ c_{ij} & d_{ij} \end{bmatrix}$$

AMDR 9635-037, APPENDIX C

I,B, Feed Line Analysis Complex Arithmetic Subroutine List (cont.)

Then it can be shown that

$$B = \left[\begin{array}{c|c} \bar{a}_{ij} & \bar{b}_{ij} \\ \hline \bar{c}_{ij} & \bar{d}_{ij} \end{array} \right] = \text{equivalent impedance matrix}$$

where

$$\begin{aligned} [\bar{a}_{ij}] &= [a_{ij}] [c_{ij}]^{-1}, & [\bar{b}_{ij}] &= [a_{ij}] [c_{ij}]^{-1} [d_{ij}] - [b_{ij}] \\ [\bar{c}_{ij}] &= [c_{ij}]^{-1}, & [\bar{d}_{ij}] &= [c_{ij}]^{-1} [d_{ij}] \end{aligned}$$

Also, it can be shown that

$$D = \left[\begin{array}{c|c} \bar{a}_{ij} & \bar{b}_{ij} \\ \hline \bar{c}_{ij} & \bar{d}_{ij} \end{array} \right] = \text{equivalent admittance matrix}$$

where

$$\begin{aligned} [\bar{a}_{ij}] &= [d_{ij}] [b_{ij}]^{-1}, & [\bar{b}_{ij}] &= [c_{ij}] - [d_{ij}] [b_{ij}]^{-1} [a_{ij}] \\ [\bar{c}_{ij}] &= -[b_{ij}]^{-1}, & [\bar{d}_{ij}] &= [b_{ij}]^{-1} [a_{ij}] \end{aligned}$$

9. Name: MATINV

Argument List: (A, AI, N, AD) - A and AI are each N x N matrix arrays of complex elements. AD is the determinant (complex) of matrix A.

Purpose: To obtain the inverse of matrix A by use of the Banachiewicz-Cholesky-Crout Elimination Method. This may be described as follows:

AMDR 9635-037, APPENDIX C

I,B, Feed Line Analysis Complex Arithmetic Subroutine List (cont.)

The first auxiliary array

$$\begin{bmatrix} \gamma_{11} & \alpha_{12} & \alpha_{13} & \dots & \alpha_{1N} \\ \gamma_{21} & \gamma_{22} & \alpha_{23} & \dots & \alpha_{2N} \\ \gamma_{31} & \gamma_{32} & \gamma_{33} & \dots & \alpha_{3N} \\ \vdots & \vdots & \vdots & \ddots & \vdots \\ \gamma_{N1} & \gamma_{N2} & \gamma_{N3} & \dots & \gamma_{NN} \end{bmatrix}$$

is computed from the original matrix $[a_{ij}]$ by the following relations:

$$\gamma_{ik} = a_{ik} - \sum_{j=1}^{k-1} \gamma_{ij} \alpha_{jk} \quad (\text{except } \gamma_{11} = a_{11})$$

$$\alpha_{ik} = \frac{1}{\gamma_{ii}} \left[a_{ik} - \sum_{j=1}^{i-1} \gamma_{ij} \alpha_{jk} \right] \quad (\text{except } \alpha_{1k} = \frac{a_{1k}}{a_{11}})$$

The computational sequence is typified by

$$\gamma_{11}, \gamma_{12}, \dots, \gamma_{N2}, \alpha_{2(2+1)}, \alpha_{2(2+2)}, \dots, \alpha_{2N}, \gamma_{3(3+1)}, \dots$$

Next, the secondary auxiliary array, β_{ij} , is computed by

$$\beta_{ij} = \begin{cases} 0 & , j > i \\ \frac{1}{\gamma_{ii}} & , j = i \\ -\frac{1}{\gamma_{ii}} \left[\sum_{k=1}^{i-1} \gamma_{ik} \beta_{kj} \right] & , j < i \end{cases}$$

The computational sequence in this case is typified by

$$\beta_{2,2}, \beta_{3,2}, \dots, \beta_{N,2}, \beta_{3(3+1)}, \beta_{3(3+2)}, \dots, \beta_{N,(j+1)}$$

AMDR 9635-037, APPENDIX C

I, B, Feed Line Analysis Complex Arithmetic Subroutine List (cont.)

Finally, the inverse elements are obtained by

$$\delta_{ij} = a_{ij}^{-1} - \sum_{k=1}^N a_{ik} a_{kj} \quad (\text{except } \delta_{Nj} = a_{Nj}^{-1})$$

where $[\delta_{ij}] = [a_{ij}]^{-1}$

with the computational sequence being typified by

$$\delta_{Nj}, \delta_{(N-1),j}, \dots, \delta_{1,j}, \delta_{N,(j+1)}, \delta_{(N-1),(j+1)}, \dots, \delta_{1,(j+1)}$$

The determinant of the matrix is evaluated by

$$\Delta D = [\delta_{ij}] = \prod_{L=1}^N \gamma_{LL}$$

10. Name: MAGADS

Argument List: (A, B, C, N, NF) - A, B, and C are each a square matrix array of complex elements, each matrix being of order N (2 ≤ N ≤ 6).

Purpose:

$$[C_{ij}] = [A_{ij}] + (NF) [B_{ij}]$$

where $NF = \begin{cases} +1 \\ -1 \end{cases}$

Both matrix addition and subtraction are provided hereby. Thus, when NF = +1, we add B to A, and when NF = -1, we subtract B from A.

11. Name: ALVAZ

Argument List: (Z, AL) - Z is a complex impedance, and AL is a 2 x 2 complex coupling matrix.

Purpose: To form the coupling matrix when only the reciprocal of the complex admittance is available as input. Thus,

$$AL = [\alpha_{ij}] = \begin{bmatrix} 1 & 0 \\ \frac{1}{Z} & 1 \end{bmatrix}$$

AMDR 9635-037

APPENDIX D

ABSORPTIVE LINE ANALYTICAL MODEL

PRECEDING PAGE BLANK NOT FILLED.

A. MODEL WITHOUT STEADY-STATE FLOW EFFECTS

A mathematical model of an absorptive hydraulic transmission line, neglecting the effect of steady-state flow upon wave propagation, has been developed for the lossy line investigation. The analysis treats one-dimensional wave propagation in a duct lined with distributed absorptive resonators. The basic analytical model not only applies to the classical lossy line, which utilizes distributed Helmholtz resonators, but also applies to the bubble filled line, which utilizes distributed gas bubbles. The equivalency of the lossy line and the bubble filled line and their common elemental model are shown in Figure 1. It is seen that, in both cases, the series impedance term (Z_s) is caused by the inertance and resistance of the liquid in the main paths, and the shunt admittance (Y_s) is caused by the parallel combination of the liquid capacitance and the resonator admittance. In the lossy line, the second order resonator is due to the slug of liquid resonating on the cavity compliance; while in the bubble filled line, the resonator is created by the "breathing mode" (lowest frequency mode of vibration) of the bubble. The application of the results of the analysis of the generalized absorptive transmission line to the problems of predicting the wave propagation characteristics for the lossy line and the bubble filled suction line is treated in the next two sections. The remainder of this section presents the preliminary results of the analysis of the generalized absorptive transmission line.

The results of the frequency response analysis of the absorptive hydraulic transmission line are presented in dimensionless form for convenient application. The effect of frequency upon the various wave propagation parameters such as the characteristic impedance, propagation function, attenuation function, phase function, and acoustic velocity is shown explicitly by frequency response (Bode) diagrams. The following discussion summarizes the results of the frequency response analysis.

A, Model Without Steady-State Flow Effects (cont.)

The fundamental equation that governs steady-state sinusoidal pressure and flow oscillations in a long transmission line is the Fourier transformed one-dimensional wave equation. This equation may be written for either pressure or flow fluctuations:

$$\frac{d^2 P(x, \omega)}{dx^2} - [\gamma'(\omega)]^2 P(x, \omega) = 0 \quad (1)$$

$$\frac{d^2 \dot{V}(x, \omega)}{dx^2} - [\gamma'(\omega)]^2 \dot{V}(x, \omega) = 0 \quad (2)$$

where

$P(x, \omega)$ = complex amplitude of $p(x, t)$

$\dot{V}(x, \omega)$ = complex amplitude of $\dot{v}(x, t)$

$p(x, t)$ = oscillatory component of pressure at distance x

$\dot{v}(x, t)$ = oscillatory component of volume flow at distance x

$\gamma'(\omega)$ = complex propagation constant per unit length.

In general, the propagation function (per unit length) of a transmission line is a complex function of frequency with a real part, $\alpha'(\omega)$, and an imaginary part, $\beta'(\omega)$

$$\gamma'(\omega) = \alpha'(\omega) + j\beta'(\omega) \quad (3)$$

The real part of Eq (3) is called the attenuation function and the imaginary part is called the phase function. The rationale behind this nomenclature is apparent when one considers the solution of Eq (1) for sinusoidal pressure waves propagating in an infinitely long line or a line terminated in its characteristic impedance. Then

$$P(x, \omega) = P_0(\omega) e^{-\gamma'(\omega)x} = P_0(\omega) e^{-[\alpha'(\omega) + j\beta'(\omega)]x} \quad (4)$$

where $j = \sqrt{-1}$ and $P_0(\omega)$ is the complex amplitude at the source (at $x=0$). If $|P_0(\omega)|$ and θ are the absolute amplitude and phase angle, respectively of $P_0(\omega)$, Eq (4) may be rewritten

A, Model Without Steady-State Flow Effects (cont.)

$$P(x, \omega) = |P_0(\omega)| e^{-\alpha(\omega)x} e^{j[\phi - \beta(\omega)x]} \quad (5)$$

Hence from Eq (5) it is obvious that $\alpha(\omega)$ controls the amplitude attenuation and $\beta(\omega)$ controls the phase shift of the traveling wave as it moves away from the source.

For the elemental model shown in Figure 1, the propagation constant is related to the series impedance and shunt admittance of an incremental length of transmission line by the following equation:

$$\gamma(\omega) = [Z'_s(\omega) Y'_s(\omega)]^{1/2} \quad (6)$$

where

$$Z'_s(\omega) = -\frac{1}{V(\omega)} \frac{\Delta P(\omega)}{\Delta X} \quad (7)$$

$$Y'_s(\omega) = -\frac{1}{P(\omega)} \frac{\Delta V(\omega)}{\Delta X} \quad (8)$$

For the circuit of Figure 1, the series impedance and shunt admittance of one stage or increment of the transmission line is given as:

$$Z_s(\omega) = Z'_s(\omega) \Delta X = j\omega L_m + R_m \quad (9)$$

$$Y_s(\omega) = Y'_s(\omega) \Delta X = j\omega C_m + \left[\frac{1}{j\omega C_c} + \frac{1}{j\omega C_s + (j\omega L_s + R_s)^{-1}} \right]^{-1} \quad (10)$$

Thus the propagation function of one transmission line stage is obtained from a combination of Eq (6), (9), and (10):

$$\gamma(\omega) = \gamma(\omega) \Delta X = \left\{ [j\omega L_m + R_m] \left[j\omega C_m + \left(\frac{1}{j\omega C_c} + \frac{1}{j\omega C_s + (j\omega L_s + R_s)^{-1}} \right)^{-1} \right] \right\}^{1/2} \quad (11)$$

where

L_m = inductance of main path

L_s = inductance of shunt path resonator

R_m = resistance of main path

R_s = resistance of shunt path resonator

C_m = capacitance of main path

C_c = coupling capacitance between main path and shunt path

C_s = capacitance of shunt path resonator

A, Model Without Steady-State Flow Effects (cont.)

If the coupling capacitance (C_g) and the main path resistance (R_m) are negligible, the expression for the propagation function may be simplified and rewritten in terms of normalized acoustic parameters:

$$\bar{V}(\omega) = j \frac{\bar{L}_a}{\left(\frac{L_a}{L_m}\right)^2} \left[\frac{\frac{C_m}{C_a} (1 + \frac{C_a}{C_m} - \Omega^2)(1 - \Omega^2) + j \frac{C_a}{C_m} \xi_a^2 \Omega^2 - j 2 \xi_a \Omega}{(1 - \Omega^2)^2 + 4 \xi_a^2 \Omega^2} \right]^{\frac{1}{2}} \quad (12)$$

where

$$\Omega = \frac{\omega}{\omega_a} = \text{dimensionless frequency}$$

$$\xi_a = \frac{R_a}{2\omega_a L_a} = \text{generalized damping constant of shunt path resonator}$$

$$\omega = \text{frequency}$$

$$\omega_a = \text{resonant frequency of shunt path resonator}$$

$$\frac{L_a}{L_m} = \text{inertance ratio}$$

$$\frac{C_a}{C_m} = \text{capacitance ratio}$$

Therefore Eq (12), combined with Eq (3), may be used to predict the attenuation function $\alpha(\omega)$, the phase function $\beta(\omega)$, and the propagation function $\bar{V}(\omega)$ as a function of the dimensionless parameters Ω , ξ_a , $\frac{L_a}{L_m}$, and $\frac{C_a}{C_m}$.

The characteristic impedance is a complex function which relates the pressure and flow oscillations at any station along the infinite transmission line:

$$Z_c(\omega) = \frac{P(x, \omega)}{\bar{V}(x, \omega)} \quad (13)$$

As in the case of the propagation constant, the characteristic impedance may be expressed in terms of the series impedance and shunt admittance for one transmission line stage:

$$Z_c(\omega) = \left[\frac{Z_s(\omega)}{Y_s(\omega)} \right]^{\frac{1}{2}} \quad (14)$$

Combining Eq (9), (10), and (14), the explicit expression for $Z_c(\omega)$ may be found:

A, Model Without Steady-State Flow Effects (cont.)

$$Z_c(\omega) = \left\{ [j\omega L_m + R_m] \left[j\omega C_m + \left(\frac{1}{j\omega C_a} + \frac{1}{j\omega C_g + \frac{1}{j\omega L_m + R_m}} \right)^{-1} \right]^{-1} \right\}^{\frac{1}{2}} \quad (15)$$

As before, this expression may be simplified by neglecting C_g and R_m . In terms of the parameters Ω , S_a , and C_a/C_m , the simplified expression becomes

$$\frac{Z_c(\omega)}{Z_{co}} = \left[\frac{(1-\Omega^2)^2 - \left(\frac{C_a}{C_m} - 4S_a^2 \right) \Omega^2 + \frac{C_a}{C_m} + j2S_a \Omega \frac{C_a}{C_m}}{(1-\Omega^2 + \frac{C_a}{C_m})^2 + 4S_a^2 \Omega^2} \right]^{\frac{1}{2}} \quad (16)$$

where Z_{co} is the characteristic impedance of a lossless transmission line ($R_m = C_a = C_g = 0$), as defined by the expression:

$$Z_{co} = \left[\frac{L_m}{C_m} \right]^{\frac{1}{2}} = \frac{\rho_o a_o}{A_m} \quad (17)$$

a_o = nominal acoustic velocity of the fluid in the main path

A_m = cross-sectional area of main path

ρ_o = nominal mass density of fluid in the main path.

The nominal acoustic velocity in the main path is governed by the main path impedance and capacitance. Again neglecting C_g and R_m , the equation for the nominal acoustic velocity is written

$$a_o = \frac{\Delta X}{[L_m C_m]^{\frac{1}{2}}} = [L_m' C_m']^{-\frac{1}{2}} \quad (18)$$

This velocity is not necessarily the velocity of sound in an infinite fluid medium. The nominal acoustic velocity may be considerably reduced by the structural compliance of the pipe walls. The equations for L_m' and C_m' are given below

$$L_m' = \frac{\rho_o}{A_m} \quad (19)$$

$$C_m' = A_m \left[\frac{1}{\rho_o a_o^2} - \frac{d}{E h} \right] \quad (20)$$

where

$a_o = [E_o/\rho_o]^{\frac{1}{2}}$ = acoustic velocity in an infinite fluid medium

E_o = adiabatic bulk modulus of the fluid in the main path

A, Model Without Steady-State Flow Effects (cont.)

E = elastic modulus of the pipe material

d = mean diameter of the pipe

h = thickness of the pipe wall.

It is seen from Eq (18) that the nominal acoustic velocity is independent of frequency; however, the actual acoustic velocity within the absorptive line is not. The effective acoustic velocity for sinusoidal waves propagating in a one-dimensional transmission line is sometimes called the phase velocity or propagation velocity, and is generally a function of frequency. The acoustic velocity is defined by the expression

$$a(\omega) = \frac{\omega \Delta x}{\beta(\omega)} = \frac{\omega}{\beta'(\omega)} \quad (21)$$

The wave propagation parameters, which have been defined for the case of the infinitely long transmission line, may be used to define the frequency response characteristics of a line of finite length. The dynamic response of a transmission line may be described by two characteristic equations, expressing the input oscillatory pressure (P_1) and the flow (\dot{V}_1) in terms of the output oscillatory pressure (P_2) and flow (\dot{V}_2).

$$\begin{aligned} P_1 &= P_2 \cosh \gamma l_t + \dot{V}_2 Z_c \sinh \gamma l_t \\ \dot{V}_1 &= \frac{P_2}{Z_c} \sinh \gamma l_t + \dot{V}_2 \cosh \gamma l_t \end{aligned} \quad (22)$$

where l_t is the total length of the transmission line. It should be noted that the parentheses containing the term " ω " after each function (which implies dependence on frequency) have been omitted for brevity. Writing Eq (22) in matrix form, the following expression is obtained:

$$\begin{bmatrix} P_1 \\ \dot{V}_1 \end{bmatrix} = \begin{bmatrix} \cosh \gamma l_t & Z_c \sinh \gamma l_t \\ \frac{1}{Z_c} \sinh \gamma l_t & \cosh \gamma l_t \end{bmatrix} \begin{bmatrix} P_2 \\ \dot{V}_2 \end{bmatrix} = [A_{ij}] \begin{bmatrix} P_2 \\ \dot{V}_2 \end{bmatrix} \quad (23)$$

where the matrix $[A_{ij}]$ is called the transmission matrix or transfer matrix of a

A, Model Without Steady-State Flow Effects (cont.)

two-port network. This matrix conveniently expresses the interrelationship between the input and output variables. It is seen that the elements of the matrix are complex functions of frequency, as defined (for the case of $C_g = R_m = 0$) by a combination of Eq (12), (16), and (17). However, a more convenient expression for the propagation function per unit length (γ') is obtained by use of Eq (9), (11), and (14).

$$\gamma'(\omega) = \frac{Z_g'(\omega)}{Z_c(\omega)} = \frac{j\omega L_m}{Z_c(\omega)} \quad (24)$$

Eq (16) and (24) are the fundamental equations which are used with Eq (23) to describe the frequency response characteristics of an absorptive transmission line when the coupling capacitance C_g and main path resistance R_m are negligible.

The transmission matrix defined by Eq (23) may be reduced to establish an algebraic equation which expresses the input impedance of the transmission line in terms of the output impedance. This equation is

$$Z_1 = \frac{P_1}{V_1} = \frac{a_{11}Z_2 + a_{12}}{a_{21}Z_2 + a_{22}} = \frac{Z_c + Z_c \tanh \gamma' \ell_t}{1 + \frac{Z_g}{Z_c} \tanh \gamma' \ell_t} \quad (25)$$

where $Z_2 = \frac{P_2}{V_2} = \text{load impedance.}$

If the transmission line is terminated by an open end, the load impedance then vanishes and the expression for the input impedance becomes

$$Z_1 = Z_c \tanh \gamma' \ell_t \quad (26)$$

Using the preceding equations, a digital computer program has been written to compute the wave propagation and frequency response parameters of a generalized absorptive transmission line. The preliminary results of this study are presented in Figures 2 through 7. The frequency response plots show the dependency of each parameter upon the frequency, capacitance ratio (C_g/C_m), and dimensionless damping constant (ξ_m).

The frequency response of the characteristic impedance of an absorptive

A, Model Without Steady-State Flow Effects (cont.)

transmission line is shown in Figure 2. These curves were obtained from Eq (16). It is seen that, for each value of the capacitance ratio C_R/C_M , the amplitude of the characteristic impedance displays a minimum or notch at the dimensionless resonator frequency ($\Omega = 1$). The maximum or peak occurs at a dimensionless frequency defined by the equation:

$$\Omega_c = \left[1 + \frac{C_R}{C_M}\right]^{\frac{1}{2}} \quad (27)$$

It will later be shown that the frequency band between $\Omega = 1$ and $\Omega = \Omega_c$ is called the "stop band" of the absorptive transmission line. Within this frequency band the magnitude of $Z_c(\omega)$ increases at approximately 6 db/octave and the phase angle of $Z_c(\omega)$ approaches 90° . Both of these observations indicate that the inertance (mass characteristics) of the shunt path is governing the response at these frequencies.

Both the low and high frequency asymptotes of the characteristic impedance are independent of frequency. The low frequency asymptote of $Z_c(\omega)$ is given by the equation:

$$\lim_{\omega \rightarrow 0} Z_c(\omega) = \frac{Z_{c0}}{\left[1 + \frac{C_R}{C_M}\right]^{\frac{1}{2}}} \quad (28)$$

Figure 2 illustrates that the high frequency asymptote of $Z_c(\omega)$ is simply Z_{c0} .

The propagation function, attenuation function, and phase functions are plotted in Figures 3, 4, and 5, respectively. These curves were obtained from Eq (24) using the following definitions for the attenuation function and phase function:

$$\alpha'(\omega) = \text{Re}[\gamma(\omega)] \quad (29)$$

$$\beta'(\omega) = \text{Im}[\gamma(\omega)] \quad (30)$$

It is interesting to note that the propagation function amplitude displays a local maximum at the resonator frequency ($\Omega = 1$) and a minimum at the frequency $\Omega = \Omega_c$. Comparison of Fig (4) and (5) reveals that the attenuation function is predominant at frequencies within the stop band ($1 \leq \Omega \leq \Omega_c$), whereas the phase function is

A, Model Without Steady-State Flow Effects (cont.)

predominant at frequencies within the "pass band" (those frequencies outside the stopband).

The attenuation function for a given transmission line is obtained from Figure 4 by multiplying the ordinate by $\frac{\omega_b}{a_0} \left(\frac{C_s}{C_m} \right)^k$ and the abscissa by ω_b . The units of $\alpha'(\omega)$ are nepers per unit length which may be converted to decibels (db) per unit length by multiplying by a factor of $20 \log_{10} e$. Using the same multiplication factors, the phase function of a given line is obtained from Figure 5. The units of $\beta'(\omega)$ are radians per unit length.

The dependence of the acoustic velocity on frequency is shown in Figure 6, which is obtained from Eq (21). It is seen that the low frequency asymptote is approximately inversely proportional to the capacitance ratio, as defined by the expression:

$$\lim_{\omega \rightarrow 0} a(\omega) = \frac{a_0}{\left[1 + \frac{C_s}{C_m} \right]^k} \quad (31)$$

The high frequency asymptote is the nominal acoustic velocity in the main path as defined by Eq (18).

$$\lim_{\omega \rightarrow \infty} a(\omega) = a_0 \quad (32)$$

Finally, the frequency response of the input impedance of an arbitrary hydraulic transmission line is shown in Figure 7. As illustrated in the sketch, the line consists of an open-ended lossy line with particular values of the parameters C_s/C_m , l_t/l_m , and S_n . Note that, for the purpose of illustration, only the absolute amplitude of the impedance is shown. The phase angle is not shown. The high amplitude peaks which occur at frequencies less than the shunt resonator frequency are caused by the lowly damped acoustic modes of the line. It is seen that these line resonances are damped as the frequency approaches the "stop band." The lowest frequency line resonance is the quarter wave length frequency given by the following dimensionless equation:

A. Model Without Steady-State Flow Effects (cont.)

$$\Omega_1 = \frac{1}{\omega_a} \left[\frac{\pi A(\omega)}{2l_t} \right] \approx \frac{\pi a_0}{2\omega_h l_t} \left[1 + \frac{C_a}{C_m} \right]^{-\frac{1}{2}} \quad (33)$$

where l_t = total length of the transmission line.

The approximation is only valid at low frequencies ($\Omega \ll 1$) when the acoustic velocity is nearly equal to the asymptotic value given by Eq (31).

B. MODEL WITH STEADY-STATE FLOW EFFECTS

It was shown in Figure 6 of the preceding section that the acoustic velocity at low frequencies may be greatly reduced by the increase of the resonator capacitance C_a . In certain cases the acoustic velocity may indeed approach the nominal flow velocity, so that the acoustic waves travel faster downstream than they travel upstream. As a consequence, the absorptive transmission line behaves in a non-reciprocal manner. A discussion of this phenomenon is presented in Bibliography entries B.8, B.20, B.21, B.23, B.24. Experimental data presented in entry B.23 indicates that the effect of flow through an absorptive line with distributed lowly damped resonators may be to cause an amplification of a downstream traveling wave! Hence, it is important to understand the effect of flow upon wave propagation so that the desired attenuation characteristics of the absorptive transmission line may be obtained.

The mathematical model of the generalized absorptive transmission line, as presented in the foregoing discussion, is valid only when the mean flow velocity (\dot{u}_0) is much less than the acoustic velocity $A(\omega)$. The operating conditions of most propellant feed systems are such that the criterion $\dot{u}_0 \ll A(\omega)$ is usually satisfied. However, in the case of an absorptive line with a very large distributed compliance (C_a) this condition may be violated since the acoustic velocity at low frequencies ($\Omega \ll 1$) is greatly reduced and may indeed approach the nominal flow velocity. Considering the relatively low flow velocity in the Saturn propellant lines, the

B, Model With Steady-State Flow Effects (cont.)

criterion that $(\dot{u}_g \ll a_0 c)$ may be violated in the following two cases: (1) the lossy suction line with very large resonator compliance, and (2) the gas bubble filled line with a very large volume ratio of gas to liquid.

The influence of flow on wave propagation may be attributed to three fundamental effects: (1) change in the effective acoustic velocity (and hence wavelength), (2) change in the transverse acoustic pressure distribution across the duct, and (3) change of the admittance characteristics of the shunt path resonator. It is felt that the first effect, that of the change in the acoustic wavelength, is the most important effect in the case of a hydraulic transmission line with distributed compliant resonators. The second effect is due to the velocity gradient causing a distortion of the "phase plane" (or points of equal amplitude and phase) of a traveling wave. It is shown in Bibliography entry B.25 that the oscillatory pressure amplitude at the duct wall may be greatly affected, even for low speed flow ($\dot{u}_g/a_0 \cong 0.2$), when the acoustic wavelength (λ) approaches the transverse dimension (d) of the duct. However, for the frequencies and dimensions of this investigation, the condition that $d/\lambda \ll 1$ will always prevail. Finally, the third effect is important only in the case of the "classical" lossy line where a series of Helmholtz resonators is uniformly distributed in such a way that each resonator inlet is perpendicular to the flow vector \vec{U}_0 . This shearing action of this flow, acting on the part of slug of liquid which oscillates in the neck of the resonator, will result in a change of the reactance as well as the resistance of the resonator impedance. However, the resonator admittance at frequencies well below its resonant frequency is probably not affected by flow since it is controlled by the cavity compliance at these frequencies. Thus, it is seen from the above discussion that the change in the effective acoustic velocity is the primary consideration in the prediction of

B, Model With Steady-Stage Flow Effects (cont.)

the flow effects upon wave propagation in an absorptive transmission line. Therefore, the following analysis accounts for only this effect of flow.

The Fourier transformed equations that govern sinusoidal pressure and flow fluctuations in a moving medium are given as

$$\frac{dP(x,\omega)}{dx} + Z'_s(\omega)\dot{V}(x,\omega) + \frac{\dot{u}_0 Z'_s(\omega)}{j\omega} \frac{d\dot{V}(x,\omega)}{dx} = 0 \quad (34)$$

$$\frac{d\dot{V}(x,\omega)}{dx} + Y'_s(\omega)P(x,\omega) + \frac{\dot{u}_0 Y'_s(\omega)}{j\omega} \frac{dP(x,\omega)}{dx} = 0 \quad (35)$$

where \dot{u}_0 is the nominal flow velocity and the remaining nomenclature is the same as that of Eq (7) and (8). Note the similarity of these differential equations to the limits (as $\Delta x \rightarrow 0$) of Eq (7) and (8). Combining Eq (34) and (35) yields the Fourier transformed one-dimensional wave equations:

$$[1 - \psi^2(\omega)] \frac{d^2 P(x,\omega)}{dx^2} - 2\psi(\omega)\gamma(\omega) \frac{dP(x,\omega)}{dx} - [\gamma(\omega)]^2 P(x,\omega) = 0 \quad (36)$$

$$[1 - \psi^2(\omega)] \frac{d^2 \dot{V}(x,\omega)}{dx^2} - 2\psi(\omega)\gamma(\omega) \frac{d\dot{V}(x,\omega)}{dx} - [\gamma(\omega)]^2 \dot{V}(x,\omega) = 0 \quad (37)$$

where $\gamma(\omega) = [Z'_s(\omega) Y'_s(\omega)]^{\frac{1}{2}}$ = nominal propagation function per unit length
 $\psi(\omega) = \frac{\dot{u}_0 \gamma(\omega)}{j\omega}$ = complex Mach number.

It is seen that Eq (36) and (37) reduce to Eq (1) and (2) if the nominal flow velocity \dot{u}_0 , approaches zero. Note that the complex Mach number approaches the real Mach number if the transmission line is lossless since as the attenuation function approaches zero, the propagation function becomes purely imaginary:

$$\lim_{\alpha' \rightarrow 0} \psi(\omega) = \frac{\dot{u}_0 [j\beta(\omega)]}{j\omega} = \frac{\dot{u}_0}{\omega} \frac{\omega}{a(\omega)} = \frac{\dot{u}_0}{a(\omega)} \quad (38)$$

A discussion of the derivation and application of Eq (36) and (37) to the lossless

B, Model With Steady-State Flow Effects (cont.)

case is given in entries A.20, B.8, and B.21 in the Bibliography.

The transmission matrix for the absorptive transmission line with flow may be obtained by solving the differential equations given in Eq (36) and (37). The forward transmission matrix is defined by the following equation relating the upstream variables (subscript 1) to the downstream variables (subscript 2):

$$\begin{bmatrix} P_1 \\ \dot{V}_1 \end{bmatrix} = \begin{bmatrix} e^{-\gamma l} \cosh \gamma l & e^{-\gamma l} Z_c \sinh \gamma l \\ \frac{e^{-\gamma l}}{Z_c} \sinh \gamma l & e^{-\gamma l} \cosh \gamma l \end{bmatrix} \begin{bmatrix} P_2 \\ \dot{V}_2 \end{bmatrix} = [a_{ij}] \begin{bmatrix} P_2 \\ \dot{V}_2 \end{bmatrix} \quad (39)$$

where $\gamma = \frac{\gamma'}{1 - \psi^2}$ = effective propagation function per unit length
 $Z_c = [Z_1 / \gamma_1]^{\frac{1}{2}}$ = characteristic impedance of the line.

This matrix may be compared to the forward transmission matrix for a line without flow, as given in Eq (23). As before, the parentheses containing the term " ω " have been omitted for brevity. The reciprocity of the circuit represented by Eq (39) may be determined by examining the determinant of the matrix $[a_{ij}]$. Two-port network theory states that $\det[a_{ij}] = 1$ for a reciprocal circuit and $\det[a_{ij}] \neq 1$ for a non-reciprocal circuit (Bibliography entries H.4, H.5, H.14). Consequently, it is seen that the absorptive line with flow is non-reciprocal since

$$\det [a_{ij}] = e^{-2\gamma l} \quad (40)$$

The input impedance at the upstream station may be found from manipulation of Eq (39). The following equation results which may be compared to Eq (26):

$$Z_1 = \frac{Z_2 + Z_c \tanh \gamma l}{1 + \frac{Z_2}{Z_c} \tanh \gamma l} \quad (41)$$

The pressure gain (the complex ratio of downstream pressure to upstream pressure) of the line with flow effects is also obtained from Eq (39):

B, Model With Steady-State Flow Effects (cont.)

$$\frac{P_2}{P_1} = \frac{Z_2 e^{\psi \gamma^+ l}}{Z_2 \cosh \gamma^+ l + Z_0 \sinh \gamma^+ l} \quad (42)$$

If the downstream impedance, Z_2 , equals the characteristic impedance, Z_0 , then there will be no reflection at Port 2 and the pressure gain will be:

$$\frac{P_2}{P_1} = e^{\psi \gamma^+ l - \gamma^+ l} = e^{-\frac{\gamma^+ l}{1+\psi}} \quad (43)$$

This expression is equivalent to Eq (4) which was given for the line with negligible steady-state flow. Equation (43) is seen to be the solution for a downstream traveling wave. In a similar fashion, the solution for a upstream traveling wave in a line with no reflection is:

$$\frac{P_1}{P_2} = e^{-\frac{\gamma^- l}{1-\psi}} \quad (44)$$

Equations (43) and (44) may be used to define the upstream and downstream propagation functions:

$$\gamma^- = \frac{\gamma'}{1-\psi} = \text{upstream propagation function} \quad (45)$$

$$\gamma^+ = \frac{\gamma'}{1+\psi} = \text{downstream propagation function} \quad (46)$$

As in the case of negligible flow velocity, the attenuation function and phase function are, respectively, the real and imaginary parts of the complex propagation function. Hence

$$\alpha^+ = \text{Re}[\gamma^+] = \text{downstream attenuation function} \quad (47)$$

$$\alpha^- = \text{Re}[\gamma^-] = \text{upstream attenuation function} \quad (48)$$

$$\alpha^* = \text{Re}[\gamma^*] = \text{effective attenuation function} \quad (49)$$

$$\beta^+ = \text{Im}[\gamma^+] = \text{downstream phase function} \quad (50)$$

$$\beta^- = \text{Im}[\gamma^-] = \text{upstream phase function} \quad (51)$$

$$\beta^* = \text{Im}[\gamma^*] = \text{effective phase function} \quad (52)$$

B, Model With Steady-State Flow Effects (cont.)

The acoustic velocity (phase velocity) for each condition of wave propagation is again obtained from the phase function for the particular condition:

$$\alpha^+(\omega) = \omega / \beta^+(\omega) = \text{downstream phase velocity} \quad (53)$$

$$\alpha^-(\omega) = \omega / \beta^-(\omega) = \text{upstream phase velocity} \quad (54)$$

$$\alpha^*(\omega) = \omega / \beta^*(\omega) = \text{effective phase velocity} \quad (55)$$

It is easily shown that for frequencies within the "pass band" of the absorptive line, i.e., dimensionless frequencies defined by the expression $[\Omega < 1, (1 + \omega/C_m)^2 < \Omega]$, the downstream phase velocity is simply $\alpha^+(\omega) = a(\omega) + u_0$ while the upstream phase velocity is simply $\alpha^-(\omega) = a(\omega) - u_0$. It should be noted that $a(\omega)$ is the phase velocity in the absence of flow.

The equations presented in the foregoing discussion of the effect of flow upon wave propagation has been programmed for digital computer solution. The frequency responses of the various parameters have been computed and are presented in Figures 8 through 11. These dimensionless frequency response plots show the effect of flow for a particular value of the capacitance ratio (C_A/C_M) and damping ratio (ξ_A). The effect of changing these variables has not been studied.

In these studies the flow velocity (u_0) has been normalized to the acoustic velocity (a_0) through the main path, as defined by Eq (18). The parameter u_0/a_0 , called the dimensionless flow velocity, was varied through the interval

$[0 \leq u_0/a_0 \leq .300]$. The upper limit was selected to insure that the flow velocity approaches the phase velocity (neglecting flow) at low frequencies ($\Omega \ll 1$). Use of Eq (31) allows the calculation of the dimensionless acoustic velocity at low frequencies for a capacitance ratio of 10:

$$\lim_{\omega \rightarrow 0} \frac{a(\omega)}{a_0} = (11)^{1/2} = .3015$$

Figure 8 illustrates the variation of the complex Mach number with frequency

B, Model With Steady-State Flow Effects (cont.)

for an absorptive line with $C_a/C_m = 10$ and $S_a = 0.1$. These results, obtained from the definition of $\Psi(\omega)$ (see Eq (36) and (37)), substantiate Eq (38). It is seen that the low and high frequency asymptotes are given by the expressions

$$\lim_{\omega \rightarrow 0} \Psi(\omega) = \frac{\dot{u}_0}{a_0} \left[1 + \frac{C_a}{C_m} \right]^{\frac{1}{2}} \quad (56)$$

$$\lim_{\omega \rightarrow \infty} \Psi(\omega) = \frac{\dot{u}_0}{a_0} \quad (57)$$

A comparison of the frequency response of the various propagation functions for the absorptive line with $C_a/C_m = 10$, $S_a = 0.1$ and $\dot{u}_0/a_0 = 0.1$ is shown in Figure 9. The propagation functions γ' , γ^* , γ^+ , and γ^- , as defined by Eq (24), (39), (45), and (46) respectively, are plotted versus frequency. The effect of flow is seen to reduce the frequency of the peak in the upstream propagation function γ^- and the effective propagation function γ^* . Note that the curves tend to converge at frequencies above the stopband ($\Omega > 3.33$). The low frequency asymptotes of these curves may be used to compute the phase velocity for each case. Using Eq (21), (53), (54), and (55), the following values of phase velocity are obtained:

phase velocity without flow	=	$\lim_{\omega \rightarrow 0} a(\omega)$	=	$.301 a_0$
downstream phase velocity	=	$\lim_{\omega \rightarrow 0} \bar{a}^+(\omega)$	=	$.401 a_0$
upstream phase velocity	=	$\lim_{\omega \rightarrow 0} \bar{a}^-(\omega)$	=	$.201 a_0$
effective phase velocity	=	$\lim_{\omega \rightarrow 0} \bar{a}^*(\omega)$	=	$.267 a_0$

These observations support the statements made previously concerning upstream and downstream phase velocities. Note that the effective phase velocity at low frequencies is decreased by the effect of flow. As a result, the frequencies of the acoustic "organ-pipe" modes which exist at low frequencies will be reduced by approximately 11% for this flow condition ($\dot{u}_0 = .10 a_0$).

Figure 10 illustrates the effect of flow upon the effective propagation function

B, Model With Steady-State Flow Effects (cont.)

The results show that the low frequency ($\Omega < 1$) part of the curve is greatly affected as the flow velocity approaches the acoustic velocity. Note that the phase angle of $\bar{\gamma}^{\#}$ is negative at low frequencies for the larger flow velocities. These negative phase angles occur whenever the absolute amplitude of the complex Mach number exceeds one.

Frequencies at which the Mach number amplitude is greater than one create a "stopband" of the absorptive line with flow. Upstream wave propagation is prohibited at these frequencies. It is seen that the phase angle of the upstream propagation function, shown in Figure 11, becomes negative at these frequencies. Hence the stopband of the absorptive line with steady-state flow effects is defined to be the range of frequencies such that the following condition is satisfied:

$$\beta(\omega) = \text{Im}[\bar{\gamma}(\omega)] \leq 0$$

At frequencies that satisfy this criterion, the input impedance of the absorptive line, looking upstream, equals the characteristic impedance. Therefore, any acoustic modes that would normally occur at frequencies within this range in the case of negligible steady-state flow effects will be suppressed.

C. RESONANCE AND ANTIRESONANCE IN A HYDRAULIC TRANSMISSION LINE

In the preceding two sections of this appendix, the equations that describe the general wave propagation parameters, as functions of frequency, were presented. Graphical results have been presented that indicate there are certain conditions which may cause large attenuations of a sinusoidal acoustic wave traveling through the absorptive transmission line. However, the application of these results to the practical problem of predicting the frequencies and effective damping of the acoustic modes in a hydraulic line has not as yet been discussed. The use of the analytical results to achieve this goal is discussed in this section.

C, Resonance and Antiresonance in a Hydraulic Transmission Line (cont.)

The following discussion may be simplified if we consider the most simple boundary conditions of the hydraulic line. Obviously, these end conditions must be satisfied by the vibrating fluid at the resonant frequency. For the purposes of our preliminary investigation, a line with one end open and the opposite end closed may be considered because of its close similarity to the Saturn suction line. As shown in Figure 12, the line resembles a closed-open end organ pipe.

Theoretically, the closed-open end line has an infinite number of acoustic resonances. The oscillatory pressure and flow distribution (mode shape) for the first three "organ-pipe" modes is sketched in Figure 12. These mode shapes are shown for the line with small attenuation. It is seen that these standing waves identify the first three acoustic modes as the quarter-wavelength, the three-quarter-wavelength, and five-quarter-wavelength modes, respectively. Note that the oscillatory pressure is always distributed in such a way that a pressure "node" ($P=0$) is obtained at the open end; whereas the flow is such that a flow "node" ($\dot{V}=0$) is obtained at the closed end. The resonant frequencies at which these boundary conditions are satisfied are given by the expression:

$$f_n = \frac{(2n-1)a}{4l_e} \quad (58)$$

where n = positive integer
 a = acoustic (phase) velocity in the line
 l_e = effective length of the line.

The condition for resonance may be expressed in terms of β' , the phase function per unit of length of the line. Substituting Eq (21) in Eq (49), it is found that for resonance to occur, the phase function must equal the product of an odd integer and $\pi/2$:

$$\beta'_{res} l_e = (2n-1)\frac{\pi}{2}, \quad n = 1, 2, 3 \dots \quad (59)$$

C, Resonance and Antiresonance in a Hydraulic Transmission Line (cont.)

Recall that the input impedance of the transmission line, immediately upstream of closed end (and looking toward the open end), is expressed in terms of a hyperbolic function of a complex variable as given in Eq (26)

$$Z_m = Z_c \operatorname{Tanh}(\alpha' l_c + j\beta' l_c) \quad (60)$$

This impedance is plotted in Figure 13 as a function of the attenuation function ($\alpha' l_c$) and phase function ($\beta' l_c$) of the line. Note that the maximum amplitude of the dimensionless impedance Z/Z_c is obtained when the line is at resonance, so that the phase function $\beta' l_c$ satisfies Eq (59). The effect of increasing the attenuation function $\alpha' l_c$ is to decrease the value of impedance at resonance. Most textbooks on transmission line theory (see Bibliography entry H.19) list the following equation for the dimensionless impedance at the resonant frequency:

$$\left| \frac{Z_{res}}{Z_c} \right| = \frac{4Q_n}{(2n-1)\pi} = \frac{2\beta'_{res}}{(2n-1)\pi\alpha'} \quad (61)$$

where Q_n = quality factor of the n^{th} mode.

Substituting Eq (60) in Eq (61) we obtain the following expression:

$$\left| \frac{Z_{res}}{Z_c} \right| = \frac{1}{\alpha' l_c} \quad (62)$$

The expressions given in Eq (61) and (62) are valid only for relatively small values of $\alpha' l_c$, such that $\alpha' l_c < .5$. For larger attenuations, the value of $|Z_{res}/Z_c|$ may be obtained from Figure 13.

The antiresonant frequencies for the closed-open end line are those frequencies where the input impedance at the closed end is minimum. The value of the phase function for this condition is given as

$$l_c \beta'_{\text{antiresonance}} = l_c \beta'_{\text{antires}} = n\pi \quad n=1,2,3,\dots \quad (63)$$

The antiresonant value of impedance is merely the reciprocal of the resonant

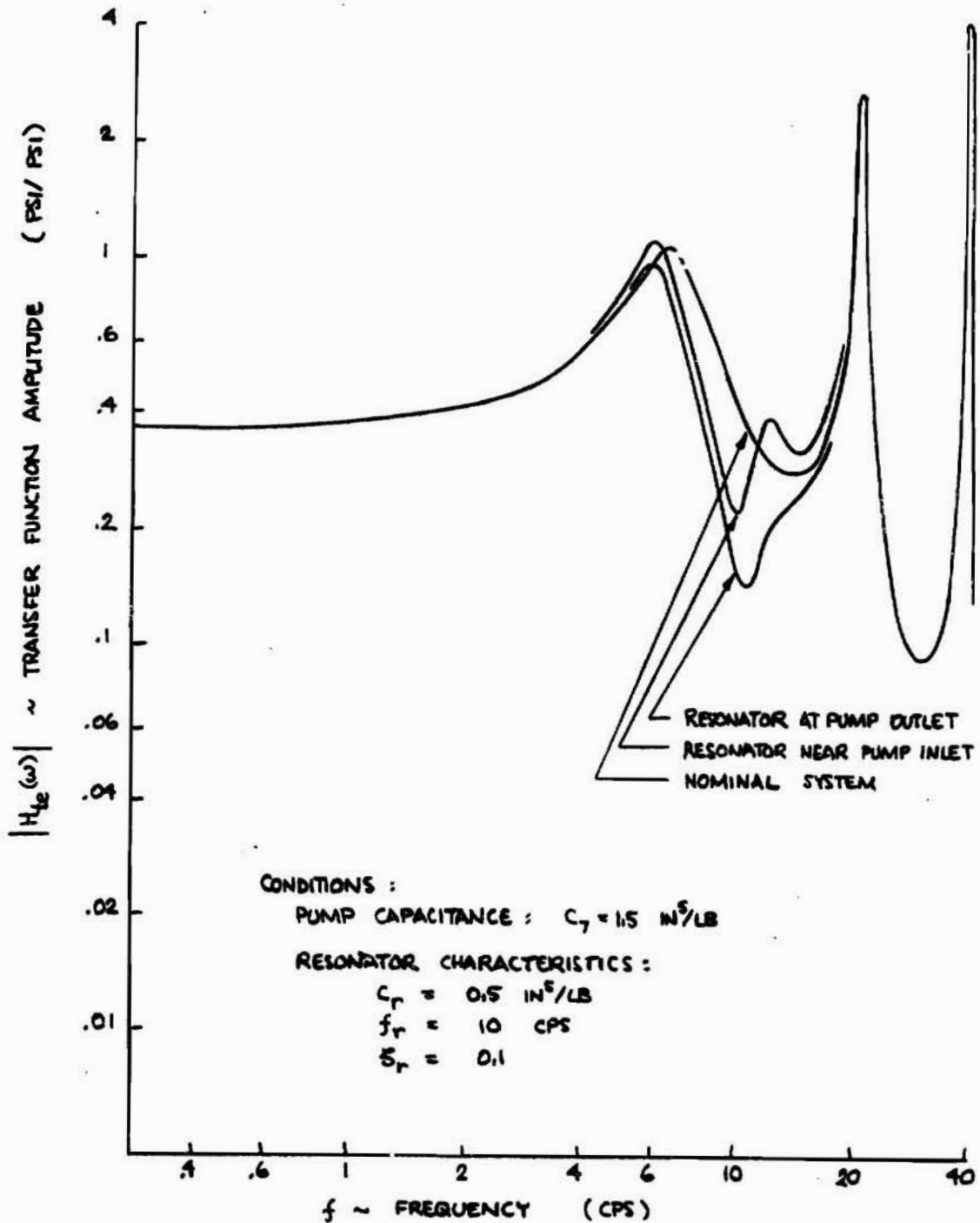


FIGURE 26 FREQUENCY RESPONSE FOR THE SIC LOX SYSTEM WITH RESONATOR

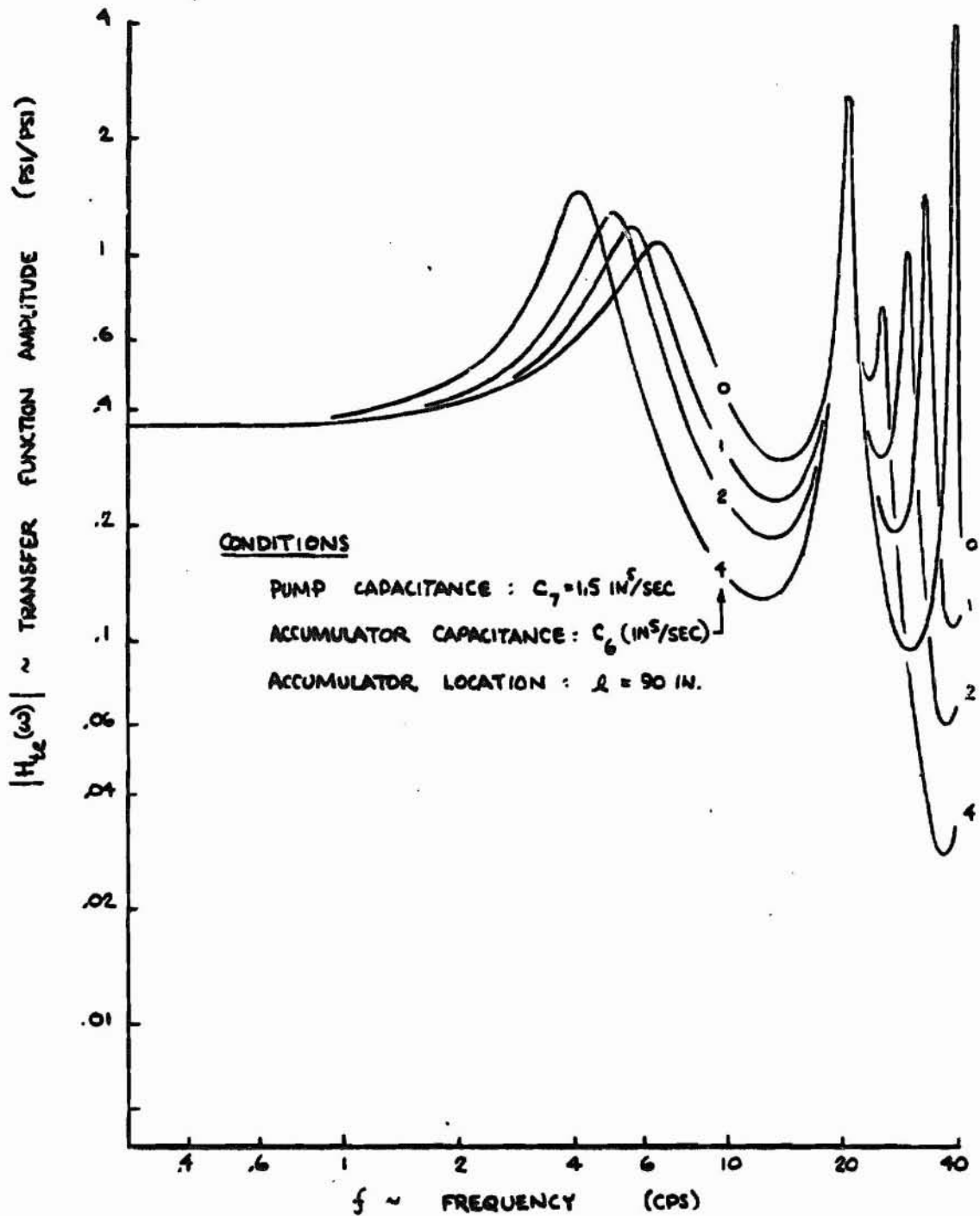


FIGURE 27 FREQUENCY RESPONSE FOR THE SIC LOX SYSTEM WITH SUCTION ACCUMULATOR

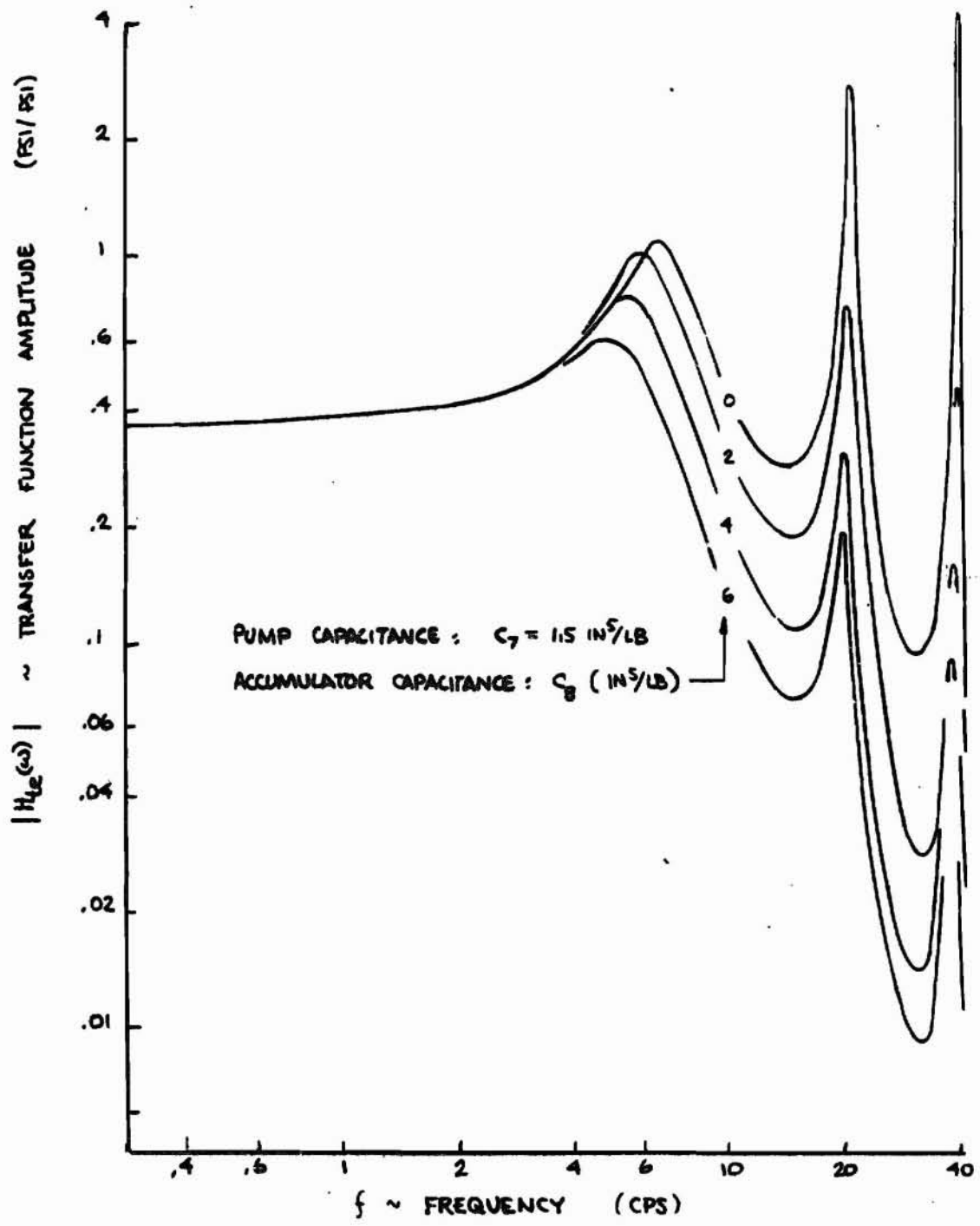


FIGURE 28 FREQUENCY RESPONSE FOR THE SIC LOX SYSTEM WITH DISCHARGE ACCUMULATOR

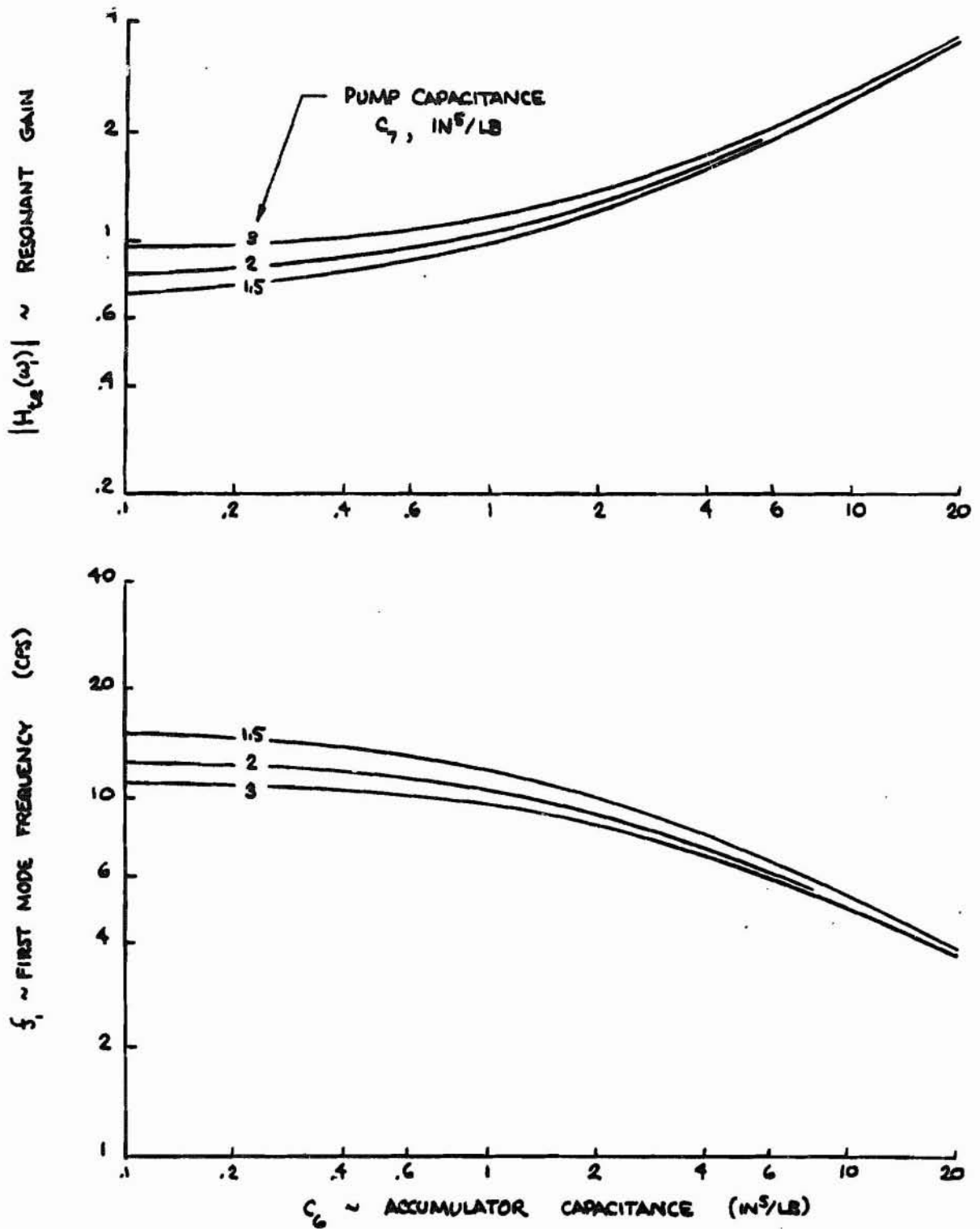


FIGURE 29 RESONANT GAINS AND FREQUENCIES FOR THE SIC LOX SYSTEM WITH SUCTION ACCUMULATOR

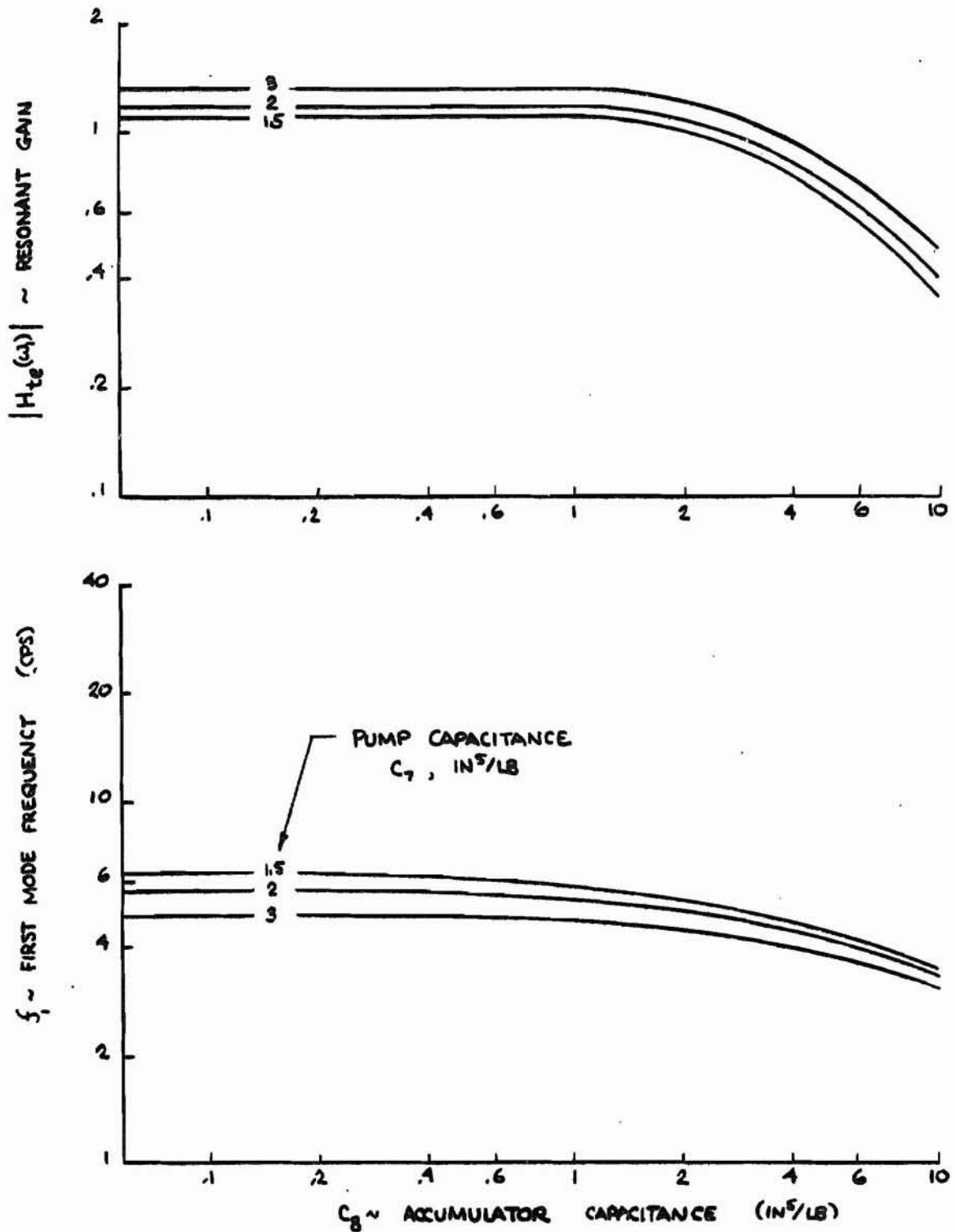


FIGURE 30 RESONANT GAINS AND FREQUENCIES FOR THE SIC LOX SYSTEM WITH DISCHARGE ACCUMULATOR

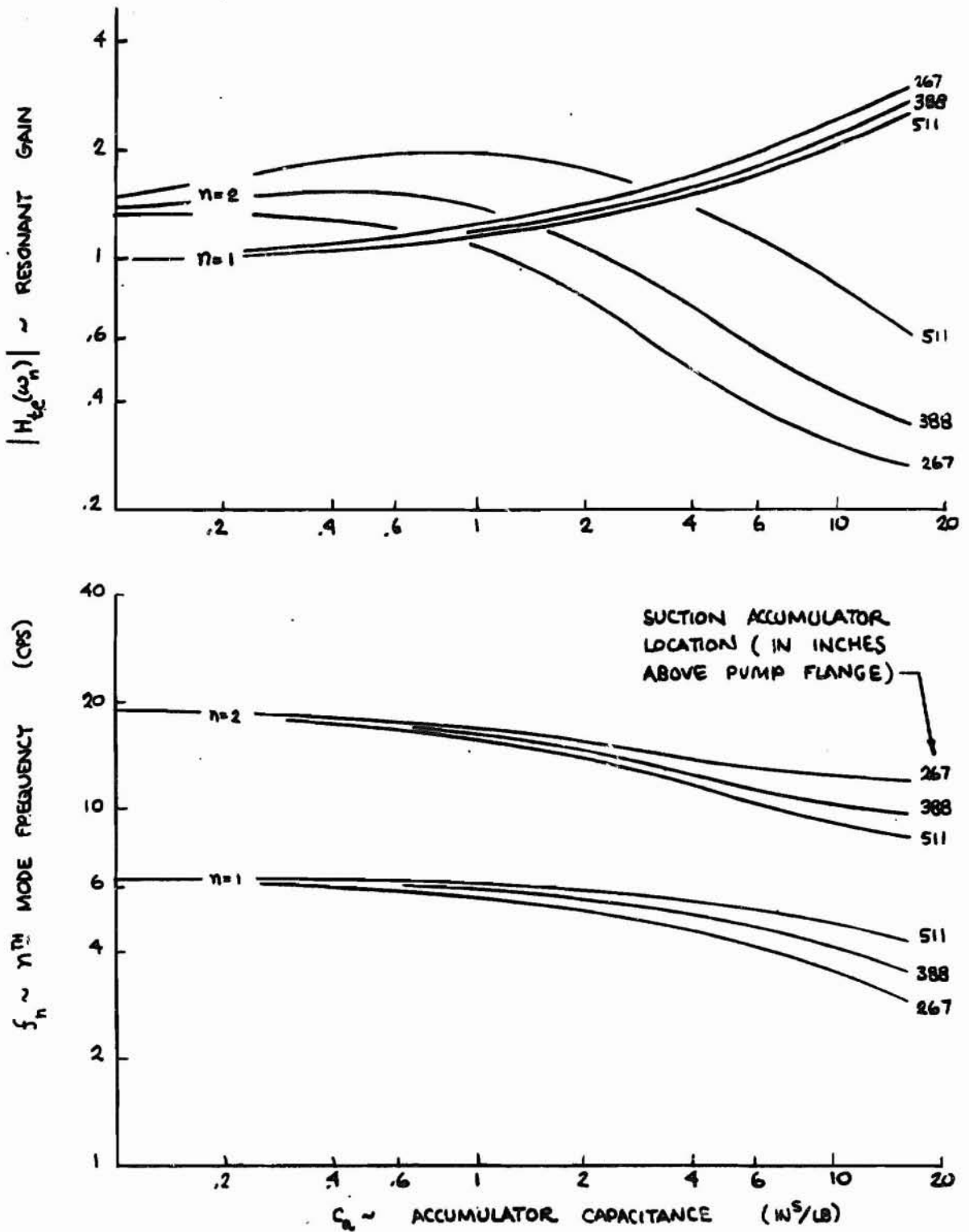


FIGURE 31 EFFECT OF SUCTION ACCUMULATOR LOCATION FOR THE SIC LOX SYSTEM

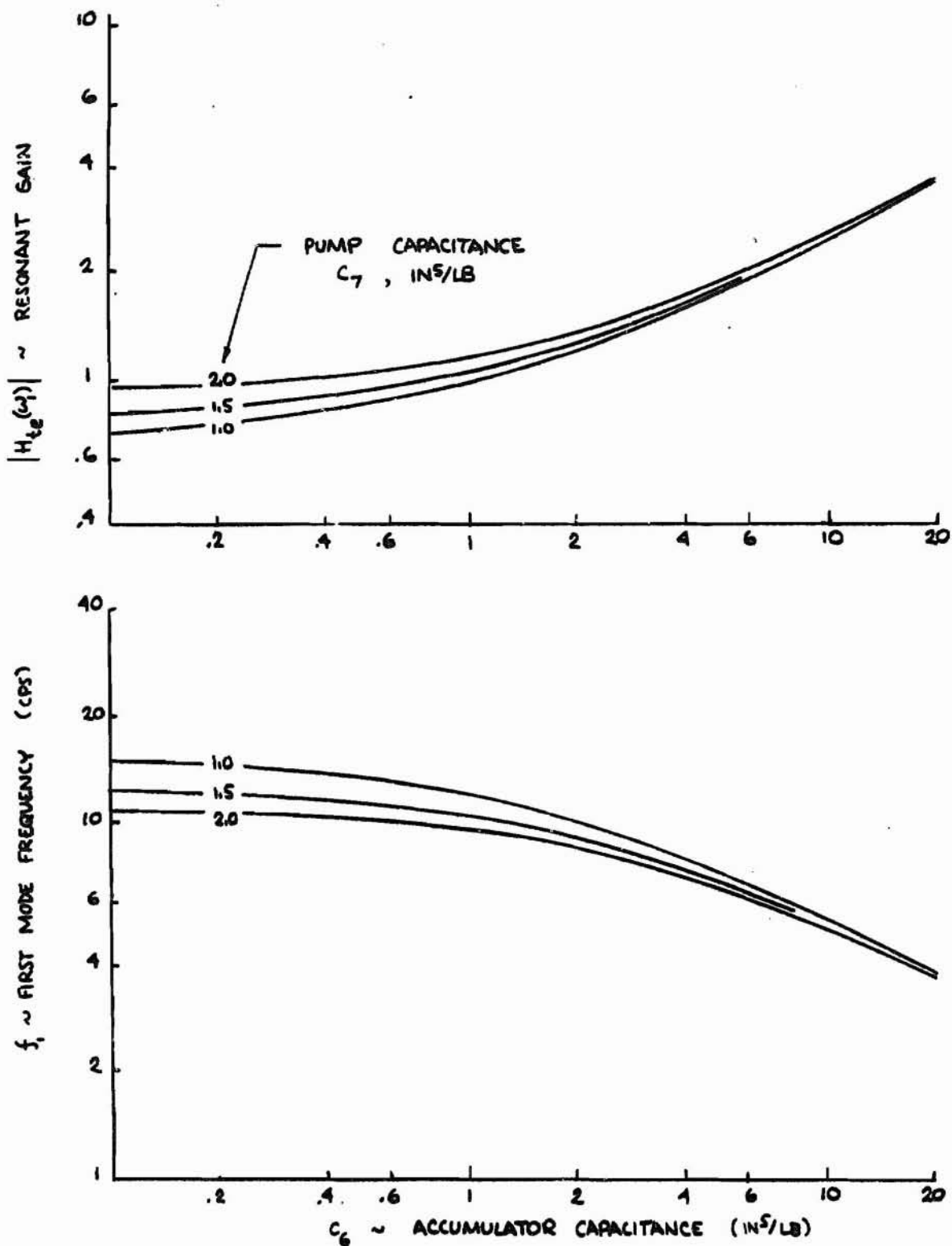


FIGURE 32 RESONANT GAINS AND FREQUENCIES FOR THE SIC FUEL SYSTEM WITH SUCTION ACCUMULATOR

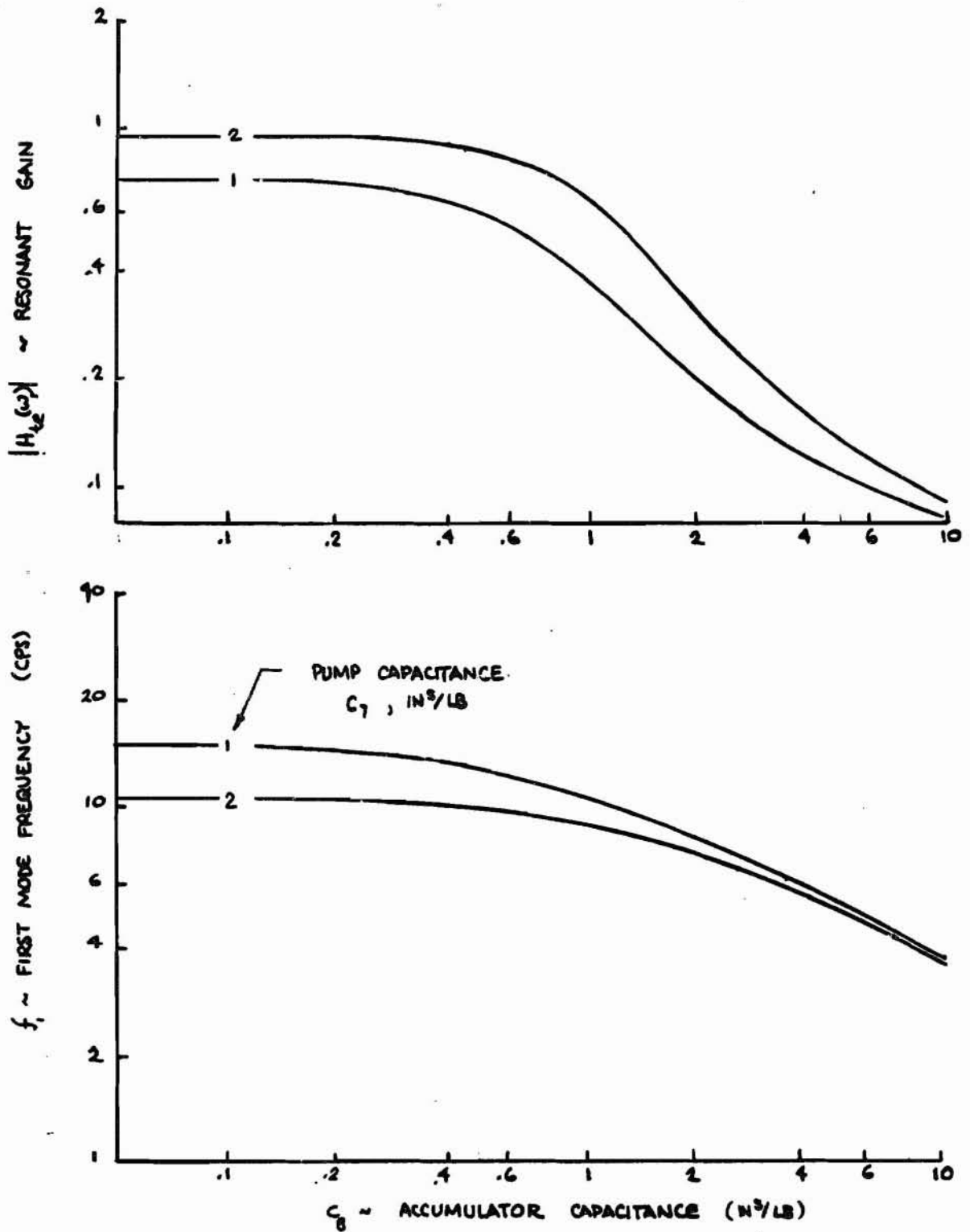


FIGURE 33 RESONANT GAINS AND FREQUENCIES FOR THE SIC FUEL SYSTEM WITH DISCHARGE ACCUMULATOR

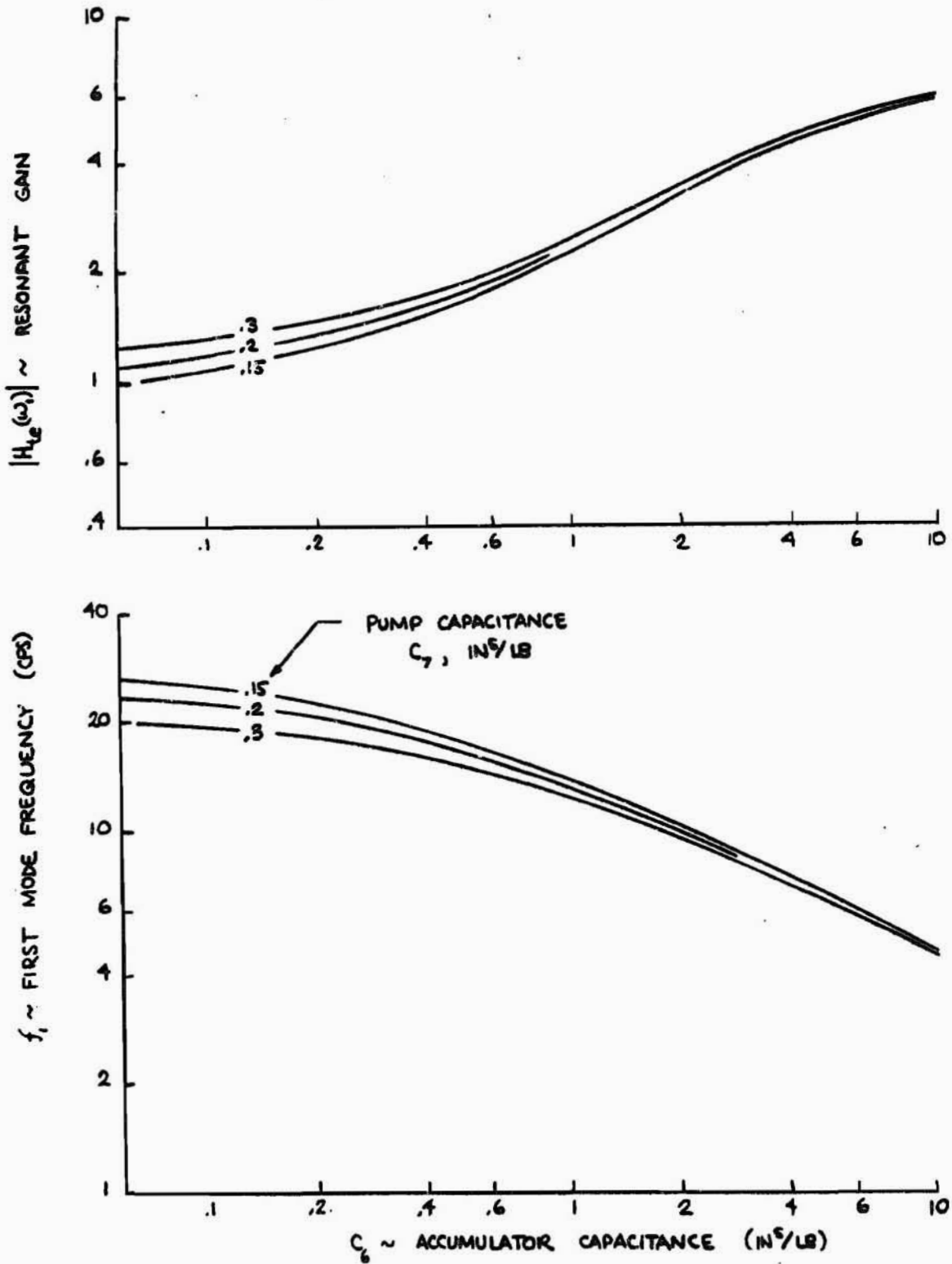


FIGURE 34 RESONANT GAINS AND FREQUENCIES FOR THE SIB LOX SYSTEM WITH SUCTION ACCUMULATOR

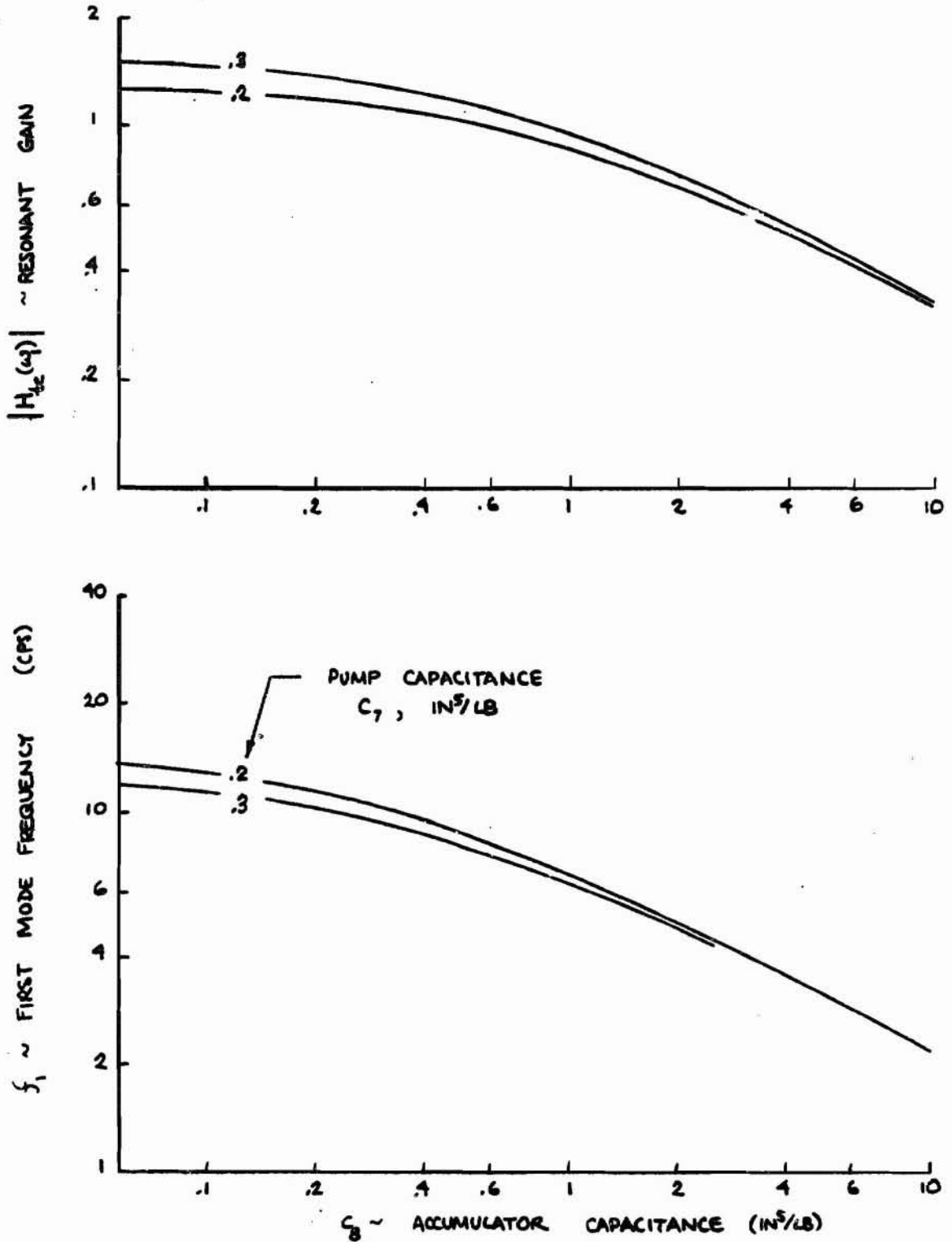


FIGURE 35 RESONANT GAINS AND FREQUENCIES FOR THE SIB LOX SYSTEM WITH DISCHARGE ACCUMULATOR

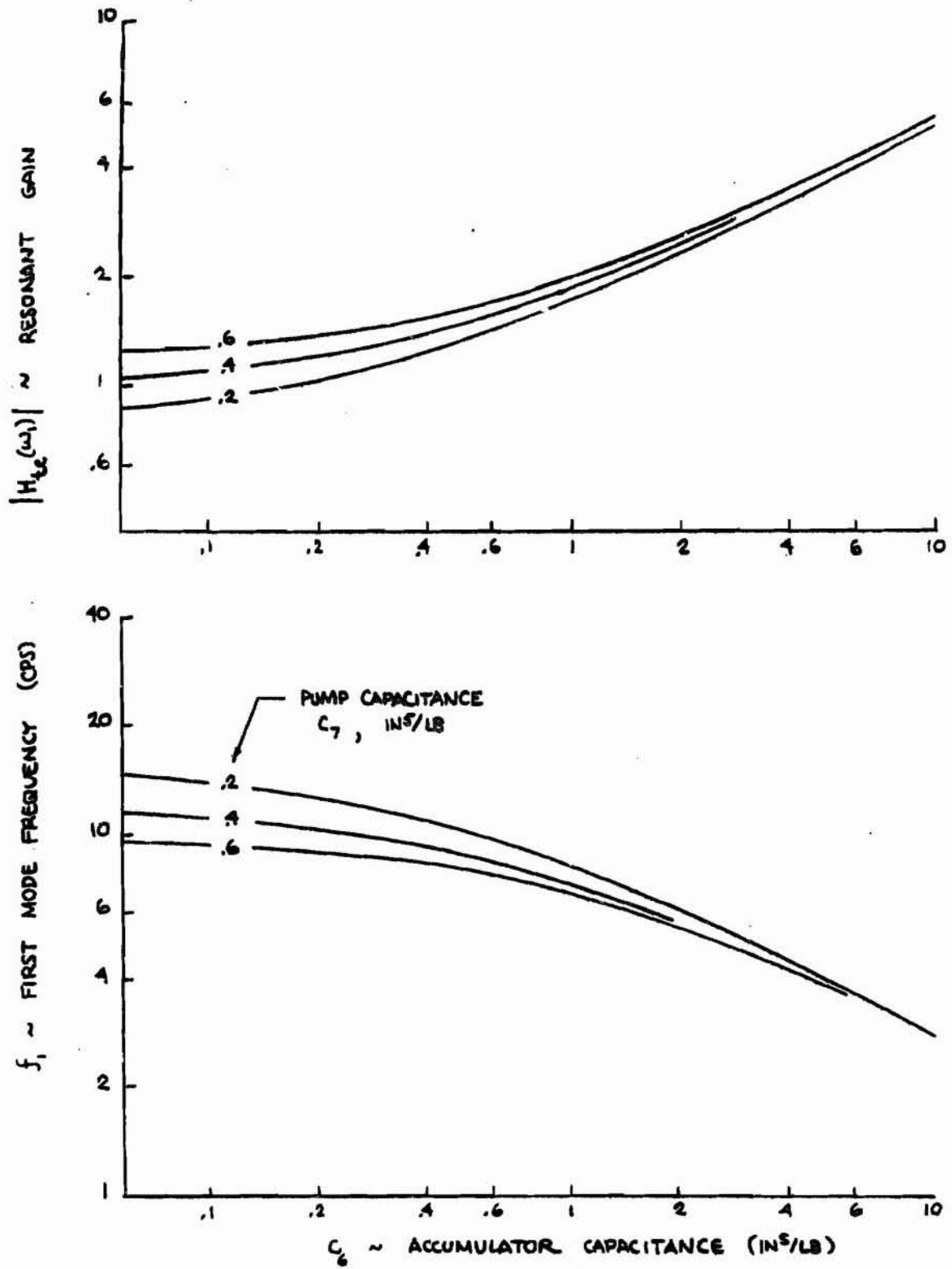


FIGURE 36 RESONANT GAINS AND FREQUENCIES FOR THE SIB FUEL SYSTEM WITH SUCTION ACCUMULATOR

REPRODUCIBILITY OF THE ORIGINAL PAGE IS POOR

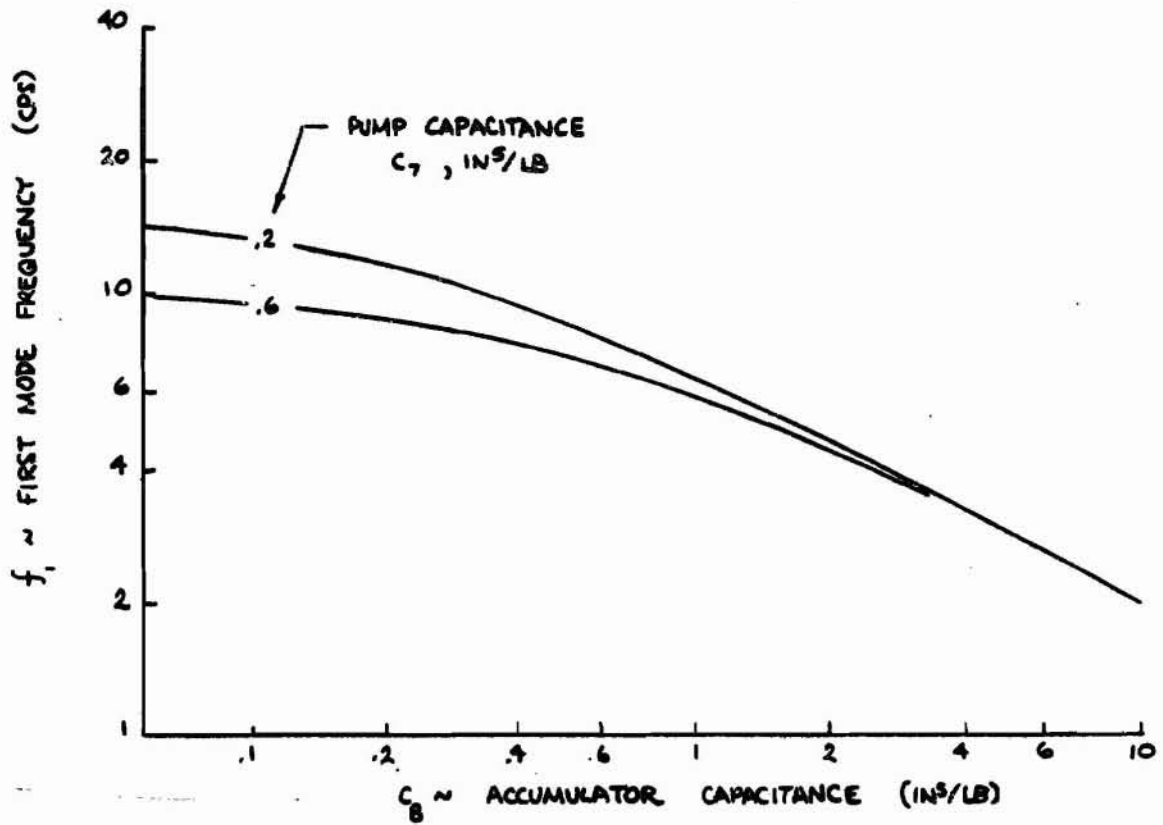
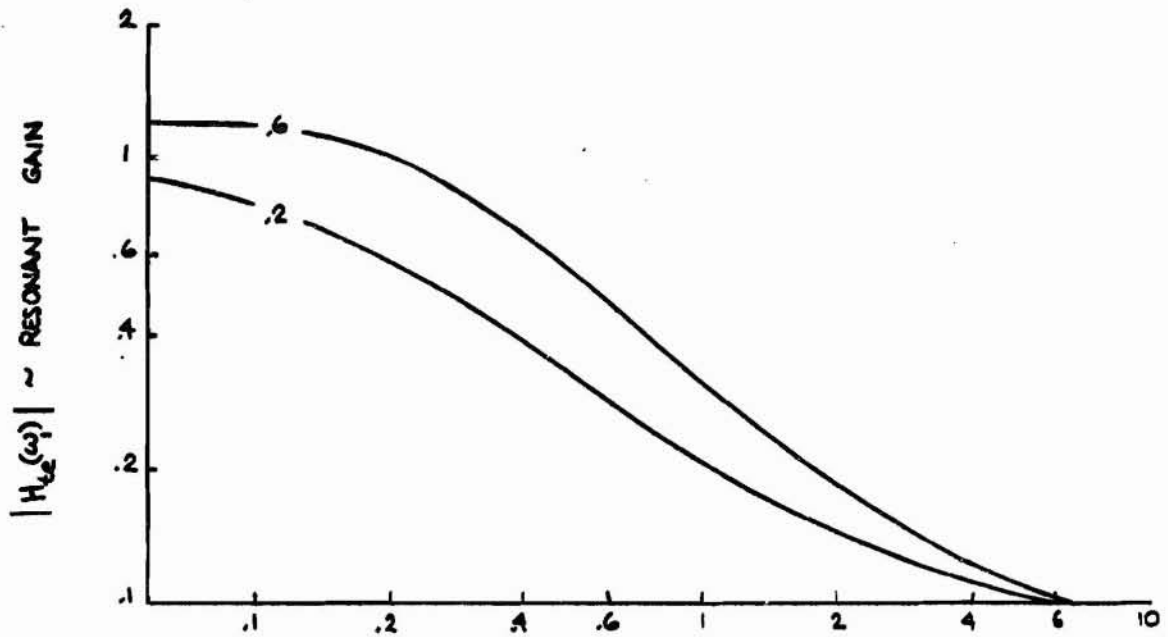


FIGURE 37 RESONANT GAINS AND FREQUENCIES FOR THE SIB FUEL SYSTEM WITH DISCHARGE ACCUMULATOR

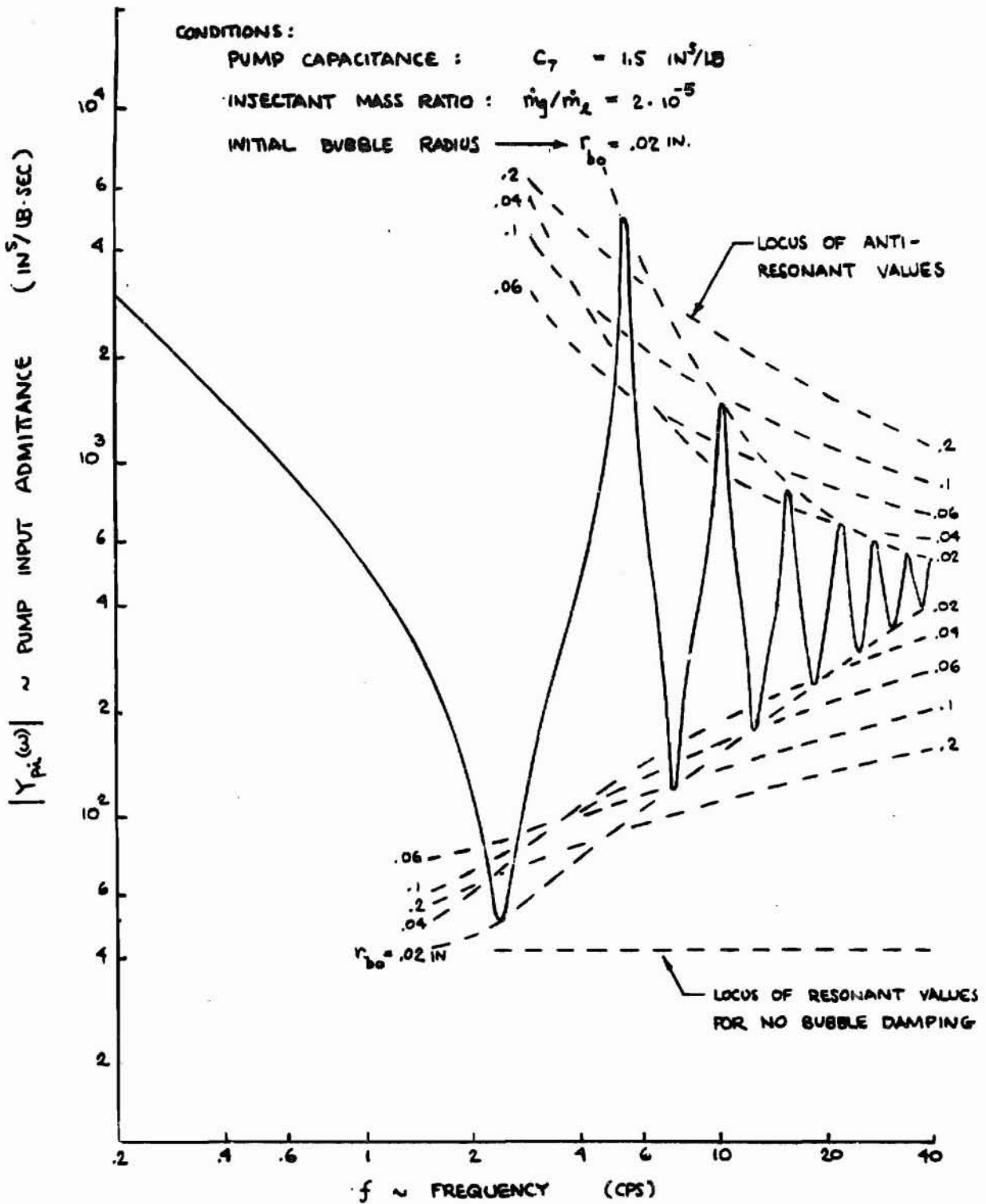


FIGURE 38 FREQUENCY RESPONSE OF $Y_{pi}(\omega)$ FOR THE SIC LOX SYSTEM WITH GAS INJECTION

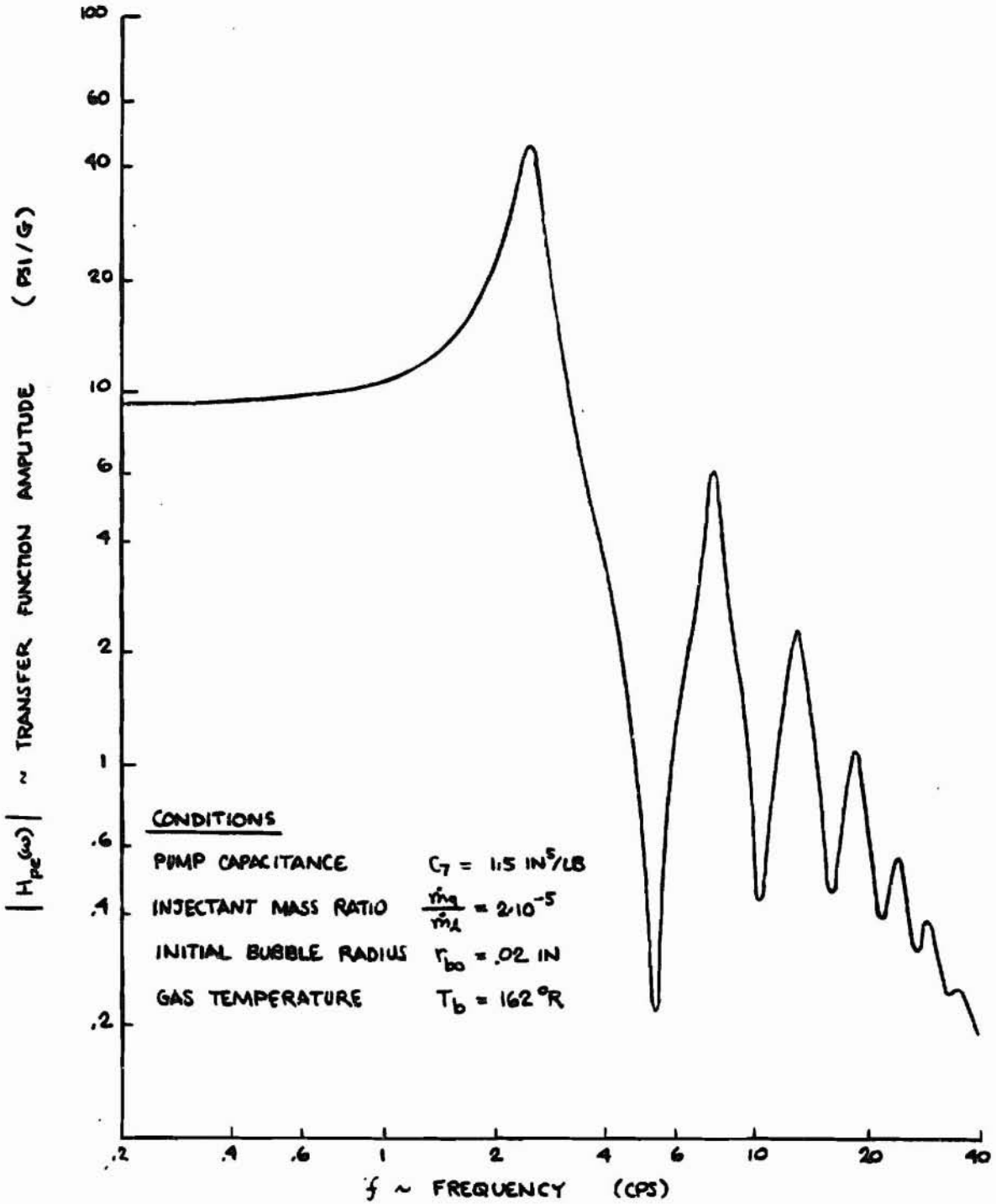


FIGURE 39 FREQUENCY RESPONSE OF $H_{pe}(\omega)$ FOR THE SIC LOX SYSTEM WITH GAS INJECTION

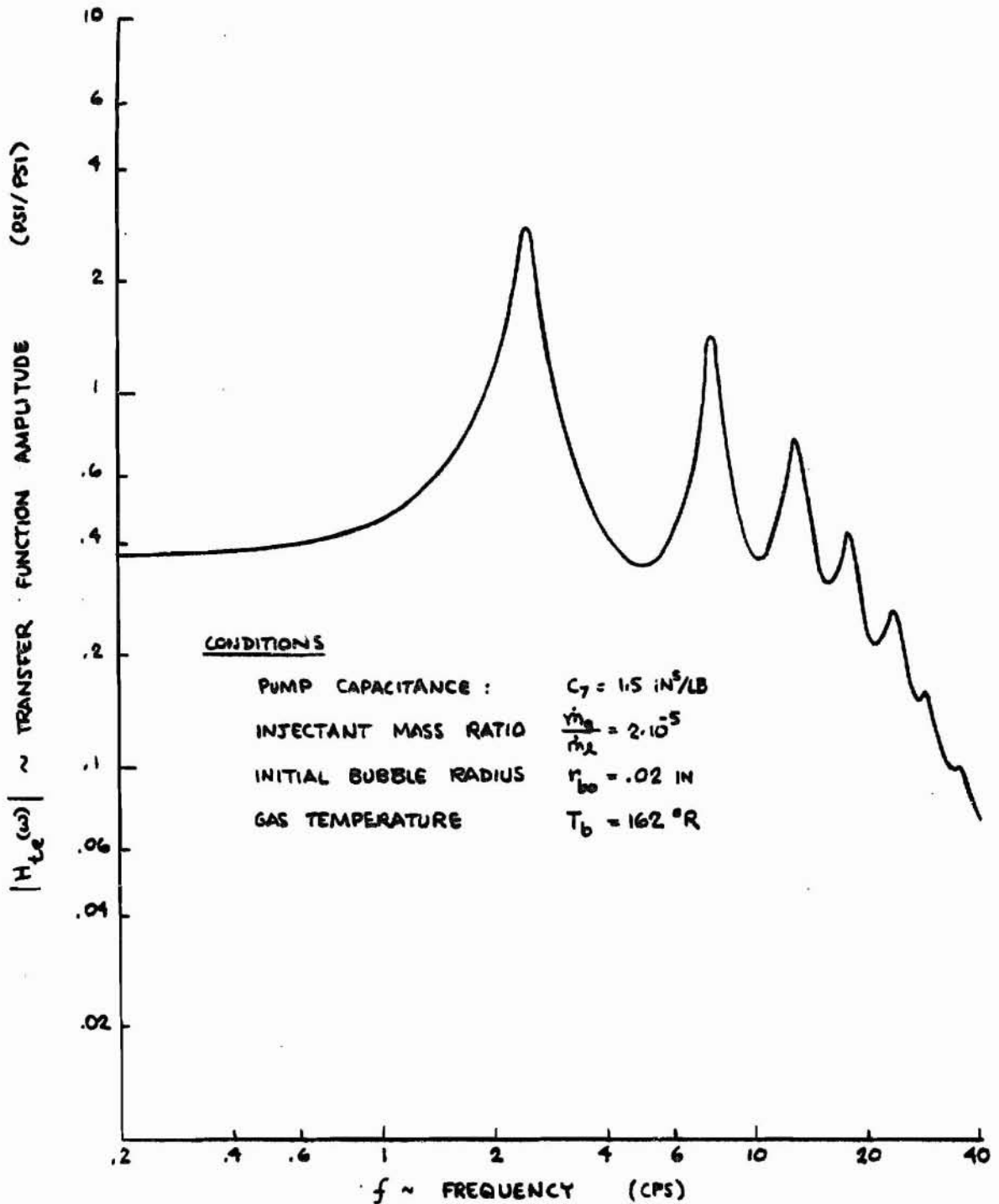


FIGURE 40 FREQUENCY RESPONSE OF $H_{te}(\omega)$ FOR THE SIC LOX SYSTEM WITH GAS INJECTION

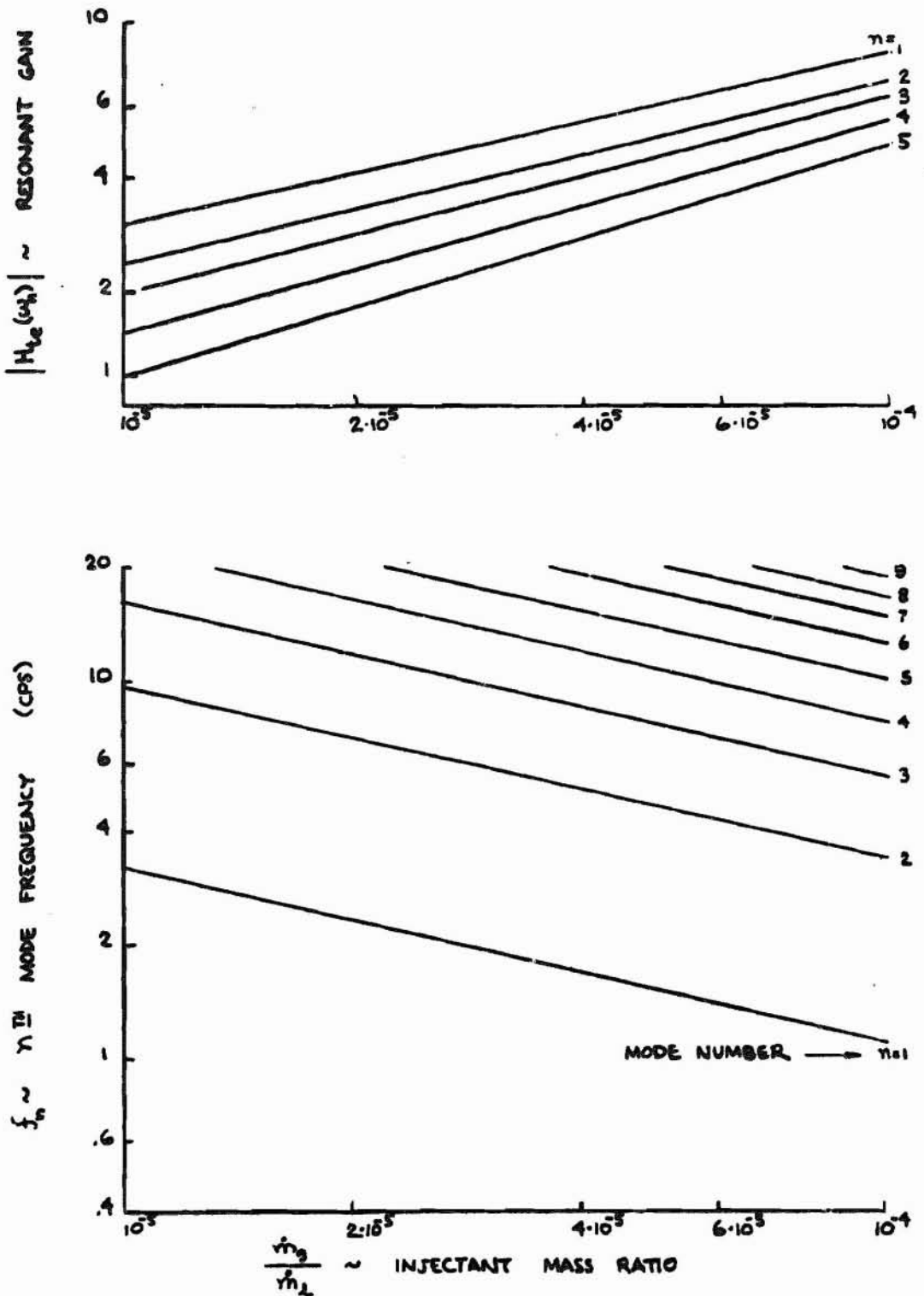


FIGURE 41. RESONANT GAINS AND FREQUENCIES FOR THE SIC LOX SYSTEM WITH GAS INJECTION AND NO BUBBLE DAMPING

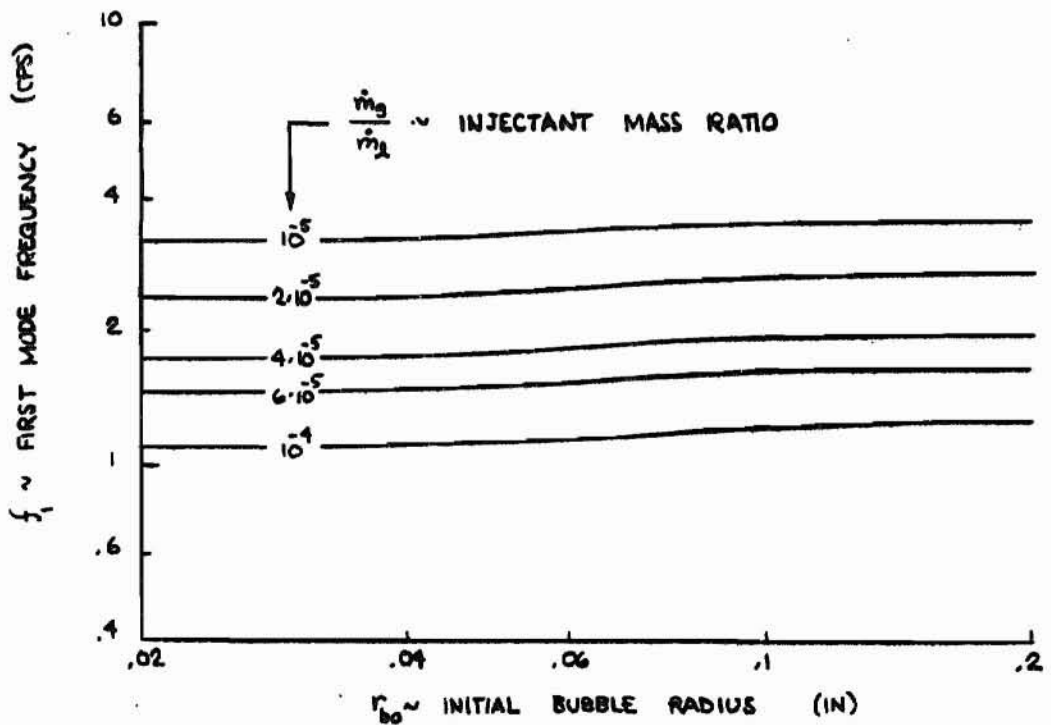
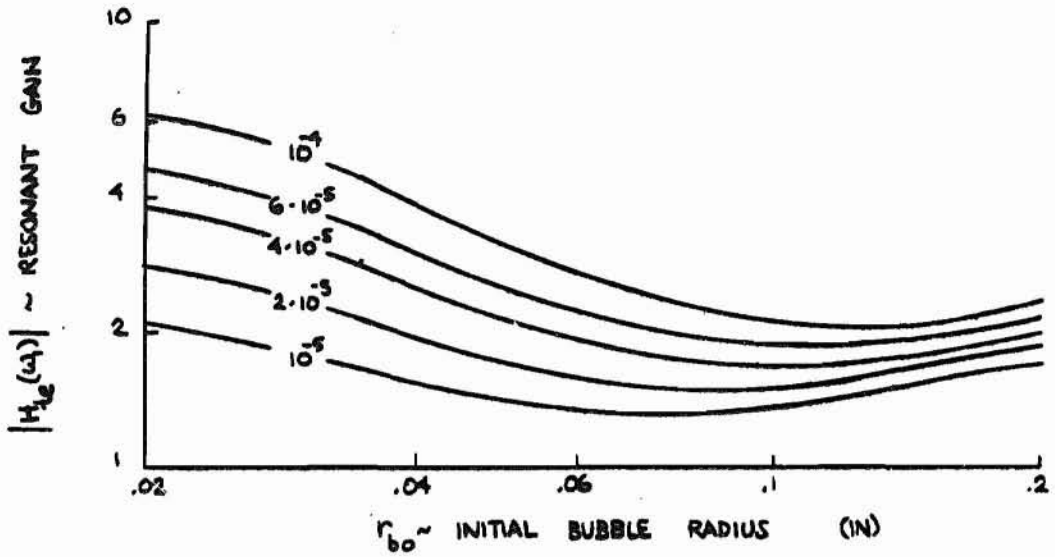
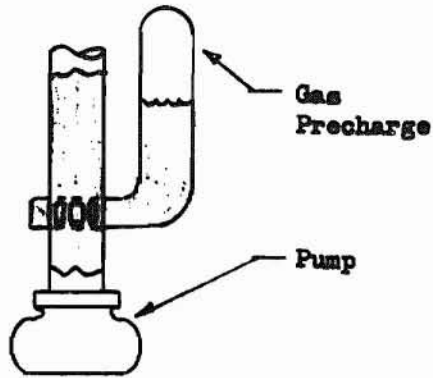
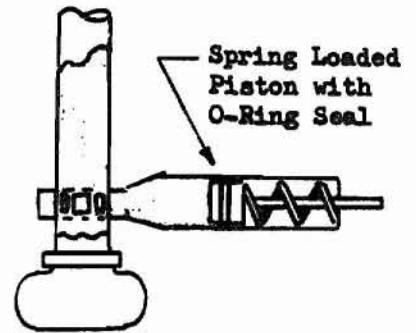


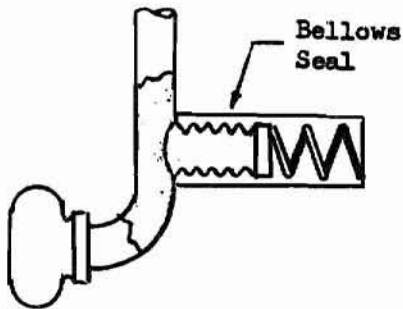
FIGURE 42 FIRST MODE RESONANT GAIN AND FREQUENCIES FOR THE SIC LOX SYSTEM WITH GAS INJECTION AND BUBBLE DAMPING



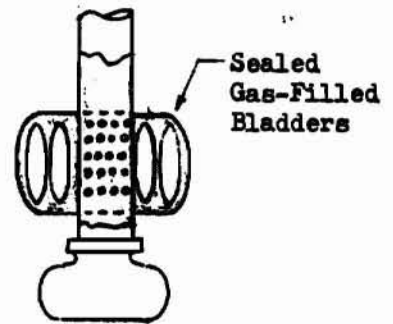
a) Standpipe Accumulator
(Used on Gemini Oxidizer)



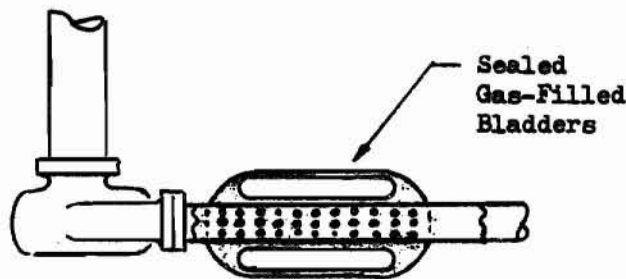
b) Piston Accumulator
(Used on Gemini Fuel)



c) Piston Accumulator
(Proposed for Thor)

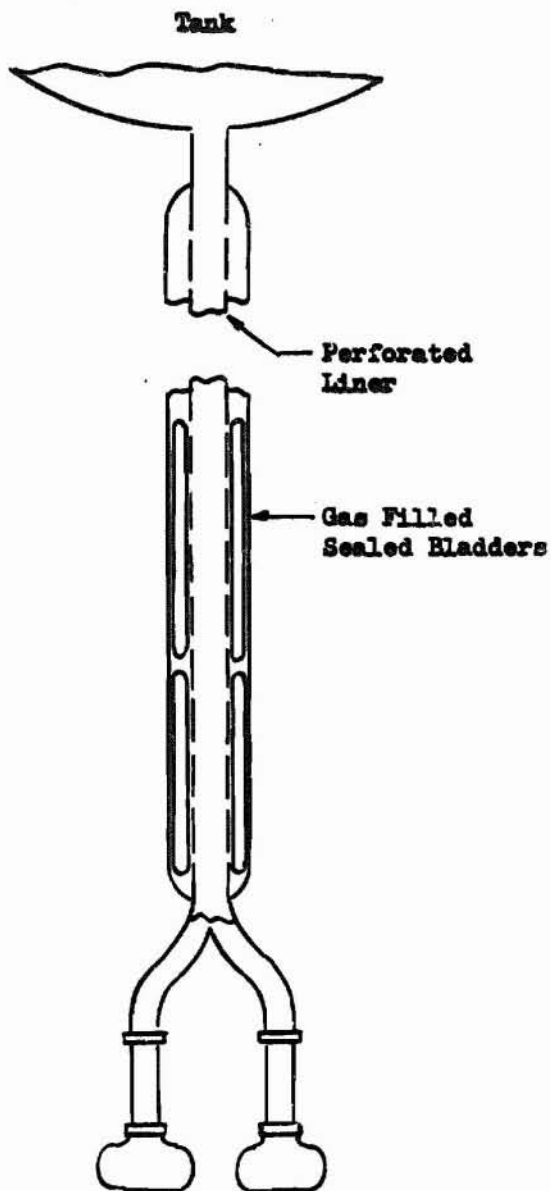


d) Bladder Accumulator
(Used on Titan IIIB Fuel
Proposed for Titan IIM)

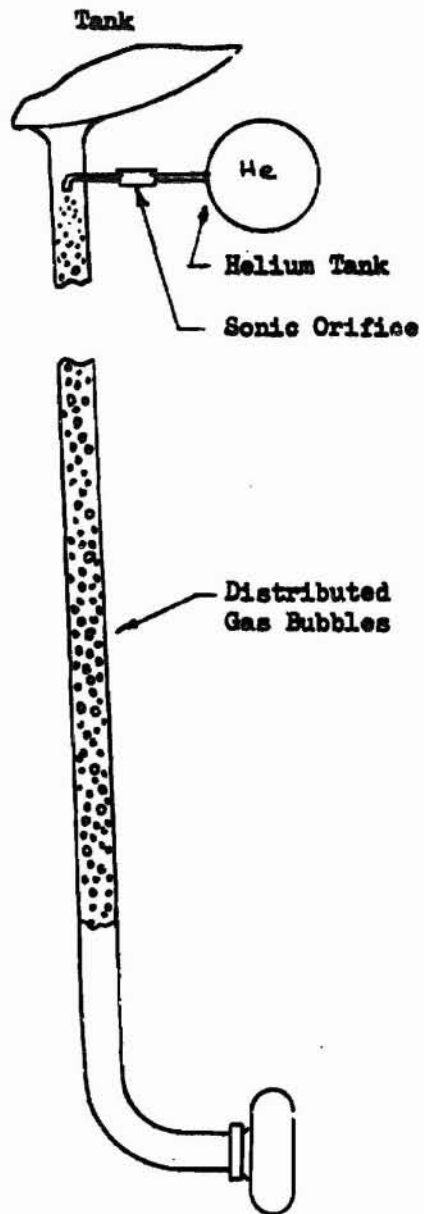


e) Discharge Accumulator
(Proposed for Titan II/Gemini)

FIGURE 43 LUMPED PARAMETER POGO FIX DEVICES

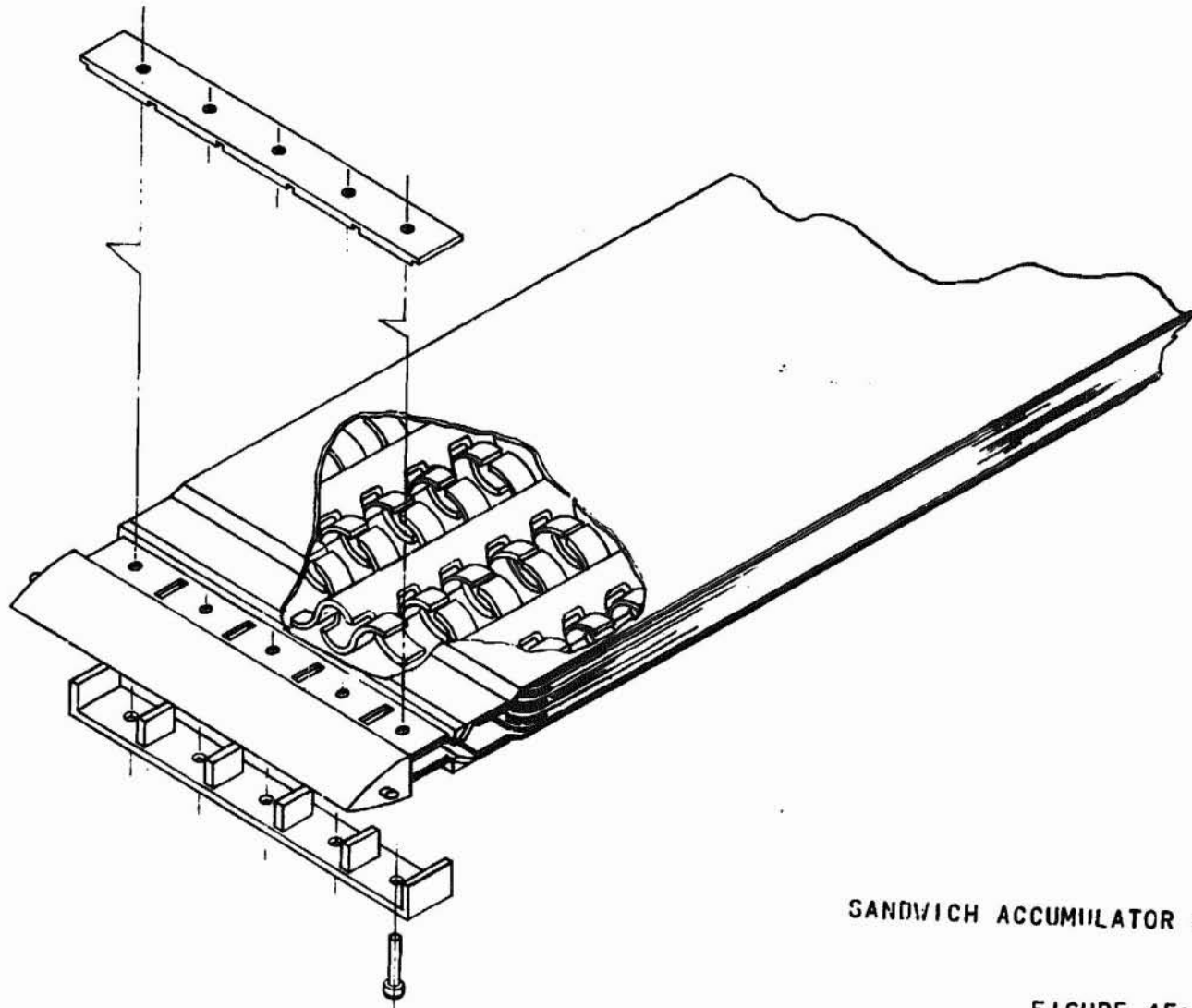


a) Bladder Type Lossy Line
(Proposed for Titan/Gemini)



b) Inert Gas Injection
(Proposed for Saturn SIB/SIC)

FIGURE 44 DISTRIBUTED PARAMETER POGO FLX DEVICES



SANDWICH ACCUMILATOR DESIGN

FIGURE 45a

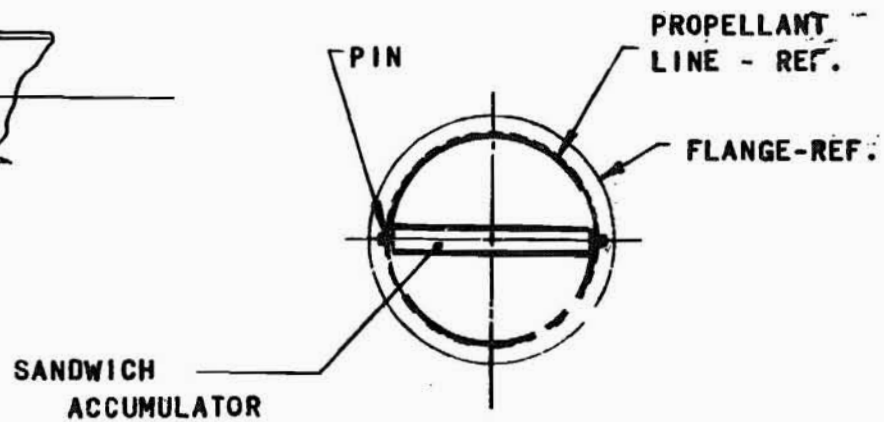
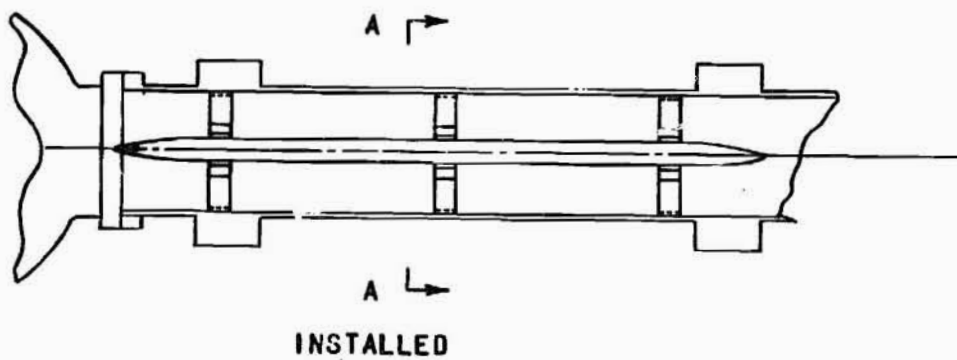
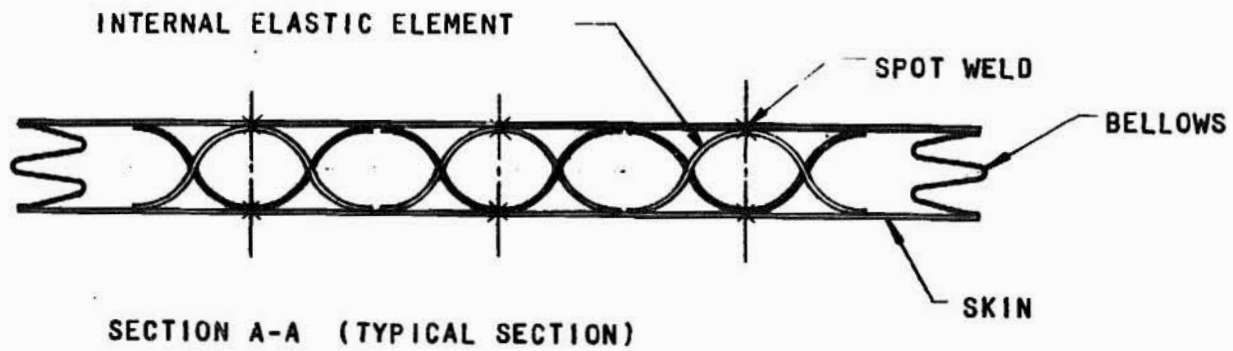
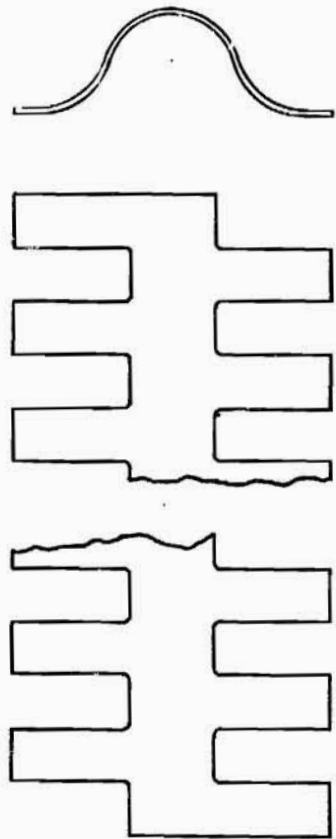


FIGURE 45b



ELASTIC ELEMENT
DETAIL

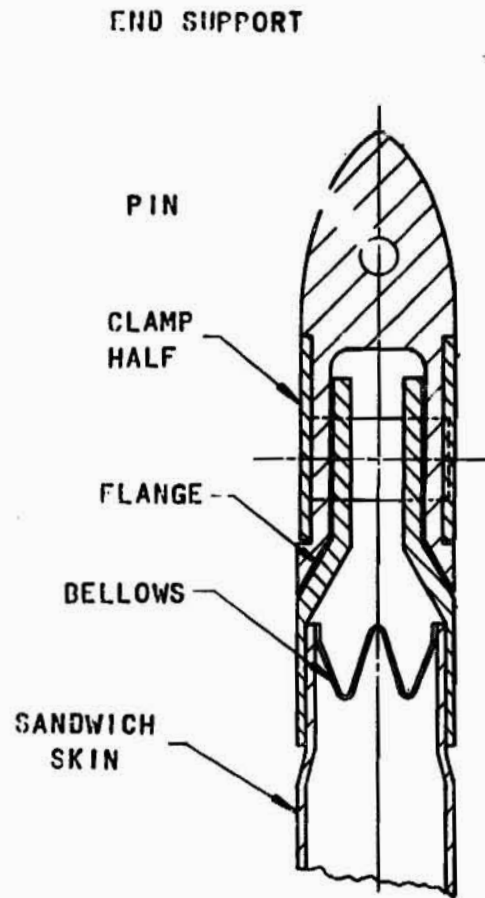


FIG 45c

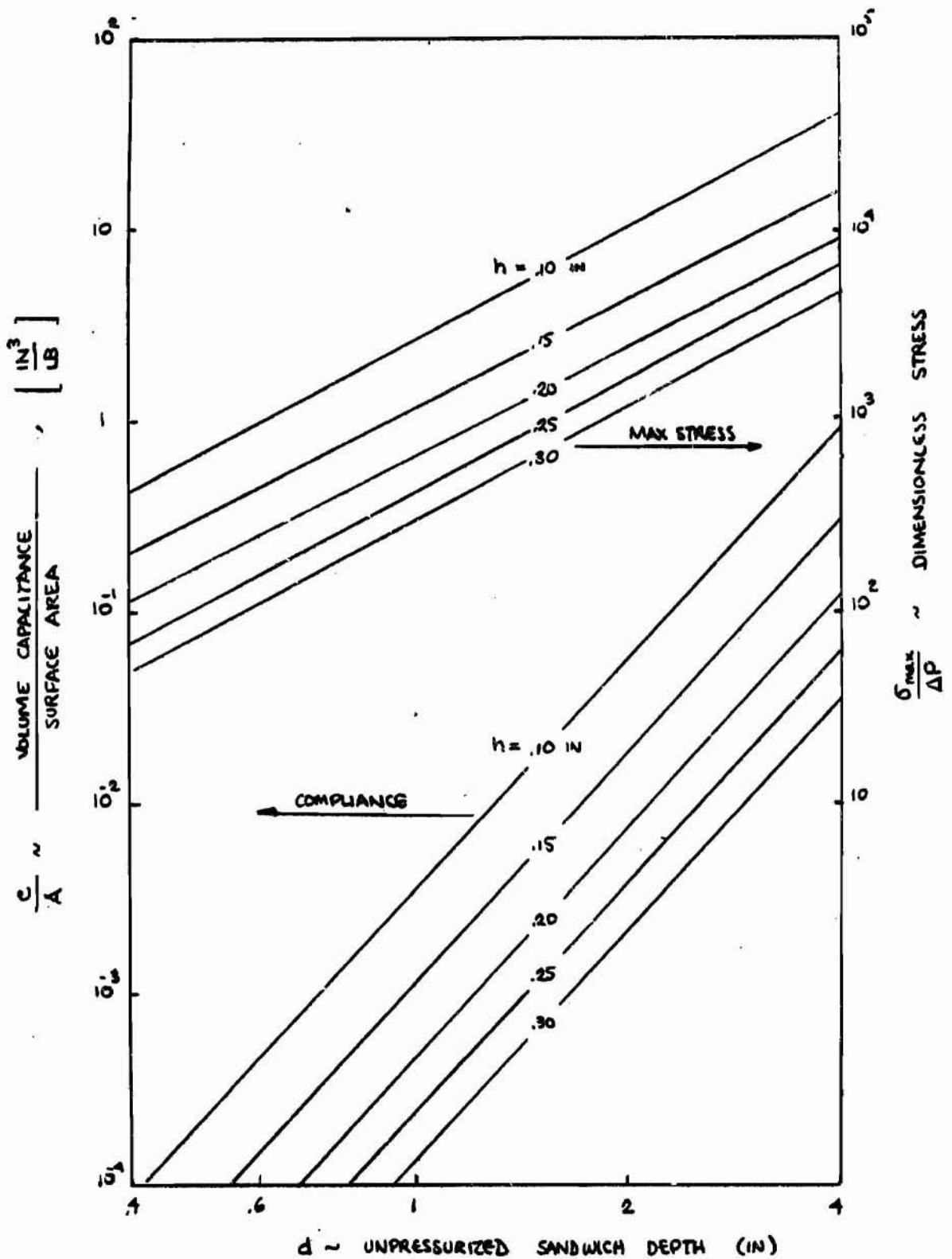


FIGURE 46 SANDWICH ACCUMULATOR DESIGN CURVES

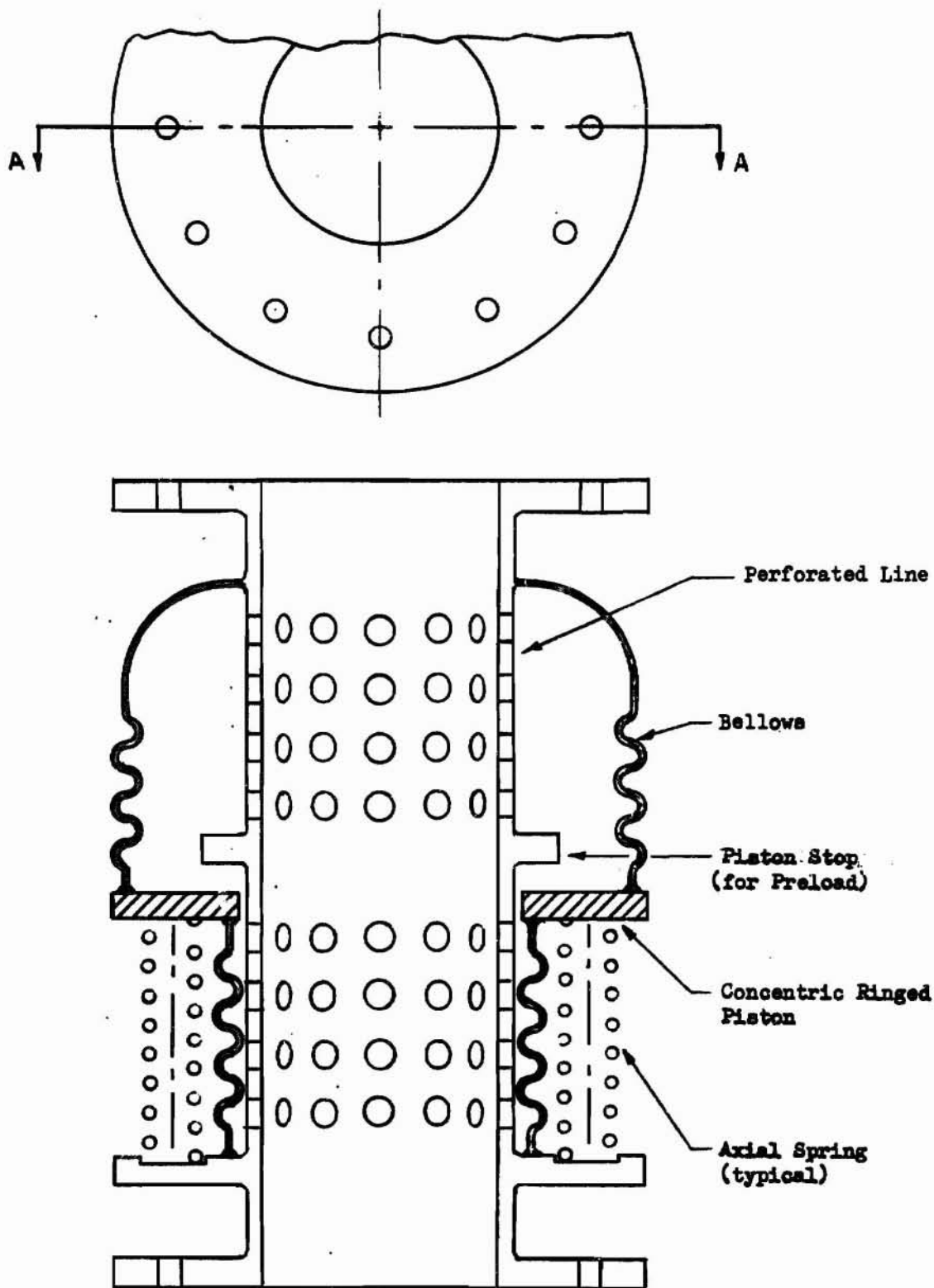


FIGURE 47. TROMBONE ACCUMULATOR DESIGN

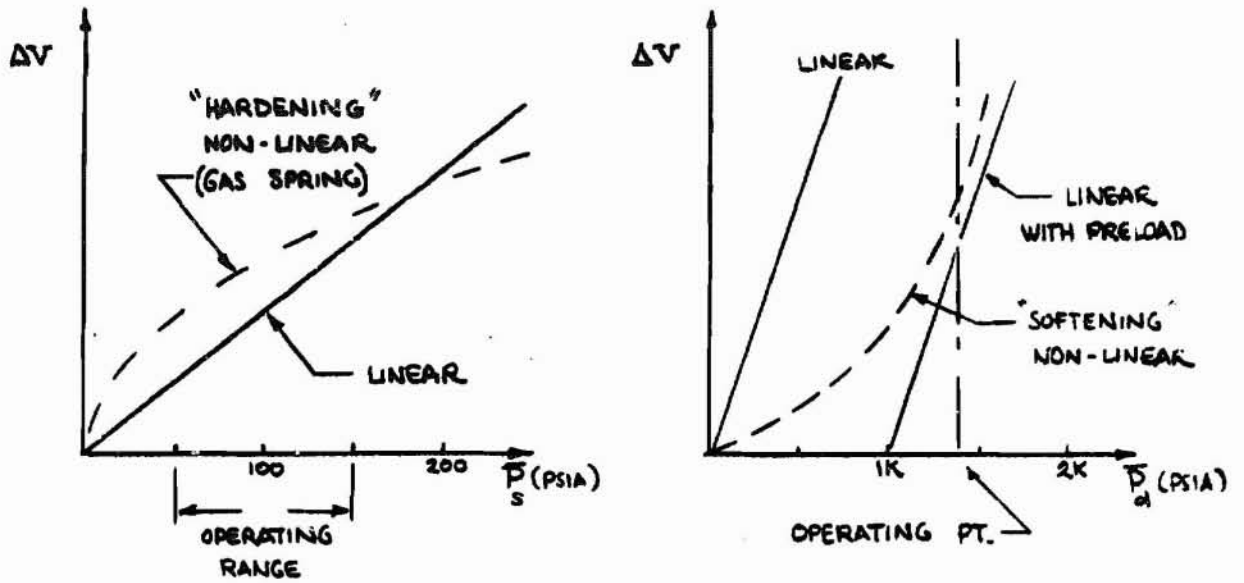


FIGURE 48. TYPICAL ACCUMULATOR COMPLIANCE CHARACTERISTICS

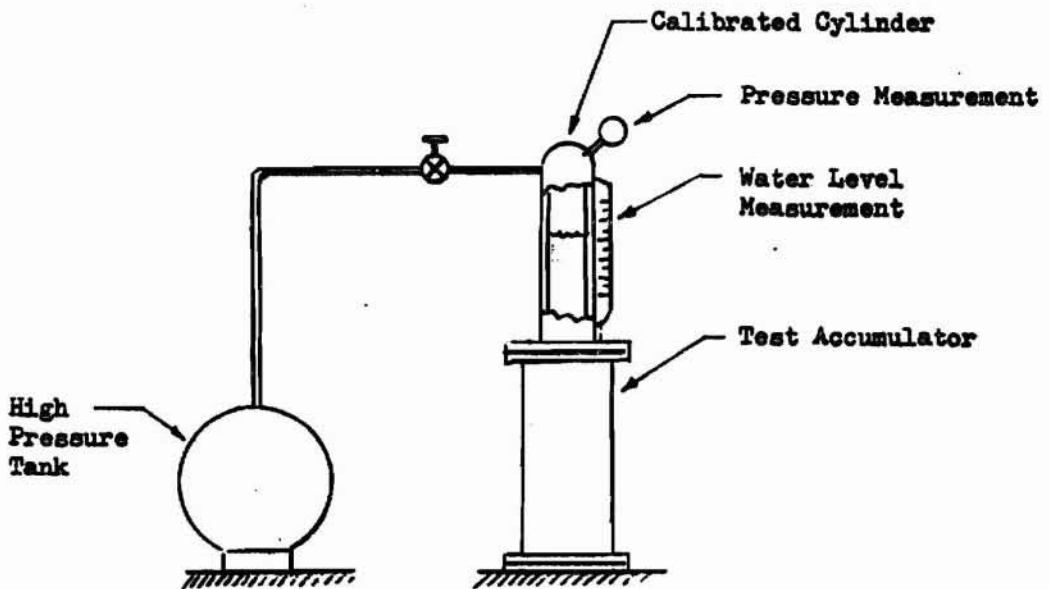
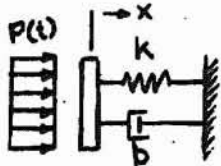
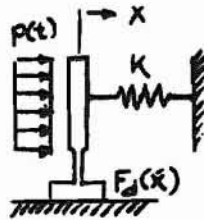


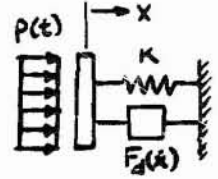
FIGURE 49. SKETCH OF THE COMPLIANCE TEST FACILITY



Viscous

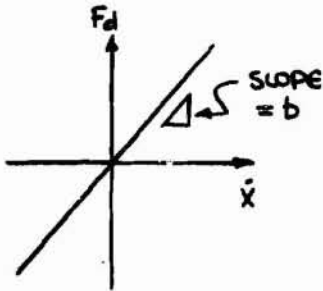


Coulomb

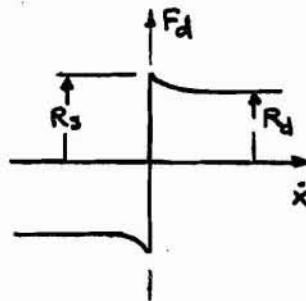


Arbitrary

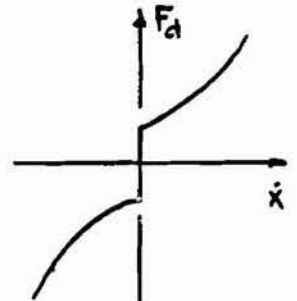
a) Spring-Damper Models



Viscous

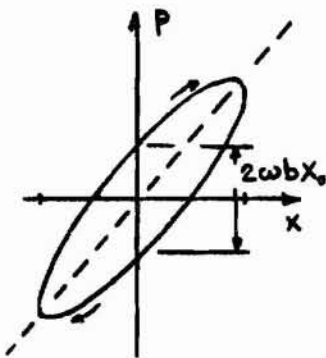


Coulomb

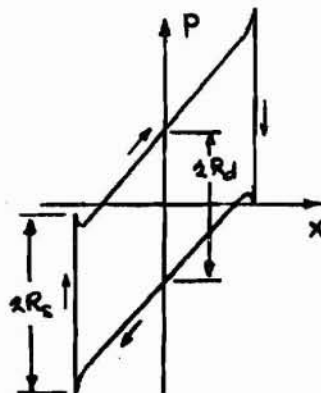


Arbitrary

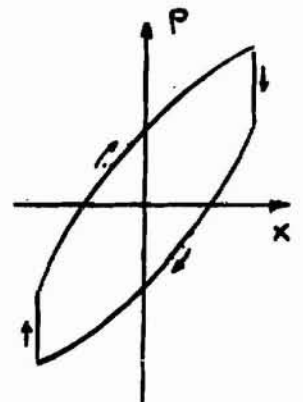
b) Damper Characteristics



Viscous



Coulomb



Arbitrary

c) Hysteresis Curves for Spring-Damper Combinations

FIGURE 50. DAMPING MECHANISMS AND HYSTERESIS

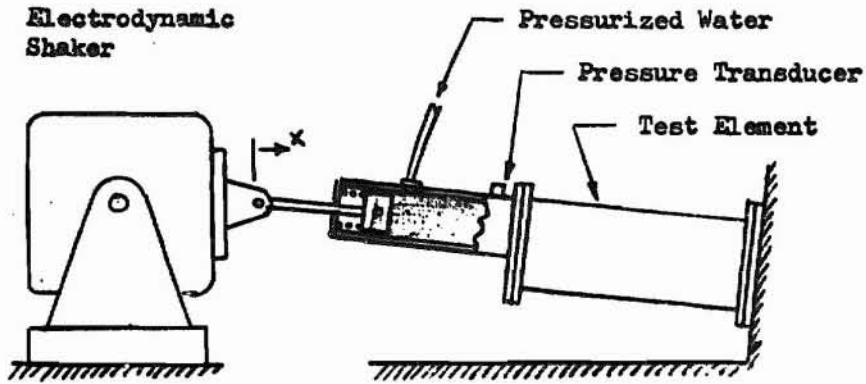


FIGURE 51. SKETCH OF THE HYSTERESIS TEST FACILITY

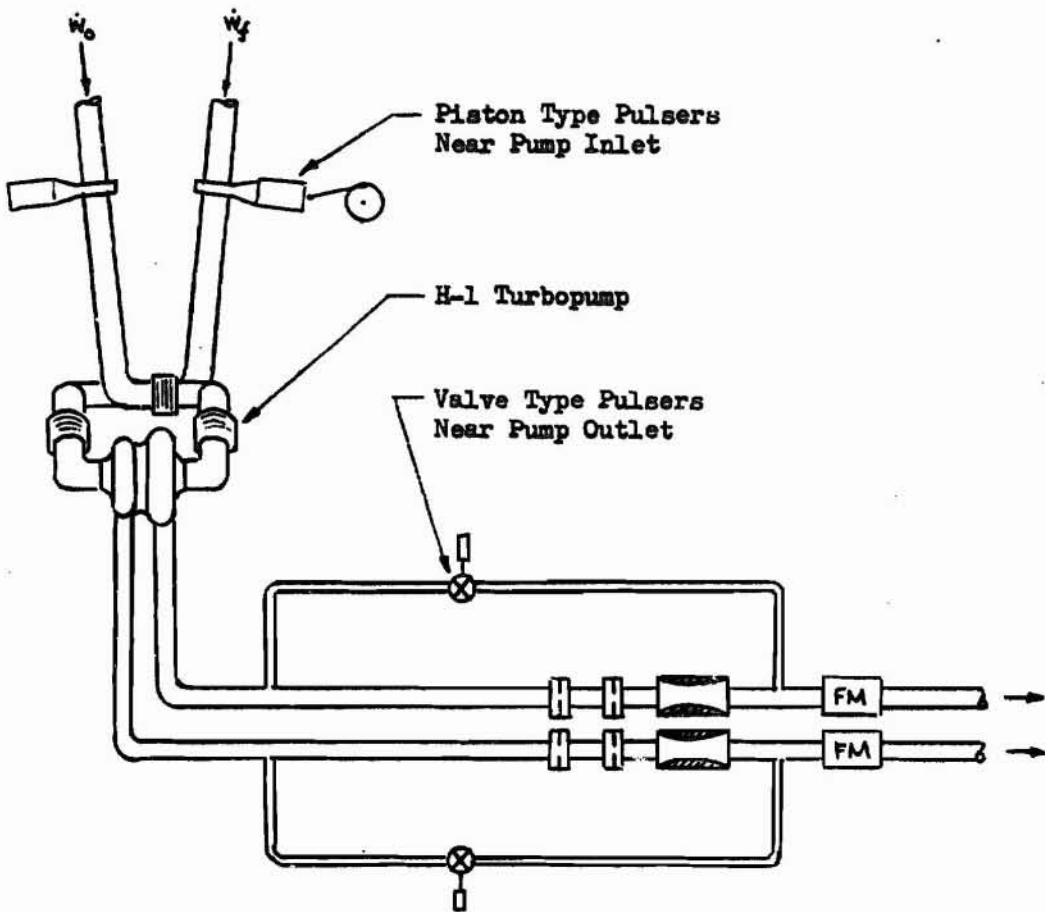
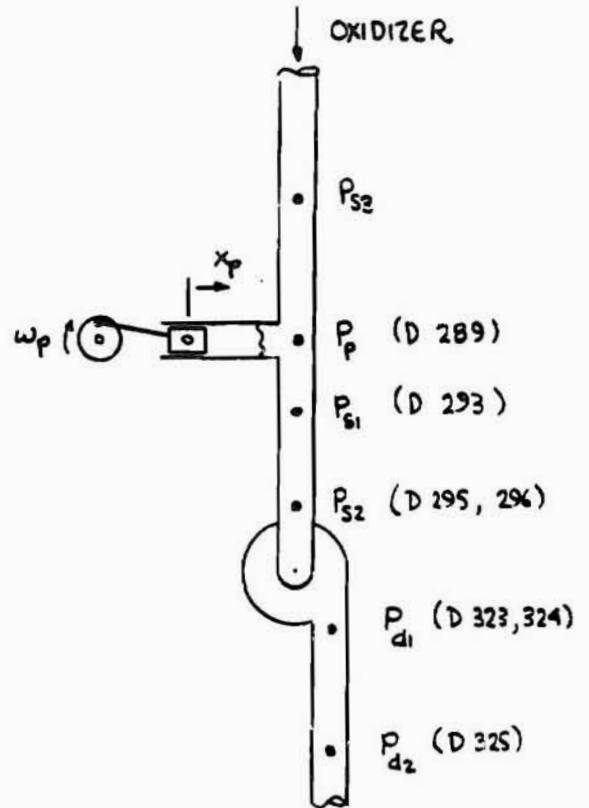
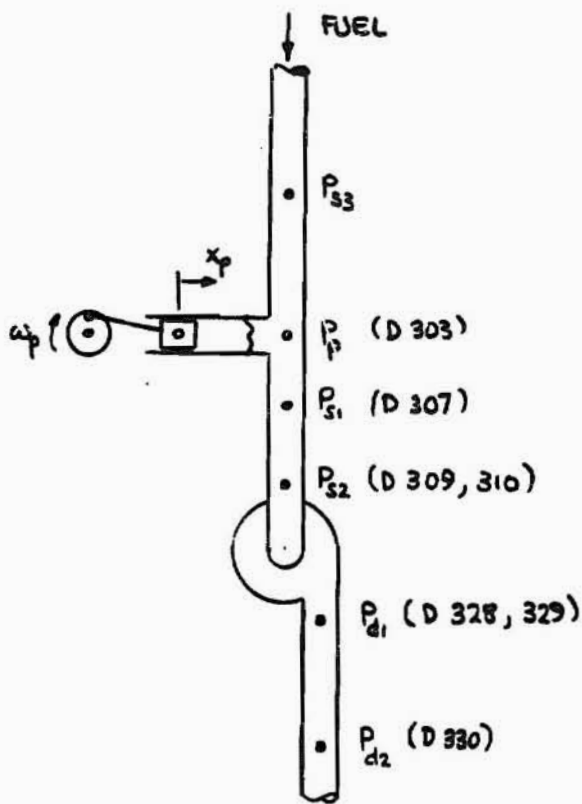
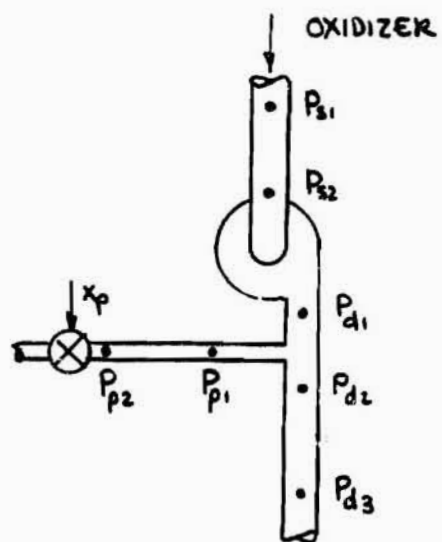
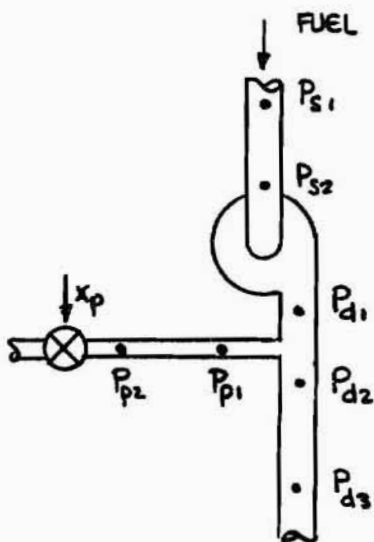


FIGURE 52. SCHEMATIC OF THE H-1 TURBOPUMP TEST FACILITY



a) Pulsing Suction Side of Turbopump



b) Pulsing Discharge Side of Turbopump

FIGURE 53. H-1 BOBTAIL TEST MEASUREMENTS

APPENDIX A

**AEROJET-GENERAL
"POGO" EXPERIENCE**

PRECEDING PAGE BLANK NOT FILMED.

A. INTRODUCTION

The problem of eliminating system coupled instabilities involving the propellant feed system, combustion process, and structural dynamics of a rocket vehicle has motivated Aerojet-General dynamicists to develop generalized methods of solution of such problems. During the development of the Titan II/Gemini Launch Vehicle, considerable effort was devoted to the development of analytical and experimental techniques for the solution of the Titan II "FOGO" longitudinal instability problem. The purpose of this appendix is to present a description of the methodology resulting from this effort and related programs.

B. ANALYSIS

1. Basic Considerations and Techniques

The stability analysis procedures employed at Aerojet-General rely heavily on the concepts developed for linear control system stability analysis (Ref 7). The procedures are valid for small amplitude sinusoidal oscillations of relatively low frequencies. Thus, the procedures discussed herein apply to system instabilities in the initial stages of development.

Because Aerojet-General is primarily concerned with the rocket propulsion system rather than the vehicle, the primary emphasis has been placed on the combustion and feed system dynamics. The result has been the development of techniques for detailed dynamic analysis of the propellant feed system.

B.1 (cont.)

a. The "POGO" System

Figure 1 illustrates schematically the type of system considered in the "POGO" longitudinal oscillation problem. The schematic diagram illustrates the physical relationship between the missile structure and propulsion system composed of the tank, propellant suction lines, turbopumps, discharge lines, and thrust chambers. The complex interaction of these elements is represented by the block diagram shown in Figure 2. Note that the main "loop" which affects the liquid system POGO mode of oscillation is shown in heavy print whereas the subsidiary loops are shown in light print. Since the structural response to the thrust oscillation input results in an oscillatory motion input to the tank bottoms and pump inlets, it is seen that the vehicle structure provides the feedback loop for the system. The following discussion will present the equations which describe the frequency response characteristics of the main system elements. A brief description of the method of performing the closed-loop stability analysis of the system is also presented.

b. Feed System Dynamics

(1) General Methods

The propulsion system is treated as a linearized hydraulic/acoustical network which is analogous to an electrical network. The impedance analog, which is utilized here, is applicable to systems with relatively small amplitudes of oscillation. This analogy, discussed in Ref 8, is based on the similarity between the equations of motion which describe pressure and flow rate oscillations and those which describe voltage and current oscillations. For the

AMDR 9635-037, APPENDIX A

B.1.b.(1) (cont.)

purpose of a linearized frequency response analysis of a hydraulic circuit, each circuit element may be represented by a combination of acoustical inductors, resistances, and capacitances. If the characteristic length of the feed line elements is short relative to an acoustic wavelength (less than 1/8 wavelength), the utilization of a lumped parameter representation is permissible. For the purpose of a lumped parameter analysis the dynamic characteristics of each hydraulic element are defined in terms of the following parameters:

$$L = \frac{\rho l}{A} = \text{acoustical inertance} \quad (1)$$

$$R = \frac{2\Delta P}{\dot{V}} = \text{linearized acoustical flow resistance} \quad (2)$$

$$C = \lambda A \left[\frac{1}{\rho a_0^2} + \frac{d}{Eh} \right] = \text{acoustical capacitance} \quad (3)$$

A method successfully employed at Aerojet-General for frequency response analysis of feed system circuits composed of many interconnected hydraulic elements is to consider each dynamic element as a two-port (four terminal) network and use matrix methods to account for their dynamic interaction. As discussed in Appendix B, the frequency response of the two-port network may be described in matrix form as

$$\begin{bmatrix} P_1(\omega) \\ \dot{V}_1(\omega) \end{bmatrix} = \begin{bmatrix} a_{11}(\omega) & a_{12}(\omega) \\ a_{21}(\omega) & a_{22}(\omega) \end{bmatrix} \begin{bmatrix} P_2(\omega) \\ \dot{V}_2(\omega) \end{bmatrix} \quad (4)$$

The 2 x 2 matrix $\begin{bmatrix} a_{11}(\omega) & a_{12}(\omega) \\ a_{21}(\omega) & a_{22}(\omega) \end{bmatrix}$ will be referred to as a transmission matrix. For a given load impedance at port "2", the input impedance at port "1" may be expressed as

B.1.b.(1) (cont.)

$$Z_1(\omega) = \frac{P_1(\omega)}{V_1(\omega)} = \frac{a_{11}(\omega) Z_2(\omega) + a_{12}(\omega)}{a_{21}(\omega) Z_2(\omega) + a_{22}(\omega)}, \text{ where } Z_2(\omega) \triangleq \frac{P_2(\omega)}{V_2(\omega)} \quad (5)$$

A similar expression may be written for the input impedance at port "2." For other transformations of the characteristic matrices that describe n-port hydraulic networks, Appendix B should be consulted. The digital program which performs these matrix manipulations to compute the frequency response of the complete engine-feed system is contained in Appendix C.

(2) System Components

As indicated in the previous sections, a thorough feed system dynamic analysis required that the feed system be divided into its different dynamic components. The analysis techniques are the same for both the fuel and the oxidizer systems. The different component parts of the feed system are described below.

(a) Propellant Tank

The dynamic modeling of the fluid in the tank depends upon whether the tank ullage pressure is affected by the structural oscillations and whether the tank bottom pressure is affected by the response of the feed lines. It has been experimentally noted that for the liquid system "POGO" problem the tank ullage tank pressure oscillations are negligible. Furthermore, because of the large impedance discontinuity at the tank bottom/feed line interface, the tank fluid motion is not affected by oscillations present in other parts of the feed system. Therefore, the tank bottom pressure may be determined from the modal analysis of the vehicle structure which includes the mass of the fluid in the tank and the volume compliance of the tank structure, but ignores the feed system response.

B.1.b.(2) (cont.)

(b) Hydraulic Transmission Line

For the case of a hydraulic transmission with constant fluid inertance, capacitance and resistance uniformly distributed along its length, the transmission matrix may be written

$$\begin{bmatrix} P_1(\omega) \\ \tilde{V}_1(\omega) \end{bmatrix} = \begin{bmatrix} \cosh \gamma(\omega)l & Z_c(\omega) \sinh \gamma(\omega)l \\ \frac{\sinh \gamma(\omega)l}{Z_c(\omega)} & \cosh \gamma(\omega)l \end{bmatrix} \begin{bmatrix} P_2(\omega) \\ \tilde{V}_2(\omega) \end{bmatrix} \quad (6)$$

where

$$\gamma(\omega)l = \left[j\omega C(j\omega L + R) \right]^{\frac{1}{2}}, \quad \text{propagation angle}$$

$$Z_c(\omega) = \left[\frac{j\omega L + R}{j\omega C} \right]^{\frac{1}{2}}, \quad \text{characteristic impedance}$$

It is shown in Appendix D that this expression does not hold for the case of an acoustical lossy line or gas injection. However, it is a good approximation for the case of turbulent flow through a liquid filled propellant line. For a transmission line with a length less than 1/8 of the smallest acoustic wave length, a lumped parameter representation may be employed to represent the line as follows:

$$\begin{bmatrix} P_1(\omega) \\ \tilde{V}_1(\omega) \end{bmatrix} = \begin{bmatrix} 1 + \Upsilon(\omega)Z(\omega) & Z(\omega) \\ \Upsilon(\omega)[2 + \Upsilon(\omega)Z(\omega)] & 1 + \Upsilon(\omega)Z(\omega) \end{bmatrix} \begin{bmatrix} P_2(\omega) \\ \tilde{V}_2(\omega) \end{bmatrix} \quad (7)$$

where

$$Z(\omega) = j\omega L + R, \quad \text{series impedance}$$

$$\Upsilon(\omega) = \frac{1}{2} [j\omega C], \quad \text{shunt admittance}$$

B.1.b.(2) (cont.)

(c) Closed Propellant Valves

Many of the transmission lines branching from the main line are terminated with closed propellant valves. It is generally assumed that the structural compliance of the valve is negligible and the acoustic impedance at the valve is infinitely large.

(d) Turbopump

The linearized differential equations of motion of the turbopump, as illustrated in Figure 3a, may be represented by the following equations:

$$P_d(t) = \mu_f P_s(t) - L_p \ddot{V}_d(t) - R_p \dot{V}_d(t) + K_p \dot{\theta}(t) \quad (8)$$

$$\dot{V}_d(t) - \dot{V}_s(t) = C_p \dot{P}_s(t) \quad (9)$$

where

 μ_f = pump forward pressure gain R_p = pump resistance L_p = pump inertance K_p = pump speed constant C_p = pump inlet capacitance

As a first approximation, the constants μ_f , R_p and K_p may be estimated from the steady state pump performance data. Consider the partial derivative expressions

$$\mu_f = \left. \frac{\partial \bar{P}_d}{\partial \bar{P}_s} \right|_{\bar{V}_d, \bar{\theta}} \quad (10)$$

B.1.b.(2).(d) (cont.)

$$R_p = \left. \frac{\partial \bar{P}_d}{\partial \bar{V}} \right|_{\bar{P}_s, \bar{\theta}} \quad (11)$$

$$K_p = \left. \frac{\partial \bar{P}_d}{\partial \bar{\theta}} \right|_{\bar{P}_s, \bar{V}_d} \quad (12)$$

where the bars indicate the steady state component of the pump variables. The pump gain and resistance are shown as the slopes of the \bar{P}_d vs \bar{P}_s curve and \bar{P}_d vs \bar{V}_d curve in Figure 3b, respectively. Although the predicted values of μ_f , R_p and K_p obtained by this method are not accurate, they should qualitatively agree with the actual values. Dynamic pulse tests of the turbopump are required to obtain the precise values of these constants as well as to evaluate the parameters C_p and L_p .

Relative to sinusoidal pressure and flow oscillations, equations (8) and (9) may be written

$$\begin{bmatrix} P_d(\omega) \\ \dot{V}_d(\omega) \end{bmatrix} = \begin{bmatrix} \mu_f & -Z_p(\omega) \\ 0 & 1 \end{bmatrix} \begin{bmatrix} P_s(\omega) \\ \dot{V}_s(\omega) \end{bmatrix} \quad (13)$$

$$\begin{bmatrix} P_s(\omega) \\ \dot{V}_s(\omega) \end{bmatrix} = \begin{bmatrix} 1 & 0 \\ -Y_p(\omega) & 1 \end{bmatrix} \begin{bmatrix} P_s(\omega) \\ \dot{V}_s(\omega) \end{bmatrix} \quad (14)$$

where

$$\begin{aligned} Z_p(\omega) &= j\omega L_p + R_p &&= \text{pump series impedance} \\ Y_p(\omega) &= j\omega C_p &&= \text{admittance due to inlet capacitance} \end{aligned}$$

The use of these equations requires the assumption that the pump speed fluctuations are negligible. In the case of the Titan system, this assumption was justified for small amplitude oscillations at the frequencies of interest (5 to 20 cps).

B.1.b.(2).(d) (cont.)

Combining eqs (13) and (14) yields the rearward transmission matrix for the pump, including the effect of inlet compliance

$$\begin{bmatrix} P_d(\omega) \\ \dot{V}_d(\omega) \end{bmatrix} = \begin{bmatrix} \mu_f + Y_p(\omega)Z_p(\omega) & -Z_p(\omega) \\ -Y_p(\omega) & 1 \end{bmatrix} \begin{bmatrix} P_s(\omega) \\ \dot{V}_s(\omega) \end{bmatrix} \quad (15)$$

The forward transmission matrix of the pump may be obtained from the inverse of eq (15)

$$\begin{bmatrix} P_s(\omega) \\ \dot{V}_s(\omega) \end{bmatrix} = \mu_r \begin{bmatrix} 1 & Z_p(\omega) \\ Y_p(\omega) & \mu_f + Y_p(\omega)Z_p(\omega) \end{bmatrix} \begin{bmatrix} P_d(\omega) \\ P_s(\omega) \end{bmatrix} \quad (16)$$

where

$$\mu_r = \mu_f^{-1} = \text{reverse pressure gain}$$

(e) Injector/Cooling Tubes

For low frequencies, the discharge line, cooling tubes and thrust chamber injector may be lumped and represented as a single hydraulic resistance and inertance. For higher frequencies, the distributed fluid capacitance of the discharge lines and cooling tubes must be accounted for. Indeed, the cooling tube capacitance may become quite large if appreciable nucleate boiling of the propellant occurs in the nozzle throat section of tubes.

In the case of the Titan feed system, it was found that the discharge system capacitance was negligible. With this assumption the transmission matrix for the lumped discharge line and injector may be written

$$\begin{bmatrix} P_d(\omega) \\ \dot{V}_d(\omega) \end{bmatrix} = \begin{bmatrix} 1 & Z_d(\omega) \\ 0 & 1 \end{bmatrix} \begin{bmatrix} P_c(\omega) \\ \dot{V}_c(\omega) \end{bmatrix} \quad (17)$$

$$Z_d(\omega) = j\omega L_d + R_d + R_j = \text{total discharge impedance}$$

$$L_d = \text{discharge line inertance}$$

$$R_d = \text{discharge line resistance}$$

$$R_j = \text{injector resistance}$$

B.1 (cont.)

c. Combustion Dynamics

A simplified model of the combustion chamber dynamics has been found to be valid for the low frequencies of interest in the "POGO" model. The model includes the effects of the injection transport time delay and the time delay due to the residence time of the hot combustion gases in the combustion chamber. In addition, the effects of mixture ratio fluctuations are considered. The equation for the combustion chamber dynamic response is as follows:

$$P_c(\omega) = \frac{c^*}{A_t g} \frac{e^{-j\omega\tau_1}}{1+j\omega\tau_2} \left[K_f \dot{W}_f(\omega) + K_o \dot{W}_o(\omega) \right] \quad (18)$$

where

- A_t = nozzle throat area
- c^* = $\bar{P} A_t g / \bar{W}_c$ = characteristic exhaust velocity
- g = gravitational acceleration
- K_f = $\frac{A_t g}{c^*} \cdot \frac{\partial \bar{P}_c}{\partial \bar{W}_f} = 1 - \frac{\bar{r}(\bar{r}+1)}{c^*} \frac{\partial c^*}{\partial \bar{r}}$
- K_o = $\frac{A_t g}{c^*} \cdot \frac{\partial \bar{P}_c}{\partial \bar{W}_o} = 1 + \frac{\bar{r}+1}{c^*} \frac{\partial c^*}{\partial \bar{r}}$
- \bar{r} = \bar{W}_o / \bar{W}_f , steady state mixture ratio
- $\frac{\partial c^*}{\partial \bar{r}}$ = slope of c^* versus \bar{r} curve
- P_c = chamber pressure
- τ_1 = injection - combustion time lag
- τ_2 = residence time of gases in combustion chamber

The factors K_f and K_o are called the mixture ratio combustion constants. These constants are obtained from the partial derivatives of the combustion surface illustrated in Figure 4.

AMDR 9635-037, APPENDIX A

B.1.c (cont.)

The combustion time delay, τ_1 , may be estimated by the equation

$$\tau_1 = \frac{l_j}{\bar{u}_j} \quad (19)$$

where l_j = distance from the injector face to the combustion zone

\bar{u}_j = mean injection velocity

The residence time delay, τ_2 , may be approximated by the following equation

$$\tau_2 = \frac{L^*}{k c^*} \left(\frac{k+1}{2} \right)^{\frac{k+1}{k-1}} \quad (20)$$

where k = specific heat ratio

L^* = (chamber volume)/(area of nozzle throat)

= characteristic length of combustion chamber,

Relative to sinusoidal pressure and flow fluctuations, eq (18) may be rewritten in terms of the equivalent hydraulic impedance Z_k^h of the combustion process:

$$P_c(\omega) = Z_k^h(\omega) [K_f \bar{W}_{cf}(\omega) + K_o \bar{W}_{co}(\omega)] \quad (21)$$

where

$$Z_k^h = \frac{c^*}{A_t g} \frac{e^{-j\omega\tau_1}}{1 + j\omega\tau_2}$$

It should be noted that this combustion dynamics equation neglects such acoustical effects as wave propagation in the thrust chamber and the variable impedance of the nozzle throat. Thermodynamic effects, such as entropy variations throughout the chamber, are also neglected. However, in the range of frequencies of interest, the aforementioned effects are negligible.

B.1 (cont.)

d. The Nozzle

At low frequencies, the action of the nozzle in converting the products of combustion into thrust is represented by the steady state thrust equation

$$F_c = n C_F A_t P_c \quad (22)$$

where

A_t = area of the nozzle throat

C_F = thrust coefficient

n = number of rocket thrust chambers

F_c = thrust

It is assumed that the effect of pressure fluctuations on the value of the thrust coefficient, C_F , is negligible.

e. Structural Dynamics

The free vibration modes and frequencies of the combined vehicle structure and propellant tank system must be determined for inclusion in the analytical model. This combined fluid-structural system is analyzed by breaking it into discrete elements and describing the compliance and inertial properties of each element. A technique commonly employed for the vibration analysis of such systems is the Holtzer-Myklestad method. This method has been programmed for the digital computer and may be employed for handling 100 different elements, each having six degrees of freedom.

An example of the Titan structural dynamic model is shown in Figure 5. Each element of the system, including the propellants in the tanks, is represented by a mass-spring system and the entire network is coupled as shown.

B.1.e (cont.)

Using the generalized coordinate approach, the following response equation may be written for each mode of vibration

$$\frac{\ddot{x}_{ik}}{Q_i} = \frac{A_{ik} \left(\frac{\omega_i}{s}\right)^2}{1 + \left(\frac{\omega_i}{s}\right)^2 + 2\xi_i \left(\frac{\omega_i}{s}\right)} \quad (23)$$

where

- A_{ik} = modal displacement at the k^{th} station in the i^{th} mode
- \ddot{x}_{ik} = acceleration at the k^{th} station in the i^{th} mode
- ξ_i = damping ratio of i^{th} mode
- ω_i = frequency of i^{th} mode
- Q_i = generalized force acting on the i^{th} mode

The modal displacement, A_{ik} , is defined as

$$A_{ik} = \frac{\phi_{ik}}{M_i} \quad (24)$$

where

- $M_i = \sum_{k=1}^n M_k \phi_{ik}^2$ = generalized mass in the i^{th} mode (25)
- M_k = mass at k^{th} station
- ϕ_{ik} = normalized modal displacement at k^{th} station

The generalized force in the i^{th} mode, caused by the application of thrust F_e at the engine station "e" and the suction pressure reaction at the pump station "p," is given by the expression

$$Q_i = \phi_{ie} F_e - \phi_{ip} (A_{sf} P_{sf} + A_{so} P_{so}) \quad (26)$$

where

- F_e = thrust of n thrust chambers
- ϕ_{ie} = normalized modal displacement of engine station
- ϕ_{ip} = normalized modal displacement of pump station
- A_{sf} = total fuel pump suction area
- A_{so} = total oxidizer pump suction area

B.1 (cont.)

f. Stability Analysis

The combined thrust chamber-feed line-structural system may be expressed as a closed loop system by the signal flow graph illustrated in Figure 6 where the transmittances are determined from the interacting dynamic equations formed by combining the previous analog network relationships (Ref 1). In such a form, the following system open loop stability equation can be developed for the system opened at the point representing system thrust.

$$\frac{F_{e \text{ out}}}{F_{e \text{ in}}} = \frac{N}{D} \quad (27)$$

where

$$N = t_{48} (1 - t_{23} t_{32}) (1 - t_{56} t_{65}) [t_{23} t_{34} (t_{12} t_{81} + t_{82}) (1 - t_{56} t_{65}) + t_{65} t_{54} (t_{87} t_{76} + t_{86}) (1 - t_{23} t_{32})]$$

$$D = \left\{ (1 - t_{32} t_{23}) (1 - t_{56} t_{65}) \left[1 - (t_{12} t_{81} + t_{82}) t_{28} - (t_{87} t_{76} + t_{86}) t_{63} \right] - t_{23} t_{32} t_{28} (t_{12} t_{81} + t_{82}) (1 - t_{56} t_{65}) \right. \\ \left. - t_{65} t_{56} t_{69} (t_{87} t_{76} + t_{86}) (1 - t_{32} t_{23}) \right\} \left[(1 - t_{32} t_{23}) (1 - t_{56} t_{65}) - t_{43} t_{34} (1 - t_{56} t_{65}) - t_{45} t_{54} (1 - t_{32} t_{23}) \right] \\ - \left[t_{32} t_{28} t_{43} (1 - t_{56} t_{65}) + t_{56} t_{68} t_{45} (1 - t_{32} t_{23}) \right] \left[t_{23} t_{34} (t_{12} t_{81} + t_{82}) (1 - t_{56} t_{65}) + t_{65} t_{54} (1 - t_{32} t_{23}) (t_{87} t_{76} + t_{86}) \right]$$

Standard techniques for stability analysis may then be employed for determining the stability characteristics of the system. The Nyquist criterion may conveniently be utilized for examining the open loop response of lumped as well as distributed parameter systems. In lumped parameter systems, the root locus technique is especially useful. Specific examples of the application of the Nyquist criteria will be discussed in subsequent sections.

AMDR 9635-037, APPENDIX A

B.1 (cont.)

g. Compensating Devices

With the aid of a stability analysis, it is usually possible to synthesize compensating devices to make the system more stable. Aerojet dynamicists have experience in the design of passive compensation devices which modify the dynamic response of the propellant feed system. Such devices are designed to detune a system by providing attenuation at a given frequency or by phase shifting the resonant frequencies of oscillation into a more stable operating regime. Figure 7 illustrates schematically the following devices: (a) a Helmholtz resonator, and (b) a quarter-wavelength resonator. The figure presents both a schematic and an electrical analog of the acoustic circuit for each device. From the latter diagram, the acoustic impedance of each device can be determined. For example, the Helmholtz resonator impedance is expressed by

$$Z_i(\omega) = \frac{P_i(\omega)}{V_i(\omega)} = \frac{1117}{j\omega C} \left[\frac{1}{C} - LC\omega^2 + j(RC)\omega \right] \quad (28)$$

and the quarter-wavelength resonator impedance is expressed by

$$Z_i(\omega) = \frac{P_i(\omega)}{V_i(\omega)} = R_i + Z_c(\omega) \coth \gamma(\omega)l \quad (29)$$

2. Titan II "POGO" Experience

a. Flight Data Analysis

During the developmental flight testing of the Titan II missile, it was discovered that the vehicle experienced a severe longitudinal oscillation during first-stage operation. Maximum oscillation amplitude occurred at 11 cps, although the frequency of instability tended to shift during the flight from 10

B.2.a (cont.)

cps at the start to 13 cps at the end of the instability. Although the amplitude of the oscillation did not cause structural damage to the vehicle, it was found that the vibration would seriously impair the effectiveness of the astronauts during the boost period of the Gemini launch vehicle. Therefore, Aerojet-General and the other Titan II contractors began a concentrated effort to suppress or eliminate the undesirable longitudinal vibration characteristics of the propulsion-vehicle system.

The Aerojet-General analysis of the flight vibration and pressure oscillation data was accomplished by use of spectral analysis and narrow-band filtering equipment. This analysis of the oscillatory pressure data was useful in defining the acoustic mode resonant frequencies of the propellant suction lines as well as the apparent "gain" or pressure amplification of the propellant pumps. The results of the analysis of the data from the first few flights revealed that the fuel pump displayed a very high gain. It was found that the magnitude of the pump gain was inversely proportional to NPSH (net positive suction head), so that the gain could be decreased by an increase in suction pressure. Although the spectral analysis of propellant suction pressures did not completely define the suction line resonant frequencies, there was some indication that the fuel and oxidizer frequencies were 10 and 18 cps, respectively. The oxidizer suction line resonant frequency was particularly hard to define by means of power spectral density plot because of the relatively high damping of this acoustic mode.

As a result of analyzing data resulting from the first Titan II flight, the following objectives were established for subsequent flight testing:

- (1) Improve the flight instrumentation-telemetry system for the purpose of the acquisition of valid dynamic amplitude and phase data.

AMDR 9635-037, APPENDIX A

B.2.a (cont.)

(2) Evaluate the effect of adding surge chambers and/or accumulators to the oxidizer and fuel suction lines near the pump inlet.

(3) Evaluate the effect of wrapping the oxidizer suction line and turbopump with thermal insulation.

(4) Evaluate the effect of increasing the propellant tank pressures and decreasing the propellant temperature.

In regard to the first objective, it was necessary to (1) add more low frequency accelerometers to define the vehicle mode shape, and (2) close couple the existing pressure transducers to obtain adequate pressure amplitude and phase data. Accelerometers were added to the pump frame, engine frame, and missile structure longeron. These additional vibration measurements revealed that each station was vibrating in phase, although each accelerometer trace displayed a distinct second harmonic component at twice the frequency of the primary component. The pump acceleration data indicated that the turbopumps displayed a rocking mode at approximately 20 cps. At the frequency of instability, the longitudinal acceleration of both the fuel and oxidizer suction flanges were approximately equal.

Increased tank pressures were first evaluated on Missile N-4. The results of this test were very encouraging in that chamber pressure oscillations at the time of maximum missile oscillation were reduced from 100 psi (p-p) to 40 psi (p-p). The next missile flight with increased tank pressures was N-13, followed by N-15. The results of these tests were more successful with the maximum P_c oscillations reduced to 25 psig, peak-to-peak. The ratio of fuel discharge pressure to fuel suction pressure were noted to be lower on these flights than any prior flights. The use of colder propellants as another method of increasing

AMDR 9635-037, APPENDIX A

B.2.a (cont.)

head pressure due to the smaller vapor pressure and greater density was considered.

During the early Titan II test flights, temperatures in the area of the first-stage engine compartment were noted to be in excess of 1000°F. It was thought by some that the intense heat might cause localized heating of the propellants at the pump, specifically the oxidizer, and thus causing the pump to see the effects of an oxidizer localized boiling condition brought on by the high engine compartment temperatures. The oxidizer lines and the upper portion of the pump were wrapped on two missiles with a thermal shielding type of material. This thermal insulation appeared to have no effect toward reducing any of the previously experienced oscillations.

On Missile N-12, surge chambers were added to the oxidizer suction lines 9-1/2 in. above the pump suction flange. The surge chambers were nothing more than a standpipe 4 in. in diameter and 26 in. in length. The surge chamber acts as an energy absorber on frequencies near its tuned range. That is, it will suppress oscillations in the 9 to 13 cps range if adjusted properly. The height of the liquid column is a function of the nominal suction pressure and original volume of entrapped gas.

The flight data from Missile N-11 revealed that the insertion of oxidizer devices caused the suppression of oxidizer pressure oscillations. However, since the fuel suction pressure was low on this flight, thus resulting in a high fuel pump gain, a relatively large amplitude instability occurred at a flight time which was later than previous flights. It was apparent from these results that accumulator devices must be used on the fuel suction line as well as

B.2.a (cont.)

on the oxidizer suction line. Therefore, Martin Co. personnel designed a fuel accumulator which utilized a piston supported by a coil spring to achieve a dynamic vibration absorber effect at 11 cps. The combined "POGO Hardware" consisting of both the oxidizer standpipe and the fuel accumulator was first tested successfully on Missile N-25, which displayed a maximum longitudinal acceleration amplitude of .125g at the payload station.

b. Titan II Fuel Pump Redesign

Early in the Titan II/Gemini "POGO" investigation, it was discovered that the fuel pump tended to display a large "gain" or amplification of suction pressure oscillations throughout the operational range of NPSH. This high gain, which contributed to the destabilization of the "POGO" loop, was attributed to the relatively poor cavitation performance of the fuel pump during operation at nominal operating conditions. Therefore, a program was initiated at Aerojet-General for the purpose of modifying the pump to improve the cavitation performance. It was decided that this objective could best be achieved by modifying the partial vane and inlet vane configuration and increasing the impeller solidity. The solidity (σ^*) is defined by the equation

$$\sigma^* = \frac{\text{blade chord}}{\text{blade spacing}} = \frac{\eta C}{2\pi r} \quad (30)$$

where

η = number of inducer blades

C = blade chord

r = inducer tip radius

B.2.b (cont.)

The effect of the pump modification is shown in Figure 8, which is a plot of the steady-state pump discharge pressure versus the steady-state suction pressure for a nominal fuel flow rate. It is seen from this steady-state performance curve that the effect of modifying the pump is to shift the knee of the curve to a lower suction pressure so that the slope of the curve, and thus the pump gain, is decreased for a particular steady-state suction pressure.

Dynamic testing of the redesigned pump, both at Aerojet-General and Martin Co., indicated that the modifications were indeed successful in reducing the pump gain. Although the gain depended on the value of nominal suction pressure (NPSH) and the suction pressure amplitude, the reduction in gain was approximately 25 to 50%. The fuel suction line resonant frequency was increased by the insertion of the redesigned pump. This increase in frequency was caused by the smaller cavitation compliance (for a given value of suction pressure) of the redesigned pump as compared to the production pump. In conclusion, the various investigators agreed that the redesigned fuel pump displayed desirable dynamic characteristics, but that its use in the manned Gemini vehicles was prohibited by the lengthy qualification test program.

C. TESTING

1. Preliminary Titan II "POGO" Testing

Early in the Titan II POGO investigation, Aerojet-General initiated a ground test program to determine the contribution of the propulsion system, including propellant feed lines and turbopumps, to the first-stage missile oscillation problem. A subsidiary objective of this preliminary test program was to achieve limited dynamic testing of the second-stage engine system since flight

C.1 (cont.)

data had revealed that the vehicle experienced low-level longitudinal instability during second-stage burning. Since the POGO oscillations were more severe during first-stage flight, more emphasis was placed on dynamic testing of the first-stage (YLR87-AJ-5) engine.

The objectives of the preliminary first-stage engine test program were:

- 1) determine the fundamental resonant frequency of the oxidizer suction line;
- 2) investigate engine oscillations at both nominal and low pump suction pressures (NPSH);
- 3) determine the oscillation transfer characteristics of the propulsion system;
- 4) determine the structural resonant frequency of the turbopump assembly;
- 5) determine the effect of adding stiffeners between the pump frame and engine frame, and
- 6) investigate the flow conditions at the pump inlet.

The fundamental acoustic mode of the oxidizer suction line was initially excited by means of sudden closure of a cut-off valve which was installed at the pump inlet location. The resulting waterhammer oscillations indicated that the quarter-wavelength frequency ranged from 17.6 to 18.6 cps, depending on the temperature of the oxidizer (N_2O_4). Comparison of this data and flight pressure spectral density data indicated that the dynamic coupling of the suction line and turbopump during engine operation tended to reduce this natural frequency to the 8-12 cps range.

Dynamic instrumentation was added to the engine to measure low amplitude pressure oscillations throughout the system. Special low amplitude delta pressure transducers were used, with one side plumbed to a steady-state reference pressure so that only the dynamic oscillatory pressure amplitude was recorded. With this special instrumentation, engine firing tests were made under nominal operating conditions. All pressure parameters displayed low frequency

C.1 (cont.)

oscillatory components; however, the observed frequencies were random within the frequency band of from 9-16 cps. When the engine was operated at a very low fuel suction pressure (13.5 psia), it was noted that the engine system experienced a very definite self excited oscillation in the 10-12 cps frequency range. It was observed that, when the fuel suction pressure was decreased still further (12 psia), the frequency of the fuel discharge pressure suddenly doubled. The result of this second harmonic in the fuel circuit was to decrease the amplitude of the chamber pressure oscillation. Although the self-induced oscillations of the engine system were noted on other low fuel suction pressure tests, the exact mechanism of the instability was never determined. It was later theorized that this phenomenon was caused by a "POGO" instability of the engine test stand combination since the frequency of the fundamental vibration mode of the test stand structure was observed to range from 8 to 13 cps, depending on the mass of propellant in the tanks. Since the structural damping of the structure is probably much greater than that of the Titan II vehicle, the fuel pump gain must be very large to cause such an instability.

The transmission of oscillations through the first-stage engine system was studied by exciting the system with a nearly sinusoidal pressure oscillation in the oxidizer suction line. The pressure oscillation was induced by use of a rotating ball valve (tweaker valve) which connected a small bleed-off line to the oxidizer suction line. The valve was driven by a varidrive motor, the frequency of which could be varied from 5 to 15 cps. The resulting oscillatory flow through this valve resulted in induced suction line pressure oscillations of 40 to 50 psi (peak-to-peak). Although this system was adequate to excite system resonances in the 8 to 11 cps frequency range, it was found that the fuel system responded to the oxidizer excitation with very small oscillatory pressure amplitudes. The

C.1 (cont.)

oscillation transfer characteristics of the fuel pump could be measured only at a frequency of approximately 10 cps when relatively large amplitude fuel pressure oscillations were experienced. The pressure amplification across the fuel pump appears to range from 3 to 10, depending on the fuel suction pressure. The oxidizer pump amplification ratio was found to vary from 1 to 2 for the normal range of pump operation.

The structural resonant frequencies of the turbopump assembly (TPA) were experimentally determined by means of a "twang" test of the TPA, when installed in the YLR87-AJ-5 engine. For the purposes of this test the engine was mounted in the engine test stand and a longitudinal load was applied to the turbopump. The sudden release of this load resulted in transient vibration response of the TPA which was measured by use of differential displacement transducers on the suction line bellows and low frequency accelerometers on the turbopump housing. The results indicated that the first and second longitudinal vibration modes of the structure had frequencies of approximately 15 and 27 cps, respectively. The 15 cps mode was associated with the test stand mass-spring resonance, whereas the 27 cps mode appears to be the "rocking mode" of the turbopump, with the pump housing pivoting about the offset mounting points.

The results of the Aerojet-General "twang" test were later verified by vibration tests of the Missile N-3 conducted at Martin Co., Denver. A test fixture was installed which was capable of transmitting a longitudinal oscillatory force from a shaker to the turbopump outboard brackets. The resulting frequency response data indicated that the pump rocking mode frequency, with the suction lines filled with propellant, is 18 cps. It was found that this resonant frequency could be increased to 22 cps by additional support of pump frame. The effect of increasing

C.1 (cont.)

the pump mode frequency by stiffening the pump frame upon engine oscillation characteristics was evaluated by a series of seven engine tests at Aerojet-General. The conclusion of these tests was that the increase in the pump rocking mode frequency was not effective in reducing the amplitude of pressure oscillations.

For the purposes of a qualitative study of the flow conditions at the pump inlet, a transparent lucite suction spool was installed on the oxidizer pump which allowed visual inspection of the pump inlet flow patterns. High-speed movies were made of the flow patterns during pump operation at both high and low suction pressures and flow rates. The results show that, although very few bubbles exist in the inducer section with high suction pressures and flows, the volume of bubbles on the backside of the inducer is increased by decreasing suction pressure. As the pump suction pressure approached the minimum NPSH condition, a definite shedding of vortices and bubble streamers was visible. No obvious 10 to 12 cps frequency was present.

2. Titan II Engine Transfer Function Tests

As the Titan II POGO investigation proceeded, it became obvious that a test program was necessary to experimentally define the dynamic characteristics of the first-stage Titan II engine system. Aerojet-General was assigned responsibility for the dynamic testing of a complete YLR87-AJ-5 engine. The main objective of this test program was to provide experimental frequency response data with which to verify or modify the various analytical models of the propulsion system transfer functions.

The Titan II Engine Transfer Function Test Program consisted of eight engine tests conducted during the period of 24 August to 13 November 1963. During

AMDR 9635-037, APPENDIX A

G.2 (cont.)

each test, fuel and/or oxidizer suction pressure oscillations were induced by operation of sinusoidal pulse generators at a frequency of from 5.6 to 19 cps. The frequency of excitation was incrementally changed during each test while the nominal fuel and oxidizer suction pressure was held constant. The effect of the nominal pump suction pressure (or NPSH) upon the frequency response characteristics of the engine system was thus determined.

A detailed description of the Titan II EFTF including engine hardware, test equipment, instrumentation, data reduction, test conditions, and significant results is presented in Ref 10. This report is presented in Appendix H.

APPENDIX A

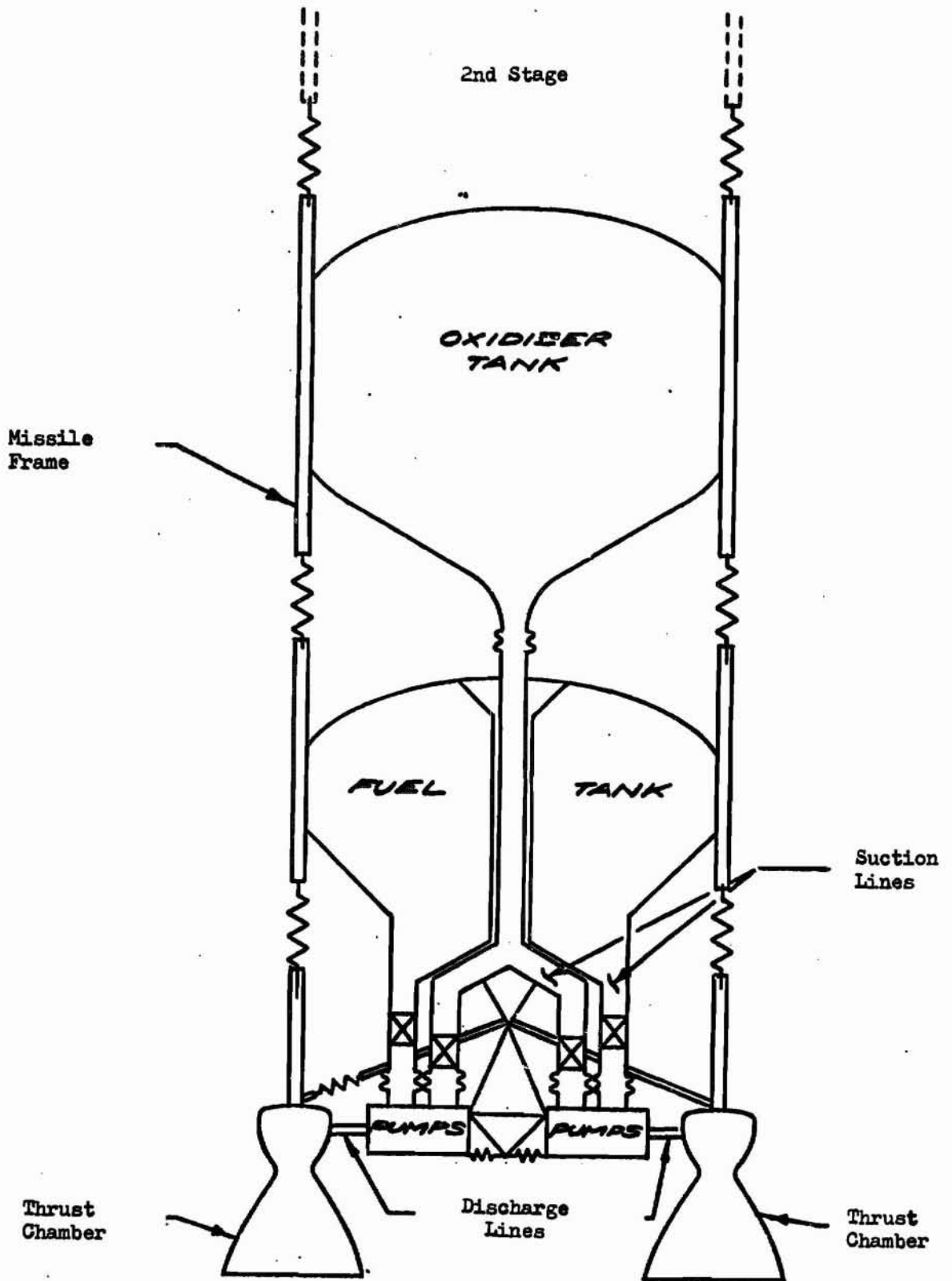
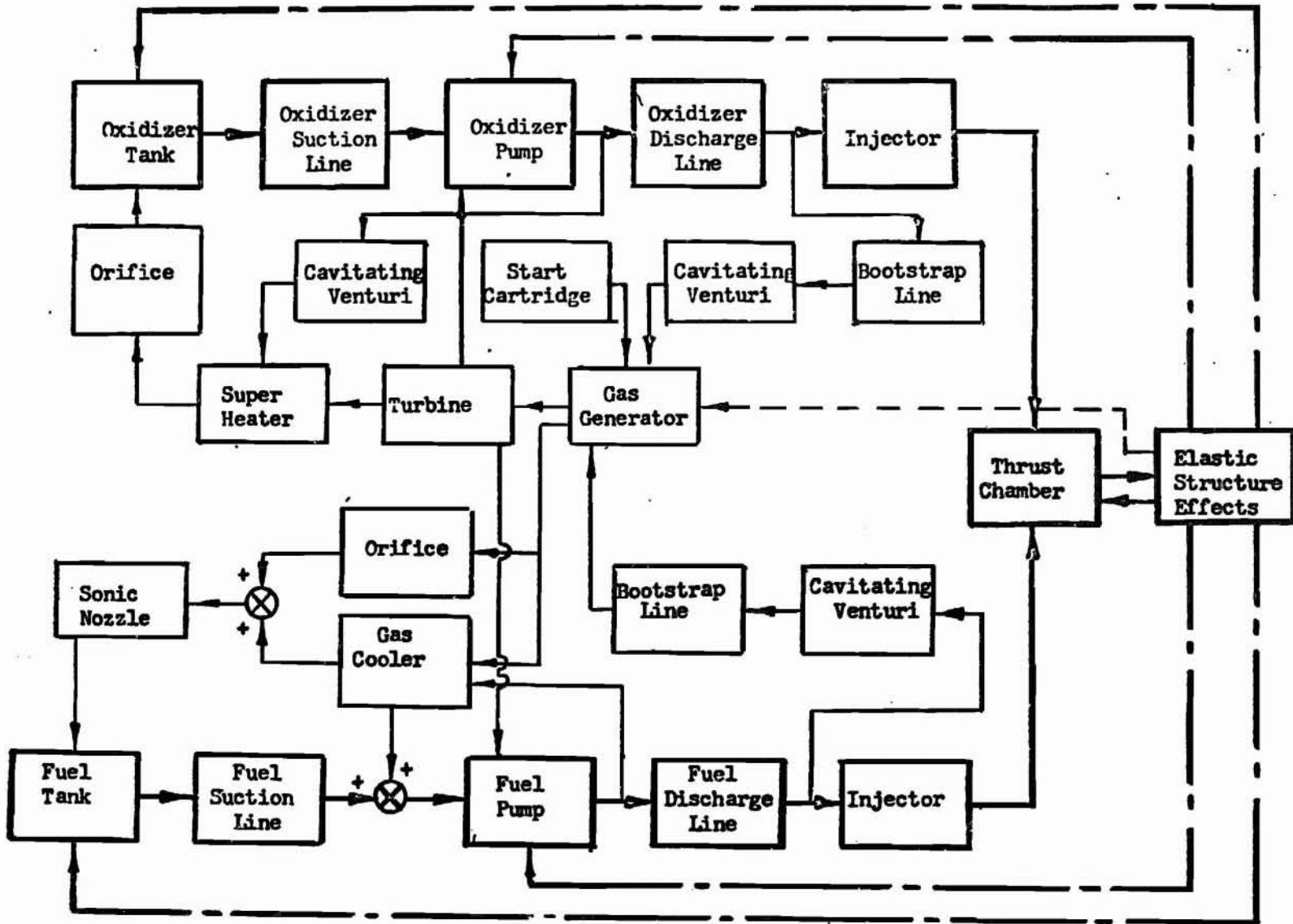


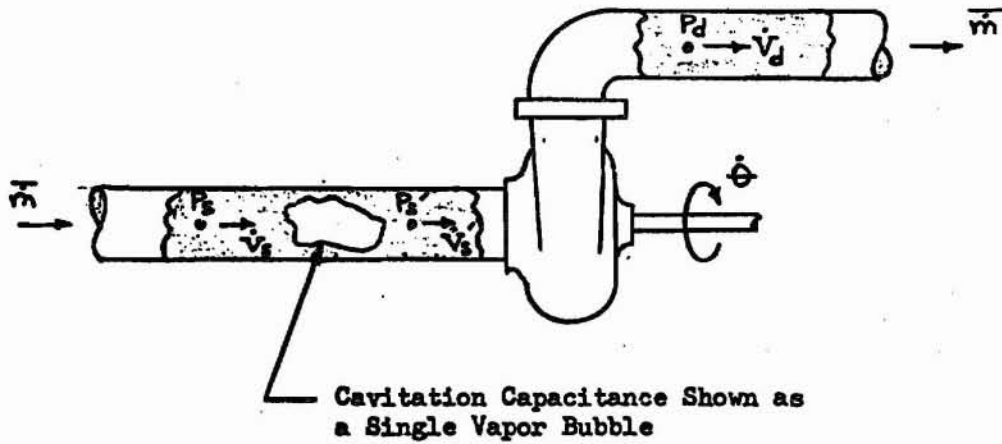
FIGURE 1 GENERAL SCHEMATIC OF THE TITAN II FIRST-STAGE ENGINE-VEHICLE COMBINATION



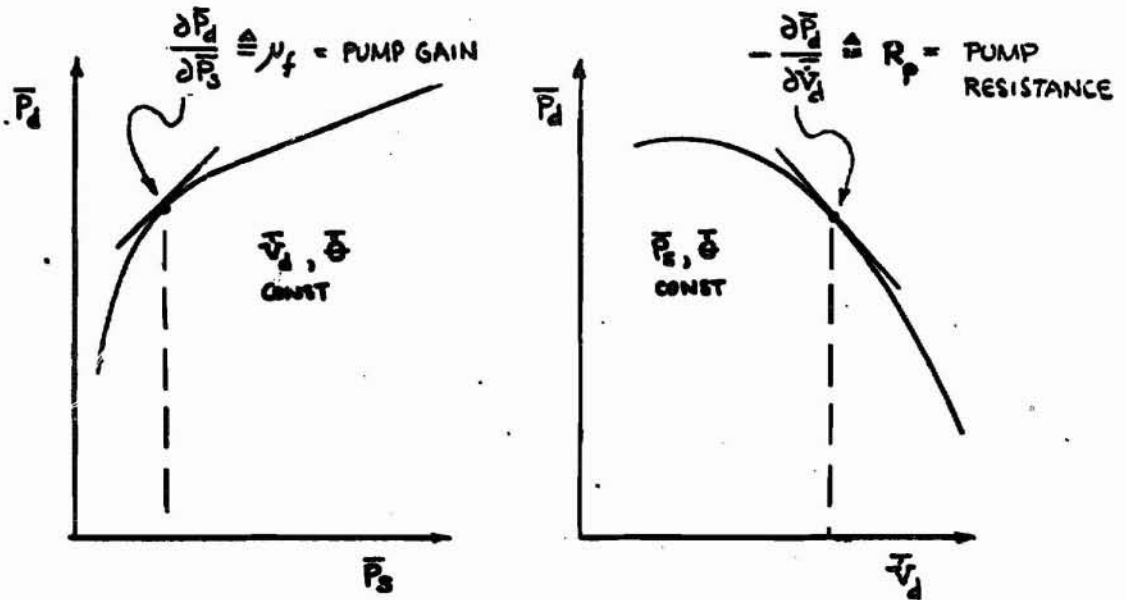
APPENDIX A

Figure 2 DETAILED BLOCK DIAGRAM OF TITAN II FIRST-STAGE ENGINE-VEHICLE COMBINATION

APPENDIX A



a) Sketch of Pump Dynamic Parameters



b) Pump Static Performance Curves

FIGURE 3 PUMP DYNAMIC CHARACTERISTICS

APPENDIX A

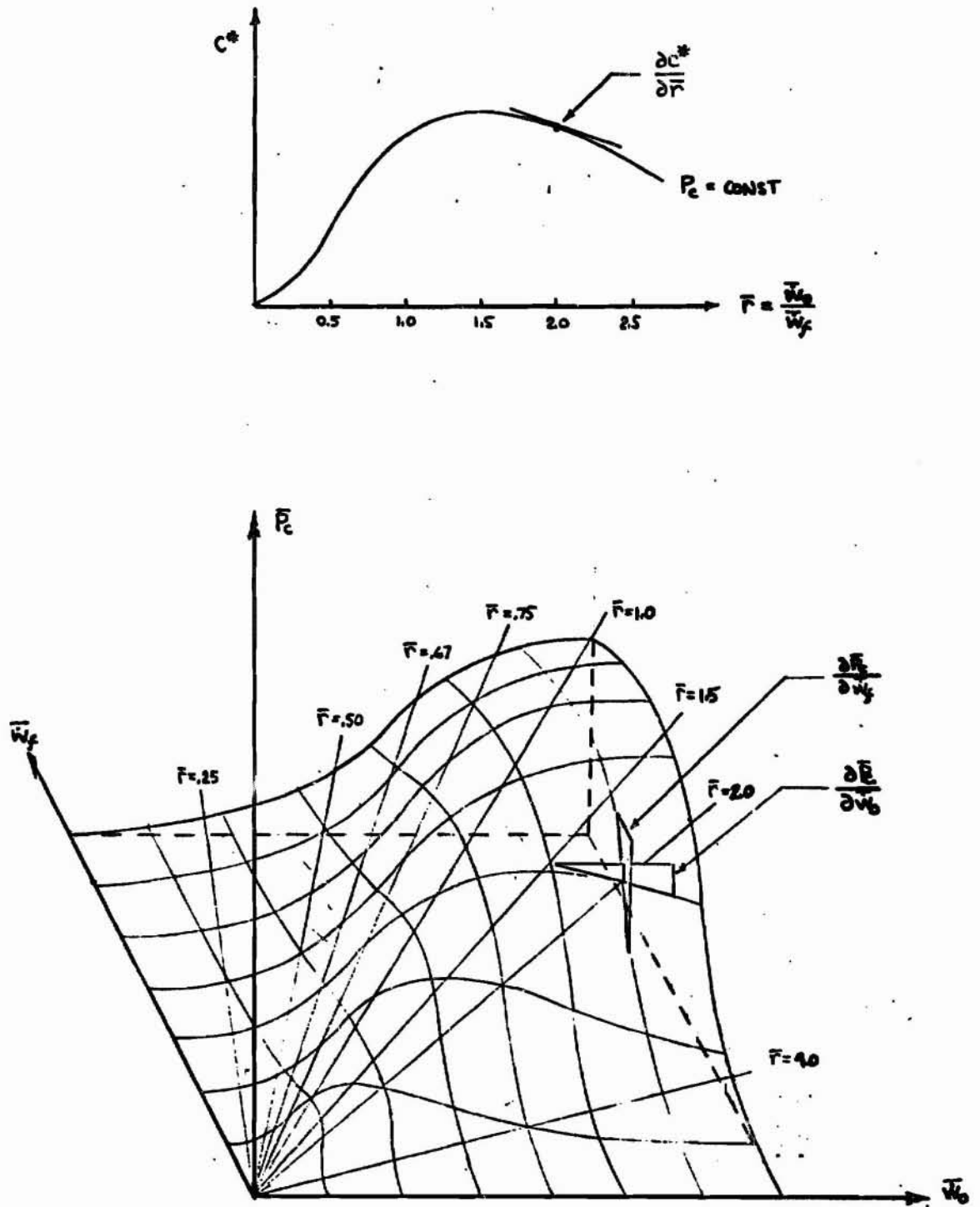


FIGURE 4 COMBUSTION CHAMBER STATIC PERFORMANCE SURFACE

APPENDIX A

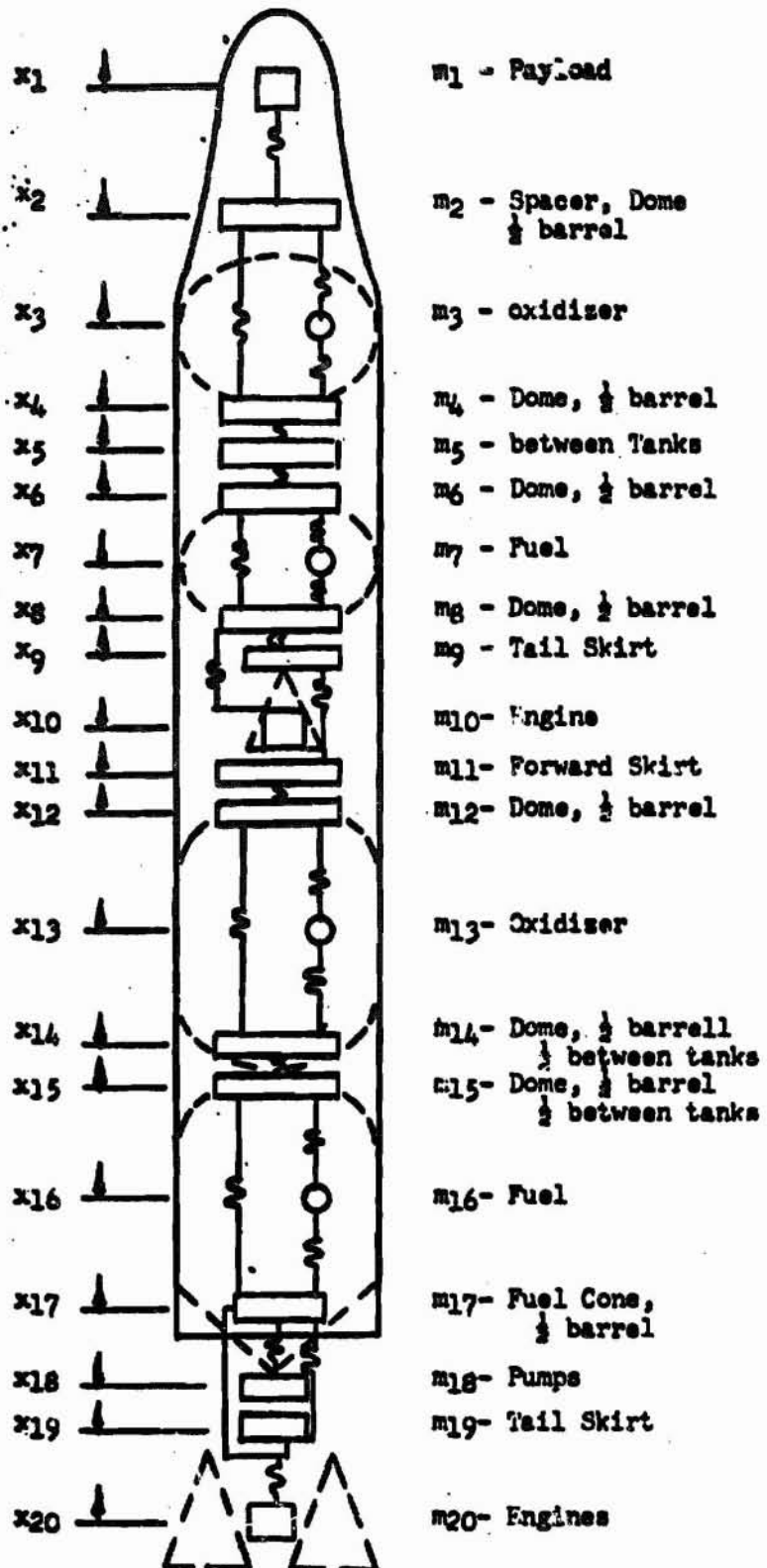


FIGURE 5 TITAN II SPRING-MASS MODEL.

V,C,2, Dynamic Tests (cont.)

represented as a spring-dashpot device, may be determined by plots of the damping force versus velocity. If a sinusoidal signal is applied to the system, then the maximum displacement is related to the maximum velocity by the simple relation

Thus the hysteresis plot for the cyclic (sinusoidal) excitation may be plotted. Hysteresis plots are shown in Figure 50, for viscous damping, coulomb (with stiction) damping and arbitrary damping.

A hysteresis test may be performed on the candidate accumulators by means of the apparatus illustrated in Figure 51. The oscillatory source could be either a small electrodynamic shaker with piston drive or a varidrive with crankshaft and piston. The oscillatory piston displacement and pressure must be accurately measured during each test. The instantaneous values of these parameters are used as inputs to an X-Y plotter to obtain the hysteresis plots. During the development of the Gemini fuel accumulator, Martin Company personnel (Ref 4) designed and used such an apparatus with good results. The static and dynamic coulomb damping constants were directly measured and minimized by the redesign of the piston O-ring seal.

The hysteresis test apparatus may also be used to measure the resonant frequency of the accumulator. The procedure is simply to increase the frequency of excitation at constant velocity until the monitored pressure amplitude is maximum. If the phase angle between the pressure and piston velocity is zero, then this frequency defines the accumulator resonance. During this test, extra care should be given to the complete removal of gas from the system.

D. ASSISTANCE IN THE ANALYSIS OF DYNAMIC TEST DATA

The objective of this task is to provide assistance to MSFC personnel (R-P&VE-PTF) in their experimental determination of the F-1 and H-1 pump dynamic characteristics from the dynamic pulse test data. The method chosen by MSFC personnel for this determination was to first obtain experimental pump frequency

V,D, Assistance in the Analysis of Dynamic Test Data (cont.)

response functions for the pump/flow facility by means of cross-spectral analysis of the oscillatory pressure data and then vary the unknown pump dynamic coefficients in the analytical model until the predicted response functions matched the measured response functions. The disadvantage of this method is that it requires that the analyst have a precise analytical description of the flow facility frequency response characteristics and that he knows the general topological "structure" of the turbopump. Thus the theoretical equations describing the dynamic performance of the pump, such as eqs 8 and 9 in Appendix A, must be assumed to be valid for all test conditions and frequencies. In order to check this assumption, it was decided that Aerojet should develop a new method for determining the pump dynamic characteristics which did not require prior knowledge of the facility dynamics and/or the pump dynamics.

The Aerojet method of pulse test data analysis, called the constrained impedance matrix method, allows the admittance matrix of the pump or any n-port hydraulic network to be determined from the measured pulse test data. This method, which is described in Appendix G, has the advantage that the "dynamic loading" effect of the fluid flow facility may be analytically removed from the data with no prior determination of its dynamic characteristics. However, the method does require that measurements be made for the system with flow pulsers operated at each of the n ports of the general network. Therefore the pump must be consecutively pulsed at both the upstream and downstream ports.

During the MSFC turbopump pulse test program, only the H-1 pump was fitted with pulsers at both the pump inlet and outlet. A sketch of the H-1 turbopump pulse test facility and pressure measurement locations are shown in Figures 52 and 53, respectively. The pressure measurements correspond to those shown in Figure 3 of Appendix G and may be used directly to obtain the pump admittance. This may be done by using eqs 9 through 14 of the Appendix, if the digitized data is numerically Fourier transformed to obtain the various pressure spectra $P_k(\omega)$. If the data is reduced by a cross-spectral density program, then eqs 13 and 14 should be replaced by the following expressions:

V,D, Assistance in the Analysis of Dynamic Test Data (cont.)

$$Z_{jk}^c(\omega) = \frac{Z_k^s(\omega) S_{jj}^s(\omega)}{S_{jk}^s(\omega) - S_{jk}^l(\omega)} \quad \left| \text{only } S_{jk}^s(\omega) - S_{jk}^l(\omega) \neq 0 \right. \quad (39)$$

$$Y_{kk}^l(\omega) = \frac{S_{kk}^s(\omega) - S_{kk}^l(\omega)}{Z_k^l(\omega) S_{kk}^s(\omega)} \quad (40)$$

where

- $S_{jk}(\omega)$ = cross power spectral density between $P_j(t)$ and $P_k(t)$
- $S_{jk}^s(\omega)$ = cross power spectral density between $P_j(t)$ and $P_k^s(t)$
- $S_{kk}^s(\omega)$ = power spectral density of $P_k(t)$
- $S_{kk}^l(\omega)$ = power spectral density of $P_k^l(t)$

Unfortunately, the H-1 turbopump pulse test data for the downstream pulsing condition was not reduced by MSFC personnel by either the Fourier analysis or cross-spectral density methods during the course of this contract. Therefore the constrained admittance matrix method could not be applied to the determination of the pump dynamic characteristics.

VI. BIBLIOGRAPHY

A. ONE-DIMENSIONAL WAVE PROPAGATION IN HYDRAULIC AND/OR PNEUMATIC LINES

- 1.* Auslander, D. M., "Frequency Response of Fluid Lines with Turbulent Flow," SM Thesis, Engineering Projects Lab, MIT, May 1964.
2. Blade, R. J., Lewis, W., Goodykoontz, J. H., "Study of Sinusoidally Perturbed Flow in a Line Including a 90° Elbow with Flexible Supports," NASA TND 1216, July 1962.
3. Brown, F. T., "The Transient Response of Fluid Lines," Jour of Basic Engr, Trans ASME, Series D, Vol 84, 1964, p 547.
- 4.* Brown, F. T., "Pneumatic Pulse Transmission with Bistable-Jet-Relay Reception and Amplification," ScD Thesis, Engineering Projects Lab, MIT, May 1962.
5. Brown, F. T. and Nelson, S. E., "Step Responses of Liquid Lines with Frequency-Dependent Effects of Viscosity," ASME Paper 64-WA/FE-6, 1964.
6. D'Souza and Oldenburger, "Dynamic Response of Fluid Lines," ASME Paper 63-WA-73, 1963.
7. D'Souza, "Dynamic Response of Fluid Flow Through Straight and Curved Lines," PhD Thesis, Purdue University, June 1963.
8. Ezekiel, F. D., Paynter, H. M., "Fluid Power Transmission," Chap 5 of Fluid Power Control, edited by Blackburn, Reethof, and Shearer, The Technology Press of MIT and John Wiley & Sons, New York, 1960, pp 130-143.
9. Ezekiel, F. D. and Paynter, H. M., "Firmoviscous and Anelastic Properties of Fluids and Their Effects on the Propagation of Compression Waves," ASME Paper 59-HYD-19, 1959.
10. Fay, R. C., "Attenuation of Sound in Tubes," Jour of Acoustical Soc of Am, Vol 12, 1940.
11. Fisher, R. C., "Theory of Sound Transmission in a Cylindrical Tube Filled with Viscous Fluid," Document No. D-18142, Boeing Aircraft Co., March 6, 1957.
12. Hunt, F. V., "Propagation of Sounds in Fluids," American Institute of Physics Handbook, McGraw-Hill, New York, 1957.

* All entries denoted by an asterisk are of special interest.

13. Iberall, A. S., "Attenuation of Oscillatory Pressures in Instrument Lines," Jour of Research, National Bureau of Standards, Vol 45, July 1950, R. P. 2115.
14. Markham, J. J., Beyer, R. T. and Lindsay, R. B., "Absorption of Sound in Fluids," Revue Modern Physics, Vol 23, No 4, 1951, pp 353-411.
15. Morse, P. M., "Transmission of Sound Inside Pipes," Jour of Acoustical Soc of Am, Vol 11, 1939, p 205.
16. Nelson, S. E., "Analysis of Viscous Dispersion Effects on Responses in Liquid Filled Lines," SM Thesis, Engineering Projects Lab, MIT, January 1964.
- 17.* Nichols, N. B., "The Linear Properties of Pneumatic Transmission Lines," Instrument Soc of Am Trans, Vol 1, No. 1, Jan 1962.
18. Oldenburger, R., Goodson, R. E., "Simplification of Hydraulic Line Dynamics by Use of Infinite Products," Jour of Basic Engr, ASME Trans, March 1964, pp 1-10.
19. Paynter, H. M., "Fluid Transients in Engineering Systems," Section 20 of Handbook of Fluid Dynamics, edited by V. L. Streeter, McGraw-Hill, New York, 1961.
20. Regetz, J. D., "An Experimental Determination of the Dynamic Response of a Long Hydraulic Line," NASA TND-576, December 1960.
- 21.* Rohmann, C. P., Grogan, E. C., "On the Dynamics of Pneumatic Transmission Lines," Jour of Basic Engr, ASME Trans, Vol 79, 1957, pp 853-874.
22. Schuder, C. B., Binder, R. C., "The Response of Pneumatic Transmission Lines to Step Inputs," Jour of Basic Engr., ASME Trans, Series D, Vol 81, 1959, p 578.
23. Thurston, G. B., "Periodic Flow Through Circular Tubes," Jour of Acoustical Soc of Am, Vol 24, 1952, pp 653-656.
24. Thurston, R. N., "Wave Propagation in Fluids and Normal Solids" Chap 1 of Physical Acoustics, Vol 1, Part A, edited by W. P. Mason, Academic Press, New York, 1965.
25. Wylie, E. B., "Resonance in Pressurized Piping Systems, ASME Paper 65-FE-6, 1965.

* All entries denoted by an asterisk are of special interest.

B. WAVE PROPAGATION THROUGH ABSORPTIVE TRANSMISSION LINES

1. A Study of the Suppression of Combustion Oscillations with Mechanical Damping Devices, Pratt & Whitney Aircraft Report PWA FR 1007, Florida Research and Development Center, September 1964.
2. Alexander, G., "Acoustic Liner Damps Rocket Combustion," Aviation Week and Space Technology, August 9, 1965, p 72.
3. Beranek, L. L., Acoustics, McGraw-Hill, New York, 1954, pp 350-360.
4. Beranek, L. L., Labate, S., "Properties of Porous Acoustical Materials," Chap 12 of Handbook of Noise Control, edited by L. L. Beranek, McGraw-Hill, New York, 1961, pp 246-279.
5. Beck, A. W. H., Space-Charge Waves and Slow Electromagnetic Waves, Pergamon Press, London, 1958.
6. Binder, R. C., "The Damping of Large Amplitude Vibrations of a Fluid in a Pipe," Jour of Acoustical Soc of Am, Vol 15, 1943, pp 41-43.
7. Blackman, A. W., "Effects of Nonlinear Losses on the Design of Absorbers for Combustion Instabilities," ARS Jour., November 1960, p 1022.
- 8.* Blokhintsev, D. I., "Acoustics of a Nonhomogeneous Moving Medium," NASA TM 1399, February 1956.
9. Bolt, R. H., Ingard, U., "Absorption Characteristics of Acoustic Materials with Perforated Facings," Jour of Acoustical Soc of Am, Vol 23, No. 5, September 1951, p 533.
10. Brittain, C. P., et al, "Attenuation of Sound in Lined Air Ducts," Engineering, February 13, 1948, p 145.
11. Bucher, R. E., "A Mathematical Analysis of the Suppression of High Frequency Combustion Instabilities by a Sound Absorbing Liner," AIAA Paper No. 65-107, Presented at AIAA 2nd Aerospace Sciences Meeting, New York, January 25-27, 1965.
12. Cremer, L., "Theory of Damping of Airborne Sound in a Rectangular Duct with Absorbing Walls and the Maximum Attenuation Constant," Acustica, Vol 3, 1953, p 249.

* All entries denoted by an asterisk are of special interest.

V,B, Wave Propagation Through Absorptive Transmission Lines (cont.)

13. Doelling, N., "Dissipative Mufflers," Chap 17 of Handbook of Noise Control, Edited by L. L. Beranek, McGraw-Hill, New York, 1960, pp 434-465.
14. Dyer, I., "Noise Attenuation of Dissipative Mufflers," Noise Control, Vol 2, May 1956, p 50.
15. Gebhardt, G. T., "Acoustic Impedance Measurements of Liquid Pipes Containing Lossy, High Compliance Inserts," Boeing Airplane Co. Report D-15871, 15 October 1954.
16. Holland, C. M., Blade, R. S., Dorsh, G. R., "Attenuation of Sinusoidal Perturbations Superimposed on Laminar Flow of a Liquid in a Long Line," NASA TN D-3099, November 1965.
17. Holland, C. M., Blade, R. S., "Attenuation of Sinusoidal Disturbances in a Non Viscous Liquid Flowing in a Long Line with Distributed Leakage," NASA TN D-3565, August 1966.
18. Ingard, U., "Attenuation and Regeneration of Sound in Ducts and Jet Diffusers," Jour of Acoustical Soc of Am, Vol 31, 1959, pp 1202-1212.
19. King, A. J., "Attenuation of Sound in Lined Air Ducts," Jour of Acoustical Soc of Am, Vol 30, 1958, p 505.
- 20.* Lambert, R. F., "Acoustic Filtering in a Moving Medium," Jour of Acoustical Soc of Am, Vol 28, 1956, pp 1054-1058.
21. Lapin, A. D., "Influence of Motion of the Medium of the Propagation of Sound in a Waveguide with Volume Resonators in the Walls," Soviet Physics Acoustics, Vol 7, No. 4, 1962, pp 360-363.
22. Lippert, W. K. R., "Sound Propagation Ducts with Side Branches," Acustica, Vol 7, No. 3, 1957, p 137.
- 23.* Myer, E., Mechel, F., Kurtze, G., "Experiments on the Influence of Flow on Sound Attenuation in Absorbing Ducts," Jour of Acoustical Soc of Am, Vol 30, No. 3, 1958, pp 165-174.
- 24.* Mechel, F., et al, "Research on Sound Propagation in Sound-Absorbent Ducts with Superimposed Air Streams," Vol I, II, III, Report No. AMRL TDR-62-140 (I,II,III), USAF Aerospace Medical Division, Wright-Patterson AFB, Ohio, December 1962.

* All entries denoted by an asterisk are of special interest.

V,B, Wave Propagation Through Absorptive Transmission Lines (cont.)

25. Pridmore-Brown, D. C., "Sound Propagation in a Fluid Flowing Through an Attenuating Duct," Jour Fluid Mechanics, Vol 6, 1958, p 393.
26. Pierce, J. R., "Coupling of Modes of Propagation," Jour of Applied Physics, Vol 25, 1954, p 179.
27. Ribner, H., "Reflection, Transmission and Amplification in a Moving Medium," Jour of Acoustical Soc of Am, Vol 29, 1957, p 435.
28. Rzhavkin, W. N., "Resonance Sound Absorber with Yielding Wall," NACA TM 1273, May 1951.
29. Sivian, L. J., "Sound Propagation in Ducts Lines with Absorbing Materials," Jour of Acoustical Soc of Am, Vol 9, 1937, p 135.

C. BUBBLE DYNAMICS AND WAVE PROPAGATION IN A LIQUID CONTAINING GAS BUBBLES

1. Baird, M., "Resonant Bubbles in a Vertically Vibrating Liquid Column," Canadian Jour of Chem Engr, April 1963, pp 52-55.
2. Baird, M., "Sonic Resonance of Bubble Dispersions," Chemical Engr Society, Vol 18, 1963, pp 685-687.
3. Chow, J. W., "Attenuation of Acoustic Waves in Dilute Emulsions and Suspensions," Jour of Acoustical Soc of Am, Vol 36, 1964, pp 2395-2401.
4. Carstensen, E. L., Foldy, L. L., "Propagation of Sound Through a Liquid Containing Bubbles," Jour of Acoustical Soc of Am, Vol 19, 1947, pp 481-501.
5. Davids, N., Thurston, E. G., "Acoustic Impedance of a Bubbly Mixture and Its Size Distribution Function," Jour of Acoustical Soc of Am, Vol 22, 1950, pp 20-23.
- 6.* Devin, G., "Survey of Thermal, Radiation and Viscous Damping of Pulsating Air Bubbles in Water," Jour of Acoustical Soc of Am, Vol 31, 1959, pp 1654-1667.
7. Epstein, P. S., Carhard, R. R., "The Adsorption of Sound in Suspensions and Emulsion. I. Water Fog in Air," Jour of Acoustical Soc of Am, Vol 25, 1953, pp 553-565.

* All entries denoted by an asterisk are of special interest.

V,C Bubble Dynamics and Wave Propagation in a Liquid Containing Gas Bubbles (cont.)

- 8.* Foldy, L. L., "General Theory of the Propagation of Sound Through a Liquid Containing Air Bubbles," OSRD Report 3601, NDRC Report 6.1-1378 PB 31027, April 1944.
9. Fox, Curley, Larson, "Phase Velocity and Adsorption Measurements in Water Containing Air Bubbles," Jour of Acoustical Soc of Am, Vol 27, 1955, pp 534-539.
10. Glasgow, V. L., "Analysis of the Effect of Gas Injection on Acoustic Velocity," Unpublished Notes by V. L. Glasgow, Fluid Mechanics & Thermodynamics Branch, Propulsion Division, MSFC, Huntsville, Ala.
- 11.* Gouse, S. W., Brown, G. A., "Some Remarks on the Velocity of Sound for Two Phase Mixtures and Flows," MIT Report 8C40-1, April 1963.
12. Hawkins, A., "Measurement of the Resonant Frequency of a Bubble Near a Rigid Boundary," Jour of Acoustical Soc of Am, Vol 37, 1965, pp 1505-1508.
- 13.* Hsieh, Din-Yu, "Some Analytical Aspects of Bubble Dynamics," Jour of Basic Engr, ASME Trans, Vol 87(3), 1965, pp 991-1005.
14. Houghton, G., "Theory of Bubble Pulsation and Cavitation," Jour of Acoustical Soc of Am, Vol 35, 1963, pp 1387-1393.
15. Laird, D. T., Kendig, P. M., "Attenuation of Sound in Water Containing Air Bubbles," Jour of Acoustical Soc of Am, Vol 24, 1952, pp 29-32.
- 16.* Silberman, E., "Sound Velocity and Attenuation in Bubbly Mixtures Measured in Standing Wave Tubes," Jour of Acoustical Soc of Am, Vol 29, 1957, pp 925-935.
- 17.* Spitzer, L., "Acoustic Properties of Gas Bubbles in a Liquid," NDRC Report No. 6, 1-sr20-918, 1943.
18. Strasburg, M., "The Pulsation Frequency of Nonspherical Gas Bubbles in Liquids," Jour of Acoustical Soc of Am, Vol 25, 1953, pp 536-537.
19. Wood, A. B., A Textbook of Sound, G. Bell & Sons, London, 1957, pp 360-363.
- 20.* Worlund, A. L., et al, "The Reduction of Pogo Effects by Gas Injection" AIAA Paper 66-560 presented at the Propulsion Joint Specialists Conf., Colorado Springs, June 1966.

* All entries denoted by an asterisk are of special interest.

D. PREDICTION OF THE SIZE AND THERMAL PROPERTIES OF GAS BUBBLES

1. Clark and Larsen, "The Dynamics of Gas-Vapor Bubbles in Binary Systems," Proc Royal Soc (London), Series A, #283, 1965, p 50-63.
2. Foster, H. K., "Diffusion in a Moving Medium with Time Dependent Boundaries," Jour AI ChE, Vol 3-4, 1957-58, p 535.
3. Foster, H. K., Zuber, N., "Growth of a Vapor Bubble in a Superheated Liquid," Jour of Applied Physics, Vol 25, 1954, p 474.
4. Han, C. Y., Griffith, P., "The Mechanism of Heat Transfer in Nucleate Pool Boiling," Tech Report 19, MIT, February 1962.
- 5.* L'Ecuyer, M. R., Murphy, N. B., "Energy Transfer from a Liquid to Gas Bubbles Forming at a Submerged Orifice," NASA TN D-2547, January 1965.
6. Mullins, W. W., Sekerka, R. F., "Morphological Stability of a Particle Growing by Diffusion or Heat Flow," Jour of Applied Physics, Vol 34, 1963, p 323.
7. Plesset, M. S., Zwick, S. A., "The Growth of Vapor Bubbles in Super Heated Liquid," Jour of Applied Physics, Vol 25, 1954, pp 493-500.
- 8.* Silberman, E., "Production of Bubbles by Disintegration of Gas Jets in Liquids," Proc Midwest Conf on Fluid Mechanics, 5th Ed, 1957, p 263.
9. Silberman, E., "Air Water Mixture Flow Through Orifices, Bends and Other Fittings in a Horizontal Pipe," St. Anthony Falls Hydraulic Lab, Univ of Minn, Report FR-63, September 1960.
10. Scriven, L. F., "On the Dynamics of Phase Growth," Chem Engr Sci., Vol 10, 1959, pp 1-13.
- 11.* Sullivan, Hardy, Holland, "Formation of Air Bubbles at Orifices Submerged Beneath Liquids," AI ChemE Jour, Vol 10, 1964, pp 685-687.
- 12.* Yang, Wen-Jei, Clark, J. A., "On the Application of the Source Theory to the Solution of Problems Involving Phase Change, Part 1 - Growth and Collapse of Bubbles," Jour of Heat Transfer, ASME Trans, Vol 86(2), 1964, pp 207-212.

* All entries denoted by an asterisk are of special interest.

V,D, Prediction of the Size and Thermal Properties of Gas Bubbles (cont.)

13. Zwick, S. A., "Growth and Collapse of Vapor Bubbles," CIT Report R-21-19, December 1954.
14. Zwick, S. A., "Growth of Vapor Bubbles in a Rapidly Heated Liquid," CIT Report R-85-13, September 1959.

E. LUMPED PARAMETER PASSIVE STABILIZING DEVICES

1. Bies, D., Wilson, O., "Acoustic Impedance of a Helmholtz Resonator at a Very High Amplitude," Jour of Acoustical Soc of Am, Vol 29, 1957, pp 711-714.
2. Bickford, L. L., Meisenholder, S. G., Moss, J. F., "Apollo Low Frequency Combustion Stability Analysis," ETRD 9647; 1.3-74R, Aerojet-General Sacramento, 2 November 1964.
3. Fox, J. L., "Preliminary Investigation of Helmholtz Resonators for Damping Pressure Fluctuations in a 3-6-inch Ramjet at Mach Number 1.90," NACA RM E51005, 1951.
4. Hixson, E. L., et al, "Resonant Side-Branch Acoustical Filters for a Liquid Piping System," Jour of Acoustical Soc of Am, Vol 34, 1962, pp 594-602.
5. Iwanicki, L. R., Fontaine, R. J., "Sensitivity of Rocket Engine Stability to Propellant Feed System Dynamics," AIAA Paper No. 65-558, AIAA Propulsion Joint Specialist Conf, Colorado Springs, Colorado, June 14-18, 1965.
6. Ingard, U., "On the Theory and Design of Acoustic Resonators," Jour of Acoustical Soc of Am, Vol 25, No. 6, November 1953, p 1037.
7. Ingard, U., Labate, S., "Acoustic Circulation Effects and the Nonlinear Impedance of Orifices," Jour of Acoustical Soc of Am, Vol 22, No. 2, March 1950, p 211.
8. Lewis, W., Blade, R. J., Dorsch, R. G., "Study of the Effect of a Closed-End Side Branch on Sinusoidally Perturbed Flow of Liquid in a Line," NASA TN D-1876, September 1963.
9. Lewis, W., Blade, R. J., "Analysis of Effect of Compensating-Bellows Device in a Propellant Line as a Means of Suppressing Rocket Pump Inlet Perturbation," NASA Report TN D-2409, August 1964.

* All entries denoted by an asterisk are of special interest.

V,E, Lumped Parameter Passive Stabilizing Devices (cont.)

10. Lippert, W. K. R., "Sound Propagation in Ducts with Side Branches," Acustica, Vol 7, No. 3, 1957, - 137.
11. Id, Y. T., "Stabilization of Low-Frequency Oscillations of Liquid Propellant Rockets with Fuel Line Stabilizer," Jet Propulsion, Vol 26, No. 1, January 1956, p 26.
12. Thurston, G., Hargrove, L., Cook, W., "Nonlinear Properties of Circular Orifices," Jour of Acoustical Soc of Am, Vol 29, 1957, p 992.

F. SERVO-MECHANISM CONTROLS TO GOVERN PROPULSION SYSTEM FEEDBACK

1. Freeman, N. G., "Proposal for a Micro-Accumulator Solution for the Titan II Axial Oscillation Problem," Martin-Denver Report TM-0451-23-63, 1963.
2. Lee, Y. C., Gore, M. R., Ross, C. G., "Stability and Control of Liquid Propellant Rocket Systems," Jour of Am Rocket Soc, Vol 23, March-April 1953, p 75.
3. Marble, F. E., Cox, D. W., Jr., "Servo-Stabilization of Low-Frequency Oscillations in a Liquid Bipropellant Rocket Motor," Jour of Am Rocket Soc, Vol 23, March-April 1953, p 63.
4. Tsien, H. W., "Servo-Stabilization of Combustion in Rocket Motors," Jour of Am Rocket Soc, Vol 22, September-October 1952, p 256.

G. REDUCTION OF DYNAMIC DATA

1. Bendat, J. W., et al, "Application of Statistics to the Flight Vehicle Vibration Problem," ASD Tech Report 61-123, 1961.
- 2.* Bendat, J. S., et al, "Analytical Study of Vibration Data Reduction Methods," Technical Products Co Report, Contract NAS8-5093) 1963.
3. Bendat, J. S., and Piersol, A. G., Measurement and Analysis of Random Data, Wiley, 1966.
- 4.* Blackman, R. B., Tukey, J. W., The Measurement of Power Spectra, Dover, 1958.

* All entries denoted by an asterisk are of special interest.

V,G, Reduction of Dynamic Data (cont.)

5. Curtis, A. J., "Concepts in Vibration Data Analysis," Chap 22 of Shock and Vibration Handbook, edited by Harris & Crede, McGraw-Hill, New York, 1961.
6. Lunney, E. L., "Introduction to Data Analysis and Testing," Chap 21 of Shock and Vibration Handbook, edited by Harris & Crede, McGraw-Hill, New York, 1961.
7. Langill, A. W., Automatic Control Systems Engineering, Vol 2, Prentice-Hall, 1965.

H. DYNAMIC ANALYSIS OF PROPELLANT FEED SYSTEMS BY USE OF MATRIX METHODS AND IMPEDANCE TECHNIQUES

1. Bolinder, "Note on the Matrix Representation of Linear Two-Port Networks," Jour of Inst Radio Eng (Trans on Circuit Theory) Vol CT-4, 1957, pp 337-339.
2. Brown, F. T., "On the Stability of Fluid Systems," Proceedings of the Fluid Amplification Symposium, Harry Diamond Labs, Vol I, Mar 1964.
3. Brown, F. T., Graber, S. D., Wallhagen, R. E., "Investigation of Stability Predictions of Fluid Jet Amplifier Systems" NASA CR 54244, October 1964.
4. Cauer, W., Synthesis of Linear Communication Networks, McGraw-Hill, New York, 1958, Chap 3,4, Appendix 1.
5. Getgen, L. E., "Application of Matrix Algebra to Circuit Design," Electro-Technology, February 1963.
6. Guillemin, E., Synthesis of Passive Networks, McGraw-Hill, New York, 1957, Chap 6.
7. Guillemin, E., Communication Networks, Wiley & Sons, New York, 1935, pp 69-75.
8. Kopp, E. H., "Matrices for Basic Two-Port Networks," Electro-Technology, March 1964.

* All entries denoted by an asterisk are of special interest.

V,H, Dynamic Analysis of Propellant Feed Systems (cont.)

9. Hixson, E. L., "Mechanical Impedance and Mobility," Chap 10 in Shock and Vibration Handbook, edited by Harris & Crede, McGraw-Hill, New York, 1961.
10. Mason, S. J. and Zimmermann, H. J., Electronic Circuits, Signals, and Systems, Wiley & Sons, New York, 1960.
11. Molloy, C. T., "Use of Four-Pole Parameters in Vibration Calculations," Jour of Acoustical Soc of Am, Vol 29, 1957, pp 842-853.
- 12.* Pestel, E., Leckie, F. A., Matrix Methods in Elastomechanics, McGraw-Hill, New York, 1963, pp 148-152, 187-191.
13. Pipes, L. A., "The Matrix Theory of Four Terminal Networks," Philosophical Magazine, Vol 30, 1940, p 370.
- 14.* Pipes, L. A., Applied Mathematics for Engineers and Physicists, 2nd Edition, McGraw-Hill, New York, 1958, pp 182-191, 295-301.
15. Pipes, L. A., Matrix Methods for Engineering, Prentice-Hall, New Jersey, 1963, Chap 12.
16. Plunkett, R. (ed.), "Colloquium on Mechanical Impedance Methods for Mechanical Vibrations," ASME, 1958.
- 17.* Rubin, S., "Transmission Matrices for Vibration and Their Relation to Admittance and Impedance," Jour of Engr for Industry, ASME Trans, Vol 86(B) 1964, pp 9-21.
18. Rubin, S., "On the Use of Eight-Pole Parameters for the Analysis of Beam Systems," Paper 925F presented at SAE Aeronautic and Space Meeting in Los Angeles, October 1964.
19. Skilling, H. H., Electric Transmission Lines, McGraw-Hill, New York, 1951, pp 313-319.

* All entries denoted by an asterisk are of special interest.

VII. REFERENCES

1. Bickford, L. L. and Meisenholder, S. G., "'Pogo' Analysis of the Saturn Propulsion System," Aerojet-General/Sacramento Report AMDR 9635-001, 26 January 1966.
2. Bikle, F. E., et al, "Titan III 'Pogo' Analysis," Martin Co./Denver Report TM III-64-42(0494), Feb 1964.
3. Thurston, R. S., The Effect of Two-Phase Flow in KIWI B Startup Studies, Los Alamos Scientific Lab Report 6C8133(CRD) Oct 1962.
4. Meisenholder, S. G., "Dynamic Analysis of the Titan IIIB Pogo Test Data," Aerojet-General/Sacramento, Report AMDR 9635-026, Sept 1966.
5. Ross, D., Kerwin, E. M., and Dyer, I., "Flexural Vibration Damping of Multiple-Layer Plates," Bolt, Beranek & Newman, Inc., Report 564 ONRC Nonr-2311(00), 26 June 1958.
6. Ruscio, D. and Ward, T., Report on the Redesigned Fuel Accumulator to Provide Low Friction, Martin Co., Denver Report, Contract AF 04(647)-576, 7 February 1964.
7. Truxal, J. G., Automatic Feedback Control System Synthesis, McGraw-Hill, New York, 1955.
8. Alexander, J. E. and Bailey, U. M., Systems Engineering Mathematics, Prentice-Hall, New Jersey, 1962.
9. Pipes, L. A., Matrix Methods for Engineering, Prentice-Hall, New Jersey, 1963.
10. Investigation of the Transfer of Oscillations Through the YLR87-AJ-5 Engine System, Aerojet-General Report BSD TR 65-54, March 1965.

LIST OF SYMBOLS

		<u>Units</u>
a	= acoustic velocity,	in/sec
A	= cross-sectional area of hydraulic element,	in ²
A_t	= nozzle throat area,	in ²
A_{jk}	= structural modal displacement,	in.
B	= acoustical susceptance ($\frac{1}{Z}$),	lb sec/in ⁵
β_l	= effective bulk modulus of liquid,	psi
β_0	= bulk modulus of liquid,	psi
C	= acoustical capacitance,	in ⁵ /lb
C_f	= thrust coefficient	
c^*	= characteristic exhaust velocity,	in/sec
d	= mean diameter of propellant line,	in
D	= thermal diffusivity,	in ² /sec
E	= elastic modulus of line wall material,	psi
\mathcal{E}	= kinetic energy of vibration,	in-lb
f	= frequency,	cps
F	= force,	lb
F_e	= engine thrust,	lb
g_i	= vibratory acceleration,	g's
g	= gravitational constant,	in/sec ²
G	= acoustical conductance ($R_0 Y$),	in ⁵ /lb sec
h	= wall thickness of propellant line,	in.
k	= specific heat ratio	
K	= cavitation index	
K_f	= fuel mixture ratio combustion constant (eq A.12)	

AMDR 9635-037

List of Symbols (cont.)

		<u>Units</u>
K_o	= ox mixture ratio combustion constant (eq A.12)	
l	= length of fluid transmission line,	in.
l_j	= distance from injector to combustion zone,	in.
L	= acoustical inertance,	lb sec ² /in ⁵
L^*	= characteristic chamber length,	in.
M_{i_1}	= generalized mass of the i^{th} structural mode,	lb sec ² /in.
M_k	= lumped structural mass at k^{th} station,	lb sec ² /in.
m	= fluid mass,	lb sec ² /in.
\dot{m}	= steady-state mass flow	lb sec/in.
m_p	= slope of pump $\bar{\Delta P}$ vs \bar{P}_s curve	
n	= number of rocket engines	
NPSH	= pump net positive suction head,	psia
Q_{i_1}	= generalized force in i^{th} structural mode,	lb
P	= oscillatory pressure,	psi
\bar{P}	= steady-state pressure,	psia
P_c	= oscillatory chamber pressure,	psi
P_d	= oscillatory pump discharge pressure,	psi
P_s	= oscillatory pump suction pressure,	psi
\mathcal{P}	= vibratory power,	in-lb/sec
$\bar{\Delta P}$	= steady-state pressure drop,	psi
\bar{r}	= steady-state mixture ratio	
r_b	= bubble radius,	in.
R	= linearized acoustical resistance ($R_e Z$),	lb sec/in ⁵
R^h	= hydraulic resistance,	sec/in ²

AMDR 9635-037

List of Symbols (cont.)

		<u>Units</u>
\mathcal{R}	= gas constant,	in/ $^{\circ}$ R
s	= Laplace operator,	(sec) $^{-1}$
S	= entropy,	in-lb/ $^{\circ}$ R
t	= time,	sec
T	= temperature,	$^{\circ}$ R
\dot{u}	= steady-state fluid velocity,	in/sec
\dot{U}	= oscillatory fluid velocity,	in/sec
\dot{V}	= oscillatory volume flow,	in 3 /sec
\bar{V}	= steady-state volume flow,	in 3 /sec
w	= weight density,	lb/in 3
\dot{W}	= oscillatory weight flow,	lb/sec
\bar{W}	= steady-state weight flow,	lb/sec
x	= axial distance,	in.
X	= acoustical reactance ($\text{dm}Z$),	lb sec/in 5
\dot{x}	= vibrational structural velocity,	in/sec
\ddot{x}_j	= vibrational acceleration of the j^{th} structural mode,	in/sec 2
Y	= acoustical admittance (complex ratio, \dot{V}/P),	in 5 /lb sec
Y^h	= hydraulic admittance (complex ratio, \dot{W}/P),	in 2 /sec
Z	= acoustical impedance (complex ratio, P/\dot{V}),	lb sec/in 5
Z^h	= hydraulic impedance (complex ratio, P/\dot{W}),	sec/in 2
Z_c	= characteristic impedance of a transmission line,	lb sec/in 5
Z_k^h	= combustion process hydraulic impedance,	sec/in 2

Bold Face Letters

		<u>Units</u>
\bar{A}	forward transmission matrix,	mixed
\bar{B}	rearward transmission matrix,	mixed
\bar{P}	pressure column matrix,	psi
\bar{P}_k	pressure vector at port set "k",	psi
\bar{H}	pressure gain matrix	
$\dot{\bar{V}}$	volume flow column matrix,	in ³ /sec
$\dot{\bar{V}}_k$	volume flow vector at port set "k",	in ³ /sec
$\dot{\bar{W}}$	weight flow column matrix,	lb/sec
$\dot{\bar{W}}_k$	weight flow vector at port set "k",	lb/sec
\bar{Y}	acoustical admittance matrix,	in ⁵ /lb sec
\bar{Z}	acoustical impedance matrix,	lb sec/in ⁵
$\bar{\Psi}_k$	state vector at set of ports "k",	mixed

Greek Letters

α'	attenuation function (eq D.29),	nepers/in.
β'	phase function (eq D.30),	rad/in.
δ'	propagation function (eq D.24),	rad/in
δ	dimensionless thermal bubble conductance (eq E.29)	
ϵ	dimensionless bubble capacitance (eq E.30)	
ζ	acoustical damping factor	
η	absolute viscosity,	lb sec/in ²
ν	gas volume to liquid volume ratio	
$\dot{\phi}$	pump speed fluctuation,	rad/sec
Θ_1	thermal bubble damping parameter (eq E.31)	
Θ_2	radiative bubble damping parameter (eq E.32)	

Greek Letters (cont.)

	<u>Units</u>
Θ_3 viscous bubble damping parameter (eq E.33)	
χ ratio of gas compressibility to liquid compressibility (eq E.13)	
χ_0 adiabatic gas compressibility ratio (eq E.18)	
λ acoustic wave length (a/f),	in.
μ_f forward pump pressure gain	
μ_r rearward pump pressure gain	
ν kinematic viscosity,	in ² /sec
ξ_i structural damping ratio for i^{th} mode	
ρ mass density,	lb sec ² /in ⁴
σ surface tension	lb
τ surface tension factor (eq E.25)	
τ_2 combustion time delay,	sec
τ_1 injection time lag,	sec
Φ_i structural mode shape for i^{th} mode	
Φ bubble parameter, $\Theta_1 \Omega^{1/2}$	
v volume perturbation,	in ³
χ gas volume to mixture volume ratio	
ψ complex mach number (eq D.37)	
ω radian frequency,	(sec) ⁻¹
ω_a resonant frequency of lossy line shunt element,	(sec) ⁻¹
ω_0 adiabatic breathing mode frequency for bubble,	(sec) ⁻¹
ω_i resonant frequency for i^{th} structural mode,	(sec) ⁻¹
Ω dimensionless frequency, ω/ω_a	
$\Omega_{1/2}$ dimensionless frequency, $\omega/\omega_{1/2}$	
Ω_0 dimensionless frequency, ω/ω_0	

Subscripts

- a refers to acoustical parameters
- b refers to gas bubble
- d refers to pump discharge
- e refers to engine
- f refers to fuel parameters
- g refers to gas or gas/vapor mixture
- j refers to injector
- k refers to combustion
- l refers to liquid
- m refers to mixture
- o refers to oxidizer parameters
- p refers to pump parameters
- s refers to pump suction
- t refers to tank

TABLE 1

Dynamic Parameters Used in the Saturn Feed Systems Analysis

ELEMENT	PARAMETER SYMBOL	SIC LOX FEED SYSTEM	SIC FUEL FEED SYSTEM	SIB LOX FEED SYSTEM	SIB FUEL FEED SYSTEM
Z ₁	l in	245	40	41	35
	u ₀ in/sec	2.93 · 10 ²	2.65 · 10 ²	4.30 · 10 ²	2.23 · 10 ²
	a ₀ in/sec	2.46 · 10 ⁴	3.6 · 10 ⁴	3.09 · 10 ⁴	3.76 · 10 ⁴
	L _m lb sec ² /in ⁴	8.34 · 10 ⁻⁵	2.69 · 10 ⁻⁵	1.46 · 10 ⁻⁴	7.25 · 10 ⁻⁵
	Z _{co} lb sec ² /in ⁴	8.41 · 10 ⁻³	2.41 · 10 ⁻²	1.10 · 10 ⁻¹	7.81 · 10 ⁻²
	w _a sec ⁻¹	2.5 · 10 ⁴	2.5 · 10 ⁴	2.5 · 10 ⁴	2.5 · 10 ⁴
	C _a /C _m	1.0 · 10 ⁻²	1.0 · 10 ⁻²	1.0 · 10 ⁻²	1.0 · 10 ⁻²
Z ₂	l in	245	40	60	162
	u ₀ in/sec	2.93 · 10 ²	2.65 · 10 ²	2.65 · 10 ²	1.67 · 10 ²
	a ₀ in/sec	2.46 · 10 ⁴	3.6 · 10 ⁴	3.00 · 10 ⁴	3.66 · 10 ⁴
	L _m lb sec ² /in ⁴	8.34 · 10 ⁻⁵	2.69 · 10 ⁻⁵	1.32 · 10 ⁻⁴	2.52 · 10 ⁻⁴
	Z _{co} lb sec ² /in ⁴	8.41 · 10 ⁻³	2.41 · 10 ⁻²	6.61 · 10 ⁻²	5.68 · 10 ⁻²
	w _a sec ⁻¹	2.5 · 10 ⁴	2.5 · 10 ⁴	2.5 · 10 ⁴	2.5 · 10 ⁴
	C _a /C _m	1.0 · 10 ⁻²	1.0 · 10 ⁻²	1.0 · 10 ⁻²	1.0 · 10 ⁻²
Z ₃	l in	206	79	90	40
	u ₀ in/sec	3.84 · 10 ²	2.75 · 10 ²	2.65 · 10 ²	2.23 · 10 ²
	a ₀ in/sec	2.90 · 10 ⁴	3.6 · 10 ⁴	3.00 · 10 ⁴	3.76 · 10 ⁴
	L _m lb sec ² /in ⁴	9.18 · 10 ⁻⁶	5.31 · 10 ⁻⁵	1.98 · 10 ⁻⁴	8.29 · 10 ⁻⁵
	Z _{co} lb sec ² /in ⁴	1.10 · 10	2.45 · 10 ⁻²	6.61 · 10 ⁻²	7.81 · 10 ⁻²
	w _a sec ⁻¹	2.5 · 10 ⁴	2.4 · 10 ⁴	2.5 · 10 ⁴	2.5 · 10 ⁴
	C _a /C _m	1.0 · 10 ⁻²	1.0 · 10 ⁻²	1.0 · 10 ⁻²	1.0 · 10 ⁻²
Z ₄	C ₄ in ⁵ /lb	0	0	0	0
	w ₄ sec ⁻¹	∞	∞	∞	∞
	ξ ₄	—	—	—	—
Z ₅	L ₅ lb sec ² /in ⁴	0	0	0	0
	R ₅ lb sec/in	0	0	0	0
Z ₆	C ₆ in ⁵ /lb	1.5	1.0	0.2	0.6
	G ₆ in ⁵ /lb sec	0	0	0	0
Z ₇	L ₇ lb sec ² /in ⁴	1.03 · 10 ⁻⁴	2.55 · 10 ⁻⁴	5.58 · 10 ⁻⁴	9.8 · 10 ⁻⁴
	R ₇ lb sec/in	3.75 · 10 ⁻²	5.34 · 10 ⁻²	1.045 · 10 ⁻¹	1.07 · 10 ⁻¹

TABLE 2
Frequencies of the
Longitudinal Vibration Modes of the Saturn Vehicles

Mode	SATURN IB VEHICLE (201 configuration)		SATURN V VEHICLE (501 configuration)	
	Modal Frequency @ 126 sec (cps)	Modal Frequency @ 147 sec (cps)	Modal Frequency @ 135 sec (cps)	Modal Frequency @ 150 sec (cps)
1	8.26	8.68	5.68	5.44
2	9.98	12.18	6.76	7.96
3	21.1	21.2	8.66	8.66
4	23.4	23.6	9.38	9.40
5	32.5	32.6	9.81	9.87
6	36.5	39.7	13.4	14.8
7	39.0	47.9	19.2	20.6

"REPRODUCIBILITY OF THE ORIGINAL PAGE IS POOR."

TABLE 3

TABULATION OF L, C, R FOR H-1 FUEL SUCTION LINE TO PULSER

Station ξ	Length L (in)	Dia d (in)	TH t (in)	Area A (in ²)	Inertance L (sec ² /in ²)	Capacitance C_2 (in ²)	Resistance R (sec/in ²)	Description
1								Fuel Tank
2	403	15.25	.375	182.7	5.7×10^{-1}	1.53×10^{-2}		
3	20	25.0	.25	491	2.1×10^{-1}	2.6×10^{-3}		Sump Tank
4								
5	16.6							Ball Valve
6								
7	4.8	6.0	.016	28.3	4.4×10^{-4}	7.2×10^{-5}		Bellows
8	17.3	7.3 (Avg)	.134	42	1.1×10^{-3}	4×10^{-5}		
9		8.33	.148	54.5				
10								Pulser

TABLE 4

TABULATION OF L, C, R, FOR H-1 FUEL SUCTION LINE FROM PULSER TO PUMP

1		8.33	.148	54.5				
2	6	8	.016	50	3.1×10^{-4}	1.5×10^{-4}		Bellows
3	19	8.33	.148	54.5	9×10^{-4}	5.8×10^{-5}		
4	8	8	.016	50	4.1×10^{-4}	1.9×10^{-4}		Bellows
5		8.38	.148	54.5				
6	8	8	.016	50	4.1×10^{-4}	1.9×10^{-4}		Bellows
7	43	8.33	.148	54.5	2×10^{-3}	1.3×10^{-4}		
8	8	8	.016	50	4.1×10^{-4}	1.9×10^{-4}		Bellows
9		8.33	.148	54.5				

Acoustic Velocity, $a_\infty = 4000$ ft/sec @ $T = 77^\circ\text{C}$, $P = 14.7$ psi

Density, $\rho = 1.55$ lb sec²/ft⁴ = $.75 \times 10^{-4}$ lb sec²/in.⁴

Note: The above tables are incomplete because some of the bobtail facility feed system data was not available.

TABLE 5

Tabulation of L, C, R for H-1 Fuel Discharge Line

STATION #	LENGTH L (IN)	DIA d (IN)	TH t (IN)	AREA A (IN ²)	INERTANCE L (SEC ² /IN ⁶)	CAPACITANCE C (IN ²)	RESISTANCE R (SEC/IN ²)	DESCRIPTION
1	—	—	—	—	—	—	—	CATCH TANK
2	—	—	—	—	—	—	—	
3	337 (APP)	8.33	.148	54.5	1.6×10^{-2}	1.02×10^{-3}	—	
4	12	8.33	—	54.5	5.7×10^{-4}	—	—	GATE VALVE
5	406.5	8.33	.148	54.5	1.9×10^{-2}	1.24×10^{-3}	—	
6	39	—	—	—	—	—	—	VENTURI
7	48	8.33	.148	54.5	2.9×10^{-3}	1.5×10^{-4}	—	
8	—	—	—	—	—	—	—	ORIFICE
9	112	8.33	.148	54.5	5.3×10^{-3}	3.4×10^{-4}	—	
10	55	4.26	.120	14.3	10^{-2}	2.8×10^{-6}	—	
11	—	—	—	—	—	—	—	ORIFICE
12	34	4.26	.120	14.3	6.2×10^{-3}	1.7×10^{-5}	—	
13	4	4.26	—	14.3	7.3×10^{-4}	—	—	VALVE
14	16.5	4.26	.120	14.3	3×10^{-3}	8.4×10^{-6}	—	

Acoustic Velocity, $a_{00} = 4000$ ft/sec @ 77°F, $\rho = 14.7$ psi
 Density, $\rho = 1.55$ lb sec²/ft⁴ = $.75 \times 10^{-4}$ lb sec²/in.⁴

Note: The above table is incomplete because some of the hottail facility feed system data was not available.

"REPRODUCIBILITY OF THE ORIGINAL PAGE IS POOR."

TABLE 6

Tabulation of L, C, R for H-1 VOK Suction Line

Station §	L (in.)	d (in.)	L (sec ² /in. ²)	C (in. ²)	R (sec/in. ²)	Description
1	18.2	15.25	2.58x10 ⁻⁴	1.14x10 ⁻³		
2	33.5	25.	1.77x10 ⁻⁴	7.08x10 ⁻³		sump tank
3	5.1	7.75	2.80x10 ⁻⁴	8.15x10 ⁻⁵		
4	10.					ball valve
5	4.					
6	5.					bellows
7						
8						pulser
9						
10						bellows
11						
12	10	7.89	5.3x10 ⁻⁴	2.42x10 ⁻⁴		ball joint
13	9	E.C	4.64x10 ⁻⁴			bellows
14	10.5	7.89	8.75x10 ⁻⁴	3.98x10 ⁻⁴		
15	9	8.0	4.64x10 ⁻⁴			bellows
16	16.5	7.89	8.75x10 ⁻⁴	3.98x10 ⁻⁴		
17	9	8.0	4.64x10 ⁻⁴			bellows
18	42.3	7.89	2.24x10 ⁻⁴	1.02x10 ⁻³		

Acoustic Velocity, c_{ac} = 3050 ft/sec @ 162°R, P = 690 psia
 Density, ρ = 1.065 x 10⁻⁴ lb-sec²/in.⁴

Note: The above table is incomplete because some of the hobtail facility feed system data was not available.

TABLE 7
TABULATION OF L,C,R FOR N-1 LOX DISCHARGE LINE

Station S	L (in)	d (in)	L (sec ² /in ²)	C (in ²)	R (sec/in ²)	description
1	24	6.36	$1.95 \cdot 10^{-8}$	$2.73 \cdot 10^4$	$1.78 \cdot 10^3$	
2	22.					control valve
3	50.5	6.36	$4.11 \cdot 10^{-8}$	$5.74 \cdot 10^4$	$3.73 \cdot 10^{-3}$	
4	19.5	6.0	$1.78 \cdot 10^{-8}$	$4.65 \cdot 10^4$	$5.81 \cdot 10^{-2}$	bellows
5	47.5	6.36	$7.95 \cdot 10^{-8}$	$1.11 \cdot 10^3$	$7.21 \cdot 10^{-3}$	bellows
6	11.25					
7	107.5	6.36	$8.76 \cdot 10^{-8}$	$1.22 \cdot 10^3$	$7.91 \cdot 10^{-3}$	
8	12					flowmeter
9	20.	6.36	$1.63 \cdot 10^{-8}$	$2.28 \cdot 10^4$	$1.48 \cdot 10^{-3}$	
10	5.	2.17	$5.50 \cdot 10^{-8}$	$5.88 \cdot 10^6$	0	branch
11	36	6.36	$2.93 \cdot 10^{-8}$	$4.09 \cdot 10^4$	$2.65 \cdot 10^{-3}$	
12	27.7					venturi
13	25.	6.36	$2.04 \cdot 10^{-8}$	$2.84 \cdot 10^4$	$1.85 \cdot 10^{-3}$	
14	24.	6.0	$2.19 \cdot 10^{-8}$	$5.73 \cdot 10^4$	$1.12 \cdot 10^{-1}$	bellows
15						orifice
16		6.36				
17						orifice
18		6.07				6" sch 40
19						reducer
20						elbow
21						

Note: The above table is incomplete because some of the bobtail facility feed system data was not available.

TABLE 8

Tabulation of L, R, C for F-1 Fuel Suction Line
(See Note Below)

Station	Length (in)	Dia d (in)	TH t (in)	Area A (in ²)	Inertance L (sec ² /in ²)	Capacitance C (in ²)	Resistance R (sec ² /in)	Description
1								
2	86	12.4	.180	120.6	1.8×10^{-3}	2.4×10^{-3}		
3								
4								
5								
6								
7								
8								
9								
10								
11								
12								
13								
14								
15								

Note: Sections 1 through 15 represent one of two suction lines. To find the effective R, L, and C of each section for both suction lines taken together halve the inertances and resistances, and double the capacitances.

Acoustic Velocity, = 4000 ft/sec @ 77°F, P = 14.7 psi
Density, = 1.55 lb sec²/ft⁴ = $.75 \times 10^{-4}$ lb sec²/in.⁴

Note: The above table is incomplete because some of the bobtail facility feed system data was not available.

TABLE 9

Tabulation of L, C, R for F-1 Fuel Discharge Line

STATION P	LENGTH L (IN)	DIA d (IN)	TH t (IN)	AREA A (IN ²)	INERTANCE L (SEC ² /IN ⁴)	CAPACITANCE C (IN ²)	RESISTANCE R (SEC/IN ⁴)	DESCRIPTION
1	—	—	—	—	—	—	—	CATCH TANK
2	5.400	19.5	.25	298.6	4.7×10^{-2}	.394	—	EMERGENCY DUMP
3	546	10.4	.165	85.3	1.7×10^{-2}	1.06×10^{-2}	—	
4	48	19.5	.25	298.7	4.2×10^{-4}	3.5×10^{-3}	—	
5	36	12.4	.180	120.6	7.7×10^{-4}	1.02×10^{-3}	—	
6	42	19.5	.25	298.7	3.7×10^{-4}	3×10^{-3}	—	
7	—	20	—	—	—	—	—	
8	319	19.5	.25	298.7	2.8×10^{-3}	2.3×10^{-2}	—	ORIFICE # 1
9	20	16 (AVE)	.180	201	2.5×10^{-4}	1.02×10^{-3}	—	
10	—	—	—	—	—	—	—	
11	54	12.4	.180	120.6	1.2×10^{-3}	1.5×10^{-3}	—	ORIFICE # 2
12	12	11 (AVE)	.165	95	3.3×10^{-4}	2.7×10^{-4}	—	
13	—	5.17	—	—	—	—	—	ORIFICE # 3
14	48	10	.365	78.9	1.6×10^{-3}	7.4×10^{-4}	—	
15	—	4.76	—	—	—	—	—	
16	15	8.5	1.125	56.8	6.8×10^{-4}	1.5×10^{-4}	—	2 each
17	139	8.5	1.125	56.8	6.3×10^{-3}	1.4×10^{-3}	—	
18	90	5.2	.718	21.2	1.1×10^{-2}	3.3×10^{-4}	—	2 each

Acoustic Velocity, $a_{00} = 4000$ ft/sec @ 77°F, P = 14.7 psi
 Density, $\rho = 1.55$ lb sec²/ft⁴ = $.75 \times 10^{-4}$ lb sec²/in.⁴

Note: The above table is incomplete because some of the hottail facility feed system data was not available.

TABLE 10
TABULATION OF L, C, R FOR F-1 LOX SUCTION LINES

Station 5	l (in)	d (in)	L (sec ² /in ²)	C (sec/in ²)	R (sec/in ²)	Description
1	33.6	27	1.515×10^{-4}	1.124×10^{-2}		
2	40.5	20	3.34×10^{-4}	1.03×10^{-2}		
3	7.5	21	5.62×10^{-5}	1.35×10^{-3}		bellows
4	9.0	20	7.42×10^{-5}	2.30×10^{-3}		
5	7.25	21	5.43×10^{-5}	1.49×10^{-3}		bellows
6	467.3	20	3.86×10^{-3}	1.43×10^{-1}		
7	7.5	17.75	7.86×10^{-5}	1.40×10^{-3}		bellows
8	7.14	17	8.15×10^{-5}	8.70×10^{-4}		
9	17.38	17	1.98×10^{-4}	3.43×10^{-3}		
10	8.25	17.75	8.65×10^{-5}	9.83×10^{-4}		bellows
11	3.50	17	3.99×10^{-5}			
12	27.6					
13	5.4					
14	30	4.03	6.07×10^{-3}	1.20×10^{-4}		4" sch 40
15	12	4.0	2.46×10^{-3}	9.52×10^{-5}		bellows
16	12	4.03	2.43×10^{-3}	4.79×10^{-5}		4" sch 40
17	15.4					
18	4.88	18.8	4.55×10^{-5}	1.06×10^{-3}		bellows
19	16.3	17.13	1.83×10^{-4}	2.93×10^{-3}		
20	17.1	24.7	9.24×10^{-5}	8.12×10^{-3}		
21	16.3	17.13	1.83×10^{-4}	2.93×10^{-3}		
22	6.38	18.8	5.95×10^{-5}	1.39×10^{-3}		bellows
23						

Note: The above table is incomplete because some of the bobtail facility feed system data was not available.

TABLE II

TABULATION OF L, C, R FOR F-1 LOX DISCHARGE LINES

Station S	L (in)	d (in)	L (sec ² /in ²)	C (sec/in ²)	R (sec/in ²)	Description
1	96	13.5	1.74×10^{-3}	5.04×10^{-3}		14" sch 10
2	15					valve
3	213	13.5	3.86×10^{-3}	1.12×10^{-2}		14" sch 10
4	96	13.5	1.74×10^{-3}	5.04×10^{-3}		14" sch 10
5	15					valve
6	17	13.5	3.08×10^{-4}	8.98×10^{-4}		14" sch 10
7	165	19.5	1.43×10^{-3}	1.99×10^{-2}		20 sch 10
8	18.8	20	1.55×10^{-4}			bellows
9	87	19.5	7.53×10^{-4}	1.05×10^{-2}		20 sch 10
10	18.8	20	1.55×10^{-3}			bellows
11	236.3	19.5	2.05×10^{-3}	2.84×10^{-2}		20" sch 10
12	87	29.38	3.32×10^{-4}	2.52×10^{-2}		30" sch 10
13	24	6.36	1.96×10^{-3}	2.73×10^{-3}		6" sch 10
14	418.4	27.38	1.60×10^{-3}	1.21×10^{-1}		30" sch 10
15	31.38	30	1.15×10^{-4}			bellows
16	36	29.38	1.38×10^{-4}	1.04×10^{-2}		30" sch 10
17	42	13.5	7.67×10^{-4}	2.19×10^{-4}		14" sch 10
18	16	14	2.69×10^{-4}			bellows
19	61	13.5	1.10×10^{-3}	3.20×10^{-3}		14" sch 10
20	16	14	2.69×10^{-4}			bellows
21	885	13.5	1.60×10^{-2}	4.64×10^{-2}		14" sch 10
22	36	29.38	1.38×10^{-4}	1.04×10^{-2}		30" sch 10
23	121.8	19.5	1.06×10^{-3}	1.34×10^{-2}		20" sch 10

Table 11 (cont.) Tabulation of L, C, R for F-1 LOX Discharge Lines

Station ξ	L (in)	d (in)	L (sec ² /in ²)	C (sec/in ²)	R (sec/in ²)	Description
24	60	29.38	2.29×10^{-4}	1.73×10^{-2}		30" sch 10
25	16.25	30	5.95×10^{-5}			bellows
26	109.5	29.38	4.19×10^{-4}	3.16×10^{-2}		30" sch 10
27	69.7	19.5	6.05×10^{-4}	8.39×10^{-3}		20" sch 10
28	17.37	20	1.43×10^{-4}			bellows
29	36	19.5	3.12×10^{-4}	4.33×10^{-3}		30" sch 10
30	-		0	0		orifice
31	38.3	19.5	3.33×10^{-4}	4.63×10^{-3}		20" sch 10
32	-		0	0		orifice
33		19.5				20" sch 10
34	-		0	0		orifice
35		19.5				20" sch 10
36						dome cavity
37	15					dome inlet
38	15					" "
39	15					" "
40	15					" "
41						valve
42						valve
43	54					pump discharge
44	81					pump discharge

Note: The above table is incomplete because some of the bobtail facility feed system data was not available.

REPRODUCIBILITY OF THE ORIGINAL PAGE IS POOR

TABLE 12. F-1 TURROPUMP TEST DYNAMIC PARAMETERS

Index 1	Symbol	Parameter No.	Description	Tape Designation		
				A	B	C
1	Psf-1 ^a	-	Pr fuel suction line #1	x		
2	Psf-1 ^b	L-118	Pr fuel pump inlet #1	x		
3	Psf-2 ^b	D-120	Pr fuel pump inlet #2	x		
4	Pdf-1 ^a	L-124	Pr fuel pump outlet #1	x		
5	Pdf-2 ^a	L-126	Pr fuel pump outlet #2	x		
6	Pmf-1	D-371	Pr main fuel valve inlet #1	x		
7	Porf-1	D-221	Pr U. S. fuel discharge #1 orifice	x		
8	Ppf-a	D-383	Pr fuel pulser line, upstream	x		
9	Ppf-b	D-384	Pr fuel pulser line, downstream	x		
10	$\bar{x}_{t, pf}$	F-084	Vibration fuel pump inlet	x		
11	x _{pf}	G-029	Position fuel pulser	x		
12	Pso-z	D-372	Pr LOX suction line transition		x	
13	Pso-b	D-277	Pr LOX pump inlet 90" point		x	
14	Pso-c	D-180	Pr LOX pump inlet		x	
15	Pso-d	L-181	Pr LOX pump inlet, dia/opp		x	
16	Puo-1 ^a	D-128	Pr LOX pump outlet #1		x	
17	Pdo-2 ^a	D-130	Pr LOX pump outlet #2		x	
18	Pmvo-1	-	Pr main LOX valve inlet #1		x	
19	Ppo-a	D-381	Pr LOX pulser line, upstream		x	
20	Ppo-b	D-382	Pr LOX pulser line downstream		x	
21	$\bar{x}_{t, po}$	E-075	Vibration LOX pump inlet		x	
22	x _{po}	G-030	Position LOX pulser		x	
23	Psf-2 ^a	-	Pr fuel suction line #2			x
24	Psf-1 ^c	-	Pr fuel pump inlet #1, Dia/opp			x
25	Psf-2 ^c	D-355	Pr fuel pump inlet #2, Dia/opp			x
26	Paf-1 ^b	L-358	Pr fuel pump outlet #1, Dia/opp			x
27	Paf-2 ^b	L-359	Pr fuel pump outlet #2, Dia/opp			x
28	Pdo-1 ^b	-	Pr LOX pump outlet #1, Dia/opp			x
29	Pdo-2 ^b	-	Pr LOX pump outlet #2, Dia/opp			x
30	$\dot{\theta}_p$	T-001	Pump speed	x	x	x

Note: The above table is incomplete because some of the bobtail facility feed system data was not available.

TABLE 13. NECESSARY SPECTRA FOR THE F-1 TURBOPUMP TEST DATA REDUCTION

A. Spectra for Fuel Pulse Test	S _{2,2}	S _{4,4}	S _{8,8}	S _{9,9}	S _{11,11}						
B. Cross Spectra for Fuel Pulse Test	S _{1,4}	S _{2,4}	S _{3,4}	S _{3,4}	S _{6,4}	S _{7,4}	S _{8,4}	S _{9,4}	S _{10,4}	S _{11,4}	
	S _{1,11}	S _{2,11}	S _{3,11}	S _{4,11}	S _{5,11}	S _{6,11}	S _{7,11}	S _{8,11}	S _{9,11}	S _{10,11}	
C. Spectra for Oxidizer Pulse Test	S _{14,14}	S _{16,16}	S _{19,19}	S _{20,20}	S _{22,22}						
D. Cross Spectra for Oxidizer Pulse Test	S _{12,16}	S _{13,16}	S _{14,16}	S _{15,16}	S _{17,16}	S _{18,16}	S _{19,16}	S _{20,16}	S _{21,16}	S _{22,16}	
	S _{12,22}	S _{13,22}	S _{14,22}	S _{15,22}	S _{16,22}	S _{17,22}	S _{18,22}	S _{19,22}	S _{20,22}	S _{21,22}	
E. Optional Spectra and Cross Spectra	S _{23,26}	S _{24,26}	S _{25,26}	S _{26,26}	S _{27,26}	S _{28,28}	S _{29,28}				

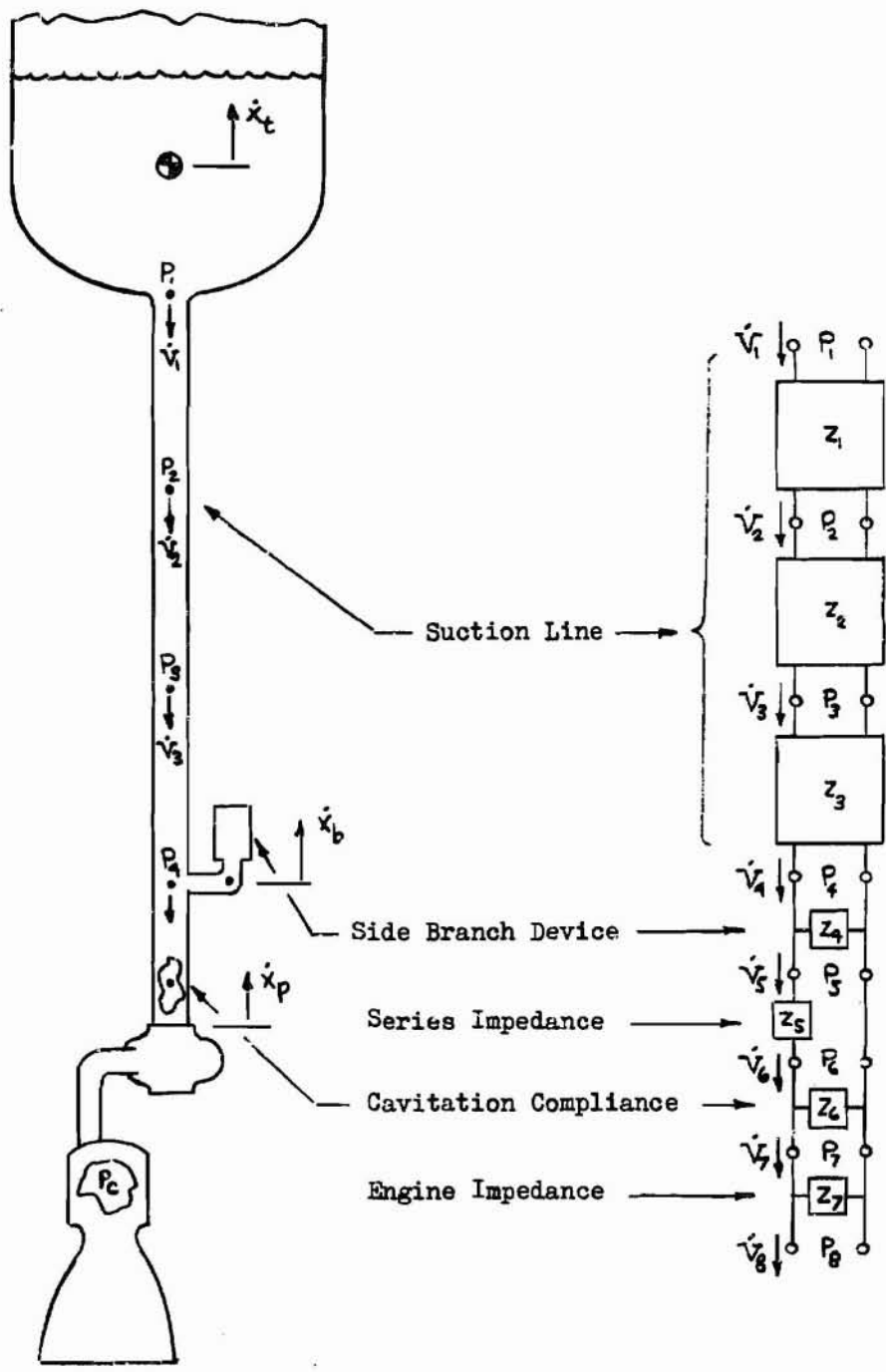


FIGURE 1. SKETCH OF THE PROPELLANT FEED SYSTEM MODEL FOR PART I

"REPRODUCIBILITY OF THE ORIGINAL PAGE IS POOR."

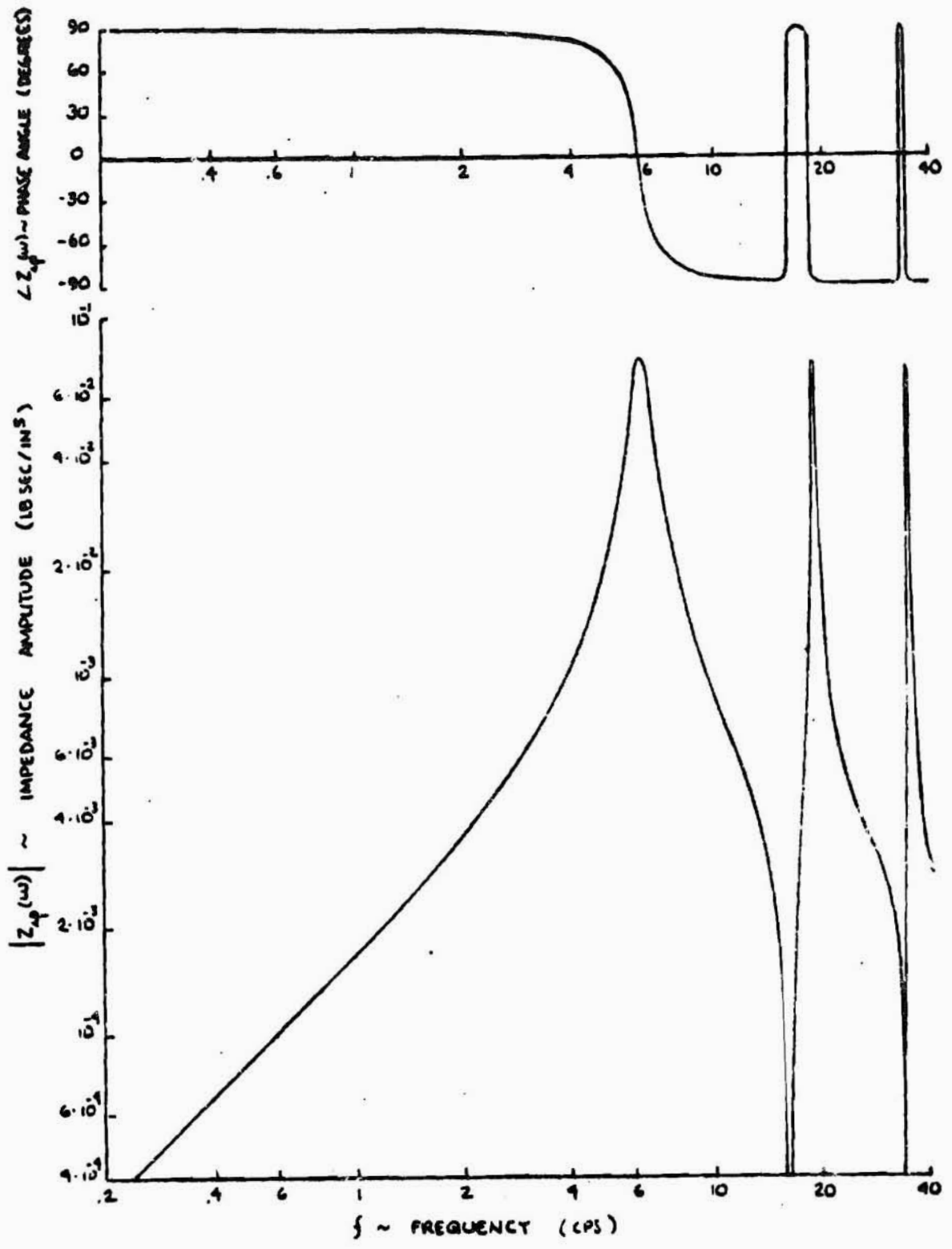


FIGURE 2. FREQUENCY RESPONSE OF $Z_{1p}(\omega)$ for the SATURN IC LOX FIRED SYSTEM

"REPRODUCIBILITY OF THE ORIGINAL PAGE IS POOR."

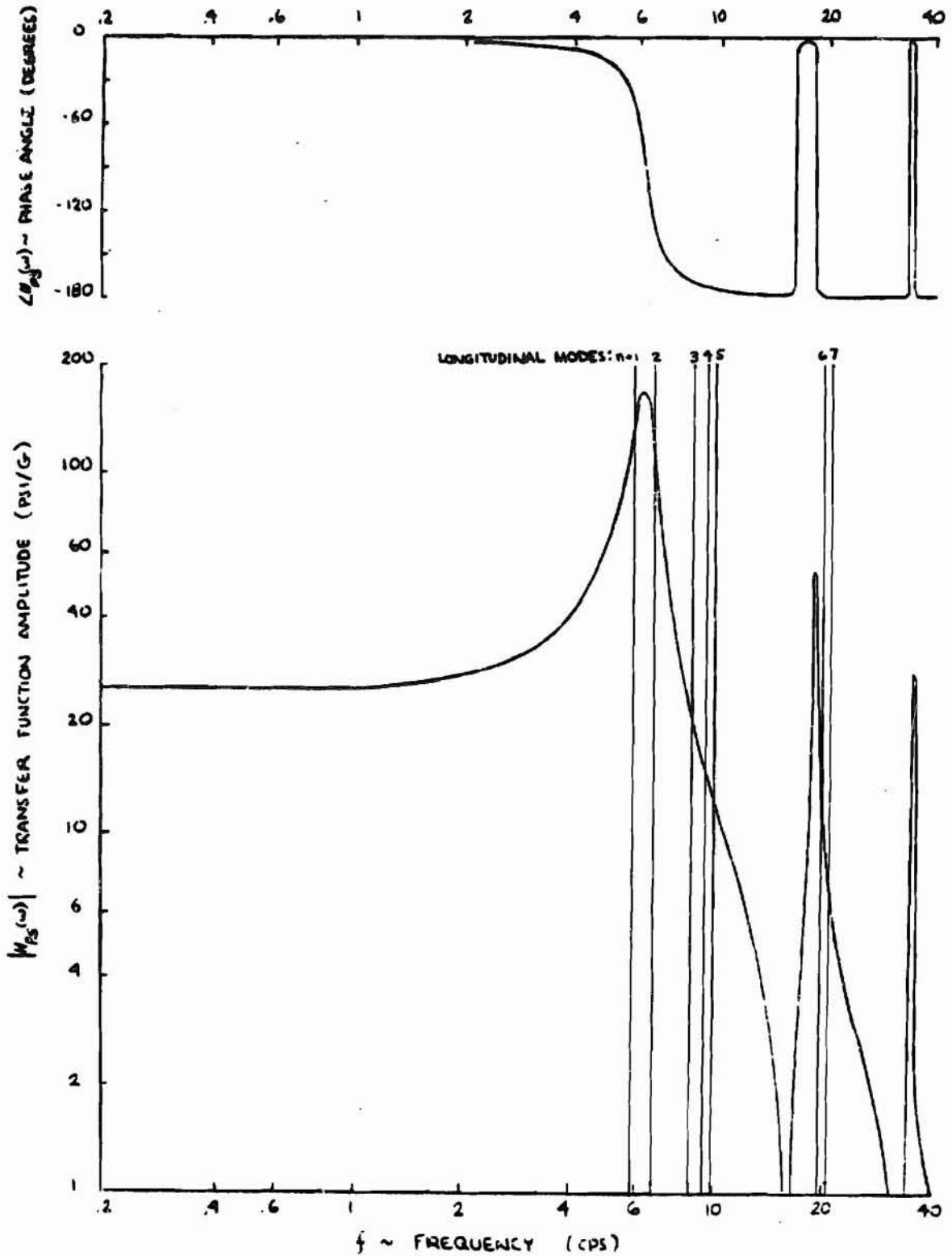


FIGURE 3. FREQUENCY RESPONSE OF $H_{ps}(\omega)$ for the SATURN IC LOX FEED SYSTEM

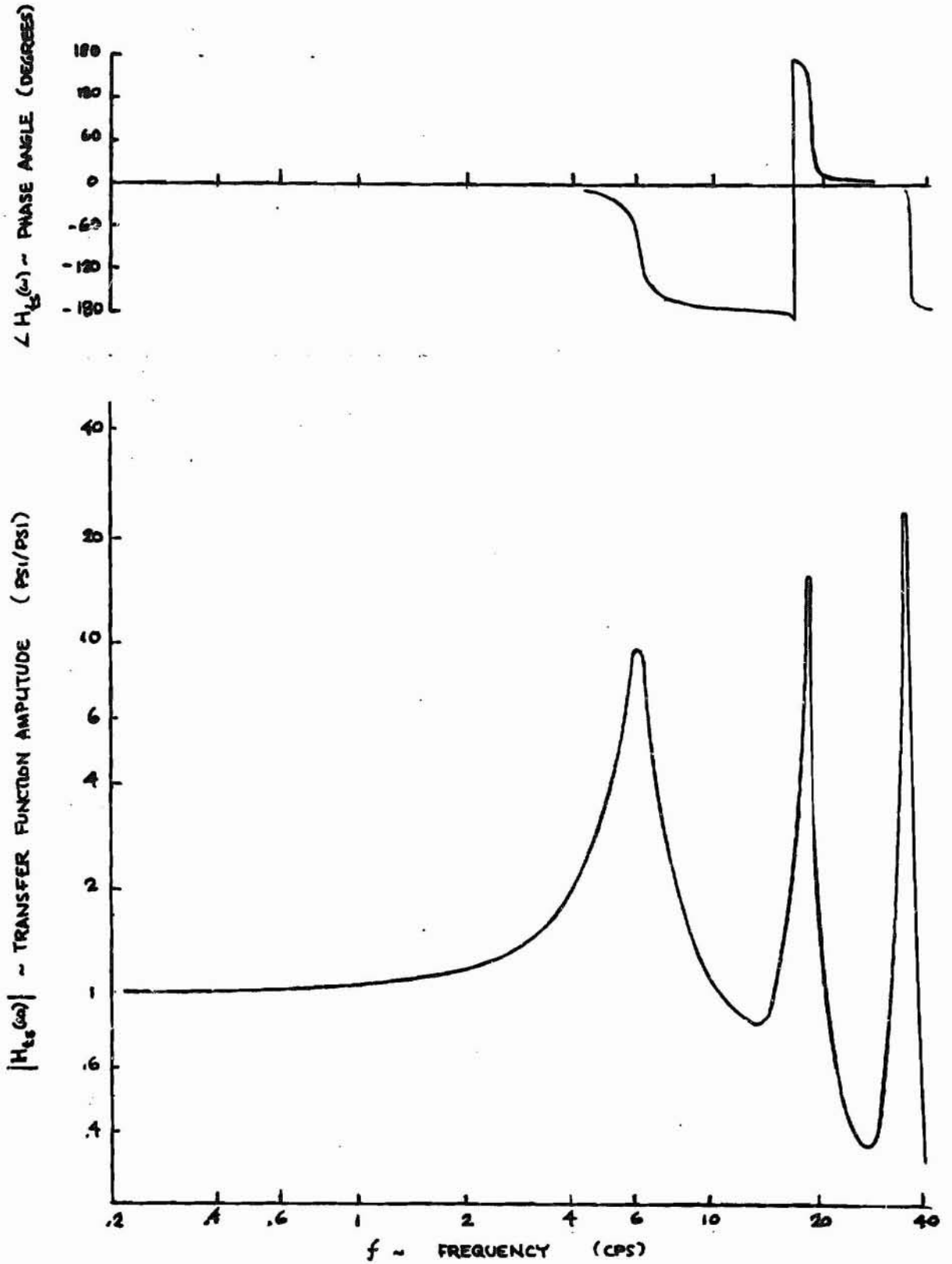


FIGURE 4. FREQUENCY RESPONSE OF $H_{t_B}(\omega)$ for the SATURN IC LOX FEED SYSTEM

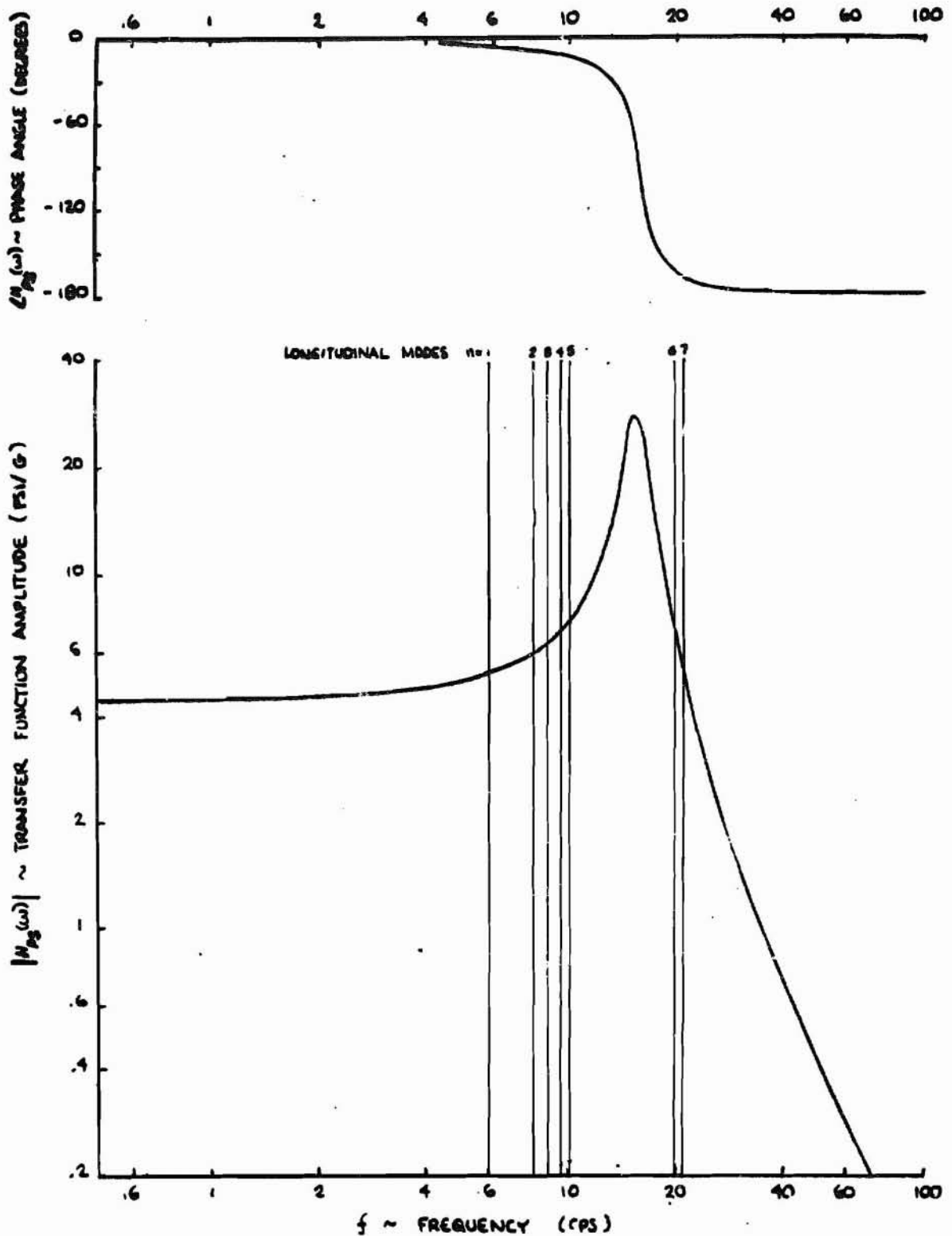


FIGURE 5. FREQUENCY RESPONSE OF $H_{Pb}(\omega)$ for the SATURN IC FUEL FEED SYSTEM

"REPRODUCIBILITY OF THE ORIGINAL PAGE IS POOR."

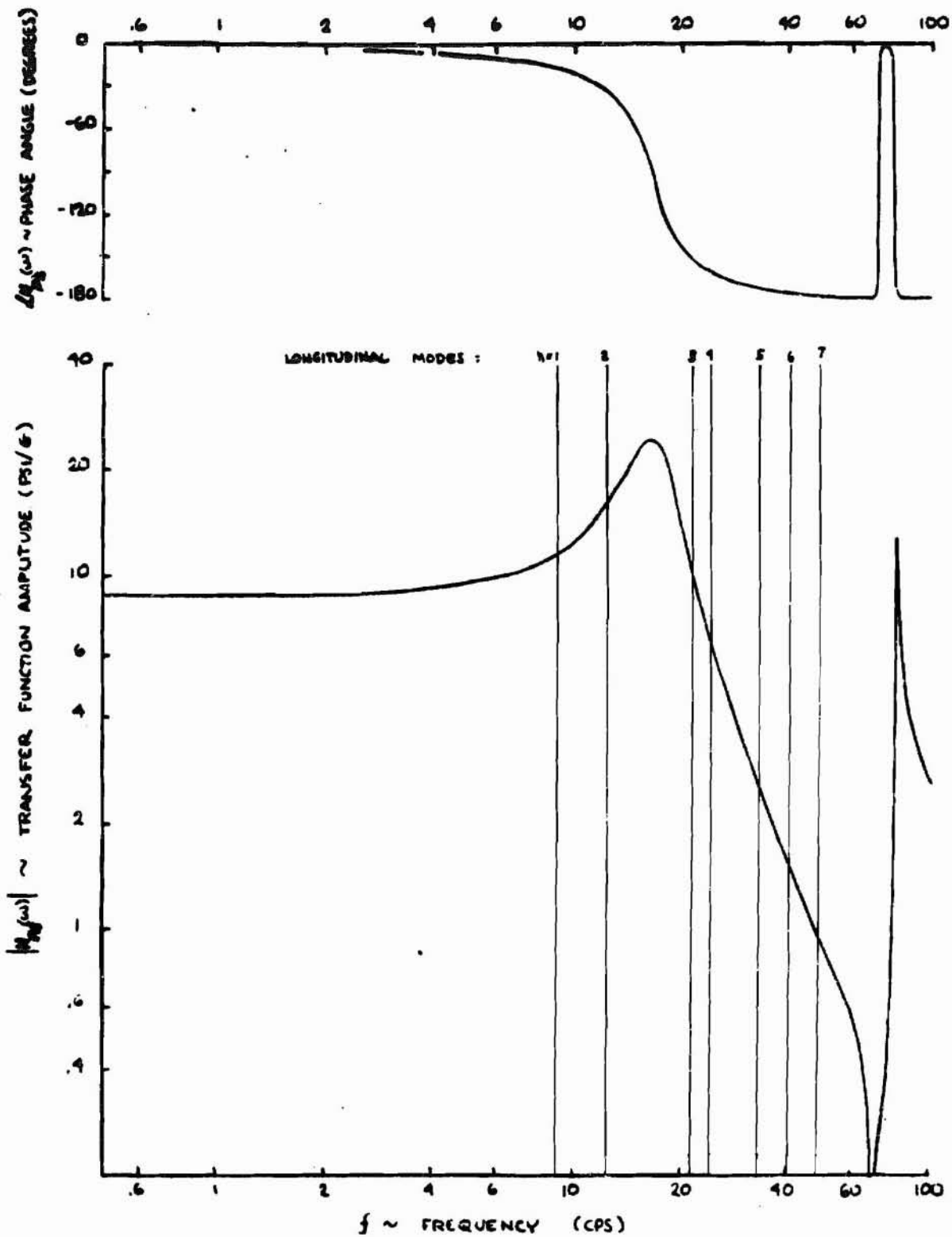


FIGURE 6. FREQUENCY RESPONSE OF $H_{sp}(\omega)$ for the SATURN IB LOX FEED SYSTEM

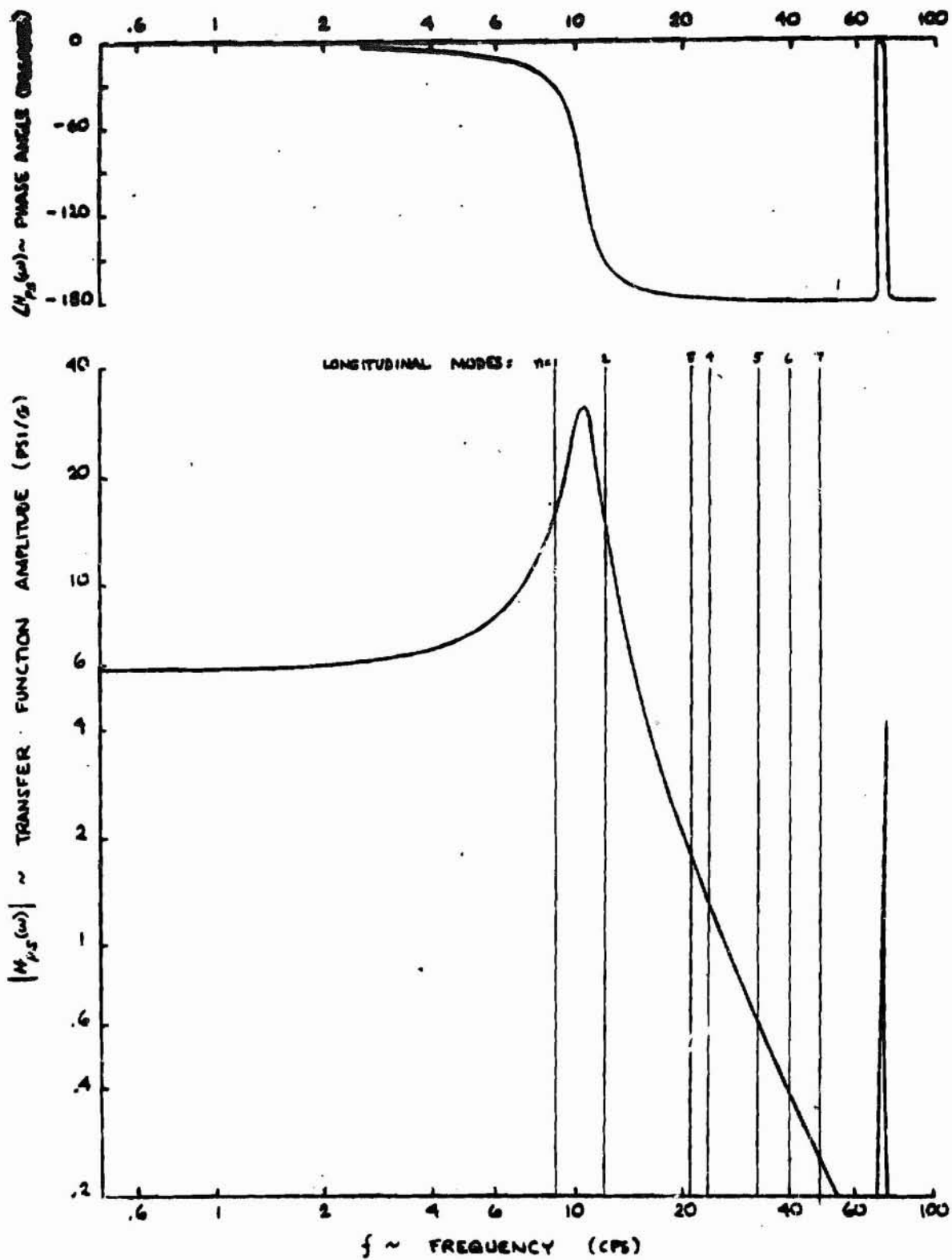


FIGURE 7. FREQUENCY RESPONSE OF $H_{ps}(\omega)$ for the SATURN IB FUEL FEED SYSTEM

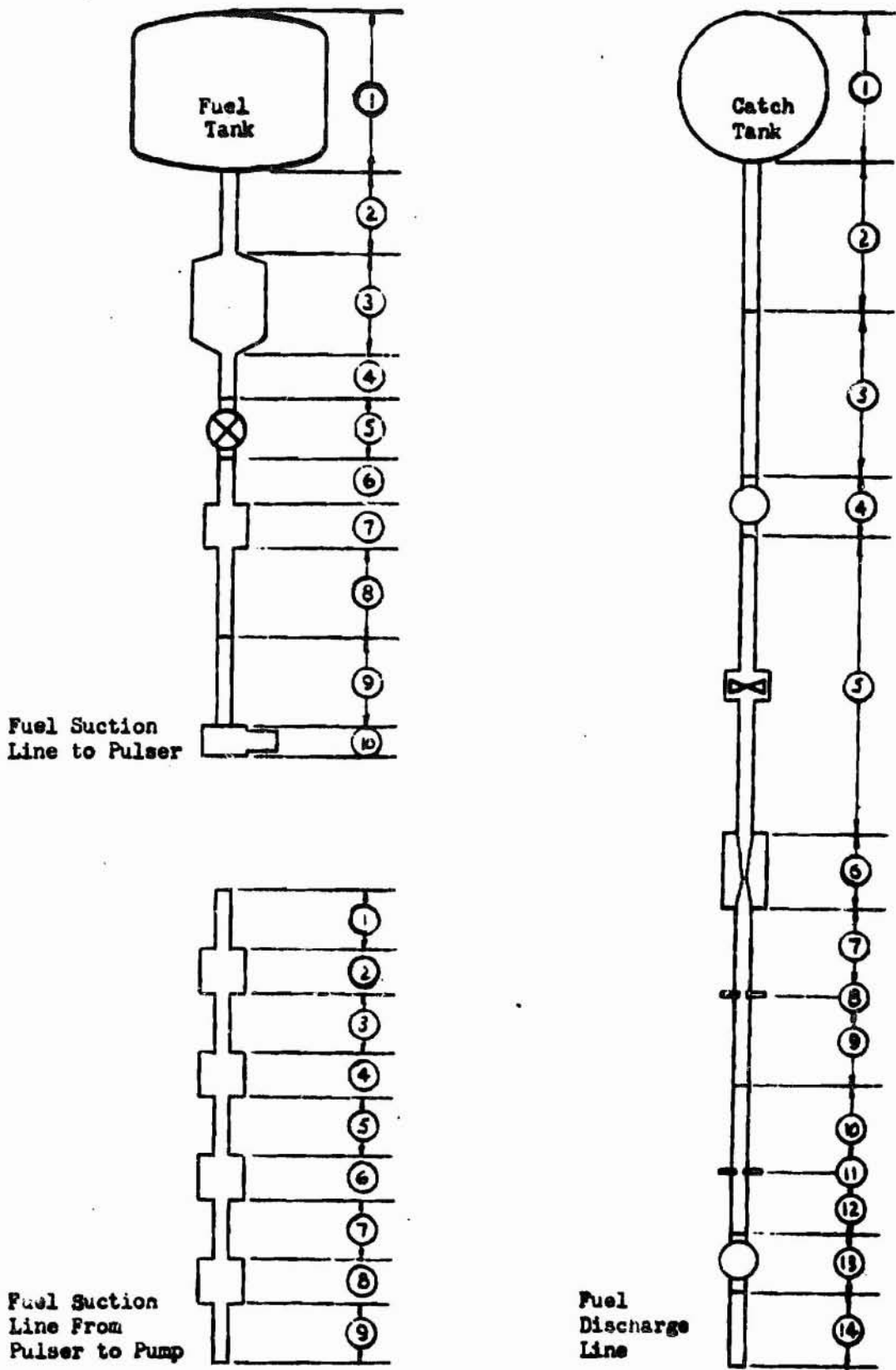


FIGURE 8. SCHEMATIC OF H-1 FUEL FEED SYSTEM (BOBTAIL FACILITY)

"REPRODUCIBILITY OF THE ORIGINAL PAGE IS POOR"

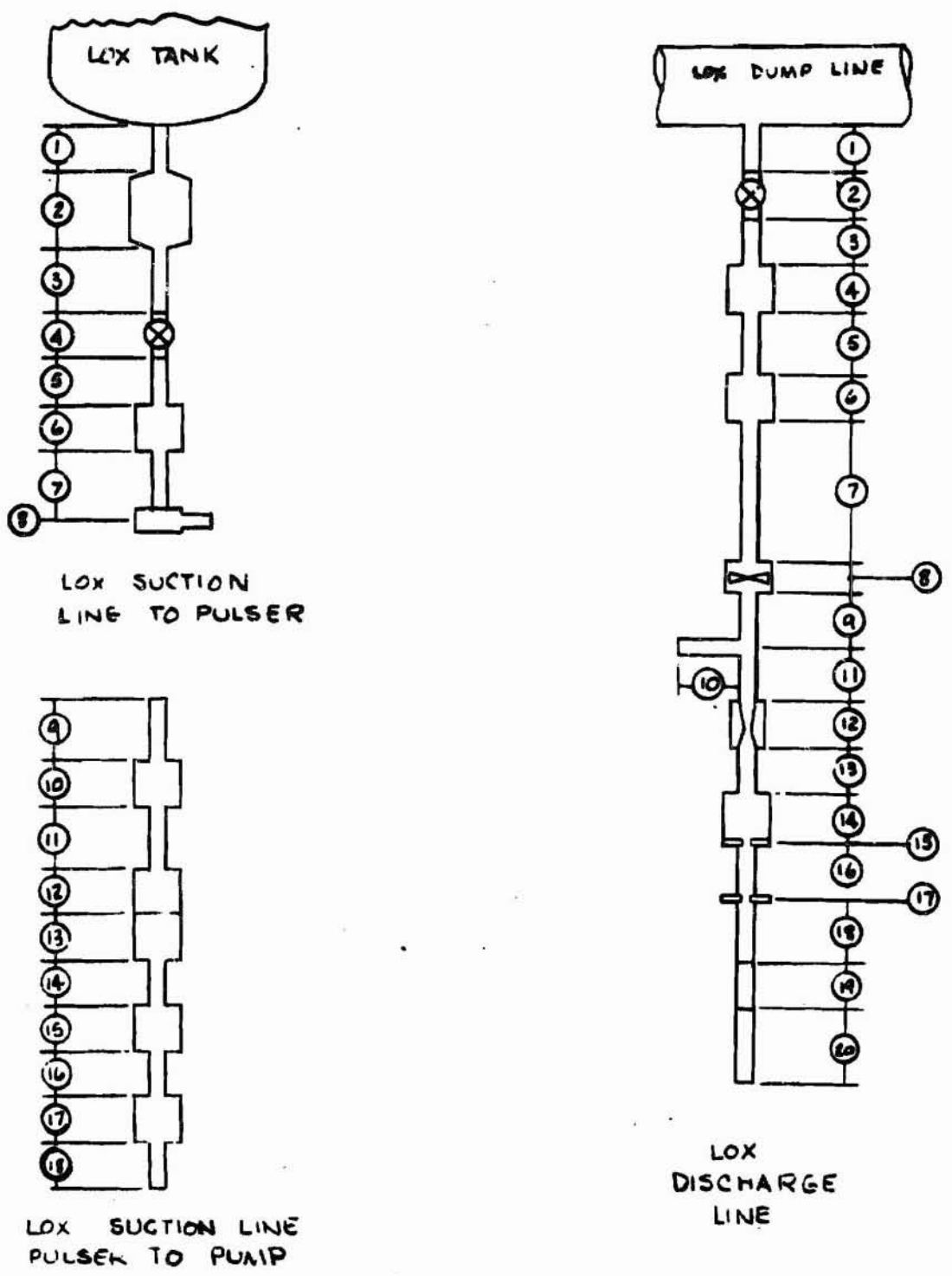
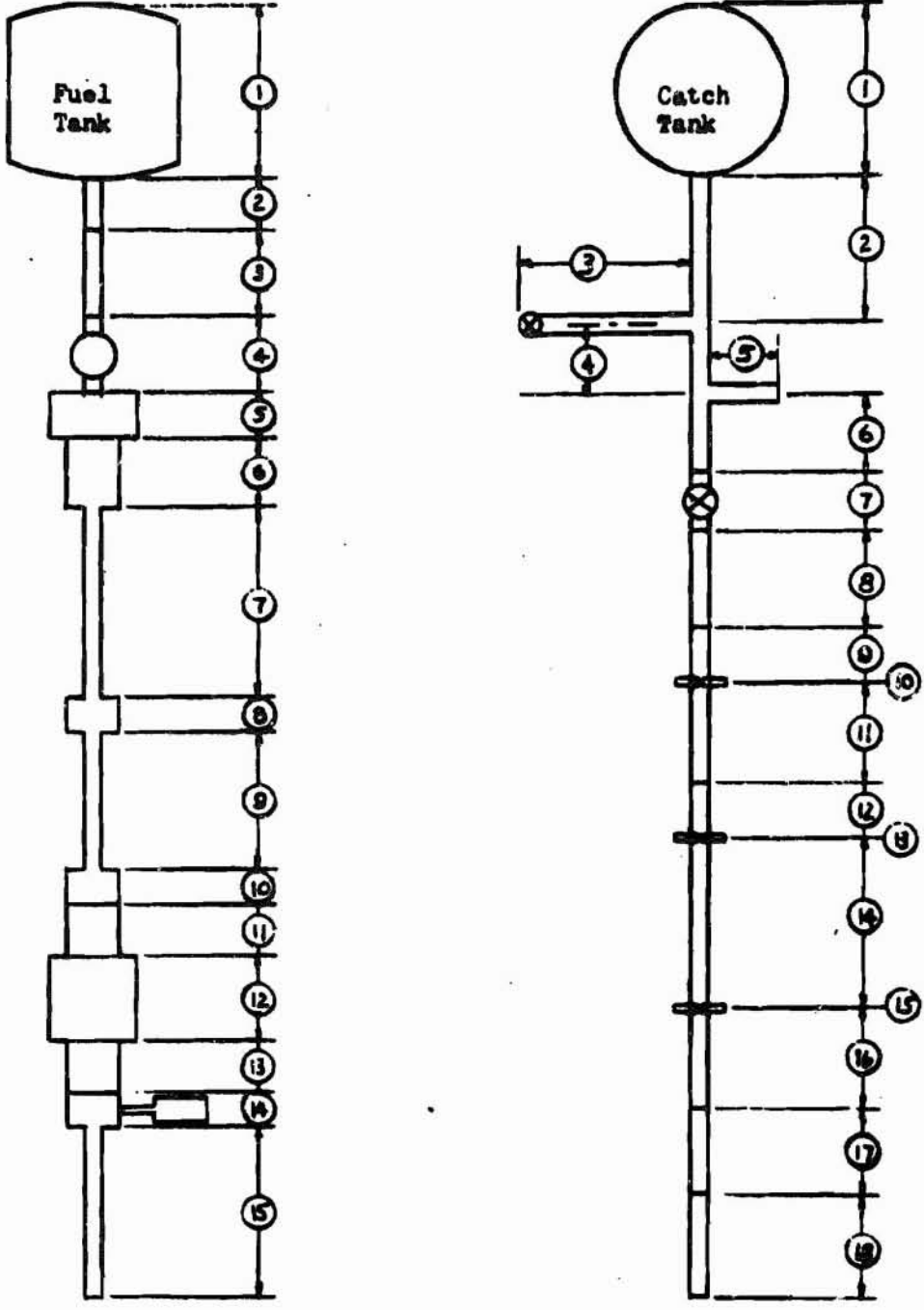


FIGURE 9. SCHEMATIC OF H-1 LOX FEED SYSTEM (BOBTAIL FACILITY)

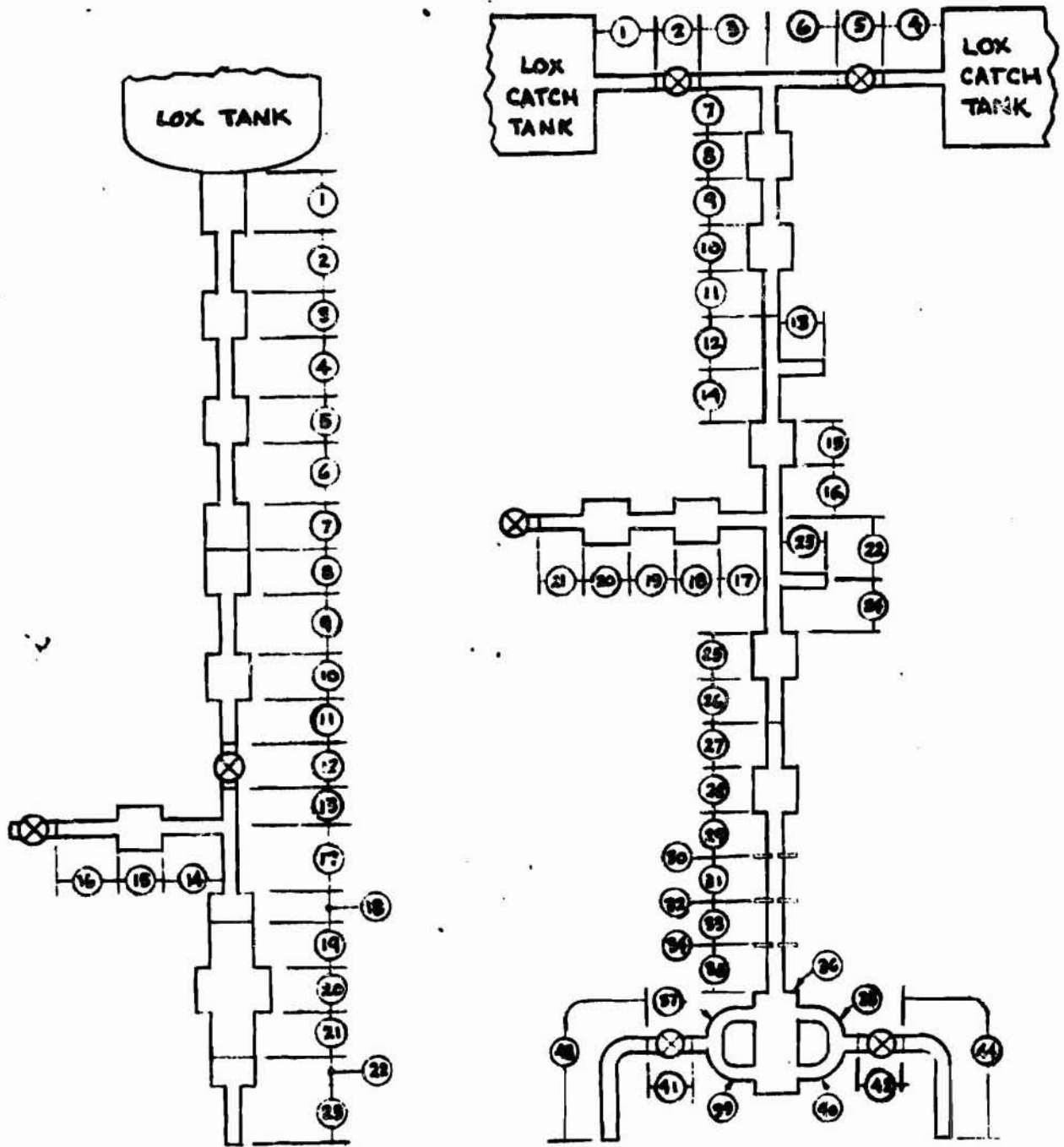
"REPRODUCIBILITY OF THE ORIGINAL PAGE IS POOR"



Fuel Suction Line to Pump (1 of 2)

Fuel Discharge Line

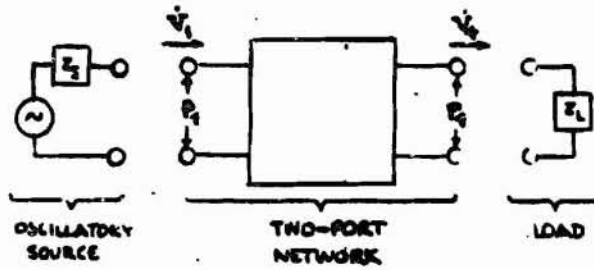
FIGURE 10. SCHEMATIC OF F-1 FUEL FEED SYSTEM (ROBTAIL FACILITY)



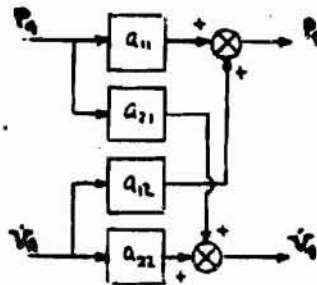
LOX SUCTION LINE

LOX DISCHARGE LINE

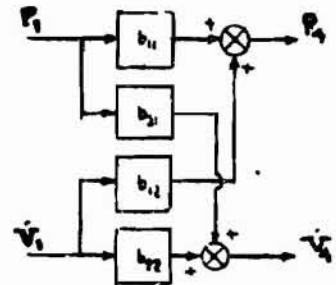
FIGURE 11. SCHEMATIC OF F-1 LOX FEED SYSTEM (BOBTAIL FACILITY)



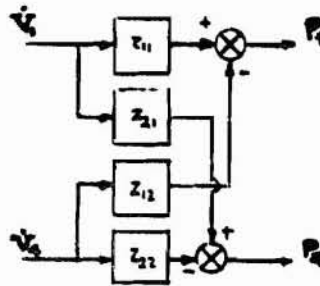
8) ELECTRIC ANALOG NETWORK OF A HYDRAULIC ELEMENT



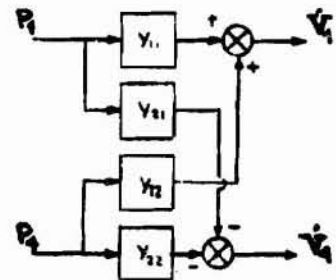
9) BLOCK DIAGRAM FOR EQ (1)



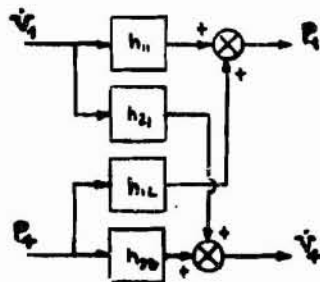
10) BLOCK DIAGRAM FOR EQ (2)



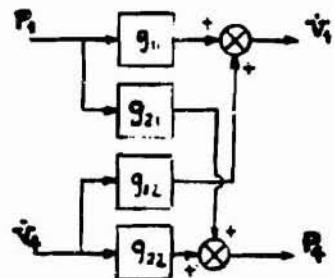
11) BLOCK DIAGRAM FOR EQ (3)



12) BLOCK DIAGRAM FOR EQ (4)

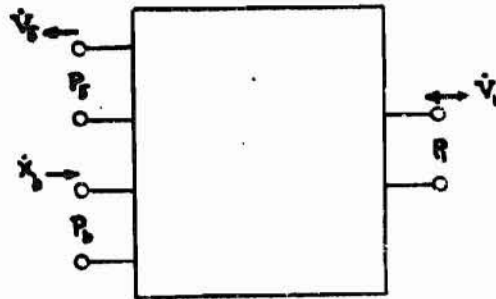


13) BLOCK DIAGRAM FOR EQ (5)

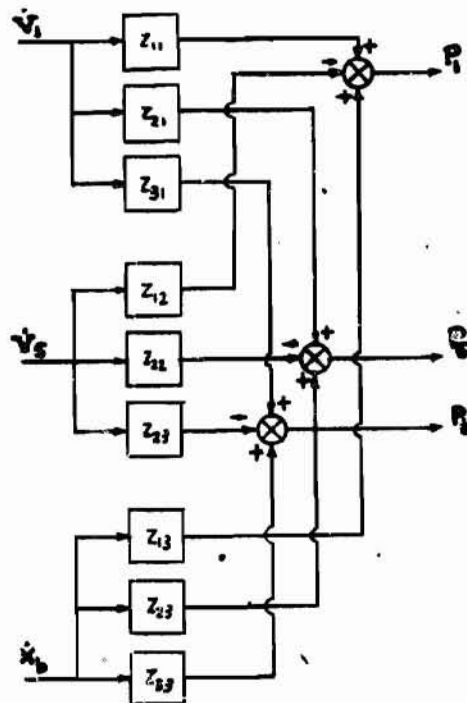


14) BLOCK DIAGRAM FOR EQ (6)

FIGURE 12. ANALOG NETWORK AND EQUIVALENT BLOCK DIAGRAMS FOR A HYDRAULIC ELEMENT



a) Three-Port Analog Network



b) Multivariable Block Diagram

FIGURE 13. BLOCK DIAGRAM FOR THE COMBINED SUCTION LINE AND STABILIZATION DEVICE

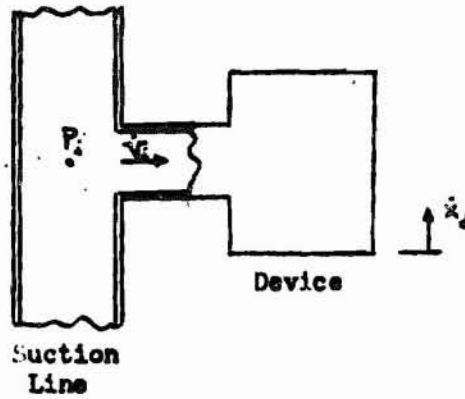


FIGURE 14. SCHEMATIC REPRESENTATION OF A FLUID CORRECTIVE DEVICE

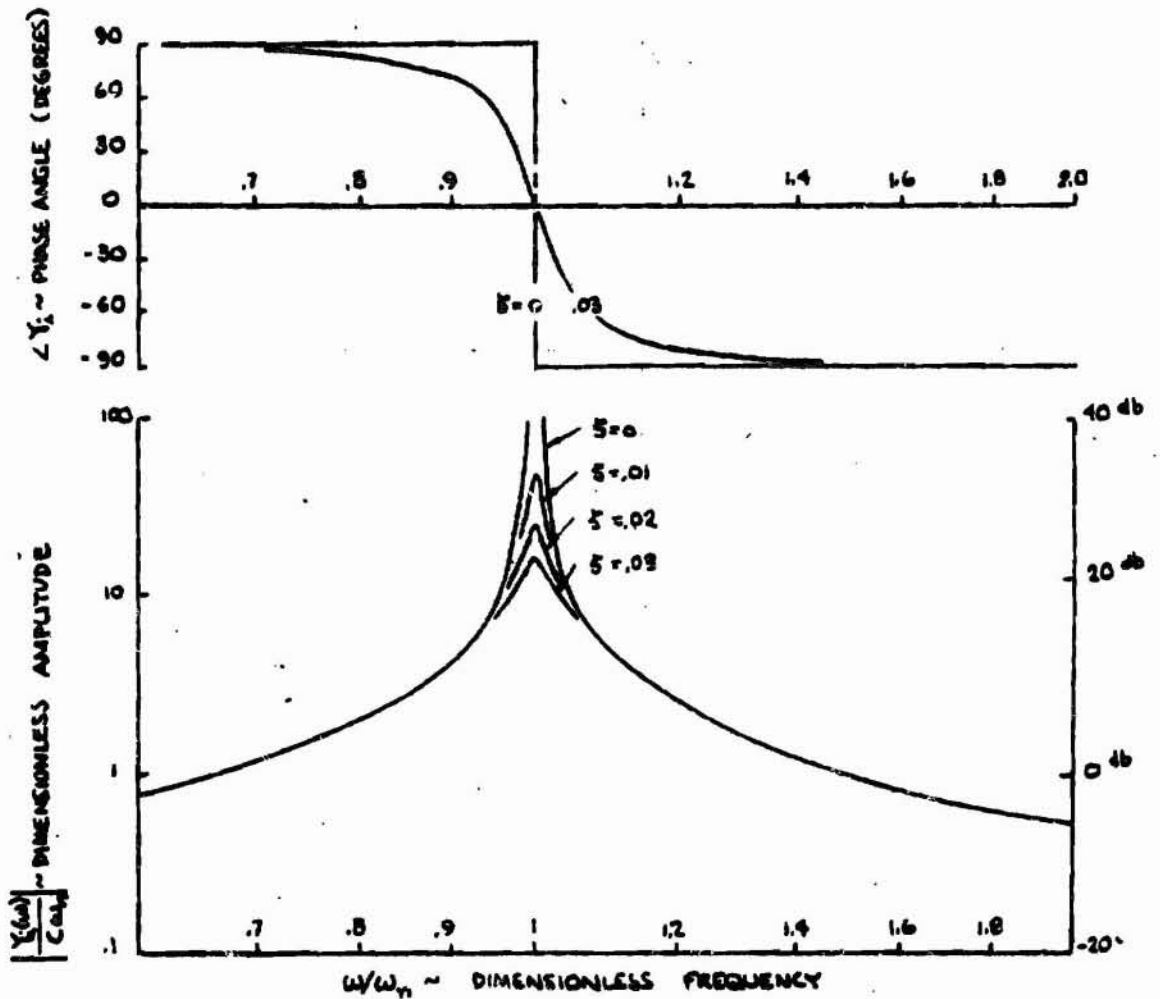


FIGURE 15. INPUT ADMITTANCE OF A SIDEBRANCH DEVICE

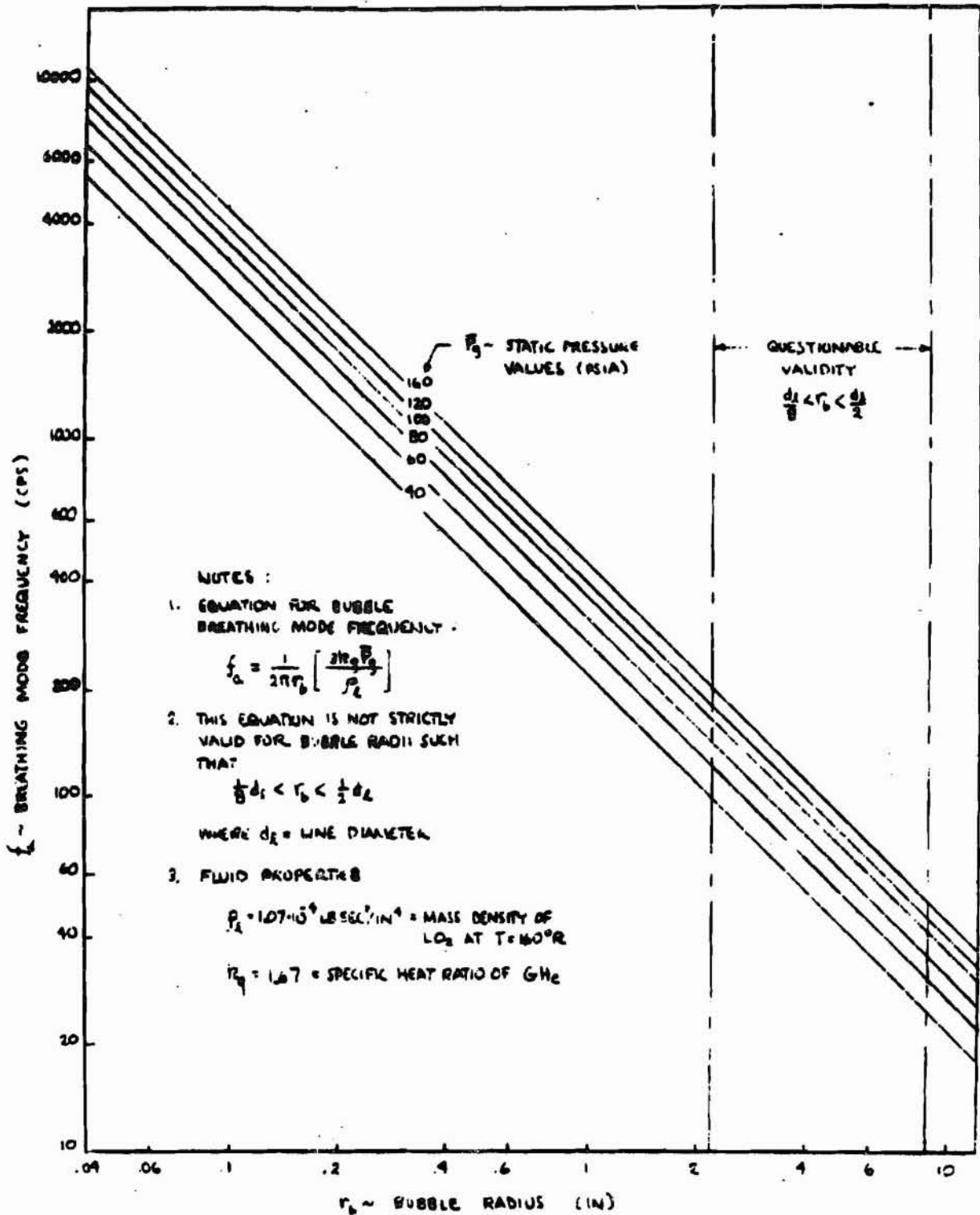


FIGURE 16. BREATHING MODE FREQUENCY FOR GASEOUS H_2 BUBBLES IN LIQUID O_2

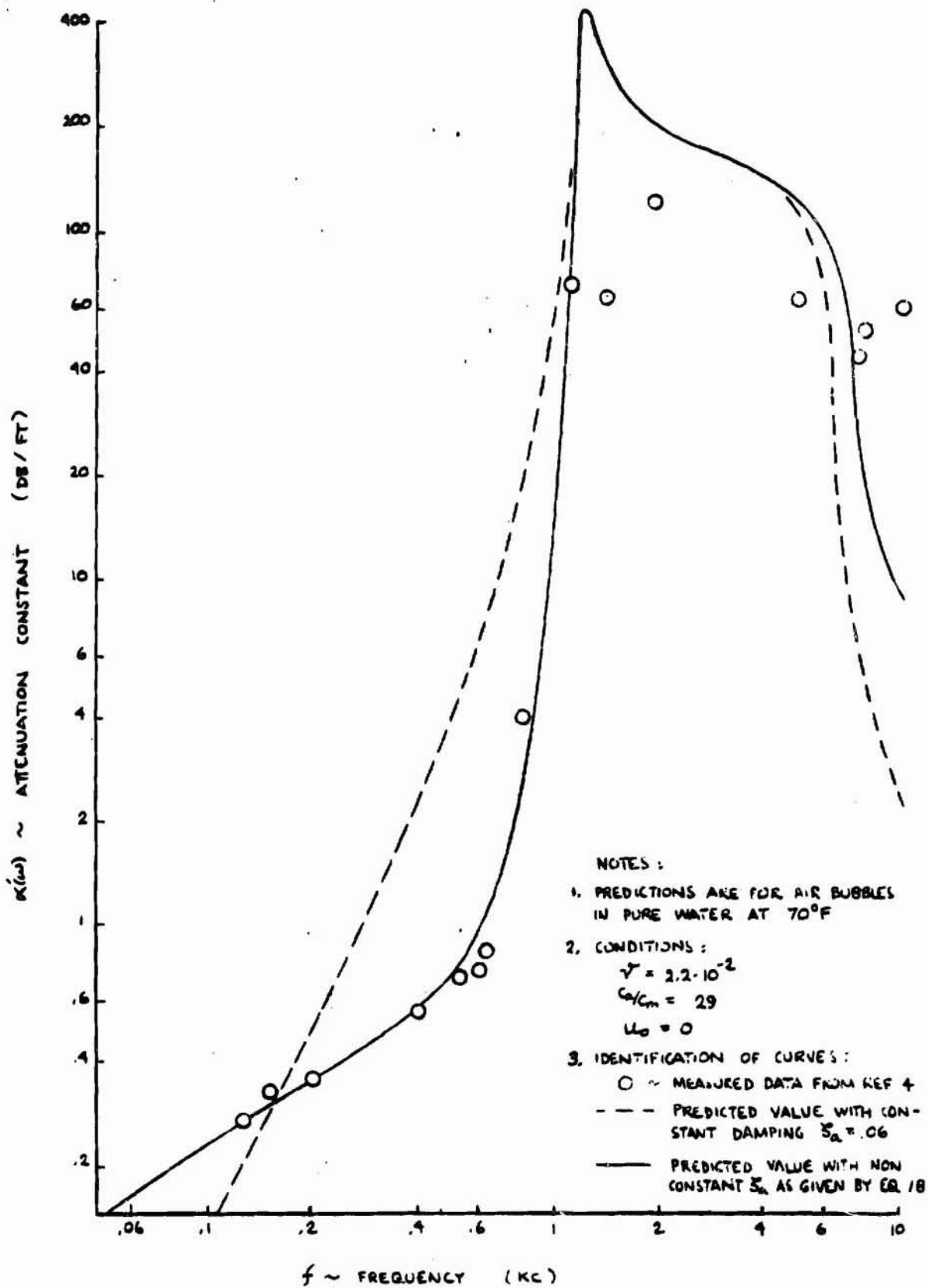


FIGURE 17. ATTENUATION CONSTANT FOR WAVE PROPAGATION IN A BUBBLY MIXTURE

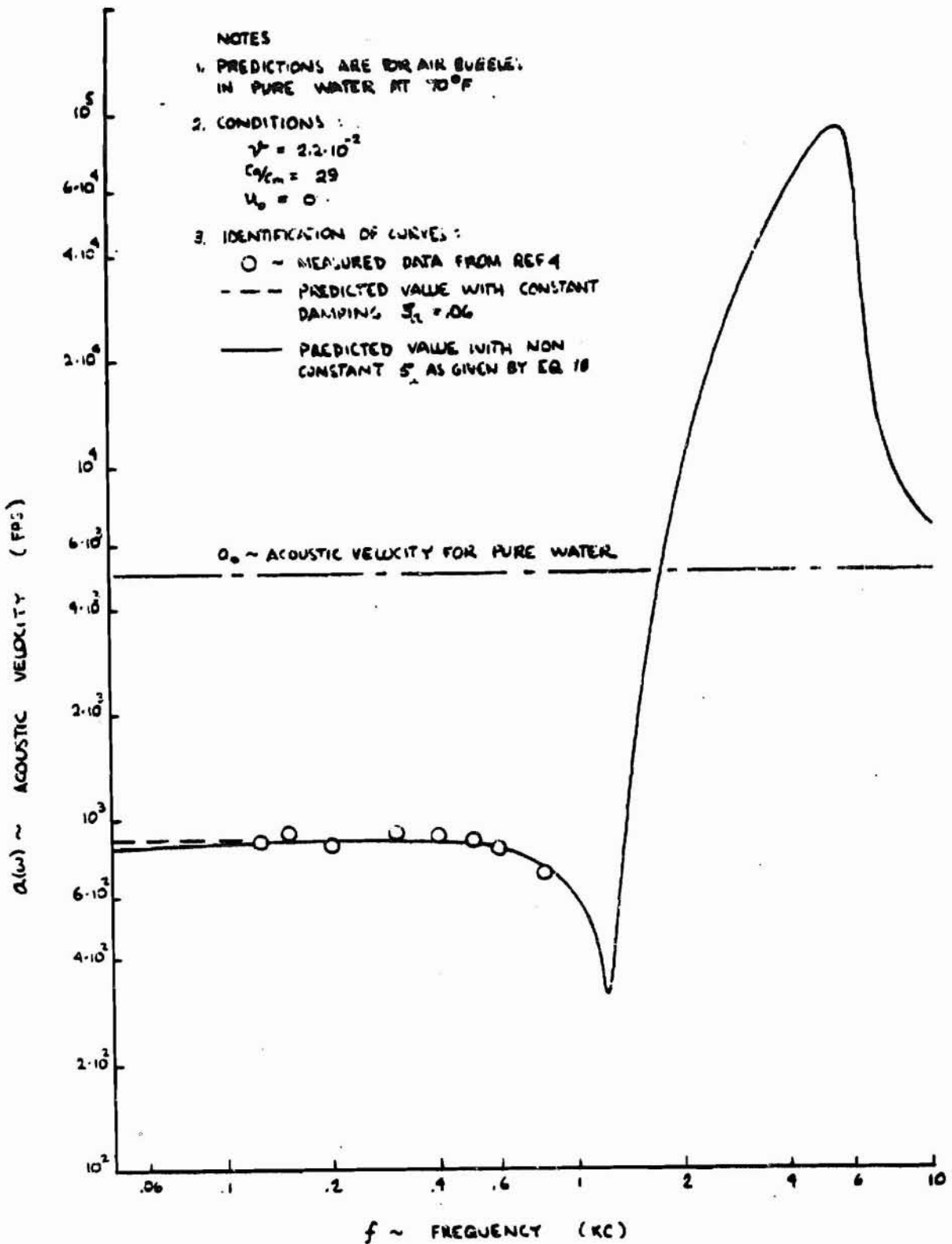
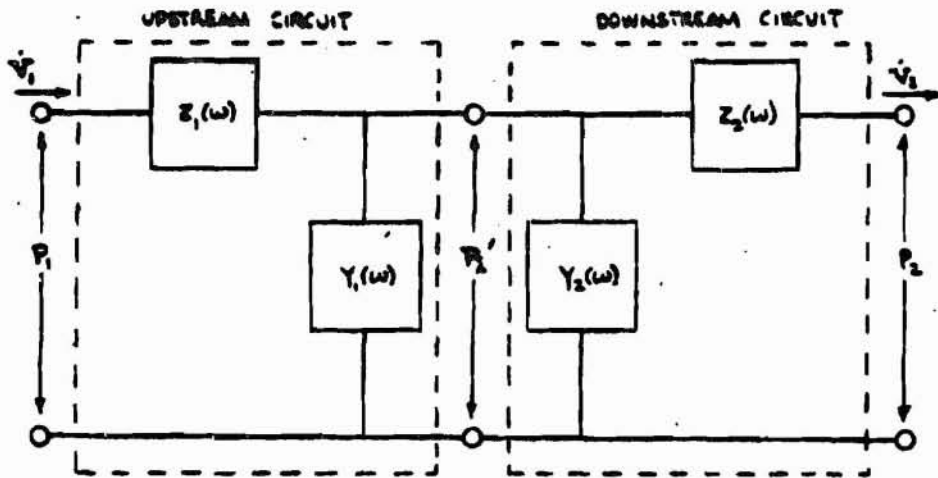
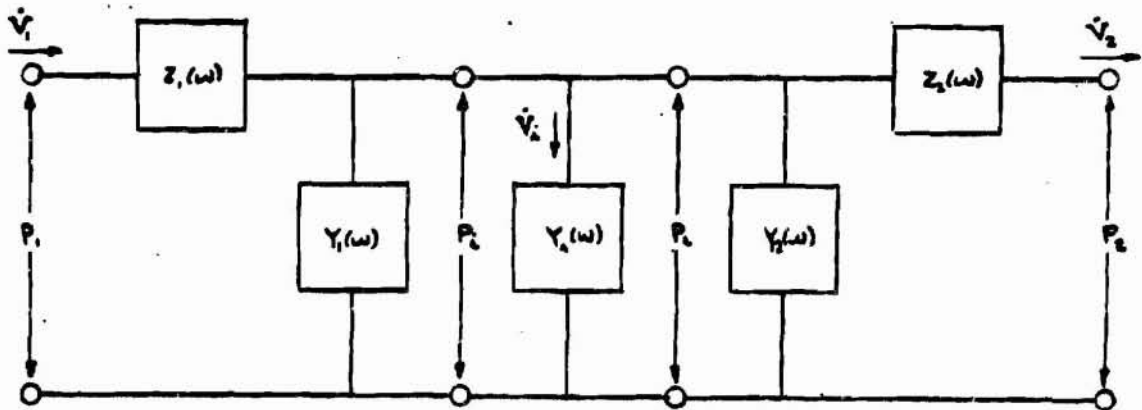


FIGURE 18 ACOUSTIC VELOCITY FOR WAVE PROPAGATION IN A BUBBLY MIXTURE



a. Network without Sidebranch Device



b. Network with Sidebranch Device Inserted

FIGURE 19. GENERAL ANALOG NETWORK FOR THE FEED SYSTEM

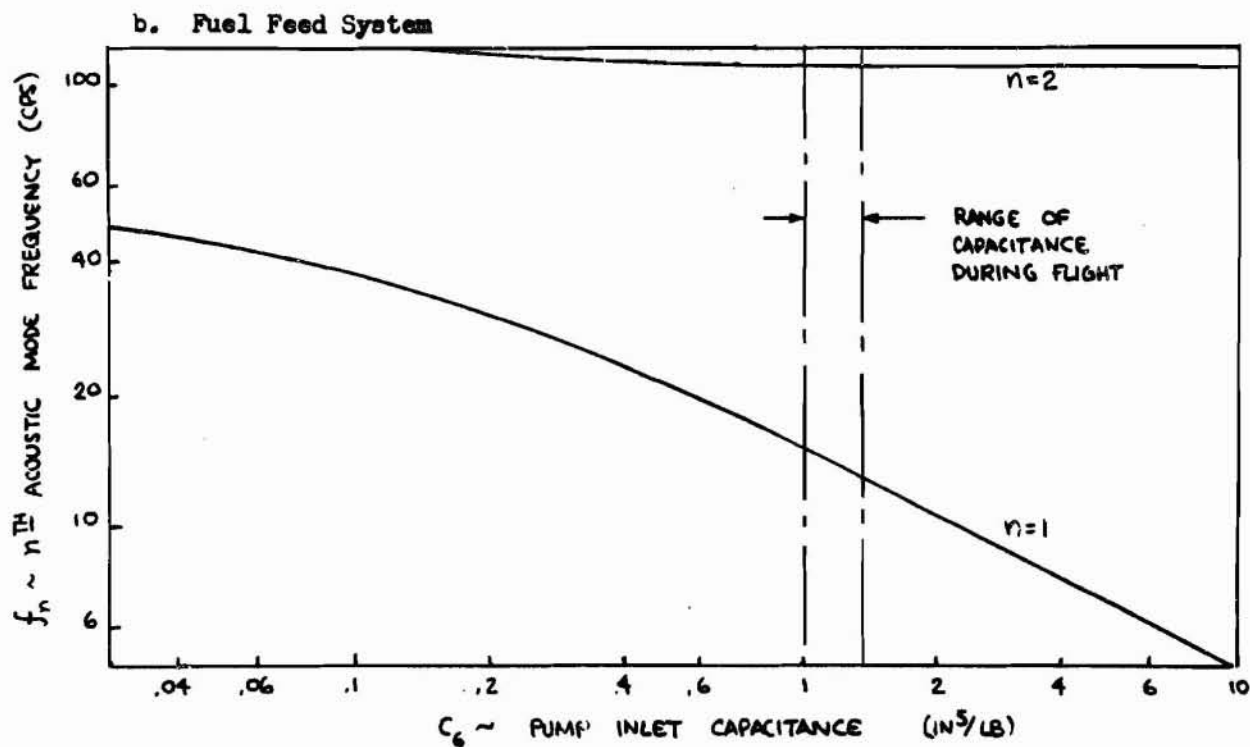
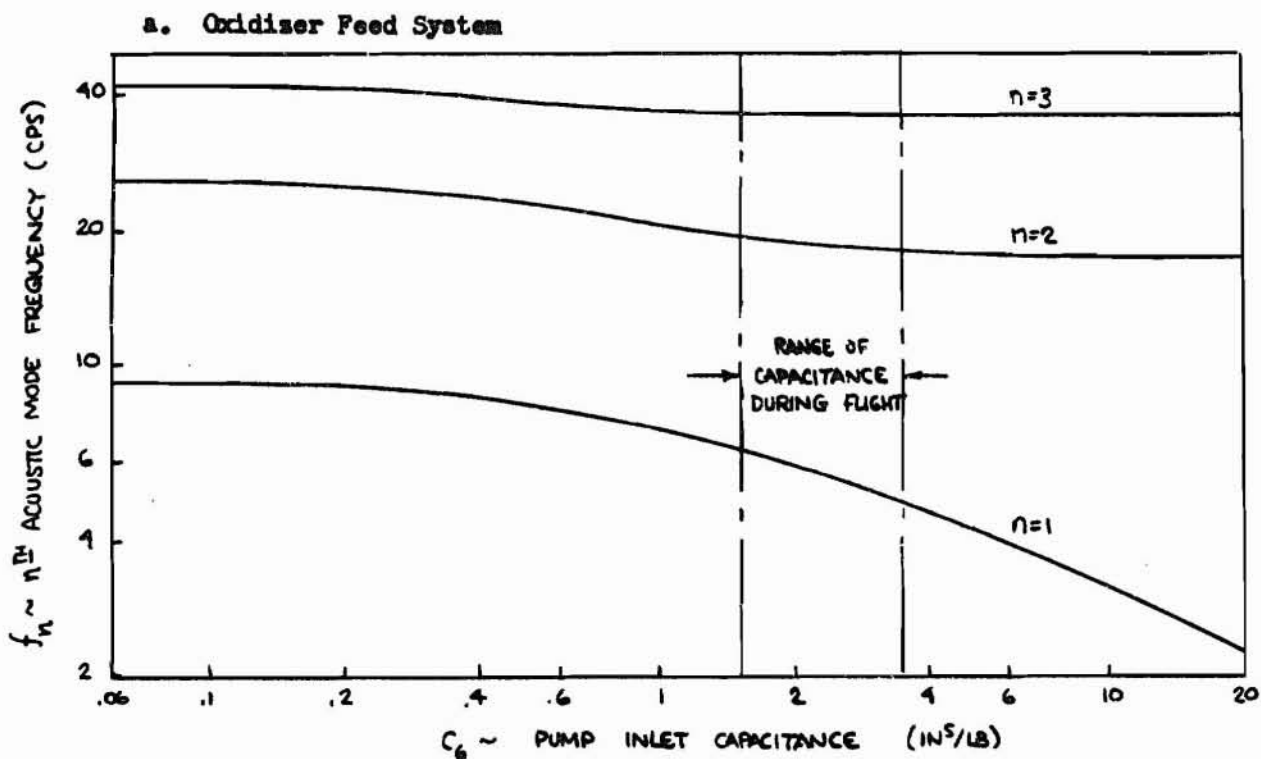


FIGURE 20. ACOUSTIC MODE FREQUENCIES FOR THE SATURN IC FEED SYSTEMS

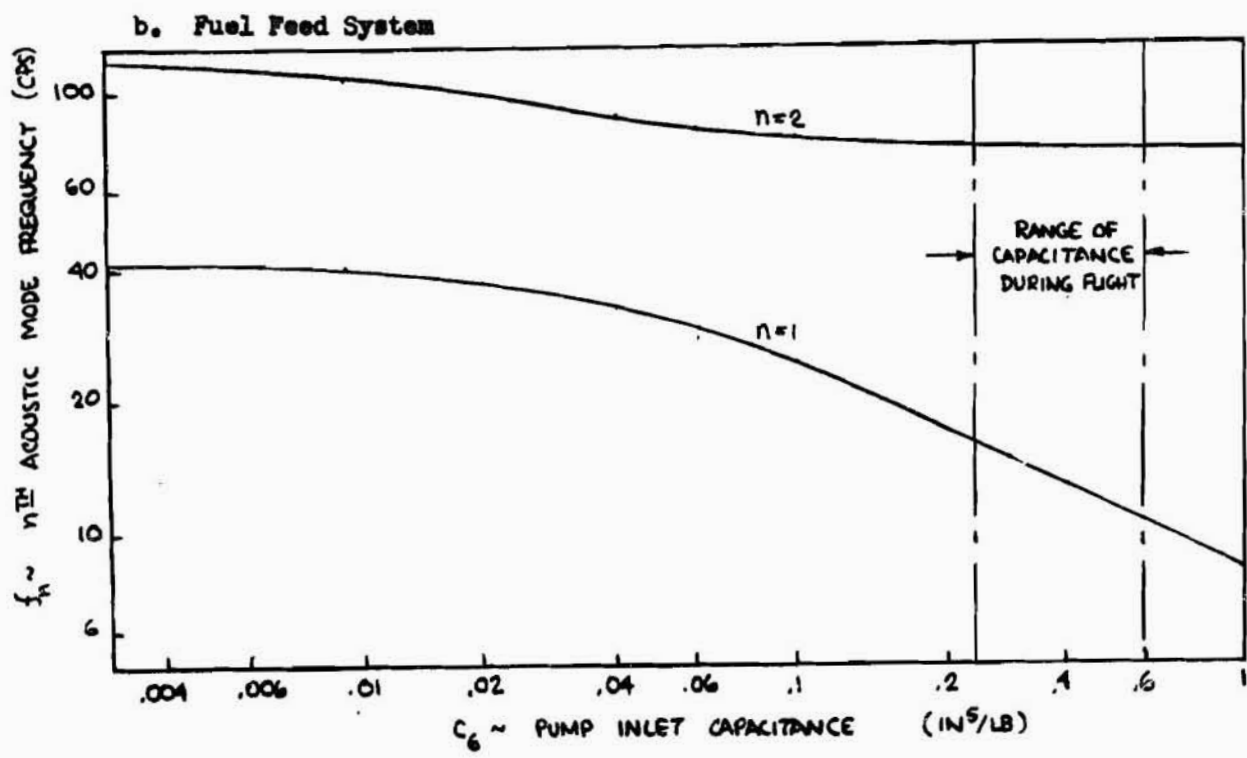
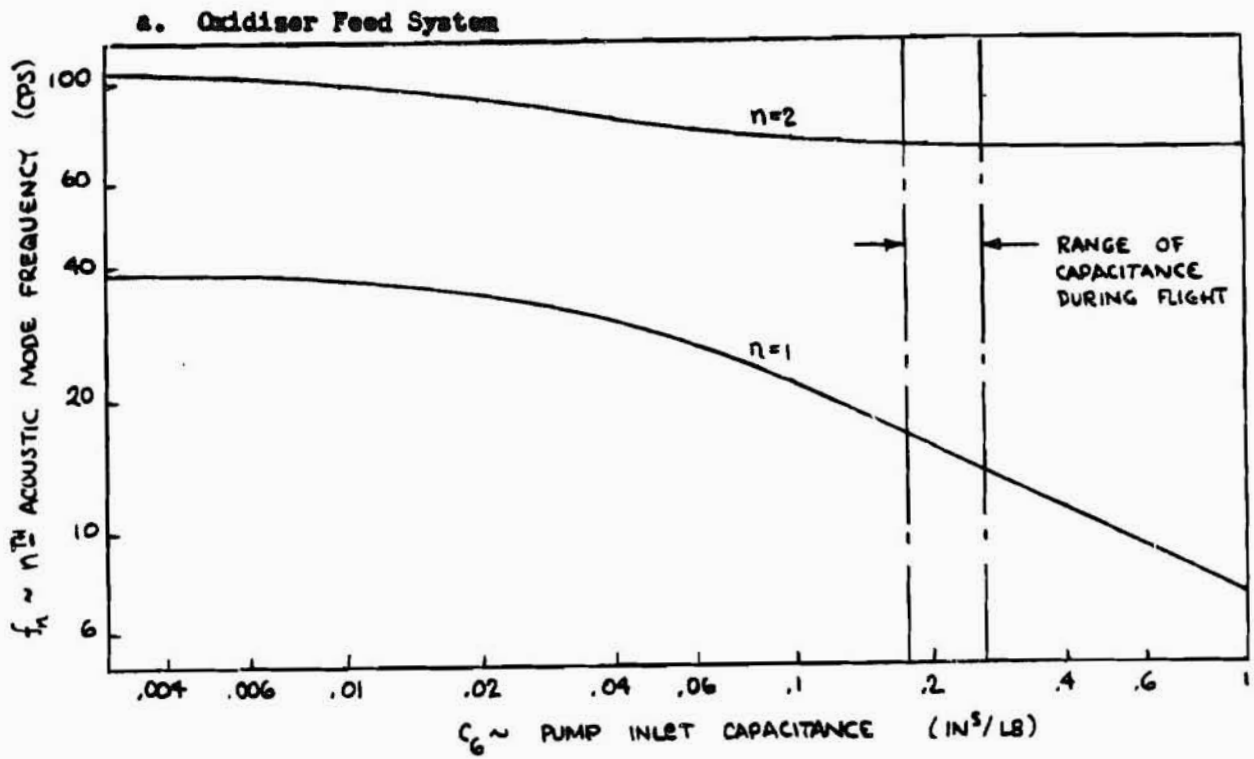


FIGURE 21. ACOUSTIC MODE FREQUENCIES FOR THE SATURN IB FEED SYSTEMS

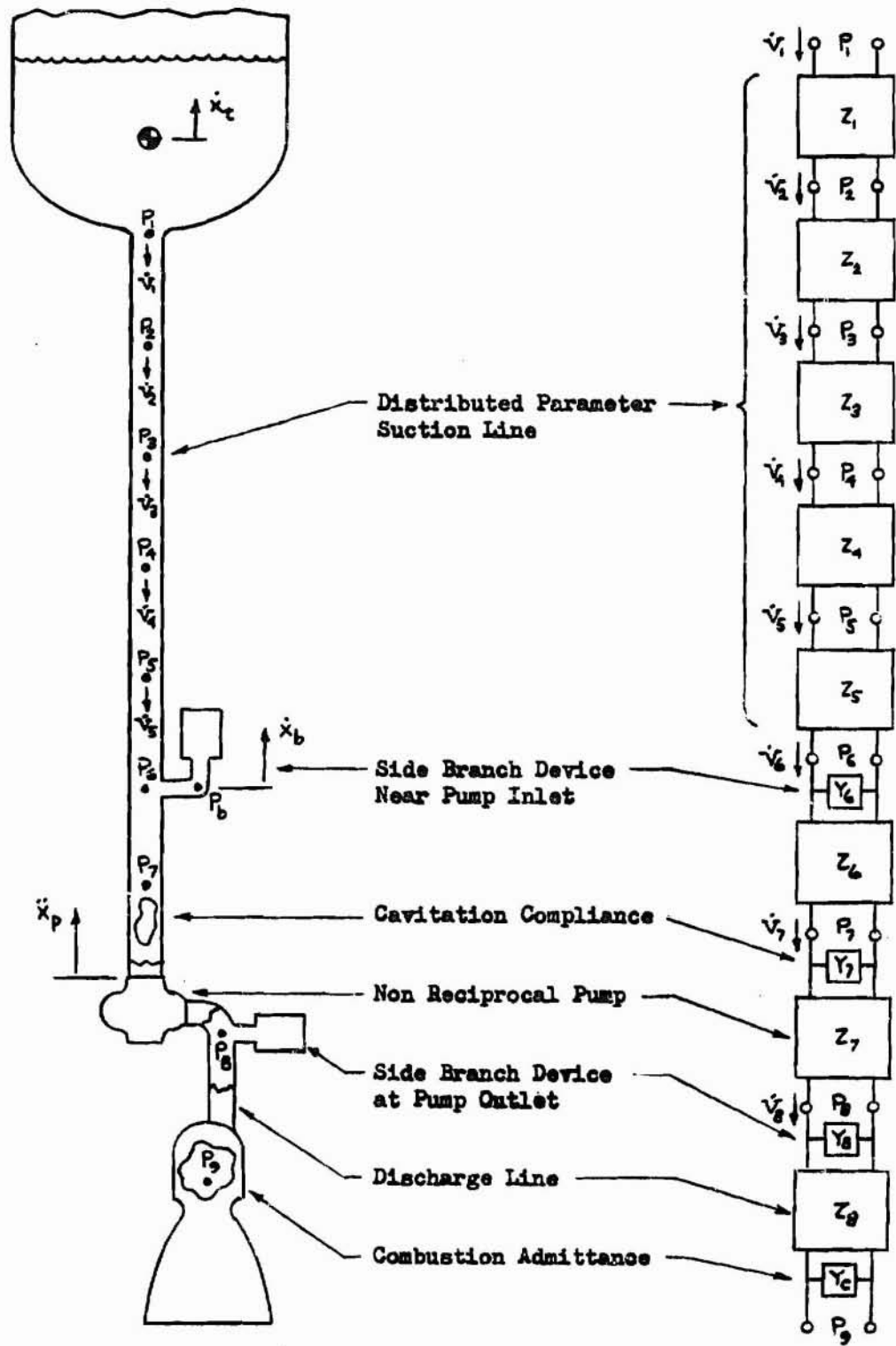


FIGURE 22 PROPULSION SYSTEM MODEL USED IN PART II

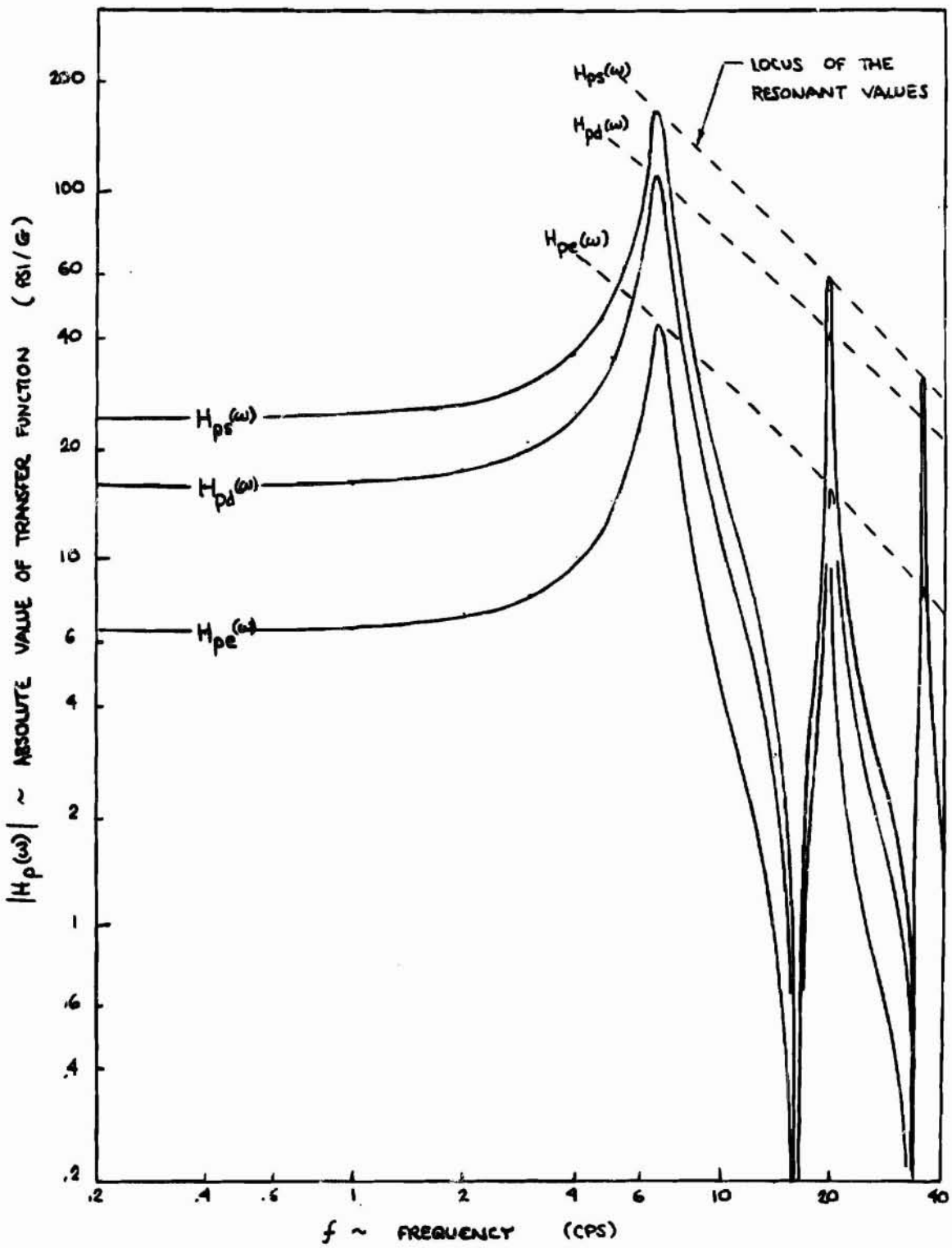


FIGURE 23. FREQUENCY RESPONSE OF $H_p(\omega)$ FOR THE SATURN IC LOX FEED SYSTEM

"REPRODUCIBILITY OF THE ORIGINAL PAGE IS POOR"

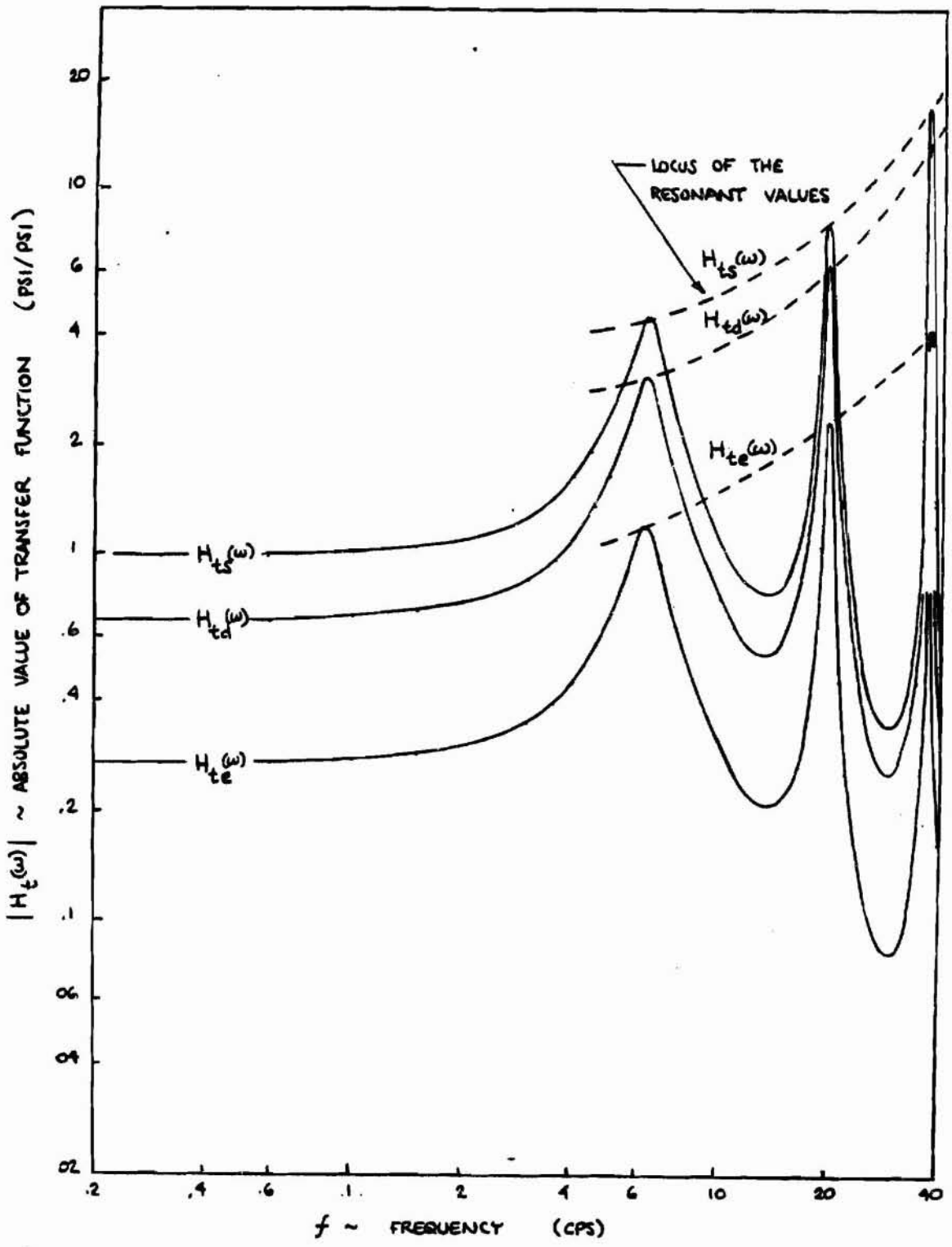


FIGURE 24. FREQUENCY RESPONSE OF $H_{ts}(\omega)$ FOR THE SATURN IC LOX FEED SYSTEM

REPRODUCIBILITY OF THE ORIGINAL PAGE IS POOR

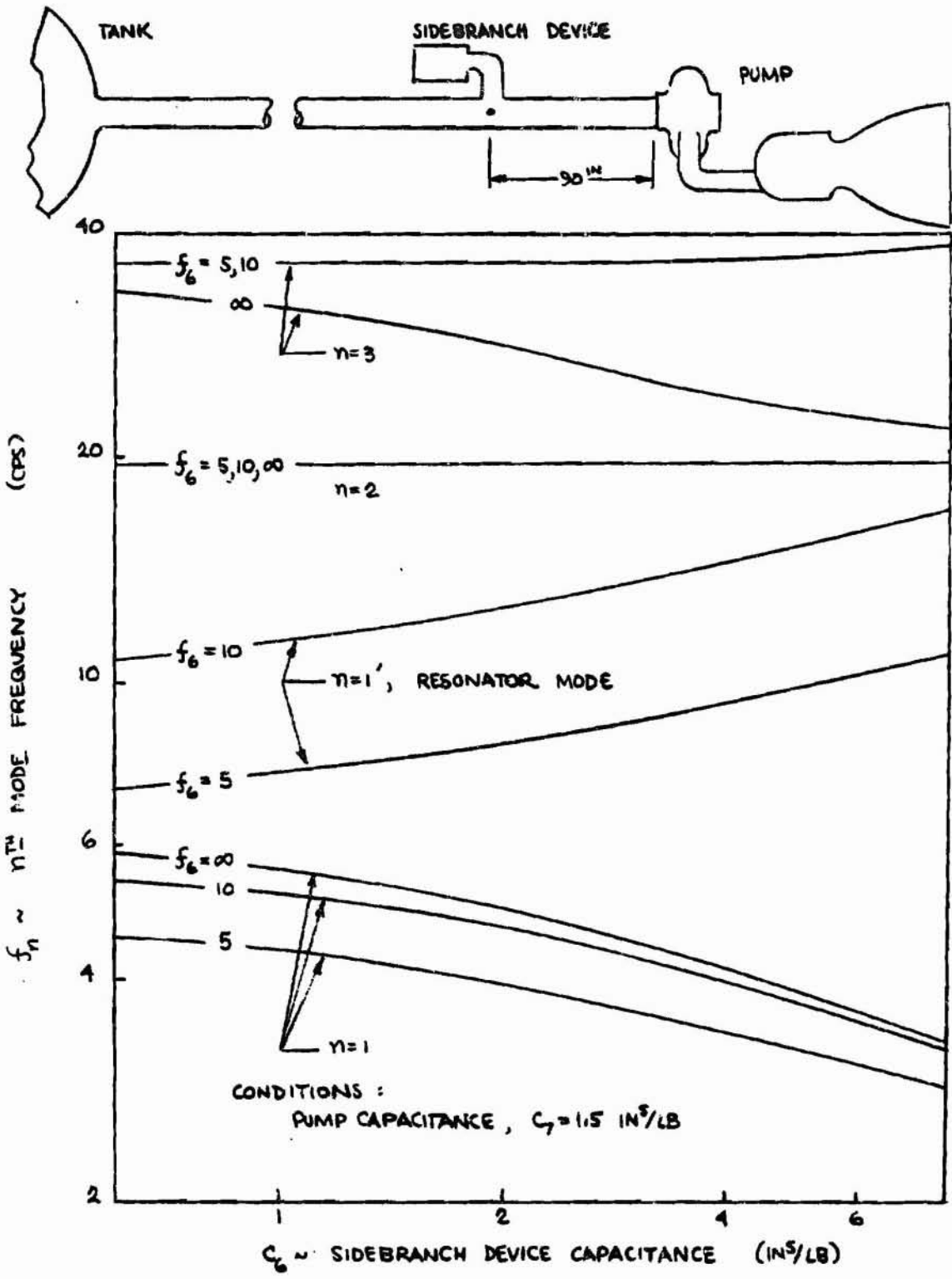


FIGURE 25. ACOUSTIC MODE FREQUENCY SHIFT DUE TO SIC LOX SIDEBRANCH DEVICE

The classified or limited status of this document applies to each page thereof unless otherwise marked. Separate page printouts **MUST be marked accordingly.**

104. 998

SACRAMENTO PLANT

"POGO" ANALYSIS OF THE SATURN PROPULSION SYSTEM

AMDR 9635-037

NAS 8-20401

3 APRIL 1967

FACILITY FORM 608

X67-17093
(ACCESSION NUMBER)

457
(PLACES)

CR-87632
(NASA CR OR TMX OR AD NUMBER)

(THRU)

20
(CODE)

38
(CATEGORY)



Report AMDR 9635-037

Date: 3 April 1967

"POGO" ANALYSIS OF THE SATURN PROPULSION SYSTEM

Prepared by:

S. G. Meisenholder
L. L. Bickford

Prepared for:

George C. Marshall Space Flight Center
National Aeronautics and Space Administration
Huntsville, Alabama

Final Report, Contract No. NAS 8-20401

Control No. DCN 1-6-57-01134 (1F) & SI (1F)

AEROJET-GENERAL CORPORATION
Liquid Rocket Operations
Sacramento, California

U. S. Government Agency and
Contractors File

FOREWORD

This report was prepared under Contract NAS 8-20401, "Pogo Analysis of the Saturn Propulsion System" for the George C. Marshall Space Flight Center of the National Aeronautics and Space Administration, which is an extension of Contract NAS 8-20068. For completeness, the results from both the initial and follow-on contract are presented in this report as Part I and Part II, respectively. All research and analysis discussed herein was performed by personnel of the Dynamics Section, Applied Mechanics Department, Liquid Rocket Engineering Division of the Aerojet-General Corporation. The project engineer was L. L. Bickford for Part I and S. G. Meisenholder for Part II. Assistance was provided by Messrs. J. Angulo, G. Hosmer, E. L. Kessler and R. Wesley; with contributions from Drs. F. M. Bonnell and J. D. Graham. Special recognition is due to F. H. Brady who developed all computer programs used in both parts of this study.

This investigation was authorized and technically directed by personnel of the Propulsion Division, Propulsion & Vehicle Engineering Lab. The program managers were D. Davis for the first contract and A. L. Worlund for the second.

ABSTRACT

The problem of longitudinal (Pogo) instabilities due to the coupling of the liquid propellant rocket propulsion system with the longitudinal vibration mode of the rocket vehicle structure has caused considerable concern in the development of manned space vehicles. This report documents the results of studies involving: review of Aerojet Titan "Pogo" experience; review of the Saturn propellant feed systems; definition, evaluation and preliminary design of passive feed system "Pogo" fix devices, and assistance in analysis and utilization of pump pulse test dynamic data. In support of these activities, an extensive frequency domain analytical model of the Saturn propulsion system has been developed. This model allows the evaluation of the effect of the pressure oscillation suppression devices; such as accumulators, resonators, "lossy" lines and gas injection.

TABLE OF CONTENTS

	<u>Page</u>
I. Introduction	1
II. Summary	2
A. Part I	2
B. Part II	3
III. Conclusions and Recommendations	3
A. Conclusions	3
1. Part I	3
2. Part II	4
B. Recommendations	5
1. Part I	5
2. Part II	6
IV. Discussion, Part I	6
A. Review of Aerojet Titan "Pogo" Experience	6
B. Review of Saturn Propellant Feed System	7
1. Flight Vehicle Feed System	7
2. Pump Test Facility Feed System	10
C. Define Saturn "Pogo" Fixes	10
1. General Discussion	10
2. Sidebranch Corrective Device	15
3. Lossy Line	16
4. Gas Injection, Approximate Model	18
5. Fix Evaluation	22

Table of Contents (cont.)

	<u>Page</u>
D. Review Test Procedures and Facilities	23
1. F-1 Turbopump Facility	24
2. H-1 Turbopumps	26
3. General Recommendations	27
E. Assist in Utilizing Dynamic Test Data	28
1. Recording	29
2. Data Presentation	29
3. Data Reduction	29
V. Discussion, Part II	33
A. Evaluation of Fix Devices	33
1. General Considerations	33
2. Lumped Parameter Devices	35
3. Distributed Parameter Devices	37
B. Preliminary Design of Fix Devices	39
1. General Considerations	39
2. Sandwich Accumulator	41
3. Trombone Accumulator	43
4. Lossy Line	44
C. Determination of Fix Device Tests	45
1. Static Tests	45
2. Dynamic Tests	45
D. Assistance in the Analysis of Dynamic Test Data	46

Table of Contents (cont.)

	<u>Page</u>
VI. Bibliography	49
A. One-Dimensional Wave Propagation in Hydraulic and/or Pneumatic Lines	49
B. Wave Propagation Through Absorptive Transmission Lines	51
C. Bubble Dynamics and Wave Propagation in a Liquid Containing Gas Bubbles	53
D. Prediction of the Size and Thermal Properties of Gas Bubbles	55
E. Lumped Parameter Passive Stabilizing Devices	56
F. Servo-Mechanism Controls to Govern Propulsion System Feedback	57
G. Reduction of Dynamic Data	57
H. Dynamic Analysis of Propellant Feed Systems by Use of Matrix Methods and Impedance Techniques	58
VII. References	60
List of Symbols	61

APPENDICES

- A. Aerojet-General "Pogo" Experience
- B. Matrix Methods in Frequency Response Analysis
- C. Engine-Feed System Frequency Response Computer Program
- D. Absorptive Transmission Line Analysis
- E. Bubble Dynamics & Wave Propagation through a Bubbly Mixture
- F. Analytical Model of the Saturn Propulsion System
- G. Measurement of an Acoustical Admittance Matrix
- H. Investigation of the Transfer of Oscillation through the YLR87-AJ-5 Engine System
- I. Distribution List

LIST OF FIGURES

1. Sketch of the Propellant Feed System Model for Part I
2. Frequency Response of $Z_{ip}(\omega)$ for the Saturn IC LOX Feed System
3. Frequency Response of $H_{ps}(\omega)$ for the Saturn IC LOX Feed System
4. Frequency Response of $H_{ts}(\omega)$ for the Saturn IC LOX Feed System
5. Frequency Response of $H_{ps}(\omega)$ for the Saturn IC Fuel Feed System
6. Frequency Response of $H_{ps}(\omega)$ for the Saturn IB LOX Feed System
7. Frequency Response of $H_{ps}(\omega)$ for the Saturn IB Fuel Feed System
8. Schematic of H-1 Fuel Feed System (Bobtail Facility)
9. Schematic of H-1 LOX Feed System (Bobtail Facility)
10. Schematic of F-1 Fuel Feed System (Bobtail Facility)
11. Schematic of F-1 LOX Feed System (Bobtail Facility)
12. Analog Network and Equivalent Block Diagrams for a Hydraulic Element
13. Block Diagram for the Combined Suction Line and Stabilization Device
14. Schematic Representation of a Fluid Corrective Device
15. Input Admittance of a Sidebranch Device
16. Breathing Mode Frequency for Gaseous He Bubbles in Liquid O_2
17. Attenuation Constant for Wave Propagation in a Bubbly Mixture
18. Acoustic Velocity for Wave Propagation in a Bubbly Mixture
19. General Analog Network for the Feed System
20. Acoustic Mode Frequencies for the Saturn IC Feed Systems
21. Acoustic Mode Frequencies for the Saturn IB Feed Systems
22. Propulsion System Model used in Part II

List of Figures (cont.)

23. Frequency Response of $H_p(\omega)$ for the SIC LOX Feed System
24. Frequency Response of $H_t(\omega)$ for the SIC LOX Feed System
25. Acoustic Mode Frequency Shift due to SIC LOX Sidebranch Device
26. Frequency Response for the SIC LOX System with Resonator
27. Frequency Response for the SIC LOX System with Suction Accumulator
28. Frequency Response for the SIC LOX System with Discharge Accumulator
29. Resonant Gains and Frequencies for the SIC LOX System with Suction Accumulator
30. Resonant Gains and Frequencies for the SIC LOX System with Discharge Accumulator
31. Effect of Suction Accumulator Location for the SIC LOX System
32. Resonant Gains and Frequencies for the SIC Fuel System with Suction Accumulator
33. Resonant Gains and Frequencies for the SIC Fuel System with Discharge Accumulator
34. Resonant Gains and Frequencies for the SIB LOX System with Suction Accumulator
35. Resonant Gains and Frequencies for the SIB LOX System with Discharge Accumulator
36. Resonant Gains and Frequencies for the SIB Fuel System with Suction Accumulator
37. Resonant Gains and Frequencies for the SIB Fuel System with Discharge Accumulator
38. Frequency Response of $\gamma_{p_i}(\omega)$ for the SIC LOX System with Gas Injection
39. Frequency Response of $H_{pe}(\omega)$ for the SIC LOX System with Gas Injection
40. Frequency Response of $H_{te}(\omega)$ for the SIC LOX System with Gas Injection

List of Figures (cont.)

41. Resonant Gains and Frequencies for the SIC LOX System with Gas Injection
42. Effect of Bubble Size on the SIC LOX First Mode Gain and Frequency
43. Lumped Parameter Fix Devices
44. Distributed Parameter Fix Devices
45. Sandwich Accumulator Design
46. Sandwich Accumulator Design Curves
47. Trombone Accumulator Design
48. Typical Accumulator Compliance Characteristics
49. Sketch of the Compliance Test Facility
50. Damping Mechanisms and Hysteresis
51. Sketch of the Hysteresis Test Facility
52. Schematic of the H-1 Turbopump Test Facility
53. H-1 Bobtail Test Measurements

LIST OF TABLES

1. Dynamic Parameters Used in the Saturn Feed Systems Analysis
2. Frequencies of the Longitudinal Vibration Modes of the Saturn Vehicles
3. Tabulation of L, C, R for H-1 Fuel Suction Line to Pulser
4. Tabulation of L, C, R for H-1 Fuel Suction Line from Pulser to Pump
5. Tabulation of L, C, R for H-1 Fuel Discharge Line
6. Tabulation of L, C, R for H-1 LOX Suction Line
7. Tabulation of L, C, R for H-1 LOX Discharge Line
8. Tabulation of L, C, R for F-1 Fuel Suction Line
9. Tabulation of L, C, R for F-1 Fuel Discharge Line
10. Tabulation of L, C, R for F-1 LOX Suction Line
11. Tabulation of L, C, R for F-1 LOX Discharge Line
12. F-1 Turbopump Test Dynamic Parameters
13. Necessary Spectra for the F-1 Turbopump Test Data Reduction

BLANK PAGE

I. INTRODUCTION

The longitudinal instability of liquid-propellant rocket engine/vehicle systems, commonly called "Pogo" instability, is an important problem in the development of large rocket launch vehicles. "Pogo" instability is caused by an unstable coupling of the longitudinal vibration modes of the vehicle with the propulsion system. As a result, the vehicle payload will experience vibratory oscillations that may build up to relatively large limit cycle amplitudes during booster engine operation. Because of the serious implications of this problem, the various contractors involved in developing liquid rocket propelled launch vehicles have devoted considerable effort to analytical and experimental "Pogo" investigations.

The object of this final report is to document the effort expended by Aerojet-General personnel in assisting Marshall Space Flight Center personnel in their studies of the "Pogo" problem associated with the Saturn IB and V vehicles. The Saturn "Pogo" investigation at MSFC is primarily composed of two main tasks:

- (1) Perform pulse tests of the Saturn H-1 and F-1 engine turbopumps;
- (2) Perform a stability analysis of the Saturn "Pogo" loop.

Aerojet-General has been granted two contracts, NAS 8-20068 and 8-20401, for the purpose of assisting in the MSFC Saturn Pogo study. The objectives of the initial contract were (1) provide a review of Aerojet Titan "Pogo" experience, (2) review the Saturn propellant feed system, (3) define feed system "Pogo" fix devices, (4) review test procedures and facilities for the engine-feed system pulse testing, and (5) assist in utilizing dynamic pump test data. The objectives of the second contract were (1) evaluate "Pogo" fix devices, (2) preliminary design of fix devices, (3) determine fix device test procedures, (4) assist in the analysis of pump dynamic data and (5) assist in utilization of information from the Aerojet analysis.

II. SUMMARY

A. PART I

The results of the initial contract (NAS 8-20068), originally documented in Reference 1, will be referred to as Part I in this report. The results of the follow-on contract (NAS 8-20401) will be referred to as Part II.

The analytical and experimental techniques used by Aerojet-General personnel to study the Gemini/Titan II "Pogo" problem are summarized in Appendix A. The mathematical model of the combustion and feed system dynamic response characteristics makes use of acoustical impedance representations and matrix methods which are convenient for application to a system dynamic analysis utilizing classical control system theory.

The review of the Saturn propellant feed systems has resulted in the analysis of both the Saturn vehicle feed systems and the turbopump test facility feed systems. The results of the frequency response analysis of the vehicle feed system are presented in Figures 1 through 7. The analysis of the impedance characteristics of the "Bobtail" turbopump test facility feed systems involved the determination of the impedance characteristics of the individual feed system elements.

The initial investigation of "Pogo" fixes for the Saturn systems concentrated on the modification of the dynamic characteristics of the Saturn SIB and SIC feed systems by means of increasing the effective pump inlet capacitance (compliance). During this initial analysis other fix concepts were briefly considered, such as side-branch resonators, lossy lines, and gas bubble injection.

A review of the test procedures and facilities associated with the MSFC H-1 and F-1 turbopump pulse test program was conducted. Specific changes were suggested with regard to the improvement of the oscillatory pressure and flow instrumentation. These recommendations as well as a brief description of the usage of cross and input power spectral densities to determine transfer functions from test data is contained in this report. Table 12 contains the dynamic parameters associated with the F-1 turbopump pulse test and Table 13 contains a listing of the necessary spectra for determining transfer functions from the dynamic test data.

II, Summary (cont.)

B. PART II

The analytical model of the Saturn SIB and IC propulsion system frequency response developed in Part I was modified for the purpose of the evaluation of "Pogo" fix devices in Part II. This evaluation is based on the effect of the various fix devices upon the frequency response characteristics of the system. All feed system oscillation suppression concepts are passive devices inserted in the feed system, such as the 1) suction line accumulator, 2) suction line resonator, 3) discharge line accumulator, 4) lossy line and 5) gas injection.

The design of two candidate fix devices, the sandwich accumulator and the trombone accumulator, is discussed and compared to gas injection with respect to the satisfaction of the design criteria. The use of the sandwich accumulator concept in the design of a lossy line for the LO₂ system is also discussed. The test methods that apply to the development of these accumulators are presented.

The matrix methods which may be used to obtain the admittance matrix or transfer functions of the turbopump from pulse test data are presented. It is shown that this admittance matrix may be used to completely characterize linear oscillation transmission through the pump.

III. CONCLUSIONS AND RECOMMENDATIONS

A. CONCLUSIONS

1. Part I

The review of the Saturn IB and IC propellant feed systems has resulted in a frequency response analysis of the nominal feed system configurations. By comparing the frequencies of the feed system modes to those of the structural longitudinal vibration modes, certain conclusions may be made concerning the destabilizing effect of the feed system dynamics on the overall "Pogo" loop. The results of this comparison indicate that coincidence of these resonances is possible for at least one frequency in both the Saturn IB

III,A,1, Part I (cont.)

and Saturn IC configurations. Therefore, it is desirable to either shift the feed system resonant frequencies to prevent this coincidence or to lower the gain of the feed system transfer function.

The stabilization devices or fixes that have been considered appear to be effective for shifting the frequency of the feed system acoustic mode and/or lowering the feed system gain at resonance. The basic analytical model which was developed for absorptive lines applies to both the bubble filled line, which utilizes distributed gas bubbles, and the lossy line, which utilizes distributed side branch resonators. The effect of the mean flow velocity upon the absorptive transmission line dynamics is significant when the acoustic velocity is greatly reduced due to (1) very large-lossy line resonator compliance, or (2) a very large volume ratio of gas to liquid in a bubble filled line.

As a result of the review of the H-1 and F-1 turbopump test facilities, it was concluded that the apparatus and instrumentation for the measurement of the pump dynamic response characteristics required modification. In particular, it was deemed necessary to flush-mount or at least close-couple the pressure transducers to the measurement location. This was necessary to prevent either the compliance of the trapped gas or the structural mounting bracket from causing a low-frequency transducer resonance which would invalidate the dynamic data. It was also concluded that additional pressure measurements plus direct oscillatory flow measurements would be desirable.

2. Part II

The evaluation of "Pogo" fix devices, using the Saturn S-IB and SV propulsion system frequency response model, has revealed that a feed system dynamic accumulator is most effective when used as a pure compliance instead of a tuned resonator. The effectiveness also depends on the magnitude of the capacitance of the accumulator and its insertion point. Analytically, the discharge line accumulator has been shown to be much more effective than the suction line accumulator in the attenuation of pressure oscillations transmitted through the feed system to the combustion chamber. However, the

III,A,2, Part II (cont.)

problems in designing a compliant device to withstand the extremely high operating pressures outweigh this theoretical advantage.

The suction line accumulator and gas injection appear to be equally effective in the reduction of the frequency of the fundamental feed system mode to achieve separation from the vehicle structural modes. However, the accumulator does not reduce the frequencies of all higher feed system modes as does the gas injection concept. The injection of gas causes a uniform increase in the distributed suction line capacitance so that all feed line acoustic modes are lowered. A secondary effect of gas injection is the increased damping of the feed system modes caused by the energy dissipation in the bubbles. Therefore, even if the frequencies of the higher acoustic modes of the feed system are reduced so that they are within the range of the vehicle structural modes, these modes tend to be less destabilizing because of their increased damping.

Of the two Aerojet conceptual fix device designs, the sandwich accumulator displays more attractive features. It satisfies all design criteria and is superior to all other lumped compliant devices considered. When compared to the gas injection concept proposed by MSFC, the sandwich accumulator appears to have the same attractive features of minimum installation time and negligible performance loss. However, the necessary hardware development program would take longer for the sandwich accumulator, thus causing more schedule impact.

B. RECOMMENDATIONS

1. Part I

It is recommended that additional work be performed to evaluate the various feed system fixes in conjunction with the overall longitudinal (Pogo) stability model. This is necessary to evaluate the effect of shifts in feed system resonant frequencies and the gain reduction of the feed system transfer functions.

III,B,1, Part I (cont.)

It is recommended that MSFC personnel, with the aid of AGC personnel, perform a pump transfer function determination program. This program would be based on the cross and input power spectral density analysis of the tape recorded frequency response data resulting from the H-1 and F-1 turbopump pulsing tests.

2. Part II

It is recommended that MSFC personnel complete the evaluation of "Pogo" fix devices by use of the analytical descriptions provided in this report. The MSFC stability model should be used to determine the effect of the fixes on the open loop gain of the complete vehicle/propulsion system.

It is suggested that the effect of bubble damping in the use of gas injection be further evaluated. The results presented in this report imply that the gas temperature and injection scheme may be empirically optimized to yield maximum energy dissipation.

Finally, the use of the sandwich accumulator is recommended as a "backup" fix device. If this approach is considered, then a prototype should be built and tested immediately.

IV. DISCUSSION, PART I

A. REVIEW OF AEROJET TITAN "POGO" EXPERIENCE

A report which describes the analysis, testing, and stabilizing compensation experience related to the "Pogo" problem was completed and forwarded to MSFC during the course of the initial contract as Aerojet Report PTDR 9647-031, "Aerojet-General 'Pogo' Experience." This report, which constitutes Appendix A, presents a detailed discussion of the analytical and experimental techniques that were applied to the Titan II/Gemini "Pogo" investigation at Aerojet.

IV, Discussion, Part I, (cont.)

B. REVIEW OF SATURN PROPELLANT FEED SYSTEM

The primary objective of the review of the Saturn propellant feed system was to define the dynamic response characteristics of the Saturn IB and Saturn IC vehicle feed systems and identify the critical components that may have a destabilizing influence on the overall "Pogo" loop. In addition to the analysis of the vehicle feed system, a dynamic analysis of the H-1 and F-1 "Bobtail" turbopump test facilities was initiated. The purpose of this secondary investigation was to define the impedance characteristics of the propellant feed systems on the Bobtail facilities by means of a distributed parameter frequency response analysis. The results of this analysis were then to be compared to the results of the lumped parameter analysis performed by MSFC (R-P&VE-PTF) personnel.

1. Flight Vehicle Feed System

The frequency response characteristics of the nominal Saturn IB and Saturn IC propellant feed systems have been analytically determined by use of the analytical model described in Appendix F. The results of this study are presented in the form of frequency response plots, of certain propulsion system transfer functions, which have been selected because of their importance in the overall "Pogo" loop. Comparison of the propellant feed system resonant frequencies, as obtained from these plots, with the overall vehicle longitudinal structural resonant frequencies provides a basis for qualitative evaluation of the destabilizing effect of the feed system dynamics. This evaluation is based on the observation that longitudinal instability is generally possible only when there is a coincidence of the resonant frequencies of at least one of the propellant feed systems and the vehicle structure.

Figure 1 presents the schematic and corresponding analog circuit of the propellant feed system. The same analog circuit applies to all configurations of the Saturn IB and Saturn IC propellant feed systems. This basic circuit was used to derive the basic equations that govern the frequency response of the system, as presented in Appendix F. The numerical values of the various dynamic parameters to be used with these equations are presented

IV,B,1, Flight Vehicle Feed System (cont.)

in Table I. Table II lists the frequencies of the longitudinal modes of vibration of the Saturn IB and Saturn V vehicles. These resonant frequencies were obtained from MSFC structural dynamics (R-P&VE-SLR) personnel.

The results of the frequency response of the nominal propellant feed systems are presented in Figures 2 through 7. It should be noted that the nominal feed system is the basic feed system configuration with no fix devices inserted. Furthermore, the values of the pump cavitation compliance used in this analysis occur late in the first-stage engine operating period. These compliance values were selected because the results of a preliminary stability analysis performed by MSFC (R-P&VE-SLR) personnel indicated that both the Saturn IB and the Saturn V are potentially unstable near the end of the first-stage burn period.

The frequency response characteristics of the nominal Saturn IC LOX feed system are shown in Figures 2, 3 and 4. Figure 2 illustrates the variation of the pump input impedance $Z_{ip}(\omega)$ with respect to frequency. This curve was computed by means of Eq (5) in Appendix F, using the numerical values of the feed system parameters given in Table 1. It is seen that the amplitude of the impedance is maximum at the frequencies of the feed system acoustic modes. The resonant values of the impedance, $|Z_{ip}|_{res}$, are governed by the resistance of the feed system. In the case of the nominal Saturn IC configuration, the suction line was assumed to be lossless, so that $|Z_{ip}|_{res}$ is determined by the resistance of the series combination of the pump, discharge line and thrust chamber. The resonant frequencies corresponding to the first three acoustic modes are 6.2 cps, 18.9 cps and 35.4 cps, respectively. The first two antiresonant frequencies are 16.2 cps and 34.2 cps. As explained in Section C of Appendix D, these antiresonances generally occur at integer multiples of the half wavelength frequency, relative to the suction line length.

In Figure 3 is shown the frequency response of the transfer function $H_{ps}(\omega)$. As defined by Eq (7) of Appendix F, this transfer function indicates the relative sensitivity of the oscillatory suction pressure (P_{s0}) to the longitudinal vibratory acceleration of the oxidizer pump (\ddot{x}_{p0}). Note

IV,B,1, Flight Vehicle Feed System (cont.)

that the peaks in the amplitude of $H_{ps}(\omega)$ occur at the same frequencies as the peaks of $Z_{ip}(\omega)$, but are not constant in amplitude. Since these resonant values, $H_{ps}(\omega)|_{res}$, are inversely proportional to frequency, it is seen that the low frequency acoustic modes are the most sensitive to oscillatory pump acceleration. Also shown in Figure 3 are the longitudinal mode frequencies of the Saturn V (501 configuration) at 150 seconds after lift-off, as obtained from Table II. It is seen that the first and sixth structural modes are practically coincident with the first and second acoustic modes. Because of the relatively small separation between the feed system acoustic modes and the two structural modes, the S-V Pogo loop is potentially unstable at the frequencies of the first and sixth structural modes.

The transfer function $H_{ts}(\omega)$ is plotted as a function of frequency in Figure 4. This transfer function, defined by Eq (8) in Appendix F, describes the transmission of pressure oscillations from the tank to the pump inlet. It is seen from Figure 4 that the frequencies at which the amplitude of $H_{ts}(\omega)$ is maximum are the same resonant frequencies at which $H_{ps}(\omega)$ was maximized.

The frequency response of the transfer function $H_{ps}(\omega)$ is plotted in Figure 5 for the Saturn IC fuel feed system. Comparison of Figures 3 and 5 reveals that, because of the shorter suction lines and higher acoustic velocity, fuel feed system displays fewer acoustic modes than the oxidizer feed system within the frequency range of interest. Only the first acoustic mode, with a frequency of 15.5 cps, is within the range of structural frequencies. It is noted that the frequency of this mode is adequately separated from all structural modes at 150 seconds after lift-off. However, inspection of Table II shows that the sixth structural mode will be coincident with the fuel system acoustic mode at some time late in the S-IC stage operation.

Figures 5 and 6 present the results of the frequency response analysis of the nominal Saturn IB oxidizer and fuel feed systems. As in the case of the analysis of the nominal Saturn IC configuration, these plots illustrate the frequencies of the acoustic modes that may couple unstably with the

IV,B,1, Flight Vehicle Feed System (cont.)

longitudinal modes of the Saturn IB structure. The structural mode frequencies, which are superimposed on these frequency response plots, have been computed for the S-IB (201 configuration) for the flight times given in Table II.

The results presented in Figure 5 indicate that the oxidizer acoustic mode frequency is not coincident with any structural mode frequency. However, the results plotted in Figure 6 show a possible coincidence of the fuel acoustic mode and the second structural mode at a time just before outboard engine cut-off.

2. Pump Test Facility Feed System

An analytical investigation of the dynamic characteristics of the H-1 and F-1 "Bobtail" pump test facilities was performed for the purpose of defining the hydraulic impedance characteristics of each pump circuit. The impedance function of the overall circuit were to be computed by use of a distributed parameter frequency response analysis, using the methods outlined in Appendix A. Schematics of the various pump test feed systems are shown in Figures 8 through 11. The values of the dynamic parameters which describe the individual components are presented in Tables 3 through 11.

It was the original intent of Aerojet-General personnel that the dynamic data presented in Tables 3 through 11 be utilized to compute the frequency response of the impedance, both upstream and downstream of the turbo-pump. Unfortunately, complete feed system information was not available during the course of the initial contract, thus resulting in an incomplete impedance representation.

C. DEFINE SATURN "POGO" FIXES

1. General Discussion

The goal of these studies has been to define the set of compensation devices which will most efficiently attenuate energy propagation in the system at Saturn "Pogo" frequencies. During the course of the contract, Aerojet personnel agreed to provide MSFC structures (R-P&VE-SLR) personnel with

IV,C,1, General Discussion (cont.)

analytical descriptions of specific stabilizing devices for the H-1 and F-1 propulsion systems. At present, these candidate devices are all passive elements which modify the dynamic response of the suction lines. Therefore, since the discharge side of the feed lines is not affected, the following engine transfer functions (which are presently provided by Rocketdyne) remain unchanged:

$$H_1(s) = \frac{\dot{W}_{d0}(s)}{P_{s0}(s)}, H_2(s) = \frac{\dot{W}_{d1}(s)}{P_{s0}(s)}, H_3(s) = \frac{\dot{W}_{d0}(s)}{P_{s1}(s)}, H_4(s) = \frac{\dot{W}_{d1}(s)}{P_{s1}(s)}, H_5(s) = \frac{T(s)}{P_{s0}(s)}, H_6(s) = \frac{T(s)}{P_{s1}(s)}$$

In order to establish a mutually acceptable form for the analytical representation of the dynamic response characteristics of the suction line and/or sidebranch stabilizing devices, a description of alternate equation forms was transmitted to MSFC personnel (R-P&VE-SLR). This transmittal presented a general discussion of the available methods by which the dynamic response of the suction line and stabilizing device may be described. For example, there are six characteristic matrices which may be used to represent the dynamic performance of the suction line, depending on the grouping of the pressure and flow variables. Referring to the schematic of Figure 1, the following equations may be written by arranging the oscillatory parameters, P_1 , \dot{V}_1 , P_4 , and \dot{V}_4 in different pairs of independent and dependent variables:

Forward Transmission Matrix

$$\begin{aligned} P_1(s) &= a_{11}(s)P_4(s) + a_{12}(s)\dot{V}_4(s) \\ \dot{V}_1(s) &= a_{21}(s)P_4(s) + a_{22}(s)\dot{V}_4(s) \end{aligned} \iff \begin{bmatrix} P_1(s) \\ \dot{V}_1(s) \end{bmatrix} = \begin{bmatrix} a_{1j}(s) \\ a_{2j}(s) \end{bmatrix} \begin{bmatrix} P_4(s) \\ \dot{V}_4(s) \end{bmatrix} \quad (1)$$

Rearward Transmission Matrix

$$\begin{aligned} P_4(s) &= b_{11}(s)P_1(s) + b_{12}(s)\dot{V}_1(s) \\ \dot{V}_4(s) &= b_{21}(s)P_1(s) + b_{22}(s)\dot{V}_1(s) \end{aligned} \iff \begin{bmatrix} P_4(s) \\ \dot{V}_4(s) \end{bmatrix} = \begin{bmatrix} b_{1j}(s) \\ b_{2j}(s) \end{bmatrix} \begin{bmatrix} P_1(s) \\ \dot{V}_1(s) \end{bmatrix} \quad (2)$$

IV,C,1, General Discussion (cont.)

Impedance Matrix

$$\begin{aligned} P_1(s) &= Z_{11}(s)\dot{V}_1(s) - Z_{12}(s)\dot{V}_4(s) \\ P_4(s) &= Z_{21}(s)\dot{V}_1(s) - Z_{22}(s)\dot{V}_4(s) \end{aligned} \iff \begin{bmatrix} P_1(s) \\ P_4(s) \end{bmatrix} = \begin{bmatrix} -Z_{11}(s) \\ -Z_{21}(s) \end{bmatrix} \begin{bmatrix} \dot{V}_1(s) \\ \dot{V}_4(s) \end{bmatrix} \quad (3)$$

Admittance Matrix

$$\begin{aligned} \dot{V}_1(s) &= Y_{11}(s)P_1(s) + Y_{12}(s)P_4(s) \\ \dot{V}_4(s) &= -Y_{21}(s)P_1(s) - Y_{22}(s)P_4(s) \end{aligned} \iff \begin{bmatrix} \dot{V}_1(s) \\ -\dot{V}_4(s) \end{bmatrix} = \begin{bmatrix} Y_{11}(s) \\ Y_{21}(s) \end{bmatrix} \begin{bmatrix} P_1(s) \\ P_4(s) \end{bmatrix} \quad (4)$$

Series-Parallel Coupling Matrix

$$\begin{aligned} P_1(s) &= h_{11}(s)\dot{V}_1(s) + h_{12}(s)P_4(s) \\ \dot{V}_4(s) &= h_{21}(s)\dot{V}_1(s) + h_{22}(s)P_4(s) \end{aligned} \iff \begin{bmatrix} P_1(s) \\ \dot{V}_4(s) \end{bmatrix} = \begin{bmatrix} h_{11}(s) \\ h_{21}(s) \end{bmatrix} \begin{bmatrix} \dot{V}_1(s) \\ P_4(s) \end{bmatrix} \quad (5)$$

Parallel-Series Coupling Matrix

$$\begin{aligned} \dot{V}_1(s) &= g_{11}(s)P_1(s) + g_{12}\dot{V}_4(s) \\ P_4(s) &= g_{21}(s)P_1(s) + g_{22}\dot{V}_4(s) \end{aligned} \iff \begin{bmatrix} \dot{V}_1(s) \\ P_4(s) \end{bmatrix} = \begin{bmatrix} g_{11}(s) \\ g_{21}(s) \end{bmatrix} \begin{bmatrix} P_1(s) \\ \dot{V}_4(s) \end{bmatrix} \quad (6)$$

In these equations $P(s)$ refers to the Laplace transform of the oscillatory component of pressure and $\dot{V}(s)$ refers to the Laplace transform of the oscillatory component of volume flow. Figure 12 illustrates the equivalent multi-variable block diagrams for each of the above equations.

Communication with MSFC (R-P&VE-SLR) personnel indicated that the impedance matrix form given in Eq (3) is most convenient for use in the stability analysis of the overall "Pogo" loop.

AMDR 9635-037

IV,C,1, General Discussion (cont.)

The combined suction line and sidebranch device may be represented by a 2 x 4 transmission matrix which is formed by postmultiplying the 2 x 2 forward transmission matrix of the suction line (superscript "t") by the 2 x 4 transmission matrix of the device (superscript "d"):

$$\begin{bmatrix} P_1 \\ \dot{V}_1 \end{bmatrix} = \begin{bmatrix} a_{11}^t & a_{12}^t \\ a_{21}^t & a_{22}^t \end{bmatrix} \begin{bmatrix} a_{11}^d & a_{12}^d & a_{13}^d & a_{14}^d \\ a_{21}^d & a_{22}^d & a_{23}^d & a_{24}^d \end{bmatrix} \begin{bmatrix} P_5 \\ P_b \\ \dot{V}_5 \\ \dot{x}_b \end{bmatrix} = \begin{bmatrix} a_{11}^r & a_{12}^r & a_{13}^r & a_{14}^r \\ a_{21}^r & a_{22}^r & a_{23}^r & a_{24}^r \end{bmatrix} \begin{bmatrix} P_5 \\ P_b \\ \dot{V}_5 \\ \dot{x}_b \end{bmatrix} \quad (7)$$

Note that the S term within parentheses after each Laplace transformed variable has been omitted for brevity. Using the preferable impedance matrix form of Eq (7), we may write

$$\begin{bmatrix} P_1 \\ P_5 \\ P_b \end{bmatrix} = \begin{bmatrix} Z_{11}^r & Z_{12}^r & Z_{13}^r \\ Z_{21}^r & Z_{22}^r & Z_{23}^r \\ Z_{31}^r & Z_{32}^r & Z_{33}^r \end{bmatrix} \begin{bmatrix} \dot{V}_1 \\ \dot{V}_5 \\ \dot{x}_b \end{bmatrix} \quad (8)$$

The multivariable block diagram representation of Eq (8) is shown in Figure 13. The functions $Z_{ij}(s)$ that comprise the matrix given in Eq (8) are generally irrational functions of the Laplacian variable s. These transcendental functions arise as a result of the distributed parameter nature of the suction line. It is shown in Appendix D that the solution of the one-dimensional wave equation results in hyperbolic functions and/or exponentials of fractional powers of s. Since these irrational functions are not convenient for use in the overall stability analysis of the Saturn "Pogo" loop, a method must be devised to obtain approximate rational fraction expressions for each element, $Z_{ij}(s)$, of the matrix expressed in Eq (8).

IV,C,1, General Discussion (cont.)

The most obvious method to obtain rational fraction expressions for the matrix $[Z_{ij}(s)]$ is to reconstruct the mathematical model of the suction line so that it is composed of a series of lumped parameter elements. However, this model would not be as general as the distributed parameter hydraulic line model presented in Appendix B, and would not allow evaluation of certain concepts such as the lossy line and the injection of gaseous Helium in large quantities. Therefore, it is desirable to use the exact distributed parameter analytical model of the suction line and then obtain rational fraction approximations of the resultant impedance matrix elements. The following two methods of obtaining these rational fraction expressions have been considered: (1) curve fitting the frequency response of a rational fraction to that of the exact function, and (2) obtaining a rational fraction by means of an infinite product expansion of the exact function. The infinite product expansion method, as explained in bibliography entry A.18, is the more direct method which becomes quite arduous in the case of three cascaded absorptive transmission lines. Therefore, the rational fraction curve fit procedure using a digital computer is desirable.

During the course of the contract, work was initiated to develop a computer program capable of approximating any arbitrary frequency response function as a rational fraction expression, which is valid over some finite frequency interval. This program will determine the coefficients of the polynomials in s by means of curve fitting orthogonal functions as components, using least squares as the curve fit criterion. However, the curve fit program was not completed during the course of the initial contract with the result that Aerojet personnel were not able to provide MSFC personnel with specific analytical descriptions of the suction line dynamics in the form of rational fractions of s .

A partial evaluation of "Pogo" fixes has been accomplished by use of the analytical model of the frequency response of the Saturn propellant feed systems, as described in Appendix F. The following sections describe the general representations of the fix devices as well as the results obtained from the fix evaluation.

AMDR 9635-037

IV,C, Define Saturn "Pogo" Fixes (cont.)

2. Sidebranch Corrective Device

A general analytical representation of sidebranch corrective devices begins with the schematic representation of such devices as shown in Figure 14. This basic model of a sidebranch device may be used to represent various hydraulic suppression devices such as gas and spring loaded accumulators, standpipes with gas entrapment, constant area bellows, Helmholtz resonators, and hydraulic capacitors.

It can be seen from Figure 14 that the relationship between the oscillatory volume flow into the sidebranch device (\dot{V}_i), the oscillatory pressure at the branch (P_i), and the longitudinal vibratory motion of the device (\dot{x}_d) is given by:

$$\dot{V}_i = Y_i P_i + H_d \dot{x}_d \quad (9)$$

where $Y_i = Y_i(s)$ = input admittance of the device
 $H_d = H_d(s)$ = structural transfer function

The variables of Eq (9) are generally related to each other as well as to other variables in the overall stability loop. For example, the vibratory velocity of the device \dot{x}_d may be related to the modal velocities of each longitudinal vibration mode of the vehicle structure:

$$\dot{x}_d = \sum_{k=1}^n \phi_{dk} \dot{q}_k \quad (10)$$

where q_k = generalized coordinate velocity in the k^{th} structural mode
 ϕ_{dk} = normalized modal displacement at the device.

AMDR 9635-037

IV,C,2, Sidebranch Corrective Device (cont.)

As mentioned in the preceding discussion, the sidebranch device, represented as a pure compliance at the pump inlet, has been evaluated as a candidate fix for the Saturn "Pogo" problem by use of the frequency response analysis described in Appendix F. This evaluation is based on the assumption that the effect of the structural motion, \dot{x}_d , upon the dynamic performance is negligible. Hence the oscillatory flow into the branch device is simply a function of the branch point pressure, as defined by Eq (9). The input admittance of the sidebranch device is given by the expression

$$Y_i = \left. \frac{\dot{V}_i}{P_i} \right|_{\dot{x}_d=0} = \frac{C_s}{1 + RCs + LCs^2} = \frac{C_s}{1 + \left(\frac{2S}{\omega_n}\right)s + \left(\frac{S}{\omega_n}\right)^2} \quad (11)$$

This expression corresponds to Eq (12) in Appendix F which is used to represent the frequency response of the device. The frequency response of a sidebranch device, obtained by letting $s = j\omega$ in Eq (11), is plotted in Figure 15. The results obtained from the fix evaluation using the analytical model of the Saturn feed system with a branch device inserted are presented in Section C.5 of this discussion.

3. Lossy Line

The "lossy line" concept has been considered as a method of suppressing the feed system acoustic resonances within the frequency band of interest. Conceptually, the suction line may be made a lossy line by means of uniformly distributing compliant elements along its length. The investigation of the frequency response of such a "lined duct" has been the subject of numerous papers, most of which are presented in Section B of the Bibliography. Most of these papers are concerned with sinusoidal wave propagation through an absorptive line containing a gaseous medium. However, the same basic theory applies to a liquid medium. The analytical model of the absorptive line is presented in Appendix D. This model may be applied to both the lossy line and the gas injection concept which will be described in the next section.

AMDR 9635-037

IV,C,3, Lossy Line (cont.)

As shown in Figure 1 of Appendix D, the lossy line may display either one or two axial acoustic transmission paths, depending on its construction. If the resonator cavity is partitioned, then there is only axial acoustic wave propagation along the main path. However, if the cavity is not partitioned, then there is acoustic wave propagation along the backside path as well as the main path. The analytical results presented in Appendix D are theoretically valid only for the case of the lossy line with a partitioned resonator cavity.

The results of the absorptive line study have been dimensionalized for convenient application to the design of a lossy line for the Saturn feed lines. In the case of negligible flow velocity, Figures 2 through 10 of Appendix D may be used to estimate the attenuation function, phase function, and acoustic velocity for various frequencies. The effect of the increase in the attenuation function, α' , upon the damping of suction line resonant response may be investigated by considering the resonant value of the input impedance. The expression for $|Z|_{res}$, as a function of α' , is given in Eq (61) in Appendix D. The values of $|Z|_{res}$, as predicted by Eq (61), are conservative since the simplified analysis does not account for the added resistance of the pump, discharge lines, and thrust chamber.

Certain configurations of the lossy line have been considered which cause a drastic reduction of the acoustic velocity at low frequencies. As shown in Appendix D, the low frequency asymptote of the acoustic velocity is inversely proportional to the term $[1 + C_a/C_m]^{1/2}$. Thus if the capacitance ratio $C_a/C_m = 1000$, the acoustic velocity will be 3.16% of the nominal acoustic velocity a_0 . For the Saturn V LOX suction line, the nominal acoustic velocity is $a_0 = 2050$ fps (at $T = 165^\circ R$, including the effect of the radial compliance of the pipe walls) and the flow velocity is 32 fps (in the downstream section of the suction line). Thus at low frequencies, the complex Mach number (for $C_a/C_m = 1000$) is:

$$\lim_{\omega \rightarrow 0} \psi(\omega) \approx \frac{u_0}{a} \left[\frac{C_a}{C_m} \right]^{1/2}, \quad \text{for } \frac{C_a}{C_m} \gg 1 \quad (12)$$

$$\therefore \lim_{\omega \rightarrow 0} \psi(\omega) = \frac{32}{(2050)(.0316)} = .494$$

IV,C,3, Lossy Line (cont.)

Results presented in Appendix D show that when the amplitude of the complex Mach number exceeds 0.2, the effective propagation function is significantly altered. Therefore, the steady-state effect of flow must be considered in the frequency response analysis of a lossy line with a large capacitance ratio.

4. Gas Injection, Approximate Model

During the initial contract, an attempt was made to apply the absorptive line analysis to the case of gas bubbles uniformly distributed throughout the propellant line. This attempt resulted in an approximate analysis which is valid for large bubbles or higher frequencies. However, it was later found that for the case of low frequency wave propagation through a mixture of LO₂ and helium, this analysis was not accurate. Therefore, an exact analysis, which is valid for all frequencies and bubble sizes was developed during the second contract. The application of this analysis (Appendix E) will be discussed in Section V. The approximate gas injection model is discussed here.

As mentioned in Appendix D, the generalized absorptive line analysis may be applied to the case of helium bubbles distributed throughout the oxidizer suction line. Expressions are required for the resonant frequency (ω_a), generalized damping ratio (ζ_a), and effective capacitance ratio (C_a/C_m) of the bubbles. However, the assumption of constant fluid inertance in the main path (L_m) is valid only for a gas volume ratio, (vol of gas)/(vol of liquid), of less than 5%. It is felt that this restriction is minor since engine performance considerations probably dictate a maximum gas volume ratio of the same order.

First, consider the case of adiabatic bubble pulsations. The resonant frequency of the adiabatic bubble is expressed by the equation:

$$\omega_o = \left[\frac{1}{L_b C_{bo}} \right]^{\frac{1}{2}} \quad (13)$$

IV,C,4, Gas Injection, Approximate Model (cont.)

From entries C.6 and C.18 in the Bibliography, the approximate equations for the bubble inertance and adiabatic capacitance are given by:

$$L_b = \frac{\rho_l}{4\pi r_b} \quad (14)$$

$$C_{bo} = \frac{4\pi r_b^3}{3k\bar{P}_b} \quad (15)$$

where

ρ_l = mass density of the liquid surrounding the bubble

k = ratio of specific heats of the gas in the bubble

\bar{P}_b = average static pressure in the bubble

r_b = radius of the bubble

Combining Eqs (13) through (15), the expression for the adiabatic resonant frequency of the bubble may be written:

$$\omega_o = \frac{1}{r_b} \left[\frac{3k\bar{P}_b}{\rho_l} \right]^{\frac{1}{2}} \quad (16)$$

This frequency is associated with the adiabatic breathing mode of the bubble which results in simple volume pulsations of the nearly spherical bubble. This frequency corresponds to actual breathing mode only for small bubbles since larger bubbles will display oscillatory heat transfer across the bubble surface. For a small helium bubble of radius .04 in. in LO_2 , the breathing mode frequency is approximately 10,000 cps. Figure 16 shows the breathing mode frequency as a function of the bubble radius and static pressure for helium bubbles in liquid oxygen. It is seen that impossibly, large bubbles are necessary to achieve resonant frequencies in the 20 to 50 cps range.

The expression for the capacitance ratio, C_a/C_m , may be derived by again assuming that the bubble capacitance (compliance) is adiabatic.

IV,C,4, Gas Injection, Approximate Model (cont.)

The ratio C_a/C_m is then simply the product of the gas volume ratio, \mathcal{V} , and the adiabatic gas compressibility ratio, χ_o :

$$\left. \frac{C_a}{C_m} \right|_{\text{adiabatic}} = \frac{G}{C_m} = \mathcal{V} \chi_o \quad (17)$$

where

$$\mathcal{V} = \frac{\bar{V}_g}{\bar{V}_l} = \frac{\text{gas volume flow}}{\text{liquid volume flow}}$$

$$\chi_o = \frac{B_l}{k P_g} = \frac{\text{adiabatic gas compressibility}}{\text{liquid compressibility}}$$

$$B_l = f_l a_o^2 = \text{bulk modulus including the effect of pipe wall elasticity.}$$

Applying Eq (17) to the case of the LOX suction line for a temperature of 165°R and pressure of 65 psia, the nominal acoustic velocity (accounting for pipe wall elasticity), bulk modulus, and compressibility ratio are given respectively, as $a_o = 2050$ fps, $B_l = 6.48 \times 10^4$ psi, and $\chi_o = 6.0 \times 10^2$. Therefore, the maximum capacitance ratio corresponding to a gas volume ratio of 5% is $C_a/C_m = 30$.

The damping mechanism involved in the volume pulsation of gas bubbles is quite complicated. Fundamentally, the three sources of energy dissipation are heat conduction, reradiation of sound energy from the bubbles, and viscous damping at the boundary of the bubble. Bibliography entry C.16 gives the following expression for the damping constant, as a function of frequency:

$$\zeta_a = \zeta_{th} + \zeta_{rad} + \zeta_{vis} \quad (18)$$

IV,C,4, Gas Injection, Approximate Model (cont.)

The three terms comprising S_a are defined by the following equations:

$$S_{th} \approx \frac{3}{2\Theta} \frac{k-1}{\Omega^{3/2}} \quad , \quad \Omega^{1/2} > \frac{50}{\Theta} \quad (19)$$

$$S_{rad} \approx \left[\frac{3}{4} \frac{1}{\chi_0} \right]^{1/2} \Omega^2 \quad , \quad \Omega^{1/2} > \frac{50}{\Theta} \quad (20)$$

$$S_{vis} \approx \frac{2\eta_l}{r_b} \left[\frac{\rho_l}{3k\bar{P}_g} \right]^{1/2} \quad , \quad \Omega^{1/2} > \frac{50}{\Theta} \quad (21)$$

where

$$\Omega = \frac{\omega}{\omega_a}$$

$$\omega_a \approx \left[\frac{3k\bar{P}_g}{r_b^2 \rho_l} \right]^{1/2} \quad , \quad \Omega^{1/2} > \frac{50}{\Theta}$$

$$\Theta = \left[\frac{2r_b}{D_g} \right]^{1/2} \left[\frac{3k\bar{P}_g}{\rho_l} \right]^{1/4}$$

D_g = thermal diffusivity of gas in bubble

η_l = kinematic viscosity of liquid

The range $\Omega^{1/2} > 50/\Theta$, defines nearly adiabatic bubble pulsations. Unfortunately, this assumption is invalid for the frequencies of interest (1 - 40 cps). Therefore, the exact theory will be developed and applied to this condition in Part II.

The parameters ω_a , C_a/C_m , and S_a may be used with Eqs (15) and (24) of Appendix D to obtain the wave propagation parameters $Z_c(\omega)$ and $\chi(\omega)$. Since the propagation constant is composed of the attenuation constant, $\alpha'(\omega)$, and the phase constant, $\beta'(\omega) = \omega/a(\omega)$, both the attenuation and acoustic velocity may be obtained from the above-mentioned equations.

IV,C,4, Gas Injection, Approximate Model (cont.)

Experimental data obtained for one-dimensional wave propagation in a mixture of air bubbles and water is presented in Figures 17 and 18. This data has been obtained from bibliography entry G.16. In Figure 17, the theoretical predictions of the attenuation constant, obtained from Eq (24) of Appendix D are plotted with the experimental values of attenuation. It is seen that the correlation of theory and experimental data is quite good at these frequencies if the frequency dependence of the damping factor is included.

5. Fix Evaluation

In the process of defining the best set of compensation devices, various criteria can be applied. For example, a lumped parameter device such as a sidebranch resonator can be considered to fit into a general feed system in the manner shown in the general impedance network of Figure 19. Applying network theorems to the system of Figure 19 yields P_{λ} (with device) and P_{λ}' (without device). The ratio, P_{λ}'/P_{λ} is known as the insertion ratio and is given by the expression

$$\frac{P_{\lambda}'}{P_{\lambda}} = 1 + Y_{\lambda} \left[\frac{Z_1 Z_2}{Z_1 + Z_2 + Z_1 Z_2 (Y_1 + Y_2)} \right] \quad (22)$$

where Z_1 and Z_2 are the upstream and downstream impedances and Y_1 and Y_2 are the downstream admittances. It can be seen from Eq (22) that the filtering action of the device is dependent on upstream and downstream fluid dynamics. It is also apparent that the input admittances, Y_{λ} , associated with various devices will yield a relative comparison of filtering effectiveness. Recall that the input admittance of a sidebranch resonator, as shown in Figure 15, displays an admittance maxima at the resonant frequency. Therefore, it is common practice to "tune" such a device to achieve the maximum insertion ratio at the desired frequency.

Analytical models of the S-IB and S-IC propellant feed systems have been developed to allow the preliminary evaluation of the candidate stabilization devices. The preliminary analytical model utilizes the analog circuit

IV,C,5, Fix Evaluation (cont.)

of the feed system shown in Figure 1. A frequency response analysis of each circuit, with the conceptual fix device inserted, allows the evaluation of the effect of the device on the response characteristics of the feed system.

The main design criterion that is used in these studies is the minimization of the primary feed system transfer function amplitudes at the frequencies of the vehicle longitudinal modes. Recall that this transfer function is defined by Eq (7) of Appendix F. Since the peaks in the amplitude of this transfer function occur at the feed system acoustic mode frequencies, it is apparent that, to satisfy the abovementioned criterion, either the frequencies of the acoustic modes must be shifted or the modes must be suppressed by the addition of damping.

During the course of the contract, the effect of the insertion of a compliant sidebranch device upon the frequency of the Saturn feed system acoustic modes was investigated. This investigation utilized the analytical model of the Saturn propellant feed system with the values of dynamic parameters presented in Table I. The results of this analysis are presented in Figures 20 and 21. Note that, since the impedance Z_5 of the length of suction line between the pump and the branch point was assumed negligible, it is possible to lump the two capacitances C_4 and C_6 . Thus, the effect of the variable cavitation compliance upon the feed system resonant frequencies may also be determined.

D. REVIEW TEST PROCEDURES AND FACILITIES

The experience gained by Aerojet-General personnel during the Titan II/Gemini engine transfer function test program (Appendix A) was applied to the similar pulse test program which was conducted for the H-1 and F-1 feed systems on the bobtail test facilities. In particular, the objective of this review was to evaluate the adequacy of the test apparatus and dynamic data acquisition system with regard to experimentally defining the frequency response characteristics of the turbopumps associated with the H-1 and F-1 engine systems.

IV,D, Review Test Procedures and Facilities (cont.)

A review of the H-1 and F-1 bobtail testing facility was conducted at MSFC by personnel from the Aerojet Test Instrumentation Division which resulted in the following recommendations.

1. F-1 Turbopump Facility

a. Oxidizer Pump Dynamic Instrumentation

The original suction line dynamic instrumentation consisted of two diametrically opposed strain gage pressure transducers which were installed immediately above the suction flange. Both transducers were tube-connected: one with a 6-in. tube length, the other with an approximate 18-in. tube length. One measurement device, which was located 90 in. above the suction flange, was installed with an approximate 24-in. tube length to a strain gage transducer. Two diametrically opposed strain gage transducers were installed on each discharge line immediately below the discharge flange with tube connections of 18-in. to 36-in. line lengths.

In view of the poor frequency response characteristics of non-flush pressure transducers, it was also recommended that all pressure transducers for dynamic measurement be flush mounted. This was necessary because the compliance of entrapped gas or the mounting structure may lower the resonant frequency of the transducer so that it is within the frequency range of interest. In particular, it may be shown that the "bubble" mode of the non-flush mounted pressure transducers, which is caused by the resonance of the liquid in the connector and the gas compliance, may exist at frequencies of less than 20 cps.

One problem that precluded the flush-mounting of the pressure transducers in the IO_2 circuit was the potential cracking of transducer diaphragms due to the freezing of the water in the transducer cavity. As a consequence of this problem, it was recommended that the IO_2 pressure transducers be "close-coupled," using the following criterion for the minimum coupling tube lengths:

IV,D,1,a, Oxidizer Pump Dynamic Instrumentation (cont.)

- (1) Shorten all suction measurement connector tubes to 2 in.
- (2) Shorten all discharge measurement connector tubes to 6 in.

These lengths were specified to insure that the "bubble mode" frequency is greater than 50 cps. In addition, it was recommended that the strain gage pressure transducers be temperature compensated for cryogenic temperatures. The following additional transducers were recommended to insure consistent dynamic measurement: (1) additional transducers at each discharge line (preferably at available boss 6 in. downstream of original measurement), and (2) two transducers in LO₂ bleed-off line with maximum distance between them. The pressure transducers in the bleed-off line were necessary to compute the oscillatory flow in this line. The oscillatory component of flow is calculated by taking the product of the measured oscillatory pressure drop and the theoretical admittance of the section of line.

Originally it was recommended that the oscillatory component of flow in the bleed-off line be directly measured by use of a fast response turbine-flowmeter. Although a modified Potter flowmeter was located which was suitable for this application, it was found that installation of this device in the bleed-off line was considered a major change by MSFC personnel.

b. Fuel Pump Dynamic Instrumentation

The original dynamic instrumentation for the F-1 fuel pump consisted of four diametrically opposed flush-mounted Photocon Model 207 transducers, two of which were installed in each suction line above the flange, and with the remaining two installed in each discharge line immediately below the discharge flange.

It was recommended that all Photocons remain in their originally installed location. It was further recommended that (1) at least one flush-mounted transducer be added at the 90-in. suction point of each line, (2) two flush-mounted transducers be added in each discharge line at the two

IV,D,1,b, Fuel Pump Dynamic Instrumentation (cont.)

stations where bosses are located, and (3) two flush or close-coupled transducers be added in the fuel bleed-off line at two stations. As in the case of the LO_2 bleed-off line, direct measurement of the flow fluctuations by use of a fast response flowmeter was recommended.

2. H-1 Turbopumps

a. Oxidizer Pump Dynamic Instrumentation

The original suction line dynamic instrumentation consisted of three suction line measurements which were instrumented with tube connections, 18-in. to 36-in. lengths, to strain gage transducers. One of the suction line measurements was located in the suction flange; the other two measurements were located between the pulser and suction flange. One measurement was installed in the discharge flange and was connected by a 24-in. tube to a strain gage transducer.

It was recommended that all pressure transducers be flush mounted to insure adequate frequency response. As an alternative to flush-mounting, it was suggested that the transducers be close-coupled using tube lengths of less than 2 in. in the suction line and less than 6 in. in the discharge line.

Because of the extreme closeness of the original discharge pressure transducer location to the turbulent rotational flow at the outlet of the pump, the validity of the dynamic data resulting from this measurement is suspect. Therefore, it was recommended that two additional transducers be added at two stations further downstream of the discharge flange.

b. Fuel Pump Dynamic Instrumentation

The original suction line dynamic instrumentation for the H-1 fuel pump consisted of two suction pressure measurements which were instrumented with tube connections to strain gage pressure transducers of 18-in. to 36-in. tube lengths. The dynamic discharge pressure transducer was connected to the fuel pump discharge flange by a tube length of approximately 24 in.

IV,D,2,b, Fuel Pump Dynamic Instrumentation (cont.)

It was recommended that all pressure transducers be flush-mounted. In lieu of flush-mounting, the transducers may be close-coupled using the 2-in. and 4-in. maximum coupling tube lengths for the suction and discharge measurements, respectively. As in the case of the LO₂ discharge pressure measurement, the addition of two discharge pressure measurements was recommended.

3. General Recommendations

Technical information concerning the dynamic problems associated with non-flush-mounting of pressure transducers has been transmitted to Marshall Space Flight Center. In particular, it was suggested that Kistler or Photocon 2775 or 2765 pressure transducers could be flush-mounted to the oxidizer propellant system without danger of freezing and subsequent contamination of the LO₂ circuit.

In addition to measuring oscillatory pressure during the H-1 and F-1 turbopump pulsing tests, it is desirable to measure oscillatory flow at the pump inlet and outlet. Aerojet personnel investigated the availability of a commercial flowmeter which would be compatible with the propellants, and measure flow fluctuations at frequencies of 2 to 20 cps. In addition, an investigation was initiated to study the possibility of using the existing F-1 propellant flowmeters to measure oscillatory flow in the pump suction line. The existing units were Potter turbine flowmeters which were located in the prevalves. It was planned to utilize experimental step response data (available from the manufacturer) to obtain a dynamic calibration. Use of these meters would have required a modification of the associated pulse-counting data processing hardware. However, it was found that the frequency of the output signal was too low (80 cps) to achieve adequate frequency response. According to the Potter Corp. representatives, there was no simple modification possible which would increase the frequency output at nominal flow. Therefore, it was not feasible to use the F-1 Potter meters to measure flow fluctuations in the suction lines.

A survey of the commercially available flowmeters indicated that there were no readily available oscillatory flow transducers which met all

IV,D,3, General Recommendations (cont.)

of the following requirements:

High frequency response (first order lag ≤ 5 msec).

Compatible with both RP-1 and LOX.

Same size as H-1 and F-1 suction lines and/or discharge lines.

Since oscillatory flow measurement was apparently not feasible in the suction and discharge lines of the F-1 turbopump facility, it was recommended that direct measurement of the oscillatory flow in the discharge pulser bleed-off line be obtained. As a result of a review of the available flowmeters, it was determined that a modified Potter turbine flowmeter would best meet the requirements. Specifically, the flowmeter recommended was a 3-in.-line flowmeter designed by Aerojet-General and manufactured by Potter to comply with AGC specification No. S770: 1550, per Aerojet Drawing 258857. Briefly, this flowmeter met the following requirements:

Operating temperature range	- -425°F to +200°F
Maximum rated flow (water)	- 700 gpm
Output frequency (at maximum flow rate)	- 455 cps
Nominal LOX flow rate	- 377 gpm at 10 psid
Theoretical response time constant	- 4 msec
Practical response time constant	- 10 to 20 msec

Information describing the dynamic relationship between fluid pulser piston travel and pump inlet suction pressure was provided to MSFC in Aerojet Report PTDR 9647-031, "Aerojet-General 'Pogo' Experience" which constituted Appendix H of this final report.

E. ASSIST IN UTILIZING DYNAMIC TEST DATA

The dynamic response data which was obtained from the pulse tests of the H-1 and F-1 engine systems will be used by the various contractors to

IV, E, Assist in Utilizing Dynamic Test Data (cont.)

verify or modify their respective analytical models. The objective of this task was to insure that the final response data was valid and consistent.

In particular, the following improvements in data handling were considered necessary to obtain meaningful dynamic data from the F-1 and H-1 pulse test programs.

1. Recording

Recording of all dynamic data was accomplished on Ampex FR600 14-channel FM tape recorders. Full signals were recorded on tape; that is, static data with dynamic data on the same trace.

Since the dynamic portion of the trace represents only 1 to 10% of the trace value on the discharge side, it was highly recommended that all traces be high-passed approximately 1 cycle and amplified onto the tape for better dynamic data presentation. It was further recommended that dynamic calibration be placed on tape and also a phase calibration prior to run by placing an AC signal at discrete frequencies 2 to 30 cycles in 5-cycle steps or frequencies of major interest on all channels simultaneously, ahead of any filters used in the system.

2. Data Presentation

Traces were played back to an oscillograph, one to a record displayed in three forms: one DC presentation and two filtered presentations of the same trace. Filtered traces were amplified after filtering from the tape recorder. Dynamic data of this type were subject to a high noise-to-signal content making a qualified data analysis extremely difficult.

It was recommended that with high-passed data onto tape, grouping of traces could be displayed on the same oscillograph record for quick-look, phase-amplitude check. Grouping should be for each pump circuit.

3. Data Reduction

It was understood that Rocketdyne had been assigned the responsibility for the reduction and interpretation of the frequency response

IV,E,3, Data Reduction (cont.)

data resulting from the H-1 and F-1 turbopump pulsing tests. Because of the relative importance and large expense of the experimental pump transfer function program, it was recommended that MSFC personnel initiate a small-scale transfer function determination program using a partial set of pulse test data as a check on the results of the Rocketdyne data analysis. The MSFC effort may be simplified by use of the existing dynamic data reduction facilities at the Computation Laboratory.

Communication between Aerojet and MSFC (R-Comp) personnel has revealed that the Computation Laboratory has an existing digital computer program which may be used to directly compute transfer functions from tape recorded frequency response data. The proposed frequency response function determination is based on the relationship:

$$H_{jk}(\omega) = \frac{S_{kj}(\omega)}{S_{kk}(\omega)} \quad (23)$$

where $H_{jk}(\omega) \triangleq \frac{P_j(\omega)}{P_k(\omega)}$ = frequency response function between $P_j(\omega)$ and $P_k(\omega)$

$P_j(\omega)$ = Fourier transform of j^{th} parameter (output), $P_j(t)$

$P_k(\omega)$ = Fourier transform of k^{th} parameter (input), $P_k(t)$

$S_{kj}(\omega)$ = cross power spectral density (or simply cross spectrum) of the j^{th} and k^{th} parameters

$S_{kk}(\omega)$ = power spectral density (or simply spectrum) of the k^{th} parameter

The cross spectrum, $S_{jk}(\omega)$, is generally a complex function of frequency having a real part, $S_{cjk}(\omega)$, called the cospectrum, and an imaginary part, $S_{qjk}(\omega)$, called the quadrature spectrum. Consequently the absolute amplitude of the

IV, E, 3, Data Reduction (cont.)

cross spectrum is

$$|S_{jk}(\omega)| = \left\{ [S_{cjk}(\omega)]^2 + [S_{qjk}(\omega)]^2 \right\}^{\frac{1}{2}} \quad (24)$$

and the phase angle of the cross spectrum is:

$$\angle S_{jk}(\omega) = \text{Tan}^{-1} \left[\frac{-S_{qjk}(\omega)}{S_{cjk}(\omega)} \right] \quad (25)$$

Since the spectrum $S_{kk}(\omega)$ is always real, the expression for the absolute magnitude of the transfer function is:

$$|H_{jk}(\omega)| = \frac{|S_{kj}(\omega)|}{S_{kk}(\omega)} \quad (26)$$

It is seen that the phase angle of the transfer function is simply the phase angle of the cross spectrum:

$$\angle H_{jk}(\omega) = \angle S_{kj}(\omega) \quad (27)$$

MSFC Computation Laboratory personnel have an established program capable of directly computing the spectrum and cross spectrum for any tape recorded dynamic parameter, $P_i(t)$. In the case of the F-1 pulse tests, the parameters, $P_i(t)$, are listed in Table 12. For example, the second parameter in the table (corresponding to $i = 2$) is the fuel suction pressure at the #1 inlet; therefore, we may write

$$P_2(t) = P_{sf-1b}$$

Using this nomenclature, the transfer function relating the oscillatory pressure at the #1 pump outlet to the oscillatory pressure at the #1 pump inlet is written

$$H_{3,2}(\omega) = \frac{P_3(\omega)}{P_2(\omega)} = \frac{P_{df-1a}}{P_{sf-1b}} \quad (28)$$

IV,E,3, Data Reduction (cont.)

From Eqs (26) and (27), the absolute magnitude and phase of the transfer function are easily found once the spectrum of $P_2(t)$ and cross spectrum of $P_1(t)$ are computed.

It is observed from Table 12 that there are 29 dynamic parameters which may be arranged in different ratios to yield a total of 812 different transfer functions. However, if we take a common reference parameter $P_n(t)$, then only 29 cross spectra need be computed since an arbitrary transfer function may be found from the relationship

$$H_{ij}(\omega) = \frac{H_{in}(\omega)}{H_{jn}(\omega)} = \frac{S_{ni}(\omega)}{S_{nj}(\omega)} \quad (29)$$

Table 13 has been constructed to show explicitly what cross spectra are needed. Note that the two reference parameters, in the case of the tapes A and B, are the pulser position and the pump discharge pressure at outlet #1. Hence all cross spectra are relative to parameters P_4 and P_{11} for fuel pulsing data, and to parameters P_{16} and P_{22} for oxidizer pulsing data. In addition to computing spectra of these reference parameters, the spectra of certain other important parameters are desired. This will provide a check of the random noise background. Finally, Table 13 indicates that although the spectral analysis of the tape C data is optional, the reference parameter is the alternate pump discharge pressure at outlet #1.

The following discussion concerns the operation of the computer program to determine the spectra $S_{kk}(\omega)$ and the cross spectra $S_{jk}(\omega)$. The operation of the program is affected by several considerations that arise when the magnetic taped data is digitized. The following parameters must be considered:

- N = number of data points in digitized data
- t = sampling interval
- m = number of lags

IV,E,3, Data Reduction (cont.)

Δf = calculation resolution

B = spectrum bandwidth

The value of m normally is chosen such that

$$40 \leq \frac{2N}{m} \leq 200$$

If the parameter m does not obey this criterion, the resultant spectra may be invalid because of either of the following problems: (1) confidence level too low (if $20m < N$), or (2) resolution too low (if $N < 100m$).

The calculation resolution, Δf , is usually chosen so that

$$\Delta f = \frac{1}{2m\Delta t}$$

This insures that the frequency interval is covered in a manner such that the estimates completely overlap each other. The spectrum bandwidth is given by

$$B = \frac{1}{m\Delta t}$$

The parameters N, Δt , and m are functions of the maximum frequency cutoff which can be established by filtering the data. A particularly suitable form of filtering used at Aerojet-General is a digital filter having a cutoff rate of over 200 db/octave and zero degrees phase shift in the pass band. A description of this filter can be found in entry G.6 of the Bibliography.

The complete description of N, Δt , and m in terms of maximum frequency cutoff, record length, and maximum lag is given in entry G.3 of the Bibliography.

V. DISCUSSION, PART II

A. EVALUATION OF FIX DEVICES

1. General Considerations

The evaluation of various "Pogo" fix devices may be performed on an open-loop basis by comparing their effect in the suppression of propulsion system resonant gains and the separation of system resonant frequencies.

V,A,1, General Considerations (cont.)

This frequency domain analysis was accomplished by use of the Saturn propulsion system model described in Appendix F. The analog circuit corresponding to this model is shown in Figure 22. It may be noted that this model is more complete than the model used in Part I, in that it 1) allows for gas injection in the suction line, 2) includes the gain of the nonreciprocal pump, and 3) predicts the chamber pressure response. The analog circuit for this model is shown in Figure 22, which may be compared to Figure 1. Both models require the assumption that the dynamic interaction of fuel and oxidizer systems, due to cross flow of oscillations through the common combustion chamber, is negligible. It is also assumed that the "bootstrap" (gas generator/turbine) loop gain is sufficiently attenuated at the frequencies of interest so that it may be ignored.

Before investigating the effect of feed system fix devices, the nominal feed system frequency response, as predicted by the improved model, should be reconsidered. The frequency response characteristics of the nominal SIC LOX feed system are shown in Figures 23 and 24. The frequency response functions $H_p(\omega)$ and $H_t(\omega)$ describe the respective oscillatory responses of the propulsion system to oscillatory acceleration at the pump inlet and pressure oscillations at the tank bottom, which are the two major input variables. These functions are defined by the following expressions:

$$H_{ps}(\omega) = \frac{P_s}{\ddot{x}_p} = \frac{P_7(\omega)}{\ddot{x}_p(\omega)} \Big|_{P_1(\omega)=0} \quad (30)$$

$$H_{pd}(\omega) = \frac{P_d}{\ddot{x}_p} = \frac{P_8(\omega)}{\ddot{x}_p(\omega)} \Big|_{P_1(\omega)=0} \quad (31)$$

$$H_{pe}(\omega) = \frac{P_e}{\ddot{x}_p} = \frac{P_9(\omega)}{\ddot{x}_p(\omega)} \Big|_{P_1(\omega)=0} \quad (32)$$

$$H_{ts}(\omega) = \frac{P_s}{P_t} = \frac{P_7(\omega)}{P_1(\omega)} \Big|_{\ddot{x}_p(\omega)=0} \quad (33)$$

$$H_{td}(\omega) = \frac{P_d}{P_t} = \frac{P_8(\omega)}{P_1(\omega)} \Big|_{\ddot{x}_p(\omega)=0} \quad (34)$$

$$H_{te}(\omega) = \frac{P_e}{P_t} = \frac{P_9(\omega)}{P_1(\omega)} \Big|_{\ddot{x}_p(\omega)=0} \quad (35)$$

V,A,1, General Considerations (cont.)

These definitions correspond, respectively, to eqs (33), (34), (35), (36), (37), and (38) in Appendix F. Note that $H_{ps}(\omega)$ and $H_{ts}(\omega)$ correspond to the transfer functions that were predicted by the original model used in Part I.

Returning to Figures 23 and 24, it is seen that pressure oscillations are attenuated as they are transmitted from the pump inlet to the engine combustion chamber. In other words, at any frequency ω ,

$$H_{ps}(\omega) > H_{pd}(\omega) > H_{pe}(\omega) ; H_{ts}(\omega) > H_{td}(\omega) > H_{te}(\omega) \Rightarrow P_s(\omega) > P_d(\omega) > P_e(\omega)$$

This attenuation of downstream traveling oscillations is caused by the presence of large acoustical resistances in the pump/discharge system and the lack of pump amplification due to the assumed unity gain of the pump. As explained in Appendix A, the forward pump "gain" μ_f is a measure of the amplification of pressure oscillations transmitted from the pump inlet to the outlet. This gain is assumed to be unity because of the small degree of cavitation exhibited by the H-1 and F-1 pumps at normal operating conditions.

Comparing the results of Figures 23 and 24, the maximum gains of all functions are found to occur at approximately the same frequencies, which are the feed system acoustic mode frequencies. It is important to define the effect of the various stabilizing concepts upon these acoustic mode frequencies and upon the resonant amplitude (gain) of the most pertinent propulsion system transfer functions. As previously mentioned, a stabilizing influence is achieved if the feed system modes are separated from the vehicle structural modes and/or the transfer function resonant gains are reduced. For this investigation, the effect of the fix devices upon the pump-to-engine transfer function, H_{pe} , and the tank-to-engine transfer function, H_{te} , were considered. The parametric results from the fix concept evaluation will be presented for the function H_{te} only since the same relative effects were noted for the function H_{pe} .

2. Lumped Parameter Devices

As discussed in Appendix A, a device may be classified as lumped parameter when its characteristic length is less than $1/8$ wavelength at the highest frequency of interest. For our purposes, the lumped parameter

V,A,2, Lumped Parameter Devices (cont.)

"Pogo" fix device to be considered is a generalized sidebranch element, as described by eq 11. Recall that this equation describes either an accumulator or a sidebranch resonator, depending on the selection of the resonant frequency, ω_n .

The effect of a sidebranch resonator or capacitive device (accumulator) upon the SIC LOX system acoustic mode frequencies is illustrated by the parametric plot presented as Figure 25. The uncoupled resonant frequency (f_6) and capacitance (C_6) of the device have been varied to determine the effect on the natural frequencies of the coupled system. The insertion point is constant at 90 inches above the turbopump inlet flange. One obvious effect of the resonator is to introduce an additional system acoustic mode (called the $n = 1$ resonator mode) because of its added degree-of-freedom. However, it may be shown that this mode is generally more highly damped than other modes, due to the selection of a relatively large resonator damping factor ($\zeta_6 = 0.1$).

In Figure 26, the effect of placing a tuned resonator at the pump inlet or outlet is shown. This plot illustrates the increased damping of the resonator mode is much more apparent on the discharge resonator. However, neither device is effective in appreciably shifting the coupled system mode frequencies. Referring to Figure 25, it is seen that the effectiveness of the resonator could be increased if either 1) its capacitance is increased or 2) its uncoupled resonant frequency is set equal to the original system mode frequency that must be shifted. Because of the difficulty of tuning the resonator device, it is concluded that the side branch device should be used as a simple capacitance (accumulator) rather than a tuned vibration absorber (resonator). Therefore, subsequent studies of lumped parameter devices consider only the capacitive accumulator.

A comparison of the benefits of suction and discharge accumulators may be obtained by comparing Figures 27 and 28. Although both accumulators are equally effective in shifting the first mode frequency, the discharge accumulator is more efficient in the suppression (attenuation) of the resonant

V,A,2, Lumped Parameter Devices (cont.)

value of the propulsion system gain, $|H_{te}|_{\max}$. The first mode resonant gain and frequency of the SIC LOX system are shown explicitly as a function of accumulator capacitance in Figures 29 and 30 for the suction and discharge accumulators, respectively. Note that the effect of increased capacitance is to increase the resonant gain for the suction accumulator but decreases the resonant gain for the discharge accumulator. However, a suction accumulator may still be used to stabilize the system, providing the feed system mode frequencies are decreased enough to yield adequate separation from the lowest vehicle mode frequency.

The effect of the location of the SIC LOX suction accumulator is shown in Figure 31. The effectiveness of the accumulator, in reducing the first mode ($n = 1$) frequency, is decreased as it is moved up the suction line. Also, the second mode ($n = 2$) frequency is strongly affected by accumulator location and tends to be reduced by moving the accumulator away from the pump inlet. It is thus desirable to insert the accumulator as close to the pump inlet as possible. This conclusion is quite general and applies to other systems such as Titan (Ref 2).

The above-mentioned results all apply to the SIC LOX feed system, although similar conclusions may be drawn when the other Saturn feed systems are considered. Figures 32 through 37 present the results for these feed systems.

3. Distributed Parameter Devices

The primary distributed parameter device considered in this evaluation is the helium gas injection concept, which has been developed by MSFC personnel. As mentioned in Part I of the Discussion, the original Aerojet model of gas injection was invalid for the general case of polytropic bubble pulsations. Therefore, an exact analysis of the effect of bubbles upon wave propagation was developed for the evaluation of gas injection. This analysis, which is presented in Appendix E, accounts for the frequency dependent capacitance and damping of the distributed gas bubbles.

The main variables in the gas injection investigation are the injectant mass ratio (mass flow of gas/mass flow of LOX) and the initial gas

V,A,3, Distributed Parameter Devices (cont.)

bubble size. The mass ratio mainly controls the gas capacitance and hence the resultant acoustic mode frequencies, whereas the bubble size governs the bubble damping.

The effect of bubble damping is particularly important in the analytical model of the Saturn feed system with gas injection since it largely influences the resonant gain. Figure 38, which is a plot of the input admittance at the pump inlet, illustrates that in the frequency range of interest the system damping is strongly dependent on bubble size. The damping of the propulsion system, as indicated by the distance between the envelope of the resonant and anti-resonant values of admittance, tends to be increased as the bubble radius is decreased. The "no-damping" case corresponds to perfectly isothermal pulsations of the bubbles. As explained in Appendix E, the thermal damping of the bubbles is caused by irreversible heat transfer as a result of polytropic bubble pulsations.

Figures 39 and 40 show the effect of bubble damping on the propulsion system transfer functions H_{pe} and H_{te} , respectively. The bubble radius (.02 in.) has been chosen to optimize the suppression of the higher acoustic modes. Note that the injectant mass ratio has been assumed constant in these curves.

The injectant mass ratio is a very important parameter in the adjustment of the feed system acoustic mode frequencies. The reduction of the resonant frequencies by the increase of this parameter is shown in Figure 41 for the isothermal case (no bubble damping). An undesirable effect of increasing the injectant mass ratio is the resultant increase in the resonant gains for the higher acoustic modes, which are shifted into the range of the vehicle structural mode frequencies.

For the case of polytropic bubble pulsations (with bubble damping), the bubble size is also important in the adjustment of the feed system acoustic mode frequencies and resonant gains. This effect is shown for the fundamental mode in Figure 42. The resonant frequency is decreased with increasing bubble radius due to the transition of the bubble capacitance from the isothermal case (r_b very small) to the adiabatic case (r_b very large).

V, Discussion, Part II (cont.)

B. PRELIMINARY DESIGN OF FIX DEVICES

1. General Considerations

a. Introduction

The objective of this task is to conceptually design two candidate oscillation suppression devices for the Saturn propellant feed system. These "Pogo" fix devices shall be compared to gas injection, which is the preferred MSFC fix concept. The fix concepts are compared with respect to the satisfaction of various design criteria, which are described in the following section.

b. Design Criteria

(1) Minimum Schedule Impact

The device shall be designed such that it requires little modification of the existing propulsion system hardware and may be installed in the field with the minimum period of "down-time."

(2) Negligible Performance Loss

Any loss of engine performance due to the insertion of the device shall be no larger than the normal 3 deviation allowance.

(3) Minimum Weight and Envelope

Because of potential interference between any feed system fix device and the structure of the Saturn engine frame (thrust complex), it is desirable to minimize the increase in the envelope of the propulsion system. Obviously, the weight of the device should also be minimized, consistent with the other components in the system.

(4) Material Compatibility

The materials used in any feed system fix device should be compatible with the Saturn propellants. The cryogenic environment imposed by the LO₂ shall not cause any degradation of these materials.

V,B,1,b, Design Criteria (cont.)

(5) Low Amplitude Operating Threshold

Since the fix device must stabilize the system for small amplitude pressure oscillations, it must not display significant "stiction" or "preload" nonlinearities about the operating point.

(6) Control Vaporization of LO_2

In order to precisely control the compliance of a side-branch device in a cryogenic feed system, it is necessary to either eliminate or precisely predict the amount of vaporization of the quiescent liquid that is trapped in the device. The reduction of vaporization can be achieved either by thermally insulating the side-branch cavity or designing it so that it no longer traps large volumes of stagnant fluid. The accurate prediction of the amount of vaporization due to the transient heat transfer from the walls of the device to the cavity liquid is an intractable problem. Although attempts at this prediction have been made (Ref 3) it is clearly desirable to design any oxidizer system accumulator so that there is negligible LO_2 vaporization.

c. Conventional "Pogo" Fix Concepts

The passive feed system suppression devices considered by various "Pogo" investigators are sketched in Figures 43 and 44. These devices may be classified as either lumped parameter or distributed parameter, as determined by their characteristic length relative to an acoustic wave length. The lumped parameter devices shown in Figure 43 all act as "soft" springs to lower the feed system resonant frequencies by introducing additional compliance. The added capacitance is normally inserted at a point near the turbopump and is of the same magnitude as the pump cavitation capacitance. The desired flexibility of the accumulator is obtained by careful design of the structural or gas spring.

Considering the accumulator designs shown in Figure 43, it is seen that only the piston accumulator with bellows (Figure 43c) is applicable to a cryogenic propellant. However, because of the relatively large volume of the side-branch cavity, this device has potential LO_2 vaporization problems and displays an undesirable large inertance (fluid mass). Also, the design of the

V,B,1,c, Conventional "Pogo" Fix Concepts (cont.)

spring/piston support should be improved to eliminate any tilting of the piston.

The gas-spring devices shown in Figure 43 are quite well suited to storable propellants. In particular, the bladder accumulator has been used successfully on the Titan LIIB fuel system. Note that this device displays a toroidal configuration which minimizes the liquid inertance. The most difficult design problem in the development of a bladder accumulator is the selection of a plastic or elastomeric bladder material with the necessary compatibility, strength and porosity requirements.

The distributed parameter "Pogo" fix devices illustrated in Figure 44 are intended to lower the effective acoustic velocity in the suction line, thus reducing the feed system resonant frequencies. This effect is achieved by adding a large, distributed compliance by the addition of a compressible gas, which is either contained in a flexible bladder or injected directly into the liquid. Also, these concepts cause an attenuation of acoustic waves traveling through the line. This energy dissipation ("lossy") effect is caused by the damped nature of the resonators which are distributed along the length of the line.

2. Sandwich Accumulator

The sandwich accumulator design is illustrated in Figures 45a, 45b, and 45c. It is composed of two rectangular sandwich skins which are connected at the edges by a peripheral bellows to allow relative translation. The primary source of compliance is a network of distributed internal elastic elements, which are simply convoluted spring steel sheets located between the sandwich skins. Details of these elastic elements and the structural support of the sandwich device are shown in Figure 45b. Note that the end support provides axial restraint, by benefit of a pin inserted in the milled slot provided in the propellant suction line flange. Lateral support is provided by semi-circular retaining spring, as shown in Figure 45c.

The sandwich accumulator is proposed as a lumped parameter compliant device which could be installed in the suction line with the minimum

V,B,2, Sandwich Accumulator (cont.)

schedule impact. This device is also well suited to the satisfaction of the other design criteria. It has better hydrodynamic efficiency than a conventional side-branch accumulator because of its low-drag shape and position along the center of the line.

When used in the cryogenic oxidizer it is superior to any of the side-branch accumulators because of the absence of any accumulator cavity which could trap LO_2 and create gas/vapor bubbles.

The structural design of sandwich accumulator is easily accomplished with the use of the design curves provided in Figure 46. These curves present the results of a parametric structural analysis for the purpose of sizing the necessary sandwich initial depth and wall thickness to achieve a specified accumulator capacitance. The structural analysis, which utilized energy methods and the theory of plates and shells, allows the prediction of the structural capacitance per unit surface area and the maximum stress in the elastic element for a given configuration. Note that both curves must be used in a complementary fashion; first to estimate the wall thickness for a given compliance, and then to determine the resulting maximum flexural stress corresponding to P_{max} .

The total capacitance of the sandwich accumulator is equal to the sum of the structural capacitance caused by the internal elastic elements and the gas capacitance caused by the gas which is trapped in the sealed accumulator. This gas compliance may be predicted by assuming the gas behaves as a perfect gas undergoing an isothermal compression/expansion process. Thus the accumulator gas volume, \bar{V}_a , is related to the applied pressure, \bar{P}_a , by the well known expression

$$\bar{V}_a = K(\bar{P}_a)^{-1} \quad (36)$$

where K is a constant. The isothermal gas capacitance, C_g , is found from this relationship

$$C_g = -\frac{\partial \bar{V}_a}{\partial \bar{P}_a} = \frac{K}{\bar{P}_a^2} = \frac{\bar{P}_0 \bar{V}_0}{\bar{P}_a^2} \quad (37)$$

V,B,2, Sandwich Accumulator (cont.)

where \bar{P}_0 and \bar{V}_0 are the original or "charge" pressure and volume, respectively. The validity of this expression for the prediction of the gas spring compliance has been experimentally verified (Ref 4). For the sandwich accumulator the capacitance per unit surface is simply

$$\frac{C_g}{A} = \frac{\bar{P}_0}{\bar{P}_a^2} d_0 \quad (38)$$

where d_0 is the original depth of the sandwich.

It may be shown by use of eq (38) that, for the range of Saturn operating pressures (40 to 100 psia) and an atmospheric original pressure (\bar{P}_0), the gas capacitance is on the same order as the structural capacitance. However, because of the difficulty of controlling this gas spring in a cryogenic environment, it is recommended that the gas capacitance be reduced until it is much smaller than the structural capacitance. This may be accomplished by creating a vacuum in the internal cavity of the sandwich accumulator, in order to reduce the magnitude of \bar{P}_0 in eq (38).

3. Trombone Accumulator

The trombone accumulator design, as shown in Figure 47, is intended for use in the discharge line as a lumped parameter compliant device. This device is comprised of a system of bellows connected to a ringed piston which is supported by an axial spring. The design of this spring is very critical because it must be compliant enough to suppress the discharge pressure oscillations but yet be stiff enough to limit the axial excursion due to the high operating pressures. Because of these conflicting requirements, the use of either a linear spring with pre-load or a spring with a "softening" type nonlinearity is suggested. In Figure 48, the curves of spring excursion versus operating pressure illustrate the reduction in excursion available with these springs. The use of a linear helical spring with a preload provided by a restraining liner appears to be the simplest method to limit excursion. A more difficult approach is to use either Belleville conical disk springs or a buckling-type elastomeric spring to achieve the softening type nonlinearity.

V,B,3, Trombone Accumulator (cont.)

In summary, it is seen that the trombone accumulator design is much more complex and more difficult to install than the sandwich accumulator. It must be made stronger than the sandwich device because of the severe operating environment it is subjected to. Furthermore, the contradictory requirements of a soft spring rate and minimum excursion requires the use of a nonlinear spring. Therefore the design, fabrication, and installation of the trombone discharge accumulator is much more difficult than that of the sandwich suction accumulator.

4. Lossy Line

The design of a lossy line for a cryogenic propellant was not emphasized in this study because of the serious schedule impact that a complete redesign of the suction lines would have on the Saturn program. Obviously, a configuration similar to that shown in Figure 44a would require a massive redesign and development effort. Therefore it is desirable to design the lossy line in the form of segmented "inserts" which can be inserted in the existing suction line sections, in a similar manner to the sandwich accumulator. The sandwich accumulator could be adapted to a lossy line by redesigning the internal elastic elements so that they would dissipate energy as they are subjected to flexural vibration. Energy dissipation might be achieved by using a laminated construction for the elastic elements with viscoelastic shear layers. This method of construction has been used by vibration isolator designers to obtain greater damping in electronic equipment structures (Ref 5). However, since the viscoelastic damping material is not suitable for cryogenic temperatures, a method of providing thermal insulation between the elastic elements and sandwich skin would be required.

V, Discussion, Part II (cont.)

C. DETERMINATION OF FIX DEVICE TESTS

1. Static Tests

The objective of this task is to determine the test facility and instrumentation requirements for meaningful component tests of the candidate "Pogo" fix devices. These component tests may be classified as either (1) static tests or (2) dynamic tests. The methods to be used in the static test will be discussed in this section.

Since both the sandwich accumulator and trombone accumulator are simple compliant devices, the most meaningful static test is one that measures the acoustical compliance (capacitance) of the device. In other words, the fluid volume versus pressure relationship must be experimentally determined. This measurement is quite simple with the apparatus shown in Figure 49. The apparatus consists of a pressure source, water-filled accumulator, calibrated cylinder, and pressure and water level measuring devices.

The procedure for the accumulator compliance test is as follows:

- 1) Install accumulator in adaptor
- 2) Fill with water to top calibration in cylinder
- 3) Open valve until pressure increases by
- 4) Close valve and measure
- 5) Repeat Steps 3 and 4 until entire pressure operating range is covered
- 6) Reduce pressure by repeating all previous steps in reverse order.

By plotting ΔV versus ΔP , the compliance of the device may be estimated from the slope of the curve. Typical plots are sketched in Figure 48.

2. Dynamic Tests

A dynamic test is useful to measure the damping characteristics of the accumulator. As shown in Figure 50, the damping of the accumulator,